Nanomaterials and Supramolecular Structures

Anatoliy Petrovych Shpak · Petr Petrovych Gorbyk
Editors

Nanomaterials and Supramolecular Structures

Physics, Chemistry, and Applications

Springer

Editors
Prof. Anatoliy Petrovych Shpak
National Academy of Sciences of Ukraine
G.V. Kurdiumov Inst. Metal Physics
Blvd. Akademika
Vernadskogo, 36
Kiev 03680
Ukraine
metall@imp.kiev.ua

Prof. Petr Petrovych Gorbyk
National Academy of Sciences of Ukraine
A. A. Chuiko Inst. Surface Chemistry
General Naumov St., 17
Kiev 03164
Ukraine
petr_gorbik@isc.gov.ua

ISBN 978-90-481-2308-7 e-ISBN 978-90-481-2309-4
DOI 10.1007/978-90-481-2309-4
Springer Dordrecht Heidelberg London New York

Library of Congress Control Number: 2009926979

Preface

The book contains scientific articles dealing with problems in physics, chemistry, and application of nanomaterials and supramolecular structures. It focuses on experimental investigations using a variety of modern methods and theoretical modeling of surface structures and physicochemical processes occurring at solid surfaces based on analytical approaches and computational methods. Special attention is focused on biomedical nanocomposites based on nanosilica and magnetite and their interactions with components of biosystems, as well as self-organizing of water–organic systems in nanopores of adsorbents, cells, and tissues; and immobilization of biopolymers, drugs, antioxidants at a surface of nanomaterials without the loss of their native properties. Techniques of chemical modification of nanomaterials and mesoporous nanostructured films, synthesis and studies of physicochemical properties of photo-active nanomaterials, nanotubes, and other materials are described. The results of investigations of supramolecular structures with biomolecules bound to a surface of highly disperse silica are generalized.

The first part describes theoretical investigations of physicochemical processes occurring at a surface. A problem of interaction of electromagnetic radiation with surface excitations of a small particle ensemble at a solid surface was solved using the electrostatic approximation. The structural and total potentials of interaction of two quartz crystals separated by a nanosized gap were derived using Green functions with nonlocal Poisson's equation. Conditions of initializing of ordered motion of nanoparticles along a surface under the effect of external fluctuations of different nature were described, as well as examples of highly efficient Brownian and molecular motors, photo-induced molecular and dipole rotators, whose unidirectional rotation was accomplished by linearly polarized AC field. The mechanism of laser desorption/ionization of ionic dyes interacting with chemically modified surface of porous silicon was suggested.

The second part deals with studies of interactions of nanomaterials with components of biosystems, development of new medicines based on nanosilica, their application efficiency, chemical engineering of multilevel magnetosensitive nanocomposites with a hierarchical architecture, and functions of biomedical nanorobots. The process of hydration of bone tissue and products of its thermal and chemical dehydration were analyzed with the help of low-temperature NMR spectroscopy and cryoporometry.Regularities in the behavior of nanomaterials interacting with

bioobjects in different media were analyzed considering surface structures and morphology of solid nanoparticles.

The third part is devoted to the problem of geometrical, chemical, and adsorption modification of nanomaterials. Chemical design of carbon coating of nanoparticles of fumed alumina and thin films of silicium, titanium, and zinc oxides doped with Au and Ag nanoparticles is reported. It was shown that catalytic activity of these films in photooxidation of dyes correlates with an increase of specific surface area and acidity and depends strongly on the effectiveness of photogenerated charge carrier separation. The influence of conditions of template synthesis on structural and adsorption characteristics of ordered mesoporous silica comprising spherical microparticles was analyzed. Application of silica matrices in synthesis of carbon nanotubes for obtaining gold and silver nanoparticles by reducing the metal ions from solutions was described. The processes of synthesis of magnetosensitive nanocomposites based on nanocrystalline Fe_3O_4 or γ-$Fe_2O_3$and highly dispersed silicon dioxide were studied. It was shown that silica matrix stabilizes the size of Fe_3O_4 nanocrystallites at 5–8 nm. An effective and ecologically safe technique of adsorption modification of nanosilica by nonvolatile organic compounds was developed which allows production of the required coatings of the nanoparticles practically without the loss of the nanosilica dispersion properties. Functionalized mesoporous silica was synthesized; the structure of its surface and adsorptive properties were analyzed. It was shown that silylated nanosilica could be effective in formation of fibers of polypropylene–copolyamide blends. Hollow spherical silica and magnetite particles were synthesized and investigated. Conditions and growth features of Si and ZnO nanowhiskers at a surface of single-crystal silicon plates were studied for the vapor–fluid–crystal mechanism. Quantum-dimensional effects in multilayer epitaxial Si–Ge heterostructures were described. A technique of synthesis of metal oxide nanoparticles incorporated into a silica matrix was developed comprising chemical modification of the silica surface by acetyl acetonate Ce. Sol–gel synthesis of quartz glasses and optical composites containing the metal oxide nanoparticles was proposed.

The fourth part deals with supramolecular structures. Reactive sites for adsorption of Hg(II) were designed at the nanosilica surface using chemically attached β-cyclodextrin molecules. Formation of inclusion complexes between β-cyclodextrin and nitrate ions at the ratio 1:1 and supramolecules of the composition $C_{42}H_{70}O_{34}\cdot 4Hg(NO_3)_2$was proven. Interaction of such polymer as chitosan with nanosilica surface was investigated in order to develop a method of estimation of quantities of adsorbed chitosan segments directly interacting with the surface and free segments on the basis of the desorption mass spectrometry data. Dependence of hemolysis degree of red blood cells on the quantity of the free segments of adsorbed chitosan was revealed. A new supramolecular antioxidant composed of C and E vitamins and silylated nanosilica was prepared and studied. Regularities of adsorption interaction of supramolecular complexes of flavonoids with nanosilica were studied as functions of the chemical nature of the surface, biomacromolecules, and the solution characteristics. Adsorption of bilirubin and bile salts from the individual and mixed aqueous solutions onto a hydrophobic surface of modified silica was studied.

The supramolecular structures formed by blood plasma proteins with nanoparticles of highly disperse silica were analyzed as well as the behavior of water confined in these systems.

The fifth part describes new techniques for creation of nanotubes and nanoconductors with different materials, synthesis of carbon nanotubes and polymers filled by these materials, as well as new nanocomposites based on graphite and polymers and used as gas sensors, films, and disperse materials based on diamond-like carbons and related materials.

In conclusion, the editors express their gratitude to authors of the articles for given materials, creative cooperation, fruitful discussion of this book, and valuable advices. They offer special thanks to Usov D.G., Turelyk M.P., and Tsendra O.M. for assistance in creation of the book.

This book is intended for students, advanced undergraduates, and specialists in nanophysics and nanochemistry, chemistry and physics of surfaces, physical chemistry, biochemistry, bioengineering, polymer and material science, pharmaceutical chemistry, and chemical engineering.

Ukraine A.P. Shpak
P.P. Gorbyk

Contents

Contributors

M.V. Abramov O.O. Chuiko Institute of Surface Chemistry of the National Academy of Sciences of Ukraine, General Naumov St. 17, Kyiv 03164, Ukraine

S.A. Alekseev Chemistry Department, Kiev National Taras Shevchenko University, 60 Vladimirskaya St., Kiev 01033, Ukraine

T.A. Aleksyeyeva O.O. Chuiko Institute of Surface Chemistry of the National Academy of Sciences of Ukraine, General Naumov St. 17, Kyiv 03164, Ukraine

I.V. Babich O.O. Chuiko Institute of Surface Chemistry of the National Academy of Sciences of Ukraine, General Naumov St. 17, Kyiv 03164, Ukraine

D. Barbier Lyon Institute of Nanotechnologies, INL, CNRS UMR-5270, INSA de Lyon, 7 avenue Jean Capelle, Bat. Blaise Pascal, 69621 Villeurbanne cedex, France

V.M. Barvinchenko O.O. Chuiko Institute of Surface Chemistry of the National Academy of Sciences of Ukraine, General Naumov St. 17, Kyiv 03164, Ukraine

L.A. Belyakova O.O. Chuiko Institute of Surface Chemistry of the National Academy of Sciences of Ukraine, General Naumov St. 17, Kyiv 03164, Ukraine
e-mail: isc412@ukr.net

I.S. Berezovska O.O. Chuiko Institute of Surface Chemistry of the National Academy of Sciences of Ukraine, General Naumov St. 17, Kyiv 03164, Ukraine

J.P. Blitz Eastern Illinois University, Department of Chemistry, Charleston, IL 61920, USA

V.M. Bogatyrev O.O. Chuiko Institute of Surface Chemistry of the National Academy of Sciences of Ukraine, General Naumov St. 17, Kyiv 03164, Ukraine

A.A. Boiko Gomel State Technical University, Prospekt Oktyabrya 48, Gomel 246746, Belarus

T.V. Borodavka O.O. Chuiko Institute of Surface Chemistry of the National Academy of Sciences of Ukraine, General Naumov St. 17, Kyiv 03164, Ukraine

M.V. Borysenko O.O. Chuiko Institute of Surface Chemistry of the National Academy of Sciences of Ukraine, General Naumov St. 17, Kyiv 03164, Ukraine
e-mail: borysenko@naverex.kiev.ua

V.F. Chekhun R.E. Kavetsky Institute of Experimental Pathology, Oncology, and Radiobiology of the NAS of Ukraine, Vasilkovskaya St., 45, Kyiv 03022, Ukraine

O.O. Chuiko O.O. Chuiko Institute of Surface Chemistry of the National Academy of Sciences of Ukraine, General Naumov St. 17, Kyiv 03164, Ukraine

A.A. Dadykin Institute of Physics, NAS of Ukraine, 46 Nauki Avenue, Kyiv 03164, Ukraine

Yu.A. Demchenko O.O. Chuiko Institute of Surface Chemistry of the National Academy of Sciences of Ukraine, General Naumov St. 17, Kyiv 03164, Ukraine

A.O. Dobrodey Gomel State Technical University, Prospekt Oktyabrya 48, Gomel 246746, Belarus

I.V. Dubrovin O.O. Chuiko Institute of Surface Chemistry of the National Academy of Sciences of Ukraine, General Naumov St. 17, Kyiv 03164, Ukraine

L.S. Dzyubenko O.O. Chuiko Institute of Surface Chemistry of the National Academy of Sciences of Ukraine, General Naumov St. 17, Kyiv 03164, Ukraine
e-mail: dzyubenko@i.ua

A.M. Eremenko O.O. Chuiko Institute of Surface Chemistry of the National Academy of Sciences of Ukraine, General Naumov St. 17, Kyiv 03164, Ukraine

T.V. Fedyanina O.O. Chuiko Institute of Surface Chemistry of the National Academy of Sciences of Ukraine, General Naumov St. 17, Kyiv 03164, Ukraine

S. Field Teer Coatings Ltd., Kidderminster, UK

S. FitzGerald Jobin Yvon Ltd., 2 Dalston Gardens, Stanmore, Middlesex HA7 1BQ, UK

F. Fucassi University of Brighton, Brighton BN2 4GJ, UK

O.L. Gabchak O.O. Chuiko Institute of Surface Chemistry of the National Academy of Sciences of Ukraine, General Naumov St. 17, Kyiv 03164, Ukraine

M.V. Galaburda O.O. Chuiko Institute of Surface Chemistry of the National Academy of Sciences of Ukraine, General Naumov St. 17, Kyiv 03164, Ukraine

N.P. Galagan O.O. Chuiko Institute of Surface Chemistry of the National Academy of Sciences of Ukraine, General Naumov St. 17, Kyiv 03164, Ukraine

I.I. Gerashchenko O.O. Chuiko Institute of Surface Chemistry of the National Academy of Sciences of Ukraine, General Naumov St. 17, Kyiv 03164, Ukraine

Yu.I. Gnatyuk O.O. Chuiko Institute of Surface Chemistry of the National Academy of Sciences of Ukraine, General Naumov St. 17, Kyiv 03164, Ukraine

A.P. Golovan O.O. Chuiko Institute of Surface Chemistry of the National Academy of Sciences of Ukraine, General Naumov St. 17, Kyiv 03164, Ukraine

L.P. Golovkova O.O. Chuiko Institute of Surface Chemistry of the National Academy of Sciences of Ukraine, General Naumov St. 17, Kyiv 03164, Ukraine

E.V. Goncharuk O.O. Chuiko Institute of Surface Chemistry of the National Academy of Sciences of Ukraine, General Naumov St. 17, Kyiv 03164, Ukraine

P.P. Gorbyk O.O. Chuiko Institute of Surface Chemistry of the National Academy of Sciences of Ukraine, General Naumov St. 17, Kyiv 03164, Ukraine e-mail: gorbyk_petro@isc.gov.ua; pgorbyk@mail.ru

L.G. Grechko O.O. Chuiko Institute of Surface Chemistry of the National Academy of Sciences of Ukraine, General Naumov St. 17, Kyiv 03164, Ukraine e-mail: lgrechko09@rambler.ru

E.Yu. Grischuk O.O. Chuiko Institute of Surface Chemistry of the National Academy of Sciences of Ukraine, General Naumov St. 17, Kyiv 03164, Ukraine e-mail: elenayug85@rambler.ru

V.M. Gun'ko O.O. Chuiko Institute of Surface Chemistry of the National Academy of Sciences of Ukraine, General Naumov St. 17, Kyiv 03164, Ukraine e-mail: gun@voliacable.com

N.V. Guzenko O.O. Chuiko Institute of Surface Chemistry of the National Academy of Sciences of Ukraine, General Naumov St. 17, Kyiv 03164, Ukraine

C. Hofer Institute of Physics, Montanuniversitaet Leoben, Franz Josef Str. 18, Leoben A-8700, Austria

A.V. Il'chenko O.O. Chuiko Institute of Surface Chemistry of the National Academy of Sciences of Ukraine, General Naumov St. 17, Kyiv, 03164, Ukraine

L.G. Il'chenko O.O. Chuiko Institute of Surface Chemistry of the National Academy of Sciences of Ukraine, General Naumov St. 17, Kyiv, 03164, Ukraine

V.V. Il'chenko National Taras Shevchenko University of Kyiv, the Faculty of Radiophysics, 64, Volodymyrska St, Kyiv 01033, Ukraine

M. Jablonski Department of Orthopaedics and Rehabilitation, Medical University, Lublin 20-094, Poland

V.O. Kandyba G.V. Kurdyumov Institute of Metallophysics of the National Academy of Sciences of Ukraine, Acad. Vernadsky blvd. 36, Kyiv 03680, Ukraine

M.T. Kartel O.O. Chuiko Institute of Surface Chemistry of the National Academy of Sciences of Ukraine, General Naumov St. 17, Kyiv 03164, Ukraine e-mail: nikar@ kartel.kiev.ua

V.A. Kaspersky O.O. Chuiko Institute of Surface Chemistry of the National Academy of Sciences of Ukraine, General Naumov St. 17, Kyiv 03164, Ukraine

K.V. Katok O.O. Chuiko Institute of Surface Chemistry of the National Academy of Sciences of Ukraine, General Naumov St. 17, Kyiv 03164, Ukraine

O.A. Kazakova O.O. Chuiko Institute of Surface Chemistry of the National Academy of Sciences of Ukraine, General Naumov St. 17, Kyiv 03164, Ukraine

S.V. Kondratenko Kiev National Taras Shevchenko University, Physics Department, 2 Acad. Glushkov Ave, Kiev 03022, Ukraine

O.M. Korduban G.V. Kurdiumov Institute of Metal Physics of the NAS of Ukraine, Bulvar Akademika Vernadskogo, 36, Kyiv 03680, Ukraine

N.I. Kovtyukhova Department of Chemistry, The Pennsylvania State University, University Park, PA 16802, USA; O.O. Chuiko Institute of Surface Chemistry of the National Academy of Sciences of Ukraine, General Naumov St. 17, Kyiv 03164, Ukraine e-mail: nina@chem.psu.edu

Yu.N. Kozyrev O.O. Chuiko Institute of Surface Chemistry of the National Academy of Sciences of Ukraine, General Naumov St. 17, Kyiv 03164, Ukraine e-mail: kozyrev@iop.kiev.ua

Ya.I. Kruchek O.O. Chuiko Institute of Surface Chemistry of the National Academy of Sciences of Ukraine, General Naumov St. 17, Kyiv 03164, Ukraine

K.S. Kulyk O.O. Chuiko Institute of Surface Chemistry of the National Academy of Sciences of Ukraine, General Naumov St. 17, Kyiv 03164, Ukraine

T.V. Kulyk O.O. Chuiko Institute of Surface Chemistry of the National Academy of Sciences of Ukraine, General Naumov St. 17, Kyiv 03164, Ukraine e-mail: tanyakulyk@gala.net

O.I. Kutel'makh O.O. Chuiko Institute of Surface Chemistry of the National Academy of Sciences of Ukraine, General Naumov St. 17, Kyiv 03164, Ukraine

P.O. Kuzema O.O. Chuiko Institute of Surface Chemistry of the National Academy of Sciences of Ukraine, General Naumov St. 17, Kyiv 03164, Ukraine

I.V. Laguta O.O. Chuiko Institute of Surface Chemistry of the National Academy of Sciences of Ukraine, General Naumov St. 17, Kyiv 03164, Ukraine e-mail: laguta@i.com.ua

O.Yu. Lavrynenko Chemistry Department, Kiev National Taras Shevchenko University, 60 Vladimirskaya St., Kiev 01033, Ukraine

R. Leboda Faculty of Chemistry, Maria Curie-Sklodowska University, Lublin 20-031, Poland

L.B. Lerman O.O. Chuiko Institute of Surface Chemistry of the National Academy of Sciences of Ukraine, General Naumov St. 17, Kyiv 03164, Ukraine

N.O. Lipkovska O.O. Chuiko Institute of Surface Chemistry of the National Academy of Sciences of Ukraine, General Naumov St. 17, Kyiv 03164, Ukraine
e-mail: lipkovska@ukr.net

V.V. Lobanov O.O. Chuiko Institute of Surface Chemistry of the National Academy of Sciences of Ukraine, General Naumov St. 17, Kyiv 03164, Ukraine
e-mail: isc-sec@isc.gov.ua

N.Yu. Lukyanova R.E. Kavetsky Institute of Experimental Pathology, Oncology, and Radiobiology of the NAS of Ukraine, Vasilkovskaya St., 45, Kyiv 03022, Ukraine

N.B. Lutsyuk O.O. Chuiko Institute of Surface Chemistry of the National Academy of Sciences of Ukraine, General Naumov St. 17, Kyiv 03164, Ukraine

D.Yu. Lyashenko O.O. Chuiko Institute of Surface Chemistry of the National Academy of Sciences of Ukraine, General Naumov St. 17, Kyiv 03164, Ukraine

M. Makkee DelfChemTech, Delft University of Techology, Julianalaan 136, 2628 BL Delft, The Netherlands

E.V. Manuilov O.O. Chuiko Institute of Surface Chemistry of the National Academy of Sciences of Ukraine, General Naumov St. 17, Kyiv 03164, Ukraine

A.V. Melezhik O.O. Chuiko Institute of Surface Chemistry of the National Academy of Sciences of Ukraine, General Naumov St. 17, Kyiv 03164, Ukraine

L.I. Mikhalovska University of Brighton, Brighton BN2 4GJ, UK

S.V. Mikhalovsky University of Brighton, Brighton BN2 4GJ, UK

J.A. Moulijn DelfChemTech, Delft University of Techology, Julianalaan 136, 2628 BL Delft, The Netherlands

A.G. Naumovets Institute of Physics of the National Academy of Sciences of Ukraine, 46 Prospect Nauki, Kiev 03028, Ukraine

O.V. Nechypor O.O. Chuiko Institute of Surface Chemistry of the National Academy of Sciences of Ukraine, General Naumov St. 17, Kyiv 03164, Ukraine

L.V. Nosach O.O. Chuiko Institute of Surface Chemistry of the National Academy of Sciences of Ukraine, General Naumov St. 17, Kyiv 03164, Ukraine

Y.M. Nychiporuk O.O. Chuiko Institute of Surface Chemistry of the National Academy of Sciences of Ukraine, General Naumov St. 17, Kyiv 03164, Ukraine

E.M. Pakhlov O.O. Chuiko Institute of Surface Chemistry of the National Academy of Sciences of Ukraine, General Naumov St. 17, Kyiv 03164, Ukraine

B.B. Palyanytsya O.O. Chuiko Institute of Surface Chemistry of the National Academy of Sciences of Ukraine, General Naumov St. 17, Kyiv 03164, Ukraine

A.A. Pentyuk O.O. Chuiko Institute of Surface Chemistry of the National Academy of Sciences of Ukraine, General Naumov St. 17, Kyiv 03164, Ukraine

A.L. Petranovska O.O. Chuiko Institute of Surface Chemistry of the National Academy of Sciences of Ukraine, General Naumov St. 17, Kyiv 03164, Ukraine

P. Pissis Department of Physics, National Technical University of Athens, Athens 15780, Greece

I.V. Plyuto Institute of Metal Physics, National Academy of Sciences of Ukraine, Vernadsky Blvd. 36, Kiev 03142, Ukraine

Y.V. Plyuto O.O. Chuiko Institute of Surface Chemistry of the National Academy of Sciences of Ukraine, General Naumov St. 17, Kyiv 03164, Ukraine

E.N. Poddenezhny Gomel State Technical University, Prospekt Oktyabrya 48, Gomel 246746, Belarus

V.K. Pogorelyi O.O. Chuiko Institute of Surface Chemistry of the National Academy of Sciences of Ukraine, General Naumov St. 17, Kyiv 03164, Ukraine

V.A. Pokrovskiy O.O. Chuiko Institute of Surface Chemistry of the National Academy of Sciences of Ukraine, General Naumov St. 17, Kyiv 03164, Ukraine

G.P. Prikhod'ko O.O. Chuiko Institute of Surface Chemistry of the National Academy of Sciences of Ukraine, General Naumov St. 17, Kyiv 03164, Ukraine

N.M. Rezanova Kiev National University of Technologies and Design, 2 Nemirovich-Danchenko Street, Kiev 01011, Ukraine

V. M. Rozenbaum O.O. Chuiko Institute of Surface Chemistry of the National Academy of Sciences of Ukraine, General Naumov St. 17, Kyiv 03164, Ukraine
e-mail: vrozen@mail.kar.net

M.Yu. Rubezhanska O.O. Chuiko Institute of Surface Chemistry of the National Academy of Sciences of Ukraine, General Naumov St. 17, Kyiv 03164, Ukraine

A.A. Rugal O.O. Chuiko Institute of Surface Chemistry of the National Academy of Sciences of Ukraine, General Naumov St. 17, Kyiv 03164, Ukraine

A.A. Sapyanenko O.O. Chuiko Institute of Surface Chemistry of the National Academy of Sciences of Ukraine, General Naumov St. 17, Kyiv 03164, Ukraine

Yu.I. Sementsov O.O. Chuiko Institute of Surface Chemistry of the National Academy of Sciences of Ukraine, General Naumov St. 17, Kyiv 03164, Ukraine

T.V. Semikina O.O. Chuiko Institute of Surface Chemistry of the National Academy of Sciences of Ukraine, General Naumov St. 17, Kyiv 03164, Ukraine

L.S. Semko O.O. Chuiko Institute of Surface Chemistry of the National Academy of Sciences of Ukraine, General Naumov St. 17, Kyiv 03164, Ukraine

O.V. Severinovskaya O.O. Chuiko Institute of Surface Chemistry of the National Academy of Sciences of Ukraine, General Naumov St. 17, Kyiv 03164, Ukraine

L.F. Sharanda O.O. Chuiko Institute of Surface Chemistry of the National Academy of Sciences of Ukraine, General Naumov St. 17, Kyiv 03164, Ukraine
e-mail: lyusharanda@yahoo.com

I.V. Shmigol O.O. Chuiko Institute of Surface Chemistry of the National Academy of Sciences of Ukraine, General Naumov St. 17, Kyiv 03164, Ukraine
e-mail: ivshmigol@ukr.net

A.P. Shpak O.O. Chuiko Institute of Surface Chemistry of the National Academy of Sciences of Ukraine, General Naumov St. 17, Kyiv 03164, Ukraine

E.I. Shtat'ko O.O. Chuiko Institute of Surface Chemistry of the National Academy of Sciences of Ukraine, General Naumov St. 17, Kyiv 03164, Ukraine

O.M.Shvets O.O. Chuiko Institute of Surface Chemistry of the National Academy of Sciences of Ukraine, General Naumov St. 17, Kyiv 03164, Ukraine

V.K. Sklyar O.O. Chuiko Institute of Surface Chemistry of the National Academy of Sciences of Ukraine, General Naumov St. 17, Kyiv 03164, Ukraine

J. Skubiszewska-Zieba Faculty of Chemistry, Maria Curie-Skłodowska University, Lublin 20-031, Poland

N.P. Smirnova O.O. Chuiko Institute of Surface Chemistry of the National Academy of Sciences of Ukraine, General Naumov St. 17, Kyiv 03164, Ukraine
e-mail: smirnat@i.com.ua

O.N. Stavinskaya O.O. Chuiko Institute of Surface Chemistry of the National Academy of Sciences of Ukraine, General Naumov St. 17, Kyiv 03164, Ukraine

J. Stoch Institute of Catalysis and Surface Chemistry, Polish Academy of Sciences, ul. Niezapominajek, Kracow 30239, Poland

L.P. Storozhuk O.O. Chuiko Institute of Surface Chemistry of the National Academy of Sciences of Ukraine, General Naumov St. 17, Kyiv 03164, Ukraine

D.G. Teer Teer Coatings Ltd., Kidderminster, UK

C. Teichert Institute of Physics, Montanuniversitaet Leoben, Franz Josef Str. 18, Leoben A-8700, Austria

V.A. Tertykh O.O. Chuiko Institute of Surface Chemistry of the National Academy of Sciences of Ukraine, General Naumov St. 17, Kyiv 03164, Ukraine
e-mail: tertykh@public.ua.net

P. Tomlins Materials Centre, National Physical Laboratory, Teddington, Middlesex TW11 0LW, UK

I.A. Tsebrenko Kiev National University of Technologies and Design, 2 Nemirovich-Danchenko Street, Kiev 01011, Ukraine

M.V. Tsebrenko Kiev National University of Technologies and Design, 2 Nemirovich-Danchenko Street, Kiev 01011, Ukraine e-mail: mfibers@i.com.ua

S.P. Turanska O.O. Chuiko Institute of Surface Chemistry of the National Academy of Sciences of Ukraine, General Naumov St. 17, Kyiv 03164, Ukraine

M.P. Turelyk O.O. Chuiko Institute of Surface Chemistry of the National Academy of Sciences of Ukraine, General Naumov St. 17, Kyiv 03164, Ukraine

A.V. Turov Taras Shevchenko University, Kiev 01030, Ukraine

V.V. Turov O.O. Chuiko Institute of Surface Chemistry of the National Academy of Sciences of Ukraine, General Naumov St. 17, Kyiv 03164, Ukraine e-mail: v_turov@ukr.net

A.A. Turova O.O. Chuiko Institute of Surface Chemistry of the National Academy of Sciences of Ukraine, General Naumov St. 17, Kyiv 03164, Ukraine

D.G. Usov O.O. Chuiko Institute of Surface Chemistry of the National Academy of Sciences of Ukraine, General Naumov St. 17, Kyiv 03164, Ukraine

O.V. Vakulenko Kiev National Taras Shevchenko University, Physics Department, 2 Acad. Glushkov Ave, Kiev 03022, Ukraine

Y.P. Verbilovsky O.O. Chuiko Institute of Surface Chemistry of the National Academy of Sciences of Ukraine, General Naumov St. 17, Kyiv 03164, Ukraine

A.A. Vil'tsanyuk O.O. Chuiko Institute of Surface Chemistry of the National Academy of Sciences of Ukraine, General Naumov St. 17, Kyiv 03164, Ukraine

N.N. Vlasova O.O. Chuiko Institute of Surface Chemistry of the National Academy of Sciences of Ukraine, General Naumov St. 17, Kyiv 03164, Ukraine e-mail: vlabars@i.com.ua; vlasova@uni-mainz.de

E.F. Voronin O.O. Chuiko Institute of Surface Chemistry of the National Academy of Sciences of Ukraine, General Naumov St. 17, Kyiv 03164, Ukraine e-mail: e.voronin@rambler.ru

V.V. Yanishpolskii O.O. Chuiko Institute of Surface Chemistry of the National Academy of Sciences of Ukraine, General Naumov St. 17, Kyiv 03164, Ukraine

V.N. Zaitsev Chemistry Department, Kiev National Taras Shevchenko University, 60 Vladimirskaya St., Kiev 01033, Ukraine

V.I. Zarko O.O. Chuiko Institute of Surface Chemistry of the National Academy of Sciences of Ukraine, General Naumov St. 17, Kyiv 03164, Ukraine

Y.L. Zub O.O. Chuiko Institute of Surface Chemistry of the National Academy of Sciences of Ukraine, General Naumov St. 17, Kyiv 03164, Ukraine e-mail: zub_yuriy@isc.gov.ua

Part I
Modeling of Physico-chemical Processes with Participating Surface

The breakdown of regular three-dimensional framework of an ideal crystal is accompanied by radical changes in distribution of electron density, electrostatic potential, and formation of its limiting surface. Such macroscopic violation of crystal periodic structure leads to changes in atoms' interaction character, their surface valent orbitals' hybridization and localization of uncompensated charges, originating of new electron states and unsaturated valencies. Moreover in real crystals, accumulation of point (vacant lattice sites, interstitial atoms) and lengthy (growth steps, dislocations, flaws, pores) defects result from impurities and structural disorder. The impossibility of an abrupt transition from the ordered state to the disordered one causes existence of an amorphous near-surface interlayer for crystalline substances. Valence-saturated surface atoms are chemically active centers, and interaction of adsorbed molecules with them may cause formation of functional coverage, for example, with hydroxyl groups. The data obtained testifies to surface being a complicated object, experimental studies and numerical modeling of which provide only an approximate and average pattern of its structure.

This part focuses on modeling physico-chemical processes with surface participation. The urgency of the question is caused, in particular, by search for efficient methods for obtaining coatings with desired electrodynamic characteristics. So, multipole interaction of nanoparticles allocated closely to a phase boundary surface occurs among themselves and with the boundary surface and originates from polarization effects upon electromagnetic irradiation of the system. This process is especially strongly displayed in spectra of optical adsorption and scattering. The indicated interactions are sensitive to shape and size of the nanoparticles and play an important role in self-organization of nano- and supramolecular structures of inorganic, organic, and biological nature.

The surface effects play a very important role in the systems of nanoparticles interacting among themselves and with the environment. Identification of the basic laws for such interactions of particles of various chemical natures (dielectrics, conductors, metals) is important for theoretical justification of creation of new types of ultradisperse materials for technical and medico-biological applications. The nonlocal electrostatics approximation provides a tool for examination of interactions

at distances big enough to exclude overlapping of surface atoms of approaching particles.

Studies of directed transport of nanoparticles along surfaces carrying an orientation-ordered monolayer of polar atom groups are extremely important from both the scientific and the practical points of view. The mechanism of its formation is described by the model of potential energy fluctuation. The processes of mass transport against the concentration gradient in a non-equilibrium spatially asymmetric system can be traced using this model. Such phenomena occur in biological membranes. The results of their studies may be used in nanobiotechnologies.

The usage of nanoporous silica as a universal ionization substrate in the method of mass-spectrometry with laser-assisted desorption and ionization is an example of successful practical realization of theoretical approaches to and model concepts built on their basis of the interactions in the system "electromagnetic radiation–small particles–surface." Nanoporous silica is characterized by a high density of surface defects, an effective absorption in the ultraviolet range, and low thermal conductivity, which plays an important role in the ionization processes of low molecular organic compounds in laser-assisted desorption mass-spectrometry. However, special attention should be paid to clarification of the influence of local electric fields and surface heatingon laser irradiation on ionization and desorption of adsorbed molecules.

Chapter 1
Surface Plasmons in Assemblies of Small Particles

L.G. Grechko, E.Yu. Grischuk, L.B. Lerman, and A.P. Shpak

Abstract The electrodynamical response of small particles' systems in external electric field $\mathbf{E}_0$ is investigated. Calculation of the electric field at any point of the space in a system of spherical particles of different radii R_i ($i = 1,2, \ldots n$) with different dielectric permittivities $\varepsilon_i(\omega)$ above a substrate is carried out. Analytical expressions for polarizability of two particles are obtained with an allowance for their multipole interactions between themselves and with the substrate. For the case of one spherical particle above the substrate, frequencies of surface modes are calculated, and salient features of the external electric field interaction with such a system are analyzed. Similar problem is solved for a case of two different spherical particles with radii R_1 and R_2 arranged at distance d (center to center) from each other. Electrostatic approximation is used in all calculations. Surface plasmons in a metallic spheroid are calculated for different eccentricities of ellipse.

1.1 Introduction

Last years, more and more attention is paid in dielectric and optical spectroscopy for investigation of surface electromagnetic modes (polaritons, plasmons, exitones, and so on) on the mediums' interfaces [1, 2], for small particles (SP) and matrix disperse systems (MDS) [1–3] on their base. Though the basic properties of surface electromagnetic waves for spatially confined media follow directly from solutions of Maxwell equations, and they were actively learned by Arnold Sommerfeld on the eve of nineteenth century, the interest in them ceases from time to time. Only recently, mainly after surface physics and chemistry evolution and discovery of the surface enhancement Raman scattering [4], it became clear that spectroscopy of surface electromagnetic modes can be a powerful investigation method of surface properties and the structure of MDS.

L. Grechko (✉)
O.O. Chuiko Institute of Surface Chemistry of the National Academy of Sciences of Ukraine, General Naumov St. 17, Kyiv 03164, Ukraine
e-mail: lgrechko09@rambler.ru

A.P. Shpak, P.P. Gorbyk (eds.), *Nanomaterials and Supramolecular Structures*,
DOI 10.1007/978-90-481-2309-4_1,

The peculiarity of the surface electromagnetic modes (SEM) appears to be a condition of their origin. It is necessary for their origin that the real part of permittivity of one of the matters of interfaces of media or small particles and matrix in MDS be negative ($\mathrm{Re}\varepsilon(\omega) \leq -1$ where ε is a permittivity and ω is a radiation frequency). But in most cases through analyzing processes of light reflection and scattering, it was assumed in explicit or implicit form that $\mathrm{Re}\varepsilon(\omega) > 0$, though the condition $\mathrm{Re}\varepsilon(\omega) > 0$ even with absence of spatial dispersion ($\vec{k} = 0$ where $\vec{k}$ is a wave vector) is fulfilled only in case when $\omega \to 0$ [3]. As an example, for metals in case of Droude free electrons $\varepsilon(\omega) = 1 - \omega_p^2/[\omega(\omega + i\nu)]$ (ω_p is a plasmon frequency, ν is an absorber factor for solid). From expression of dependence $\varepsilon(\omega)$ when $\nu \to 0$ and all $\omega < \omega/\sqrt{2}$, it follows that $\mathrm{Re}\varepsilon(\omega) \leq -1$ (the equality corresponds to generation of a surface plasmon). For aluminum at $\omega_p/\sqrt{2} = 10.6$ eV at the interface "aluminum–vacuum" (in small metallic parts at $\omega \leq \omega_p/\sqrt{3} = 6.24$ eV) initiation is possible of surface plasmons with the spectral region of their existence extending from far ultraviolet radiation to far infra-red. Analogical assertions take place for many other metals and semiconductors [3, 5–7].

In dielectrics, electric induction $\mathbf{D} = \mathbf{E} + 4\pi\mathbf{P} = \varepsilon(\omega)\mathbf{E}$ where $\mathbf{P}$ is a vector of electric polarizability, and for negative $\mathrm{Re}\varepsilon(\omega)$, increase in $\mathbf{P}$ due to external field $\mathbf{E}$ should be more in absolute value and shifted of phase on 180° concerning the field $\mathbf{E}$. Such situation is realized in dielectrics near media absorption bands at frequencies Ω_0 when the frequency of applied field appears to be a small bit higher than Ω_0 (the frequency of the main transition). Note then on analyzing SEM in SP and MDS on their base, a strong dependence was found of spectral characteristics SEM on the SP form.

At first, as in works [8–10], we developed a mathematical technique for solving electrostatic boundary-value problem for a system of spatially distributed and homogeneous spheres placed in a homogeneous external electric field near a flat and semi-infinite homogeneous substrate. This technique is based on a multipole expansion for the electrostatic potential and is a generalization of the method developed in [10]. It is neither assumed that the spheres are of the same material and radii nor assumed that they are necessarily lying on the substrate. So, the initial problem is reduced to multipole coefficient's calculations which define each sphere's field in the outer region. The coefficients are defined using an infinite set of coupled algebraic equations. In view of the infinite size and complexity of the set, obtaining exact analytical results is impossible in the general case. However, approximate analytical results can be obtained using simple systems. Note that the main results of this section were briefly reported in [11]. Further, we consider as an example, a system of two different spheres above a substrate in the dipole approximation. This simple but instructive case is comparatively easy to solve and allows us to demonstrate how the developed technique works. By using the solution for the multipole coefficients and their relation to the so-called cyclic coordinates of the polarizability tensor (the relation is derived in [10]), we determine the expression for the polarizability of each spherical particle for this special case and show its relation to those known for systems of two spheres and for sphere–substrate systems. All the above serves not only as an illustration of possible applications of the elaborated technique, but also as a basis for further consideration.

After that, influence of the substrate on the optical properties of a small sphere is examined in the electrostatic approximation. In order to extract the effects of substrate–particle interaction and to exclude those due to interparticle interaction, we turn to a more simple system of a single sphere above a substrate. All the analytical results are obtained here using the single-oscillator's Lorentzian model of dielectric functions for both the sphere and the substrate. The ambient region is assumed to be vacuum. For such a canonical system, analytical expressions for the sphere's resonances and strengths of the corresponding modes are obtained as an approximation of zero damping. As a particular case of the problem, we analyze the case of two metallic spherical parts with distance d between them in external (variable in time) electric field with wave length λ_0 which is much more than the particles' dimension and d.

The substrate influence on both the frequency and the intensity of the resonances is analyzed, too. A multi-dipole interaction for one gold particle near gold substrate is taken into account [10, 11]. As well, we obtain an equation for calculating spectrum of surface plasmons in metallic spheroid for the general case. Some numerical and graphic results are presented.

1.2 Physical System, Initial Problem, and Multipole Expansions

Let us consider a model system of homogeneous spheres of different sizes and materials embedded in a semi-infinite homogeneous medium (ambient) occupying one half of the space. The other half space is filled with another homogeneous medium (substrate). The system is placed in an external homogeneous electric field $\mathbf{E}_0$. The spheres are assumed to be of arbitrary sizes and located at arbitrary distances both from each other and from the substrate. Additionally, the spheres may touch each other and the substrate, or they may not be touching each other. Therefore, results of this section can be applied to a wide variety of systems of spherical particles.

Under certain conditions, the results of this work can provide a good description of the properties of various real systems, such as MDS, films deposited on a substrate, aerosols, and colloids placed in an alternative electromagnetic field with $\mathbf{E} = \mathbf{E}_0 \exp\left[i\left(kr - \omega t\right)\right]$. One of these conditions is the satisfaction of the electrostatic approximation: all the characteristic lengths in the system (radii, distances, etc.) must be much smaller than the wavelength of the external field. Another condition is connected with the semi-infinite sizes of the ambient and substrate regions. Of course, any real system is always space-limited and all of its bounding surfaces influence its properties. Therefore, our results will be quite correct for those systems in which the influence of boundaries is negligible.

Let ε_a, ε_s, and ε_i be the dielectric constants of the ambient, substrate, and the i th sphere, respectively, and R_i be the radius of the i th sphere. The resulting electric field is caused by the interaction of the external field $\mathbf{E}_0$ with all the components of the system. The corresponding potential satisfies Laplace's equation [3]

$$\Delta\psi\ (r) = 0 \tag{1.1}$$

in the regions a (inside ambient, outside spheres), i (inside i th sphere), and s (inside substrate) together with the standard boundary conditions

$$\psi^u_{\sigma_{u-b}} = \psi^v, \varepsilon_u \frac{\partial \psi^u}{\partial n_u \sigma_{u-v}} = \varepsilon_v \frac{\partial \psi^v}{\partial n_v}, \tag{1.2}$$

where ε_u is the permittivity of the matter filling the u th region ($u = a, i, s$), ψ^u is the resulting field potential in the u th region, subscript σ_{u-v} under the equal sign denotes that the expression is valid for observation points lying on the common boundary surface σ_{u-v} of regions u and v.

Using the superposition principle to represent the resulting potential in regions a and s, together with the image method and multipole expansion techniques for solving electrostatic problems, we seek a solution of problems (1.1) and (1.2) in the following form [10–13]:

$$\begin{aligned} \psi^a &= \psi^a_{ext} + \sum_i \psi^a_{i\,th\ sphere} + \psi^a_{substrate} \\ &= -\mathbf{E}_0 \times \mathbf{r} + \sum_{ilm} A_{ilm} F_{lm}\ (\rho_i) + \sum_{ilm} A'_{ilm} F_{lm}(\rho'_i) \end{aligned} \tag{1.3}$$

in the region a,

$$\psi^i = \sum_{lm} B_{ilm} G_{lm}\ \left(\boldsymbol{\rho}_i\right) \tag{1.4}$$

in the region i, and

$$\psi^s = \psi^s_{ext} + \psi^s_{indused} = -\mathbf{E}_0 \times \mathbf{r} + \psi^s_0 + \sum_{ilm} C_{ilm} F_{lm}\ \left(\rho'_i\right) \tag{1.5}$$

in the region s, where $\psi^a_{ext} = -\mathbf{E}_o \times \mathbf{r}$ is the potential of the given external field $\mathbf{E}_0$, in the ambient, $\psi^s_{ext} = -\mathbf{E'}_0 \times \mathbf{r} + \psi^s_0$ is that in the substrate, $\mathbf{E'}_0$ is a constant vector representing the given external field in the substrate (note that $\mathbf{E'_0} \neq \mathbf{E_0}$ due to "refraction" of the force lines on the ambient–substrate boundary), ψ^s_0 is a constant contribution to the potential ψ^s_{ext} related with a choice of the origin point location, $\psi^a_{ith\,sphere} = \sum_{lm} A_{ilm} F_{lm}\ (\rho_i)$ is the contribution to ψ^a due to the induced charge distribution of the i th sphere, $\psi^a_{substrate} = \sum_{ilm} A'_{ilm} F_{lm}\ \left(\rho'_i\right)$ is that due to the induced charge distribution of the substrate, $\psi^s_{induced} = \sum_{ilm} C_{ikm} F_{lm}\left(\rho'_{\mathbf{i}}\right)$ is the contribution to ψ^s due to all the induced charges (of both the substrate and all the spheres), $F_{lm}(\mathbf{r}) \equiv r^{-l-1} Y_{lm}\left(\hat{\mathbf{r}}\right)$ and $G_{lm}\ (\mathbf{r}) \equiv r^l Y_{lm}\ \left(\hat{\mathbf{r}}\right)$ are spherical harmonics regular, respectively, at infinity and at zero, $Y_{lm}\ \left(\hat{\mathbf{r}}\right)$ is a spherical function normalized in the usual way [13 ,14], $\hat{\mathbf{r}} \equiv \mathbf{r}/r$ is a unit vector in the $\mathbf{r}$ direction, $\rho_{\mathbf{i}} \equiv \mathbf{r} - \mathbf{r_i}$ is the radius vector of an observation point with respect to the center of the i th sphere (see Fig.1.1), $\rho'_{\mathbf{i}} \equiv \mathbf{r} - \mathbf{r'}_i$ is that with respect to the image of the i th sphere, $\mathbf{r_i}$ is the radius vector of the i th sphere's center.

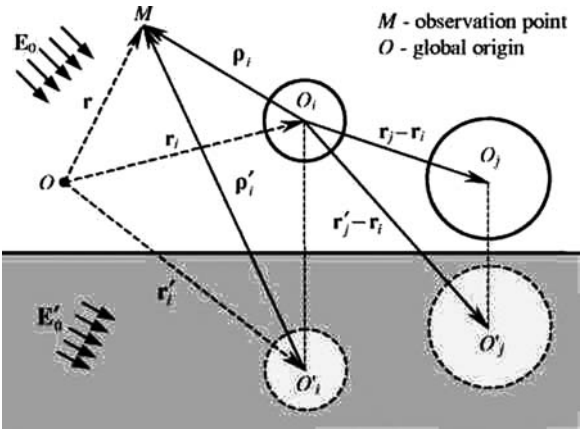

Fig. 1.1 Spheres, images, and vector description of the considered system

It should be mentioned that all the individual terms in Eqs. (1.3), (1.4), and (1.5) automatically satisfy Laplace's equation (1.1), so the unknown values A_{ilm}, A'_{ilm}, B_{ilm}, C_{ilm}, $\mathbf{E'_0}$, and ψ_0^s can be obtained after applying only the boundary conditions (1.2) to expansions (1.3), (1.4), and (1.5). Also, it is assumed that $\sum_{lm} \equiv \sum_{l=0}^{\infty} \sum_{m=-l}^{l}$ throughout this chapter.

The earlier obtained [10] equations form a full set to determine unknown coefficients A_{ilm} and B_{ilm} (recall that the values A'_{ilm} are expressed in terms of A_{ilm} and the explicit form of the expression was found earlier [10]). After some transformations the equations noted can be reduced to the form

$$\sum_{ilm} \left[\delta^{ilm}_{jl_1m_1} + K^{ilm}_{jl_1m_1} \right] A_{ilm} = U_{jl_1m_1}, \tag{1.6}$$

$$B_{ilm} = f(A_{ilm}), \tag{1.7}$$

where

$$K^{ilm}_{jl_1m_1} \equiv a_{jl_1} T^{j_1m}_{lm} \left[F'_{LM} \left(\mathrm{r}_i - \mathrm{r}_j \right) \right] + (-1)^{l+m} \frac{\varepsilon_a - \varepsilon_s}{\varepsilon_a + \varepsilon_s} F_{LM} \left(\mathrm{r'}_i - \mathrm{r'}_j \right), \tag{1.8}$$

$$a_{il} = \frac{l\left(\varepsilon_i - \varepsilon_a\right)}{l\varepsilon_i + (l+l)\,\varepsilon_a} R_i^{2\,l+1},\ U_{ilm} = \sqrt{4\pi/3 a_{il}} E_0^m \delta_l^1 = \sqrt{3/\left(4\pi\right)} \frac{\varepsilon_i - \varepsilon_a}{\varepsilon_i + 2\varepsilon_a} V_i E_0^m \delta_l^1, \tag{1.9}$$

$$T^{l_1m_1}_{lm} = (-1)^{l+m_1} \left[4\pi \frac{2\,l+1}{(2l_1+1)\,(2L+1)} \frac{(L+M)!\,(L-M)!}{(l+m)!\,(l-m)!\,(l_1+m_1)!\,(l_1-m_1)!} \right], \tag{1.10}$$

and $V_i = (4\pi/3)R_i^3$ is the volume of the i th sphere, $L = l + l_1$, $M = m - m_1$ ($l_1 = 0,1,2,...$, $m_1 = -l_1,...,l_1$).

The explicit form of the function f in Eq. (1.7) is sort of cumbersome. In this chapter, however, we are not interested in coefficients B_{ilm} representing the resulting

field inside the spheres, so the function f is not needed for further consideration and hence not given here. The expression for U_{ilm} is presented in two equivalent forms (due to $a_{il} = R_i^3(\varepsilon_i - \varepsilon_a)/(\varepsilon_i + 2\varepsilon_a)$). Both the forms are useful.

It is remarkable that the transition from a $2D$ array of identical spheres located on a substrate [9] to the system considered here (i.e., a spatial system of different spheres (above a substrate)) leads, formally, only to the appearance of the a_{il} values (known as the multipolar polarizabilities of a single sphere in the expressions for $K^{ilm}_{jl_1m_1}$ and U_{ilm} (Eqs. (1.8) and (1.10)).

Thus, we have obtained an infinite set of coupled linear algebraic equations (in indices l,m, and, possibly, i) for calculating the multipole coefficients A_{ilm} of the induced field for each sphere in the ambient. The remaining coefficients (A'_{ilm}, C_{ilm}, and B_{ilm}) are expressed in terms of A_{ilm}. Consequently, the initial problem is reduced to the determination of A_{ilm} from Eq. (1.6). Having determined the values of A_{ilm}, one can then determine all the remaining multipolar coefficients and, by using the initial expansions (1.3), (1.4), and (1.5), one can in principle calculate the electrostatic potential at any point and all other values of interest.

1.3 Two Spheres Above a Substrate: Spheres' Polarizability Tensor

Let us consider the case of two spheres located above a substrate in such a way that the line connecting the centers of the spheres is perpendicular to the substrate surface (see Fig.1.2a). By varying the parameters of this system, one can obtain

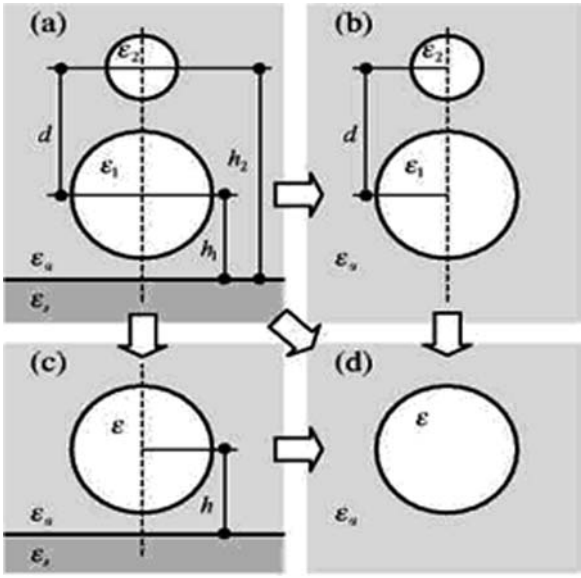

Fig. 1.2 A system of two different spheres above a substrate, and its particular cases

the particular cases shown in Fig. 1.2b–d. The more general case when the line of spheres' centers is inclined turns out to be far more analytically complicated and is not examined in this paper.

In the work [10] we obtained the expression for the mm_1th component of the i th sphere's polarizability tensor

$$\alpha^m_{im_1} = a_{i1}\frac{1+(-1)^m\eta_m\frac{a_{\bar{i}1}}{d^3}+\Delta_{\bar{i}m}}{1-\eta_m^2\frac{a_{11}a_{21}}{d^6}+\Delta_m}\delta^m_{m_1}, \tag{1.11}$$

where

$$\bar{i}\equiv\begin{cases}1, \text{ if } i=2\\ 2, \text{ if } i=1\end{cases}, \eta_m\equiv\begin{cases}1, m=\pm1\\ 2, m=0\end{cases}, \quad \Delta_{im}\equiv H_m a_{i1}\left[\frac{1}{(h_1+h_2)^3}-\frac{1}{(2h_i)^3}\right], \quad H_m\equiv\eta_m\frac{\varepsilon_s-\varepsilon_a}{\varepsilon_s+\varepsilon_a},$$

$$\Delta_m \equiv H_m^2 a_{11}a_{21}\left[\frac{1}{(2h_1)^3(2h_2)^3}-\frac{1}{(h_1+h_2)^6}\right] - H_m\left[\frac{a_{11}}{(2h_1)^3}+\frac{a_{21}}{(2h_2)^3}+(-1)^m\eta_m\frac{2a_{11}a_{21}}{d^3(h_1+h_2)^3}\right],$$

and the geometrical parameters h_1, h_2, and d are defined in Fig. 1.2. The values Δ_{lm} and Δ_m are additions to the numerator and denominator of $\alpha^m_{lm_1}$, respectively, describing the substrate's influence on the sphere's polarizability and vanishing when there is no substrate (formally, when $\varepsilon_s=\varepsilon_a$).

Starting from Eq. (1.11), expressions for $\hat{\alpha}_i$ can be easily obtained for the particular cases shown in Fig. 1.2b–d; namely, in the following cases:

(1) Two spheres without a substrate (Fig. 1.2b): by setting $\varepsilon_s=\varepsilon_a$ (or, alternatively, moving the substrate away from the spheres to infinity) we find

$$\alpha^m_{im_1}=\alpha_{i1}\frac{1+(-1)^m\eta_m a_{\bar{i}1}/d^3}{1-\eta_m^2 a_{11}a_{21}/d^6}\delta^m_{m_1}. \tag{1.12}$$

(2) A single sphere above a substrate (Fig. 1.2c): by setting $\varepsilon_{\bar{i}}=\varepsilon_a$ (or $d=\infty$) we find

$$\alpha^m_{im_1}=\frac{a_{i1}}{1-H_m\frac{a_{i1}}{(2h_i)^3}}\delta^m_{m_1}. \tag{1.13}$$

(3) A single sphere in a homogeneous medium with no substrate (Fig. 1.2d): by setting $\varepsilon_s=\varepsilon_i=\varepsilon_a$ (or $d=h_i=\infty$) we find the classical result

$$\alpha^m_{im_1}=a_{i1}\delta^m_{m_1}=\frac{3V}{4\pi}\frac{\varepsilon_i-\varepsilon_a}{\varepsilon_i+2\varepsilon_a}\delta^m_{m_1}. \tag{1.14}$$

Note that tensors (1.12), (1.13), and (1.14) are diagonal in the Cartesian frame with z axis along the system's axis of symmetry and have two different diagonal components. These components are either transversal to z axis $\alpha_i^{\perp} \equiv \alpha_{i1}^{1}$ or longitudinal to it $\alpha_i^{\sqcup} \equiv \alpha_{i0}^{0}$.

The common peculiarity among tensors (1.12), (1.13), and (1.14) is that they all differ from the spherical one because of the axial symmetry of the corresponding physical system (Fig. 1.2a–c), while the tensor, Eq. (1.14), for a single sphere (Fig. 1.2d) is simply proportional to the unit one due to the point symmetry of a sphere. This last statement means that the induced dipole moments of the spheres in the systems depicted in Fig. 1.2a–c are not parallel to $\mathbf{E}_0$, in contrast to the case of a single sphere. Thus, the dipole moment of a single sphere is changed in both its value and direction in the presence of a substrate or another sphere. These changes are caused, of course, by the interaction between the induced dipole moment of the sphere and those of neighboring objects (i.e., substrate and/or other spheres) and depend on the values as well as the relative orientation of the moments. This simple physical picture of the presence of anisotropy for initially isotropic spheres helps us to understand some peculiarities of the sphere's polarizability behavior considered below.

1.4 Investigations Surface Plasmons for Specific Systems

1.4.1 Substrate Influence on the Optical Properties of a Small Sphere

We turn now to developing analytical results and subsequent insight into the influence of a substrate on the optical properties of a sphere. To accomplish this, we shall consider a single sphere above a substrate. Its polarizability we rewrite here in the following form (from hereon, the index i is omitted):

$$\alpha_{m_1}^{m} = R^3 \frac{(\varepsilon - \varepsilon_a)(\varepsilon_s + \varepsilon_a)}{(\varepsilon + 2\varepsilon_a)(\varepsilon_s + \varepsilon_a) - \eta_m \left(\frac{R}{2h}\right)^3 (\varepsilon - \varepsilon_a)(\varepsilon_s - \varepsilon_a)} \delta_{m_1}^{m}. \tag{1.15}$$

In the optical region, all the permittivities in Eq. (1.15) become, in general, frequency dependent and complex, as does the polarizability itself. In order to analytically investigate the behavior of $\hat{\alpha}$, we shall assume ε and ε_s to be Lorentzian dielectric functions [3]

$$\varepsilon(\omega) \quad = \varepsilon_\infty + \frac{\omega_p^2}{\omega_0^2 - \omega^2 - i\gamma\omega}, \varepsilon_s(\omega) = \varepsilon_{\infty s} + \frac{\omega_{ps}^2}{\omega_{0s}^2 - \omega^2 - i\gamma_s\omega}, \tag{1.16}$$

while ε_a is assumed to be constant and equal to unity (i.e., having vacuum or rare gases as the ambient). The index s in Eqs. (1.16) denotes the values characterizing the substrate material.

Despite only a few materials being described quite well by the Lorentzian model, it often gives universal results [3, 7]. Therefore, we shall use this model here to be satisfied not so much with the quantitative fitness but in clarifying the physical picture. To accomplish this, we will first obtain the resonant frequencies for a sphere located near a substrate.

Defining the resonant frequencies as those at which the polarizability of the sphere becomes infinite (and, correspondingly, the denominator in Eq. (1.15) equals zero [5]), we find from Eq. (1.15), when accounting for Eqs. (1.16), the following algebraic equation for the resonant frequencies (in the case $\varepsilon_\infty = \varepsilon_{\infty s} = \varepsilon_a = 1$):

$$\omega^4 + a_3\omega^3 + a_2\omega^2 + a_1\omega + a_0 = 0 \tag{1.17}$$

with

$$a_3 = I(\gamma + \gamma_s),\ a_2 = -(\tilde{\omega}_0^2 + \tilde{\omega}_{0s}^2 + \gamma\gamma_s),\ a_1 = -i(\tilde{\omega}_0^2\gamma_s + \tilde{\omega}_{0s}^2\gamma),$$

$$a_0 = \tilde{\omega}_0^2\tilde{\omega}_{0s}^2 - x_m\frac{\omega_p^2}{3}\frac{\omega_{ps}^2}{2},\quad x_m \equiv \eta_m\left(\frac{R}{2h}\right)^3, \tag{1.18}$$

where

$$\tilde{\omega}_0^2 \equiv \omega_0^2 + \frac{\omega_p^2}{3} \text{ and } \tilde{\omega}_{0s}^2 \equiv \omega_{0s}^2 + \frac{\omega_{ps}^2}{2}$$

are "shifted" squared frequencies of ω_0^2 and ω_{0s}^2, and $x_m \equiv \eta_m(R/2h)^3$.

Equation (1.17) is of fourth order with complex coefficients and has, in general, four complex roots. Consequently, the resonant frequencies are, generally speaking, complex values. However, resonance occurs at real frequencies close to the real part of the corresponding complex frequencies. The exact complex solutions to Eq. (1.17) are analytically too complicate and not of interest to us here. Instead, one can determine the real roots by neglecting damping ($\gamma = \gamma_s = 0$). In this case, Eq. (1.17) is reduced to a biquadratic form with the solutions

$$\left(\omega_m^{\pm}\right)^2 = \frac{\tilde{\omega}_0^2 + \tilde{\omega}_{0s}^2}{2} \pm \sqrt{\left(\frac{\tilde{\omega}_0^2 - \tilde{\omega}_{0s}^2}{2}\right)^2 + x_m\frac{\omega_p^2}{3}\frac{\omega_{ps}^2}{2}}. \tag{1.19}$$

This expression simple enough contains useful information on the sphere resonances that allows one to trace how the substrate influences the absorption peak position of a sphere brought near it.

The main peculiarity of Eq. (1.19) is that it predicts four positive nonzero resonances for a sphere. Indeed, at each fixed value of m ($m = 0,1$) we have two resonant frequencies ω_m^+ and ω_m^- corresponding to different signs of the square root in Eq. (1.19). Thus, there are two resonances for transversal ($m = \pm 1$) and two for longitudinal ($m = 0$) components of $\hat{\alpha}$. Therefore, in the general case of the external field

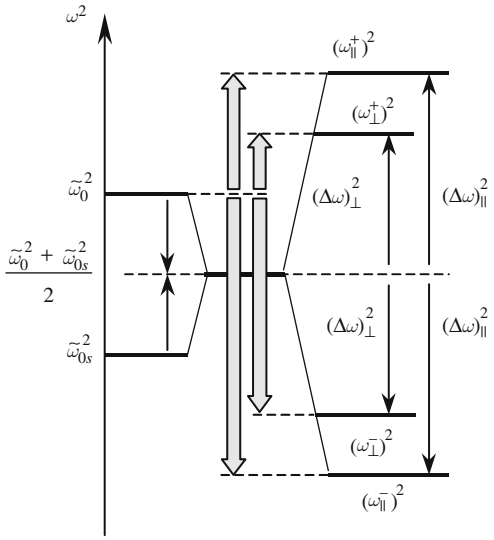

Fig. 1.3 Location of the resonant frequencies according to Eq. (1.19). The location is shown schematically for one of the components of $\hat{\alpha}$. For another component, the frequency splitting is qualitatively the same, but with another value of the $(\Delta\omega_m)^2$ being equal to the square root from Eq. (1.29). Note that the magnitude of the half-difference $(\tilde{\omega}_0^2 - \tilde{\omega}_{0s}^2)/2$ (*short arrows*) is always less than $(\Delta\omega_m)^2$ (*long arrows*)

arbitrarily oriented with respect to the substrate's normal direction, the polarizability of the sphere drastically increases at four frequencies.

Second, the resonant frequencies ω_m^+ and ω_m^- are simultaneously dependent on both sets of parameters (ω_0, ω_p) and $(\omega_{0s}, \omega_{ps})$, which characterize the sphere itself and the substrate material. Consequently, there is a "coupling" of corresponding material oscillators. Only in the limiting case of a single isolated sphere (no substrate) or an isolated substrate (no sphere) we obtain, as it must be, the single-object resonance occurring at $\omega = \tilde{\omega}_0 \equiv \left(\omega_0^2 + \omega_p^2/3\right)^{1/2}$ or $\omega = \tilde{\omega}_{0s} \equiv \left(\omega_0^2 + \omega_{ps}^2/2\right)^{1/2}$, respectively. For a sphere and substrate of fine metal ($\omega_0 = \omega_{0s} = 0$) it gives the well-known Frohlich frequencies of surface plasmons [11] $\omega_F = \omega_p/\sqrt{3}$ and $\omega_F = \omega_{ps}/\sqrt{2}$. In the general case, however, the Fröhlich resonances become entangled with those of ω_0 and ω_{0s} for bulk materials.

Third, the resonant frequency locations obey the following regularities (Fig. 1.3).

(1) The resonances for each component of the sphere's polarizability ($\alpha^{\perp}$ or $\alpha^{\sqcup}$) are located symmetrically with respect to the square root of the arithmetic mean ($(\tilde{\omega}_0^2 + \tilde{\omega}_{0s}^2)/2$) of the shifted squared frequencies $\tilde{\omega}_0^2$ and $\tilde{\omega}_{0s}^2$.

(2) The up- or down-shifts in frequency from the mean $\sqrt{(\tilde{\omega}_0^2 + \tilde{\omega}_{0s}^2)/2}$ for the resonances ω_m^+ and ω_m^- are defined by the value of the square root in Eq. (1.19). They are the same for both resonances (at fixed value of m), while being different for transversal and longitudinal components. The shifts for $\alpha^{\perp}$ ($m = \pm 1$, $\eta_m = 1$) are less than those for $\alpha^{\sqcup}$ ($m = 0$, $\eta_m = 2$).

(3) Because the radicand in Eq. (1.19) is always greater than the half-difference magnitude $\left|\tilde{\omega}_0^2 - \tilde{\omega}_{0s}^2\right|/2$, the "upper" resonances ω_m^+ $(m = 0, \pm 1)$ are always located above the greater of the two frequencies $\tilde{\omega}_0$ and $\tilde{\omega}_{0S}$, while the "lower" ones ω_m^- are located below the smaller of $\tilde{\omega}_0$ and $\tilde{\omega}_{0S}$.
(4) These shifts, being dependent on the value *h/R* (see the expression for x_m), decrease with an increase in the height h and are the same for spheres of the same material but of different radii lying on a substrate (when $h = R$), i.e., they are *scaling invariant.*

Note, finally, that the locations of these sphere resonances with respect to the resonant frequency $\tilde{\omega}_0$ of an isolated sphere define the red and blue shifts of the single-sphere eigenmode. As is clear (see Fig. 1.3), these shifts are not equal. The red shift (i.e., the shift from $\tilde{\omega}_0$ to ω_m^-) is greater than the blue shift (from $\tilde{\omega}_0$ to ω_m^+) in the case when $\tilde{\omega}_0^2 > \tilde{\omega}_{0s}^2$, and less in the opposite case.

It should be stressed that no matter how small the blue shift may be, it always exists in principle. This result is quite surprising and differs from the commonly accepted viewpoint that the substrate can cause only the red shift of an isolated sphere resonant frequency, and the blue-shifted resonances appear (if any) due to either higher multipoles [8] or nonlocality of the permittivity. From our results, such statements should be considered as erroneous. Moreover, the appearance of the four resonances due to splitting and shifting of the single-sphere resonance in the presence of a substrate is quite analogous to the same dipole approximation for a system of two unequal spheres, as well as to the production of the combination frequencies in a system of two coupled oscillators in the classical mechanics.

We can now describe the *physical picture*of the single-resonance splitting as follows. The interaction of the sphere and substrate with the external field leads at first to exciting and coupling of the corresponding bulk and surface modes ω_0, $\omega_p/\sqrt{3}$ and ω_{0s}, $\omega_{ps}/\sqrt{2}$, respectively, resulting in the natural modes of the sphere and substrate, $\tilde{\omega}_0 \equiv \left(\omega_0^2 + \omega_p^2/3\right)^{1/2}$ and $\tilde{\omega}_{0s} \equiv \left(\omega_0^2 + \omega_{ps}^2/2\right)^{1/2}$. Then, the natural modes are coupled via mutual electromagnetic interaction (dipole–dipole, in our case). The latter is what causes the splitting of $\tilde{\omega}_0$ into the set of resonances $\omega_m^{\pm}$. Increasing the distance between the sphere and the substrate leads to a weakening of their mutual interaction. In the limit $h \to \infty$, we have noninteracting modes with eigenfrequencies $\tilde{\omega}_0$ and $\tilde{\omega}_{0s}$ with no splitting.

This description of the splitting and shifting of the sphere resonance, being dependent on the combination of the values ω_0, ω_p, ω_{0s}, ω_{ps}, and h/R, can lead to various pictures of absorption band localization with respect to the fundamental frequencies ω_0 and ω_{0s} of the bulk materials, as well as to the plasma frequencies ω_p and ω_{ps}. Particularly, for a metallic sphere ($\omega_0 = 0$) near a dielectric substrate ($\omega_{ps} \ll \omega_p$), if only $\omega_{0s} \ll \omega_p$, one can derive the approximate expressions (presented in [11], but with misprints)

$$\omega_m^+ \approx \left[1 + \frac{3}{4} x_m \left(\frac{\omega_{ps}}{\omega_p}\right)^2\right] \frac{\omega_p}{\sqrt{3}}, \omega_m^- \approx \left[\omega_0^2 + (1 - x_m)\frac{\omega_{ps}^2}{2}\right]^{.1/2} \tag{1.20}$$

One can see from Eq. (1.20), for example, that the blue shift for a metallic sphere is a small value of the order of $(\omega_{ps}/\omega_p)^2$ in the presence of a dielectric substrate, but is substantial in the case of a metallic substrate.

A problem is analyzed when a small particle and substrate are metals ($\omega_0 = \omega_{0s} = 0$) and in general case we assume that $\varepsilon_\infty \neq \varepsilon_{\infty s} \neq \varepsilon_a$. For frequencies $\left(\omega_m^{\pm}\right)^2$, an expression can be obtained:

$$(\omega_m^{\pm})^2 = \frac{1}{2(1 - x_m\alpha\alpha_s)} \left\{(\bar{\omega}_f^2 + \bar{\omega}_{fs}^2)^2 \pm \left[\left(\bar{\omega}_f^2 - \bar{\omega}_{fs}^2\right)^2 + 4\bar{\omega}_f^2\bar{\omega}_{fs}^2 x_m \frac{(1-\alpha)(1-\alpha_s)}{(1 - x_m\alpha)(1 - \alpha_s x_m)}\right]^{\frac{1}{2}}\right\}, \tag{1.21}$$

where

$$\bar{\omega}_f^2 = \frac{\omega_f^2\,(1 - \alpha_s\eta_m)}{1 - \eta_m\alpha\alpha_s}, \bar{\omega}_{fs}^2 = \frac{\omega_{fs}^2\,(1 - \alpha_s\eta_m)}{1 - \eta_m\alpha\alpha_s}, \tag{1.22}$$

$$\omega_{fs}^2 = \frac{\omega_{ps}^2}{\varepsilon_{\infty s} + \varepsilon_a}, \omega_f^2 = \frac{\omega_p^2}{\varepsilon_\infty + 2\varepsilon_a}, \alpha = \frac{\varepsilon_\infty - \varepsilon_a}{\varepsilon_\infty + 2\varepsilon_a}, \alpha_s = \frac{\varepsilon_{\infty s} - \varepsilon_a}{\varepsilon_{\infty s} + \varepsilon_a}. \tag{1.23}$$

Here ω_f and ω_{fs} are independent frequencies of surface plasmons of small particles and the substrate; if $d \to \infty$, $\bar{\omega}_f^2$ and $\bar{\omega}_{fs}^2$ are the same frequencies taking into consideration dipole interaction of the substrate and small particle for finite d values (Fig. 1.2b). In case when $\varepsilon_\infty = \varepsilon_{\infty s} = \varepsilon_a = 1$ (Eq. (1.20)) at $\omega_0 = \omega_{0s} = 0$ we have

$$2(\omega_m^{\pm})^2 = \omega_f^2 + \omega_{fs}^2 \pm \left[(\omega_f^2 - \omega_{fs}^2) + 4\omega_f^2\omega_{fs}^2 A_m\right]^{\frac{1}{2}}. \tag{1.24}$$

In case when material of particle and the substrate is the same ($\omega_p = \omega_{ps}$), it follows

$$\left(\omega_m^{\pm}\right)^2 = \frac{\omega_p^2}{12}\left\{5 \pm \left[1 + 3\eta_m\left(\frac{R}{h}\right)^3\right]^{\frac{1}{2}}\right\}. \tag{1.25}$$

To determine optically active modes, it is necessary to evaluate relative oscillator strengths f_m^+ and f_m^- [10]. It follows from the analysis that only two modes $\left(\omega_m^-\right)^2$ appear to be optically active in absorption spectra. Oscillator strengths of other two modes $(\omega_m^+)^2$ tend to zero.

1.4.2 Two Metallic Spherical Particles in External Electric Field

Let us analyze the case of two metallic spherical parts with distance d between them (Fig. 1.2) in external (variable in time) electric field with wave length λ_0 which is greatly more than the particles' dimension and d. In this case it is necessaryto assign $\varepsilon_a = \varepsilon_s$, polarizability tensor of i th particle can be formed as

$$\alpha_{im_1}^m = a_{i1} \frac{1 + (-1)^m \eta_m a_{\bar{i}1}}{1 - \eta_m^2 \frac{a_{11} a_{21}}{d^6}}, \tag{1.26}$$

$$a_i = \frac{\varepsilon_i - \varepsilon_a}{\varepsilon_i + 2\varepsilon_a} R_i^3, \quad i = 1,2, \tag{1.27}$$

where R_i is i th particle radius.

All other designations are the same.

Condition for obtaining frequencies of surface plasmons (zero value of denominator in Eq. (1.27)) in this case looks like

$$\eta_m^2 \frac{R_1^3 R_2^3}{d^6} \left(\frac{\varepsilon_{1\infty} - \varepsilon_a}{\varepsilon_{1\infty} + 2\varepsilon_a} \right) \left(\frac{\varepsilon_{2\infty} - \varepsilon_a}{\varepsilon_{2\infty} + 2\varepsilon_a} \right) \left(\frac{\omega^2 - \omega_{e1}^2}{\omega^2 - \omega_{f1}^2} \right) \left(\frac{\omega^2 - \omega_{e2}^2}{\omega^2 - \omega_{f2}^2} \right) = 1. \tag{1.28}$$

Permittivities of metal spheres were taken in Drude formulation [3]

$$\varepsilon_1(\omega) = \varepsilon_{1\infty} - \frac{\omega_{p1}^2}{\omega(\omega + i\gamma_1)}; \qquad \varepsilon_2(\omega) = \varepsilon_{2\infty} - \frac{\omega_{p2}^2}{\omega(\omega + i\gamma_2)}, \tag{1.29}$$

and in case of realization expression (1.28) γ_1, γ_2 should come to zero. Additionally, in Eq. (1.28) next designations are introduced:

$$\omega_{fi}^2 = \frac{\omega_{pi}^2}{\varepsilon_{i\infty} + 2\varepsilon_a}; \qquad \omega_{ei}^2 = \frac{\omega_{pi}^2}{\varepsilon_{i\infty} - \varepsilon_a}, i = 1,2. \tag{1.30}$$

Taking into consideration these remarks, frequencies of surface plasmons are

$$2\left(\omega_m^{\pm}\right)^2 = \bar{\omega}_{f1}^2 + \bar{\omega}_{f2}^2 \pm \left[\left(\bar{\omega}_{f1}^2 - \bar{\omega}_{f2}^2 \right)^2 + 4\bar{\omega}_{f1}^2 \times \bar{\omega}_{f2}^2 \frac{(1 - \alpha_1)(1 - \alpha_2) x_m^2}{\left(1 - \alpha_1 A_m^2\right)\left(1 - \alpha_2 x_m^2\right)} \right]^{\frac{1}{2}}, \tag{1.31}$$

where

$$x_m^2 = \eta_m^2 \frac{R_1^3 R_2^3}{d^6}; \alpha_{12} = \alpha_1 \alpha_2; \alpha_1 = \frac{\varepsilon_{i\infty} - \varepsilon_a}{\varepsilon_{i\infty} + 2\varepsilon_a}$$

$$\bar{\omega}_{f1}^2 = \omega_{f1}^2 \frac{1 - \alpha_2 x_m^2}{1 - \alpha_{12} x_m^2}; \qquad \bar{\omega}_{f2}^2 = \omega_{f2}^2 \frac{1 - \alpha_1 x_m^2}{1 - \alpha_{12} x_m^2}; i = 1,2.$$

Expression (1.31) represents the basic formula for calculating frequencies of surface plasmons in a system of two different metallic spherical particles which disposed in external electric field at distance d. Corresponding frequencies of the "oscillators" force can be obtained using the method displayed in [10].

Let us analyze a particular case when particles consist of the same material $\varepsilon_1(\omega) = \varepsilon_2(\omega)$ but have different dimensions $R_1 \neq R_2$. Then from Eq. (1.31) frequencies of surface plasmons in a system of two particles are

$$\left(\omega_m^{\pm}\right)^2 = \frac{(1 \pm x_m)\omega_f^2}{1 \pm \alpha_0 x_m}, \omega_f = \frac{\omega_p^2}{\varepsilon_\infty + 2\varepsilon_0}, \varepsilon_1(\omega) = \varepsilon_2(\omega) \equiv \varepsilon(\omega),$$

$$\varepsilon(\omega) = \varepsilon_\infty - \frac{\omega_p^2}{\omega^2}, \Delta = R_2/R_1 \ (R_2 \leq R_1), \alpha_0 = \frac{\varepsilon_\infty - \varepsilon_0}{\varepsilon_\infty + 2\varepsilon_0}, x_m = \eta_m \Delta^{3/2}(R_1/d)^3,$$

$$\eta_m = \begin{cases} 2, \text{ when } m = (0; ||) \\ 1, \text{ when } m = (\pm 1; \perp) \end{cases}. \tag{1.32}$$

The sign $\parallel$ means that field $\mathbf{E}_0$ is directed along a straight line connecting the particles' centers, and longitudinal field is directed at right angle to the line:

$$(\Delta\omega)^2 = (\omega_0^+)^2 - (\omega_0^-)^2 = 3\omega_p^2 \left[\frac{(R_1 R_2)^{1/2}}{d}\right]^3. \tag{1.33}$$

At $\varepsilon_\infty = \varepsilon_0$, $\alpha_0 = 0$ expression for four frequencies of surfaces plasmons looks like

$$\left(\omega_m^{\pm}\right)^2 = \omega_f^2 \left[1 \pm \eta_m \Delta^{3/2}(R_1/d)^3\right],$$

and expression for the tensor of a polarizability of the first particle ($i = 1$) can be presented in the form

$$\alpha_{m_1}^m = R_i^3 \omega_f^2 \left[\frac{f_m^+}{(\omega_m^+)^2 - \omega^2} + \frac{f_m^-}{(\omega_m^-)^2 - \omega^2}\right] \delta_{m_1}^m,$$

where oscillator strengths, corresponded frequencies $\omega_m^{\pm}$ are $f_m^+ = (1/2)(1 + (-1)^m \Delta^{3/2})$, $f_m^- = (1/2)(1 - (-1)^m \Delta^{3/2})$ with $f_m^+ + f_m^- = 1$.

For longitudinal modes ($m = 0$), more optically active is the mode ω_0^+, and for transversal ($m = \pm 1$) it is ω_1^-. At $\Delta = 1$ and identical radii of particles there will be two modes in the spectrum of surface modes, thus a change of frequency will be equal to

$$(\Delta\omega)^2 \equiv (\omega_0^+)^2 - (\omega_1^-)^2 = 3\omega_p^2 \left[\frac{(R_1 R_2)^{1/2}}{d}\right]^3.$$

At $R_1 = R_2$ peak value of $\Delta\omega$ takes place at $d = 2R_1$. If $\varepsilon_\infty = \varepsilon_a = 1$ then

$$\Delta\omega = (1/8)^{1/2}\omega_p \approx 0{,}35\omega_p. \tag{1.34}$$

Note that value $\Delta\omega$ forms one-third of the plasma frequency ω_p of small particles' material. In real systems it is necessary to take into consideration electron's extinction γ_1,γ_2 and frequency dependencies $\varepsilon_1(\omega)$ and $\varepsilon_2(\omega)$.

1.4.3 Multipole Interaction Effect

Complex permittivities of a particle and substrate are analyzed. For ambient region, real value of permittivity ε_a is assumed. If general case of multipole interaction of one particle with substrate is taken into consideration, the following expressions are used for the polarizability tensor components $\hat{\alpha}_m$:

$$\alpha_m = \varepsilon_a r^3 A_{m1} \text{ (for } m = \perp \text{or} \parallel \text{)}, \tag{1.35}$$

where coefficients A_{m1} are to be obtained from infinite systems of linear algebraic equations ($k = 1,2,..$, δ_{kj} – Kronecker–Copelly symbols)

$$\sum_{j=1}^{\infty}\left(\delta_{kj} + \left\{\frac{k\,(\varepsilon_i - \varepsilon_a)\,(\varepsilon_a - \varepsilon_s)}{[k\varepsilon_i + (k+1)\,\varepsilon_a]\,(\varepsilon_a + \varepsilon_s)}\right\}\left[\frac{(k+j)!}{k!j!\,(2d/r)^{k+j+1}}\right]\right)\times A_{\perp j} = \frac{\varepsilon_i - \varepsilon_a}{\varepsilon_i + 2\varepsilon_a}\delta_{k1}, \tag{1.36}$$

for longitudinal constituent (with respect to the surface) of the external electric field.

Accordingly, for normal constituent

$$\sum_{j=1}^{\infty}\left(\delta_{kj} + \left\{\frac{k\,(\varepsilon_i - \varepsilon_a)\,(\varepsilon_a - \varepsilon_s)}{[k\varepsilon_i + (k+1)\,\varepsilon_a]\,(\varepsilon_a + \varepsilon_s)}\right\}\left[\frac{(k+j)!}{(k+1)!\,(j-1)!\,(2d/r)^{k+j+1}}\right]\right)\times$$
$$A_{\parallel j} = \frac{\varepsilon_i - \varepsilon_a}{\varepsilon_i + 2\varepsilon_a}\delta_{kj}. \tag{1.37}$$

The given formulas describe completely the interaction of electromagnetic radiation with a small particle near substrate and make it possible to calculate frequency response of optical characteristics for different specific systems.

The problem comes to solution of infinite systems (1.36) and (1.37). As a rule, such systems can be solved using reduction method, that is, the systems are to be replaced by systems with a finite number of equations. Such a replace is valid only in the case when the system is a regular one or, at least, quasi-regular [17]. As applied to the given problem, not enough attention is paid to the question in literature. As a rule, the problem is on the basis of general considerations restricted to dipole–dipole interaction.

To estimate impact of registering different number of multipoles on radiation spectrum, a number of calculations were done and some results are displayed in tables and figures. Let us analyze a golden particle on the gold substrate (air is ambient). For dielectric function of gold, experimental data [18, 19] are used (in 200–1900 nm range) concerning the massive material which were approximated in calculations using cubic splines. It should be noted that the next values of plasmon and extinction frequencies are $\omega_p = 1{,}37 \times 10^{16}\,Hz, \gamma_p = 0{,}33 \times 10^{14}$ Hz [1]. The particle was investigated with radius 20 nm, and all the results displayed below correspond to perpendicular polarization of the external field. There was no dimensional correction in calculations of the dielectric function because the particle is great enough.

A problem of construction of precise enough numerical solution of algebraic linear high-order systems with complex coefficients depending on real parameter (frequency) needs a separate investigation. We used in our calculations approved high-precision program SACG from IMSL library, Math. Library for Fortran Power Station, version 4.0, designed for solution systems of the type we needed.

As one would expect, the calculations made it clear that rate of convergence for solutions of infinite systems (1.6) and (1.7) depended on the frequency current value (wavelength). The values displayed in [20] of the infinite system solutions for some wavelength values and for different number l of equations are retained. Data obtained show that in case of short waves (200–500 nm) solution convergence is good enough but in plasmon resonance region it becomes worse, and more equations necessary to retain or special techniques are needed. The calculations also showed that for a long wave region (1100–2000 nm) solution convergence was good enough, too.

Scattering, absorption, and extinction spectra for remote particle are displayed in Fig. 1.4a, and for a particle on the substrate (dipole approximation) in Fig. 1.4b. In Fig. 1.4c similar spectra are displayed for quadrupole approximation ($l = 2$). Extinction spectra with multipoles taken into account for $l = 1{,}2{,}3{,}6$ are shown in Fig. 1.4d.

It follows, first of all, from the results exposed that the basic input in extinction is given by absorption (the particle is relatively small). There is only one absorption maximum in the spectra corresponding to resonance frequency of the surface plasmon. At this, the substrate increases substantially (compared with the separate particle) an absorption intensity for the resonance frequency with the extremum shift to longer waves. The result correlates with the data displayed in [9]. Taking multipole input into consideration also brings to a substantial increasing absorption (several times compared with a dipole approximation).

At increasing equation number in the system, calculations also show a shift of the resonance wavelength λ_r to greater lengths (red shift). Corresponding values of wavelengths for some l values are given in Table1.1. Note that for a separate golden $\lambda_r \approx 510$ nm. May be seen from the data is that when eight multipoles are taken into consideration, the resonance wavelength increases as much as 28% compared with that in the dipole approximation.

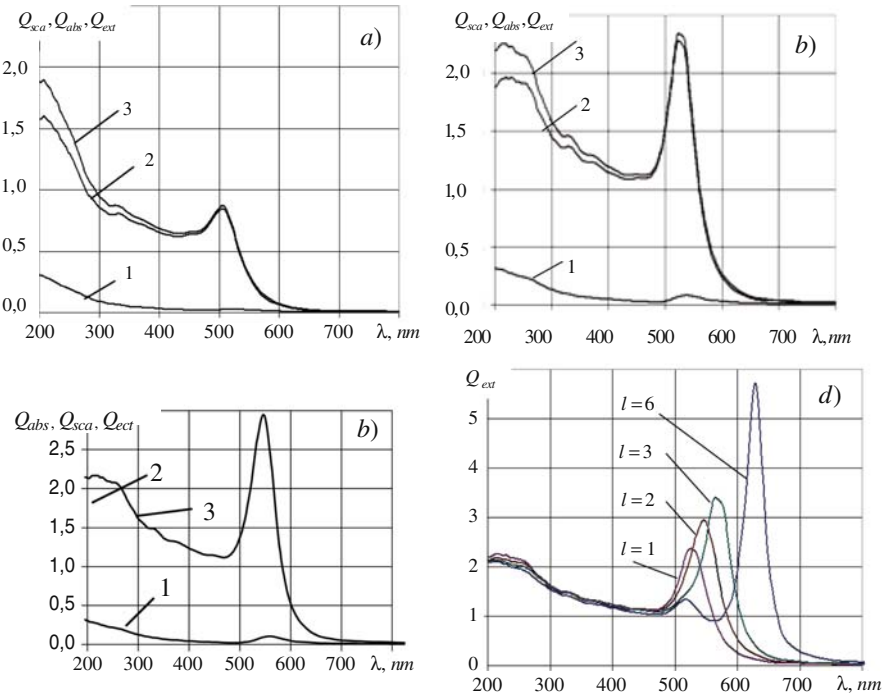

Fig. 1.4 Spectra of golden particle distant from the substrate: **a** particle alone; **b** spectra of golden particle placed on the golden substrate (dipole approximation); **c** (quadrupole approximation); **d** impact of multipoles taken into account on the extinction spectrum for the golden particle placed on the golden substrate; *1* Q_{sca} , *2* Q_{abs} , *3* Q_{ext}

Table 1.1 Values of resonance wavelengths for different number of multipoles taken into consideration (a golden particle on the golden substrate)

l	1	2	3	6	8
λ_r (nm)	521	548	563	629	669

The second example of a silver spherical particle on a silver substrate was considered in our work [20].

1.4.4 Surface Excitations of Spheroid: General Case

According to tradition, the MDS spectrum for spatially confined systems is calculated in the presence of external electromagnetic field. For spatially confined systems their polarizability and SEM frequencies are calculated on the appearance of anomalous growth of their polarizability. In other words, a heterogenous system

of differential equations is solved for corresponding system though the spectrum itself of surface MDS can be found from the homogeneous system of Maxwell equations for the specific problem as the condition of existence of nontrivial solutions [21, 22]. This method was used in the given work for calculation of surface plasmons' spectrum in spherical metallic particle. The frequencies of surface modes $\omega_{lm}(\xi)$ are calculated. Dependences of these frequencies are calculated numerically from ellipsoids' oblongness $\xi = 1/e$ (e is an ellipse eccentricity) for different values of l and m.

In any spatially confined media, fluctuations of electromagnetic field always take place [23]. The spectrum of possible excitations in the media is formed by Maxwell equation and boundary conditions corresponding to the given problem. For electrostatic approximation for the case of spheroid these equations and boundary conditions look like [7]

$$\Delta V = 0, (\vec{E} = -grad\ V), \tag{1.38}$$

$$E_t^{(in)} = E_t^{(out)}; \varepsilon_{in} E_n^{in} = \varepsilon_{out} E_n^{out}, \tag{1.39}$$

where $V(x,y,z)$ is an electric field potential in an arbitrary point of space (x,y,z),E_t^{in} and E_n^{in} the tangential and normal components to the surface arranging electrical field $\vec{E}$ inside spheroid, E_t^{out} and E_n^{out} the same components $\vec{E}$ outside of the spheroid. Taking symmetry of the problem into consideration, the solving of the problem can be exposed in a spherical coordinates' system (ξ,η,φ) [13, 14]. Cartesian coordinates (x,y,z) are connected with these coordinates with formulae [13]

$$\begin{array}{ll} x = f\,\xi\,\eta & 1 \le \xi \le \infty, \\ y = f\,(\xi^2 - 1)^{1/2}(1 - \eta^2)^{1/2}\,\cos\,\varphi & -1 \le \eta \le 1, \\ z = f\,(\xi^2 - 1)^{1/2}\,(1 - \eta^2)^{1/2}\,\sin\,\varphi & 0 \le \varphi < 2\pi, \end{array} \tag{1.40}$$

where f is a focal distance of great semi-axis for ellipsoid of revolution.

Taking into consideration a physical idea about limited nature of the potential V and its first derivatives' in any space points, solution of Eq. (1.38) for internal *(in)* and external *(out)* space regions relatively to the ellipsoid surface can be exposed:

$$V_{in} = P_l^m(\xi)\,P_l^m(\eta)\,[A\,\cos m\varphi + B\,\sin m\varphi], \tag{1.41}$$

$$V_{out} = Q_l^m(\xi)\,P_l^m(\eta)\,[C\,\cos m\varphi + D\,\sin m\varphi], \tag{1.42}$$

where $P_l^m(\xi)$, $Q_l^m(\xi)$ are Legendre polynomials of the first and the second kind.

Taking into consideration boundary conditions (1.39) and formulae (1.41), (1.42), it can be found that

$$\varepsilon_{in}\frac{P_l'^m(\xi_o)}{P_l^m(\xi_o)} = \varepsilon_{out}\frac{Q_l'^m(\xi_o)}{Q_l^m(\xi_o)}, \tag{1.43}$$

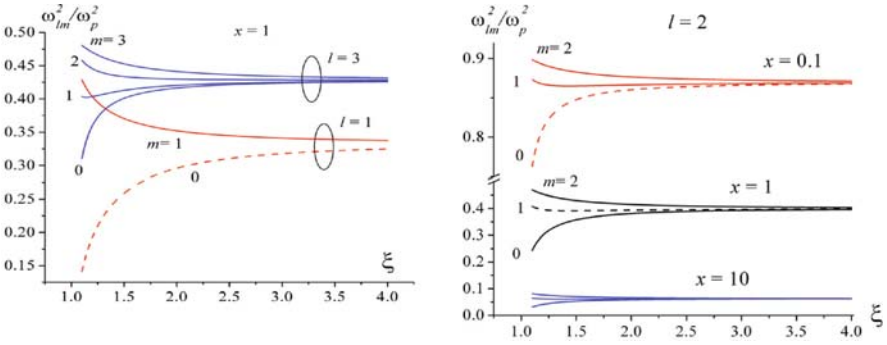

(a) (b)

Fig. 1.5 (**a**) Frequencies SP (ω_{lm}) of elongated spheroid versus $\xi = 1/e$ for $l = 1$, $l = 3$ for at $x = 1$, $\varepsilon_h = \varepsilon_\infty = 1$. (**b**) Frequencies SP (ω_{lm}) of elongated spheroid versus $\xi = 1/e$ for $l = 2$ at $x = 0{,}1$; $x = 1$; $x = 10$

where the stroke at Legendre polynomials means differentiation by ξ for specific spheroid. Equation (1.43) is the basic one for determining surface modes' frequencies of an arbitrary spheroid.

Let us analyze a metallic spheroid disposed into a dielectric space with permittivity $\varepsilon_{out} = \varepsilon_a$ independent of frequency ω. Dielectric function for spheroid is taken in Droude form [3] $\varepsilon_{in} = \varepsilon_\infty - \Omega_p^2/[\omega(\omega + i\nu)]$. Finally, we obtain an equation for calculating the spectrum of surface plasmons (SP) in metallic spheroid for the general case:

$$\left(1 - \frac{\omega_p^2}{\omega_{em}^2}\right) \frac{P_l'^m(\xi_o)}{P_l^m(\xi_o)} = x \frac{Q_l'^m(\xi_o)}{Q_l^m(\xi_o)}, \tag{1.44}$$

Where $\omega_p^2 = \Omega_p^2/\varepsilon_\infty$, $x = \varepsilon_a/\varepsilon_\infty$, and ω_{em} are the frequencies of the surface modes for the metallic spheroid.

Using recurrent dependencies for Legendre polynomials $P_l^m(\xi)$ и $Q_l^m(\xi)$ [14], numerical procedure was realized of calculating dependencies SP of the spheroid $\omega_{lm}(\xi)$ from $\xi = 1/e$ for different l and m values. The calculation results are shown in Fig. 1.5.

As follows from Fig. 1.5, in contrast to frequencies of sphere surface plasmons $\omega_l^2 \Big/ \omega_p^2 = (l\varepsilon_\infty)/[l\varepsilon_\infty + (1+l)\varepsilon_h]$, frequencies ω_{lm} depend substantially on number m (splitting on m); at that growth of spheroid's oblongness ($\xi \to 1$), the splitting increases. It is interesting to note that when the parameter $x = \varepsilon_h/\varepsilon_\infty$ changes, curves $\omega_{lm}(\xi)$ move upward (downward) at diminishing (increasing) x compared to curves $\omega_{lm}(\xi)$ at $x = 1$. This is especially important because for most of the metals $x < 1$ (for silver $\varepsilon_\infty = 4{,}5$; gold $\varepsilon_\infty = 10$) at $\varepsilon_a = 1$ (vacuum). The formulae obtained for calculating frequencies ω_{lm} of elongated ξ can be easily generalized in case of flattened ellipsoid using a simple change of ξ_0 to $i(\xi_0^2 - 1)^{1/2}$ ($i = \sqrt{-1}$). It comes from Legendre polynomials abilities [14].

1.5 Conclusion

The solution of the electrostatic boundary-value problem for a system of homogeneous spherical particles located near a homogeneous semi-infinite substrate is obtained. In the dipole–dipole approximation for two different spheres above a substrate, a system of equations was found from which expression for the polarizability tensor $\hat{\alpha}$ of each sphere was obtained. As a verification of the theory developed in this paper, we obtained the polarizability tensor both for systems of two spheres and for a sphere near a substrate.

The influence of a substrate, while not so large in the static state as might be expected, leads to new effects such as splitting and shifting of the single-sphere resonance in a time-varying external field. The quantitative characteristics of these effects were obtained by using a Lorentzian model of the permittivities for both the sphere and the substrate while neglecting damping. In the general case of an external field oriented arbitrarily with respect to the substrate's normal direction, the single-sphere resonance proves to be split into four resonances, where one pair is red shifted and the other blue shifted. This result is analogous to that obtained for a system of two spheres with no substrate and has a close analogy with the mechanical phenomenon of oscillator coupling. Not all of the new resonances are equivalent from an experimental point of view. Some of them may not be observed due to the potentially small strength of the mode.

An effective algorithm is proposed for solving an infinite system of linear algebraic equations for determination of polarizability of a small particle disposed over the substrate using reduction method whose application was proved earlier. Closed analytical formulae are elaborated for registration of dipole–dipole and quadrupole–quadrupole interaction of particle with substrate.

Registration of high multipoles gives a shift of resonance wavelength in the side of longer waves (red shift), and this shift can be a substantial one for both gold and silver. It means that in some cases registration of the dipole interaction only may be insufficient, and the registration of higher potential components (quadrupole, octupole, and interactions of higher types) is needed.

So, on the basis of elaborated general theory of small particles' interaction with various surfaces (including biological ones) as much as calculations provided it can be stated that the multipole interaction of this kind arises only in the presence of external electric field. The result is modification of electrodynamic properties of both particles and the surface: repartition of charges, shift of peaks positions, and changing absorption intensity of electromagnetic radiation by a system of particles on the surface. At this nature of changing absorption processes both particles and surface depends on the electrodynamics parameters of the surface and particles (effective permittivities, eigenmodes, physical and chemical conditions on the surface, and so on).

It can appropriately be noted that absorption intensity for the system "silver particle–silver substrate" is a few times higher then that for the system "gold particle–gold substrate."

References

1. Pitarke, J.M., Silkin, V.M., Chulkov, E.V. Echenique, P.M.: Echenique theory of surface plasmons and surface-plasmon polaritons. Rep. Prog. Phys. **70**, 1–87 (2007)
2. Angranovitch, V.M., Mills, D.D.: Electromagnetic waves on the surfaces and boundaries of matters' divisions. Nauka, Moscow (1985)
3. Bohren, C.F., Huffman, D.R.: Absorption and scattering of light by small particles. Wiley-Interscience, New York (1983)
4. Cheng, R., Furmar, T. (eds): Surface enhancement Raman scattering (tr. from Engl). Mir, Moscow (1984)
5. Kreibig, U., Volmer, M.: Optical properties of metal clusters. Springer, Berlin (1995)
6. Venger, E.F., Goncharenko, A.V., Dmitruk, M.L.: Optics of small particles and dispersion media (in Ukr). Naukova Dumka, Kyiv (1999)
7. Born, M., Wolf, E.: Principles of optics. Pergamon Press, New York (1964)
8. Haarmans, M.T., Bedeaux, D.: Optical properties of thin films up to second order in the thickness. Thin Solid Films **258**, 213–228 (1995)
9. Haarmans, M.T., Bedeaux, D.: The polarizability and the optical properties of lattices and random distributions of small metal spheres on a substrate. Thin Solid Films **224**, 117–131 (2003)
10. Gogenko, V.V., Grechko, L.G., Whites, K.W.: Electrodynamics of spatial clusters of spheres: substrate effects. Phys. Rev. B. **68**, 125422-1–125422-16 (2003)
11. Grechko, L.G., Gozhenko, V.V., Malnev, V.N., Whites, K.W.: Proceedings of the Eighth International Conference on Electromagnetics of Complex Media BIANISOTROPICS 2000, Barbosa A.M. and Topa A.L. (eds), Lisbon, 111 (2000)
12. Grechko, L.G., Whites, K.W., Pustovit, V.N., Lysenko, V.S.: Macroscopic dielectric response of the metallic particles embedded in host dielectric medium. Microelectron. Reliab. **40**, 893–895 (2000)
13. Mors, F., Feshbah, G.: Methods of Theoretical Physics Part II. McGraw-Hill (1958)
14. Abramovits, M., Stegun, A. (eds): Handbook of mathematical functions. National Bureau of Standards (1964)
15. Yamaguchi, T., Yoshida, S., Kinbara, A.: Optical effect of the substrate on the anomalous absorption of aggregated silver films. Thin Solid Films **21,** 173–187 (1974)
16. Okamoto, T., Yamaguchi, I.: Optical absorption study of the surface plasmon resonance in gold nanoparticles immobilized onto gold substrate by self-assembly technique. J. Phys. Chem. B. **107**, No. 38, 10321–10324 (2003)
17. Kantorovich, L.V., Krylov, A.I.: Approximate Methods of Higher Analysis. Gostehizdat, Leningrad-Moscow (1949) (In Russ.)
18. Jonson, P.B., Christy, R.W.: Optical constants of the noble metals. Phys. Rev. B. **6**, No. 12, 4370–4379 (1972)
19. Palik, E.D.: Handbook of optical constants of solids. Academic Press, New York (1985)
20. Vodop'yanov, D.L., Grecko, L.G., Gorbyk, P.P., Lerman, L.B., Luschenko, M.A.: Influence of multipole interaction on the spectrums of absorption of small spherical particles near-by the surface of solids (in Russ). Chem. Phys. Technol. Surf. **13**, 48–63 (2007)
21. Moussiax, A., Ronveaux, A., Lucas, A.: Surface plasmon oscillators for different geometrical shapes. Can. J. Phys. **55**, 423 (1977)
22. Brako, R., Hrncevic, J., Sunjic, M.: International Centre for Theoretical Physics. Preprint 1C/75/8
23. Barash, Yu.S., Ginsburg, V.L.: Electromagnetic fluctuations in a matter and molecular (van der Waals) forces between bodies (in Russ). UkPhJ. **116**, 1 (1975)

Chapter 2
Interaction Potential Between Two Closely Spaced Dielectric Surfaces

L.G. Il'chenko, V.V. Il'chenko, and V.V. Lobanov

Abstract The structural and total interaction potentials of the vacuum space between two dielectric quartz crystal slabs of symmetric volume features but asymmetric surface features were calculated with Green's function applied to the non-local Poisson equation.

The influence of the microscopic (atomic) structure of the surfaces and variation of the interslab width were assessed. Widths lower than 10 Å and certain co-influence of microscopic atom structures were found to increase the structural component of the total potential by forming lateral superlattices in the vacuum space with parameters exceeding the values of each dielectric surface.

2.1 Introduction

The transition from micro to nanotechnologies involves the development and use of new materials and structures with properties considerably different from the conventional ones due to the reduced size of the particles ($S < 100$ nm) and the small distance between them $L < 5$ nm [1].

In this context a detailed definition of the potential $V(\vec{r})$ becomes necessary to understand the essence of the interaction between two solid particles in the nanometer domain. The detail level must account for the differences in bulk properties of interacting particles and interparticle medium, charges, microscopic structures and adsorption layers of surfaces and external electric fields [2–9].

The decrease of the distance (L) between quasi-neutral dielectric surfaces to values lower than 5 nm is known to form a potential barrier determined by an image force potential distribution $V_j^0(x)$ [2, 3]. To allow for a continuity of $V_j^0(x)$

V.V. Lobanov (✉)
O.O. Chuiko Institute of Surface Chemistry of the National Academy of Sciences of Ukraine, General Naumov St. 17, Kyiv 03164, Ukraine
e-mail: isc-sec@isc.gov.ua

A.P. Shpak, P.P. Gorbyk (eds.), *Nanomaterials and Supramolecular Structures*,
DOI 10.1007/978-90-481-2309-4_2,

on the interfaces, a correct description of the spatial dispersion of the functions of permittivity $\varepsilon_j(\vec{k})$ in each medium is needed.

The presence of a homogeneous charge density σ_1 on the first dielectric surface and of another homogenous charge density σ_2 on the second one substantially changes the potential barrier at all values of L. Quantum-chemical calculations [6] show that the real dielectric surface is quasi-neutral. Thus, at L distances much greater than 1 nm the total interaction potential $V_2(\vec{r})$ at the centre of the vacuum space is determined by the image force potential $V_2^0(x) = V_0(x)$. Despite the quasi-neutrality of the surfaces in the macroscopic scale, at small distances ($L \leq 1$) the surfaces are essentially non-neutral, i.e., the interaction potential has a $\Delta V_2^{st}(\vec{r})$ contribution from the microscopic (atomic) structure of the surfaces [4, 5, 7–9].

This chapter deals with the calculation of the $\Delta V_2^{st}(\vec{r})$ in the hyperfine vacuum space L between two dielectric β-cristobalite crystal slabs of different microscopic surface structure. The methodology uses the Green's function as applied to the non-local Poisson equation. The calculations are carried out in the framework of local and non-local electrostatics theory taking into consideration the spatial dispersion effects in the $\varepsilon_1(\vec{k})$ and $\varepsilon_3(\vec{k})$ permittivity functions. Specifically an approximation of the Inkson interpolation model [10] is used.

The β-cristobalite surfaces are modelled with two types of ordered surface lattices ($\nu_1, \nu_2 = 2$) [6] with quasi-neutral surface charge ($\sigma_1 = \sigma_2 = 0$). The amplitude $\Delta V_2^{st}(\vec{r})$ is determined by the atomic structure, namely the values of the effective charges on the surface atoms (e_i^* and e_n^*), their two-dimensional concentration (N_i and N_n), the number and type of surface lattices (square, rectangular, triangular, etc.) and the intersurface distance L.

At small L values ($L \leq 1$nm) the structural potential $\Delta V_2^{st}(\vec{r})$ was found to determine lateral changes in the height of the potential barrier in the vacuum space between the dielectric surfaces. The interaction of the microscopic surface structures of each slab results in the formation of ordered lateral superlattices of total potential $V_2(\vec{r})$. These superlattices show parameter values that exceed those of their parent dielectric surface and promote the ordered localization of charged particles (electrons, ions) in the interslab vacuum space.

2.2 Fundamentals of the Theoretical Method

Some solutions to the problem of calculating the potential of a point charge $\pm e$ in the general (vacuum) energy level for a three-layer system of two dielectric media enclosing vacuum space can be found that use the Green's function as applied to the non-local Poisson equation [2, 3, 11, 12]. The system is commonly described by a dielectric function $\varepsilon_1(\vec{k})$ and a surface charge density $\sigma_1(y, z)$ on the first dielectric medium in the range $x \leq 0$ and with a dielectric function $\varepsilon_3(\vec{k})$ and surface charge density $\sigma_2(y, z)$ on the second one in the range of $x \geq L$. Dielectric media are separated by a vacuum space at $0 \leq x \leq L$ ($\varepsilon_2(\vec{k}) = 1$).

The Green's function of a longitudinal field $D(q; x, x')$ describing the screened Coulomb interaction between the charges at the points x and x' is determined by the

Poisson's equation [2, 3, 11, 12]:

$$\left(\frac{\partial^2}{\partial x^2} - q^2\right) \cdot D\left(q;x,x'\right) - 4\pi e^2 \int dx' \Pi(q;x,x') D\left(q;x',x\right) = \delta\left(x - x'\right), \quad (2.1)$$

where $\delta(z)$ is the delta-function, $\Pi(q;x,x')$ is the polarization operator of the heterogeneous system and $q = \left\{q_y, q_z\right\}$ is the two-dimensional component of the wave vector.

The solution of the homogeneous Poisson's equation (2.1) for $D_j(q;x,x')$ can be written in the following form:

$$\begin{aligned} &D_j(q;x,x') = \\ &-a_j(q;x)\theta(x)\partial D_j(q;0,x') + a_j(q;x)\theta(-x)\partial D_j(q;0,x') + b_{j,j-1}(q;x,x'), \end{aligned} \quad (2.2)$$

where the function $\partial D_j(q;0,x') = \left.\frac{\partial D_j(q;x,x')}{\partial x}\right|_{x=0}$ is the derivative in the case of $\varepsilon_j(\vec{k}) \to 1$ for $\vec{k} \to \infty$ and $\partial D_j(q;0,x') = \varepsilon_j \cdot \left.\frac{\partial D_j(q;x,x')}{\partial x}\right|_{x=0}$ if $\varepsilon_j(\vec{k}) \to \varepsilon_j$ while $\vec{k} \to \infty$; $\theta(x)$ is the step function.

Functions $a_j(q;x)$ and $b_{j,j-1}(q;x,x') = b_j(q;x)\delta_{j,j-1}$ have the following form [2, 11, 12]:

$$a_j(q;x) = \frac{1}{\pi} \int_{-\infty}^{\infty} \frac{dk_\perp \exp(ik_\perp x)}{\varepsilon_j(k_\perp,q) \cdot (k_\perp^2 + q^2)}, \quad (2.3)$$

$$b_j(q;x,x') = \frac{1}{2}\left[a_j(q;x-x') + a_j(q;x+x')\right], \quad (2.4)$$

where $k_\perp$ is the component of the wave vector normal to the interface and $\delta_{j,j-1}$ is the Kronecker symbol.

Under the condition of potential's continuity and considering the sharp change $4\pi\sigma_k(q)$ in the normal component of the electrostatic induction vector at the dielectric surfaces ($x = 0$ and $x = L$) the function $D_j(q;x,x)$ can be written as

$$D_j(q;x,x) = D_j^0(q;x,x) + \Delta D_j(q;x). \quad (2.5)$$

The $D_j^0(q;x,x)$ term strongly determines the total potential polarization component $V_j^0(x)$. This is related to the difference in bulk properties of three media (image force potential) [11, 12].

The $\Delta D_j(q;x)$ term determines the total potential component $\Delta V_j(\vec{r})$ caused by the interfaces charge and is defined by the following expression [4, 5, 7–9]:

$$\Delta V_j(\vec{r}) = -e \int_{-\infty}^{\infty} \int_{-\infty}^{\infty} \frac{dq_y dq_z}{(2\pi)^2} \exp\left[i(q_y y + q_z z)\right] \cdot \Delta D_j(q_y,q_z;x), \quad (2.6)$$

where the Green's function $\Delta D_j(q;x)$ in a vacuum space ($j = 2$) between two dielectric surfaces is expressed as [4, 5]:

$$\begin{aligned}\Delta D_2(q;x) = -\frac{4\pi}{B(q)} \{\sigma_1(q) \cdot a_1(q;0) \cdot [sh[(L-x)\cdot q] \\ +q \cdot a_3(q;L) \cdot ch[(L-x)\cdot q]] . + \sigma_2(q) \cdot a_3(q;L) \cdot [sh(x \cdot q) \\ +q \cdot a_1(q;0) \cdot ch(x \cdot q)]\}, (0 \le x \le L),\end{aligned} \tag{2.7}$$

In the last equation

$$B(q) = sh(q \cdot L) \cdot \left[1 + q^2 \cdot a_1(q;0) \cdot a_3(q;L))\right] + q \cdot ch(q \cdot L) \cdot [a_1(q;0) + a_3(q;L)]. \tag{2.8}$$

To account for the microscopic structure of the surfaces it is convenient to consider that the charge densities σ_1 on the first ($x \le 0$) and σ_2 on the second ($x \ge L$) dielectric surfaces are generated by the ordered lattices of the surface atoms. For the sake of simplicity of the calculations only square lattices were considered. The lattices have sides of length a_i and a two-dimensional concentration $N_i = a_i^{-2}$. The i-type atoms on the first lattice ($k = 1$) have an effective charge e_i^* on the surface. On the second lattice ($k = 2$) sides are of length b_i and a two-dimensional concentration $N_n = b_n^{-2}$. The n-type surface atoms have an effective charge e_n^*. The Fourier components of the surface atoms charge density of the first and second slabs, i.e., $\sigma_1(q)$ and $\sigma_2(q)$, can be represented in the following form [4, 5, 7–9]:

$$\begin{aligned}l\sigma_1(q) &= \sum_{i=1}^{\nu_1} \sigma_i(q) = \\ &= (2\pi)^2 \sum_{i=1}^{\nu_1} e_i^* N_i \left[\delta(q_y)\delta(q_z) + \delta\left((q_y - 2\pi/a_i)\right)\delta(q_z - 2\pi/a_i)\right],\end{aligned} \tag{2.9}$$

$$\begin{aligned}l\sigma_2(q) &= \sum_{n=1}^{\nu_2} \sigma_n(q) = \\ &= (2\pi)^2 \sum_{n=1}^{\nu_1} e_n^* N_n \left[\delta(q_y)\delta(q_z) + \delta\left((q_y - 2\pi/b_n)\right)\delta(q_z - 2\pi/b_n)\right],\end{aligned} \tag{2.10}$$

where ν_1 and ν_2 are the number of types of nuclear lattices on each of the two surfaces. The first component in (2.9) and (2.10) corresponds to the homogeneous (not modulated) charge density on the first and second surfaces.

In the absence of external fields and in the case where the slab surfaces can be considered quasi-neutral surfaces $\left(\sigma_1 = \sum_{i=1}^{\nu_1} \sigma_i = 0; \sigma_2 = \sum_{n=1}^{\nu_2} \sigma_n = 0\right)$, the distribution of the potential $V_2(\vec{r})$ in the vacuum space will be determined by the image

forces potential $V_2^0(x)$ and the structural potential $\Delta V_2^{st}(\vec{r})$. The latter is determined by the nuclear (microscopic) structure of the interfaces, i.e.,

$$V_2(\vec{r}) = V_2^0(x) + \Delta V_2^{st}(\vec{r}).$$

Let us define the structural potential $\Delta V_2^{st}(\vec{r})$ distribution for the system of two dielectric slabs enclosing a vacuum space. This is commonly referred to as the dielectric–vacuum–dielectric (DVD) system. In the framework of local electrostatics the inductivity functions meet the condition

$$\varepsilon_1(\vec{k}) = \varepsilon_1 = const,\ \varepsilon_3(\vec{k}) = \varepsilon_3 = const. \tag{2.11}$$

Taking (2.11) into account and integrating (2.3) for the expansion coefficients (2.2),

$$a_1(q;0) = \frac{1}{\varepsilon_1 q};\ a_3(q;L) = \frac{1}{\varepsilon_3 q}. \tag{2.12}$$

By substituting (2.12), (2.9) and (2.10) in (2.8) and (2.7), and then in (2.6), the distribution of the structural potential $\Delta V_2^{st}(\vec{r})$ in the vacuum space ($0 \le x \le L$) of the DVD can be expressed as

$$\begin{aligned}
&\Delta V_2^{st}(\vec{r}) = \\
&= \pm 4\pi e \cdot \left\{ \sum_{i=1}^{\nu_1} \frac{e_i^* N_i \cdot [\varepsilon_3 \cdot sh\,[(L-x)\cdot\alpha_i] + ch\,[(L-x)\cdot\alpha_i]]}{\alpha_i \cdot [(\varepsilon_1\varepsilon_3+1)\cdot sh\,(L\cdot\alpha_i) + (\varepsilon_1+\varepsilon_3)\cdot ch\,(L\cdot\alpha_i)]} \times \right. \\
&\times \cos\left(\frac{2\pi}{a_i}y\right)\cdot\cos\left(\frac{2\pi}{a_i}z\right) \\
&+ \sum_{n=1}^{\nu_2} \frac{e_n^* N_n \cdot [\varepsilon_1 \cdot sh\,(x\cdot\beta_n) + ch\,(x\cdot\beta_n)]}{\beta_n \cdot [(\varepsilon_1\varepsilon_3+1)\cdot sh\,(L\cdot\beta_n) + (\varepsilon_1+\varepsilon_3)\cdot ch\,(L\cdot\beta_n)]} \times \\
&\left. \times \cos\left(\frac{2\pi}{b_n}y\right)\cdot\cos\left(\frac{2\pi}{b_n}z\right)\right\} \quad (0 \le x \le L)\,.
\end{aligned} \tag{2.13}$$

The spatial dispersion of the dielectric functions $\varepsilon_1(\vec{k})$ and $\varepsilon_3(\vec{k})$ is conveniently treated by means of the Inkson interpolation model in which the dielectric functions are considered to have the form [10]

$$\varepsilon_{1,3}(\vec{k}) = 1 + \frac{\varepsilon_{1,3} - 1}{1 + \left(\vec{k}^2/\lambda_{1,3}^2\right),(\varepsilon_{1,3} - 1)}, \vec{k}^2 = k_\perp^2 + q^2. \tag{2.14}$$

In this equation $\varepsilon_{1,3}$ are the dielectric constants (with $\vec{k} \to 0$), $\lambda_{1,3}^{-1}$ the effective radii of the screening ion cores of the dielectric (semiconductor) crystal lattice with bound (valence) electrons.

Substituting (2.14) in (2.3) and integrating over $k_\perp$, we obtain (as compared to (2.12))

$$a_1(q,0) = \frac{1}{\varepsilon_1 q\sqrt{q^2+\Lambda_1^2}}\left[\sqrt{q^2+\Lambda_1^2}+(\varepsilon_1-1)\cdot q\right], \tag{2.15}$$

$$a_3(q,L) = \frac{1}{\varepsilon_3 q\sqrt{q^2+\Lambda_3^2}}\left[\sqrt{q^2+\Lambda_3^2}+(\varepsilon_3-1)\cdot q\right]. \tag{2.16}$$

In this equation $\Lambda_{1,3} = \lambda_{1,3}\cdot\sqrt{\frac{\varepsilon_{1,3}}{\varepsilon_{1,3}-1}}$.

Expressions for the structural potential $\Delta V_2^{st}(\vec{r})$ based on non-local electrostatics can be thus obtained by integrating (2.6) and taking into account (2.7), (2.8), (2.9), and (2.10), (2.15) and (2.16) for the DVD system. These expressions depend on the width L of the vacuum space and the bulk properties of the interacting dielectrics (semiconductors), i.e., the dielectric constants $\varepsilon_{1,3}$ of the crystal lattices and the effective screening radii of the ion cores of the crystal lattice with bound electrons, $\lambda_{1,3}^{-1}$. These are, however, too lengthy and they are spared for the sake of simplicity.

2.3 Results

The allowance for spatial dispersion effects in the functions $\varepsilon_{1,3}(\vec{k})$ of dielectrics when the Inkson interpolation model is used is known to guarantee the continuity of the image forces potential $V_2^0(x) = V_0(x)$ on the interfaces. This continuity cannot be achieved by classical representations [2, 3].

In Fig. 2.1 the solid curves represent the potential barrier formation in the vacuum space between two dielectrics. Silicon dioxide with bulk properties of β-cristobalite ($\varepsilon_{1,3} = 4.4$ and $\lambda_{1,3} = 1.603\times 10^7\text{cm}^{-1}$) was chosen as an example.

As seen in Fig. 2.1 (also see [3–5]) the image forces potential, calculated for a charge $\pm e$ with non-local electrostatics, is continuous on the interfaces. The height of the potential barrier in the vacuum space L increases with distances from the dielectric surface. The continuity of $V_0(x)$ enables a correct charging condition for each of the two dielectric surfaces.

Figure 2.2 shows the structural potential $\Delta V_2^{st}(\vec{r})$ distribution in the DVD system when the vacuum space separates two β-cristobalite monocrystals with symmetrical bulk properties, different microscopic (nuclear) structures and quasi-neutral surfaces.

Figure 2.2 shows that the shorter the L value the higher the contribution of the surface microscopic structure. The allowance for spatial dispersion effects in the dielectric functions considerably increases the contribution of the structural potential $\Delta V_2^{st}(\vec{r})$ in the total potential $V_2(\vec{r})$ as compared to the same effect calculated on the base of local electrostatics.

The total potential $V_2(\vec{r})$ ($y = 0$, $z = 0$) for positive charges $+e$ (solid curve 1) and negative charges $(-e)$ (solid curve 2) for the DVD system is shown in Fig. 2.3.

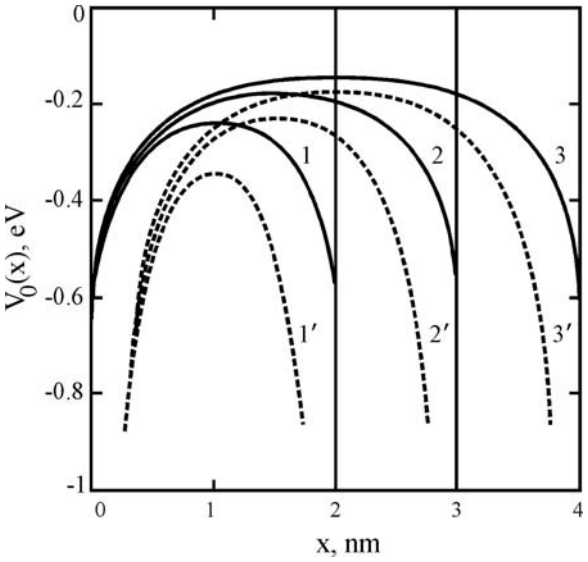

Fig. 2.1 Image force potential $V_0(x)$ for a DVD system with two identical β-cristobalite monocrystals enclosing a vacuum space with $L = 2$ nm (*1*), $L = 3$ nm (*2*) and $L = 4$ nm (*3*), respectively. *Dashed curves* $1' - 3'$: $V_0(x)$ distribution in the vacuum space as predicted by classical dielectric theory (2.11)

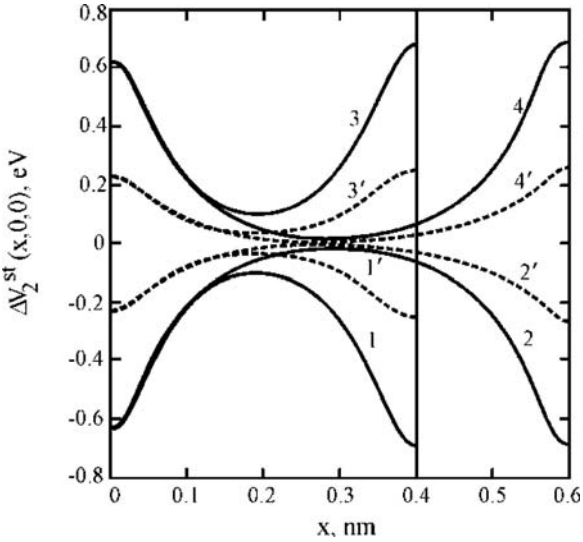

Fig. 2.2 $\Delta V_2^{st}(x,0,0)$ distribution in a $SiO_2(111)$ –vacuum– $SiO_2(100)$ system with symmetrical bulk properties plotted for two values of the vacuum space lengths ($L = 0.4$ nm and $L = 0.6$ nm). $\varepsilon_{1,3} = 4.4$; $\lambda_{1,3} = 1.603 \times 10^7$ cm^{-1}. $SiO_2(111)$ $(x \leq 0)$: $e_1^* = 1$, $N_1 = 4.5 \times 10^{14}$ cm^{-2}; $e_2^* = -0.5$, $N_2 = 9 \times 10^{14}$ cm^{-2}. $SiO_2(100)$ $(x \geq L)$: $e_1^* = 1.18$, $N_1 = 3.9 \times 10^{14}$ cm^{-2}; $e_2^* = -0.59$, $N_2 = 7.8 \times 10^{14}$ cm^{-2}. *Solid lines* (*1, 2*): positive ($+e$) charge. *Dotted lines* (*3, 4*): negative ($-e$) charge. *Dotted lines 1–4* represent the $\Delta V_2^{st}(x,0,0)$ distribution as obtained from (2.13) with local electrostatics

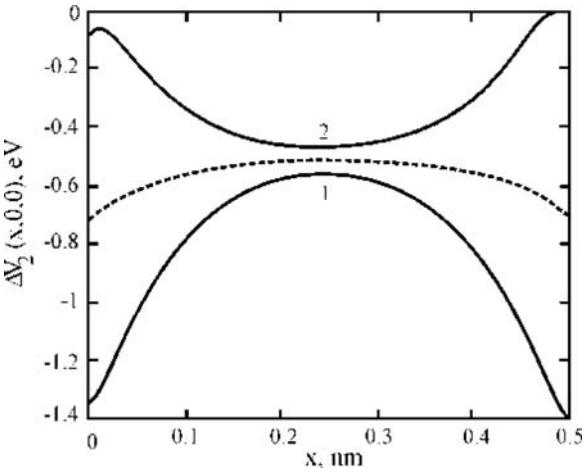

Fig. 2.3 $V_2(x,0,0)$ distribution in a $SiO_2(111)$–vacuum–$SiO_2(100)$ system with symmetrical bulk properties as obtained from non-local electrostatics (*solid curves 1* and *2*). The *dotted curve* represents the image forces potential $V_0(x)$ at $L = 0.5$ nm [3]. Parameters of surface microscopic structure as in Figure 2.2

It can be seen again that the use of spatially dispersed dielectric functions and the Inkson interpolation model (2.14) not only leads to a continuity of the image forces potential $V_0(x)$ and total potential $V_2(\vec{r})$ on the interfaces ($x = 0$, $x = L$) but also to an increase of the structural potential $\Delta V_2^{st}(\vec{r})$ contribution as compared with the same contribution calculated with local electrostatics (2.13).

Fig. 2.4 is a plot of the lateral (along the interfaces) total potential $V_2(L/2,y,0)$ distribution at the centre of the vacuum space. It can be seen that for small values of L, i.e., values smaller than 1 nm, the contribution of the structural potential $\Delta V_{st}(\vec{r})$ leads to a lateral change in the potential barrier height due to an overlapping of contributions from the microscopic (nuclear) structures of the surfaces. An ordered lattice of total potential $V_2(\vec{r})$ inside of the vacuum space is thus created.

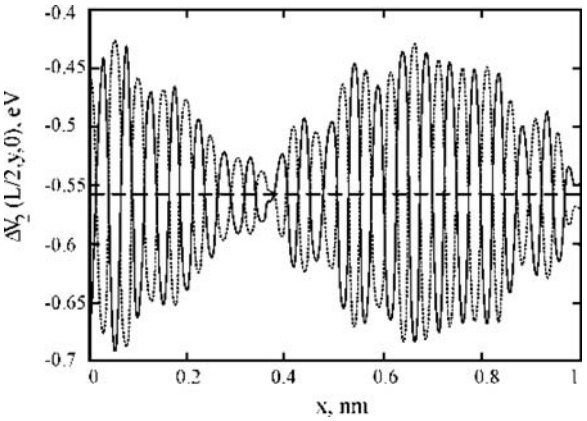

Fig. 2.4 Total potential $V_2(L/2,y,0)$ at the centre of a vacuum space of length $L = 0.4$ nm. $SiO_2(111)$ –vacuum– $SiO_2(100)$ system as depicted in Fig. 2.2 caption. The *horizontal dashed line* represents the value of the image force potential $V_0(x)$ at the centre of the vacuum space $x = L/2$

2.4 Conclusions

The structural and total interaction potentials in the vacuum space between two dielectric β-cristobalite crystal slabs with symmetrical bulk properties and different surface features have been calculated with the use of the Green's function applied to the non-local Poisson equation.

Calculations of the structural potential $\Delta V_2^{st}(\vec{r})$ in the hyperfine vacuum space show that the inclusion of spatial dispersion effects in the inductivity functions $\varepsilon_{1,3}(\vec{k})$ leads to two results: (1) a continuity of the image force potential $V_0(x)$ and the total potential $V_2(\vec{r})$ on the slabs and (2) an increase of the $\Delta V_2^{st}(\vec{r})$ contribution as compared to that predicted by local electrostatics.

The study of quasi-neutral surfaces with two types of ordered surface lattices $\nu_1, \nu_2 = 2$ shows that when the interslab space is narrowed to values in the 0.3–2 nm range the structural potential $\Delta V_2^{st}(\vec{r})$ increases (decreases) the total potential barrier in the vacuum space depending on the effective charge $e_{i,n}^*$ of the surface atoms, their two-dimensional concentration $N_{i,n}$, the type of surface lattices and the ion charge sign $\pm e$.

The influence of the microscopic (atomic) structure of the surfaces and the distance from the slab surface ($0 \leq x \leq L$) were also assessed. width lower than 1 nm and the overlap of contributions from the microscopic atom structures were found to increase the structural component $\Delta V_2^{st}(x,y,0)$ of the total potential $V_2(x,y,0)$. Lateral superlattices were formed in the vacuum space with parameters exceeding the values of each dielectric surface.

References

1. Roco M, Williams R, Alivisatos P (2000) Nanotechnology Research Directions Vision for Nanotechnology in the Next Decade. Kluwer Academic Publishers, Norwell
2. Il'chenko L, Goraychuk T (2001) Role of the image forces potential in the formation of the potential barrier between closely spaced metals. Surf Sci 478:169–179
3. Goraychuk T, Il'chenko L (2003) Image forces between closely separated dielectrics. Chem Phys Technol Surf 9:11–17
4. Il'chenko L, Lobanov V, Chuiko A (2004) Effect of surface microstructure on the interaction potential between dielectric nanoparticles. Nanosyst Nanomater, Nanotechnol 2: 1145–1158
5. Il'chenko L, Lobanov V, Chuiko A (2006) Role of surface microstructure in forming interaction potential between closely separated with vacuum space non-identical dielectric (semiconductor) nanoparticles. Chem Phys Technol Surf 11–12:4–19
6. Lobanov V, Gorlov Yu, Chuiko A et al (1999) Role of Electrostatic Interactions in Adsorption on Solid Oxide Surfaces. VEK Ltd, Kyiv
7. Il'chenko L, Grechko L, Savon A (1993) Spatial distribution of electrostatic potential near dielectric surface with modulated surface charge. 1. Atomically pure dielectric surface. Ukr Fiz Zhurn 38:415–420
8. Il'chenko L, Il'chenko V, Goraychuk T et al (2001) Microscopic structure of the semiconductor surface in the external electric field. Chem Phys Technol Surf 4–6:186–195
9. Il'chenko L (1999) Role of microscopic structure of the surface in field emission from semiconductors. 12th International Vacuum Microelectronics Conference 6–9 July 1999. Darmstadt, Germany, Technical Digest 84–85

10. Inkson J (1971) The electrostatic image potential in metal semiconductor junctions. J Phys Chem 4:591–597
11. Il'chenko L, Pashitskii E, Romanov Yu (1982) Charge interaction in layered systems with spatial dispersion. Surf Sci 121:375–395
12. Il'chenko L, Litovchenko V, Kryuchenko Yu (1995) Electron field emission (FE) from quantum size systems. Appl Surf Sci 87/88:53–60

Chapter 3
Mechanical Motion in Nonequilibrium Nanosystems

V.M. Rozenbaum

Abstract Unidirectional mechanical motion of nanoobjects along an interface can result from highly nonequilibrium processes which transmit the energy from various external sources to the system. Phenomena of this kind underlie the operation of so-called Brownian (molecular or biological) motors and have been attracting a great research interest in the last few decades. This chapter presents the main necessary conditions for directed motion of nanoparticles along the surface under the action of external nonequilibrium fluctuations; the methods to realize such conditions are also considered. Several examples are given for high-efficiency Brownian motors, molecular pumps, photoinduced molecular motors, and dipole rotators (the latter rotate unidirectionally in a linearly polarized alternating electric field).

Nonequilibrium fluctuations in asymmetric media which cause the directed motion of Brownian particles even in the absence of an external field have stimulated a great deal of interest in the recent decades [1–3]. The challenge is to gain an insight into high-efficiency energy conversion in various kinds of Brownian motors (such as nanovehicles, molecular pumps, particle segregators, etc.) mostly powered by the exothermic hydrolysis of adenosine triphosphate. On the other hand, a strong practical motivation for the research in this area is to artificially mimic the operational mechanisms of natural nanodevices aiming at significant technological and engineering breakthroughs.

As a rule, nonequilibrium fluctuations result from an external process which determines the time dependence of potential energy parameters. To exemplify, a catalytic chemical reaction proceeding on a Brownian particle gives rise to temporal fluctuations of the particle charge $q(t)$ between two values, q_+ and q_- (see the left part of Fig. 3.1). If the particle is placed in a spatially periodic asymmetric potential $\varphi(x)$, its potential energy becomes time-dependent: $U(x,t) = q(t)\varphi(x)$ [3]. A similar time dependence of the potential energy, $U(x,t) = -\boldsymbol{\mu}(t) \cdot \mathbf{E}(x)$, can be caused by

V.M. Rozenbaum (✉)
O.O. Chuiko Institute of Surface Chemistry of the National Academy of Sciences of Ukraine, General Naumov St. 17, Kyiv 03164, Ukraine
e-mail: vrozen@isc.gov.ua

A.P. Shpak, P.P. Gorbyk (eds.), *Nanomaterials and Supramolecular Structures*,
DOI 10.1007/978-90-481-2309-4_3,

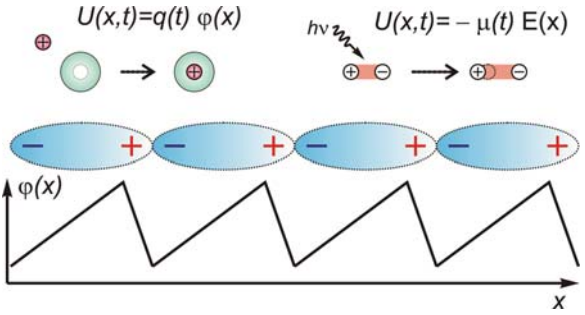

Fig. 3.1 The origin of the time-dependent potential energy of a Brownian particle near a polar substrate

fluctuations of the particle dipole moment $\boldsymbol{\mu}(t)$ in a spatially periodic asymmetric external electric field $\mathbf{E}(x)$ (see the right part of Fig. 3.1). Dipole moment fluctuations can be generated by switching on/off the resonance laser radiation, i.e., by changing the dipole moment of a molecule on its excitation/deexcitation [4]. In the above examples, the time dependence of the potential energy $U(x,t)$ represents the fluctuations between two potential reliefs, $U_+(x)$ and $U_-(x)$, which are identically shaped but differently extended along the energy axis in the "+" and "–" states. As another instance, the dichotomous fluctuations of the potential energy arise when the energy profile is shifted by half a period $L/2$ on the transitions between two states: $U_-(x) = U_+(x + L/2)$ [5]. The fluctuations concerned can occur at certain periodic time intervals or in a probabilistic manner; the former case corresponds to a deterministic and the latter to a stochastic dichotomous process. Brownian motors with the dichotomous fluctuations of the potential energy significantly differ in kinematics from those in which the potential energy continuously changes in time (e.g., from a dipole rotator in a symmetric hindered-rotation potential which rotates unidirectionally under the action of a linearly polarized alternating electric field [6, 7]).

Thus, the first necessary condition for the directed motion to occur is nonequilibrium fluctuations which supply the system with the energy drawn from various external sources. The fluctuations can be induced by fast chemical reactions or by abruptly changing electric fields if they cause jumps in the rate constants of the chemical reactions relevant to directed particle transfer [8–12]. The corresponding models include fluctuating potentials when the reaction-coordinate phase space can be introduced [13–15].

The second necessary condition implies that the system has a particular direction due to the asymmetric potential or electric field (see Fig. 3.1) which, in turn, are provided by polar substrates or orientationally ordered monolayers of adsorbed polar molecules [16]. Indeed, the ground state of two-dimensional dipole systems is represented by multichain ferroelectric or antiferroelectric structures (depending on the type of the adsorbate lattice), with dipole moments oriented parallel to chain axes.

Let the dipole chain have the period L and collinear orientations of the dipole moments μ_0 along the chain axis; the axis x is specified by the chain axis (so that the value $x = 0$ determines the position of a certain dipole) and the axis z is perpendicular to the axis x. Then the electric field potential at the point with the coordinates x, z

can be expressed as a rapidly converging series in the McDonald functions K_0 [17]:

$$\varphi_z(x) = \frac{8\pi\mu_0}{L^2}\sum_{h=1}^{\infty} hK_0\left(\frac{2\pi h}{L}z\right)\sin\left(\frac{2\pi h}{L}x\right). \tag{3.1}$$

At $z/L \geq 0.3$, the series can, to high accuracy, be restricted to the first two terms. In particular, at $z/L \approx 0.28$, the potential appears as the function

$$\varphi(x) = \left(8\pi\mu_0/L^2\right)K_0(1.76)[\sin(2\pi x/L) + 4^{-1}\sin(4\pi x/L)], \tag{3.2}$$

which is approximated well by the asymmetric sawtooth potential.

The dynamics of a Brownian particle with the fluctuating potential energy is defined by the Langevin equation:

$$ma = -\zeta v - U'_x(x,t) - f(t), \tag{3.3}$$

where m, a, v, respectively, denote the particle mass, acceleration, and velocity; ζ is the friction coefficient, and $-U'_x(x,t) = -\partial U(x,t)/\partial x$ is the position- and time-dependent force acting on the particle from the substrate. The difference between Eq. (3.3) and the equation of motion following from the second Newton law is that the former contains the random force $f(t)$ describing the random thermal impacts of environmental molecules. If time-averaged, this force vanishes and the correlation function taken at some fixed time instants accounts for a δ-correlated process (white noise):

$$\langle f(t)\rangle = 0\,,\ \ \langle f(t)f(t')\rangle = 2\zeta k_{\mathrm{B}}T\delta(t-t'), \tag{3.4}$$

where k_{B} is the Boltzmann constant and T is the absolute temperature.

For a nanosized particle in a sufficiently viscous medium, one can neglect the inertia force and turn to a statistical description using the distribution function $\rho(x,t)$ which determines the probability density for a particle to be at the point x at the time t. Such an approximation is adequate on the time interval $\Delta t >> m/\zeta$ which is long enough for thermodynamic equilibrium to be established in the velocity space and the diffusion coefficient $D = k_{\mathrm{B}}T/\zeta$ is much less than the product of the particle thermal velocity $v_T \sim \sqrt{k_{\mathrm{B}}T/m}$ and the spatial period L of the potential energy. The characteristic value of D has the order of magnitude 10^{-5} and 10^{-9} m^2/s for molecules in the gas and liquid phases, respectively. As is typical of most molecules, $v_T L \sim 10^{-7}$ m^2/s (at $L \sim 10$ Å) and hence the inequality $D << v_T L$ is valid only for a particle diffusing in a liquid. With this condition, the distribution function $\rho(x,t)$ satisfies the Smoluchowski equation [18]

$$\frac{\partial}{\partial t}\rho(x,t) = -\frac{\partial}{\partial x}J(x,t),\ J(x,t) = -D\left[\beta\rho(x,t)\frac{\partial}{\partial x}U(x,t) + \frac{\partial}{\partial x}\rho(x,t)\right], \tag{3.5}$$

($\beta = (k_B T)^{-1}$ is the inverse temperature) and is normalized as follows: $\int_0^L \rho\,(x,t)\,dx = 1$. The desired average velocity of the directed motion of a Brownian particle is specified by the average flux $J\,(x,t)$:

$$v \equiv \lim_{T\to\infty} \frac{1}{T} \int_0^T dt \int_0^L dx\, J(x,t). \tag{3.6}$$

As already mentioned, of particular interest are those dichotomous processes in which the time-dependent potential energy $U\,(x,t)$ fluctuates between two potential reliefs, $U_+\,(x)$ and $U_-\,(x)$. This time dependence is conveniently expressed in terms of the average value $u(x) = \big[U_+(x) + U_-(x)\big]/2$ and the amplitude $w(x) = \big[U_+(x) - U_-(x)\big]/2$ of the fluctuations

$$U\,(x,t) = u(x) + \sigma(t) w(x), \tag{3.7}$$

where the function $\sigma(t)$ assumes only two values ± 1. These values can be taken periodically by the following law:

$$\sigma(t) = \begin{cases} +1, & n\tau \le t \le n\tau + \tau_+\,, \\ -1, & n\tau + \tau_+ \le t \le (n+1)\,\tau\,, \end{cases} \quad n = 0, \pm 1, \pm 2, ... \tag{3.8}$$

Then the system exists in two alternate states with the potential reliefs $U_+\,(x)$ and $U_-\,(x)$, the respective lifetimes τ_+ and τ_-, and the total time period $\tau = \tau_+ + \tau_-$. Taking advantage of the time independence of the potential energy within either state, differential equation (3.5) is solved separately for each time interval $\tau_\pm$ and the solutions are linked together through their boundary conditions to provide distribution function continuity throughout the total period. Deterministic dichotomous processes defined by relation (3.8) are usually controllable by an external device, e.g., by a laser turned on/off at certain time instants (as in the case of photoinduced dipole motors).In contrast, stochastic dichotomous processes occur if potential energy fluctuations are driven, for instance, by chemical reactions.

A stochastic dichotomous process schematized by the equation below can be specified by the transition rates $\gamma_\pm$ between two states of the system (i.e., the average inverse lifetimes $\tau_\pm$ of the states):

$$\boxplus \underset{\gamma_-}{\overset{\gamma_+}{\rightleftarrows}} \boxminus. \tag{3.9}$$

Each state is characterized by the distribution functions $\rho_\pm(x,t)$ which obey the Smoluchowski equations (3.5) with the additionally included interstate transition rates:

$$\begin{aligned} \frac{\partial}{\partial t}\rho_\pm\,(x,t) &= -\frac{\partial}{\partial x} J_\pm\,(x,t) \; - \gamma_\pm \rho_\pm\,(x,t) + \gamma_\mp \rho_\mp\,(x,t)\,, \\ J_\pm\,(x,t) &= -D\left[\beta\rho_\pm\,(x,t)\,\frac{\partial}{\partial x} U_\pm\,(x) + \frac{\partial}{\partial x}\rho_\pm\,(x,t)\right]. \end{aligned} \tag{3.10}$$

Within the stochastic approach, stationary processes ($\partial\rho_{\pm}(x,t)\big/\partial t = 0$) are mainly concerned. When rewritten in time-independent terms, Eq. (3.10) is significantly simplified and the desired average velocity of the directed motion defined by Eq. (3.6) becomes

$$v = L\left[J_{+}(x) + J_{-}(x)\right]. \tag{3.11}$$

If the model includes thermal interstate transitions of the particle or addresses some peculiar cases when the transition probabilities depend on the particle position, then the transition rates should be coordinate-dependent: $\gamma_{\pm} = \gamma_{\pm}(x)$ (as an example, see the previously published description of a reciprocating nanoengine [19]).

Interestingly, an alternative treatment of stochastic dichotomous processes implies that the function $\sigma(t)$ in Eq. (3.7) becomes a random quantity to be averaged with regard to certain rules:

$$\begin{aligned}
&\langle\sigma\rangle = (\gamma_{-} - \gamma_{+})/(\gamma_{+} + \gamma_{-}),\\
&\langle\sigma(t)\sigma\left(t'\right)\rangle \underset{t>t'}{=} \langle\sigma\rangle^2 + \left(1 - \langle\sigma\rangle^2\right)e^{-\Gamma(t-t')}\,,\ \Gamma \equiv \gamma_{+} + \gamma_{-}\,,\\
&\langle\sigma(t)\sigma\left(t'\right)\sigma\left(t''\right)\rangle \underset{t>t'>t''}{=} \langle\sigma\rangle\left[\langle\sigma\rangle^2 + \left(1 - \langle\sigma\rangle^2\right)\left(e^{-\Gamma(t-t')} + e^{-\Gamma(t'-t'')} - e^{-\Gamma(t-t'')}\right)\right],\\
&\ldots
\end{aligned} \tag{3.12}$$

The Smoluchowski equation (3.5) now contains the random function $\sigma(t)$ and its solution $\rho(x,t)$ should also be averaged using relations (3.12). This is possible if the solution is expressible as an infinite series containing correlation functions (3.12) and can be restricted to the first terms due to the presence of a small parameter. As shown below, the high-temperature approximation allows this technique to be implemented.

In view of their position periodicity, the potential energy and the distribution function of the steady-state process can be Fourier-transformed into the coordinate x representation using the formula

$$f(x,t) = \sum_{q} f_q(t)\exp(ik_q x), \quad k_q = \left(2\pi\big/L\right)q, \tag{3.13}$$

where q is an integer, and $f(x + L,t) = f(x,t)$ is a function of coordinate and time. Then the differential equation (3.5) can be written in the integral form:

$$\rho_q(t) = L^{-1}\delta_{q,0} - \beta D k_q \exp(-Dk_q^2 t)\sum_{q'} k_{q'} \int_{-\infty}^{t} dt' U_{q'}(t')\rho_{q-q'}(t')\exp(Dk_q^2 t') \tag{3.14}$$

($\delta_{q,0} = 1$ at $q = 0$ and $\delta_{q,0} = 0$ at $q \neq 0$). We assume $t = -\infty$ as a starting instant in Eq. (3.14) to avoid interference of transient processes with the results obtained. The average velocity of the directed motion of a Brownian particle appears as

$$v = -i\beta DL\sum_{q} k_q \lim_{T\to\infty}\frac{1}{T}\int_{0}^{T} dt U_q(t)\rho_{-q}(t). \tag{3.15}$$

Solving Eq. (3.14) by iterations (with regard to the smallness of the parameter β) and substituting the solution into expression (3.15), the general representation of the average velocity is derived [20]:

$$\begin{aligned} v &= i\beta^3 D^3 \sum_{qq'} k_q^2 k_{q+q'}^2 k_{q'} F_{q,q'}, \\ F_{q,q'} &= \lim_{T\to\infty} \frac{1}{T} \int_0^T dt U_q(t) e^{-Dk_q^2 t} \int_{-\infty}^{t} dt' U_{q'}(t') e^{D\left(k_q^2 - k_{q+q'}^2\right)t'} \\ &\quad \int_{-\infty}^{t'} dt'' U_{-q-q'}(t'') e^{Dk_{q+q'}^2 t''}. \end{aligned} \tag{3.16}$$

Note that v becomes zero for the symmetric potentials $U_{-q}(t) = U_q(t)$ as a result of the double summation over the indices qq' of the expression containing the wave vectors to an odd power. For the same reason, $v = 0$ for the time-independent potential energy. As evident from the very structure of Eq. (3.16), it is only the interaction of several spatial harmonics of the potential that can provide nonzero values of v. Thus the directed motion is always initiated by nonlinear processes in an asymmetric and temporally fluctuating force field.

As a time-periodic function, the potential energy $U(x,t+\tau) = U(x,t)$ can be Fourier-transformed into the frequency representation:

$$U_q(t) = \sum_j U_{qj} \exp(-i\omega_j t), \quad \omega_j = \left(2\pi/\tau\right) j, \tag{3.17}$$

where j denotes integers. Then relations (3.16) are simplified:

$$v = i\beta^3 D^3 \sum_{qj,q'j'} \frac{k_q^2 k_{q+q'}^2 k_{q'} U_{qj} U_{q'j'} U_{-q-q',-j-j'}}{\left(i\omega_j + Dk_q^2\right)\left(i\omega_{j+j'} + Dk_{q+q'}^2\right)} \tag{3.18}$$

It should be noted that the contribution with $j = j' = 0$ vanishes by virtue of the identity $\sum_{q,q'} k_{q'} U_{q,0} U_{q',0} U_{-q-q',0} = 0$. Therefore, the desired average velocity is determined only by the time-dependent components of the potential energy with $j \neq 0$:

$$\begin{aligned} v = &-\beta^3 D^2 \sum_{\substack{q,q',j \\ (j\neq 0)}} \frac{\omega_j k_q^2 k_{q'} U_{-q-q',0} (U_{qj} U_{q',-j} + U_{q'j} U_{q,-j})}{(i\omega_j + Dk_q^2)(i\omega_j + Dk_{q'}^2)} \\ &+ i\beta^3 D^3 \sum_{\substack{qj,q'j' \\ (j\neq 0, j'\neq 0, j+j'\neq 0)}} \frac{k_q^2 k_{q+q'}^2 k_{q'} U_{qj} U_{q'j'} U_{-q-q',\,-j-j'}}{(i\omega_j + Dk_q^2)(i\omega_{j+j'} + Dk_{q+q'}^2)}. \end{aligned} \tag{3.19}$$

Representations (3.18) and (3.19) are particularly convenient to calculate the motion velocities for those Brownian motors in which the harmonic fluctuations of the potential energy are specified by the first harmonics ($j = \pm 1,\ \pm 2$). The theory of Brownian motors often employs the following spatially asymmetric function of the potential energy:

$$U(x,t) = U_1(t)\sin(2\pi x/L) + U_2(t)\sin(4\pi x/L). \tag{3.20}$$

A deterministic periodic dichotomous process is characterized by the period τ and the state lifetimes τ_+ and τ_- ($\tau = \tau_+ + \tau_-$). For convenience, we introduce the ratio of, e.g., the "–" state lifetime to the period τ: $\delta \equiv \tau_-/\tau$ ($0 < \delta < 1$). Then the Fourier components σ_j of the deterministic function $\sigma(t)$ can be expressed as $\sigma_j = 1-2\delta$ at $j = 0$ and $\sigma_j = i[1-\exp(-2\pi i\delta j)]/(\pi j)$ at $j \neq 0$. On substituting these relations into Eq. (3.18) and summing over the indices jj', the average velocity can be obtained for a potential relief with an arbitrary coordinate dependence. Though we omit the rather cumbersome explicit form of the resulting expression, its two important properties should be pointed out. First, if the lifetimes τ_+ and τ_- are much longer than the characteristic diffusion time L^2/D on a distance of the order L (and hence quasi-equilibrium can be achieved in both states of the dichotomous process), then the average velocity is described by the known relation [21] which assumes the following form in the high-temperature limit:

$$v = \frac{4i\beta^3 L}{\pi\tau}\sum_{qq'(\neq 0)}\frac{u_{q'}w_q w_{-q-q'}}{q}. \tag{3.21}$$

It is thus seen that at low frequencies $\gamma \equiv \tau^{-1}$ of the potential energy fluctuations, we arrive at $v \propto \gamma$ and δ-independence of v. The second important feature of the deterministic process is that $v \propto \gamma^{-2}$ at $\gamma \to \infty$. Of course, the above-mentioned regularities are valid only if δ is neither very close to zero nor to unity.

To derive the average velocity of a high-temperature Brownian motor governed by a Markovian stochastic dichotomous process (see Scheme (3.9)), one can use the high-temperature expansion of Eq. (3.10) to obtain its approximate solutions and substitute them into relation (3.11). As an alternative, formulae (3.7) and (3.16) with correlation functions (3.12) can be applied.The resulting expression [20] takes the form

$$v = \frac{4i\beta^3 D}{\tau}\sum_{qq'}\frac{Dk_q k_{q+q'}u_{q'} + (\gamma_+ - \gamma_-)\,w_{q'}}{\left(\Gamma + Dk_q^2\right)\left(\Gamma + Dk_{q+q'}^2\right)}k_{q'}w_q w_{-q-q'}. \tag{3.22}$$

It is clear that Eq. (3.22) is reduced to Eq. (3.21) at small Γ, i.e., the average velocity of the directed motion is independent of the stochastic or deterministic nature of the process provided that quasi-equilibrium can be achieved in both states of the dichotomous process. On the other hand, at large Γ and a sufficiently smooth

potential dominated by several first harmonics, we obtain the limiting relation $v \propto \gamma^{-1}$ which is not the same as in the deterministic process ($v \propto \gamma^{-2}$).

The structure of relation (3.22) is determined by the fact that the Smoluchowski equation (3.5) contains not potential energies themselves but their first derivatives with respect to coordinate (i.e., forces). The time-independent terms corresponding to the components u_0 and w_0 do not contribute to this relation and, accordingly, analysis of its properties involves only the Fourier components with $q \neq 0$.

The main inference to be made from Eq. (3.22) is that if the fluctuation amplitude w_q of the potential energy is larger than its average value u_q, then the direction of the motor motion can be reversed by varying the average frequency ratio γ_+/γ_-. At $\gamma_+ \neq \gamma_-$, temporal asymmetry arises which, along with spatial asymmetry, dictates the motion direction. Evidently, this regularity holds true only on condition that the sum of the terms containing $w_q w_{q'} w_{-q-q'}$ does not go to zero (contrary to, e.g., the case of potentials with half-period fluctuations which implies $w_q \neq 0$ only at odd q).

The case of most interest is $u_q = 0$; it is exemplified by the motors for which the charge or dipole moment fluctuates by the sign reversal. Then the directed motion arises solely due to the difference in two state lifetimes of the dichotomous process. In a longer state, a particle has an increased probability to be localized in the vicinity of the potential well minimum, whereas its position in a shorter state is determined by the dynamic effect of a steep descent along the abrupt slope of the potential relief. The resulting trend for the particle is to move to the right at $\tau_+ > \tau_-$ (if $\delta < 1/2$) and to the left at $\tau_+ < \tau_-$ as illustrated in Fig. 3.2.

Much promise is shown by the high-efficiency models of Brownian motors such as the potential fluctuating by half a period and the so-called "catalytic wheel" acting as a molecular pump. Highly efficient conversion of energy input into mechanical energy output in these models is due to (i) a high and narrow barrier blocking the reverse motion and (ii) the identical but mutually energy-shifted potential reliefs on both half-periods [5, 22–25]. Particle transport through biological membranes driven by electric-field fluctuations is described by the "catalytic wheel" model [25]. The fluctuations cause conformational changes in membrane channels which, in turn, give rise to particle capture from solution on one membrane side and release on the other; a circular flux thus originates which determines the operational velocity of the molecular pump.

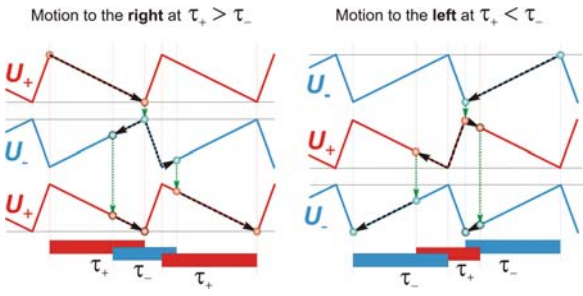

Fig. 3.2 Directed motion as a result of the competition between the spatial and temporal asymmetry of the potential energy

The directed motion of nanoparticles can also be treated as rectified reciprocating motion, reciprocation occurring at the nanoscale under the action of nonequilibrium external forces. The theory of reciprocating nanoengines, including energy aspects, has recently been developed [19]. The most significant finding is that the generalized driving force of reciprocation can arise both from the difference of potential profiles in two states of the dichotomous process and from the position dependence of interstate transition rate constants.

One of the possible implementations of near-surface molecular motors is a dipole photomotor suggested by us previously [4]. It operates due to a change in the molecular dipole moment which occurs on resonant laser-induced excitation. Another illustrative example is represented by a molecular rotor [7]. It can rotate unidirectionally only if an external alternating electric field simultaneously modulates minima and maxima of the two-well hindered-rotation potential.

To conclude, the directed motion in nanosystems can arise provided they are powered by some external sources through nonequilibrium fluctuations, on the one hand, and have spatial asymmetry, on the other hand. At the same time, temporal asymmetry, if present in a motion-generating dichotomous process, plays an equally crucial role in motor kinematics. It is the competition between the two asymmetry types that specifies the magnitude and sign of the average directed velocity thus allowing to control them by varying molecular structure, instrumental parameters, etc.

References

1. Jülicher, F., Ajdari, A., Prost, J.: Modeling molecular motors. Rev. Mod. Phys. **69**, 1269–1281 (1997)
2. Reimann, P.: Brownian motors: noisy transport far from equilibrium. Phys. Rep. **361**, 57–265 (2002)
3. Astumian, R. D.: Thermodynamics and kinetics of a Brownian motors. Science. **276**, 917–922 (1997)
4. Dekhtyar, M. L., Ishchenko, A. A., Rozenbaum, V. M.: Photoinduced molecular transport in biological environments based on dipole moment fluctuations. J. Phys. Chem. B. **110**, 20111–20114 (2006)
5. Rozenbaum, V. M.: Mechanism for the appearance of a high-efficiency Brownian motor with fluctuating potential. Pis'ma Zh. Eksp. Teor. Fiz. **79**, 475–479 (2004) [JETP Lett. **79**, 388–391 (2004)]
6. Kottas, G. S., Clarke, L. I., Horinek, D., Michl, J.: Artificial molecular rotors. Chem. Rev. **105**, 1281–1376 (2005)
7. Rozenbaum, V. M., Vovchenko, O. Ye., Korochkova, T. Ye.: Brownian dipole rotator in alternating electric field. Phys. Rev. E. **77**, 061111-1-9 (2008)
8. Tsong, T. Y., Astumian, R. D.: Absorption and conversion of electric field energy by membrane bound ATPase. Bioelectrochem. Bioenerg. **15**, 457–476 (1986)
9. Markin, V. S., Tsong, T. Y., Astumian, R. D., Robertson, R. J.: Energy transduction between a concentration gradient and an alternating electric field. Chem. Phys. **93**, 5062–5066 (1990)
10. Markin, V. S., Tsong, T. Y.: Frequency and concentration windows for the electric activation of a membrane active transport system. Biophys. J. **59**, 1308–1316 (1991)

11. Markin, V. S., Tsong, T. Y.: Electroconformational coupling for ion transport in an oscillating electric field: rectification versus active pumping. Bioelectrochem. Bioenerg. **26**, 251–276 (1991)
12. Chen, Y., Tsong, T. Y.: Comparison of kinetics of formation of helices and hydrophobic core during the folding of staphylococcal nuclease from acid. Biophys. J. **66**, 2151–2158 (1994)
13. Magnasco, M. O.: Molecular combustion motors. Phys. Rev. Lett. **72**, 2656–2659 (1994)
14. Astumian, R. D., Bier, M.: Mechanochemical coupling of the motion of molecular motors to ATP hydrolysis. Biophys. J., **70**, 637–653 (1996)
15. Keller, D., Bustamante, C.: The mechanochemistry of molecular motors. Biophys. J. **78**, 541–556 (2000)
16. Rozenbaum, V. M., Lin, S. H.: Spectroscopy and Dynamics of Orientationally Structured Adsorbates. World Scientific: Singapore (2002)
17. Korochkova, T. Ye., Rozenbaum, V. M., Chuiko, A. A.: Drift of Brownian particle due to orientationally structured adsorbate. Dop. NAN Ukr. **8**, 93–98 (2004)
18. Riskin. H.: The Fokker-Plank Equation. Methods of Solution and Applications. Springer-Verlag: Berlin (1989)
19. Makhnovskii, Yu. A., Rozenbaum, V. M., Yang, D.-Y., Lin, S. H.: Reciprocating motion on the nanoscale. J. Phys. Chem. A. **111**, 9486–9493 (2007)
20. Rozenbaum, V. M.: High-temperature Brownian motors: deterministic and stochastic fluctuations of a periodic potential. Pis'ma Zh. Eksp. Teor. Fiz. **88**, 391–395 (2008) [JETP Lett. **88**, 342–346 (2008)]
21. Parrondo, J. M. R.: Reversible ratchets as Brownian particles in an adiabatically changing periodic potential. Phys. Rev. E. **57**, 7297–7300 (1998)
22. Makhnovskii, Yu. A., Rozenbaum, V. M., Yang, D.-Y., Lin, S. H., Tsong, T. Y.: Flashing ratchet model with high efficiency. Phys. Rev. E. **69**, 021102-1-7 (2004)
23. Rozenbaum, V. M., Korochkova, T. Ye., Yang, D.-Y., Lin, S. H., Tsong, T. Y.: Two approaches toward a high-efficiency flashing ratchet. Phys. Rev. E. **71**, 041102-1-8 (2005)
24. Rozenbaum, V. M., Korochkova, T. Ye., Liang, K. K.: Conventional and generalized efficiencies of flashing and rocking ratchets: analytical comparison of high-efficiency limits. Phys. Rev. E. **75**, 061115-1-5 (2007)
25. Rozenbaum, V. M., Yang, D.-Y., Lin, S. H., Tsong, T. Y. J.: Catalytic wheel as a Brownian motor. Phys. Chem. B. **108**, 15880–15889 (2004)

Chapter 4
Surface-Assisted Laser Desorption Ionization of Low Molecular Organic Substances on Oxidized Porous Silicon

I.V. Shmigol, S.A. Alekseev, O.Yu. Lavrynenko, V.N. Zaitsev, D. Barbier, and V.A. Pokrovskiy

Abstract Desorption/ionization on silicon (DIOS) mass spectra of methylene blue (MB^+Cl^-) were studied using p^+-type oxidized monofunctional porous silicon (PS-OX_{mono}) free layers. Reduction/protonation processes of methylene blue (MB) dye were investigated. It was shown that SiH_x terminal sites on oxidized surface of porous silicon (PS-OX) are not the rate-determining factor for the reduction/protonation in DIOS. Tunneling of electron through the dielectric layer of nanostructures on silicon surface under effect of local electrostatic and electromagnetic fields is considered to be the most significant factor of adsorbate–adsorbent electron exchange and further laser-induced ion formation.

4.1 Introduction

The dependence of the ion desorption mechanism on physical and chemical properties of an ionization platform is a crucial factor for surface-assisted laser desorption ionization mass spectrometry (SALDI MS) [1]. Specifically, methods of desorption ionization on silicon mass spectrometry (DIOS MS) [2] realize matrix-free approaches in desorption mass spectrometry, i.e., do not use auxiliary agents for ionization. In particular, using porous silicon (PS) as an ionization platform for DIOS MS of low molecular organic compounds provides the absence of background mass spectrum in low mass range, a simplified procedure of sample preparation, the possibility of porous silica surface chemical modification for synthesis of ionization platforms with pregiven properties, etc. As well known [3], selectivity of surface functional groups to various types of molecules with potentialities of DIOS MS allows one to design specific high-sensitive analytical devices (chips) for desorption mass spectrometry [4].

In our early study [5] the possibility of use of ion-change reaction between modified porous silicon surface and methylene blue dye as model analyte

I.V. Shmigol (✉)
O.O. Chuiko Institute of Surface Chemistry of the National Academy of Sciences of Ukraine, General Naumov St. 17, Kyiv 03164, Ukraine
e-mail: ivshmigol@ukr.net

A.P. Shpak, P.P. Gorbyk (eds.), *Nanomaterials and Supramolecular Structures*,
DOI 10.1007/978-90-481-2309-4_4,

was investigated for receiving of qualitative mass spectrometric information by DIOS. As-prepared PS (PS-H), the PS thermally oxidized at 300°C (PS-OX), PS with chemically grafted cation-exchanging alkylsulfonic acid (PS-SO_3H) and anion-exchanging propyl-octadecyldimethylammonium chloride (PS-ODMA$^+Cl^-$) groups were tested as ionization platforms. Two mechanisms of the MB^+ desorption/ionization were proposed: (1) the formation of MBH^+ ion due to the reaction of MB^+ with H• atoms, generated under the laser-induced decomposition of Si–H surface fragments, which is predominant for PS-H and PS-OX platforms; (2) direct thermal desorption of the MB^+ cation, prevailing for PS-SO_3H. Most probably that porous silicon surface is the source of protons and electrons for reduction/protonations of methylene blue. It is well known that different terminal groups –SiH_x on PS-H, –O_3SiH and –SiOH on PS-OX are presented on native and oxidized surfaces. However, reduction of methylene blue occurred in both cases; therefore the goal of the present study is the investigation of desorption/ionization processes on monofunctional oxidized porous silicon surface PS-OX_{mono} grafted only by –SiOH terminal groups.

4.2 Experimental

4.2.1 Porous Silicon Fabrication and Oxidation

Porous silicon was prepared by anodic etching of p^+-doped ($\rho = 10$ mΩ cm) double sides polished silicon (100) wafers in HF (49%) and ethanol mixture (1:1 v/v) at the anodic current density of 150 mA cm^{-2} [6]. Samples of 55 μm in thickness and at 65% porosity (PS-H) were detached from the bulk silicon by switching to the electropolishing regime at the end of the anodization process (pulse at 1 A cm^{-2} for 5 s). PS-H samples were oxidized at 80°C for 15 min in H_2SO_4(strong) and H_2O_2(35%) mixture (7:3 v/v), affording PS-OX_{mono} samples.

4.2.2 Instrumentation

The FTIR spectra of free-standing PS samples were recorded over the 400–7800 cm^{-1} spectral range using a transmittance mode at ambient conditions using a Nicolet Nexus 470 spectrometer.

Laser desorption/ionization mass spectrometry measurements were performed using an Autoflex II time-of-flight mass spectrometer (Bruker Daltonics, Germany) with nitrogen laser (337 nm wavelength and 3 ns pulse width) and accelerating voltage 20 kV. Porous silicon samples were attached to a standard holder of a MALDI plate using a home-made clip. Presented mass spectra were collected by averaging of 100 individual laser shots. All the measurements were performed under conditions: 10 μJ/pulse laser energy and 30 ns delayed extraction period.

4.2.3 Deposition of Dyes on PS Samples

To perform the DIOS MS measurements, 1 μl probes of 10^{-3} M solution of the model dye in H_2O:EtOH mixture (1:9) were directly deposited on PS-OX_{mono} sample and dried in ambient air.

4.3 Results and Discussion

4.3.1 Chemical Composition of PS Surface Layers by FTIR Data

Usual oxidation of PS at 300°C for 1 h in dry oxygen, producing PS-OX samples, leads to the disappearance of almost all $Si_{4-x}SiH_x$ surface groups and formation of silicon oxide layer (very intense ν(Si−O) band in 1200–1000 cm^{-1} interval) (Fig. 4.1, spectrum 1). The surface of PS-OX is terminated mainly by fragments of O_2SiSiH (ν(SiH) at 2208 cm^{-1}), O_3SiH (ν(SiH) at 2264 cm^{-1}, ω(SiH) at 875 cm^{-1} [7]), isolated silanol groups Si−OH (narrow ν(O–H) band at 3745 cm^{-1}), hydrogen-bonded silanol groups, and adsorbed water (wide ν(O−H) band centered at 3400 cm^{-1}).

However, oxidation of PS at 80°C for 15 min in H_2SO_4(strong) and H_2O_2(35%) mixture, producing PS-OX_{mono} samples, leads to the disappearance of almost all O_3SiH, O_2SiSiH surface groups (Fig. 4.1, spectrum 2). Intense band between 1200 and 1000 cm^{-1} can be related to the SiO_2 lattice vibrations. Presence of surface silanol groups is indicated by the narrow band at 3745 cm^{-1} (stretching mode of isolated silanols) and the wide band centered at 3400 cm^{-1} (stretching of hydrogen-bonded silanols and adsorbed water). In the spectrum of the PS-OX_{mono}band 1640 cm^{-1} can be related to the physically adsorbed water scissors vibrations.

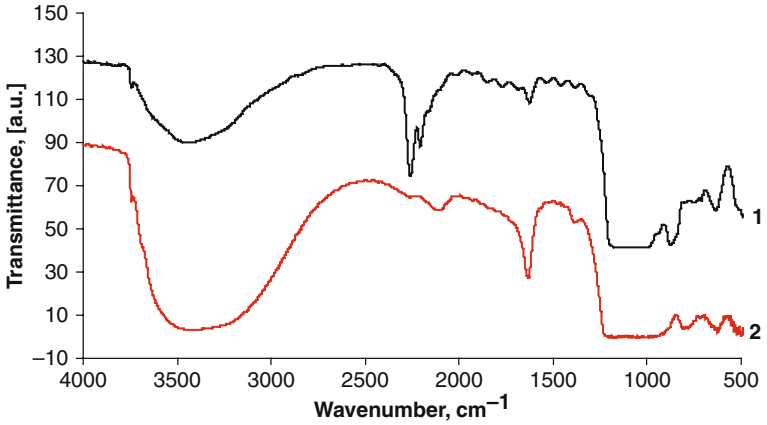

Fig. 4.1 FTIR spectra of PS-OX (*1*) and PS-OX_{mono} (*2*) samples

4.3.2 DIOS Mass Spectra of MB Dye

The DIOS mass spectra of MB dye were obtained using the proposed ionization platform PS-OX_{mono}. Interpretation of those mass spectra (Fig. 4.2) reveals significant variations in the intensity ratio for peaks at m/z=284, 285, and 286 in comparison with natural isotope distribution. This fact points to the reactions of one- (*a*) and two-electron (*b*) reduction/protonation of MB cation occurring on the modified silicon surface:

$$[\mathrm{MB}]^+ + \mathrm{e}^- \rightarrow [\mathrm{MB}]^\circ, \tag{4.1a}$$

$$[\mathrm{MB}]^+ + e^- + H^+ \rightarrow [\mathrm{MBH}]^{\cdot +}, \tag{4.2a}$$

$$[\mathrm{MB}]^+ + 2\mathrm{e}^- + \mathrm{H}^+ \rightarrow [\mathrm{MBH}]^\circ, \tag{4.1b}$$

$$[\mathrm{MBH}]^\cdot + H^+ \rightarrow [\mathrm{MBH_2}]^+. \tag{4.2b}$$

It is known that reduction of molecules under conditions of the desorption mass spectrometry measurements depends on availability of electrons and protons in the reaction space [8]. The products of the one-electron reduction (1*a*) (semi-reduced form) may appear in the protonated form $[\mathrm{MBH}]^{\bullet +}$ (2*a*). The products of two-electron reduction/protonation $[\mathrm{MBH}]^\circ$ (1*b*, leuco-form) are neutral and thus may be observed in the mass spectra only in the protonated form $[\mathrm{MBH_2}]^+$ (2*b*).

Notice that similar reduction/protonation processes are also observed at a surface of ionization platforms based on initial PS and oxidized polyfunctional PS with the $-O_3SiH$ and $-SiOH$ groups, respectively [5]. Taking into account obtained results, explanation of the reduction/ionization by desorption of hydrogen from the surface terminal SiH_x groups (350°C for Si_2SiH_2, 500°C for Si_3SiH, 550°C for O_3SiH [9])

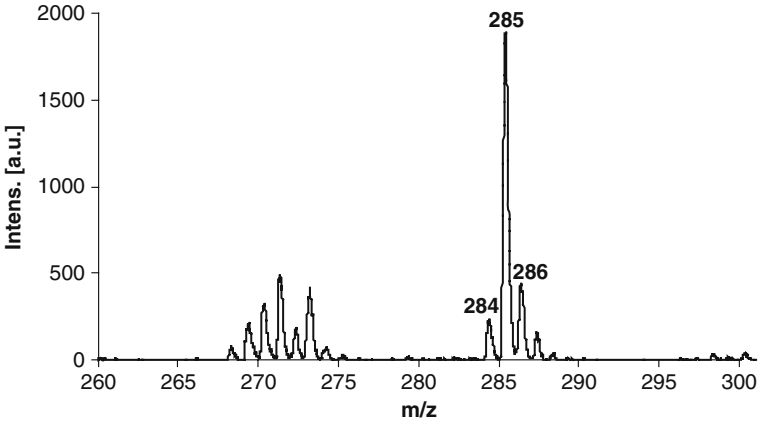

Fig. 4.2 Mass spectrum of methylene blue dye on PS-OX_{mono} surface

as a result of local heating of the ionization platform by laser irradiation [10] is not adequate because the SiH_x groups are absent at the PS-OX_{mono} surface.

Reduction/protonation of MB dye at the PS surface with monofunctional terminal groups may be explained by irradiation of the surface PS-OX_{mono} resulting in the formation of electron–hole pairs (laser photon energy is 3.6 eV at the wavelength $\lambda = 337$ nm, gap energy (E_g) of silicon monocrystal is 1.1 eV) which move to the surface and can reduce or oxidize molecules adsorbed to the ionization platform surface. A dielectric SiO_2 layer is formed at the surface as a result of oxidation which provides an energetic barrier for electrons generated by laser irradiation of the surface. The thickness of such an oxide layer is usually ~ 6 Å corresponding approximately to three monolayers of SiO_2[11].

Such thickness of surface dielectric layer allows the electron exchange between silicon surface and adsorbed molecule by tunnel effect. Probability of electron transfer depends exponentially upon electrostatic field in vicinity of nanostructured surface sites. Surface plasmons generated by laser irradiation of chemically modified porous silicon also play an important role in ionization of adsorbed molecules. And last but not least, surface migration promoted by local temperature increase, caused by laser heating, provides delivery of molecules from pores to areas where the highest values of electric field occur.

Thus, the laser-induced tunnel transition of electron through the oxide layer and subsequent ionization of adsorbed organic molecules is a complex multi-stage process depending essentially on structural details of an ionization platform, chemical composition of surface sites, and temperature of a surface layer affected by the laser irradiation.

The laser irradiation can also promote oxidation of water molecules adsorbed at the pore walls of PS. The products of water oxidation may effect directly the degradation of the MB molecules adsorbed on TiO_2 films as was shown previously [12]. But the fact that the reduction/protonation of dyes was not observed in the case of ionization PS-SO_3H platforms containing significant amounts of adsorbed water [5] confirms that the presence of water in PS pores is not the main factor in the reduction/protonation processes of MB dye on the oxidized surface of PS.

4.4 Conclusions

On the basis of the present study and the literature data [5] we revealed that chemically modified surface of PS was an exceptional proton source for reduction/protonation of ionic dyes such as MB and, evidently, certain other organic compounds.

Besides, we have found that PS-OX_{mono} modified ionization platforms provided reduction/protonation of adsorbate as efficiently as plain PS-OX surfaces with both SiH_x and SiOH groups. So, the presence of SiH_x terminal groups at the oxidized surface of PS serving as a hydrogen source on local laser-induced heating is not a rate-determining factor for the reduction/protonation in DIOS. Specific physical

and chemical properties of modified porous silicon, such as high concentration of surface defects, efficient UV absorption, high local electrostatic and electromagnetic fields make this material a promising platform to open new ways in application of laser desorption mass spectrometry.

Acknowledgment I.V.S. and V.A.P. highly appreciate financial support of this study by Science and Technology Center in Ukraine (Project # 4918).

References

1. Alimpiev S, Grechnikov A, Sunner J, Karavanskii V, Simanovsky Ya, Zhabin S, Nikiforov S. On the role of defects and surface chemistry for surface-assisted laser desorption ionization from silicon. Journal of Chemical Physics 2008; 128: 014711.
2. Wei J, Buriak JM, Siuzdak G. Desorption-ionization mass spectrometry on porous silicon. Nature 1999; 399: 243.
3. Trauger S, Go E, Shen Z, Apon J, Compton B, Bouvier E, Finn M, Siuzdak G. High sensitivity and analyte capture with desorption/ionization mass spectrometry on silylated porous silicon. Analytical Chemistry 2004; 76: 4484.
4. Meng J, Averbuj C, Lewis W, Siuzdak G, Finn M. Cleavable linkers for porous silicon-based mass spectrometry. Angewandte Chemie 2004; 43: 1255.
5. Shmigol IV, Alekseev SA, Lavrinenko OYu, Vasylieva NS, Zaitsev VN, Barbier D, Pokrovsky VA. Chemically modified porous silicon for laser desorption/ionization mass spectrometry of ionic dyes. The Journal of Mass Spectrometry 2009; DOI 10.1002/jms.1604.
6. Mery S, Alekseev SA, Zaitsev VN, Barbier D. Covalent grafting of ion-exchanging groups on porous silicon for microsystem applications. Sensors and Actuators B 2007; 126: 120.
7. Khavryuchenko VD, Natkaniec I, Tarasenko YuO, Khavryuchenko OV, Alekseev SA, Lisnyak VV. Characterization of sol-gel-derived polyhydridosiloxane pre-ceramic polymer. Materials Chemistry and Physics 2008; 108: 24.
8. Okuno S, Nakano M, Matsubayashi GE, Arakawa R, Wada Y. Reduction of organic dyes in matrix-assisted laser desorption/ionization and desorption/ionization on porous silicon. Rapid Communication in Mass Spectrometry 2004; 18: 2811.
9. Lysenko V, Bidault F, Alekseev S, Zaitsev V, Barbier D, Turpin C, Geobaldo F, Rivolo P, Garrone E. Quantitative analysis of hydrogen content in porous silicon nanostructures. The Journal of Physical Chemistry B 2005; 109: 19711.
10. Alimpiev S, Nikiforov S, Karavanskii M, Minton T, Sunner J. On the mechanism of laser-induced desorption/ionization of organic compounds from etched silicon and carbon surface. The Journal of Physical Chemistry 2001; 115: 1891.
11. Alekseev SA, Lysenko V, Zaitsev VN, Barbier D. application of infra-red interferometry for quantitative analysis of chemical groups grafted onto internal surface of porous silicon nanostructures. The Journal of Physical Chemistry C 2007; 111: 15217.
12. Gnaser H, Savina MR, Calaway WF, Tripa CE, Veryovkin IV, Pellin MJ. Photocatalytic degradation of methylene blue on nanocrystalline TiO2: surface mass spectrometry of reaction intermediates. International Journal of Mass Spectrometry 2005; 245: 61.

Part II
Interaction of Nanomaterials with Components of Biological Environments

Modern nanotechnologies provide tools for creation of unique agents for medicine and biology. Their practical usage is mostly based on knowledge about interaction of nanomaterials with the components of biological environment.

Among the large amount of known materials, oxides are of great interest for scientists. This class of compounds possesses a wide variety of properties, while accumulated knowledge is used for their further optimization with respect to certain applications. This chapter highlights highly dispersive pyrogenic oxides and magnetic nanosized oxides for various functional purposes and, in particular, for creation of an artificial bone tissue.

Silica's prominent position among oxides can be accounted for by a number of factors; in fact, the evolution of living matter took place in close contact with it; moreover, silica is a participant of many physiological processes. In the nanosized amorphous state silica possesses high biological activity and ability to modulate biotransformation and pharmacokinetics of medical preparations.

Due to a large specific surface area (200–400m^2/g) and structural features, silica is characterized by high adsorption properties with respect to water, peptides, exo- and endotoxins, and microorganisms.

"Siliks" is a medical drug, developed at O.O. Chuyko Institute of Surface Chemistry of the NAS of Ukraine on the base of nanosilica, as well as some new generations of highly effective combined medical drugs acting via various mechanisms of therapeutic effect and designed for a wide range of applications.

Magnetic oxides, magnetite in particular, which possess high biocompatibility, are of great interest for medico-biological usage. The surface of magnetite in a nanosized state may be used as a reactive component for targeted design of multilevel nanocomposites with hierarchical architecture and functions of nanorobots, which include recognition of specific microbiological objects in biological environment, targeted delivery and deposition of medicinal products into organs or cells, diagnostics and therapy of diseases at the cell level, adsorption of cell decomposition products after application of chemotherapeutic agents or hyperthermia, their removal from the organism using magnetic field. The application of polyfunctional nanocomposites of combined action, which contain monoclonal antibodies and highly efficient cytostatic compounds, in oncology may be accompanied by a

synergetic effect of chemo- and immunotherapeutic drugs and results in decreased toxico-allergic response of the organism.

One of the major problems of modern transplantology is creation of an artificial bone tissue. According to research reports, the porous type of bone tissue contains more than 30% (wt.) of bound water. Cluster structures of such water exist in strong- and weak-associated states and were detected in a number of biological objects (yeast cells, wheat seeds, etc.) and hydrated shells of bioactive amorphous nanosilica. It was found that relative amount of the indicated types of water depends on a state of a bioobject (anabiosis or the active phase) or chemical nature of the nanoparticles' surface. So, one may suppose that the detected water cluster structures may be used for monitoring and quality evaluation of artificial biomaterials, bone implants in particular. The reports dealing with analysis of textural and adsorption characteristics, structure of surface and volume phases of particles, and hierarchy of self-organized structures of pyrogenic oxide systems show regularities of interaction of the particles and the oxides with low- and high-molecular compounds, biomacromolecules, and cells and the peculiarities of the behavior in liquid medium. The relation "structure–composition–properties" for the complex oxides was derived from and their potential capabilities for redox and acid–base catalysis, adsorption of ions of heavy elements, delivery of adsorbates, polymer filling, etc., were evaluated using the obtained data.

Chapter 5
Application Efficiency of Complex Preparations Based on Nanodisperse Silica in Medical Practice

O.O. Chuiko, P.P. Gorbyk, V.K. Pogorelyi, A.A. Pentyuk, I.I. Gerashchenko, A.V. Il'chenko, E.I. Shtat'ko, N.B. Lutsyuk, A.A. Vil'tsanyuk, Y.P. Verbilovsky, and O.I. Kutel'makh

Abstract Unique physical–chemical properties of amorphous silica surface provide certain biological effects: high hydrophilia, affinity to proteins, adsorption of microorganisms and of some low-molecular substances. All of them, as well as the capability of amorphous silica to modulate pharmacokinetics and biotransformation of other medicines by joint administration, allow us to use it not only as a medication of applicational and oral therapy, but also as a matrix or a carrier to create combined drugs. A number of such perspective medical products as Aquasil, Siloglucan, Phytosilard, Lysosil, Lysetox, Flotoxan are now at different stages of development, preclinical, and clinical studies.

5.1 Introduction

Silicon compounds and Si-containing minerals belong to most widely distributed compounds in the nature and comprise almost half of the Earth's crust. There is a hypothesis that a silica surface was a matrix for spontaneous synthesis of the first biogenic molecules. Silicon compounds are not foreign substance for living organisms since it was proven that silicon is necessary for the formation and normal functioning of the vessel walls, cartilages, skin collagen, etc. Silica ($\sim$10 mg) is an irreplaceable micronutrient for man and animals. In the regions with a low content of silica which can be bioassimilable, a frequency of cardiovascular and oncologic diseases increases. At the same time crystalline forms of silica, especially on the inhalation route of entrance, can be a reason for development of a fibrous process in lungs and other organs [1–4].

Silicas of natural and synthetic origin can be used in medicine for therapeutic purposes. From ancient times kaolin, talc, bentonite, and other natural minerals were used as adsorbing means. Synthetic silicas such as porous silica gels and

P.P. Gorbyk (✉)
O.O. Chuiko Institute of Surface Chemistry of the National Academy of Sciences of Ukraine, General Naumov St. 17, Kyiv 03164, Ukraine
e-mail: gorbyk_petro@isc.gov.ua

A.P. Shpak, P.P. Gorbyk (eds.), *Nanomaterials and Supramolecular Structures*,
DOI 10.1007/978-90-481-2309-4_5, © Springer Science+Business Media B.V. 2009

amorphous nanodispersed silicas (NDS) are the objects of comprehensive investigations at O.O. Chuiko Institute of Surface Chemistry and other scientific research institutions [5–7].

Nanodispersed silica produced by burning of $SiCl_4$ in an $O_2/H_2/N_2$ flame is characterized by a relatively low content of silanols at a surface of nonporous primary nanoparticles forming secondary structures with only textural porosity. Until recently NDS was used in the pharmacy as an auxiliary substance to improve decomposition of tablets, to increase the viscosity and friability of the powders, and to reinforce the viscosity and stabilization of soft medicinal preparations. However, the physicochemical and biological properties of NDS are unique and can provide much wide spectrum of its multipurpose utilization in different branches of medicine and pharmacy. In particular, chemical structure of NDS makes it possible to utilize it not only as a means of application and enteral therapy but also as a matrix carrier to create combined medicines [8, 9].

From the chemical point of view NDS particles can be considered as a 3D polymer with $SiO_{4/2}$ as structural units connected together through the Si–O–Si bridges. Surface silanols (2–4 OH/nm^2) cause high hydrophilicity of NDS and its osmotic activity. The NDS surface possesses weak proton-donor properties in the aqueous medium. The pK value of the surface hydroxyls is in the 6–8 range, whereas the isoelectric point corresponds to 2.2 [5, 8].

The aim of this work was to describe combined preparations based on NDS being on different stages of development, preclinical, and clinical tests.

5.2 Results and Discussion

5.2.1 Biomedical Properties of NDS

The properties of NDS which cause its biomedical activity (Table 5.1) are (1) high hydrophilicity, (2) bonding of large amounts of proteins, (3) adsorption of microorganisms and viruses, (4) bonding of certain low-molecular substances predominantly N-containing [5].

The NDS properties shown in Table 5.1 and its capability to modulate the pharmacokinetics and biotransformation of medicines have been assumed as the basis of a technology to create combined preparations of a new generation. Recently our efforts were directed to the creation of new medicines with the initial NDS such as Silics (Biosil), the development of combined medicines which would combine NDS and medicines of other pharmacological groups. In the case of combined medicines special approaches were used which allow us to create preparations with both accelerated and delayed releases of an active substance from the matrix [5, 10].

Among the main directions of utilization of NDS in medicine and pharmacy it is possible to separate four ways:

(1) NDS as an auxiliary component of medicines (tablet, suppository, powders), a filler, and a stabilizer (up to 8 wt% in accordance with the pharmacopoeia)

Table 5.1 Main mechanisms of therapeutic activity of NDS

Sorption of proteins	Effects on microorganisms
Microbial toxins	Agglutination of bacteria
Antigens and the allergens	Microbial decontamination
Endotoxins	Prevention of invasion and translocation of pathogenic microflora
Lipoprotein complexes	
Receptors of enterocytes	Repression of rotting and fermentation in gastrointestinal tract
Stabilization of exoenzymes	
Hydrophilicity	Bonding of low-molecular substances
Hydro-osmotic activity	Peptides at mean molecular weight
Adsorption of water	Exotoxins
Regulation of adsorption and secretion in the intestine	Toxic metabolites

provides the necessary mechanochemical characteristics of many finished medicines, although NDS itself does not practically appear to own therapeutic activity because of a small concentration in the medicines.

(2) NDS as an autonomous medicine for enteral and local application (e.g., known preparation Silics (Biosil) and recently worked out colloidal solution of NDS (Aquasil).

(3) Combined medicines based on mechanical compositions of NDS with other preparations (antiseptics, enzymes, etc.) which combine the pharmacological effects inherent for NDS with a specific activity of other active constituents of the mixtures.

(4) Combined medicines manufactured on the basis of created technologies of immobilization of different medicines on NDS as a matrix or a carrier. In this case it is possible to create medicines with controlled release of an active substance to achieve optimization of the pharmacokinetics, and consequently, the therapeutic activity of immobilized substances. Acceleration or delay of release of immobilized substance is achieved depending on production technology and concentration of components.

5.2.2 Generations of Preparations Based on NDS

All preparations based on NDS already developed or being in different stages of development and long-range planning could be divided into three generations (Table 5.2).

The preparations of the first generation include medicines with the initial NDS powder as a substance suitable to produce the aqueous suspensions and the colloidal solution with NDS (Aquasil). The preparations of the second generation include mechanical composites with complex powders or suspensions of NDS with antiseptic, fermentation, and other components.

The preparations of the third generation include pharmacotherapeutic systems with silica nanoparticles modified by immobilized medicines capable for adjustable

Table 5.2 Generations of preparations based on NDS

Generation	Preparations
First	Biosil – Silics (powder), Aquasil (suspension)
Second	Siloglucan, Phytosilard, Lysosil, Lysetox, Flotoxan, etc. (complex powders and suspensions, plasters and bandages)
Third	Immobilized preparations with adjustable release of an active substance (including capsules and containers)

release or capsules with nanosilica nuclei. Such preparations of the first generation as Silics and Aquasil are already introduced in the medical practice.

5.2.3 List and Examples of Combined Preparations

5.2.3.1 Preparations of the Second Generation

Among preparations of the second generation there is Siloglucan, enteral rehydrational preparation with the anti-diarrhea properties, a complex powder used for preparation of suspension, includes NDS, salts, glucose, compounds for correlation adjustment of taste and odor [11]. Composition of 100g of Siloglucan [12] includes 33 g of NDS; 11.6 g of sodium chloride; 8.3 g of potassium chloride; 9.6 g of sodium citrate; 35.6 g of glucose; 0.5 g of aspartame; 0.5 g of extract of *Mentha piperita*.

It is known that correction of the disorder of water–salt metabolism is the main approach to treat infectious diarrhea. For this purpose such preparations for rehydration as salt mixtures, Rehydron (ORION, Finland), Cytraglucosolan (Russia), Orasan (Sandoz, Switzerland), Gastrolith (Polfa), etc., are used. All these preparations can more or less satisfactorily renew the disordered electrolytic balance on the intestinal infections; however, they do not have direct anti-diarrhea activity but only remove a part of complications of intestinal infections. Moreover correction of the disorder of water–salt metabolism is not always effective because the absorption of components of the rehydrational mixtures is inhibited due to injuries of the intestine as a result of damage of the transport systems of cell membranes. These disadvantages are removed by introduction of NDS to the rehydrational mixture, which (1) provides the binding of pathogenic microorganisms in the intestine, (2) possesses direct anti-diarrhea activity regulating peristalsis of the intestine, and (3) is capable to substantially activate the processes of absorption in the intestine (this is a unique property of NDS).

The results of our investigations of the NDS effects in vitro showed that it can significantly accelerate absorption of tested compounds through the intestine mucous, e.g., more than 1.5 times for glucose, chlorine anions by 30%, and sodium and potassium cations by 15%. The mechanism of this effect is not adequately

explained; however, there is evidence that it is based on the interaction of adsorbent nanoparticles with the membranes of red blood cells.

High efficiency of preparation Siloglucan was shown in the study of a model which combined diarrheal syndrome with dehydration (exicosis) of rats [13]. As a result of diarrhea and exicosis of non-treated animals, a decrease in the capacity of a liquid fraction in blood was observed, and the hematocrit index increased almost to 60%; however, concentration of chloride anions decreased in serum. Introduction of Rehydron (salt blend) provided only a partial correction of these indicators, whereas the application of Siloglucan completely normalized them. The observed powerful anti-diarrhea and rehydrational effects of Siloglucan were confirmed by clinical experiments.

One can assume that the therapeutic activity of Siloglucan is achieved because of the following effects: binding of pathogenic microorganisms and their toxins in the intestine, retardation of the intestine peristalsis, whereas the acceleration of the absorption of components of the salt mixture compensates the loss of electrolytes and fluid. Thus, Siloglucan realizes the major principle of pharmacotherapy such as actions against both exciters of intestinal infections and the pathogenetic mechanisms of the diarrheal syndrome development.

Preclinical tests were carried out for such combined preparations as Phytosilard (with Echinacea immobilized on NDS) and Phytosilard in combination with nonsteroidal anti-inflammatory preparation Nimesulide (Phytosilard-N). The investigation results testified a high anti-inflammatory activity of these preparations on the models of gingivitis and paradontosis related to inflammatory processes of soft tissues in the mouth cavity [14, 15]. The application of Phytosilard, especially Phytosilard-N, sufficiently effectively removed the clinical and laboratory symptoms of inflammation and reduced a healing period of tunica mucosa in the mouth cavity. A high efficiency of Phytosilard–Nimesulide preparation is provided by combination of keratoplastic activity of Phytosilard with the anti-inflammatory properties of Nimesulide. The latter is a selective inhibitor of cyclooxygenase-2 (enzyme controlling the synthesis of prostaglandins as mediators responsible for the development of edema, pain, and hyperthermia in inflammation nidus).

Such combined preparations as Lysosil and Lysetox were developed to treat purulent wounds [16–18]. The wound-healing composition Lysosil contains NDS (Biosil, 96 wt%), crystalline trypsin or chymopsin (1 wt%), and borax (3 wt%). The therapeutic effect of the composition on sanation of pyoinflammatory nidi is caused by complex activity of the components: protease thins exudate and causes degradation of necrotic tissues; NDS binds and neutralizes microorganisms, pathogenic proteins, and necrolysis products preventing their absorption; borax (weak antiseptic) fulfills a function of buffer to adjust the pH value (∼7) necessary for the work of the enzyme. The use of such substance as borax possessing the basic properties is also due to the fact that on the development of pyoinflammatory complications in wounds acidosis (pH < 6.5) is observed. The osmotic activity of Lysosil is close to that of NDS (∼500%).

On the development of composition Lysetox, stabilization of trypsin was achieved in the working medium due to introduction of an antimicrobial preparation

Table 5.3 Impact of Aethonium on the rate of thermoinactivation of proteases in water medium

Temperature (°C)	Constant of inactivation (kin • 10^{-3}, min^{-1})	
	Solution of native enzyme	Solution of enzyme with added 0.02% of Aethonium
	Trypsin	
37	2.5	0
84	27	1.3
	Chymotrypsin	
37	14	1.5
84	>100	2.8

Aethonium (1,2-ethylene-bis(*N*-dimethylcarbodecyloxymethyl) ammonium dichloride) possessing also the surfactant properties [17] (Table 5.3). At the physiological temperature (37°C) the activity of Aethonium-stabilized trypsin remains practically the same for 7 h and its minimum content (remaining sufficiently high proteolytic activity) can be decreased by nearly four times. Lysetox (NDS (97%), crystalline trypsin (1%), Aethonium (1.5–1.7%)) has protein adsorption capability and high hydro-osmotic activity (∼500%) similar to that of NDS.

A complex sorption bandage created as a convenient medicinal preparation based on NDS represents 6–8 layers of gauze filled by NDS and other medicinal substances pressed using a press [19]. Lysosil and Lysetox can be used as fillers, as well as other antiseptics, anesthetics, or their blends. Exact dosing of the preparations is achieved due to fixed sizes of the bandage ("tablet" of 40 mm in diameter and 3 mm in thickness). The bandage placed in a sealed packaging maintains general regime of sterilization in a steam sterilizer. On the optimization of the production technology of the bandage, it was established that optimal pressure is 10–15 bar; the composition must include 35–45% of gauze, 35–45% of NDS, and 10–20% of auxiliary substances. The bandage adhesion to a wound surface decreases in comparison with standard gauze by a factor of 2.5–3; however, its absorption properties remain the same. The wound dressings can be done once for 2–3 days because of the prolonged therapeutic activity of the developed bandage. The bandage can be input in the area of purulent leakage since its removal does not cause pain. The clinical estimations of the therapeutic efficiency of the developed compositions in comparison with the initial NDS showed that their application leads to accelerated dynamics of the wound-healing process. In particular, sloughing is accelerated and completes in 1–2 days, and the treatment period is shortened by 3–4 days [16, 19].

Flotoxan based on Silics (NDS) and used to treat the pyoinflammatory processes (Ukraine patent No. 32088A) and composed of NDS (73%), polymethylsiloxane (25%), and Aethonium (2%) has a high capability to adsorb proteins, bacteria, metabolites of mean molecular weights and to retain them [20]. The osmotic activity of Flotoxan can be regulated by the change of NDS/polymethylsiloxane ratio in contents of preparation. Flotoxan is characterized by a proteolytic activity due to protease activation in suppurative contents, since rapid cleaning of wound surface

from necrotic tissues occurs. The preparation decreases a level of endogenous intoxication due to the binding of the toxic products and stopping of their resorption through the wound surface. The hydrophilic sorbent (NDS) adsorption-active with respect to high molecular compounds (proteins and peptides) and hydrophobic sorbent (polymethylsiloxane) strongly binding acidic compounds of mean molecular weights are jointed in this preparation. The presence of Aethonium as a cationic surfactant and an active antiseptic provides high antimicrobial activity of the preparation. Flotoxan forms a stable suspension in the aqueous solutions which can be used for washing of suppurative areas. A comparative evaluation of the properties of NDS, polymethylsiloxane, and Flotoxan showed that the adsorption activity of Flotoxan with respect to proteins was 320 mg/g (activity of initial NDS was 330 mg/g under the same conditions). Flotoxan uptakes acidic compounds with mean molecular weights from the aqueous solution in the quantity of nearly 5 mg/g and about 3 mg/g of basic compounds with mean molecular weights. The application of Flotoxan on the complex treatment of patients with the pyoinflammatory processes led to shortening of the treatment period by 3 days [21–23].

5.2.3.2 Preparations of the Third Generation

The preclinical research of original medicinal preparations of such anti-arrhythmic medicine as quinidine was carried out. It is known that alkaloid quinidine is one of a few preparations capable to normalize cardiac rhythm with ciliary arrhythmia of auricles and avoiding the application of electro-cardioversion. In this case there is requirement of a medicine with accelerated absorption for rapid stopping of the ciliary arrhythmia attack, and a medicine with delayed absorption for maintaining therapeutic concentration of quinidine, i.e., a minimum level of quinidine in blood, to avoid the arrhythmia relapse. The first medicine is a simple mechano-mixture of quinidine with NDS which provides the acceleration of the absorption of quinidine from the intestine. The second medicine is quinidine immobilized on the NDS surface with the help of fastener substances. To immobilize quinidine on NDS, surfactants or proteins, e.g., albumin, could be used. This medicine was prepared by precipitation of quinidine–serum albumin complex on the NDS surface [5, 24].

A pharmacokinetic study (Fig. 5.1) showed that intragastric introduction of a simple mixture of quinidine with NDS to rats leads to acceleration of quinidine absorption with a greater peak concentration of quinidine in blood in comparison with the introduction of quinidine alone. This effect provides rapid relief of the ciliary arrhythmia attack.

On the other hand quinidine immobilized on NDS has the opposite pharmacokinetic characteristics. On the basis of biopharmaceutical and pharmacokinetic investigations one can conclude that this preparation ideally satisfies requirements for prolonged medicines [5, 24, 25]. On oral administration of quinidine–albumin–NDS conjugate to animals, a decrease in the peak concentration of quinidine in blood is observed, as well as considerable slowdown of elimination of the preparation from blood (Fig. 5.1). The period of the half-life of quinidine in blood is extended more than doubly and trace amounts of the preparation are detected in

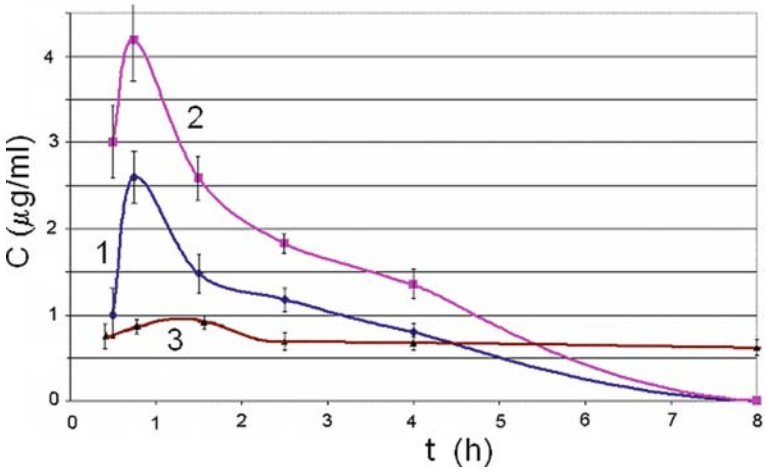

Fig. 5.1 Concentration of quinidine in blood for different preparations: (*1*) quinidine; (*2*) quinidine/NDS mixture; and (*3*) quinidine–albumin–NDS conjugate

blood in 24 h. Furthermore, on administration of this medicine, bioaccessibility of quinidine is maximal, i.e., quinidine most fully transfers from the intestine into the internal medium of organism. This medicine is capable to support the prolonged anti-arrhythmic action of quinidine.

A device (capsule) was developed with programmable release of antimicrobial means for prophylaxis of the ventral area infection by intestinal microflora in the postoperative period. This device is input in an intestine lumen on a surgical procedure [26]. This device represents a two-layered capsule with gelatin and an antiseptic Aethonium incorporated in the walls and filled by antimicrobial preparations in a mixture with NDS (Fig. 5.2).

The device works as follows: the dissolution of the outer layer begins after its introduction into the intestine lumen on the formation of interintestinal connection. In the course of this process the therapeutic concentration of antiseptic is provided in the zone of intestinal sutures. The gradual dissolution of the inner layer occurs

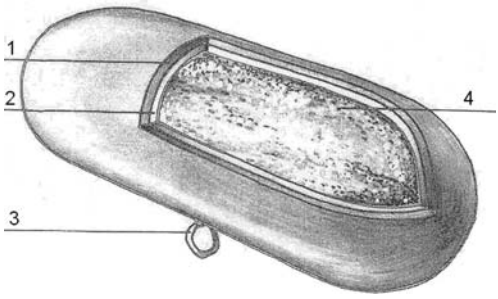

Fig. 5.2 Biosoluble device with programmed release of antimicrobial substances (Ukraine patent No. 41529A): (*1*) outer fast soluble layer; (*2*) inner slowly soluble layer; (*3*) lug for fixation of the device in the anastomosis zone; (*4*) mixture of NDS and antimicrobial preparations

during a day after a surgical procedure in consequence of which antiseptic concentration is supported at a fixed level. Since the infection of the abdominal cavity by intestinal microflora can strongly occur in the first hours after a surgical procedure (from 8 to 24 h after the application of sutures) the device was designed in such a way that the outer layer would be dissolved during the first 4 h and the internal layer would be dissolved during 24 h. After the dissolution of the inner layer the mixture of sorbents and antimicrobial means is realized into the intestine lumen and retained there in the form of gelatinous substance till the appearance of peristalsis of intestine, i.e., during 2–3 days after the surgical procedure [26, 27]. The use of the biosoluble device with programmed release of antimicrobial means and a sorption component effectively prevents the postoperative infection of the abdominal cavity through the line of intestine anastomosis and prevents the development of peritonitis. There is a decrease of the quantity of intraperitoneal complications from 19.5 to 5.9%, shortening the duration of the treatment of patients from 18.6 to 12 days, and reduction of the lethality from 13.8 to 2.9% on the use of this device [28].

5.3 Conclusion

The research and development of combined medical preparations on the basis of NDS is a promising trend in pharmacy. The medicines can be manufactured during a comparatively short time by the pharmaceutical industry and introduced in medical practice.

References

1. Iler RK (1979) The chemistry of silica. Wiley, Chichester, 1979.
2. Chuiko AA, Gorbik PP, Pogorelyi VK et al (2007) Principles of development and efficiency of application of medicines based on highly disperse silica in the experiment and clinic. In: Shpak AP, Gorbik PP (eds.), Physicochemistry of nanomaterials and supramolecular structures, Vol. 1. Naukova Dumka, Kiev, pp. 9–44.
3. Gorbik PP, Pentyk OO, Shtatko OI (2008) Perspectives of creation of combined medicinal preparations based on highly disperse silica. Nanosyst Nanomater Nanotechnol (Ukr) 6: 315–330.
4. Avtsyn AP, Zhavoronkov AA, Rish MA, Strochkova LS (1991) Human microelementoses: aetiology, classification, organopathology. AMS USSR, Medicine, Moscow, pp. 323–337.
5. Stratta P, Canavese C, Messuerotti A et al (2001) Silica and renal diseases: no longer a problem in the 21st century? J Nephrol 14: 228–247.
6. Donaldson K, Stone V, Duffin R et al (2001) The quartz hazard: effects of surface and matrix on inflammogenic activity. J Environ Pathol Toxicol Oncol 20 (Suppl 1): 101–110.
7. Chuiko AA (ed.) (2003) Medical chemistry and clinical application of silicon dioxide. Naukova Dumka, Kiev.
8. Chuiko AA (ed.) (2001) Chemistry of silica surface. UkrINTEI, Kiev.
9. Tentsova AI, Alyushin MT (eds.) (1985) Polymers in pharmacy. Medicine, Moscow.
10. Moroz VM, Chuiko OO, Pentyuk OO (1999) Achievements in development of medicines based on highly disperse silica. Vistn Vinnuts St Med Univers (Ukr) 3: 1–3.
11. Pentyk OO, Gerashchenko II, Verbilovsky YP et al (2001) Antidiarrheal preparation Siloglucan. Ukraine Patent No. 34129A (publ. 15.02.01, Bull. No. 1).

12. Verbilovsky YP, Gerashchenko II, Statko EI, Yushcenko TI (2003) Mechanochemical preparation and investigation of composite with highly disperse silica, sodium and potassium chlorides, sodium citrate and glucose. Chim Pharm J (Russ) 37(12): 45–48.
13. Verbilovsky YP, Gerashchenko II, Statko EI, Yushcenko TI (2002) Development and preclinical study of sorption-salt composite Siloglucan. Clin Pharm (Ukr) 6(3): 51.
14. Kutelmakh OI, Chumakova YG, Shtatko OI (2004) Comparative evaluation of the influence of Silics and Phytosilard on the behavior of aseptic inflammation of soft tissues of mouth cavity of rats. Vistn Stomatol (Ukr) 2: 13–18.
15. Kutelmakh OI, Chumakova YG (2006) Influence of complex preparations based on Silics on paradont tissues on experimental paradontosis of rats. Vistn Stomatol (Ukr) 1: 12–18.
16. Gerashchenko II, Viltsanyuk OA, Zheliba MD et al (1998) Method of treatment of pyoinflammatory diseases. Ukraine Patent No. 20765 A (publ. 27.02.98, Bull. No. 1).
17. Gerashchenko II, Vievsky AM, Bogomaz VI (1996) Stabilization of proteolytic enzymes in solutions of some bis-quaternary ammonium compounds. Pharm J (Ukr) 5–6: 112–115.
18. Gerashchenko II, Voronin EP, Barylo AS et al (2001) Mechanosorptional preparation of composites with highly disperse silica, trypsin and cationic surfactants. Chim Pharm J (Russ) 35(2): 16–17.
19. Gerashchenko II, Sander SV, Bondarchuk OI et al (1997) Bandage for wounds. Patent 15308 A UA, A61F13/04. 94117598 (30.06.1997, Bull. No. 3).
20. Shevchenko YM, Gerashchenko II, Viltsanyuk OA (2000) Wound healing preparation and method of its preparation. Ukraine Patent UA 32088 5A 61 A 31/695, A 61 K 31/14. No. 98126795 (15.12.2000, Bull. No. 7-11).
21. Viltsanyuk OA, Khutoryansky MO, Osolodchenko TP et al (2007) Ground of utilization of cation antiseptic surfactants and sorbents for prophylaxis of septic complications. Khark Surg School (Ukr) 2: 166–170.
22. Viltsanyuk OA (2005) Experimental evaluation of efficiency of Flotoxan on treatment of purulent wounds. Vistn Morphol VNMU (Ukr) 1: 38–42.
23. Viltsanyuk OA, Gerashchenko II, Cheplyaka OM (2008) Experimental and clinical ground of utilization of hydrophilic-hydrophobic silica-containing composites for local treatment of purulent wounds. Khark Surg School (Ukr) 1: 53–57.
24. Ilchenko OV (2001) Means of increase in the amounts of adsorbed substance immobilized on unit of surface area of carrier. Ukraine Patent No. 32545, B 01 J 8/00, B 01 J 19//00, Bull. No. 1.
25. Ilchenko AV (1999) Kinetics of sorption of alkaloids on enterosobent Polysorb MP. Abstracts of presentations at All-Russian Conference “Sorptional, electrochemical and gravitational methods in modern medicine”, October 26–28, Moscow, pp. 44–45.
26. Viltsanyuk OO, Gerashchenko II, Oshovsky AI, Chuiko OO (2001) Method of prophylaxis of septic complications after surgeries of gastrointestinal tract. Ukraine Patent No. 41529A (publ. 17.09.01, Bull No. 8).
27. Oshovsky AI, Gerashchenko II, Viltsanyuk OO (2001) Preparation and preclinical study of biosoluble capsules with given properties. Pharmacom (Ukr) 3: 54–57.
28. Viltsanyuk OO, Gerashchenko II, Oshovsky AI (1999) Utilization of soluble capsules filled by sorbent for prophylaxis of postoperative peritonitis. Vistnk VMSU (Ukr) 3: 216–217.

Chapter 6
Chemical Construction of Polyfunctional Nanocomposites and Nanorobots for Medico-biological Applications

P.P. Gorbyk, I.V. Dubrovin, A.L. Petranovska, M.V. Abramov, D.G. Usov, L.P. Storozhuk, S.P. Turanska, M.P. Turelyk, V.F. Chekhun, N.Yu. Lukyanova, A.P. Shpak, and O.M. Korduban

Abstract A method for preparation of magnetosensitive nanocomposites on the basis of surface-modified magnetite carrying immobilized cisplatin and monoclonal antibody CD 95 (a medico-biological nanorobot model) was developed. Adsorption and covalent immobilization of monoclonal antibody CD 95 and human normal immunoglobulin on nanocomposites comprising magnetite coated with poly(acryl amide) and γ-aminopropylsiloxane was studied. Isotherms of covalent attachment of oxidized immunoglobulin via formation of Schiff bases and non-specific (physical) adsorption of the normal immunoglobulin were compared. Kinetics of release of the immunoglobulin to a model environment was studied. Interaction of the prepared models of nanorobots with the cell line MCF-7 was studied. It was shown that use of magnetically driven nanocomposites carrying the anti-tumour drug and the monoclonal antibody CD 95 causes a synergic cytotoxic effect which exceeds the influence of the control doses up to 50%.

6.1 Introduction

The modern level of nanotechnology permits creating unique means for medicine and biology [1]. Their introduction into practice is the basis of the contemporary progress in diagnostics and therapy, in particular, at the cell and genetic levels.

Researchers' interest in magnetosensitive biocompatible nanoparticles arises from the possibilities to control their motion in biological medium by external magnetic field, use for targeted drug delivery, form local hyperthermia zones, create new types of adsorbents, means for early diagnostics of diseases, etc. [2–4].

In the recent years, the newest direction in diagnostics and therapy based on use of hierarchically constructed magnetosensitive nanocomposites working as " nanoclinics" has been developed. For example, the authors of [5] prepared them via a multi-stage sol–gel synthesis in micelles. The surface of the nanocomposites

P.P. Gorbyk (✉)
O.O. Chuiko Institute of Surface Chemistry of the National Academy of Sciences of Ukraine, General Naumov St. 17, Kyiv 03164, Ukraine
e-mail: gorbyk-petro@isc.gov.ua

A.P. Shpak, P.P. Gorbyk (eds.), *Nanomaterials and Supramolecular Structures*,
DOI 10.1007/978-90-481-2309-4_6,

was functionalized in order to provide recognition and targeting of specific cells. The nanocomposites comprised magnetosensitive cores in silica shells up to 50 nm in diameter which might carry encapsulated optical, magnetic or electric sensors or therapeutic agents. The nanocomposites can be delivered to a cell in a targeted manner and used for diagnostics or changing the cells' function in a desired fashion. Use of local hyperthermia principally permits therapy of malignant tumours without application of chemical drugs.

The available literature data let us conclude that creation of multi-level nanocomposites possessing functions of medico-biological nanorobots which include recognition of specific microbiological objects in biological media, targeted delivery of medical drugs to specified organs or cells, diagnostics and therapy of malignant tumours at the cell level, adsorption of products of decomposition of cancer cells after impact of a chemotherapeutic agent or hyperthermia and subsequent removal from a body is of the highest priority.

Creation of magnetically controlled nanocomposites which possess the functions of nanorobots requires a number of tasks to be solved: synthesis of efficient monodomain carriers with satisfactory magnetic properties, modification and functionalization of their surface, immobilization of medical drugs, encapsulation, attachment of sensors, etc. From the practical point of view, it is important to carry out theoretical evaluation of transport conditions and calculation and optimization of the carriers' parameters.

The magnetic characteristics can be tuned within certain limits via changing the size, shape, composition and structure of the nanoparticles. However, the properties of materials cannot be always controlled upon synthesis since they depend a lot on the particles' size distribution. Thus the characteristics of the materials can vary as a function of their polydispersity.

Surface modification of the magnetic carriers with biocompatible polymers requires optimization of the functions of the polymer constituent. In such systems, polymer molecules may work as a binding matrix for a therapeutic or diagnostic drug and determine important medication parameters like solubility, bioavailability, prolonged activity period achieved due to slow release of the medical drug from the polymer matrix and shelf live. Methods of immobilization of pharmacologically active substances can vary and are determined by designation of the medical preparation and clinical features of pathology for which they are applied.

It is known that chemotherapeutic anticancer medical means cause disturbances in nucleic acids metabolism; suppress DNA functions, processes of biosynthesis, blood formation and digestion; and are cardio-, neuro- and nephrotoxic. Therefore, the task of targeted transport of medical preparations by magnetic carriers is extremely important. Their fixation and deposition in a tumour zone by magnetic field makes a substantial reduction of the preparation dose possible and, as a consequence, minimizes toxico-allergic reactions of an organism.

Use of monoclonal antibodies in oncology practice was classified by S. Rosenberg (1997) as a method of passive immunotherapy of malignant tumours [6]. Clinical data indicate that passive immunotherapy by monoclonal antibodies

is of course efficient, and its results are often as good as those of chemotherapy. At the same time, its toxicity level is substantially lower than of chemotherapy. Complex use of these methods is considered as the most prospective because it notably broadens the potential of treatment of modern drugs and promotes their efficiency.

Use of nanocomposites carrying a cytotoxic drug and a monoclonal antibody would provide recognition of specified cells, targeted delivery of the chemotherapeutic agent to a tumour, achievement of the therapeutic effect at lower concentrations and decreasing the general toxic influence of the cytostatic drug on a whole organism.

Therefore, this work is dedicated to chemical construction of multi-level biocompatible magnetosensitive nanocomposites with hierarchical structure and polyfunctional properties modelling medico-biological nanorobots, studies of immobilization of biologically active cytotoxic molecules and monoclonal antibodies (CD 95) on their surfaces and the impact of the prepared models on the cell line MCF-7 of the human mammary gland carcinoma.

Our analysis of literature data showed that there is no exact understanding of the optimized structure and composition of immunomagnetic nanocomposites and optimal amount of antibodies in the nanocomposites. There are arguments about the strength of antibody–antigen bonding. Besides that, there are only few reports of creation of combined magnetosensitive preparations via step-by-step attachment of medical drugs and antibodies to the surface of nanocomposites.

6.2 Synthesis and Properties of Magnetite

Highly disperse magnetite was prepared via co-precipitation of salts [7, 8] in accord to the reaction

$$Fe^{+2} + 2Fe^{+3} + 8NH_4OH \rightarrow Fe_3O_4 + 4H_2O + 8NH_4^+. \qquad (6.1)$$

Fractionation of the prepared magnetite was carried out with magnetic field.

The method [7, 8] permits obtaining magnetite with broad size distribution of the particles (from microns to nanometres) which requires additional fractionation.

In order to achieve a better control over size distribution, we developed a cryochemical method of heterogeneous synthesis of magnetite at the interface of solid (frozen iron II and III salts solution) and liquid (ammonia solution of a certain concentration) phases [3]. The ammonia solution is taken in excess, while the second phase melts and releases the solution which has predetermined concentrations of the reactive components. A permanent concentration gradient is maintained at the thin interface upon melting the iron-containing solid. Contrary to the homogeneous synthesis, growth of the nanoparticles is terminated at a certain distance from the solid phase due to absence of the iron salts. This prevents further growth of the formed nanoparticles and preserves their initial size. The nanoparticles are collected with non-uniform magnetic field, and the supernatant solution is removed.

The precipitate is washed many times with water in order to dispose off the anions present in the solution.

Samples of the nanocrystalline magnetite with specific surface area of ~ 90–180 m^2/g (measured by thermal desorption of Ar) were prepared using the cryochemical method. Depending on the synthetic conditions, the particles' size comprised 6–50 nm revealing a quite narrow distribution interval. The fraction of the mostly monodomain magnetite particles of 20–50 nm in diameter was used for preparation of the magnetic carriers.

The advantages of the proposed method comprise the increased yield of the monodomain magnetite particles directly from the synthesis and their narrower size distribution.

6.3 Coating of Magnetite Surface with Poly(acryl amide)

Stabilization and biocompatibilization of the nano-sized magnetite particles were achieved via coating their surface with cross-linked poly(acryl amide) (PAA). The PAA layer was prepared via co-polymerization of acryl amide and *N*,*N*'-methylene-*bis*-acryl amide in high-frequency (HF) discharge plasma at radiator power of 20 W [9–11]. The monomer and the cross-linker were coated onto the magnetite surface in a rotor evaporator at 303 K. Plasma polymerization was carried out in glowing discharge at 1×10^{-3} Pa. Conversion degree of carbon–carbon double bonds was measured by the method of Kaufmann based on titration in a non-aqueous solution and the ability of the C=C bonds to combine with Br_2 [12]. The obtained samples were studied in the wavelength range 400–4000 cm^{-1} with a FTIR "Perkin Elmer" spectrometer (the model 1720X) [13–15]. The spectra revealed absorption bands related to the initial magnetite and the PAA coating [16].

We studied magnetic properties of the magnetite particles modified with PAA and the impact of the coating thickness. The coating weight was varied from 5 to 50% of the total weight of the composite. The specific magnetization σ_i and its function $\sigma_i = f(H)$ were calculated from the experimental data. From them, the ultimate magnetization at saturation condition σ_s, the remnant magnetization σ_r, and the coercive force H_c were determined [17].

The experimental functions of the specific magnetization on magnetic field strength for the bare magnetite and the magnetite with various PAA coating contents showed that the coating fraction up to 15 wt.% does not cause notable deviations from the initial magnetite magnetic properties. The values σ_s, H_c, are located in the ranges from 61.5×10^{-7} to 62.0×10^{-7}T m^3/kg and from 30.94 to 29.31 kA/m, respectively, while σ_r is equal to 30.1×10^{-7}T m^3/kg. Increase in the coating weight up to 50% leads to the lower σ_s, H_c, σ_r values: down to 51.1×10^{-7} T m^3/kg, 29.31 kA/m, and 24.0×10^{-7}T m^3/kg, respectively. These results show that the increase in the weight fraction of the PAA layer up to 50% makes a negligible contribution to the specific magnetic properties.

6.4 Modification of Magnetite with γ-Aminopropylsiloxane

The surface of magnetite nanoparticles was coated with γ-aminopropylsiloxane (γ-APS) in toluene [18]. The reaction of polycondensation was carried out in accord to the scheme

$$-\mathrm{OH} + (\mathrm{C_2H_5O})_3\,\mathrm{Si}\,(\mathrm{CH_2})_3\,\mathrm{NH_2} \rightarrow -\mathrm{O}-\mathrm{Si}\,(\mathrm{CH_2})_3\,\mathrm{NH_2} + 3\mathrm{C_2H_5OH} \quad (6.2)$$

γ-Aminopropyltriethoxysilane (γ-APTES) was dried over molecular sieves and purified by distillation in vacuum. Magnetite was exposed to a solution of γ-APTES (10% vol.) in toluene for 8 h, precipitated in a centrifuge, washed with toluene and acetone and dried at 293 K.

Contents of functional groups on the surface of magnetite was measured with X-ray photoelectron spectroscopy (XPS) and differential scanning calorimetry (DSC) combined with differential thermo-gravimetric analysis (DTA). The thermal graphs were recorded in the temperature range 293–1273 K at the heating rate 0.16°/s on a Q-1500D thermal analyzer purchased from the company MOM (Hungary). Concentration of the –OH groups at the surface of the magnetite nanoparticles calculated from the DTA data was equal to 2.2 mmol/g or 2.4 μmol/m^2 at $S_{\text{specific}} = 90$ m^2/g [19].

Presence of the amino groups at the surface of the obtained nanocomposite was confirmed with XPS [20]. The XPS spectra were recorded on a spectrometer EC-2402 with an analyzer "PHOIBOS-100" SPECS using the Kα radiation of a Mg anode (EMgKα = 1253.6 eV). The spectrometer was calibrated using the line Au $4f_{7/2}$ which has the binding energy $E_{\text{b}} = 84$ eV.

Fourier transform infrared spectra were recorded on a spectrometer "Perkin Elmer" (model 1720X) in the range 400–4000 cm^{-1}. Pronounced absorption bands at 1037 and 1130 cm^{-1} of approximately equal intensities indicates formation of a polymer layer Si–O–Si at the magnetite surface resulted from hydrolytic polycondensation of the modifier molecules [19].

6.5 Surface Immobilization of Human Immunoglobulin

We developed procedures for immobilization of antibodies at surfaces of the magnetite-based nanocomposites coated with poly(acryl amide) (PAA) [16] and polysiloxane (γ-APS) [19] using a model preparation of human normal immunoglobulin (Ig) produced by Biofarma, Kyiv. The Ig was purified via dialysis in order to remove low molecular weight preserving compounds.

We measured isotherms of physical adsorption of Ig to the surfaces of the nanocomposites. Samples of the nanocomposites (100 mg) were introduced into Ig solutions (5 ml) of varying concentration.

Adsorption of Ig was carried out in physiological conditions during 2 h upon shaking at ambient temperature. The amount adsorbed at the surfaces of the nanocomposites was determined from the difference between the Ig concentrations

Table 6.1 Isotherm of non-specific adsorption of human normal immunoglobulin to the nanocomposite Fe_3O_4/PAA

C_0(mg/ml)	D (280 nm)	$C_{eq.}$(mg/ml)	$A_{phys.}$(mg/g)
0.35	0.485	0.33	0.84
0.45	0.629	0.43	0.90
0.55	0.776	0.53	0.85
0.71	0.966	0.66	2.32
0.86	1.153	0.79	3.40
1.40	1.762	1.21	9.48

Table 6.2 Isotherm of non-specific adsorption of human normal immunoglobulin to the nanocomposite Fe_3O_4/γ-APS

C_0(mg/ml)	D (280 nm)	$C_{eq.}$(mg/ml)	A_{phys}(mg/g)
0.15	0.249	0.18	0.00
0.25	0.305	0.22	0.00
0.45	0.607	0.44	0.64
0.55	0.745	0.54	0.66
0.71	0.964	0.69	0.80
0.86	1.178	0.85	0.57
1.00	1.361	0.98	0.97
1.40	1.911	1.38	1.18

before and after adsorption. The concentrations were measured on Spectrometer Lambda 35 uv/vis supplied by Perkin Elmer Instruments at the wavelength $\lambda = 280$ nm using a calibration curve. The results are presented in Tables 6.1 and 6.2 and Fig. 6.1a, b.

We recorded isotherms of covalent binding of Ig to the surfaces of the nanocomposites. The chosen mechanism of the covalent binding comprises reaction of aldehyde groups created upon periodate oxidation of Ig-side carbohydrate chains

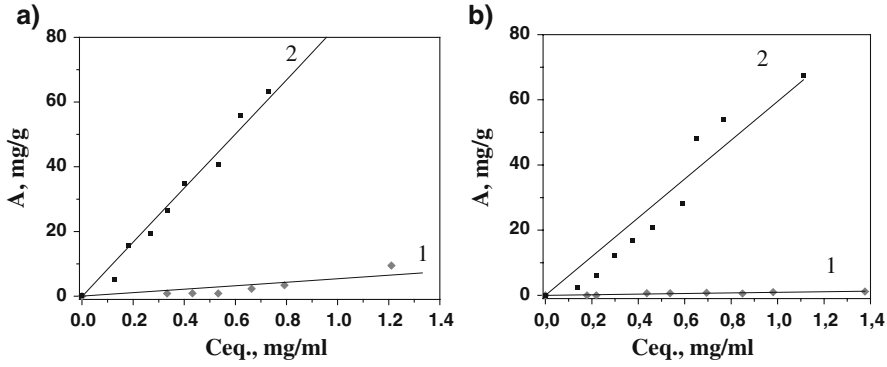

Fig. 6.1 Comparison of isotherms of physical adsorption of human normal Ig (*1*) and the covalent binding of the oxidized human Ig (*2*) to the nanocomposites: **a** Fe_3O_4/PAA; **b** Fe_3O_4/γ-APS

with amino groups located at the grafting surfaces leading to formation of Schiff bases (imines). An advantage of this mechanism is oriented immobilization of the antibody molecules with the Fc fragment (fragment crystallizable) facing the surface and the Fab fragment (fragment antigen binding) sticking out [21, 22].

The nanocomposites consisting of magnetite nanoparticles coated with PAA were activated by ethylenediamine (ED) in order to form amino groups at the surface in accord to the reaction scheme [23]

$$-\mathrm{PAA}-\mathrm{CO}-\mathrm{NH_2}+\mathrm{H_2N}-(\mathrm{CH_2})_2-\mathrm{NH_2} \rightarrow |-\mathrm{PAA}-\mathrm{CO}-\mathrm{NH}-(\mathrm{CH_2})_2-\mathrm{NH_2} \tag{6.3}$$

Since the surface of the nanocomposite Fe_3O_4/γ-APS contains native amino groups, no additional treatment was carried out.

Oxidation of human normal immunoglobulin was carried out in 0.1 M $NaIO_4$ solution prepared on the basis of aqueous 0.02 M acetate buffer (pH 5.0) in accord to the reaction scheme

$$\mathrm{Ig}-\mathrm{gly}+\mathrm{NaIO_4} \rightarrow \mathrm{Ig}-\mathrm{COH}+\mathrm{NaIO_3} \tag{6.4}$$

The oxidized Ig was purified with dialysis against 2 l of 0.02 M acetate buffer (pH 5.0). The solution obtained after the dialysis was set to pH 8–9 with 0.06 M carbonate–hydrocarbonate buffer based on 0.15 M NaCl (pH 9.5).

Covalent binding of Ig to the nanocomposites Fe_3O_4/PAA activated by ED and Fe_3O_4/γ-APS (30 mg) was carried out from 7 ml solution of 0.06 M carbonate–hydrocarbonate buffer (pH 9.0) and 0.15 M NaCl during 2 h at the ambient temperature upon shaking in accord to the reaction scheme

$$\mathrm{carrier}-\mathrm{R}-\mathrm{NH_2}+\mathrm{OCH}-\mathrm{Ig} \rightarrow \mathrm{carrier}-\mathrm{R}-\mathrm{N}=\mathrm{CH}-\mathrm{Ig}+\mathrm{H_2O}\ \text{Schiffbase}. \tag{6.5}$$

The bound Ig amount was determined from the difference between the initial and final concentrations of the contact solution. The concentrations were measured by UV absorption at $\lambda = 280$ nm using a calibration curve. The data on isotherms of the covalent binding are shown in Tables 6.3 and 6.4 and Fig. 6.1a, b.

Table 6.3 Isotherm of the covalent binding of oxidized human normal immunoglobulin to the nanocomposite Fe_3O_4

C_0 (mg/ml)	D (280 nm)	$C_{eq.}$ (mg/ml)	A(Ig/PAA) (mg/g)
0.15	0.201	0.128	5.07
0.25	0.288	0.184	15.52
0.35	0.420	0.268	19.14
0.45	0.528	0.337	26.48
0.55	0.630	0.402	34.59
0.71	0.841	0.536	40.57
0.86	0.974	0.621	55.79
1.00	1.144	0.730	63.04
1.40	1.416	0.903	116.00

Table 6.4 Isotherm of covalent binding of oxidized human normal immunoglobulin to the nanocomposite Fe_3O_4/γ-APS

C_0 (mg/ml)	D (280 nm)	$C_{eq.}$ (mg/ml)	A(Ig/PAA) (mg/g)
0.15	0.282	0.140	2.42
0.25	0.352	0.224	6.14
0.35	0.468	0.298	12.07
0.45	0.594	0.379	16.67
0.55	0.723	0.461	20.70
0.71	0.924	0.590	28.08
0.86	1.025	0.653	48.19
1.00	1.207	0.770	53.71
1.40	1.742	1.111	67.41

The obtained isotherms of non-specific adsorption (Tables 6.1 and 6.2) and the covalent binding (Tables 6.3 and 6.4) of Ig to the nanocomposites are linear functions with no saturation in the studied concentration range (Fig. 6.1a, b). The experimental data were converted to the analytical form using the equation $y = E \times x$, and the respective distribution coefficients E (ml/g) were calculated. The coefficients reflect the Ig distribution between the nanocomposites' surfaces and the contacting solutions. The coefficients (E) and the Ig amounts immobilized at the nanocomposites' surfaces at the concentration of the Ig initial solution 1.4 mg/ml (the maximal in the experiment) are summarized in Table 6.5.

The coefficients for the covalent binding exceed the respective coefficients for non-specific adsorption by more than an order and reflect equilibrium shift towards surface immobilization of Ig.

It should be noted that a significant part of Ig (64–80%) remains in the solution upon covalent binding since the reaction of Schiff base formation is reversible (Tables 6.3 and 6.4).

Nature of nanocomposite's surface influences the values of both the physical and the covalent immobilization of Ig. The amounts of immobilized Ig and the distribution coefficients are higher for the nanocomposite Fe_3O_4/PAA.

We studied the kinetics of release of Ig to model environment (0.15 M NaCl) for the nanocomposites Fe_3O_4/PAA and Fe_3O_4/γ-APS which carried physically and covalently bound Ig and had been prepared upon measurements of the respective isotherms. The samples of the nanocomposites (0.030 g) carrying physically or covalently bound Ig were placed into 5 or 7 ml of 0.15 M NaCl, respectively, and the UV absorption at 280 nm of the solution was measured after gentle shaking for

Table 6.5 Values of human Ig adsorption to the nanocomposites' surfaces of different nature at the concentration of the initial Ig solution $C = 1.4$ mg/ml

Nanocomposite	$A_{phys.}$ (mg/g)	$E_{phys.}$ (ml/g)	$A_{cov.}$ (ml/g)	$E_{cov.}$ (ml/g)
Fe_3O_4/PAA	9.48	6.1	116.00	83.53
Fe_3O_4/γ-APS	1.18	0.92	67.41	59.51

Table 6.6 Parameters of the equation $y = y_0 + Ae^{-x/t}$ describing release kinetics of covalently bound human immunoglobulin from the nanocomposite Fe_3O_4/PAA

	$y(0) =$ 55.8 mg/g	$y(0) =$ 40.6 mg/g	$y(0) =$ 34.6 mg/g	$y(0) =$ 19.1 mg/g	$y(0) =$ 15.6 mg/g
y_0	49.77±3.25	30.40±41.22	25.94±0	11.09±0	0±0
A	2.76±5.62	11.35±0	8.65±0	8.05±0	15.52±0
t	0.27±1.45	1.80±19.54	2.64±1.24	4.37±1.35	6.51±2.45

Table 6.7 Parameters of the equation $y = y_0 + Ae^{-x/t}$ describing release kinetic of covalently bound human immunoglobulin from the nanocomposite Fe_3O_4/γ-APS

	$y(0) = 48.2$ mg/g	$y(0) = 28.1$ mg/g	$y(0) = 12.1$ mg/g
y_0	28.69±3.89	9.13 ± 0	0±0
A	17.60±4.89	18.93 ± 3.11	12.06±3.97
t	60.15±55.12	14.93 ± 8.03	12.18±17.68

certain time intervals. The concentration of the desorbed Ig was calculated using the calibration curves.

Physically immobilized Ig desorbed during 1–2 min; the desorption curves are not shown. The data on desorption of covalently bound Ig are summarized in Tables 6.6 and 6.7 and Fig. 6.2a, b. Parameters of the release kinetic curves were calculated by the method of least squares using the equation $y(x) = y_0 + Ae^{-x/t}$, where y_0 is the amount of bound Ig which is not released at the given conditions, A is the amount of bound Ig which is being released, $1/t$ characterizes release dynamics and curvature of the kinetic function.

The obtained kinetic data show that the released Ig amount decreases upon increase of the amount initially immobilized at the surfaces of both nanocomposites. For small amounts of immobilized Ig 15.5 mg/g (Fe_3O_4/PAA) and 12.0 mg/g

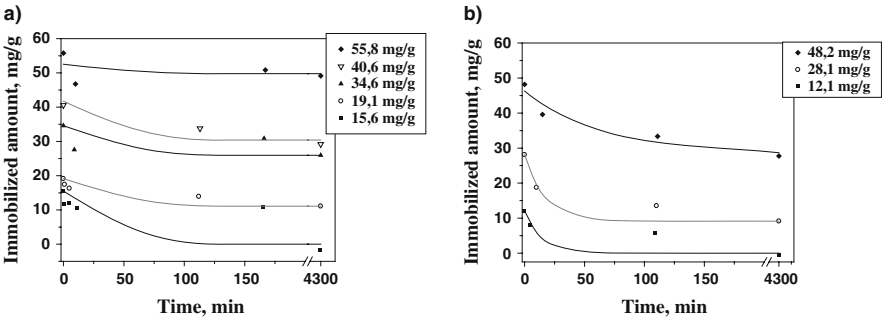

Fig. 6.2 Kinetics of release of covalently bound human immunoglobulin from the surface of the nanocomposites **a** Fe_3O_4/PAA, **b** Fe_3O_4/γ-APS. The initial bound amounts of immunoglobulin are shown in the *right* panels. The curves $y = y_0 + Ae^{-x/t}$ were calculated from the experimental data by the method of least squares

(Fe_3O_4/γ-APS), up to 30% of the Ig is released during the first 5–10 min. For higher immobilized Ig amounts 55.8 mg/g (Fe_3O_4/PAA) and 48.2 mg/g (Fe_3O_4/γ-APS), 16–18% of the Ig is released during the first 10–15 min. Release of surface-immobilized Ig bound via Schiff bases occurs slower and at lower extent than of physically bound Ig.

6.6 Immobilization of the CD 95 Antibody

We prepared nanocomposites carrying anti-tumour drug cisplatin and monoclonal mouse antibody CD 95 against the human Fas-antigen of the isotype IgG1, kappa, the clone DX2 produced by DakoCytomation (Denmark). The concentration of the initial solution of the antibody was 20 μg/ml.

We studied both non-specific (physical) adsorption and the covalent binding of the monoclonal antibody CD 95 to the nanocomposites Fe_3O_4/PAA and Fe_3O_4/γ-APS. We prepared four samples (0.03 g). Each sample was introduced into 1.0 ml solution of the antibody or 1.7 ml solution of the oxidized antibody, respectively:

1. Fe_3O_4/PAA + CD 95;
2. Fe_3O_4/γ-APS + CD 95;
3. Fe_3O_4/PAA + CD $95_{oxidized}$;
4. Fe_3O_4/γ-APS + CD $95_{oxidized}$.

Physical adsorption of the monoclonal antibody CD 95 (20 μg/ml) to the nanocomposites (samples 1 and 2) was carried out in 0.15 M NaCl (1.0 ml) during 2 h upon shaking at ambient temperature.

Oxidation of the monoclonal antibody CD 95 was carried out in acetate buffer-based solution of 0.1 M $NaIO_4$ (pH 5.0). The oxidized CD 95 was purified by dialysis against 2 l of 0.02 M acetate buffer (pH 5.0). The solution of the oxidized antibody was set to pH 8–9 after dialysis against a solution of 0.06 M carbonate-hydrocarbonate buffer (pH 9.5) and 0.15 M NaCl. The concentration of the antibody CD 95 after the dialysis was equal to 13 μg/ml.

Covalent binding of the oxidized and purified monoclonal antibody to the nanocomposites Fe_3O_4/PAA (activated with ED, see Section 6.5 for details) and Fe_3O_4/γ-APS (samples 3 and 4) was carried out in a solution of 0.06 M carbonate–hydrocarbonate buffer (pH 9.0) and 0.15 M NaCl during 2 h upon shaking at ambient temperature. Then the nanocomposites were separated using magnetic field, and the antibody concentrations in the contact solution were measured using a combined reader for a microplate Synergy HT, Model SIAFRTD, Serial Number 202993 (Bio Tek).

Quantitative measurements of protein contents in the solutions were carried out by the method of Bradford [24]. The method is based on recording light absorption of a complex between Coomassie Blue G-250 dye and protein which has a maximum at 595 nm. The antibody concentration was determined from

Table 6.8 Immobilization of the monoclonal antibody CD 95 at the surfaces of magnetosensitive nanocomposites Fe_3O_4/PAA and Fe_3O_4/γ-APS

Nanocomposite	C_0, μg/ml	D	$C_{eq.}$, μg/ml	A(CD 95), μg/g
Fe_3O_4/PAA + CD 95	20.00	0.44	19.93	2.3
Fe_3O_4/γ-APS + CD 95	20.00	0.42	19.96	1.2
Fe_3O_4/PAA + CD $95_{oxidized}$	3.88	0.73	1.00	163.2
Fe_3O_4/γ-APS + CD $95_{oxidized}$	3.88	0.72	1.45	137.7

a calibration curve. The adsorbed amount of the antibody was calculated from the difference between its concentrations in the contact solution prior and after adsorption (Table 6.8).

C_0 is the initial antibody concentration; D is the optical density; C_{eq} is the equilibrium concentration of the antibody upon adsorption; A is the adsorbed amount of CD 95 at the surfaces of the nanocomposites.

The obtained results show that the covalent binding via Schiff bases has the following advantages with respect to non-specific adsorption: higher thermodynamic stability of the immobilized layer originating from the covalent bonding and better kinetic stability due to hampered release arising from slow hydrolysis of the Schiff bases.

6.7 Immobilization of Cisplatin at the Surfaces of the Nanocomposites

Cisplatin (CP) is an anti-tumour platinum-containing drug supplied as aqueous solution. Mechanism of the anti-tumour activity of platinum derivatives comprises DNA chains bifunctional alkylating which suppresses biosynthesis of nucleic acids and induces cell apoptosis.

CP passes poorly through the hematoencephalic barrier and is quickly transformed into inactive metabolites. Binding to proteins in the state of the metabolites reaches 90%.

The period $\tau_{1/2}$ of half-excretion of the drug from blood is equal to 20–49 min at the initial stage, 58–73 h at the final stage assuming normal excretion kidney function and 240 h upon anuria. The drug is excreted by kidneys in the amount of 27–43 % in 5 days, while platinum can still be found in tissues during 4 months after introduction.

We studied stability of CP by measuring its cytotoxic activity after 10, 20 and 30 days and found that it remains constant within a month.

Adsorption kinetics of CP at surfaces of the nanocomposites [25] was measured upon shaking an aqueous solution of CP (50 ml) with magnetic particles of the nanocomposites (200 mg) during 18 h at the ambient temperature. Probes (5 ml) were taken from the solutions every 2 h. The adsorbed amounts were determined as

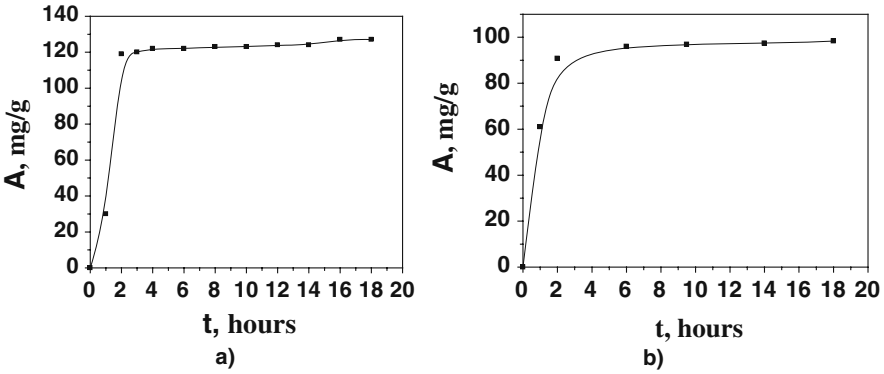

Fig. 6.3 Kinetic curves of adsorption of cisplatin at the surfaces of the magnetosensitive nanocomposites Fe_3O_4/PAA (**a**) and Fe_3O_4/γ-APS (**b**)

the difference between the initial and current concentrations of Pt^{2+} ions in the contact solutions. The measurements were carried out with a single beam two-channel atomic-absorbance spectrophotometer C-115 M1 with flame atomizer, deuterium background corrector and digital registration. A hollow cathode lamp for platinum (the analytical line 265.9 nm) and the fuel–oxidizer system acetylene–air were used.

The adsorption kinetic curves are shown in Fig. 6.3a, b.

The adsorbed amounts of cisplatin (calculated for Pt^{2+}) at the surfaces of the nanocomposites Fe_3O_4/PAA and Fe_3O_4/γ-APS comprise 128 and 98.3 mg/g, respectively. The major part of the drug is adsorbed during the first 2–3 h.

6.8 Preparation and Cytotoxic Properties of Magnetically Driven Polyfunctional Nanocomposites (Models of Nanorobots)

We prepared the following samples for studies of impact of the magnetically driven nanocomposites carrying the cytostatic drug and the monoclonal antibody on vital activity of cancer cells:

1. Fe_3O_4/PAA + CD 95;
2. Fe_3O_4/PAA + CP;
3. Fe_3O_4/PAA + CD 95 + CP;
4. Fe_3O_4/γ-APS + CD 95;
5. Fe_3O_4/γ-APS + CP;
6. Fe_3O_4/γ-APS + CD 95 + CP.

The antibody CD 95 was bound to the nanocomposites via formation of Schiff bases (samples 1, 3, 4, 6). The samples 3 and 6 were prepared in two steps: first,

the oxidized monoclonal antibody CD 95 was conjugated with the nanocomposites Fe_3O_4/PAA (activated with ED) and Fe_3O_4/γ-APS, then the cytostatic drug was adsorbed.

Oxidation of the monoclonal antibody CD 95 was carried out in accord to the procedure described in Section 6.6 and the reaction scheme (6.4).

Covalent binding of the monoclonal antibody CD 95 ($V = 1.7$ ml, $C = 3.88$ μg/ml) to the surfaces of the nanocomposites Fe_3O_4/PAA (activated with ED) and Fe_3O_4/γ-APS was carried out during 1.5 h upon shaking at the ambient temperature in accord to the reaction scheme (6.5). The obtained magnetic samples were collected in magnetic field of a permanent magnet.

The nanocomposites containing the covalently bound monoclonal antibody (the immobilized amounts of CD 95 were 163.2 mg/g for Fe_3O_4/PAA and 137.7 mg/g for Fe_3O_4/γ-APS) were introduced into 10 ml of CP aqueous solution (1 mg/ml). Adsorption was carried out for 4 h upon shaking. The precipitate was collected in magnetic field of a permanent magnet. The adsorbed amounts of CP were 128 mg/g for Fe_3O_4/PAA and 98.3 mg/g for Fe_3O_4/γ-APS.

Cytotoxic impact of the nanocomposites carrying immobilized monoclonal antibody and the cytostatic drug on cancer cells was studied in vitro. The nanocomposites were taken in the amounts which contained the quantity of CP equal to the biological equivalent of efficiency IC_{25}, i.e. 25% of the IC concentration which 100% suppresses the cells. Our earlier experiments showed that $IC_{50} = 5$ μg/ml, therefore $IC_{25} = 2.5$ μg/ml. At that concentration of the nanocomposites, the concentration of the monoclonal antibody CD 95 was equal to 0.2 μg/ml (the doze used for clinical treatment is equal to 10–30 μg/ml). The studies of cytotoxicity were carried out at P.E. Kavetsky Institute of Experimental Pathology, Oncology, and Radiobiology of the National Academy of Sciences of Ukraine [26]. The cytotoxic impact of the nanocomposites Fe_3O_4/PAA and Fe_3O_4/γ-APS carrying immobilized monoclonal antibody CD 95 and CP was measured for the human mammary gland cancer cell line MCF-7. The cytotoxic activity of the respective nanocomposites carrying only CP or only the monoclonal antibody was also measured for comparison. The following solutions were used as the control samples: pure nutrient medium, CP (2.5 μg/ml) and the monoclonal antibody CD 95 solution (0.2 μg/ml). We also studied the cytotoxic effect of the bare magnetite nanoparticles and the bare nanocomposites Fe_3O_4/PAA and Fe_3O_4/γ-APS.

The volumes 100 μl of the MCF-7 line cells (1×10^5cells/ml) were deposited into 96-cavity microplates. The cells were cultivated in a modified medium Dulbecco – ISCOV (Sigma, Germany) with addition of 10% embryonic calve serum and antibiotic gentamycin at 40 μg/ml in standard conditions at 37°C and air saturation with 5% CO_2. The samples being studied were added to the cells after a 24 h period of the cells' adapting to the cultivating conditions. Each sample was added in three parallels and incubated in the same conditions. Cytotoxicity was measured after 24 h.

The impact was evaluated with the MTT-colorimetric test. The method is based on the ability of mitochondrion ferments of living cells to convert 3-[4,5-dimethylthiazol-2-yl]-2,5-diphenyltetrazolium bromide (MTT) (yellow salt) into

Table 6.9 Impact of the magnetosensitive nanocomposites Fe_3O_4/PAA and Fe_3O_4/γ-APS carrying adsorbed cisplatin (CP) and the conjugated monoclonal antibody CD 95 on the vital activity of the MCF-7 line cells

	Fe_3O_4/ γ-APS+ CP	Fe_3O_4/γ-APS + CD 95	Fe_3O_4/γ-APS + CP+ CD 95	Fe_3O_4/ PAA+ CP	Fe_3O_4/PAA +CD 95	Fe_3O_4/PAA + CP+ CD 95
Suppressed cells (%)	31	20	46	38	21	57

	CP, 2.5 μg/ml	CD 95, 0.2 μg/ml	CP, 2.5 μg/ml + CD 95, 0.2 μg/ml
Suppressed cells (%)	25	10	38

crystalline MTT-formazan (lilac) [26]. The MTT solution (Sigma, 20 μl, 5 mg/ml in phosphate–saline buffer) was added to the cavities of the plastic plate and incubated for 3 h. Then the plate was centrifuged at 1500 rev/min for 5 min and the supernatant was removed with an automated suction. Dimethylsulfoxide (Serva, 100 μl) was added to each cavity to dissolve the formazan crystals. The optical absorbance was measured with a multi-cavity spectrophotometer at the wavelength 540 nm. The results of the study are summarized in the Table 6.9.

In accord to the obtained data, the magnetosensitive nanocomposites carrying adsorbed CP in quantity twice below the therapeutic range and the amount of the monoclonal antibody CD 95 almost by one order lower cause death of 46–57 % of the tumour cells which exceeds the impact of the control solution (CP + CD 95) by up to 50%. This synergy effect can be explained as follows. First, the targeted delivery of the complex cytostatic drug–antibody to the tumour cells was accomplished. The cytotoxic effect of CP is achieved through formation of covalent bonds between the drug and DNA. Traumatic effect of the nanocomposite on the cell membrane facilitates the process and improves transport of the therapeutic preparation through the membrane barrier. Bifuctional products of the interaction, the so-called DNA-adducts, block replication, transcription and, as a consequence, cell proliferation. Second, the system ligand/receptor plays an important role in apoptosis of malignant cells. The antibody binding its receptor launches a system of signal transmission which leads to apoptosis. There are also reports [6] that this system may cause death of tumour cells upon influence of cytotoxic drugs.

Consequently, the impact of the magnetically driven nanocomposites (models of nanorobots) carrying the anti-tumour drug and the monoclonal antibody CD 95 on the cancer cells MCF-7 exerts a synergic effect and provides the desired cytotoxicity at lower concentrations. Thus the toxic effect of the medical chemotherapeutic preparation on a whole organism can be decreased. Magnetic properties of the nanorobot models, peculiarities of their transport in the vascular system, their use

for creation of hyperthermia zones, desorption kinetics of the cytostatic drug and efficiency of its influence on cell lines are discussed elsewhere [3].

6.9 Conclusions

The complex of nanotechnologic stages of constructing the biocompatible nanocomposites with hierarchic architecture of the type magnetite–biocompatible coating–chemotherapeutic drug–antibody was worked out.

Processes of adsorption of the chemotherapeutic drug cisplatin, physical adsorption and covalent immobilization of human normal immunoglobulin and covalent binding of the antibody CD 95 to surfaces of magnetically driven nanocomposites Fe_3O_4/γ-APS and Fe_3O_4/PAA were studied.

The isotherms of covalent and physical binding of human normal immunoglobulin to the magnetically driven nanocomposites were compared. We determined the ratios of the immunoglobulin distribution coefficients for the covalent binding via formation of Schiff bases and physical adsorption for each of the nanocomposites: $E_{cov.}/E_{phys.}(Fe_3O_4/PAA)=13.7$; $E_{cov.}/E_{phys.}(Fe_3O_4/\gamma\text{-APS})=64.7$.

A technique of preparation of magnetosensitive nanocomposites on the basis of modified magnetite carrying immobilized cisplatin and the monoclonal antibody CD 95 (the nanorobot models) was worked out. Interaction of the models with the cell line of human mammary gland cancer MCF-7 was studied in vitro. We showed that the cytotoxic impact of the magnetically driven nanocomposites containing the anti-tumour drug and the monoclonal antibody CD 95 exerts synergic effect and exceeds the impact of the control cisplatin dose by 50%.

References

1. Roco MC, Williams RS, Alivisatos P (2002) Nanotechnology research directions. Vision for nanotechnology R&D in the next decade, Vol. 156. Kluwer Academic Publishers, Dordrecht
2. Gubin SP, Koksharov YuA, Khomutov GB, Yurkov GYu (2005) Magnetic nanoparticles: methods of preparation, structure, and properties. Adv Chem. 74(4):539–574 (in Russian)
3. Shpak AP, Gorbyk PP (2007) Physico-chemistry of nanomaterials and supramolecular structures. 1. Naukova Dumka, Kyiv (in Russian)
4. Turanskaya SP, Turov VV, Gorbyk PP (2007) Magnetic nanoparticles and nanocomposites in diagnostics and treatment of diseases. In: Chemistry, physics, and technology of surface: interagency research works collection. Institute of Surface Chemistry of the NAS of Ukraine, 13:272–294 Naukova Dumka, Kyiv (in Russian)
5. Levy L, Sahoo Y, Kim K-S, Bergey JE (2002) Synthesis and characterization of multifunctional nanoclinics for biological applications. Chem Mater 4:3715–3721
6. Moiseenko VM (2002) Abilities of monoclonal antibodies in treatment of malignant tumors. Pract Oncol 3(4):253–260 (in Russian)
7. Sviridov VV (1987) Chemical precipitation of metals from aqueous solutions. Vysshaya shkola, Minsk (in Russian)
8. Sviridov VV (1996) Inorganic synthesis. Vysshaya shkola, Minsk (in Russian)
9. Mikhailik OM, Povstugar VI, Mikhailova SS (1991) Surface structure of finely dispersed iron powders. 1. Formation of stabilizing coating. Colloid Surf 52:315–324

10. Yasuda H (1988) Polymerization in plasma. Mir, Moscow (in Russian)
11. Salianov FA (1997) Basics of low temperature plasma physics, plasma devices and technologies. Nauka, Moscow (in Russian)
12. Dziuba NP (1987) Method of titration in non-aqueous solvents in analysis of medical means. Chem Pharm Ind. 2:1–17 (in Russian)
13. Tarutina LI, Pozdniakova FO (1986) Spectral analysis of polymers and auxiliary compounds. Khimia, Leningrad (in Russian)
14. Dekhant I, Danz R, Kimmer V, Shmolke R (1976) Infrared spectroscopy of high molecular weight polymers. Khimia, Moscow (in Russian)
15. Krylov OV, Kiselev VF (1981) Adsorption and catalysis on transition metals and their oxides. Khimia, Moscow (in Russian)
16. Petranovska AL, Fedorenko OM, Gorbyk PP, Chuiko OO, Chekhun VF, Dubrovin IV, Semko LS, Storozhuk LP, Abramov MV, Revo SL (2005) Development and properties of magnetosensitive nanocomposites for targeted transport of medical means. Nanosyst Nanomater Nanotechnol. 3(3):817–823 (in Ukrainian)
17. Semko LS, Ogenko VM, Revo SL, Mishenko VN et al (2002) Electric and magnetic properties of composite materials in the polyethylene-nanocrystalline nickel system. Funct Mater 9(3):513–518
18. Chuiko AA (2001) Chemistry of silica surface. 1, 2. UkrINTEI, Kyiv (in Russian)
19. Petranovska AL, Fedorenko OM, Storozhuk LP, Gorbyk PP, Chuiko OO, Dziubenko LS, Oranska OI (2006) Modification of magnetite nanoparticles with γ-aminopropyltriethoxysilane from solution. Reports of NAS of Ukraine 1:157–162 (in Ukrainian)
20. Storozhuk LP (2007) Synthesis and properties of polyfunctional magnetosensitive nanocomposites. Ph.D. thesis. Kyiv (in Ukrainian)
21. Wilson BM, Nakane PK (1978) Recent developments in the periodate method of conjugating horseradish peroxidase (HRPO) to antibodies. Immunofluoresc Rel Staining Techn 215–244
22. Shmanai VV, Nikolaeva TA, Vinokurova LG, Litoshka AA (2001) Oriented antibody immobilization to polystyrene macrocarriers for immunoassay modified with hydrazide derivatives of poly(meth)acrylic acid. BMC Biotechnol 1(4):128–133
23. Korshak VV, Shtilman MI (1984) Polymers in processes of immobilization and modification of natural compounds. Nauka, Moscow (in Russian)
24. Doson R (1991) Biochemists' handbook. Nauka, Moscow (in Russian)
25. Gorbyk PP, Petranovska AL, Storozhuk LP, Dubrovin IV, Semko LS, Chekhun VF (2006) Medico-biological nanocomposites on the basis of magnetite: synthesis, modification, functionalization of surface for in vitro applications. In: Surface chemistry, physics, and technology: Interagency collection of research works. Institute of surface chemistry of the NAS of Ukraine. Naukova Dumka, Kyiv, 11–12:374–397 (in Ukrainian)
26. Mosmann T (1983) Rapid colorimetry assay for cellular growth and survival: application to proliferation and cytotoxic assays. J Immunol Methods 65:55–63

Chapter 7
Self-Organization of Water–Organic Systems in Bone Tissue and Products of Its Chemical Degradation

V.V. Turov, V.M. Gun'ko, O.V. Nechypor, A.P. Golovan, V.A. Kaspersky, A.V. Turov, R. Leboda, M. Jablonski, and P.P. Gorbyk

Abstract Hydration of bone tissue and products of its thermal and chemical degradation in the presence of organic solvents was studied using low-temperature ^{1}H NMR spectroscopy and cryoporometry. It was revealed that water filling nanosized cavities between structural elements of bone tissue can be assigned to two types of clustered structures corresponding to strongly and weakly associated water reflecting in the ^{1}H NMR spectra as separate signals with chemical shift $\delta_H = 1.3$ and 5 ppm. It was shown that the chloroform medium stabilizes weakly associated water and reduces interaction of strongly associated water with the phase boundaries. The same tendency is outlined in protein and mineral components of bovine bone. The presence of electron-donor solvents (acetonitrile, DMSO) leads to formation of clustered structures (with electron-donor molecules, strongly associated water or water solution in organic solvents) in the hydrate shells of structural elements of bone materials. In contrast to the native bone material, individual model systems with proteins or mineral components are characterized by a considerable diminution or complete disappearance of weakly associated water.

7.1 Introduction

Bone tissue as a multicomponent material includes hydroxyapatite (HAP) ($Ca_{10}(PO_4)_6{\cdot}(OH)_2$) as the main mineral component, whose crystallites are included in collagen matrix [1–5]. Bone tissue formed around cells (osteocytes) includes an organic fraction with collagen fibers, carbohydrates, and lipids. In bones of many mammals, concentration of collagen can reach to 90% of the organic fraction. On normal osteogenesis calcium and phosphates are delivered by blood to develop a mineral skeleton together with organic components produced by bone cells. On

V.V. Turov (✉)
O.O. Chuiko Institute of Surface Chemistry of the National Academy of Sciences of Ukraine, General Naumov St. 17, Kyiv 03164, Ukraine
e-mail: v_turov@ukr.net

A.P. Shpak, P.P. Gorbyk (eds.), *Nanomaterials and Supramolecular Structures*,
DOI 10.1007/978-90-481-2309-4_7,

deficiency of calcium or phosphorus a portion of the mineral component can be decomposed and transferred by the circulatory system to other organs. The possibility of this mass transfer is provided by high hydration of bone substances because in different parts of bones water content can be 30–50 wt%. Osteoclasts (special bone macrophages) take part in the mentioned process producing enzymes which effectively decompose bone substances. The processes of formation and decomposition of bone tissue can depend on the structure of water layers and clusters being in nanocavities within bone tissue. In bones, water predominantly is in bound state in biomacromolecules and fills cavities between structural elements of protein molecules and HAP crystallites. Since the size of these cavities is in nanometer scale, bound water is in a clustered state. The structure and properties of clustered water can strongly differ from that of bulk water. Many unique properties of water can be explained using cluster models [6–9] including two-state water model with high (HDW) and low (LDW) densities, icosahedral nanodomains with ideal (such as hexagonal ice with LDW) and collapsed structures with HDW [7–9]. Equilibrium between HDW and LDW depends on temperature, pressure, presence of dissolved compounds, or phase boundaries.

^{1}H NMR spectroscopy, one sufficiently accurate method, allows the determination of water structure [10–13], the average number of the hydrogen bonds (n_H) of water molecules, changes in the Gibbs free energy of bound water on the basis of temperature dependence of amounts of unfrozen water, clustered structure of water using the Gibbs–Thomson relation for the freezing point depression, etc. The chemical shift of the proton resonance of water (δ_H) can be used to estimate the n_H value assuming that non-associated water (in gas phase or dissolved in nonpolar solvents) has $\delta_H = 1$–2 ppm [14] and $\delta_H = 7$ ppm for ice Ih [15]. Notice that the presence of dissolved ions, strong acids, or bases in water can significantly change the δ_H values because cations or anions change the hydrogen bond network structure on relatively large distances.

The value of interaction energy of water with phase boundaries can be determined using the ^{1}H NMR spectroscopy with layer-by-layer freezing-out of liquid bulk and bound phases [10, 11] that allows the determination of the amounts of four types of water such as strongly (C^s_{uw}, SBW frozen at $T < 250$ K and $\Delta G <$ –0.5 kJ/mol) and weakly (C^w_{uw}, WBW frozen at $T > 250$ K and $\Delta G > -0.5$ kJ/mol) bound and strongly (SAW, C^{sa}_{uw} at $\delta_H = 3$–5 ppm) and weakly (WAW, C^{wa}_{uw} at $\delta_H = 1$–2 ppm) associated waters, as well as the value of interfacial energy (γ_S, as summary change in the Gibbs free energy of solid phase/water caused by the presence of the phase boundary), maximum decrease in the Gibbs free energy in layers of strongly (ΔG_s) and weakly (ΔG_w) bound waters. To estimate the size distribution functions of pores filled by unfrozen water at $T < 273$ K, NMR-cryoporometry [16] based on the Gibbs–Thomson (GT) relation for the freezing point depression [17] can be used. Water or other liquids can be frozen in narrower pores at lower temperatures described by the GT equation

$$\Delta T_m = T_m(R) - T_{m,\infty} = \frac{2\sigma_{sl} T_{m,\infty}}{\Delta H_f \rho R} = -\frac{k}{R}, \tag{7.1}$$

where $T_m(R)$ is the melting temperature of a frozen liquid in pores of radius R, T_m the bulk melting temperature, ρ the density of the solid, σ_{sl} the energy of solid–liquid interaction, ΔH_f the bulk enthalpy of fusion, and k a constant.

A study of water state in whole bones of rat tails [18] and a porous component of bone tissue (human vertebral bone) [19] using the low-temperature ^{1}H NMR spectroscopy revealed that water bound in bone tissue corresponds to SAW and WAW characterized by slow molecular exchange between them in the NMR time scale. In this case two signals of water at $\delta_H = 5$ ppm (SAW) and 1.3 ppm (WAW) were observed. The aim of this chapter was to study the effects of organic solvents and chemical destruction of organic components of bone tissue on the amounts of SAW and WAW as well as of SBW and WBW.

7.2 Materials and Methods

A sample of human vertebral bone tissue (Medical University, Lublin) was from healthy bone [19]. Two samples (BB1 and BB2) of degradation products of bovine tubular bone tissue were used. Bovine bone sample was boiled in water in a reactor for 0.5 h and treated at 70°C for 5 h, then hydrolyzed in 0.1 M HCl for several hours, washed off by water, and dried at 150°C in a drying chamber. For degreasing, cutting bone chips (5–10 mm length, 0.1–0.2 mm thickness) were washed off by 0.5% solution of sodium carbonate on stirring for 2 h, decanted, and secondly washed off for 2 h. After removal of the alkaline solution, the sample was washed off by distilled water. For removal of mineral component, the sample was treated by 1.35 g-eq/l solution of HCl on stirring for 15 min, decanted, and washed off by water to neutral pH controlled using an indicator. After drying at 105–110°C the sample (BB1) as a white powder at the specific surface area ~50 m^2/g included predominantly protein fraction of bone tissue. The decanted solution included a dissolved mineral fraction of bone. For precipitation, potassium phosphate (1.6 g) was added to 100 ml of the solution and neutralized to pH 7.0–7.3 by sodium hydroxide on stirring. The precipitate of white color was washed off by water and dried at 105–110°C. The obtained powder sample (BB2) corresponds to re-crystallized hydroxyapatite.

The ^{1}H NMR spectra were recorded using a Varian 400 Mercury spectrometer of high resolution using the 90° probe pulses with a duration of 2 μs. The temperature was controlled with a Bruker VT-1000 device with relative mean errors of ±1 K. Changes in concentration of unfrozen water were determined with an accuracy of ±2–3% that was provided by computer processing of the spectra including baseline correction and deconvolution of the spectra using the Gaussian functions. To prevent supercooling of the studied systems, the measurements of the amounts of unfrozen water were carried out on heating of samples preliminarily cooled to 210 K and equilibrated for 5–7 min for each temperature. The ^{1}H NMR spectra recorded here at $T < 273$ K include the signals only of nonfreezable mobile water molecules. The signals of water molecules from ice, as well as protons from the materials, do not contribute to the ^{1}H NMR spectra because of features of the measurement technique and the short duration (~10^{-6} s) of transverse relaxation of

protons in immobile structures which is shorter by several orders than that of mobile water. The characteristics of bound water layers were computed as described previously [10–13]. Organic solvents were used in the H and D forms, and the deuterated solvents included > 99% D.

7.3 Results and Discussion

The ^{1}H NMR spectra of human bone tissue containing 30 wt% (initial sample) and 60 wt% of water are shown in Fig. 7.1. The temperature dependences of the amounts of unfrozen water (C_{uw}) and the relationships between the C_{uw} and ΔG values calculated as described previously [10–13] for SAW and WAW are given in Fig. 7.2. The characteristics of the bound water layers are shown in Table 7.1.

The ^{1}H NMR spectra of porous component of bone tissue (Fig. 7.1a) were recorded at $T = 210$–280 K. The spectra include two overlapping signals at $\delta_H \approx 1.5$ ppm (more intense signal) and 5 ppm. The intensity of both signals decreases with lowering temperature and they are not observed at 210 K. These signals can be attributed to different forms of water: WAW ($\delta_H \approx 1.5$ ppm) and SAW ($\delta_H \approx 5$ ppm) [18, 19]. Water addition (+30 wt%) to the initial sample (Fig. 7.1b) leads to redistribution of the signal intensity, since in the initial sample, the amounts of SAW and WAW were $C_{uw}^{sa} = 75$ mg/g and $C_{uw}^{wa} = 220$ mg/g and after addition of water they were 350 and 240 mg/g, respectively.

From the data (Fig. 7.1 and Table 7.1), an increase in the amounts of SAW in bone tissue is accompanied by a predominate increase in the amounts of WBW. An increase in a WBW fraction in WAW occurs due to a decrease in the amounts of SBW. The total amounts of SBW increase by ~30%. Bone tissue as other biotissues is a soft material, internal structure of which depends on a quantity of adsorbate (e.g., water). Therefore, the increase in the amounts of SBW can be explained by an increase in the volume of soft cavities accessible for water and characterized by a high adsorption potential.

The investigations carried out for a large number of rigid mineral and carbon adsorbents characterized by developed system of micro- and mesopores or relatively soft (with respect to secondary particles) nanooxides with developed surface area showed that self-organizing of water/organic mixtures can occur with re-arrangement of the interfacial layers. In this case weakly polar or nonpolar organic component interacting with the surface predominantly by the dispersion mechanism can displace water from the surface toward broader pores or on the outer surface of adsorbent particles, where SAW becomes predominant [10, 20–24]. Notice that the strongest re-arrangement of the interfacial layers occurs if the pore walls are mosaic with hydrophilic and hydrophobic patches. Notice that cavities in biotissues can have mosaic walls with hydrophilic and hydrophobic functionalities. Therefore, the effects of self-organizing of water/organic mixtures bound in these cavities can be similar to that observed for mosaic or hybrid adsorbents.

Addition of a certain quantity of nonpolar organic solvent (benzene) to the bone tissue sample leads to significant changes in the shape of the ^{1}H NMR spectra

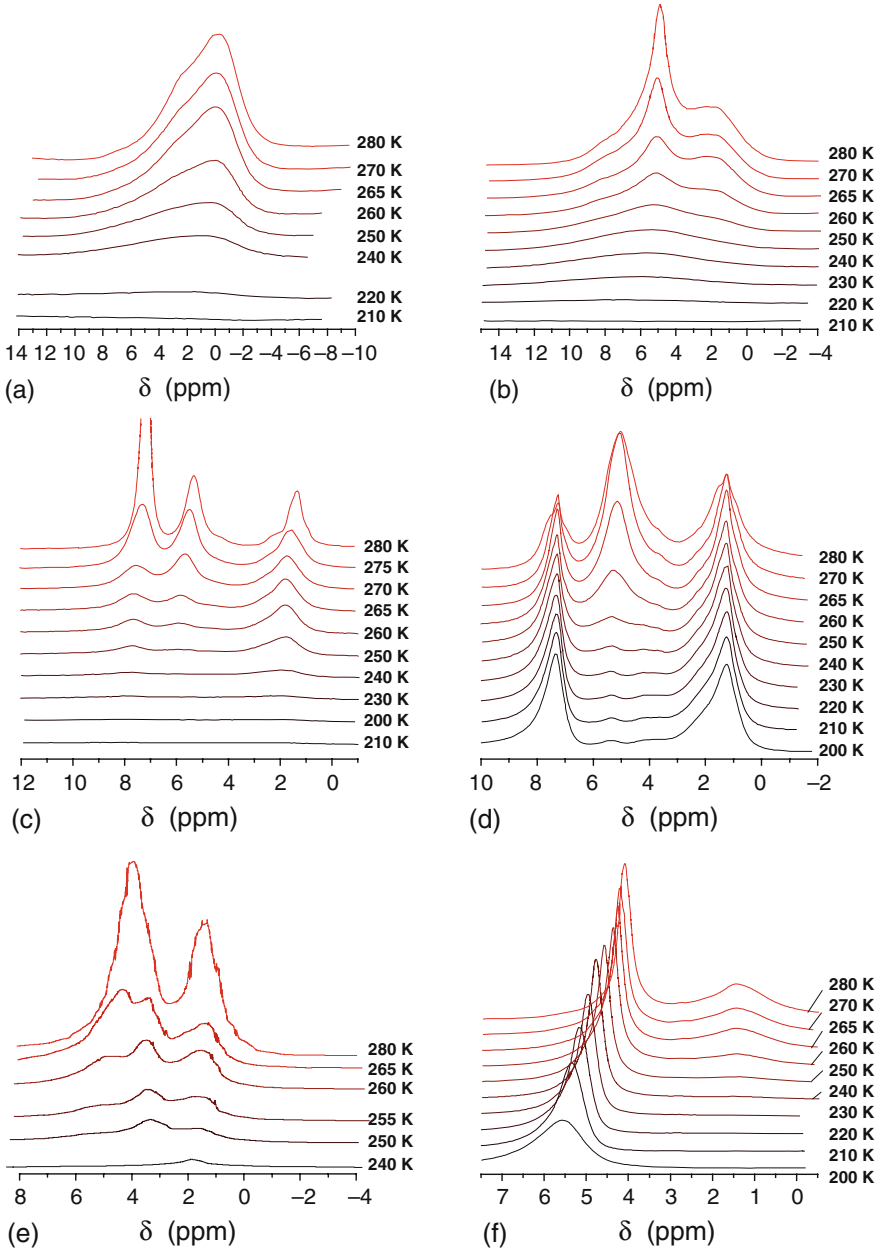

Fig. 7.1 Influence of solvents on water state in human bone tissue: (**a**) initial sample; (**b**) after addition of 30 wt% of water; initial sample in (**c**) benzene, (**d**) chloroform (100 wt%), and (**e**) CD_3CN (80 wt%), and (**f**) sample with added 30 wt% of water in DMSO-d_6

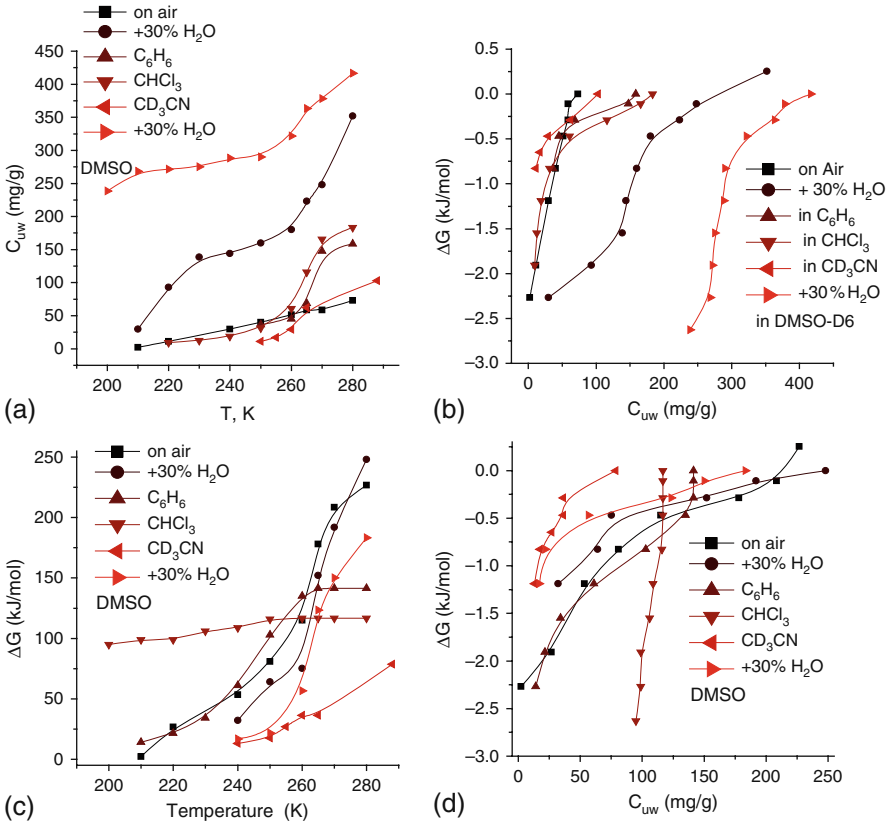

Fig. 7.2 Influence of solvents on water state in human bone tissue for (**a**, **b**) SAW and (**c**, **d**) WAW for initial sample, after addition of 30 wt% of water or in benzene, chloroform, and acetonitrile, and in DMSO-d_6 (after addition of 30 wt% of water)

(Fig. 7.1c). The signal width of bound water sharply decreases, and the signals of SAW and WAW become easily resolved. Notice that besides the signals of water (Fig. 7.1) the signal of CH groups of benzene and chloroform is observed at δ_H = 7.2–7.3 ppm. Redistribution of the signal intensities of SAW and WAW and the amounts of SBW and WBW (Table 7.1) occurs simultaneously with decreasing signal width. The amount of SAW increases by a factor of 1.5, and the corresponding decrease in the concentration of WAW is observed. These changes occur due to a decrease in the amounts of WBW which completely vanishes in the WAW structures. In the SAW structures, a quantity of SBW decreases by a factor of 1.5. Similar changes in the spectra are observed with the presence of weakly polar deuterochloroform (Fig. 7.1d); however, in this case the decrease in the WAW fraction is larger. Features of the water–chloroform mixture are caused by changes in WAW becoming such strongly bound that it does not practically freeze over the used temperature range.

Table 7.1 Characteristics of water bound in human bone tissue with addition of organic solvents

Water type	Solvent	Water content (wt%)	C^s_{uw} (mg/g)	C^w_{uw} (mg/g)	$-\Delta G_s$ (kJ/mol)	γ_S (J/g)	S_{uw} (m^2/g)	V_{uw} (cm^3/g)
SAW	–	30	65	10	2.40	4.2	4.4	0.061
	–	60	200	150	2.46	19.5	15.8	0.269
	C_6H_6	30	40	120	2.54	5.3	22.0	0.158
	$CHCl_3$	30	40	140	2.95	5.8	24.8	0.169
	CD_3CN	30	20	85	2.50	2.2	15.3	0.076
	DMSO-d_6	60	305	115	5.16	60.0	551.0	0.385
WAW	–	30	120	100	2.34	10.3	21.0	0.214
	–	60	90	150	2.50	7.1	31.5	0.204
	C_6H_6	30	140	–	2.93	10.2	71.2	0.141
	$CHCl_3$	30	115	–	2.50	36.2	218.4	0.117
	CD_3CN	30	38	42	2.37	2.4	5.7	0.050
	DMSO-d_6	60	28	152	2.52	5.2	26.9	0.157

In the presence of acetonitrile as well as in the case of nonpolar or weakly polar solvents, an increase in the SAW fraction is observed (Table 7.1); however, this effect is weaker. At $T < 280$ K, the signal of SAW splits into two signals at $\delta_H \approx 4$–5 and 3 ppm. The SAW signal shifted toward the strong magnetic fields corresponds to water dissolved in acetonitrile. This mixture can be formed in pores of bone tissue or out of them. Since bone tissue has a high affinity to water and a quantity of acetonitrile is not large (80 wt% of dry bone material), it is possible to consider that a certain portion of water–acetonitrile complexes forms within pores.

An increase in the signal intensity and appearance of a strong temperature dependence of the chemical shift value for SAW (δ_H decreases from 5.5 to 4 ppm with elevating temperature) are observed for hydrated bone tissue placed in DMSO. In this case a major fraction of WAW becomes WBW (Table 7.1). The strong temperature dependence of the chemical shift testifies about the existence of several types of water–DMSO structures (frozen at different temperatures) such as small water clusters or individual water molecules surrounded by DMSO molecules, confined water nanodomains with small amounts of dissolved DMSO molecules, and water structures located out of pores.

The obtained results (Table 7.1, Figs. 7.1 and 7.2) suggest that in the case of samples being in solvent media (chloroform, benzene, and acetonitrile), an increase in the quantity of WBW is characteristic for the SAW structures. However, in contrast to inorganic adsorbents [20–24], this growth occurs due to a decrease in a quantity of WAW. As a result the value of interfacial free energy (with exception of water–acetonitrile) has a tendency to increase. For DMSO as the most polar solvent among studied ones, a substantial fraction of water is dissolved in the solvent. This leads to a sharp increase in the γ_S value (Table 7.1), which reflects interaction of water rather with DMSO than with the pore walls of bone tissue.

Figure 7.3 shows temperature changes in the ^{1}H NMR spectra of BB1. The initial powder does not practically contain water (Fig. 7.3a) since a small quantity of

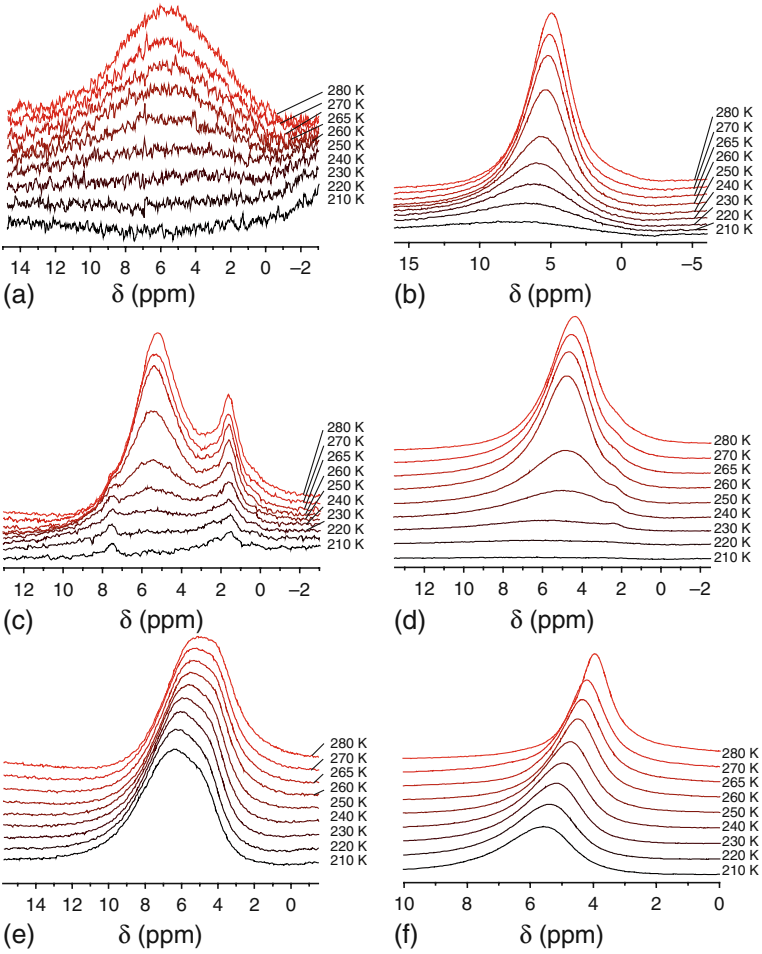

Fig. 7.3 ^{1}H NMR spectra of water bound in BB1 recorded at different temperatures for (**a**) initial sample, (**b**) after addition of 10 wt% of water, and then addition of (**c**) 60 wt% of $CDCl_3$, (**d**) 80 wt% of CD_3CN, (**e**) 30 wt% and (**f**) 80 wt% of DMSO-d_6

residual water appears in the spectra in the form of very broad signal with a maximum at $\delta_H \approx 5$ ppm. Estimation of the signal intensity shows that the amount of water in this sample is smaller than 1 wt%. Addition of 10 wt% of water to this sample leads to a certain decrease in the signal width (Fig. 7.3b) and its chemical shift is displaced from 5 to 5.8 ppm with lowering temperature. The replacement of air medium by such weakly polar solvent as deuterochloroform leads to the appearance of WAW, whose quantity is equal to 2 wt% at 280 K (Fig. 7.3c). In contrast to SAW, practically total amount of WAW corresponds to SBW. In contrast to the native bone material (Fig. 7.1), addition of electron-donor organic solvents (acetonitrile-d_3 and DMSO-d_6) to BB1 did not lead to stabilization of WAW (Fig. 7.3, Table 7.2).

Table 7.2 Characteristics of water bound in BB1 at 10 wt% of water and after addition of solvents

Solvent	Solvent content (wt%)	C^{s}_{uw} (mg/g)	C^{w}_{uw} (mg/g)	$-\Delta G_s$ (kJ/mol)	γ_S (J/g)	S_{uw} (m^2/g)	V_{uw} (cm^3/g)
–	–	80	20	4.01	8.3	7.3	0.094
$CDCl_3$ (WAW)	100	10	7	3.71	1.2	2.6	0.017
$CDCl_3$ (SAW)	100	50	33	2.31	4.8	6.1	0.077
CD_3CN	10	100	0	2.42	6.8	53.1	0.100
CD_3CN	30	96	4	2.38	5.6	49.1	0.100
CD3CN	100	90	10	2.71	6.1	38.0	0.100
$(CD_3)_2SO$	10	90	10	5.47	15.7	24.7	0.100
$(CD_3)_2SO$	30	100	0	14.76	43.8	93.7	0.100
$(CD_3)_2SO$	100	100	0	5.00	17.3	65.9	0.100

In the presence of acetonitrile besides the signal of SAW, a weak signal of CHD_2 groups of non-deuterated acetonitrile is observed at $\delta_H \approx 2$ ppm (Fig. 7.3d). In the case of a relatively small concentration of DMSO (30 wt%), two close signals of SAW and the solution of water in DMSO (signal shifted toward the strong magnetic field) are observed in the spectra (Fig. 7.3e).

In the DMSO medium (Fig. 7.3f), there is dynamic equilibrium between these forms of water, and the signal shifts from 6 ppm at 210 K to 3.5 ppm at 280 K. Since the δ_H value at low temperatures is slightly larger than that of liquid water, one can assume that SAW and DMSO form clustered structures in which the DMSO molecules surround water clusters. Sample BB1 includes mainly protein component of bone tissue; therefore, one can assume that WAW localizes in cavities with mainly hydrophobic walls (hydrophobic side groups of certain amino acids). A similar effect was previously observed for frozen-dried serum albumin [10].

Figure 7.4 shows the temperature dependences of the amounts of unfrozen water $C_{uw}(T)$ and the corresponding relationships between the ΔG and C_{uw} values, and the characteristics of bound water layers are shown in Table 7.2.

These results suggest that the amount of SBW in SAW is significantly decreased only in the presence of chloroform. In the case of added electron-donor solvents, entire water becomes SBW and partially freezes out only at low temperatures. The proximity of the ΔG_s values (characterizing changes in the Gibbs free energy in the first adsorbed water layer [10, 11]) for practically all samples (with exception of samples with DMSO) to that for the initial BB1 without solvents suggests that water is concentrated in the solvation shells of collagen structures. A significant increase in the ΔG_s and γ_S values is observed for samples containing DMSO that can be caused by a great energy of hydration of DMSO molecules and dissolution of water molecules in DMSO. The maximum γ_S value for sample containing 30 wt% of DMSO can be caused by the maximal clusterization of the DMSO/water structures. The presence of several water signals at $\delta_H = 6$ and 4–4.5 ppm is due to heterogeneity of these structures. Stabilization of a considerable quantity of WAW

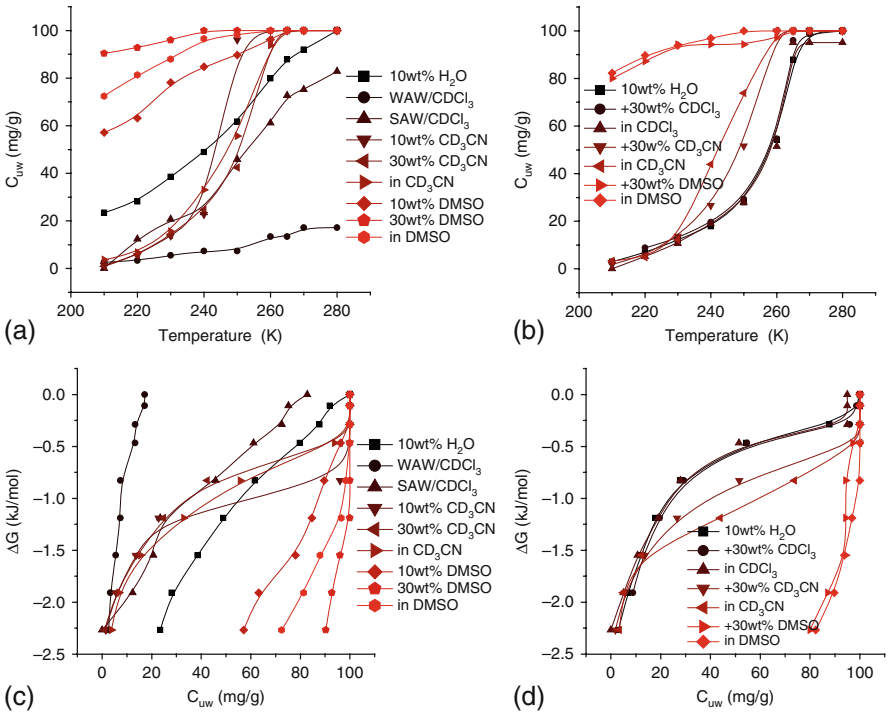

Fig. 7.4 Influence of solvents on (**a**, **b**) temperature dependence of the amounts of unfrozen water and (**c**, **d**) relationships between the C_{uw} and ΔG values for (**a**, **c**) BB1 and (**b**, **d**) BB2 with added 10 wt% of water and different amounts of solvents

by chloroform does not occur for sample BB2 (mineral component of bone tissue) (Fig. 7.5). In the presence of deuterochloroform, WAW is observed as a weak signal whose intensity is difficult to be measured against the background of the signal of SAW. In other respects features of changes in the spectral characteristics of BB2 with organic solvents are close to that observed for BB1. Chloroform slightly reduces a quantity of SAW (Table 7.3); however, this decrease is considerably less than for BB1. In the presence of acetonitrile, the signals of SAW and a solution of water in acetonitrile are distinguished but a fraction of the solution is higher than that for BB1. In the case of DMSO, this equilibrium shifts toward the solution of water in DMSO. Probably this is due to a smaller value of the specific surface area of the HAP crystallites/water interfaces because a smaller γ_S value is for the initial BB2 in comparison with the initial BB1. The characteristics of bound water layers in the presence of 30 and 100 wt% of DMSO for BB2 are close to that for BB1 with addition of 100 wt% of DMSO.

In the presence of DMSO, the ΔG_s values are equal to 5–6 kJ/mol for the majority of samples of native human bone tissue and protein or mineral components of bovine bone tissue. Probably, this value is affected by the free energy of solvation

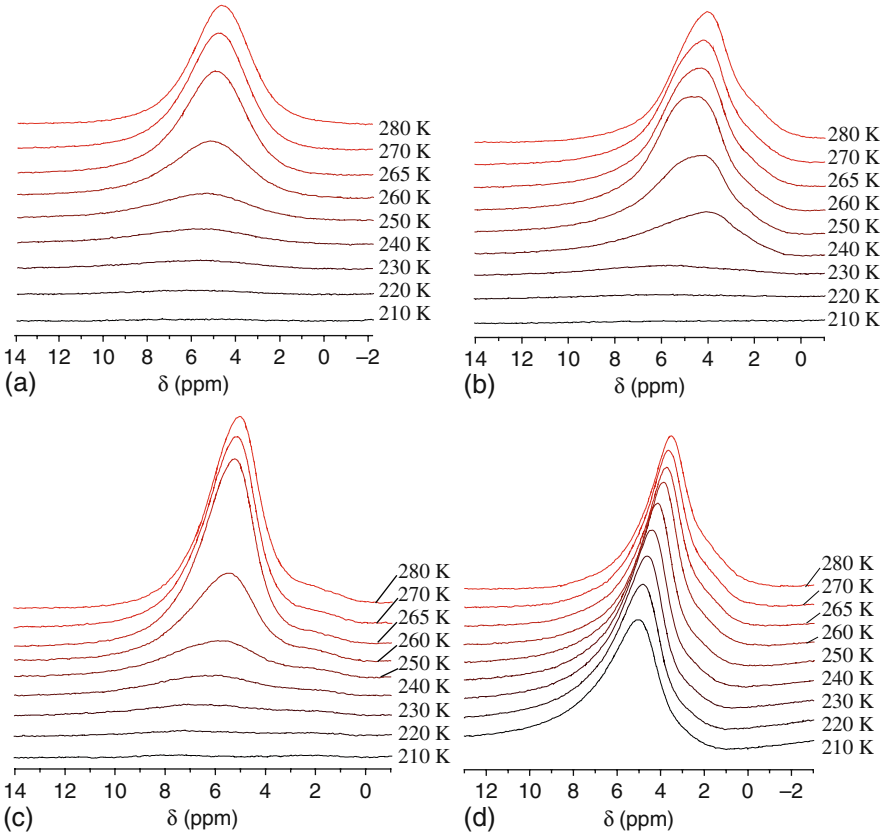

Fig. 7.5 ^{1}H NMR spectra of water bound in BB2 recorded at different temperatures after addition of (**a**) 10 wt% of water and then 80–100 wt% of solvents (**b**) $CDCl_3$, (**c**) CD_3CN, and (**d**) DMSO-d_6

of water in DMSO in the interfacial layers under action of the surface forces of the materials.

Taking into account that the heat effect of water crystallization is 4 kJ/mol one can conclude that the solvation energy of water in DMSO ($T < 273$ K) is higher than the interaction energy of water with functionalities of both protein and mineral components of bone tissue.

For the majority of samples addition of solvents leads to an increase in the surface area of bone structures being in contact with unfrozen water (Tables 7.1, 7.2, and 7.3, S_{uw}). This effect is strongest on addition of DMSO because contribution of narrow cavities filled by water (or water/DMSO mixture) increases (Fig. 7.6). In other words, DMSO/water mixture can penetrate into narrower cavities than water alone. The observed results are in agreement with well-known properties of DMSO as a carrier of other compounds and a cryoprotectant [25, 26].

The effect of DMSO is stronger for SAW than WAW (Table 7.1, Fig. 7.6) because WAW as water bound in the form of small interfacial clusters possesses a lower

Table 7.3 Characteristics of water bound in BB2 with added 10 wt% of water and solvents (30 or 100 wt%)

Solvent	Solvent content (wt%)	C^{s}_{uw} (mg/g)	C^{w}_{uw} (mg/g)	$-\Delta G_s$ (kJ/mol)	γ_S (J/g)	S_{uw} (m^2/g)	V_{uw} (cm^3/g)
–	–	60	40	2.57	4.36	23.2	0.100
$CDCl_3$	30	60	40	2.31	4.52	21.6	0.099
$CDCl_3$	100	55	35	2.31	4.25	15.7	0.095
CD_3CN	30	100	0	2.47	5.91	41.1	0.100
CD3CN	100	100	0	3.04	6.76	49.3	0.100
$(CD_3)_2SO$	30	100	0	6.04	20.30	19.5	0.100
$(CD_3)_2SO$	100	100	0	6.02	20.76	74.4	0.100

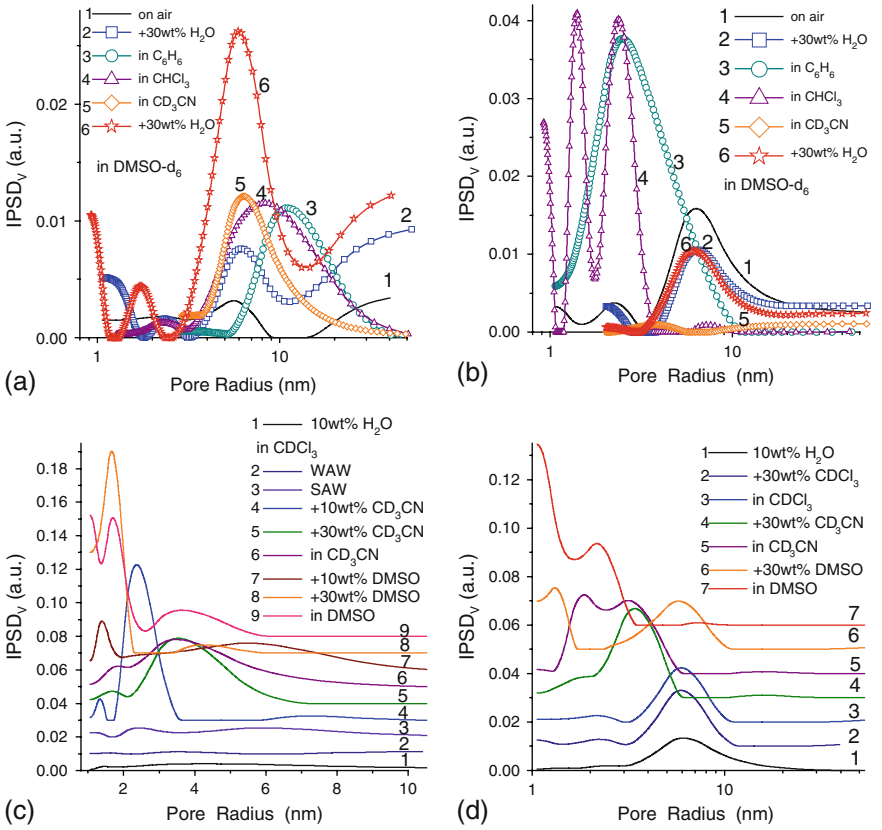

Fig. 7.6 Size distributions of pores filled by unfrozen water for (**a**) SAW and (**b**) WAW in human bone tissue initially and after addition of water and solvents; (**c**) BB1 and (**d**) BB2 after addition of water and solvents

ability to form mixtures with DMSO (or other polar solvents) than SAW present in the form of nanodomains. Therefore, the effects of nonpolar (benzene) or weakly polar (chloroform) solvents (which can more strongly interact with hydrophobic functionalities than water) on WAW is stronger than that of DMSO (Table 7.1, S_{uw} and γ_S). Notice that the effects of CD_3CN (as more polar than C_6H_6 but less polar than DMSO) for both SAW and WAW are minimal.

In the case of protein or mineral components of bovine bone tissue, the influence of solvents on bound water differs from that for human bone tissue (Tables 7.1, 7.2, and 7.3 and Fig. 7.6). Addition of less polar solvents gives smaller changes in the S_{uw}, γ_S, and ΔG_s values. These results can be explained by a lower heterogeneity of BB1 and BB2 samples than native one; i.e., model samples BB1 and BB2 have less mosaic (hydrophilic/hydrophobic) surfaces than native bone tissue.

7.4 Conclusion

Water in bone tissue is present in two forms of spatially divided clustered structures as strongly associated water characterized by $\delta_H = 4.5$–6 ppm and weakly associated water at $\delta_H = 1$–2 ppm. Weakly associated water is more strongly bound and freezes at temperatures considerably lower than the freezing point of the major fraction of SAW.

The chloroform medium stabilizes weakly associated water and decreases the interaction of water with the surfaces of the bovine bone materials. The same tendency is outlined for protein and mineral components of the bone material.

The presence of such electron-donor solvents as acetonitrile and DMSO leads to the formation of clustered structures (with the electron-donor molecules and SAW or the solution of water in the solvents) in the hydrate shells of structural elements of the bone material. The ^1H NMR signals of these structures are observed in the form of separate signals.

A small fraction of weakly associated water is characteristic for protein and mineral components in contrast to the native bone tissue. For protein component in chloroform medium, contribution of this fraction increases, while for the mineral component, it is present only in the form of a broad and weak signal. There are several factors in the native bone material, which are appropriate for the formation of weakly associated water structures, such as hydrophilic hydroxyapatite nanoparticles in hydrophilic/hydrophobic collagen matrix and hydrophobic grease functionalities as weakly polar or nonpolar components creating mosaic hydrophilic/hydrophobic structures.

References

1. Katz EP (1969) The kinetics of mineralization in vitro. I. The nucleation properties of 640-Å collagen at 25°C. Biochim Biophys Acta Protein Struct 194: 121–130.
2. Lipson SF, Katz JL (1984) The relationship between elastic properties and microstructure of bovine cortical bone. J Biomech 17: 231–235.

3. Wilson RM, Elliott JC, Dowker SEP, Rodriguez-Lorenzo LM (2005) Rietveld refinements and spectroscopic studies of the structure of Ca-deficient apatite. Biomaterials 26: 1317–1327.
4. Cortet B, Marchandise X (2001) Bone microarchitecture and mechanical resistance. Joint Bone Spine 68: 297–305.
5. Weiner S, Traub W, Wagner HD (1999) Lamellar bone: structure–function relations. J Struct Biol 126: 241–255.
6. Bernal JD, Fowler RH (1933) A theory of water and ionic solutions with particular reference to hydrogen and hydroxyl ions. J Chem Phys 1: 515–548.
7. Wiggins PM (1990) Role of water in some biological processes. Microbiol Mol Biol Rev 54: 432–449.
8. Wiggins PM (1995) High end low density water in gel. Prog Polym Sci 20: 1121–1163.
9. Chaplin MF (1999) A proposal for structuring of water. Biophys Chem 83: 211–221.
10. Gun'ko VM, Turov VV, Bogatyrev VM et al (2005) Unusual properties of water at hydrophilic/hydrophobic interfaces. Adv Colloid Interface Sci 118: 125–172.
11. Turov VV, Leboda R (1999) Application of ^{1}H NMR spectroscopy method for determination of characteristics of thin layers of water adsorbed on the surface of dispersed and porous adsorbents. Adv Colloid Interface Sci 79: 173–211.
12. Gun'ko VM, Turov VV (1999) Structure of hydrogen bonds and ^{1}H NMR spectra of water at the interface of oxides. Langmuir 15: 6405–6415.
13. Turov VV, Gun'ko VM, Bogatyrev VM et al (2005) Structured water in partially dehydrated yeast cells and at partially hydrophobized fumed silica surface. J Colloid Interface Sci 283: 329–343.
14. Pople JA, Schneider WG, Bernstein HJ (1959) High-Resolution Nuclear Magnetic Resonance. McGraw-Hill Book Co, New York.
15. Kinney DR, Chaung IS, Maciel GE (1993) Water and the silica surface as studied by variable temperature high resolution ^{1}H NMR. J Am Chem Soc 115: 6786–6794.
16. Gun'ko VM, Turov VV, Leboda R et al (2007) Comparative analysis of heterogeneous solid and soft materials by adsorption, NMR and thermally stimulated depolarisation methods. Appl Surf Sci 253: 5640–5644.
17. Aksnes DW, Kimtys L (2004) Characterization of mesoporous solids by ^{1}H NMR. Solid State Nucl Magn Reson 25: 146–163.
18. Turov VV, Gun'ko VM, Zarko VI et al (2006) Weakly and strongly associated nonfreezable water bound in bones. Colloids Surf B 48: 167–175.
19. Gun'ko VM, Turov VV, Shpilko AP et al (2006) Relationships between characteristics of interfacial water and human bone tissues. Colloids Surf B 53: 29–36.
20. Gun'ko VM, Turov VV, Skubiszewska-Zieba J et al (2003) Structural characteristics of a carbon adsorbent and influence of organic solvents on interfacial water. Appl Surf Sci 214: 178–189.
21. Turov VV, Gun'ko VM, Leboda R et al (2002) Influence of organics on structure of water adsorbed on activated carbons. J Colloid Interface Sci 253: 23–34.
22. Turov VV, Gun'ko VM, Tsapko MD et al (2004) Influence of organic solvents on interfacial water at surface of silica gel and partly sililated fumed silica. Appl Surf Sci 229: 197–313.
23. Gun'ko VM, Turov VV, Leboda R et al (2005) Influence of organics on structure of water adsorbed on activated carbons. Adsorption 11: 163–168.
24. Gun'ko VM, Turov VV, Turov AV et al (2007) Behaviour of pure water and water mixture with benzene or chloroform adsorbed onto ordered mesoporous silicas. Cent Eur J Chem 5: 420–454.
25. Hubalek Z (2003) Protectants used in the cryopreservation of microorganisms. Cryobiology 46: 205–229.
26. Tsutsaeva AA (ed) (1983) Cryopreservation of Cell Suspensions. Naukova Dumka, Kiev.

Chapter 8
Regularities in the Behaviour of Nanooxides in Different Media Affected by Surface Structure and Morphology of Particles

V.M. Gun'ko, V.I. Zarko, V.V. Turov, E.V. Goncharuk, Y.M. Nychiporuk, A.A. Turova, P.P. Gorbyk, R. Leboda, J. Skubiszewska-Zięba, P. Pissis, and J.P. Blitz

Abstract Textural and adsorptive characteristics, surface structures, and the volume of individual, binary and ternary nanooxide particles with SiO_2, Al_2O_3 and TiO_2 were investigated. These materials' interactions with low and high molecular weight compounds were investigated using adsorption, NMR, TSDC, DRS, FTIR, TPD–MS, Auger spectroscopy, optical spectroscopy, DLS, titration and microcalorimetry. The presence of a structural hierarchy of particles from primary (10–50 nm), their aggregates (50–1000 nm) and agglomerates of aggregates (> 1 μm) to visible flocculi affects textural features of the oxides, adsorption of different compounds and the behaviour of materials in liquid media.

8.1 Introduction

Adsorbents possessing internal and textural porosities can be divided into three groups [1–9]: (i) materials with particles in the micron to millimetre size range with internal porosity; (ii) materials comprised of nonporous nanoparticles forming aggregates and agglomerates responsible for textural porosity as voids between nanoparticles; and (iii) materials comprised of porous nanoparticles with internal porosity of 10^1–10^2 or hundreds of nanometre size range, and forming secondary particles with textural porosity. Features of the textural characteristics determining adsorption properties of materials dependent on surface chemistry determine the application area of adsorbents [1–4]. Adsorbents with internal microporosity practically do not adsorb high molecular weight compounds, but effectively adsorb low molecular compounds penetrating into micropores. Adsorbents with textural porosity effectively adsorb high molecular weight compounds from solution but are poor adsorbents of low molecular weight compounds since the adsorption energy is comparable to the energy of desolvation caused by adsorption. The aim of this chapter

V.M. Gun'ko (✉)
O.O. Chuiko Institute of Surface Chemistry of the National Academy of Sciences of Ukraine, General Naumov St. 17, Kyiv 03164, Ukraine
e-mail: gun@voliacable.com

A.P. Shpak, P.P. Gorbyk (eds.), *Nanomaterials and Supramolecular Structures*,
DOI 10.1007/978-90-481-2309-4_8,

is to study regularities in the behaviour of individual and complex nanooxides in different media affected by surface structure and particle morphology.

8.2 Materials and Methods

Materials. Fumed silica, alumina, titania and related mixed nanooxides with silica/titania (ST), silica/alumina (SA) and alumina/silica/titania (AST) with different concentrations of components (Table 8.1, prepared at the pilot plant of the Institute

Table 8.1 Structural characteristics and the heat of immersion of nanooxides in water

Sample	C_{SiO_2} (wt%)	C_{TiO_2} (wt%)	$C_{Al_2O_3}$ (wt%)	S_{BET} (m^2/g)	V_p (cm^3/g)	Δw_{sph}	ΔH_{im} (J/m^2)
A-50	99.9			52	0.126	0.378	0.22
A-100	99.9			87	0.193	0.028	
A-150	99.9			144	0.312	0.300	
A-200	99.9			206	0.463	0.031	
A-300	99.9			232	0.483	0.222	0.18
A-300	99.9			294	0.518	0.174	
A-300	99.9			331	0.689	0.356	
A-380	99.9			378	0.780	0.051	
A-400	99.9			409	0.859	0.351	
A-500	99.9			492	0.874	0.063	0.14
SA1	98.7		1.3	203	0.416	0.251	0.28
SA3	97		3	185	0.405	0.344	0.21
SA5	94.6	0.1	5.3	266	0.719	0.234	
SA8	92		8	303	0.688	0.330	0.12
SA23	77		23	347	0.788	0.233	0.13
SA30	70		30	238	0.643	0.260	
SA75	25		75	118	0.320	0.233	0.34
SA96	3.8	0.1	96.1	81	0.163	0.418	0.54
Al_2O_3			99.9	125	0.262	0.164	0.37
ST2	98	2		77	0.263	0.353	0.36
ST9	91	9		235	0.580	0.246	0.18
ST14	86	14		156	0.386	0.385	0.26
ST20	80	20		84	0.174	0.402	0.34
ST29	71	29		73	0.180	0.386	
ST40	60	40		148	0.333	0.420	0.24
ST63	33	63		84	0.215	0.309	
ST65	35	65		34	0.080	0.380	0.40
ST94	6	94		30	0.100	0.254	0.33
TiO_2		100		42	0.117	0.317	0.26
AST03	2.75	0.25	97.0	125	0.308	0.315	0.35
AST06	20.0	0.6	79.4	97	0.234	0.327	0.51
AST1	10.0	1.0	89.0	99	0.253	0.328	0.55
AST50	28	50	22	37	0.095	0.306	0.47
AST71	8	71	21	74	0.127	0.429	0.59
AST82	6	82	12	39	0.150	0.265	0.49
AST87	4	87	9	42	0.148	0.203	0.72
AST88	8	88	4	39	0.123	0.300	0.64

of Surface Chemistry, Kalush, Ukraine) were used as the initial powder materials. The chemical composition of mixed oxides (Table 8.1) was analysed using a XRF (Canberra, USA) spectrophotometer with a ^{55}Fe (or ^{109}Cd) radioactive source, and an amplitude analyser (Canberra) coupled with a computer with the AXIL program. Before the XRF measurements all samples were heated at 723 K for 8 h to remove adsorbed compounds and residual HCl and MCl groups remaining after pyrogenic synthesis in the $O_2/H_2/N_2$ flame using precursors MCl_n (M = Si, Al, Ti). The synthesis of similar individual and composite nanooxides was described previously [10–20].

Nitrogen, water, DMAAB and polymer adsorption. To analyse the structural characteristics of nanooxides, low-temperature (77.4 K) nitrogen adsorption–desorption isotherms were recorded using a Micromeritics ASAP 2405 N adsorption analyser. The nitrogen desorption data were utilised to compute pore size distribution (PSD) recalculated to incremental values (IPSD) [12–20]. To analyse the adsorptive characteristics, water adsorption–desorption on nanooxides was studied by an adsorption apparatus with a McBain–Bark quartz scale at 293 ± 0.2 K and relative pressure $p/p_0 = 0.01$–0.999.

(Dimethylamino)azobenzene ($pK_a = 3.3$) was chosen as a colour indicator to study the active site distributions on the oxide surfaces by optical spectroscopy. The diffuse reflectance spectra of adsorbed DMAAB were recorded using a SF-18 (LOMO, St. Petersburg) spectrophotometer.

Polymer adsorption measurements from aqueous solutions (0.1–1.0 wt%) were added to oxide powders, agitated at 298 K for 2 h and then centrifuged (6000 rpm) for 0.5 h. The value of the adsorption of poly(vinyl alcohol) (PVA), poly(ethylene glycol) (PEG), poly(vinyl pyrrolidone) (PVP), poly(ethylene oxide) (PEO), polydimethyldisiloxane (PDMS) and lecithin was determined using viscosimetry. The concentration of adsorbed proteins was determined by analysis of the residual liquid after centrifugation using the Biuret method and UV/vis spectrophotometry [20].

TPD–MS. Water desorption from nanooxides was studied by the one-pass (OP) temperature-programmed desorption (TPD) time-of-flight (TOF) mass spectrometry (MS) method. Relevant conditions were pressure in chamber 4×10^{-4} Pa, sample weight 5 mg, heating rate 1.67 K/s, with a short distance (~0.5 cm) between sample and MS detector with a MSC-3 ("Electron," Sumy, Ukraine) TOF mass spectrometer (sensitivity 2.2×10^{-5} A Torr^{-1}, accelerating voltage 0.5 kV, pulse frequency 3 kHz), and rehydration time was 15 min.

FTIR. Variable temperature diffuse reflectance FTIR spectra of nanooxides were acquired at 4 cm^{-1} nominal resolution by co-addition of 64 scans using a Digilab FTS3000 FTIR spectrometer equipped with a liquid nitrogen cooled MCT detector [16, 17]. The sample temperature was monitored and controlled with a temperature controller from Omega Engineering. A 5% (w/w) dispersion of nanooxide was dispersed in ground and dried KCl (particle size approximately 5 μm). The dispersion was heated to 200°C for a minimum of 15 min prior to spectral data acquisition and ratioed to a spectrum of pure KCl acquired under the same conditions.

NMR spectroscopy. The ^{29}Si (resonance frequency 59.595 MHz) cross-polarisation magic angle spinning (CP/MAS) NMR spectra and the ^{27}Al (resonance frequency 78.172 MHz) MAS NMR spectra (program ZG) of mixed oxides were

recorded by a Bruker Avance^{TM} 300 NMR spectrometer (magnetic field of 7.046 T, spinning rate of 8 kHz, 4 mm zirconia rotor). Chemical shifts of ^{29}Si and ^{27}Al were referenced to tetramethylsilane and an $Al(NO_3)_3$ aqueous solution, respectively, i.e. the resonance of $Si(CH_3)_4$ and $Al(H_2O)_6^{3+}$ was set to 0 ppm. The ^{1}H NMR spectra were recorded using a Varian 400 Mercury spectrometer or a Bruker WP-100 SY spectrometer of high resolution with a bandwidth of 10–50 kHz. The 90° probe pulses with a duration of 2–4 μs were used to record the ^{1}H NMR spectra. The temperature was controlled with a Bruker VT-1000 device. Relative mean errors were ±10% for ^{1}H NMR signal intensity (by comparison of signals with widely varying intensities) and ±1 K for temperature [21].

Thermally stimulated depolarisation current (TSDC). Thermally stimulated depolarisation current measurements of oxide samples were polarised by an electrostatic field at an intensity $F = (1–5)\times10^5$ V/m at 265 K for 2 min, then cooled to 90 K with the field still applied and then heated without the field at a heating rate of 0.05 K/s. Relative mean errors for the measured TSD current were ±5%, ±2 K for temperature and ±5% for the heating rate. The TSDC method was described in detail elsewhere [22].

Broadband dielectric relaxation spectroscopy (DRS). DRS measurements of complex dielectric permittivity was determined as a function of frequency ($f = 10^{-1}$ to 3×10^6 Hz) at T = 123–293 K (controlled better than ±0.1 K). The dielectric constant (ϵ') is indicative of the ability of a material to store energy and polarise when subjected to an electric field, while the dielectric loss factor (ϵ'') is associated with loss of electric field energy in a material which is dissipated as heat [23]. An Alpha dielectric analyser with a Quatro Cryosystem for temperature control was employed (both from Novocontrol GmbH, Germany). The samples were placed between parallel disk-shaped electrodes, and the distance between the electrodes was kept constant using a Teflon ring spacer of 1 mm thickness.

Metal ion adsorption. Pb(II) and Ni(II) adsorption on oxide surfaces (oxide concentration C_{ox} = 0.2 wt%) was carried out from aqueous solution of PbX_2 or NiX_2 (X = ClO_4). The initial concentration was 10^{-3}–10^{-6} M (concentration of radioactive species ^{210}Pb(II) and ^{59}Ni(II) was 10^{-6} M) with addition of a neutral electrolyte (10^{-3} M $NaClO_4$) using a Teflon cell (50 cm^3) temperature-controlled at $T = 298\pm0.2$ K. The pH value was varied by addition of 0.1 M HCl or NaOH solutions. The gamma radioactivity of the solution was determined using a Beckman Gamma 5500B counter.

Microcalorimetry. A study of oxide adsorbents was carried out by means of a DAC 1.1A (EPSE, Chernogolovka, Russia) differential automatic calorimeter. Before measurements of the heat of immersion (ΔH_{im}), a sample (∼50 mg) was degassed at 473 K and 0.01 Pa for 2 h. The 50 mg sample per 3 cm^3 of distilled water was exposed for several hours. The average errors of the ΔH_{im} measurements repeated several times were smaller than ±10%.

Dynamic light scattering (DLS). Electrophoretic and particle size distribution investigations were carried out using a Zetasizer 3000 (Malvern Instruments) apparatus (λ = 633 nm, Θ = 90°, software version 1.3) at 298 K. Deionised distilled

water and oxide samples (1–10 g of oxide per dm^3 of water) were utilised to prepare suspensions which were ultrasonicated for 5 min using an ultrasonic disperser (Sonicator Misonix, power 500 W and frequency 22 kHz). The pH values were adjusted by addition of 0.1 M HCl or NaOH solutions, and the salinity was 0.001 M NaCl.

Surface charge density and Debye screening length. To evaluate the surface charge density (σ_0), potentiometric titrations were performed using a thermostated Teflon vessel in nitrogen atmosphere free from CO_2 at 25 ± 0.2°C. The solution pH was measured using a PHM240 Research pH-meter (G202C and K401 electrodes) coupled with an REC-61 recorder. The surface charge density was calculated using the potentiometric titration data for a blank electrolyte solution and oxide suspensions (C_{ox} = 0.2 wt% for all oxides), at a constant salinity of 10^{-3} M NaCl. Calculations of the Debye screening length (κ^{-1}) were carried out using the Loeb equation from the results of the DLS and potentiometric titrations measurements [17].

8.3 Surface Structure and Properties

Complex nanooxides (Table 8.1, SA, ST and AST) are characterised by nonlinear changes in surface content of Al_2O_3 and TiO_2 (Fig. 8.1, C^s_X) versus their total content in the materials. The relationships between the specific surface area (S_{BET}) or the pore volume (V_p) of these mixed oxides and the$C_{Al_2O_3}$ and C_{TiO_2} values are nonlinear; however, there is the tendency of a decrease in S_{BET} and V_p values at $C_{Al_2O_3} \geq 23$ wt% and $C_{TiO_2} \geq 40$ wt% (Table 8.1). In SA and AST samples, a maximum in the content of surface alumina is observed at $C_{Al_2O_3}$ = 8–12 wt% and a minimum

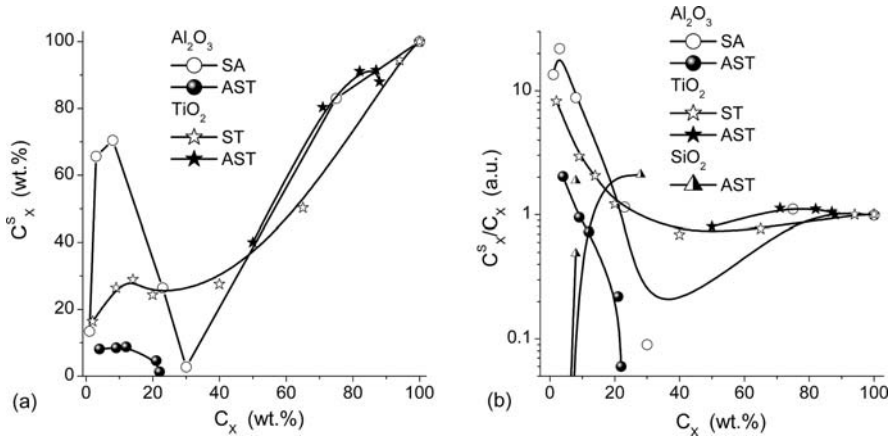

Fig. 8.1 Relationships between total C_X and surface content C^s_X of (**a**) alumina and titania in SA, ST and AST samples; (**b**) relationship between the ratio C^s_X/C_X and the total content of the second phases

at $C_{Al_2O_3} = 21$–30 wt% (Fig. 8.1). In contrast to surface alumina the surface titania increases with the total content of TiO_2 in ST and AST without significant deviation. Notice that a shallow minimum in $C_{TiO_2^s}$ at $C_{TiO_2} = 20$ wt% corresponds to a maximal number of≡SiOTi≡ bridges in ST, and the largest number of Brønsted acid sites is in SA23 [24, 25]. These structural features, as well as changes in the size of primary particles and their aggregation, and Brønsted (B) and Lewis (L) acidity affect interfacial phenomena: the adsorption (gaseous phase) and structurisation (aqueous suspension) of water, the adsorption of metal ions, polymers and proteins and other effects [8, 9].

One can expect the interfacial relaxation phenomena to depend on oxide surface composition as observed by NMR, TSDC, DRS and other methods [10, 21, 22].

The FTIR spectra of nanooxides (Fig. 8.2) in the OH stretching region were acquired at 200°C to minimise the effects of surface adsorbed water. The free silanol peak at 3740 cm^{-1} is readily detected in SA at $C_{Al_2O_3} \leq 30$ wt% and in ST at $C_{TiO_2} \leq 65$ wt%. However, for certain samples there is only a shoulder at 3740 cm^{-1}. This free silanol peak is not seen at the highest alumina (75%) or titania (94%) contents. For both SA and ST samples, the free silanol peak intensity decreases with increasing surface alumina or titania content. As alumina content increases an increase in absorbance at lower frequencies is observed. These broad bands may arise from hydrogen-bonded hydroxyls on the alumina, silica, mixed metal sites

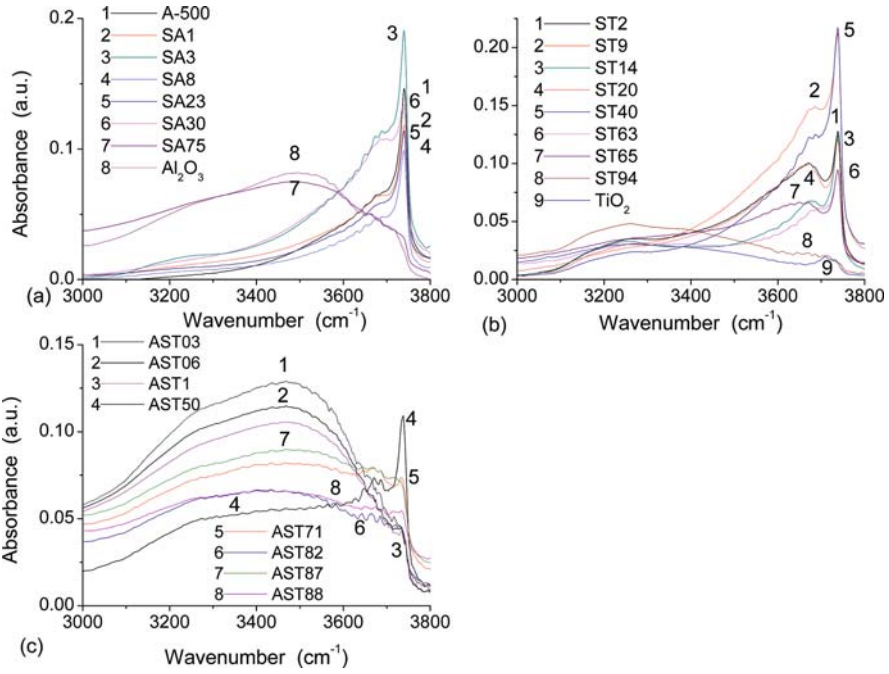

Fig. 8.2 FTIR spectra acquired at 200°C of nanosilica A-500, SA (**a**), ST (**b**) and AST (**c**) samples at different alumina and titania contents in the OH stretching region

correlating with Brønsted acid sites, and residual water which may be held more tightly by the mixed oxides. Spectra of the ST samples exhibit similar behaviour. It is interesting to note that a small but distinct set of peaks in the 3300–3200 cm^{-1} region is seen in the ST and titania samples (Fig. 8.2b). The AST sample spectra (Fig. 8.2c) exhibit characteristics of both the SA and ST sample spectra, e.g. peaks in the 3700–3600 cm^{-1} region which are not characteristic for individual silica. These bands can be assigned to different terminal ≡MOH and bridging $\equiv M_1O(H)M_2\equiv$ hydroxyls (M = Si, Ti and Al).

On the basis of the analysis of the FTIR spectra (Fig. 8.2) and the literature, the bands at 3730 and 3710 cm^{-1} observed for pure titania (Fig. 8.2b) can be attributed to ≡TiOH and ≡TiO(H)Ti≡ groups.

The bands at 3650–3640 cm^{-1} are linked to ≡SiO(H)Al≡ and the bands at 3670–3660 cm^{-1} can be assigned to ≡SiO(H)Ti≡ in AST. The bands at 3690–3680 cm^{-1} can be assigned to ≡AlO(H)Ti≡ or ≡AlO(H)Si≡ [16, 17]. A broad band at 3670 cm^{-1} is characteristic of disturbed silanols of pure silica. Thus the FTIR spectra demonstrate a certain heterogeneity of mixed oxides with respect to the characteristics of the surface hydroxyls, which can impact the adsorption properties of the materials, since surface hydroxyls are the main adsorption sites on metal oxides.

The adsorption (Fig. 8.3a) and desorption (Figs. 8.3b and 8.4) of water from nanooxides depend on the concentration and kind of surface hydroxyls, S_{BET} (Table 8.1) and the type of packing of nanoparticles in aggregates [5, 10–12]. For instance, the adsorption/desorption of water is largest for SA23 among SA samples because SA23 has the largest S_{BET} value (Table 8.1) and greatest Brønsted acidity (Fig. 8.5) because of a low $C^s_{Al_2O_3}$ value (Fig. 8.1). Typically the lower the $C^s_{Al_2O_3}$ value in amorphous (e.g. fumed) or crystalline (e.g. zeolites) SA, the higher the Brønsted acidity. The sample SA8 has larger S_{BET} and $C^s_{Al_2O_3}$ values than SA3. Therefore desorption of water (Fig. 8.3b) from SA8 is greater at $T < 550$ K (effect of surface alumina and Al_2O_3/SiO_2 interfaces) and lower at $T > 550$ K (effect of surface silica) because associative desorption of water from surface hydroxyl condensation occurs more easily from SA than silica (Figs. 8.3 and 8.4). However, the adsorption of water is higher on SA3 than SA8 (Fig. 8.3a).

Since the volume of adsorbed water is less than the total pore volume measured by N_2 adsorption (V_p, Table 8.1), water fills just a fraction of the total pore volume in these SA materials.

Therefore, even though SA8 has larger S_{BET} and V_p values, the lower adsorption of water onto SA8 may be caused by a difference in packing of primary particles in aggregates. Deviation from the model of pores as voids between spherical particles (Table 8.1, Δw_{sph}) varied from 0.05 to 0.43 and depends on nanooxide composition because it is smaller for silicas and larger for mixed oxides.

This difference appears in the IPSDs (Fig. 8.3d) for both narrow pores at R between 1 and 5 nm and for broader pores at $R > 20$ nm. Water more effectively fills narrow pores ($V_w < V_p$), and the IPSD of SA3 is higher at $1 < R < 5$ nm than that of SA8 (Fig. 8.3d). Therefore the adsorption of water is higher for SA3 than SA8 (Fig. 8.3a). The shape of the IPSDs of SA (Fig. 8.3d) and nanosilica (Fig. 8.3c)

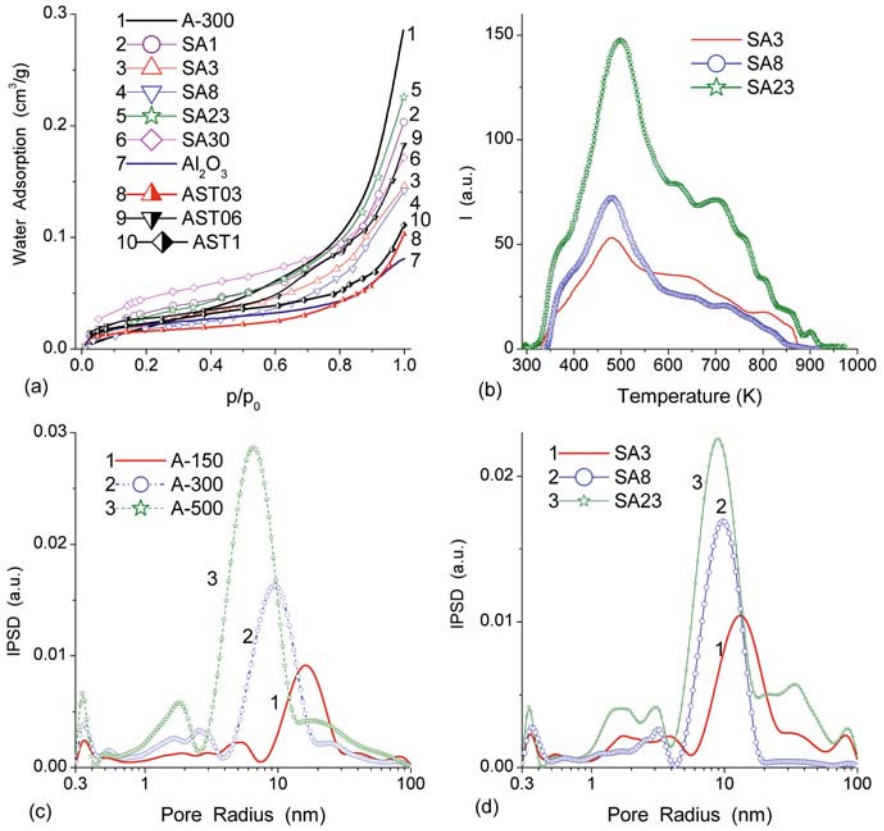

Fig. 8.3 (**a**) Adsorption isotherms of water, (**b**) TPD–MS spectra of water (*m*/*z* 18), and IPSD for (**c**) nanosilica and (**d**) SA samples

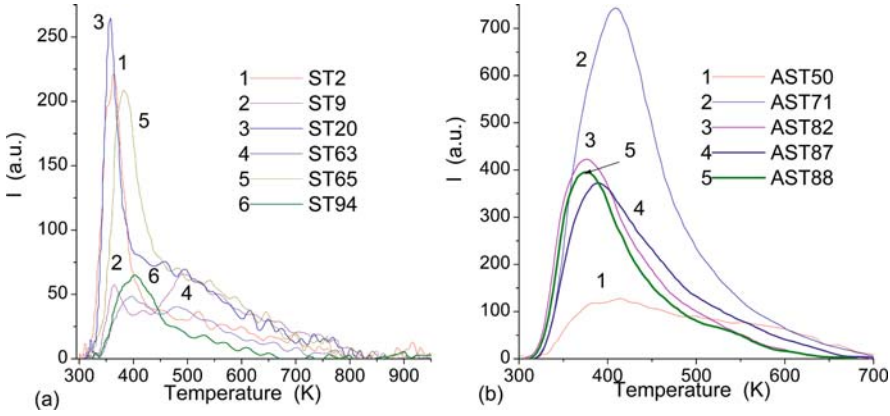

Fig. 8.4 TPD–MS spectra of water (*m*/*z* 18) desorbed from degassed (**a**) ST and (**b**) AST

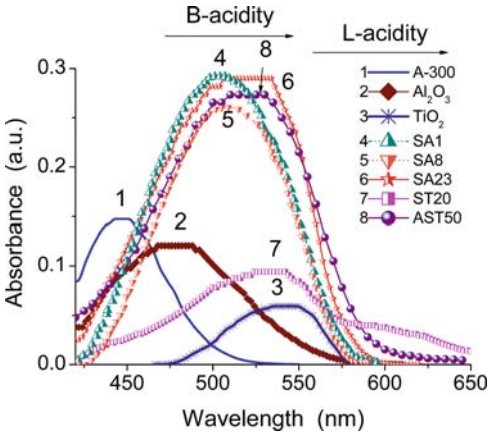

Fig. 8.5 Optical spectra of DMAAB adsorbed on nanooxides

samples differ over the ranges of narrow mesopores and macropores. This can be caused by the presence of surface alumina and silica in SA samples, leading to changes in particle–particle interactions influencing formation of aggregates and agglomerates, whose sizes are larger for SA than nanosilica samples [10]. Of the low titania content AST samples, AST06 exhibits the largest water adsorption while also having relatively small S_{BET} and V_p values (Table 8.1). Since AST06 has a relatively high silica content, this results in a relatively large number of surface acid (SiO(H)Al) sites. Therefore, the ΔH_{im} value is higher for AST06 than AST03 with minimal silica content.

The main water desorption peak from ST is at $T = 330$–450 K and from AST at $T = 330$–550 K (Fig. 8.4). However, the tail of this desorption is longer for both ST and SA samples (Fig. 8.3b) than for AST samples. Water desorption from AST stops at $T = 650$–700 K because of the small content of silica in these samples. The influence of silica on water desorption from mixed nanooxides is much less than for CVD-TiO_2/A-300 (Fig. 8.4c) (high-temperature portions of the water desorption curves for A-300 and CVD-TiO_2/A-300 are similar). In the case of grafted CVD-TiO_2, separate titania particles form and their contacts with silica particles are weak [26]. This result confirms the importance of the formation of bridges ≡SiO(H)M≡ and ≡SiOM≡ and tight contacts between different phases in mixed nanooxides for different surface processes. These structural features can play a specific role on the relaxation of interfacial water in aqueous suspensions of these oxides, as shown below.

The larger number of different surface sites at a mixed oxide surface [16, 17, 24] leads to broadening of the TPD–MS spectra for ST samples in comparison with individual titania (Fig. 8.4). For AST samples, desorption of water from AST82, AST87 and AST88 is similar, water desorption from AST50 and AST71 differs (Fig. 8.4) due to the effect of larger S_{BET} (AST71) and lower$C^s_{TiO_2}$ values (AST50). The TPD–MS spectra of desorbed water (Fig. 8.4) is dependent on oxide composition. Several factors, in addition to the surface content of the second oxide, can be responsible

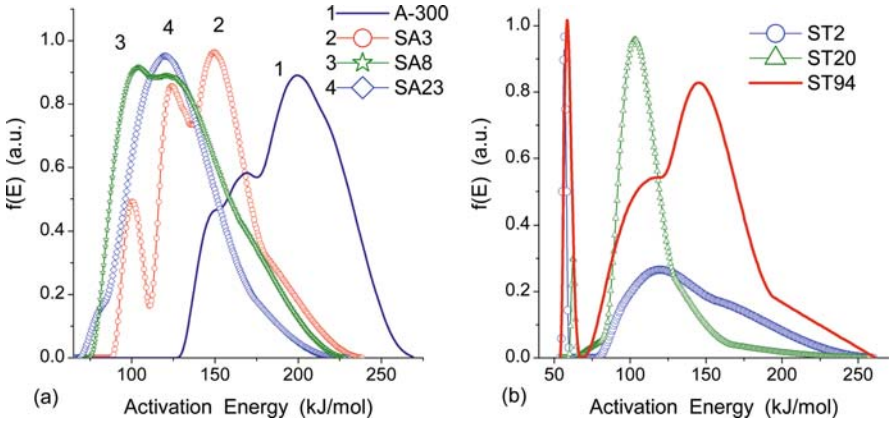

Fig. 8.6 Distribution functions of the activation energy of water desorption (m/z =18) from (**a**) A-300 and SA and (**b**) ST samples

for this effect: (i) different contents of terminal and bridging hydroxyls for different samples; (ii) different topology and morphology of primary and secondary particles; (iii) different S_{BET} values; and (iv) different amounts of adsorbed intact water. These factors also affect the distribution functions of the activation energy (E) of water desorption (Fig. 8.6). The difference between the $f(E)$ shape for SA, ST and AST is much smaller than for A-300, because silica has only terminal hydroxyls (single ≡SiOH and twin =$Si(OH)_2$). An increase in the surface B acidity of SA23 (Fig. 8.5), evidenced by the DMAAB spectrum being slightly shifted towards longer wavelengths in comparison with other SA samples because of a relatively low surface content of alumina at a higher S_{BET} value for SA23, results in a higher intensity of $f(E)$ at $E > 150$ kJ/mol for SA3 and SA8 than for SA23 (Fig. 8.6a). ST20 has the largest number of bridging hydroxyls ≡SiO(H)Ti≡ with maximal B acidity among ST samples.

Therefore the high-energy band of $f(E)$ at $E > 130$ kJ/mol is lower for ST20 in comparison with ST2 and ST94 (shown as boundary ST samples). The TPD activation energy of 70–80 kJ/mol for desorption of water from titania corresponds to the initial portion of the $f(E)$ function for mixed oxides (Fig. 8.6), related to desorption of intact water molecules.

Features of mixed oxides are reflected in the amounts of Si atoms in the structures $Si(OM–)_4$ (Q^4_{Si} in Table8.2, Fig. 8.7), $Si(OM–)_3(OH)$ (Q^3_{Si}) and $Si(OM–)_2(OH)_2$ (Q^2_{Si}) (where M = Si, Al or Ti). Their contributions, as well as of sites with different O-coordination numbers of aluminium atoms, change with increasingC_{TiO_2} or$C_{Al_2O_3}$ value. Contributions of six-, five- and fourfold O-coordinated Al atoms also vary. For a large titania content material such as ST94 or AST88 (C_{SiO_2} = 6 and 8 wt%, respectively), silica does not represent a separate phase because it forms a solid solution in titania. However, titania in ST9 or ST with largerC_{TiO_2} values forms its own phase, observed in XRD patterns. The distribution of alumina in SA, and titania in ST, at the particle surface as a function of the total content of alumina

Table 8.2 Contributions (in %) of different centres with Si and Al in SA, ST and AST samples determined as relative integral intensity of the bands obtained on deconvolution of the ^{29}Si CP/MAS and ^{27}Al MAS NMR spectra

Sample	Q^4_{Si}	Q^3_{Si}	Q^2_{Si}	$Q_{Al(VI)}$	$Q_{Al(V)}$	$Q_{Al(IV)}$
SA1	45.7	33.3	21.0	60.3		39.7
SA3	31.1	52.6	14.2	77.9	1	21.1
SA8	48.0	45.0	7.0	73.4		26.6
SA23	45.5	33.4	21.1	55.9	3.5	40.6
SA30	28.8	50.7	20.5	51.0	4.2	44.8
ST9	33.6	44.7	21.7			
ST14	44.0	31.8	24.2			
ST20	29.1	54.6	16.3			
ST63	57.3	16.6	26.1			
ST65	64.9	19.5	15.6			
AST50	68.1	23.6	8.3	86.2		13.8
AST82				94.1	3.4	2.5

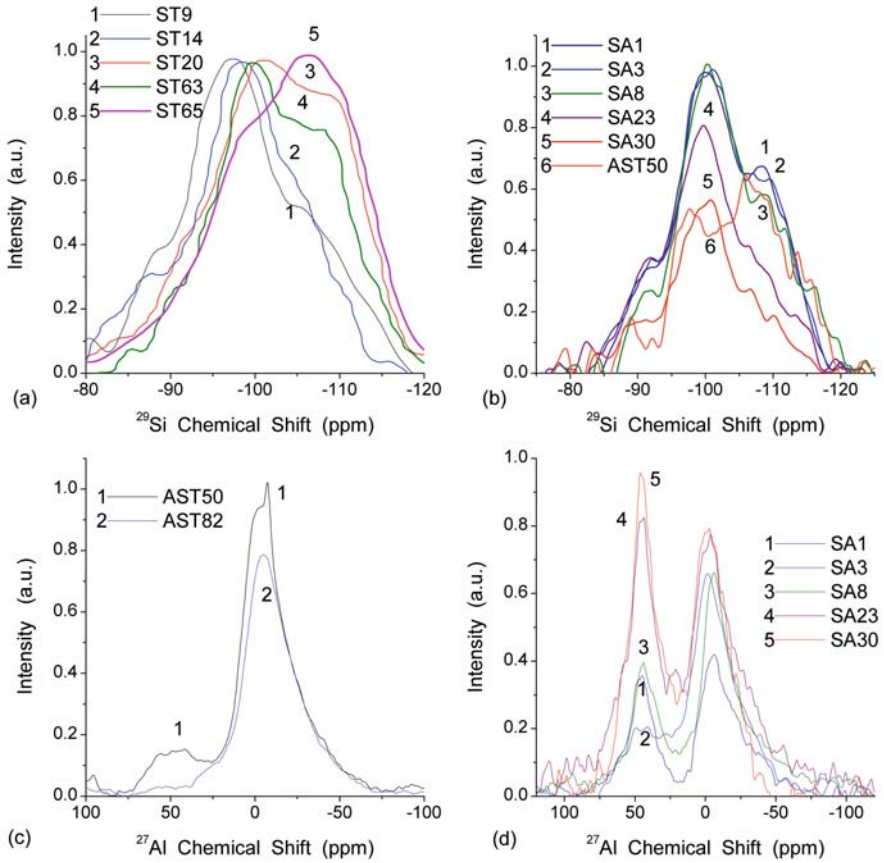

Fig. 8.7 (**a**, **b**) ^{29}Si and (**c**, **d**) ^{27}Al MAS NMR spectra of (**a**) ST, (**b**, **d**) SA and (**c**) AST samples

or titania differs (smoother curve for ST than SA). A small amount of Si atoms at the surface of ST samples at high C_{TiO_2} values causes results in small signals from Q^3_{Si} and Q^2_{Si} sites, and a large signal from Q^4_{Si} sites (Fig. 8.7a) corresponding to Si atoms in the bulk. This is in agreement with the FTIR spectra (Fig. 8.2) showing decreased intensity of the O–H stretching vibrations of free silanols at 3740 cm^{-1} with increasing surface content of alumina or titania in mixed oxides. A similar tendency for SA samples is more complex than for ST samples because the surface content of alumina as a function of total alumina content is extremely nonlinear.

An increase in the content of alumina in SA samples and titania in ST samples leads to the opposite results with respect to contribution of Q^4_{Si} at −110 ppm (Fig. 8.7 and Table 8.2) because of the difference in the electronic properties of titania (semiconductor) and alumina (dielectric). However, changes in Q^3_{Si} at −101 ppm and Q^2_{Si} at −91 ppm do not seem to correlate with $C_{Al_2O_3}$ and C_{TiO_2} values. Deviation from a linear dependence of contribution of these sites on the $C_{Al_2O_3}$ and C_{TiO_2} values are caused by nonlinear changes in the surface content of these oxides (Fig. 8.1). The Q^3_{Si} and Q^2_{Si} sites correspond to surface silanols, whose content directly depends on the surface content of alumina and titania (the effects of titania on shielding the Si nuclei can affect the position of the corresponding components of the ^{29}Si CP/MAS NMR spectra). A semiconducting titania phase, as an electron-donor for the silica phase, can change shielding of the Si nuclei; additionally, the $Si(OM–)_4$ structure (i.e. bond lengths and valence angles) changes if $M \neq Si$.

Therefore, the ^{29}Si NMR spectra shift slightly and the Q^4_{Si} intensity increases with increasing C_{TiO_2} value in ST samples (Fig. 8.7a). The electronic properties of dielectric alumina and silica (as well as the sizes of Si and Al atoms) are closer than titania; therefore, a similar displacement of the ^{29}Si NMR spectra is not observed for SA samples with increasing $C_{Al_2O_3}$ value (Fig. 8.7b). The number of Q^2_{Si} sites decreases with increasing surface content of alumina or titania (Table 8.2); for instance, it is lowest for SA8 with the largest content of surface alumina (Fig. 8.1). The number of Q^3_{Si} sites is greatest for ST20 and SA3 for several reasons related to the surface content of the second oxide: its distribution form in the bulk, the particle size and surface patches, the number of contacts of these patches with silica and the number of centres with isomorphic substitution of Si for Al or Ti atoms.

According to the ^{27}Al MAS NMR spectra (Fig. 8.7c, d), the content of sixfold O-coordinated Al(VI) (^{27}Al resonance at ∼0 ppm) in the alumina phase is larger than that of fourfold O-coordinated Al(IV) (^{27}Al resonance at ∼50 ppm) in SA samples (Table 8.2). This suggests that alumina preferentially forms in a separate phase (e.g. γ-Al_2O_3 (which represents ∼20% in individual nanoalumina) includes approximately 80% Al(VI) and 20% Al(IV) or individual amorphous phase) than a solid solution in the silica matrix with substitution of fourfold O-coordinated Si, keeping this coordination state. Although the peak intensity of the Al(IV) resonance is higher than Al(VI) for SA23 and SA30, the Al(VI) band is broader (Fig. 8.7) and a larger FWHM (full-width at half-maximum) value causes a greater integral contribution of Al(VI) sites (Table 8.2). In the case of AST82 synthesised at a higher temperature

(> 1700 K) than SA samples, the alumina phase includes mainly Al(VI) because (i) patches of individual alumina can have a structure similar to a high-temperature modification of alumina (e.g. α-Al_2O_3 with only Al(VI)); and (ii) a dense solid solution of alumina in titania corresponds to substitution of sixfold O-coordinated Ti(VI) by Al(VI). In AST50 possessing a larger content of silica but a smaller content of titania (Table 8.1), and synthesised at a lower temperature than AST82, an individual alumina phase can include patches with a structure close to that of γ-Al_2O_3 or amorphous alumina including both Al(VI) and Al(IV). Contribution of Al(VI) in AST50 is greater than that of γ-Al_2O_3 because of the reasons mentioned above with respect to AST82. However, a lower synthesis temperature and possible incorporation of Al(IV) into the silica lattice (as AST50 includes 28% silica) gives a larger amount of Al(IV) in AST50 than AST82. The ^{29}Si CP/MAS NMR spectrum of AST82 (not shown) in contrast to AST50 does not have clear bands, and the Si–O(Si) stretching vibrations at 1100 cm^{-1} are not observed in the FTIR spectrum of AST82 or AST88. These results suggest that silica is absent as an individual phase in AST82, AST87 and AST88 forming only a solid solution in titania and alumina. The opposite effects of titania and alumina on the ^{29}Si chemical shift provide a very small ^{29}Si (at the noise level) in the AST samples, with the exception of AST50. A low amount of Al(V) (^{27}Al chemical shift at 30 ppm) is observed for certain samples (Table 8.2); however, a clear Al(V) band is observed only for SA23 (Fig. 8.7d) characterised by a low amount of surface alumina (Fig. 8.1).

If the ratio $Q_{Al(VI)}/Q_{Al(IV)} \approx 4$ corresponds to an individual Al_2O_3 phase (γ-Al_2O_3 or amorphous) in mixed oxides, then the value $\beta = Q_{Al(IV)}/(Q_{Al(IV)} + Q_{Al(IV)}) - 0.2$ can be used as a measure of the number of Al atoms isomorphically substituting Si atoms in the silica lattice. This estimation for SA3 ($\beta = 0.011$) shows that nearly all alumina is at the surface in agreement with AES data. However, in the case of other SA samples a fraction of the Al atoms can be embedded in the silica matrix. The greatest number of these Al atoms ($\beta > 0.2$) is observed for SA30 and SA23 (Table 8.2), characterised by relatively low surface content of alumina according to the AES data (Fig. 8.1).

The dependence of Brønsted acidity on the$C^s_{Al_2O_3}$ value and the nonlinear dependence of surface alumina concentration on the total content of alumina in SA and AST samples (Fig. 8.1), as well as differences in the morphology of particles and the size distribution of gaps between these particles (Fig. 8.3), can cause nonlinearity of the interfacial characteristics of both mixed oxides and adsorbed water or water layers structured by the oxide surface in aqueous suspensions. For analysis of the interfacial phenomena in aqueous suspensions, the data related to dry powders and dried solid residues obtained from suspensions of nanooxides can be used. This comparison allows the elucidation of some changes in the characteristics of oxides occurring on their transfer from the gaseous medium to liquid and then into air.

A minimal$C^s_{Al_2O_3}$ value for SA23 (Fig. 8.1a) results in the smallest amounts (C_{uw}) of structured water unfrozen at $T < 273$ K (Fig. 8.8) determined by ^{1}H NMR spectra. Larger C_{uw} values are found for the suspensions of alumina and SA3 (high$C^s_{Al_2O_3}$ value). Changes in the Gibbs free energy of the structured water are between -0.2 and -2.7 kJ/mol (Fig. 8.8b).

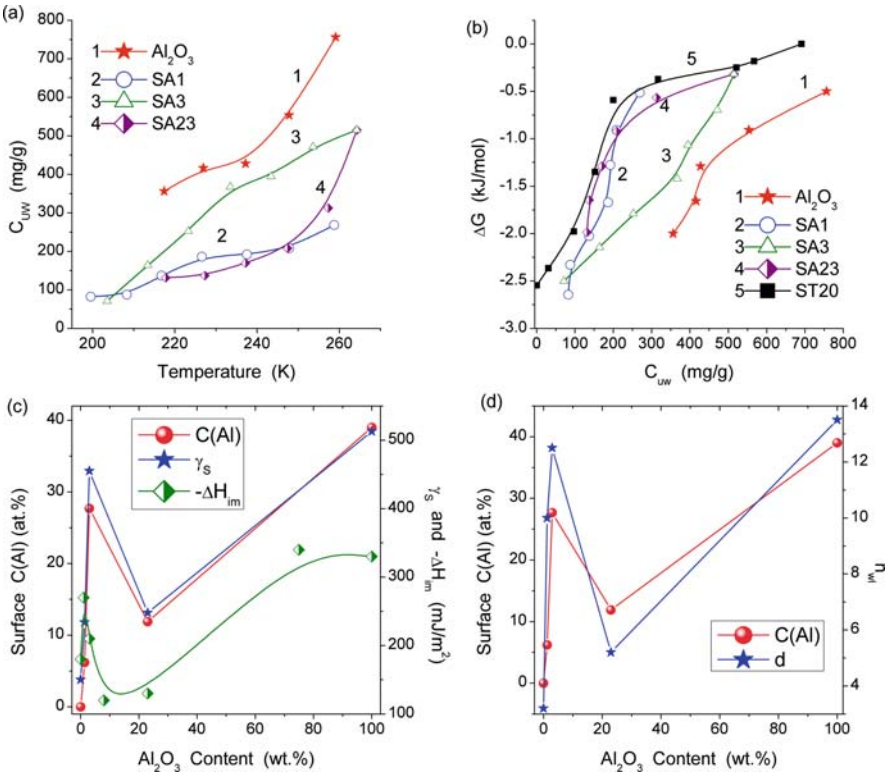

Fig. 8.8 (**a**) Concentration of unfrozen water (C_{uw}) as a function of temperature for aqueous suspension (5 wt%) of alumina and SA samples determined from the ^{1}H NMR spectra; (**b**) relationship between Gibbs free energy ΔG and C_{uw} (curve for ST20 is also shown); (**c**, **d**) relationships between total content of alumina is SA samples and surface content of aluminium and (**e**) interfacial free energy γ_S and the enthalpy of immersion in water (ΔH_{im}), and (**d**) the number of statistical water layers (n_{wl}) at a thickness of each of them of 0.3 nm

The structure of interfacial water can be also characterised by the Debye screening length (κ^{-1}) as a function of pH (Fig. 8.9) and ζ potential as a function of pH and the surface charge density (Fig. 8.10).

Notice that the ζ potential and the surface charge density deal with different planes (i.e. shear and surface planes, respectively). In the case of individual oxides (e.g. silica, titania and alumina), the κ^{-1}(pH) function has only one maximum observed in the pH range close to the isoelectric point (IEP) of the materials (Fig. 8.9a) since IEP(SiO_2) $\approx$ 2.2, IEP(TiO_2) $\approx$ 6 and IEP(Al_2O_3) $\approx$ 9.8. The κ^{-1}(pH) function is determined on the basis of three factors ζ(pH), σ_0(pH) and effective diameter of particles D_{ef}(pH) (with consideration for the porosity of aggregates), and these are nonlinear functions of pH (Fig. 8.10). However, for mixed oxides the κ^{-1}(pH) function can have an unexpected shape, e.g. SA23 (low amount of surface alumina and high Brønsted acidity) exhibits a maximum far from

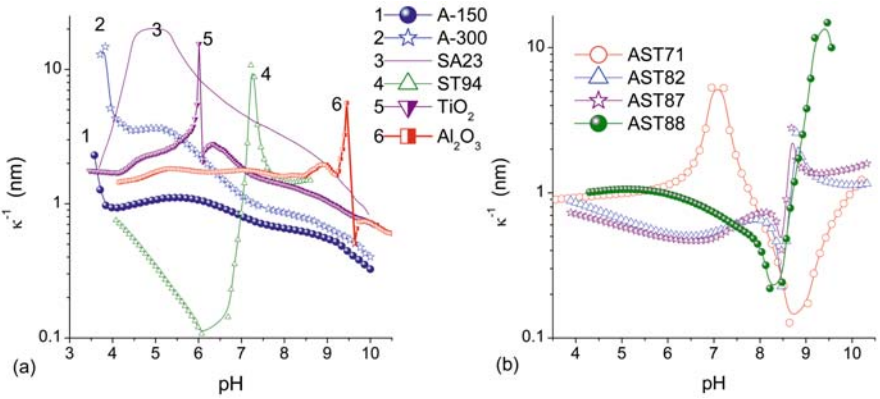

Fig. 8.9 Debye screening length (κ^{-1}) for dispersions with (**a**) nanosilica A-150 and A-300, SA23, ST94, TiO_2 and Al_2O_3 (**b**) AST samples

$IEP(SiO_2)$ and $IEP(Al_2O_3)$ (Fig. 8.9a). There is a difference in the peak position of the κ^{-1}(pH) function for TiO_2 and titania-containing ST and AST oxides because of the complex structure of their surface. The difference in the surface composition of AST samples (Figs. 8.1 and 8.2) causes noticeable differences in their behaviour in aqueous media (Figs. 8.9 and 8.10), especially for AST71 in comparison with other AST samples, because of the maximal content of alumina and specific surface area among AST samples (Table 8.1). This results in the differences (discussed above and below) in many of the properties of AST71 and other samples. Complex

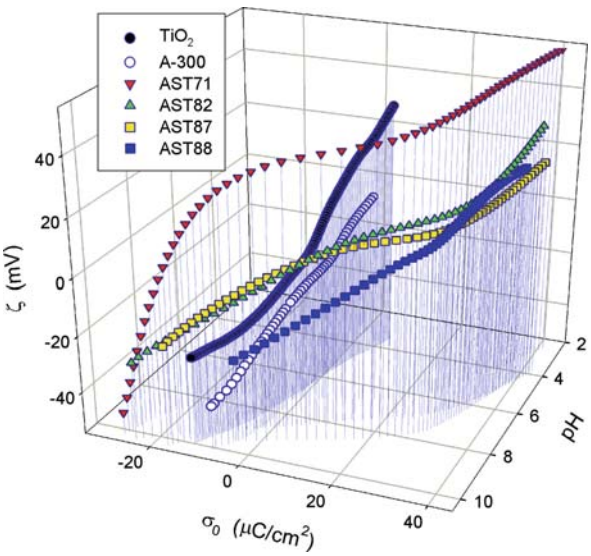

Fig. 8.10 ζ potential as a function of pH and surface charge density of A-300, TiO_2 and AST samples

shapes of the κ^{-1}(pH) function as well as the ζ(pH) potential and σ_0(pH) can lead to complex pH dependences of other properties of the nanooxide dispersions such as aggregation of particles (i.e. D_{ef}(pH)), adsorption of dissolved compounds and metal ions, suspension viscosity, etc.

The spectra of DMAAB adsorbed onto SA23 and ST20 have similar widths (Fig. 8.5) because of a wide range of surface sites; however, ST20 has a larger amount of L sites. This similarity in the types of surface sites results in a similar shape of the $\Delta G(C_{uw})$ graphs for interfacial water in aqueous suspensions of these oxides (Fig. 8.8b). However, relationships between the enthalpy of immersion in water (ΔH_{im}) and surface content of Al, versus the total content of the second oxides differ for SA and ST [16, 17]. This can be caused by differences in the distribution of alumina and titania, and the corresponding active sites at the surface of mixed oxides.

The γ_s and ΔH_{im} values as functions of $C_{Al_2O_3}$ in SA correlate with the surface content of aluminium C^s_{Al} (Fig. 8.8c), as well as the thickness of the interfacial structured water (Fig. 8.8d). These correlations are caused by several factors: (i) number and acidity of surface sites; (ii) nonuniformity of the surface; and (iii) specific surface area (γ_s and ΔH_{im} are calculated per unit surface area). The influence not only of the number of B sites but also of other factors on the surface properties of mixed oxides is clearly depicted in the data (Fig. 8.8) [16, 17].

The effects of not only B sites but also other surface structures (and several adsorption mechanisms) on the adsorption of metal ions are clearly observed in Fig. 8.11. The shapes of the plateau adsorption curves of Pb(II) onto SA samples, and Ni(II) onto ST samples, correlate with the surface content of alumina and titania, respectively. A larger deviation in the curve shapes for the adsorption of Pb(II) onto the SA samples corresponds to a similar deviation in the relationship between the S_{BET} and $C^s_{Al_2O_3}$ versus the total $C_{Al_2O_3}$ values (Table 8.1), because the ion adsorption is calculated per unit surface area. The observed correlations show that

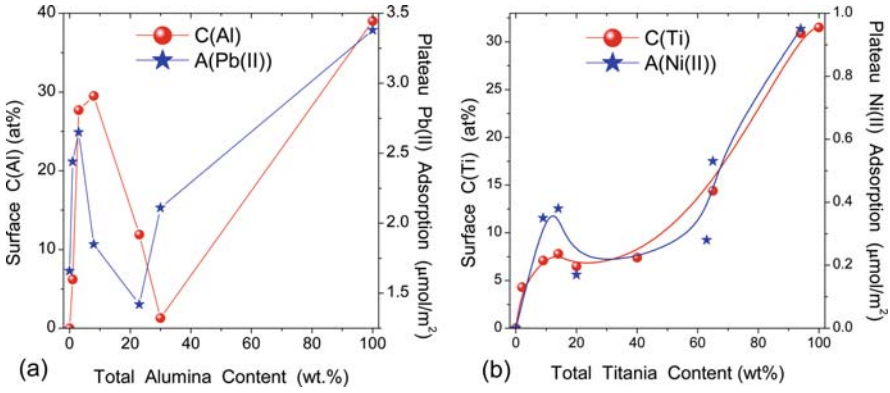

Fig. 8.11 Surface content of (**a**) Al in SA and (**b**) Ti in ST and the plateau adsorption of (**a**) Pb(II) and (**b**) Ni(II) as a function of the total (**a**) alumina and (**b**) titania content in mixed nanooxides

the number of B sites is not limiting for the plateau adsorption of Pb(II) and Ni(II), because this maximal adsorption is observed at relatively high pH values (close to 7–8) when the contribution of hydroxy species of Pb(II) and Ni(II) increases.

8.4 Interaction of Nanooxides with Polymers and Proteins

The adsorption of several types of polymers onto nanosilica A-300 gives different interfacial layer structures. PEG and PEO having the same segment structure are characterised by a close $\Phi(C_{pol})$ shape (Fig. 8.12a). Despite weak polymer–polymer interactions, PDMS gives the lowest $\Phi(C_{pol})$ values (as a function of C_{pol} in mg/g) because of (i) a large segment (m_{seg}) weight $-(CH_3)_2Si-O-Si(CH_3)_2-$, (ii) its weak interaction with silanols due to relatively poor electron-donor properties of oxygen atoms in the siloxane bonds, (iii) steric effects of the CH_3 groups and (iv) the helical structure of the PDMS chain. PVA molecules can form strong hydrogen bonds with both silanols and OH groups of neighbouring molecules, leading to low Φ values as a function of C_{pol} and the lowest Φ values as a function of C_{pol}/m_{seg} (Fig. 8.12b). PVP has a larger segment weight than PEG, PEO and PVA by a factor of 2.4. Therefore, $\Phi(C_{pol})$ for PVP is lower than PEG or PEO, but close to that of PVA (Fig. 8.12a). PVP molecules can more effectively interact with surface silanols than other linear polymer molecules because of the rotational mobility of the side groups responsible for the formation of hydrogen bonds (Fig. 8.12b).

BSA molecules demonstrate relatively low $\Phi(C_{pol})$ values because of the high average m_{seg} value, and the globular protein shape. Therefore, a significant portion of the molecules cannot be in contact with the silica surface. However, protein

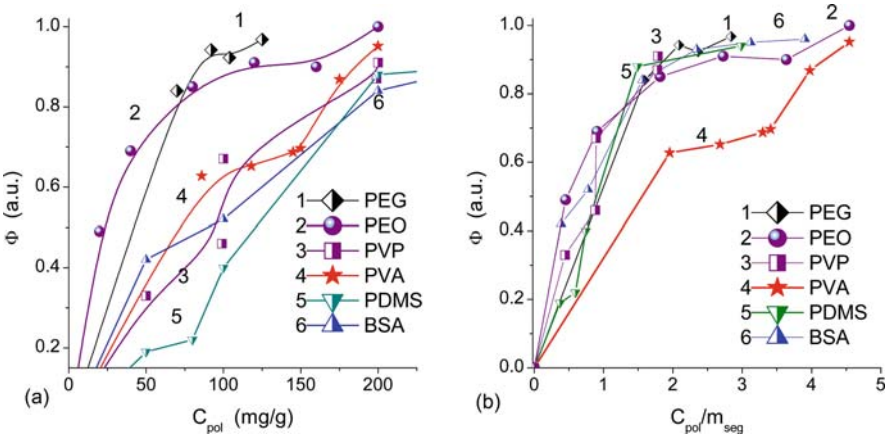

Fig. 8.12 Perturbation degree (Φ) of free surface silanols as a function of the polymer loading (**a**) C_{pol} in mg per gram of silica, and (**b**) C_{pol} normalised by dividing by the molecular weight of a segment (m_{seg}) for PEG (35 kDa), POE (600 kDa), PVP (12.7 kDa), PVA (43 kDa), PDMS (8 kDa) and BSA (67 kDa) onto A-300

molecules have several types of polar side groups in addition to the polypeptide chain which can form strong hydrogen bonds with silanols, which can partially compensate for the effect of the globular shape of the molecules on the $\Phi(C_{pol})$ values. Normalisation of C_{pol} by dividing by the segment m_{seg} molecular weight (Fig. 8.12b) results in similar $\Phi(C_{pol}/m_{seg})$ graphs for all A-300/polymer systems except A-300/PVA. The effects of strong hydrogen bonds between PVA molecules are the likely cause of this result. The globular structure of BSA molecules prevents strong lateral interactions, therefore $\Phi(C_{pol}/m_{seg})$ for BSA is similar to other systems characterised by relatively weak polymer–polymer interactions. The effects of residual interfacial water, which can disturb silanols and form hydrogen bond bridges between polar groups of polymer molecules and surface silanols, can provide a small difference in the $\Phi(C_{pol}/m_{seg})$ graphs for different polymers (especially at $C_{pol}/m_{seg} > 1$) (Fig. 8.12b). Thus a minimal loss of the specific surface area for the nanooxide/polymer powders results from a monolayer coating of nanoparticles by PEO or PEG. This is a result of the formation of strong hydrogen bonds with silanols and weak polymer–polymer interactions, which result in a dense coverage with stronger interactions between polymer molecules and surface silanols.

The strong interaction of adsorbed polymers with oxide surfaces causes changes during their thermal decomposition. Additionally, the catalytic effect of active surface sites on mixed oxides on thermolysis of adsorbed PVA and PEG molecules (Fig. 8.13) causes displacement of the TPD peaks towards lower temperatures in comparison with thermolysis on silica.

There is a difference in the catalytic effects for PVA and PEO, because of their structural differences and the type of surface interactions. Dehydration of PVA/silica is complete at 650 K, but the dehydration of nanosilica alone occurs at much higher temperatures (up to 1000 K and higher). The strong hydrogen bonding of OH groups of PVA and silica is the main reason for this difference. Since the sample mass used in all of the TPD–MS measurements was almost identical, differences in the TPD peak intensities of eliminated water and CO on decomposition of PVA and PEG (Fig. 8.13) are likely caused by differences in the catalytic effects of SA and ST samples and the differences in the specific surface area of nanooxides and the amounts of polymers.

Assuming that the glass transition temperature (T_g) for PVA/A-300 corresponds to the maximum on the $\varepsilon''(f,T)$ and $\varepsilon'(f,T)$ curves at low frequencies, i.e. $T_g = 341$ K (Fig. 8.14) and $T_g = 358$ K for bulk PVA, one can estimate the amounts of water bound in the PVA phase to be 0.6 wt%.

Since t total amount of water in PVA/A-300 is $\approx$1.7 wt%, the amount of water adsorbed on the silica surface from air is approximately 1.1 wt%. There are three types of relaxations (α, β and γ, in order of increasing frequency/decreasing temperature) of different intensity and strong ion conductivity at low frequencies/high temperatures caused by adsorbed water promoting the mobility of protons (Figs. 8.14 and 8.15). Contribution of the conductivity increases with increasing temperature because of enhanced mobility of bound water molecules [23]. According to ^{1}H NMR spectra of similar systems, mobile water molecules appear in the strongly

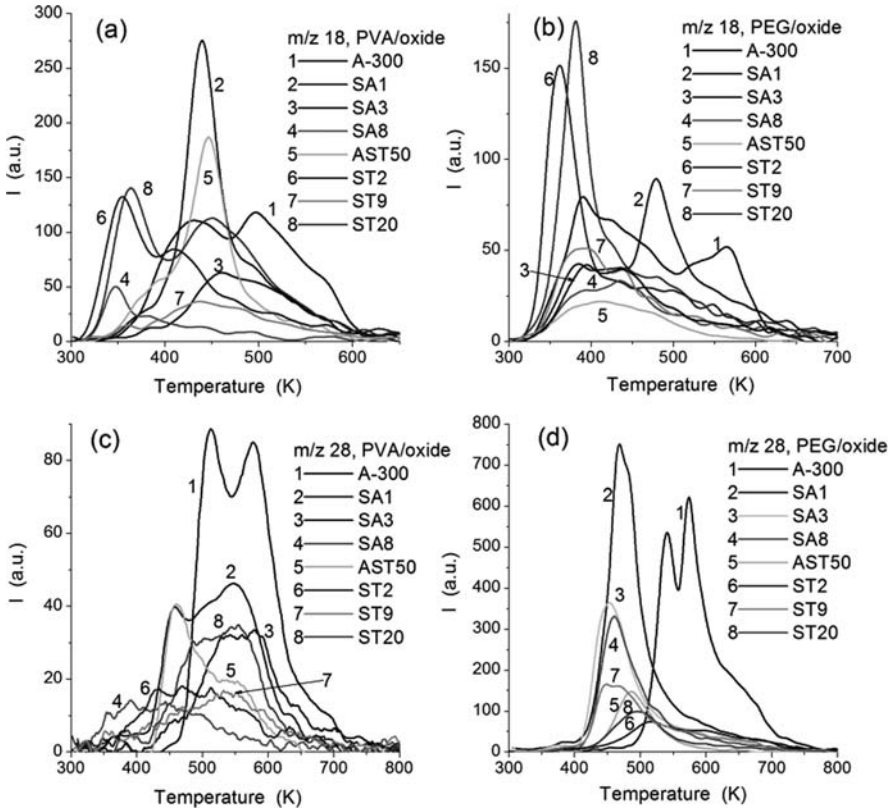

Fig. 8.13 TPD–MS thermograms at *m*/*z* (**a**, **b**) 18 (water) and (**c**, **d**) 28 (CO) formed on decomposition of PVA (**a**, **c**) and PEG (**b**, **d**) adsorbed on silica A-300, silica/alumina SA1, SA3, SA8, silica/titania ST2, ST9, ST20 and alumina/silica/titania AST50

adsorbed layer at $T > 200$–210 K and at $T > 250$–260 K in the weakly bound water layer. With a small amount of adsorbed water (as in this case), all water is strongly bound. Even low amounts of interfacial water result in relatively large ε'' and ε' values at low frequencies, due to the contribution of the conductivity term. Therefore, the intensity of the relaxation processes related to the polymer molecules is low, and it is difficult to decompose the $\varepsilon''(f)$ curves especially at low temperatures [23].

Several time-dependent effects can be responsible for the secondary particle rearrangement: (i) decomposition of residual secondary particles of silica upon interaction with the first layer of adsorbed organics (OC-I), followed by a second layer (OC-II), because of a stronger binding of organics to the silica surface than silica to silica particles; (ii) coagulation of silica nanoparticles with polymer or protein molecules to form new secondary hybrid particles due to electrostatic, polar and hydrogen bonding interactions; (iii) rearrangement of adsorbed OC-I/silica aggregates upon interaction with OC-II because of the displacement of adsorbed smaller molecules by larger ones (i.e. due to the Vroman effect);

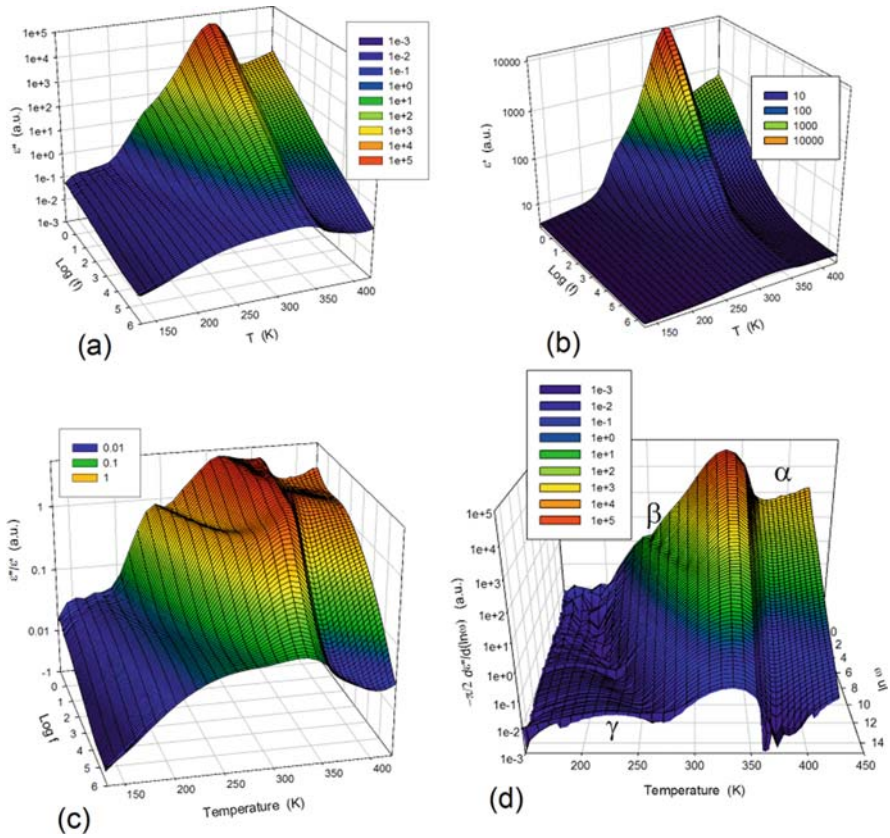

Fig. 8.14 (**a**) Dielectric loss, (**b**) permittivity, (**c**) tan $\varepsilon = \varepsilon''/\varepsilon'$ and (**d**) derivative $d\epsilon''/d(\ln \omega)$ as functions of frequency and temperature for PVA/A-300

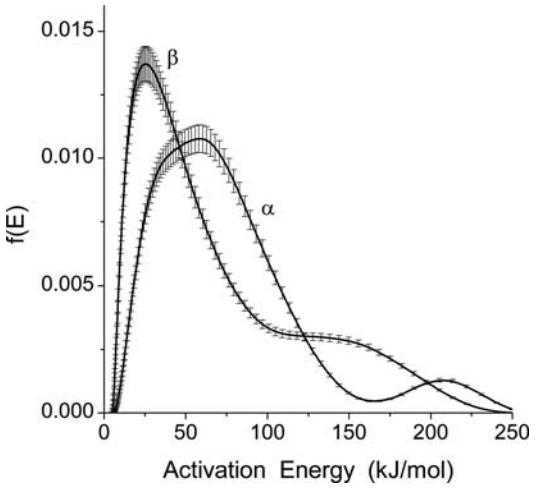

Fig. 8.15 Distribution functions of activation energy for the α and β relaxations in PVA/A-300

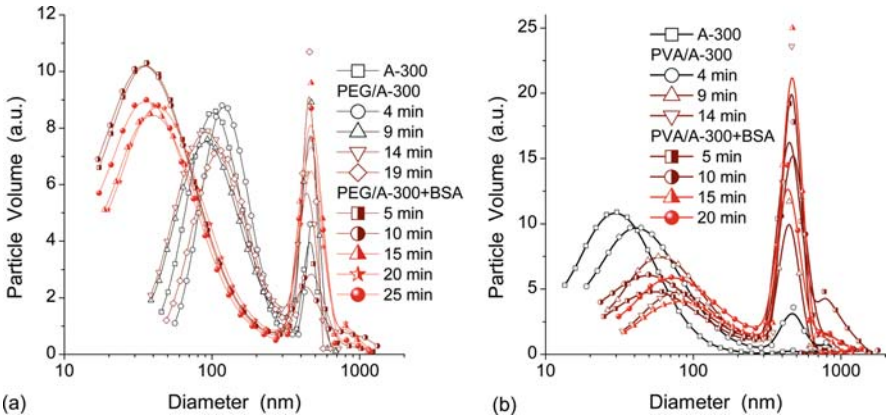

Fig. 8.16 Particle size distributions with respect to particle volume in the aqueous suspension of (**a**) A-300, PEG (2 kDa)/A-300 and BSA(II)/PEG(I)/A-300 and (**b**) A-300, PVA/A-300 and BSA(II)/PVA(I)/A-300

and (iv) rearrangement of aggregates with adsorbed OC-II/OC-I/silica with time because of perikinetic and orthokinetic aggregation and differential sedimentation of organics/solid particles [10, 28]. Figure 8.16 depicts the time-dependent interaction of PEG(I)-BSA(II) and PVA(I)-BSA(II) with A-300 ($C_{SiO2} = 0.1$ wt% and salinity 0.9 wt% of NaCl) at polymer concentrations close to their monolayer coverage [28].

For the first pair, smaller particles appear after addition of the BSA solution to the PEG/A-300 suspension. However, a certain amount of large particles at a size $d > 600$ nm are observed (Fig. 8.16). The behaviour of the second pair is radically altered, large particles form after addition of the BSA solution to the PVA/A-300 suspension. This enlargement of aggregates increases with time. BSA molecules can destroy hybrid aggregates composed of primary silica particles and relatively small PEG molecules, which can weakly block the silica surface against much larger BSA molecules. Therefore the PSD_V and PSD_N peaks for PEG/A-300 at $d \approx 100$ nm disappear but the peaks at 20–40 nm appear after interaction with BSA. The second PSD_V peak at 400–500 nm is also time-dependent and affected by adsorbed BSA as well as PSD_I. In the case of pre-adsorbed PVA, decomposition of aggregates of PVA/A-300 by BSA molecules is not observed because aggregates of electron-donor/proton-donor PVA/silica can strongly interact with BSA without decomposition. Additionally, PVA molecules can more strongly shield the silica surface against BSA molecules than smaller PEG molecules (the W_M value is 2 kDa (PEG) and 43 kDa (PVA)). PEG has only electron-donor groups, which can more effectively interact with ≡SiOH groups than with other PEG molecules. Therefore the interactions between PEG-PEG molecules are weaker than between PEG and BSA molecules. More detailed analysis of subsequent adsorption of different organics on nanosilicas was given elsewhere [27,28].

8.5 Conclusion

The processes of adsorption/desorption, relaxation and diffusion near or on a surface of individual and mixed nanooxides depend on textural characteristics, morphology of primary and secondary particles and chemical structure of the surface of primary particles. The adsorption, relaxation and energetic parameters of the powders and suspensions of mixed oxides correlate with the surface Al_2O_3 content in SA and AST materials and the surface TiO_2 content in ST and AST. These concentrations determine the quantity and properties of active sites responsible for processes occurring at the interfaces of mixed oxides. Investigations by broadband dielectric relaxation spectroscopy of weakly hydrated powders with PVA/A-300 depict concentration- and temperature-dependent structural reorganisation of the systems and the effects of nanoparticles on the relaxation of adsorbed polymer molecules and their glass transition temperature. The time-dependent rearrangement of secondary particles is observed in aqueous suspensions of polymer/BSA/nanosilica. This rearrangement depends on the type of polymers, especially the formation of hydrogen bonds between polymer molecules (PVA).

References

1. Adamson AW, Gast AP (1997) Physical chemistry of surface. John Wiley & Sons, New York.
2. Bonneviot L, Belard F, Danumah C, Giasson S, Kaliaguine S (eds) (1998) Mesoporous molecular sieves. Studies in Surface Science and Catalysis, V. 117. Elsevier, Amsterdam.
3. Legrand LP (ed) (1998) The surface properties of silicas. John Wiley & Sons, New York.
4. Gregg SJ, Sing KSW (1982) Adsorption, surface area and porosity. Academic Press, London.
5. Iler RK (1979) The chemistry of silica. Wiley, Chichester.
6. Fendler JH (ed) (1998) Nanoparticles and nanostructured films. Wiley-VCH, Weinheim.
7. Gun'ko VM, Leboda R, Turov VV et al (2002) Structural and energetic heterogeneities of hybrid carbon-mineral adsorbents. Appl Surf Sci 191:286–299.
8. Chuiko AA (ed) (2003) Medical chemistry and clinical application of silicon dioxide. Naukova Dumka, Kiev.
9. Blitz JP, Gun'ko VM (eds) (2006) Surface chemistry in biomedical and environmental science. NATO Science Series II: Mathematics, Physics and Chemistry, V. 228. Springer, Dordrecht.
10. Gun'ko VM, Zarko VI, Leboda R, Chibowski E (2001) Aqueous suspensions of fumed oxides: particle size distribution and zeta potential. Adv Colloid Interface Sci 91:1–112.
11. Gun'ko VM, Mironyuk IF, Zarko VI et al (2001) Fumed silicas possessing different morphology and hydrophilicity. J Colloid Interface Sci 242:90–103.
12. Gun'ko VM, Mironyuk IF, Zarko VI et al (2005) Morphology and surface properties of fumed silicas. J Colloid Interface Sci 289:427–445.
13. Bergna HE (ed) (2005) Colloidal silica: fundamentals and applications. Taylor & Francis LLC, Salisbury.
14. Shpak AP, Gorbyk PP (eds) (2007) Physicochemistry of nanomaterials and supramolecular structures. Naukova Dumka, Kiev.
15. Gun'ko VM, Myronyuk IF, Chelyadin VL et al (2007) Structural and adsorption properties of fumed oxides TiO_2, TiO_2/SiO_2 and TiO_2/Al_2O_3. Phys Chem Solids (Ukr) 8:357–362.
16. Gun'ko VM, Blitz JP, Gude K et al (2007) Surface structure and properties of mixed fumed oxides. J Colloid Interface Sci 314:119–130.
17. Gun'ko VM, Nychiporuk YM, Zarko VI et al (2007) Relationships between surface compositions and properties of surfaces of mixed fumed oxides. Appl Surf Sci 253:3215–3230.

18. Gun'ko VM, Leboda R, Skubiszewska-Zieba J et al. (2008) Influence of different treatments on characteristics of nanooxide powders alone or with adsorbed polar polymers or proteins. Powder Technology 187:146–158.
19. Gun'ko VM, Zarko VI, Turov VV et al. Morphological and structural features of individual and composite nanooxides with alumina, silica, and titania in powders and aqueous suspensions. Powder Technology, in press.
20. Gun'ko VM, Zarko VI, Voronin EF et al (2002) Impact of some organics on structural and adsorptive characteristics of fumed silica in different media. Langmuir 18:581–596.
21. Gun'ko VM, Turov VV, Bogatyrev VM et al (2005) Unusual properties of water at hydrophilic/hydrophobic interfaces. Adv Colloid Interface Sci 118:125–172.
22. Gun'ko VM, Zarko VI, Goncharuk EV et al (2007) TSDC spectroscopy of relaxational and interfacial phenomena. Adv Colloid Interface Sci 131:1–89.
23. Gun'ko VM, Pissis VM, Spanoudaki A et al (2007) Relaxation phenomena in poly(vinyl alcohol)/fumed silica affected by interfacial water. J Colloid Interface Sci 312:201–213.
24. Gun'ko VM, Zarko VI, Turov VV et al (1999) The effect of second phase distribution in disperse X/silica (X=Al_2O_3, TiO_2, and GeO_2) on its surface properties. Langmuir 15: 5694–5702.
25. Gun'ko VM, Zarko VI, Turov VV et al (1999) Characterization of fumed alumina/silica/titania in the gas phase and aqueous suspension. J Colloid Interface Sci 220:302–323.
26. Gun'ko VM, Zarko VI, Turov VV et al (1998) CVD-titania on fumed silica substrate. J Colloid Interface Sci 198:141–156.
27. Gun'ko VM, Goncharuk EV, Nechypor OV et al (2006) Integral equation for calculation of distribution function of activation energy of shear viscosity. J Colloid Interface Sci 304: 239–245.
28. Gun'ko VM, Zarko VI, Voronin EF et al (2006) Successive interaction of pairs of soluble organics with nanosilica in aqueous media. J Colloid Interface Sci 300:20–32.

Part III
Geometrical, Chemical, and Adsorptive Modification of Nanomaterials

The substance in a nanosized state possesses features not usual for massive samples. New properties of nanomaterials may be caused by sized energy quantization, exceeded influence of surface electronic states, bioactivity and bioaccessibility of nanoparticles.

So, quantum-sized effects may develop in nanostructures at room temperature, when the distance between energy levels of the spectrum of sized quantization at least becomes commensurable with the energy of corresponding phonons. And the prohibition rules for electron transition of Pauli–Fermi principle may be modified. Chemical activity of the surface of nanomaterials is closely connected with an increasing influence of surface atoms and hence of uncompensated valencies. Bioactivity and bioaccessibility of nanomaterials may be caused by a direct effect of surface-active sites on corresponding terminal fragments of a cell membrane and by specific structure of hydrated shells, which contain cluster structures, recognizable by bioobjects.

The ways of further improvement and development of nanotechnologies may be connected with the usage of geometrical, chemical, and adsorption methods of modification, which will allow treatment of nanomaterials for obtaining new properties and considerable extension of functional capabilities. These methods are classified and widely used in surface chemistry of disperse solid state. As a rule, one-step synthesis does not give a desired result; however, in such cases multi-step modification allows surface assemblage of compounds with given structure and properties.

Besides that in the last years, special attention has been paid to studies of geometrical, chemical, and adsorptive modification of materials and their usage as nanoreactors for synthesis of nanotubes, nanowires, and noble metal nanoparticles. Nanovolume of such chemical reactors may accommodate metal-containing compounds for further reduction, immobilize reagents with reduction properties, and limit the growth of nanoparticles. One should consider that special conditions of chemical transformation may result from the superposition of electric fields of ions localized closely to the surface of nanosized pores.

This part reviews the results of our studies in the field.

Chapter 9
Chemical Design of Carbon Coating on the Alumina Support

Lyudmila F. Sharanda, Igor V. Plyuto, Anatoliy P. Shpak, Igor V. Babich, Michiel Makkee, Jacob A. Moulijn, Jerzy Stoch, and Yuri V. Plyuto

Abstract The developed approach to the synthesis of carbon-coated alumina is described. It includes grafting of 4,4′-methylenebis(phenylisocyanate) (MDI) due to reaction of isocyanate groups (N═C═O) with hydroxyl groups on the alumina surface via N═C bond opening and subsequent pyrolysis of MDI surface species at 700°C in vacuum. Carbon-coated alumina supports with carbon loading up to 17.5 wt.% were synthesised by repetition of grafting–pyrolysis cycles. SEM analysis shows that surface structure of the initial alumina support is retained and no separate carbon phase is observed. It has been found out that carbon coating does not substantially influence the pore structure of the initial alumina support. The mechanism of formation of carbon coating as well as the structure of the synthesised carbon-coated alumina was studied by FTIR, TG/DTG-DTA, XPS, XRD, SEM and adsorption measurements.

9.1 Introduction

Combination of physico-chemical properties of individual carbon and alumina in carbon-coated alumina or carbon–alumina hybrid results in novel materials promising for the development of advanced sorbents [1], catalyst supports and catalysts [2–9], electrically conductive fillers and coatings [10–12], membranes [13, 14] and functional coatings [15]. The synthesis of carbon-coated alumina or carbon–alumina hybrid is by pyrolytic methods.

In the case of carbon-coated sorbents [1], the synthesis may include, for example, combining of the alumina particles with sucrose followed by carbonisation at 700°C. Electrically conducting carbon coatings over alumina foams were prepared by the alumina foams' impregnation in a polyurethane solution with subsequent pyrolysis of the polymer layer [12]. An optimal coating procedure was developed, using a commercial polyurethane lacquer. Pyrolysis was performed by heating

L.F. Sharanda (✉)
O.O. Chuiko Institute of Surface Chemistry of the National Academy of Sciences of Ukraine, General Naumov St. 17, Kyiv 03164, Ukraine
e-mail: lyusharanda@yahoo.com

A.P. Shpak, P.P. Gorbyk (eds.), *Nanomaterials and Supramolecular Structures*,
DOI 10.1007/978-90-481-2309-4_9,

the coated foams to 650–1200°C. In a similar way the electrically conductive dense and porous alumina with in situ-synthesised nanoscale carbon networks was prepared [11].

The proposed alternative CVD approach [10] is based on the ability of organic compounds to pyrolyse on the surface of the alumina and silica–alumina supports at elevated temperatures in the range of 600–700°C. Among the tested organic pyrolysable substances, such hydrocarbons as hexane, benzene, toluene, naphthalene, anthracene, cyclohexene and cyclohehene were found to be the most promising for making carbon–alumina and carbon–silica–alumina catalyst supports [2–9]. By CVD route, the carbon-coated alumina membranes [13, 14] and decorating carbon-coated thin anodic aluminium oxide films of tunable colour [15] were also developed.

The novelty of the present work is in the development of a two-step method of coating of alumina with carbon. Carbon-coated alumina was synthesised by grafting and subsequent pyrolysis of 4,4′-methylenebis(phenylisocyanate) on the support surface. The mechanism of formation of the carbon coating as well as the structure of the synthesised carbon-coated alumina were studied by FTIR, XPS, XRD, SEM, TG/DTG-DTA and adsorption measurements.

9.2 Experimental

9.2.1 Material

The as-received precipitated alumina support (CK 300, Ketjen, $S_{BET}(N_2) = 266\ m^2\ g^{-1}$) was crushed, sieved to a particle size of 0.25–0.50 mm and calcined in air at 500°C for 2 h in a muffle furnace in order to remove organic impurities. 4,4′-Methylenebis(phenylisocyanate) (MDI) obtained from Bayer AG was dissolved in *o*-xylene preliminary dried with NaX molecular sieves. The weighted amount (15 g) of the support was contacted with 340 ml of 1% *o*-xylene solution of MDI at room temperature for 1 day, filtered and the sample was washed with approximately 100 ml of pure *o*-xylene followed by drying at 60°C for 2 h. Then, the sample was placed into a quartz cell and evacuated at room temperature to the pressure of 1×10^{-2} Pa. The temperature of the sample was increased to 700°C within a period of 10 h under continuous pumping. The sample was kept at this temperature and a pressure of 1×10^{-2} Pa for 2 h in order to complete pyrolysis of the grafted MDI and to remove the volatile products.

To prepare the samples with increased carbon content, the grafting–pyrolysis cycle was repeated up to three times. The above procedure resulted in samples with carbon content of 7.7, 12.3 and 17.5 wt.%, denoted hereafter as C(7.7)/Al_2O_3, C(12.3)/Al_2O_3 and C(17.5)/Al_2O_3, respectively.

9.2.2 Experimental Methods

IR spectra in a reflectance mode were recorded in the range from 4000 to 400 cm^{-1} with a spectral resolution of 8 cm^{-1} using a Nexus Nicolet FTIR spectrometer

(Thermo Scientific) equipped with a Smart Collector reflectance accessory. Alumina samples were powdered with KBr in 1:10 ratio.

Thermal studies (TG/DTG-DTA) were carried out with a STA-1500 H thermobalance (PL Thermal Sciences) at a heating rate of 10°C/min in an airflow of ~50 cm^3/min. The carbon content in the synthesised samples was determined gravimetrically from the weight loss within the temperature interval 300–650°C.

Surface area (BET) and porosity were determined by nitrogen adsorption/desorption at 77 K using a Quantachrome Autosorb-6B equipment. The samples were preliminary heated in vacuum at 150°C for 16 h.

X-ray diffraction (XRD) patterns were recorded in the range 5–80° (scanning step 0.1°) with a DRON-3 M automated diffractometer using the Cu-K_α (Å=1.54178 A) radiation and Ni filter.

SEM images were obtained with a LEO 1550 high-resolution electron microscope. An electron beam of 2.5 kV was used to analyse the surface details of the samples.

X-ray photoelectron spectra (XPS) were recorded on a Vacuum Generator ESCA-3 photoelectron spectrometer using Al-K$\alpha_{1,2}$ radiation (1486.6 eV) from an X-ray source operating at 10 kV and 12 mA. The working pressure inside the chamber was less than 2.5×10^{-6} Pa. All spectra were recorded with a step size of 0.1 eV in the constant pass energy mode at 50 eV. Samples were mounted for the analysis by dusting their powder onto a double-sided polymer-based adhesive tape.

9.3 Results and Discussion

The contact of the alumina support with MDI dissolved in *o*-xylene resulted in partial discoloration of the solution and the initial white colour of the alumina samples turned yellow which means interaction of MDI with the support surface. This interaction is strong and irreversible since the sample does not lose yellow colour even after washing with *o*-xylene.

The interaction of MDI with the alumina surface was investigated by FTIR spectroscopy. In FTIR spectrum of MDI, the intense absorption band at 2268 cm^{-1} typical for isocyanate group (N=C=O) [16] is observed (Fig. 9.1(1)).

This band is not present in the spectrum of the alumina sample which contacted with MDI. Instead, one can see the broad band at 3450 cm^{-1} which corresponds to N–H vibrations (Fig. 9.1(2)). Besides, the band around 1512 cm^{-1} which corresponds to C–N vibrations is also observed [16]. These changes mean that MDI grafting should proceed via N=C bond opening upon the reaction of N=C=O groups with hydroxyl groups of the alumina support. Grafting of MDI on the alumina surface is shown in Fig. 9.2.

Thermal analysis using TG/DTG-DTA technique was used to ensure quantitative control over MDI grafting on the alumina support and determine carbon yield after pyrolysis of grafted MDI species. Thermoanalytical characterisation of carbon-coated samples (Fig. 9.3) exhibits intense weight loss in DTG patterns around 500°C that coincides with the exothermic peak in DTA curves.

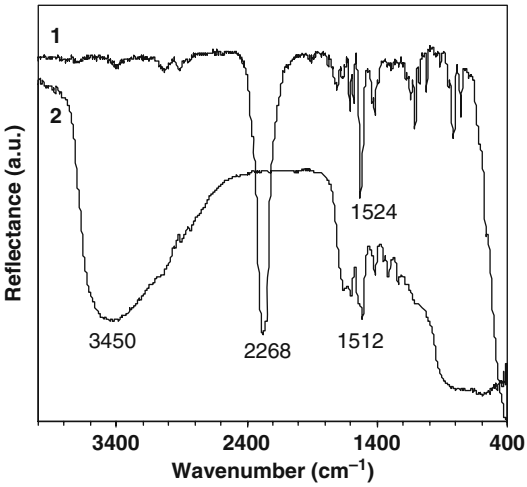

Fig. 9.1 FTIR spectra of individual MDI (*1*) and alumina sample after contact with MDI (*2*)

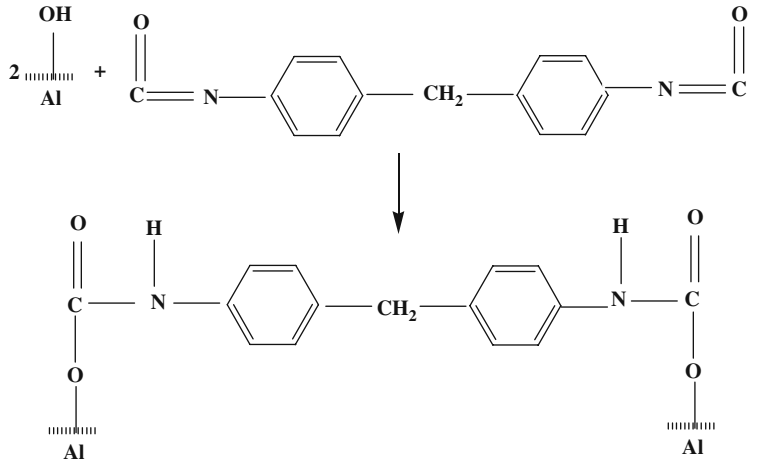

Fig. 9.2 Grafting of 4,4′-methylenebis(phenylisocyanate) (MDI) on the alumina surface

Oxidation starts at 300°C and proceeds in one step in a narrow temperature interval. This suggests that oxidation of a single carbon phase occurs. Table 9.1 illustrates the formation of carbon coating upon pyrolysis of MDI grafted to the surface of the alumina support.

One can see that on the initial alumina support the amount of the grafted MDI reaches 16.2 wt.%. The carbon loading in this samples after pyrolysis was 7.7 wt.% that corresponds to 66% of carbon yield. The synthesised C(7.7)/Al_2O_3 sample was contacted with solution of MDI in *o*-xylene again. In this case the adsorption of MDI also proceeded since discoloration of the solution was observed. The adsorption of MDI appeared to be somewhat lower as compared to that on the initial alumina

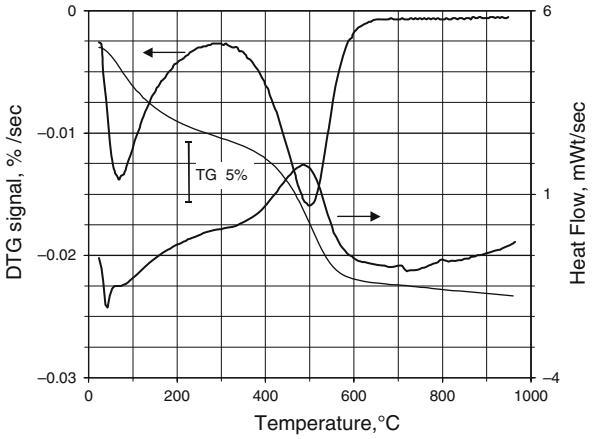

Fig. 9.3 TG/DTG-DTA curves for C(7.7)/Al_2O_3 sample

Table 9.1 Synthesis of carbon coating on the alumina support by pyrolysis of grafted MDI

			Pyrolysis of grafted MDI	
Sample	Initial carbon loading (wt.%)	Grafted MDI (wt.%)	Yield of elemental carbon (wt.%)	Final carbon loading (wt.%)
Al_2O_3	0	16.2	66.0	7.7
C(7.7)/Al_2O_3	7.7	10.6	60.3	12.3
C(12.3)/Al_2O_3	12.3	10.2	71.0	17.5
C(17.5)/Al_2O_3	17.5	–	–	–

support; however, the carbon yield after pyrolysis remains sufficiently high. Similar results were obtained for the sample C(12.3)/Al_2O_3 and the increase of the carbon loading in this case reached 5.2 wt.%. After threefold repetition of the grafting–pyrolysis cycle the carbon loading on the alumina surface was 17.5 wt.%.

It appears that up to 16 wt.% of MDI can be grafted on the initial alumina surface. High loading of MDI surface species is due to reaction of N=C=O groups with hydroxyl groups of the alumina support. In the case of carbon-coated alumina supports, the reactive C(OH) and C(O)OH groups which exist in carbon coating can also react with MDI. This explains a sufficient grafting of MDI not only on the initial alumina support but also on carbon-coated alumina and high carbon yield upon each repetition of the grafting–pyrolysis cycle.

Characterisation of the synthesised samples with XRD does not reveal any peaks which should be attributed to the ordered carbon structures [17]. Therefore, the presence of either amorphous carbon coating or a thin graphitic layer can be assumed.

The nitrogen adsorption–desorption isotherms were recorded in order to clarify the influence of carbon coating on textural characteristic of the synthesised supports

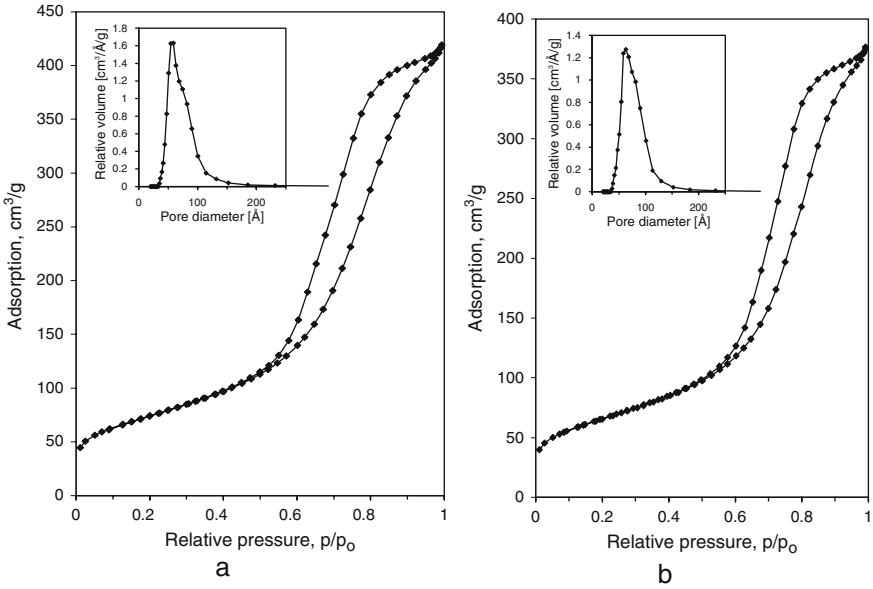

Fig. 9.4 Nitrogen adsorption–desorption isotherms of the initial Al_2O_3 support (**a**) and $C(7.7)/Al_2O_3$ (**b**) samples

(see Fig. 9.4). One can see that the shape of the nitrogen adsorption–desorption isotherms and the hysteresis loops is similar for all samples.

The structural characteristics of the initial and the synthesised supports are summarised in Table 9.2.

The apparent surface area of all carbon-coated samples appeared to be somewhat less than that of the initial alumina support. The increase of carbon loading resulted in the decrease of the total pore volume. The dependence of the mean pore diameter on carbon loading appeared more complex. Deposition of the first carbon layer on the initial Al_2O_3 support resulted in the increase of mean pore diameter from 55 to 61 Å that indicates the filling or shielding of micropores. Further increase of carbon loading is accompanied with a steady decrease of the mean pore diameter from 61 to 55 Å convincing the uniformity of the carbon covering.

Table 9.2 Textural properties of the initial and carbon-coated alumina supports

Sample	Carbon loading (wt.%)	S_{BET} (N_2) (m^2/g)	Total pore volume (cm^3/g)	Mean pore diameter (Å)
Al_2O_3	0	266	0.65	55
$C(7.7)/Al_2O_3$	7.7	234	0.57	61
$C(12.3)/Al_2O_3$	12.3	230	0.52	58
$C(17.5)/Al_2O_3$	17.5	212	0.47	55

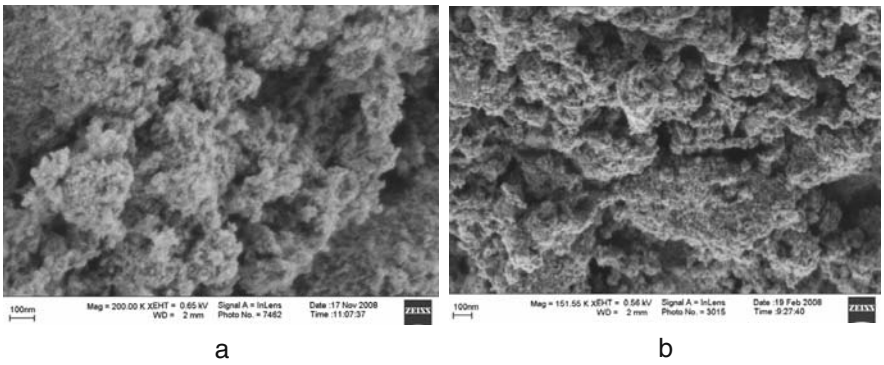

Fig. 9.5 SEM images of the initial Al_2O_3 support (**a**) and C(17.5)/Al_2O_3 (**b**) sample

This means that the porous structure of the initial alumina support was not changed upon carbon deposition. Moreover, a pore mouth plugging did not occur and carbon appeared to be uniformly distributed over the surface of alumina support. Therefore, we may suppose that carbon uniformly coats the alumina surface.

The surface morphologies of the initial alumina support and the synthesised carbon-coated samples were compared using SEM. As one can seen in Fig. 9.5a, the initial alumina support possesses distinct grain boundaries between individual particles. The SEM image of the carbon-coated alumina with carbon content 17.5 wt.% which was synthesised by a threefold repetition of grafting–pyrolysis cycles (Fig. 9.5b) shows that surface structure of the initial alumina support is retained and no separate carbon phase is observed. Besides, the boundaries between the alumina grains are clearly seen that indicates the uniform nature of the carbon coating.

Thus, the proposed synthesis of the carbon-coated alumina support by MDI grafting and subsequent pyrolysis leads to formation of uniform carbon coating on the alumina surface.

All synthesised carbon-coated alumina samples were analysed by XPS in the regions of the binding energy of the Al2p and C1s electrons. The recorded Al2p and C1s envelopes (Fig. 9.6) show asymmetry that decreases with the increased carbon loading. This means that the spectra have a complex character and are composed of a number of overlapping individual components.

A curve synthesis procedure was used in order to extract the overlapping component peaks from the experimental XPS envelopes. The experimental envelopes were reconstructed manually using an increasing number of individual peaks.

The position and intensity of individual component peaks were determined using a minimum variation of their full width at half maximum (FWHM) and the constant 80% Gaussian/20% Lorentzian mixing ratio of the fitting function.

We succeeded in curve reconstruction of the experimental XPS envelopes in the region of the binding energy of the Al2p electrons with two individual components and in the region of the binding energy of the C1s electrons with four individual components (Fig. 9.6a, b).

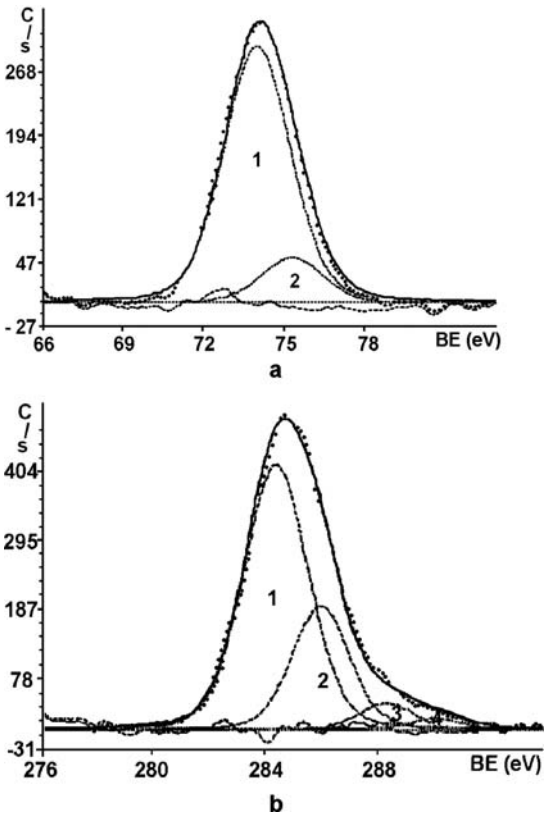

Fig. 9.6 XPS spectra of $C(7.7)/Al_2O_3$ sample in the region of the Al2p (**a**) and C1s (**b**) binding energies

Table 9.3 Peak position in experimental XPS envelopes of carbon-coated alumina supports after curve synthesis

Sample	Binding energy[a] (eV)					
	Al2p		C1s			
$C(7.7)/Al_2O_3$	74.00 (2.9)	75.31 (2.7)	284.40 (2.7)	286.00 (2.4)	288.34 (2.3)	290.08 (2.3)
$C(12.3)/Al_2O_3$	74.00 (2.4)	75.37 (2.3)	284.29 (2.3)	286.00 (2.5)	288.05 (2.3)	290.27 (2.3)
$C(17.5)/Al_2O_3$	74.00 (2.1)	75.88 (2.3)	284.34 (2.1)	285.88 (2.3)	288.16 (2.3)	290.58 (2.3)

[a]Values in parentheses correspond to full width at half maximum in eV.

The binding energies were referenced to the low-energy individual component at 74.0 eV in the experimental Al2p envelope. The position of the individual components and their width, which resulted from the curve synthesis, are summarised in Table 9.3.

In all experimental Al2p envelopes the high-energy individual components at 75.3–75.9 eV are present (Fig. 9.6a) along with the normally observed low-energy ones. In the case of the C1s envelope, the number of high-energy individual components reaches three (Fig. 9.6b). It should be mentioned that for each considered sample, the absolute difference between the binding energy of the individual low- and high-energy components in the Al2p envelopes and between the low-energy and the neighbouring components in the C1s envelopes appeared to be very close.

The presence of the high-energy Al2p components can be explained if one considers the occurrence of a steady-state charging of the different parts of insulating alumina support. The variation of the charging effect that can appear owing to a difference in the contact of alumina particles with the conducting sample holder is minimised by application of insulating adhesive tape. Therefore, a differential charging should relate to the chemical composition of the synthesised samples. This is the case since the insulating alumina support is covered with a conducting carbon. As a result, the charging of the parts of the insulating alumina support, which are not covered with carbon, exceeds the charging of those parts that are in direct contact with the carbon coating, increasing a probability of charge compensation by acquisition of slow or thermal electrons from the vacuum. Therefore, Al2p peaks with different binding energies are observed. It is self evident that the high-energy components originate from those parts of the alumina support that are not covered with the carbon coating and, hence, have a higher steady-state charging.

The relative intensities of the individual components in the Al2p and C1s envelopes depend on the carbon content in the synthesised samples. The relative intensity of the low-energy individual component appears to be higher for samples with an increased carbon loading. If we compare the intensities of the Al2p peaks, the contribution of the high-energy individual components at 75.3–75.9 eV into the overall intensity of the Al2p envelopes decreases with an increase in carbon loading on the alumina surface, which is negligible for $C(17.5)/Al_2O_3$ sample. Taking this into account, one can conclude a complete coverage of the alumina surface with carbon layer in the case of the $C(17.5)/Al_2O_3$ sample.

In the C1s envelopes, the number of the high-energy individual components reaches three (Fig. 9.6b). The contribution of the high-energy individual components at 286.0–291.0 eV into the overall intensity of the C1s envelope is more pronounced as compared to that in the case of the Al2p envelopes. Although the contribution of the high-energy individual C1s components to the overall intensity of the C1s envelopes decreases with an increase in carbon loading their role is still important even for the $C(17.5)/Al_2O_3$ sample with the highest carbon loading.

The proposed model enables us to explain a complex character of the XPS envelope in the region that corresponds to the binding energy of the C1s electrons (Fig. 9.6a). The component around 284.3–284.4 eV can be attributed to carbon, which constitutes the coating and, hence, ensures surface conductivity. One can assume that the component around 285.9–286.0 eV is connected with carbon in carbonaceous surface species, which do not form a conducting layer on alumina support.

It should be noted that the contribution of the high-energy individual components at 286.0 eV to the overall intensity of the C1s envelope is still high even for the C(17.5)/Al_2O_3 sample whose surface should be considered as completely covered with carbon layer as concluded from the analysis of the Al2p envelope. Thus, the high-energy individual components at 286.0 eV in the C1s envelope are connected not just with a steady-state charging. The presence of the high-energy C1s components in XPS envelopes of coals was also reported [18–21].

In order to explain the origin of the components around 285.9–286.0, 288.0–288.3 and 290.1–290.6 eV in experimental C1s envelopes (Fig. 9.6b), one should refer to the chemical shifts for the C1s electrons in organic compounds.

Experimentally determined chemical shifts of C1s electrons in a wide range of model organic compounds [22] divides them into four classes with (1) carbon atoms bonded only to carbon and/or hydrogen (i.e. carbon atoms in C–C or C–H groups and not directly bonded to oxygen) – binding energies around 285.0 eV; (2) carbon atoms bonded to a single oxygen in C–O groups – binding energies around 286.6 eV and chemical shifts reaching 1.6 ± 0.1 eV; (3) carbon atoms bonded to two single (non-carbonyl) oxygens or to a single carbonyl oxygen in O–C–O or C═O groups, respectively – binding energies of 287.9 ± 0.2 eV and chemical shifts reaching 2.9 ± 0.2 eV; (4) carbon atoms bonded to a carbonyl and non-carbonyl oxygen in O═C–O carboxyl groups – binding energies of 289.1±0.2 eV and chemical shifts reaching 4.1 ± 0.2 eV.

From this viewpoint, the components around 285.9–286.0, 288.0–288.3 and 290.1–290.6 eV in Fig. 9.6b should be attributed to carbon, which is bound to oxygen in surface species. Most likely they relate to carboxylate surface structures in carbon coating on the alumina support.

From Table 9.4, one can see that upon increasing of carbon content, the proportion between the integral intensity of the C1s component at 284.3–284.4, which relates to the carbon coating, and the integral intensity of the overall Al2p envelope constantly changes. Therefore, it was possible to compare the bulk and the surface C/Al ratio and to analyse the dependence of the latter on carbon content. In order to do this, the bulk values were calculated assuming a complete and homogeneous dispersion of carbon in an alumina matrix. Surface values, related to the probed surface layer, were calculated using the following equation [23]:

$$\frac{\mathrm{C}}{\mathrm{Al}} = \frac{I_\mathrm{C}}{I_\mathrm{Al}} \cdot \frac{S_\mathrm{Al}}{S_\mathrm{C}}, \tag{9.1}$$

where I_C is the integral intensity of the overall C1s envelope, I_{Al} is the integral intensity of the overall Al2p envelope, S_{Al} and S_C are atomic sensitivity factors of

Table 9.4 XPS analysis of carbon-coated alumina supports

Sample	C loading (wt.%)	Bulk C/Al ratio	*I*(C1s)/*I*(Al2p)	Surface C/Al ratio
C(7.7)/Al_2O_3	7.7	0.35	1.69	1.25
C(12.3)/Al_2O_3	12.3	0.60	2.05	1.52
C(17.5)/Al_2O_3	17.5	0.90	2.64	1.95

Al (0.185) and C (0.250) for the 2p and 1s electrons, respectively [18], determined from the empirical peak area values [19].

The intensity ratio data enable to estimate the surface atomic concentration of carbon in the synthesised samples (Table 9.4). One can see that for $C(7.7)/Al_2O_3$ sample, the surface C/Al ratio is more than three times higher as compared to that of the bulk one. This means that carbon is preferably concentrated at the external surface of the alumina support. With increasing of carbon loading, the difference between the surface and bulk C/Al ratio decreases. Thus for $C(17.5)/Al_2O_3$ sample, the proportion between the surface and bulk C/Al ratio falls ca. to 2. One can conclude that the carbon coating becomes more uniformly distributed within the internal and the external surfaces of the alumina support.

9.4 Conclusions

Carbon coating can be synthesised on the alumina support by grafting of 4,4′-methylenebis(phenylisocyanate) (MDI) via reaction of isocyanate groups (N═C═O) with hydroxyl groups on the alumina surface due to N═C bond opening and subsequent pyrolysis of MDI surface species at 700°C in vacuum. By repetition of grafting–pyrolysis cycles, the carbon loading on the alumina surface can be increased from 7.7 wt.% (one grafting–pyrolysis cycle) to 17.5 wt.% (three grafting–pyrolysis cycles). The possibility of repetition of the adsorption cycles is connected with the ability of isocyanate groups in MDI to react not only with surface hydroxyl groups on the alumina support but with C(OH) and C(O)OH groups which were detected by XPS in carbon coating. SEM analysis shows that surface structure of the initial alumina support is retained after carbon coating deposition and no separate carbon phase is observed. It has been found that carbon coating does not substantially influence the pore structure of the initial alumina support.

Acknowledgments This work was financially supported by the European Community in the frame of the research project "Development of environmentally benign technology for deep recovery of elemental sulphur from technological off-gasses of metallurgical coke plants and chemical refineries of crude oil" (Contract N ICA2-CT2000-10021).

References

1. Pullen JB (1967) Carbon-Coated Alumina and Process for Making Same. US Patent 3360134
2. Vissers JPR, Mercx FPM, Bouwens SMAM, De Beer VHJ and Prins R (1988) Carbon-Covered Alumina as a Support for Sulfide Catalysts. J Catal 114:291–302
3. Rama Rao KS, Kanta Rao P, Masthan SK, Kaluschnaya L and Shur VB (1990) New Type of Carbon Coated Alumina Supports for the Preparation of Highly Active Ruthenium Catalysts for Ammonia Synthesis. Appl Catal 62:L19–L22
4. Boorman PM, Chong K, Kydd RA and Lewis JM (1991) A Comparison of Alumina, Carbon, and Carbon-Covered Alumina as Supports for Ni-Mo-F Additives: Carbon Deposition and Model Compound Reaction Studies. J Catal 128:537–550
5. Boorman PM, Kydd RA, Sorensen TS, Chong K, Lewis JM and Bell WS (1992) A Comparison of Alumina, Carbon and Carbon-Covered Alumina as Supports for Ni-Mo-F additives: Gas Oil Hydroprocessing Studies. Fuel 71:87–93

6. Boorman PM and Chong K (1993) Preparation of Carbon-Covered Alumina Using Fluorohydrocarbons. A New Acidic Support Material. Appl Catal A 95:197–210
7. Zhang T, Jacobs PD and Haynes HW Jr (1994) Laboratory Evaluation of Four Coal Liquefaction Catalysts Prepared from Modified Alumina Supports. Catal Today 19:353–366
8. Leon y Leon CA, Scaroni AW and Radovic LR (1992) Physicochemical Characterization of Carbon-Coated Alumina. J Colloid Interface Sci 148:1–13
9. Comolli AG and Ganguli PS (1991) Porous Metal Oxide Supported Carbon-Coated Catalysts and Method for Producing Same. US Patent 5037791
10. Youtsey KJ, Holt WC, Carnahan.RD Jr and Spielberg DH (1977) Method of Forming a Conducting Material for a Conducting Device. US Patent 4018943
11. Menchavez RL, Fuji M and Takahashi M (2008) Electrically Conductive Dense and Porous Alumina with In-Situ-Synthesized Nanoscale Carbon Networks. Adv Mater 20:2345–2351
12. Mann M, Shter GE and Grader GS (2006) Preparation of Carbon Coated Ceramic Foams by Pyrolysis of Polyurethane. J Mater Sci 41:6046–6055
13. Liu PKT, Gallaher GR and Wu JCS (1993) Method of Producing a Carbon Coated Ceramic Membrane and Associated Product. US Patent 5262198
14. Kyotani T, Xu W, Yokoyama Y, Inahara J, Touhara H and Tomita A (2002) Chemical Modification of Carbon-Coated Anodic Alumina Films and Their Application to Membrane Filter. J Memb Sci 196(2):231–239
15. Wang X.H, Akahane T, Orikasa H, Kyotani T and Fu YY (2007) Brilliant and Tunable Color of Carbon-Coated Thin Anodic Aluminum Oxide Films. Appl Phys Lett 91: 011908-1–011908-3
16. Dechant J, Danz R, Kimmer W and Schmolke R (1972) Ultrarotspektroskopische Untersuchungen An Polymeren. Akademie-Verlag, Berlin
17. Sanders JV, Spink JA and Pollack. SS (1983) The Structure of Carbon Deposits on HDS Catalysts. Appl Catal 5:65–84
18. Briggs D and Seah MP (eds) (1990) In Practical Surface Analysis, Vol. 1. Wiley, Chichester
19. Wagner CD, Davis LE, Zeller MV, Taylor JA, Raymond RM and Gale LH (1981) Empirical Atomic Sensitivity Factors for Quantitative Analysis by Electron Spectroscopy for Chemical Analysis. Surf Interface Anal 3:211–225
20. Buckley AN and Lamb RN (1996) Surface Chemical Analysis in Coal Preparation Research: Complementary Information from XPS and ToF-SIMS. Intern J Coal Geol 32:87–106
21. Clark DT and. Wilson R (1983) ESCA Applied to Aspects of Coal Surface Chemistry. Fuel 62:1034–1040
22. Clark DT and Thomas HR (1976) Application of ESCA to Polymer Chemistry. X. Core and Valence Energy Levels of a Series of Polyacrylates. J Polym Sci Polym Chem Ed 14: 1671–1700
23. Moulder JF, Stickle WF, Sobol PE and Bomben KD (1992) Handbook of X-ray Photoelectron Spectroscopy. Chastain J (ed.), Perkin-Elmer, Eden Prairie, MN

Chapter 10
Design of Ag-Modified TiO_2-Based Films with Controlled Optical and Photocatalytic Properties

N.P. Smirnova, E.V. Manuilov, O.M. Korduban, Yu.I. Gnatyuk, V.O. Kandyba, A.M. Eremenko, P.P. Gorbyk, and A.P. Shpak

Abstract TiO_2-based functional coatings doped with Ag nanoparticles were prepared via template assisted sol–gel method with an attempt to enhance the decomposition reaction rate of industrial water pollutants. The films were characterized by X-ray diffraction (XRD), atomic force microscopy (AFM), X-ray photoelectron (XPS), and UV–vis spectroscopies. Catalytic activity in photooxidative organic dyes decomposition remarkably enhances TiO_2/ZnO samples with homogeneously distributed noble metal nanoparticles. Ag nanoparticles in TiO_2 matrix improve an efficiency of charge separation and charge-transfer processes, acting as traps for photoinduced electrons.

10.1 Introduction

Many processes related to the elimination of toxic and hazardous chemical substances from air and wastewaters require photocatalysts (especially coatings and films) with developed porous structure and high surface area [1, 2]. The most widely used catalyst is titanium dioxide that has many interesting properties: chemical stability and high refractive index, good transmittance in the visible region, strong oxidation power, and superhydrophilicity under UV illumination. Coupling of two semiconductors [3], in particular TiO_2 and ZnO [4, 5], is useful for achievement of more efficient separation of photogenerated electron–hole pairs that leads to improvement of the photoactivity, for example, in the process of methyl orange photo-cleavage [5]. Zinc–titanium oxide materials have great potentials for use as catalysts [4, 6], superhydrophilic coatings [7], semiconductive ceramics [8]. A common way to enhance the quantum efficiency is to add the noble metal on the surface of semiconductor powder or film [9, 10]. The noble metal, which acts as a sink

N.P. Smirnova (✉)
O.O. Chuiko Institute of Surface Chemistry of the National Academy of Sciences of Ukraine, General Naumov St. 17, Kyiv 03164, Ukraine
e-mail: smirnat@i.com.ua

A.P. Shpak, P.P. Gorbyk (eds.), *Nanomaterials and Supramolecular Structures*,
DOI 10.1007/978-90-481-2309-4_10,

for photoinduced charge carriers, promotes interfacial charge-transfer processes. Such semiconductor–metal composite films can play an important role in photoelectrochemical cells. Several fabrication techniques including sol–gel process with thermoinduced [11], photo- or chemical reduction of metal ions deposited on the TiO_2 surface [12], as well as combination of ion-exchange and reduction process [13] ,were proposed for the preparation of the films containing small particles of metals and semiconductor.

In our previous work we reported direct photoelectrochemical investigations of the TiO_2/Ag and TiO_2/ZnO/Ag heterojunctions that showed cathode shift of the flat-band potential position and increase of photocurrent quantum yield in comparison with unmodified TiO_2 electrodes. Modification of TiO_2-based films with Ag nanoparticles gives the possibility to decrease overvoltage in the process of electrochemical oxygen reduction and extends the potential range for oxygen determination [14]. Questions still remain regarding stability of Ag nanoparticles deposited on semiconductor surface, the effect of the electronic structure of nanocomposites on their optical and photocatalytic properties. This work is devoted to the photochemical deposition of Ag nanoparticles onto mesoporous TiO_2 and TiO_2/ZnO (1% ZnO) films, prepared via templated sol–gel route, investigation of surface morphology, optical properties, electronic structure, and photocatalytic activity in the process of xantene dye Rhodamine B photodegradation.

10.2 Experimental

Mesoporous TiO_2 and TiO_2/ZnO films were obtained as described in our previous papers [2, 7, 11] using titanium tetra-isopropoxide and zinc acetate as Ti and Zn sources and triblock copolymer Pluronic P123 as the templating agent. Ag-modified films were prepared via photoreduction of Ag^+ ions deposited on the mesoporous TiO_2 and ZnO/TiO_2 (1 at.% ZnO) films from aqueous solution $[Ag(NH_3)_2]NO_3$ under UV irradiation followed by heat treatment at 20–500°C.

Atomic force microscopy (AFM) was carried out using a Digital Nanoscope (Nanoscope IIIa). UV–vis optical absorption spectra were recorded by a Perkin-Elmer Lambda 35 spectrophotometer.

Chemical analysis of films was performed using atomic absorption spectrometer SELMI M-150.

The electronic structure of the sol–gel film surface was explored by X-ray photoelectron spectroscopy (XPS) with an electron spectrometer (E MgKα =1253.6 eV, $P = 10^{-7}$ Pa) with PHOIBOS-100 energy analyzer SPECS (USA). The spectra of Ag*3d* level were decomposed into peak couples with parameters of spin–orbit separation ΔE_p ($3d_{3/2} - 3d_{5/2}$) = 6.0 eV and ratio of intensities was $I\ 3d_{3/2}/3d_{5/2}$= 0.66. Full width at the half maximum height (FWHM) was 1.0 eV. The deconvolution was carried out by Gauss–Newton method; the area of peaks was determined after subtraction of background by Shirley method.

Photocatalytic activity of synthesized films was checked in the photodegradation process of xantene dye Rhodamine B ($C_M = 5\times10^{-5}$ M) as described previously [11].

10.3 Synthesis of Mesoporous TiO_2 and TiO_2/ZnO Films Modified with Ag

Optically transparent mesoporous TiO_2/ZnO films were prepared via the adopted sol–gel method from [15]. Calculated thickness of one-coating films ranged between 70 and 90 nm; refractive index was 1.9–2.1. Total surface area ($S_{BET} \sim 300$ m^2/g) value was obtained from BET analysis of the isotherms for all TiO_2 and TiO_2/ZnO samples [7]. The absorption onset for TiO_2/ZnO films was slightly red-shifted as compared with unmodified TiO_2 films giving the band-gap E_g values 3.4 and 3.5 eV for TiO_2/ZnO and TiO_2 films, respectively. The increase of the E_g values up to 3.5 eV in comparison with E_g of bulk TiO_2 (3.2 eV) revealed the formation of nanocrystalline structure for synthesized films. Band-gap energy values were calculated by extrapolation of the linear parts of the dependences $(\alpha hv)^{1/2} \sim f(hv)$ to abscissa axis assuming indirect electronic transitions to prevail for the above-indicated TiO_2-based semiconductors [16].

Ag nanoparticles were deposited on the mesoporous TiO_2 and TiO_2/ZnO film surfaces via a two-step procedure, adopted from [13]: semiconductor films were dipped in a 10^{-3} M aqueous solution of $[Ag(NH_3)_2]NO_3$ (pH 10), washed with ultrapure water and dried, then irradiated with UV light at 254 nm to reduce the deposited Ag^+ ions to Ag^0 nanoparticles. Basic $[Ag(NH_3)_2]NO_3$ complex salt was used because an ion-exchange process effectively occurs on negatively charged TiO_2 surface under basic conditions:

$$\equiv Ti - O^- + \left[Ag\,(NH_3)_2\right]^+ \leftrightarrow \equiv Ti - O - \left[Ag\,(NH_3)_2\right].$$

Furthermore NH_3 acts as an additional electron donor facilitating silver reduction.

Silver ion reduction is caused by electron attachment from conduction band of TiO_2 generated under UV irradiation. Initiation of silver ion reduction demands strong reductive agents because the potential $Ag^+/Ag^0{}_{atom}$ is −1.8 V [17]. As first clusters are formed, the potential grows to 0.79 V (aqueous solution) for $Ag^+/Ag^0{}_{metal}$, and the reduction process is facilitated. The bond energy of Ag–O is low and more preferable bonding corresponds to Ag–Ag. Therefore, on thermal treatment, the silver atoms and clusters will tend to agglomerate forming nanoparticles [10]. An initial distribution of noble metal cations is uniform on the film surface. However, reduction of cations causes their consolidation as the free energy of solvation of Ag^+ in water is negative and very low $\Delta Gs = -75.7$ kcal/mol (calculated using the B3LYP/SDD/IEFPCM method). Positive $\Delta Gs = 4.3$ kcal/mol for Ag^0; and $\Delta Gs = 8.1$ ($Ag_4{}^0$), −42.3 ($Ag_4{}^+$), 22.5 ($Ag_8{}^0$), −24.4 ($Ag_8{}^+$) kcal/mol are

observed. Consequently, the average positive value of free energy of solvation per Ag atom for reduced metal clusters decreases with its growth [18].

Available Ag^+ concentration on the film surface was adjusted by repetition of dipping/irradiation procedure and controlled by UV–vis measurements. The increase of Ag surface plasmon absorption at 400–450 nm is a sign of the Ag accumulation.

The concentration of Ag^+ ions determined by atomic absorption analysis was 13% Ag in TiO_2/Ag and 14% in TiO_2/ZnO/Ag as-prepared samples. During contact of TiO_2/ZnO films with basic $[Ag(NH_3)_2]NO_3$ solution, partial dissolution of ZnO followed by exchange of Zn^{2+} ions in the film with Ag^+ leads to more homogeneous distribution and stabilization of Ag^0 nanoparticles generated through the Ag^+ photoreduction on the surface [10].

10.4 Characterization of TiO_2/Ag and /TiO_2/ZnO/Ag Films by XRD, AFM, and UV–Vis Spectroscopy

The obtained Zn to Ti atomic ratios (Table10.1) reveals that the stoichiometry of as-prepared TiO_2/ZnO films is disturbed. Zn is present in near-surface region at about 3 and 35 at.% instead of 1 and 10 at.% in precursor.

Partial dissolving of Zn^{2+} ions in the sample treated with NH_4OH (pH 10) basic solution leads to the redistribution of Zn ions along the film profile and rise in Zn/Ti surface ratio for TiO_2/1%ZnO samples up to 0.07.

TiO_2/10%ZnO films with Zn ions-enriched surface at the same condition of NH_4OH treatment lose a significant part of Zn^{2+} ions that precipitate as $Zn(OH)_2$ in solution. We suggested the same mechanism of $[Ag(NH_3)_2]^+$ action on the Zn-rich sites of the film surface. Zn/Ti ratio in Ag+-doped films was estimated to be 0.04 after ion-exchange procedure. These data coincide with chemical analysis by atom absorption spectroscopy that gives us 1.03% Zn in TiO_2/1%ZnO film before and 0.70% Zn after contact with $[Ag(NH_3)_2]^+$ ions.

Crystalline structure of TiO_2/Ag and TiO_2/ZnO/Ag nanocomposites with 1% Zn content was investigated by XRD analysis of film scratched off from the glass substrate (Fig. 10.1). The XRD pattern of TiO_2/Ag exhibits only anatase diffraction lines. No observable rutile phase is found in all samples. For TiO_2/1%ZnO sample the new peaks characteristic to cubic $Zn_2Ti_3O_8$ phase [8] appears. According to [8] during sintering, ZnO reacts with TiO_2 and transforms into $Zn_2Ti_3O_8$ phase and further (at 600°C) to hexagonal $ZnTiO_3$ phase.

As we reported previously [7], initial crystallinity of titania films (60%) was slightly decreased when Zn concentration in the films grew. The average size of

Table 10.1 A summary of the Zn to Ti atomic ratios before and after contact with ammonia solution calculated from XPS survey spectra

Sample	TiO_2/1%ZnO	TiO_2/1%ZnO NH_3	TiO_2/10%ZnO	TiO_2/10%ZnO NH_3
Zn/Ti ratio	0.03	0.07	0.35	0.24

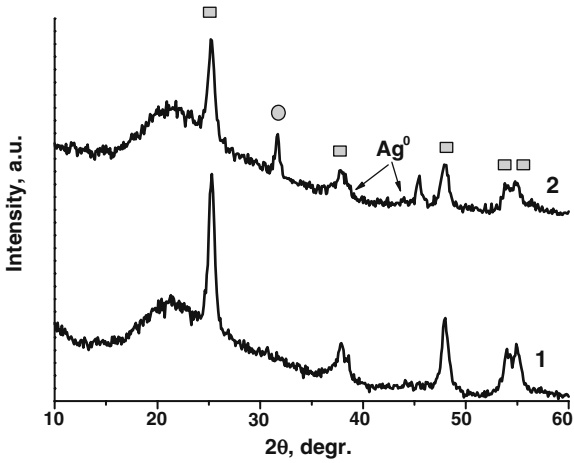

Fig. 10.1 X-ray diffraction patterns of TiO_2/Ag *1*, TiO_2/1%ZnO/Ag *2* films, ■ – anatase, • – new phase $Zn_2Ti_3O_8$

anatase crystallites estimated according to the Scherrer equation increases from 9 nm for TiO_2 to 11 nm for TiO_2/ZnO powders. The characteristic peak at $2\theta = 38.1°$ of Ag^0 was not observed in the XRD pattern due to the overlapping of the structural lines of TiO_2 anatase and silver. Only weak peak near $2\theta = 44.3°$ of silver (331) can be seen indicating that very small Ag species uniformly dispersed within the film surface.

Surface morphology of mesoporous TiO_2/ZnO/Ag films with photodeposited Ag nanoparticles before and after thermal treatment at 500°C was studied using AFM microscopy. Surface of non-treated TiO_2/ZnO/Ag films consists of the agglomerates of silver nanoparticles with sizes of $\sim$ 1.1 μm and heights in the range of 10–160 nm (maximum at 70 nm). Root mean square roughness of the film is 21.3 nm. After annealing at 500°C the surface of TiO_2/ZnO/Ag films is composed of rows of smaller Ag particles (height 10–95 nm with maximum ~45 nm) oriented along one direction that follows mesoporous TiO_2 film topology (root mean square roughness is 21.5 nm).

From AFM data and broad surface plasmon resonance band (SPR) (450 nm) in absorption spectra of TiO_2/ZnO/Ag films (Fig. 10.2) we can conclude nonhomogeneous distribution of Ag nanoparticles on the surface of as-prepared films; after heat treatment smaller particles oriented along one direction (b) were obtained giving bright yellow color and the intensive plasmon resonance peak at 400 nm typical for particles with narrow size distribution. Only wide band in the visible region was registered in absorption spectra of TiO_2/Ag films prepared in the same manner that could be attributed to the formation of large silver particles and/or silver oxide [19].

Subsequent thermal treatment leads to the decrease of absorption in visible range of spectra and discoloration of films. One possible explanation could be that we obtained extremely small (<2 nm) nanoparticles dispersed on the titania surface without characteristic plasmon resonance absorption (Fig. 10.3).

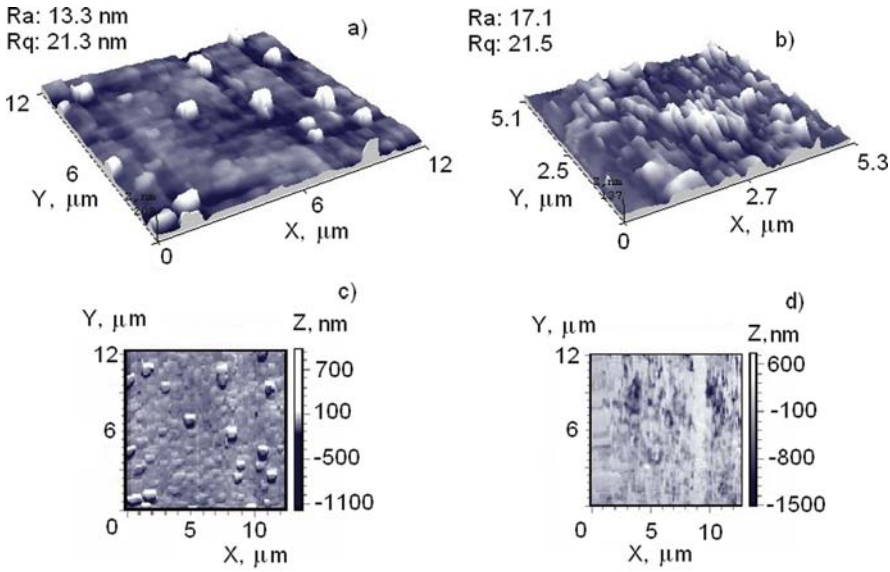

Fig. 10.2 3D and 2D AFM images of the surface of TiO_2/ZnO/Ag films deposited onto glass substrate: **a**, **c** film with as-deposited Ag particles; **b**, **d** film treated at 500°C

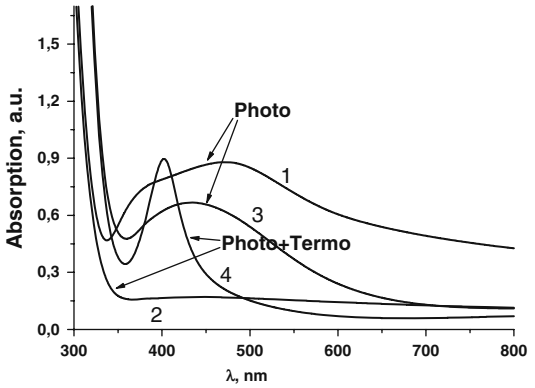

Fig. 10.3 Absorption spectra of the TiO_2 (*1*, *2*) and TiO_2/ZnO (*3*, *4*) films with photodeposited silver nanoparticles as-prepared (*1*, *3*) and after thermal treatment at 500°C (*2*, *4*)

10.5 Surface Analysis of TiO_2/Ag and TiO_2/ZnO/Ag Nanocomposites by X-Ray Photoelectron Spectroscopy

In order to elucidate the nature of SPR peak transformation in optical spectra of TiO_2/Ag and TiO_2/ZnO/Ag films during thermal treatment the analysis of photoemission spectra of as-prepared and thermal treated at 500°C samples was performed.

The composition and chemical state changes occurring on the film surface during thermal treatment are characterized according to the peak intensity, shape changes, and binding energy (E_B) shift in the X-ray photoelectron spectra.

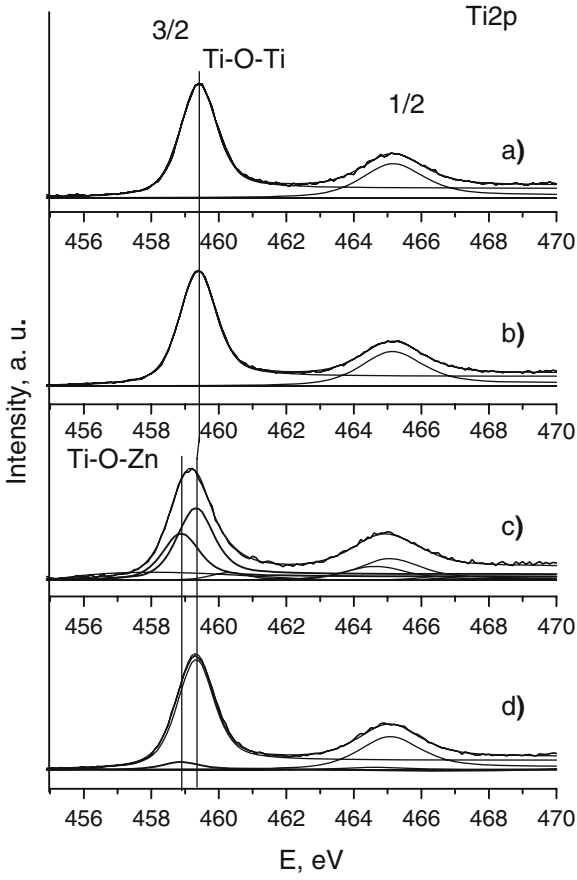

Fig. 10.4 Peak synthesis for Ti2*p* level for as-prepared samples (**a**, **c**) and after thermal treatment at 500°C (**b**, **d**) of TiO_2/Ag (**a**, **b**) and TiO_2/ZnO/Ag (**c**, **d**) films

XPS analysis of the atomic level Ti2*p* is presented in Fig. 10.4. The Ti2*p* binding energy for all Ag-doped samples is slightly shifted to higher E_B as compared to that of unmodified TiO_2.

This is because the Fermi level of Ag is lower than that of TiO_2, so that the conduction band electrons of TiO_2 may transfer to the Ag species deposited on the surface of TiO_2, resulting in decrease of the outer electron density of Ti ions [20].

The Ti$2p_{3/2}$ line of TiO_2/Ag samples is composed of a single peak at E_B = 459.4 eV for as-prepared and annealed at 500°C films, leaving no doubt of the existence of $Ti^{(IV)}O_2$ as major titanium species [21].

For the TiO_2/1%ZnO/Ag samples the Ti$2p_{3/2}$ peak becomes broader and more asymmetric that represents the existence of additional peak at 458.9 eV shifted by 0.5 eV from the main peak at 459.4 eV (Fig. 10.4c, d). This peak could be attributed to the formation on the surface of Zn–O–Ti bonds. The obtained E_B values are similar to those reported by C.T. Wang and J.C. Lin for nanosized zinc–titanium oxide

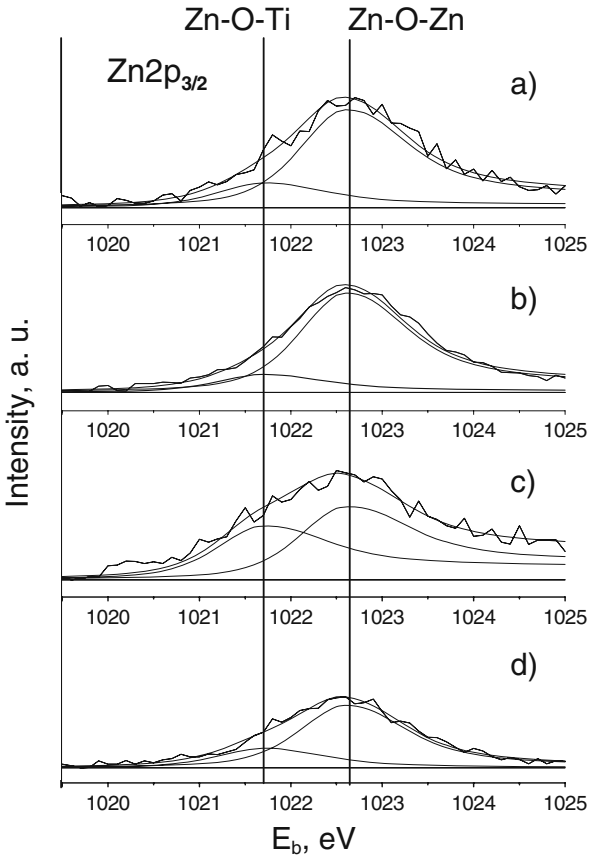

Fig. 10.5 Peak synthesis for Zn2*p* level for TiO_2/1%ZnO films. Initial TiO_2/1%ZnO film (**a**), TiO_2/1%ZnO leached in NH_4OH solution (**b**), TiO_2/1%ZnO after Ag photodeposition (**c**), TiO_2/1%ZnO/Ag annealed at 500°C (**d**)

aerogel [6]. Lower E_B value than in TiO_2 indicates stronger electronic interaction between Zn and Ti atoms in the mixed oxide structure. This peak is diminished after additional thermal treatment due to further $Zn_2Ti_3O_8$ phase crystallization (see XRD pattern in Fig. 10.1).

Figure 10.5 presents XPS spectra of the TiO_2/1%ZnO films and TiO_2/1% ZnO/Ag films after photodeposition of silver and following calcination at 500°C. TiO_2/1%ZnO/Ag film showed higher E_B values for Zn2$p_{3/2}$ than in ZnO [6]. Due to asymmetry, the Zn2*p* peak can be decomposed into two components: one at 1022.7 eV that according to [6] can be assigned to Zn^{2+} ions in Zn–O–Ti bonds of $Zn_2Ti_3O_8$ structure and peak at 1021.7 eV that corresponds to Zn–O–Zn bonds in ZnO. This peak decreases after calcination at 500°C giving rise to the 1022.7 peak of $Zn_2Ti_3O_8$ phase that can be seen in diffractogram (Fig. 10.1). It seems Ag loading accelerates this process.

XPS spectra of TiO_2/1%ZnO films treated with NH_4OH solution (Fig. 10.5b) confirm that such treatment does not lead to significant changes in electronic structure of Zn$2p_{3/2}$ levels.

Silver is a metal that has anomalous properties in E_B shifts when being oxidized, i.e., the Ag*3d* peaks shift to lower E_B values [22]. Usually, positive E_B shifts in the metal core-level peaks are observed when the metal is oxidized, which are explained by considering the electronegativity differences between the metal atom and cation. Factors such as lattice potential, work function changes, and extra-atomic relaxation energy lead to negative E_B shift in the case of Ag and some Cd compounds [23].

The XPS spectra of Ag*3d* level and results of their decomposition into peaks are shown in Fig. 10.6.

Ag$3d_{5/2}$ component for as-prepared TiO_2/Ag and TiO_2/ZnO/Ag films stands at 368.2 and 368.0 eV, respectively (Fig. 10.6a, c). Thermal treatment results in

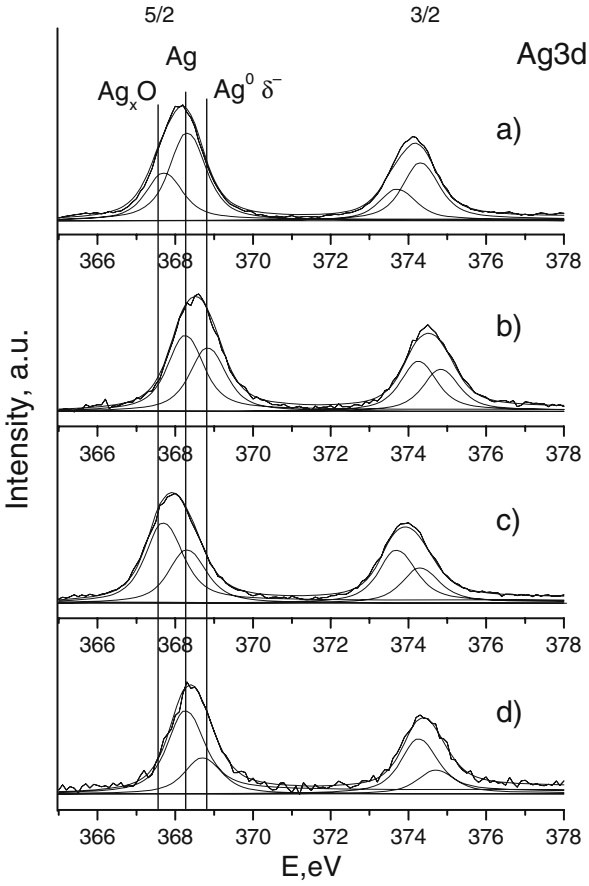

Fig. 10.6 Peak synthesis for Ag*3d* level for as-prepared samples (**a**, **c**) and after thermal treatment at 500°C (**b**, **d**) of TiO_2/Ag (**a**, **b**) and TiO_2/ZnO/Ag (**c**, **d**) films

peak narrowing and their shift toward higher binding energy by 0.4 eV. The peak decomposition reveals the presence of Ag in metallic state peaked at 368.35 eV and Ag_2O with peak at $E_B = 367.7$ eV. The values are in good agreement with those (368.22 eV) reported herein [22, 24]. These results indicate that the silver nanoparticles formed on TiO_2 under given experimental conditions (UV irradiation, ambient atmosphere, room temperature) are chemically very reactive and were easily oxidized with Ag_2O shell formation. The authors [25] reported that the growth of silver oxide overlayer up to 6 nm on Ag^0–TiO_2 interface is a function of plasma exposure time at room temperature. Higher intensity of oxide peak for TiO_2/ZnO/Ag film as compared to TiO_2/Ag supports our assumption about more homogeneous distribution of smaller Ag nanoparticles on this surface. Tendency to oxidation might increase significantly with decrease of particle size and increase of portion of surface atoms exposed to interface.

Annealing at 500°C results in the complete decomposition of silver oxide; no peaks are observed at low E_B side near 367.7 eV for TiO_2/Ag as for TiO_2/ZnO/Ag samples (Fig. 10.6b, d). For the last one Ag_2O decomposition leads to Ag^0 peak intensity growth (Fig 10.6d) that coincides with narrow SPR band appearance in the absorption spectra (Fig. 10.3, 4).

For both samples two components were found to form Ag$3d_{5/2}$ peak: one of them at 368.4 eV corresponds to metallic silver and the other one that has binding energy higher by 0.4 eV (368.8 eV) than that for Ag^0. Observed shift toward higher E_B after thermal treatment is similar to that reported for Ag nanoparticles in SiO_2, SiN_x, and TiO_2 thin films [26]. This effect was also observed for Pt [27] indicating the charge transfer from semiconductor matrix to the metal.

Calculated Ag to Ti atomic ratios (Table 10.2) show that the silver content in the near-surface region is significant and equal for both samples.

The different Ag / Ti ratio values of the films treated at 500°C and as-prepared one indicate the decrease of the total Ag^0 amount on the TiO_2/Ag surface as well as on the surface of TiO_2/1%ZnO/Ag film.

XPS data confirm our suggestion that Ag^0 is still present on the TiO_2/Ag film, but the disappearance of SPR band in the TiO_2/Ag spectra could be caused by the formation of very small Ag particles on the TiO_2 surface or by partial "dissolving" of certain critical-size silver nanodrops in the crystalline matrix as was described

Table 10.2 A summary of the Ag content and Ag to Ti atomic ratios before and after annealing at 500°C

E_BAg$3d_{5/2}$	TiO_2/Ag[a](%)	TiO_2/1%ZnO/Ag[a] (%)	TiO_2/Ag[b] (%)	TiO_2/1%ZnO/Ag[b] (%)
367.7 eV	35.9	54.2	–	–
368.3 eV	64.1	45.8	60.7	70.1
368.8 eV	–	–	39.3	29.9
Ag/Ti	0.60(13%)	0.60(14%)	0.11(2.3%)	0.09(2.1%)

[a]With photodeposited silver.
[b]Thermally treated at 500°C.

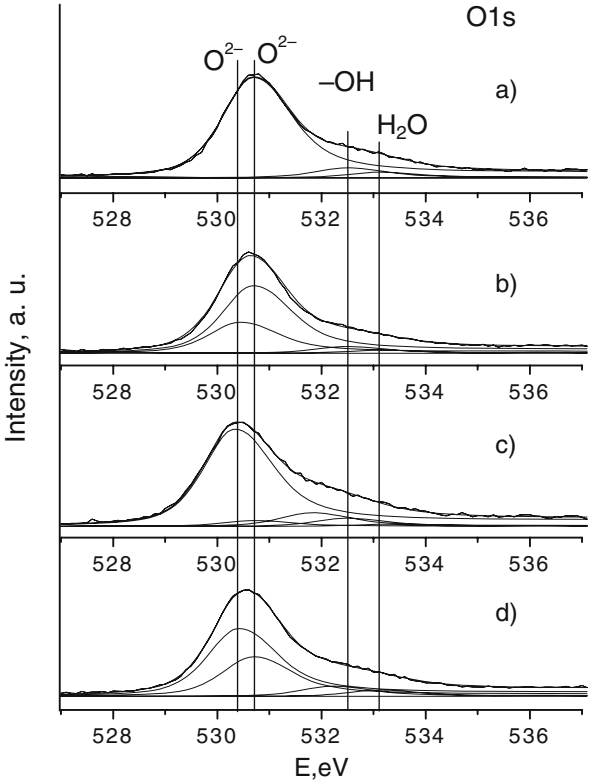

Fig. 10.7 Peak synthesis for O*1s* level for as-prepared samples (**a**, **c**) and after thermal treatment at 500°C (**b**, **d**) of TiO_2/Ag (**a**, **b**) and TiO_2/ZnO/Ag (**c**, **d**) films

elsewhere [13, 18]. Escape of the metal nanoparticles from TiO_2/1%ZnO/Ag film after 500°C treatment leads to more homogeneous particle size distribution through the film profile because of more intensive evaporation of silver droplets from the outer surface of the films. The smaller particles that manifested in the intensive SPR peak in the absorption spectra were formed in restricted media inside the film pores, where Zn^{2+} ions were replaced by Ag^{+} ones and converted to Ag^0 as a result of photoreduction. Similar results are reported for temperature dependence of Ag nanoparticles distribution through the depth profile of Ag–TiO_2 sol–gel films [28].

The O*1s* spectra presented in Fig. 10.7 were separated into two main contributions that were assigned to the "O^{2-}" anions of the crystalline network (near 530.0 eV) and integrated as –OH (532.5 eV) and adsorbed H_2O (533.0 eV). The first peak is slightly shifted to lower E_B value for the TiO_2/ZnO and thermal-treated TiO_2/Ag due to the increase of basic strength of the metal oxide with Ti–O–Zn and Ti–O–Ag bonds formation [29].

10.6 The Photocatalytic Activity of Prepared Nanocomposites

On the basis of literature [12, 30] the heterogeneous photocatalytic process of Rhodamine B degradation can be expressed as follows: the photogenerated holes of the valence band migrate to the surface of photocatalyst. Due to the fact that Fermi level of TiO_2 is higher than Ag^0, electrons allow transfer to Ag nanoparticles and avoid recombination with holes [9]. The oxidative pathway can be performed by direct hole attack or mediated by OH radicals that formed when holes react with OH^- groups on the TiO_2 surface. Photoinduced electrons of the conduction band interact with the electron acceptors, commonly dissolved O_2, which are transformed in superoxide radical anion $O_2^{\cdot -}$. These radicals ($\bullet OH$, $O_2^{\cdot -}$) possess high oxidative potential for complete mineralization of Rhodamine B (RB).

The activity of prepared samples was estimated in processes of RB decomposition. Photooxidation rates were calculated in pseudo first order reaction approach under equal conditions and presented in Fig. 10.8. As we can see from the figure improved efficiency of photodegradation is caused by Zn doping due to the photogenerated charge separation between TiO_2 and $Zn_2Ti_3O_8$ phase [4]. Silver-modified samples prepared via photodeposition procedure exhibit enhanced activity (3–4 times) toward the undoped TiO_2 and TiO_2/ZnO coatings. Efficiency of dye photodegradation grows in correlation with the flat-band potential shift to more negative values (from −0.51 V for TiO_2 to −0.71 V for photodeposited and −1.51 V for additionally treated at 500°C TiO_2/ZnO/Ag samples) [14].

The decrease of activity of the TiO_2/Ag film after heat treatment in spite of the fact that Ag^0 nanoparticles are present on the surface (clearly evident from the XPS spectra) could be connected with lack of plasmon resonance band in UV–vis spectra of this nanocomposite. This observation supports "plasmonic photocatalysis" approach discussed in [31]. The authors [31] hypothesized that the enhanced near-field in the vicinity of the Ag nanoparticles could boost the excitation of the electron–hole pairs in TiO_2 and therefore increased the efficiency of the photocatalyst.

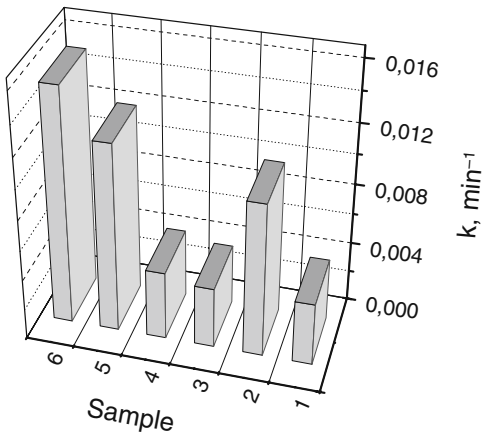

Fig. 10.8 The photocatalytic efficiency for as-prepared TiO_2 (*1*) and TiO_2/ZnO (*4*) films; TiO_2/Ag and TiO_2/ZnO/Ag before (*2*, *5*) and after heat treatment at 500°C (*3*, *6*)

10.7 Conclusions

Prepared by templated sol–gel method TiO_2/ZnO mesoporous films consist of anatase nanocrystallites and $Zn_2Ti_3O_8$ phase.

The XPS results indicate that the Ag metal was dominant in all samples modified with Ag.

The intensive sharp SPR peak in absorption spectra evidences about the formation of silver nanoparticles in restricted media inside the film pores after Zn^{2+} ions in TiO_2/ZnO matrix were replaced by Ag^+ ones and then converted into Ag^0 by photoreduction.

Thermal treatment at 500°C leads to destruction of silver oxide shell and more homogeneous distribution of Ag nanoparticles in oxide matrixes that enhanced activity in the photooxidation of Rhodamine B.

Acknowledgments The authors thank Gornikov Yu.I. for the XRD measurements; N.P. thanks STCU Project 4918 for the financial support.

References

1. Zorn ME, Tompkins DT, Zelter WA et al (2000) Catalytic and photocatalytic oxidation of ethylene on titania-based thin films. Environ Sci Technol 34:5206–5210
2. Gnatyuk Yu, Smirnova N, Eremenko A et al (2005) Design and photocatalytic activity of mesoporous TiO_2/ZrO_2 thin films. Ads Sci Technol 23:497–508
3. Kamat PV (1997) Composite semiconductor nanoclusters. In: Kamat PV, Meisel D (eds) Semiconductor Nanoclusters – Physical, Chemical and Catalytic Aspects. Elsevier Science, Amsterdam
4. Marci G, Augugliano V, López-Muňoz MJ et al (2001) Preparation, characterization and photocatalytic activity of polycrystalline ZnO/TiO_2 systems. I. Surface and bulk characterization. J Phys Chem B 105:1026–1040
5. Liao S, Donggen Y, Yu D et al (2004) Preparation and characterisation of ZnO/TiO_2, SO_4^{2-}/ZnO/TiO_2 photocatalyst and their photocatalysis. J Photochem Photobiol A 168:7–13
6. Wang CT, Lin JC (2008) Surface nature of nanoparticle zinc-titanium oxide aerogel catalysts. Appl Surf Sci 254:4500–4507
7. Ptashko T, Smirnova N, Eremenko A, Oranska E, Huang W (2007) Synthesis and photocatalytic properties of mesoporous TiO_2/ZnO films with improved hydrophilicity. Ads Sci Technol 25:35–43
8. Shi ZM, Lin LN (2009) Influence of La^{3+}/Ce^{3+} doping on phase transformation and crystal growth in TiO_2-15%ZnO gels. J Non-Cryst Solids 355:213–220
9. Subramanian V, Wolf E, Kamat P (2001) Semiconductor-metal composite nanostructures. To what extend do metal nanoparticles improve the photocatalytic activity of TiO_2 films? J Phys Chem B 105:11439–11448
10. He C, Yu Y, Hu X et al (2002) Influence of silver doping on the photocatalytic activity of titania films. Appl Surf Sci 200:239–247
11. Gnatyuk Yu, Manuilov E, Smirnova N et al (2006) Sol–gel produced mesoporous Ag/TiO_2 coatings effective in rhodamine B photooxidation. In: Kassing R et al (eds) NATO Science Series. II. Mathematics, Physics and Chemistry. Functional Properties of Nanostructured Materials, The Netherlands. Springer, Heidelberg, 223:485–490
12. Arabatis IM, Stergiopolulos T, Bernard MC et al (2003) Silver-modified titanium dioxide films for efficient photodegradation of methylorange. Appl Catal B 42:187–201
13. He J, Ichinose I, Kunitake T et al (2003) In situ synthesis of noble metal nanoparticles in ultrathin TiO_2-gel films by combination of ion-exchange and reduction processes. Langmuir 18:10005–10010

14. Vorobets V, Manujlov E, Smirnova N et al (2008) Electro- and photocatalytic properties of electrodes based on mesoporous TiO_2-ZnO-Ag films. Chem Phys Technol Surf 14:382–390
15. Yang P, Zhao D, Margolese DI et al (1998) Generalized syntheses of large-pore mesoporous metal oxides with semicrystalline frameworks. Nature 396:152–155
16. Enright B, Fitzmaurice D (1996) Spectroscopic determination of electron and hole effective masses in a nanocrystalline semiconductor film. J Phys Chem 100:1027–1035
17. Henglein A (1998) Colloidal silver nanoparticles: photochemical preparation and interaction with O_2, CCl_4, and some metal ions. Chem Mater 10:444–450
18. Krylova GV, GnatyukYuI, Smirnova NP et al (2009) Ag nanoparticles deposited onto silica, titania and zirconia mesoporous films synthesized by sol–gel template method. J Sol–Gel Sci Technol 50:216–228
19. Epifani M, Giannini C, Tapfer L et al (2000) Sol–gel synthesis and characterization of Ag and Au nanoparticles in SiO_2, TiO_2 and ZrO_2 thin films. J Am Ceram Soc 88:2385–2393
20. Hou X-G, Huang M-D, Wu X-L (2009) Preparation and studies of photocatalytic silver-loaded TiO_2 films by hybrid sol–gel method. Chem Eng J 146:42–48
21. Alam MJ, Cameron DC (2002) Preparation and characterisation of TiO_2 thin films by sol–gel method. J Sol–Gel Sci Technol 25:137–145
22. Weaver JF, Hoflund GB (1994) Surface characterization study of the thermal decomposition of AgO. J Phys Chem 98:8519–8524
23. Xin BF, Jing LQ, Ren ZY et al (2005) Effects of simultaneously doped and deposited Ag on the photocatalytic activity and the surface states of TiO_2. J Phys Chem B 109:2805–2809
24. ISO 15472:2001 Surface chemical analysis – X-ray photoelectron spectrometers – Calibration of energy scales
25. Romannyuk A, Oelhafen P (2007) Formation and electronic structure of TiO_2-Ag interface. Solar Energy Mater Solar Cells 91:1051–1054
26. Masetti E, Bulir J, Gagliardi S et al (2004) Elipsometric and XPS analysis of the interface between silver and SiO_2, TiO_2 and SiNx thin films. Thin Solid Films 455–456:468–472
27. Bahl MK, Tsai SC, Chung YW (1980) Auger and photoemission investigations of the platinum-Sr-TiO_3(100) interface: relaxation and chemical-shift effects. Phys Rev B 21: 1344–1348
28. Traversa E, Vona ML, Nunziante P et al (2001) Photoelectrochemical properties of sol–gel processed Ag-TiO_2 nanocomposite thin films. J Sol–Gel Sci Technol 22:115–123
29. Tanabe K (1970) Solid Acids and Bases, Kodansha, Tokio, Japan In: Anderson JR, Boudart M (eds) Catalysis: Science and Technology. Springer, New York
30. Sung-Suh H, Choi J, Hah H et al (2004) Comparison of Ag deposition effects on the photocatalytic activity of nanoparticulate TiO_2 under visible and UV light irradiation. J Photochem Photobiol A 163:37–44
31. Awasu K, Fujimaki M, Rockstuhl C et al (2008) A plasmonic photocatalyst consisting of silver nanoparticles embedded in titanium dioxide. J Am Chem Soc 130:1676–1680

Chapter 11
Nanoporous Silica Matrices and Their Application in Synthesis of Nanostructures

V.A. Tertykh, V.V. Yanishpolskii, K.V. Katok, and I.S. Berezovska

Abstract The effect of the presence of I-4 Me-Ph ionene in the supramolecular template (cetyltrimethylammonium bromide) on formation of porous structure of silicas was studied. We also studied the peculiarities of template synthesis of mesoporous silicas inside of large pores of silica gel. Mesoporous silicas with chemically modified surface were applied in synthesis of metallic nanostructures. Porous silicas with grafted layer of hydridepolysiloxane were used for in situ preparation of supported nanoparticles of gold and silver by reduction of metal ions from chloroauric acid and silver nitrate solutions, respectively. Nitrogen adsorption–desorption, X-ray powder diffraction analysis, scanning and transmission electron microscopies, IR-, UV–visible, and laser correlation spectroscopies were applied for characterization of adsorbents and nanostructures obtained.

Ordered mesoporous silicas of the M41S type have attracted much attention due to their application as adsorbents in separation techniques, catalysts supports, hosts for a variety of optoelectronic materials. The nature of a supramolecular template and inorganic precursors crucially influences the quality of materials with desired nanoporous architecture. Instability of their structure has considerably limited range of application of the M41S materials. Thus, porous structure control and structural stability of mesoporous silicas are the current trends in the template synthesis of ordered porous materials [1–3].

Nowadays, researchers more widely use possibilities of geometrical and chemical modification of silica matrices in synthesis of supported nanoparticles. One of the approaches of controlled synthesis of metal nanoparticles is using porous matrices whose sizes of pores confine growth of nanoparticles [4]. The second approach is attachment of appropriate metal-containing compounds with following reduction of metal [5]. The third route is application of chemically modified silicas with immobilized reagents possessing reductive properties.

V.A. Tertykh (✉)
O.O. Chuiko Institute of Surface Chemistry of the National Academy of Sciences of Ukraine, General Naumov St. 17, Kyiv 03164, Ukraine
e-mail: tertykh@public.ua.net

A.P. Shpak, P.P. Gorbyk (eds.), *Nanomaterials and Supramolecular Structures*,
DOI 10.1007/978-90-481-2309-4_11,

Reductive properties of silicon hydride groups with respect to metals in electromotive series are well known [6–8], therefore formation of gold and silver nanoparticles is necessary to be expected in close vicinity of grafted silicon hydride groups. Sizes of reduced nanoparticles could be regulated by varying concentration of metal-containing compounds in solution or using matrices with specified sizes of pores.

The main target of the work was to study the effect of polymer-containing template on the porous structure and particle morphology of silicas obtained by calcination of sol–gel products. Here, we also report the approach in improvement of mesoporous silicas' mechanical stability due to carrying out of template synthesis inside of volume of inorganic matrices with higher structural stability. Possibilities of application of chemically modified ordered mesoporous silicas of the MCM-41 type for immobilization of metal nanoparticles were investigated.

11.1 Role of Ionene in Composition of Porous Structure of Template-Synthesized Silicas

Ionic surfactants with different lengths of hydrocarbon chain are the most widely applied to form mesoporous structure because of their possibility to self-assembly into charged micelles. There has been considerable interest in studying the influence of polymers with high charge density, especially organic polymers with a quaternary nitrogen atom (polycations, ionenes), on the composition of the porous structure of template-synthesized silicas [9, 10].

Syntheses were carried out in ethanol–ammonia media using tetraethoxysilane (TEOS) as a silica precursor with molar ratio of components 1 TEOS:X:11 NH_3:144 H_2O:58 EtOH, where X is a template. The following templates were used: (a) cetyltrimethylammonium bromide (CTAB); (b) mixtures of CTAB with various amounts of I-4 Me-Ph ionene; (c) ionene of the general formula.

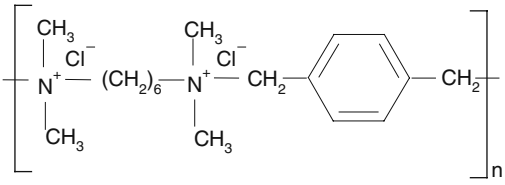

Composition of the used templates is presented in Table 11.1.

The calcined silicas were investigated by adsorption–desorption of nitrogen at 77 K (ASAP-2000). From isotherms of nitrogen adsorption, the specific surface area, pore volume, and pore size distribution were determined. The structure of samples was investigated using small-angle X-ray diffraction (XRD) (automated diffractometer DRON-4-07, CuKα-radiation). Scanning electronic microscopy (Superprobe-733, JEOL) was applied to study the form and size of the obtained silica particles.

Table 11.1 Composition of micellar templates in sol–gel synthesis of silicas

Template	Molar ratio of TEOS/template	I-4 Me-Ph content (mol%)
CTAB	0.3	–
CTAB + I-4 Me-Ph	0.3	1
CTAB + I-4 Me-Ph	0.3	10
CTAB + I-4 Me-Ph	0.3	33
I-4 Me-Ph	0.3	100

Nitrogen adsorption isotherms (Fig.11.1a) of silicas, synthesized with CTAB and mixtures of CTAB with small amounts of ionene (1–10%) as templates, show a type IV isotherm. Capillary condensation of nitrogen was observed over a narrow range of relative pressures (p/p_0 =0.15–0.27) that is evidence of the presence of mesopores. Specific surface areas determined by the BET method were 1050–1230 m^2/g, and curves of pore sizes distribution (DFT method) had two maxima of 2.5 and 1 nm (Fig. 11.1b). Increase of polymer concentration (up to 33%) led to

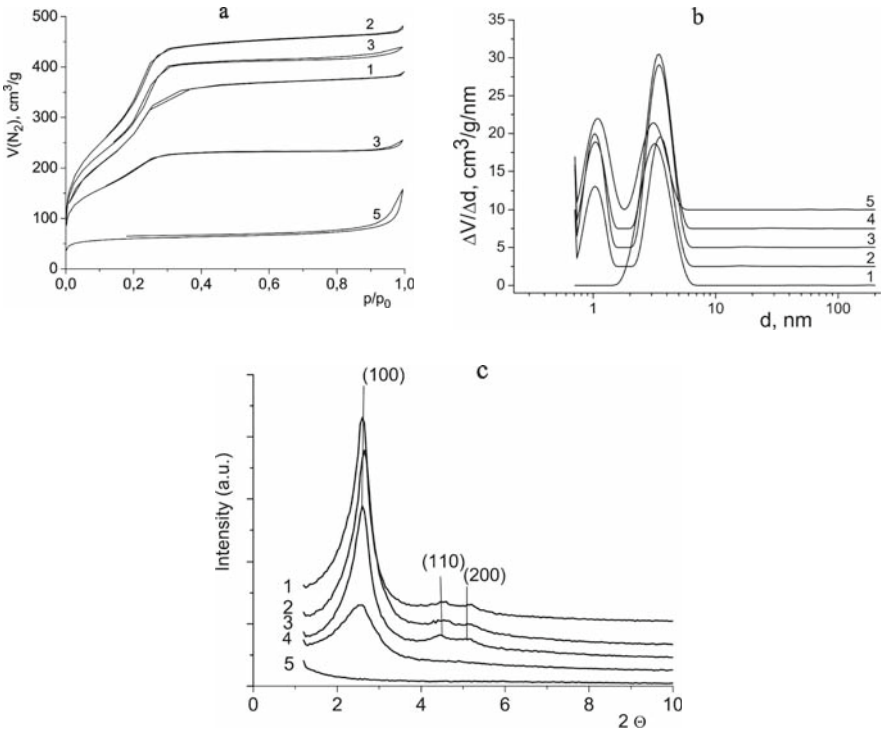

Fig. 11.1 Nitrogen adsorption isotherms (**a**), pore size distribution (**b**), and X-ray diffractograms (**c**) of silicas synthesized with different amounts of I-4 Me-Ph ionene in the template: 0% (*1*), 1% (*2*), 10% (*3*), 33% (*4*), and 100% (*5*)

Table 11.2 Adsorption-structural parameters of silicas synthesized with different amounts of I-4 Me-Ph ionene in the template

I-4 Me-Ph ionene content (%)	Surface area (m^2/g; from BET)	Parameter of lattice a_o (nm; from X-ray data)	Structure of pores (from X-ray data)
–	800	3.9	Hexagonal ordered
1	1234	3.8	Hexagonal ordered
10	1055	3.9	Hexagonal ordered
33	702	3.9	Slightly ordered
100	239	–	Disordered

decrease in surface areas up to 700 m^2/g. The adsorption isotherm of silica synthesized with the use of ionene as a template gave a type I isotherm, and the resulting material has a relatively low value of specific surface area (240 m^2/g).

The diffractograms (Fig 11.1c) of silicas synthesized using pure CTAB as a template and in the presence of small amounts of ionene (up to 10%) show three low-angle Bragg peaks in the range of 2θ=2.5–7.0° with indexation for hexagonal system and are typical for the MCM-41 materials [1, 3]. The diffractogram of silica synthesized with ionene content of 33% has one weak peak; silicas synthesized with pure ionene as a template have no peaks and are characterized by the disordered structure of pores. The distances between pore centers (lattice parameter, a_o) were determined using the formula $a_o=2d_{100}/3^{0.5}$ (d_{100} – interplanar distance of 100 planes) [11, 12].

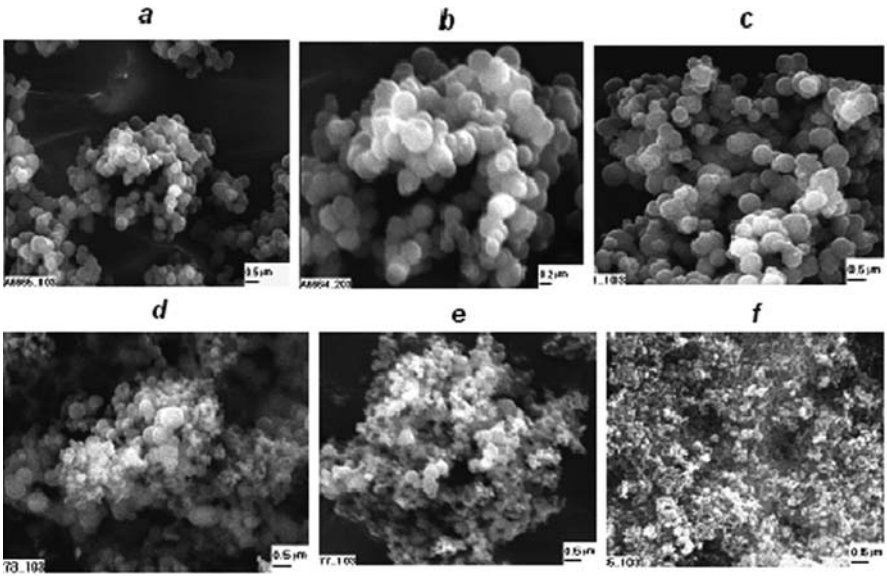

Fig. 11.2 SEM micrographs of silicas synthesized using CTAB (**a**, **b**) and CTAB with different amounts of I-4 Me-Ph ionene: 1% (**c**), 10% (**d**), 33% (**e**), 100% (**f**) as templates

Thus, the polymer of the I-4 MePh type can be applied as a molecular template to synthesize mesoporous materials with higher value of specific surface area in comparison with silicas synthesized with use of pristine CTAB. These materials have ordered bimodal structure of pores of 2.5 nm size formed by micelles of CTAB and 1 nm size that reveals structure-directing role of polyionene. Adsorption-structural characteristics of silicas synthesized with different ratios of CTAB and ionene in the template are presented in Table 11.2.

Scanning electronic micrographs (Fig. 11.2) of silicas synthesized in alcohol–ammonia media using CTAB as a supramolecular template show that a majority of particles have almost perfect spherical granulation with average particle diameter about 0.5 μm. Addition of ionene into template leads to decrease of particle sizes from 0.5 to 0.1 μm and transformation of spherical particles to irregular agglomerates.

11.2 Template Synthesis of Mesoporous Silicas Inside of Nanoreactors Based on Large Pores of Silica Gel

Together with successes in porous structure design, an increase of ordered mesoporous silica stability is an essential parameter for their potential applications [13, 14]. Here, improvement of mechanical properties by incorporation of the MCM-41 materials inside of pore volume of silicas with higher structural stability has been proposed.

Synthesis of mesoporous silicas in nanoreactors based on large pores of silica gel was carried out by step-by-step incorporations of micellar solutions inside of pore volume of silica gel with surface area about 115 m^2/g and average pore diameter about 24 nm. Micellar solution with molar ratio of components 1 TEOS:0.18 CTAB:5 NH_3:75 H_2O was prepared according to procedure [15]. After template elimination synthesized materials were characterized by low-temperature adsorption–desorption of nitrogen to estimate surface area (BET equation) and pore size distribution (DFT method) [16]. X-ray diffraction was used to determine the structure of synthesized samples.

Results of thermal analysis of template-containing mesoporous silicas synthesized inside of pore volume of silica gel are presented in Fig. 11.3. Thermogravimetric studies of uncalcined samples can provide information about approximate content of the organic template. The TG and DTG curves of the synthesized materials show a typical decomposition profile with four distinctive weight loss steps. Initial weight loss (about 4%) at the temperature up to 200°C can be explained by evaporation of ammonia and physically adsorbed water. In the temperature range from 200 to 360°C, the main decrease of mass (about 12%) with expressed exothermal effect (DTA curve) is observed because of organic template decomposition. The third peak on the DTG curve in the range of temperature 360–550°C is connected with thermal oxidation of residual organic compounds (about 7% of the lost weight). At the temperature above 550°C TG and DTG curves

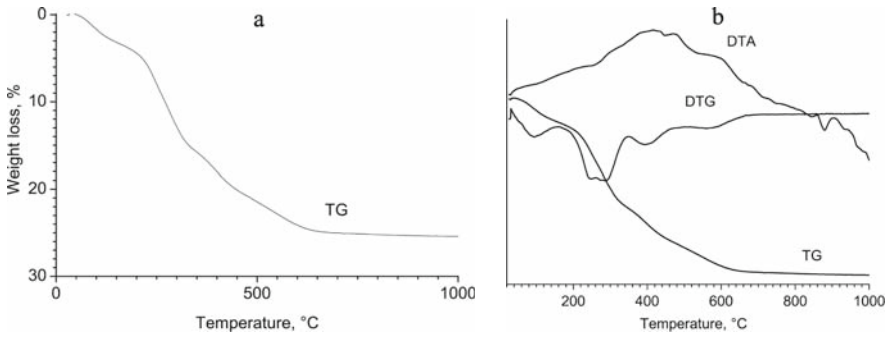

Fig. 11.3 TG , DTG, and DTA curves of mesoporous silicas synthesized inside of pore volume of silica gel

show slight weight loss (2.9%) corresponding to water loss due to condensation of silanol groups to form siloxane bonds. Total weight loss was 25.9%, and 19% of lost weight corresponds to the content of the organic template. According to molar ratio of micellar solution components, the quantity of synthesized mesoporous silicas should be equal to 3% of the total weight of the synthesized material which is in good agreement with results of thermal analysis.

Nitrogen adsorption–desorption isotherm for silica gel has a hysteresis loop at high relative pressure; it reveals existence of large pores in the samples (Fig. 11.4a, curve 1). Nitrogen adsorption–desorption isotherms for silica gel after template syntheses inside of nanopores are characterized by appearance of capillary condensation ranges ($0.3<p/p_o<0.4$) and testify the mesopores' presence. The sharpness of these regions increased after each template synthesis was accompanied by decreasing hysteresis loop which can be explained by filling silica gel pore volume with mesoporous silica (Fig. 11.4a, curves 2–7).

Specific surface area of pristine silica gel is 115 m^2/g (by BET equation), and the DFT pore size distribution curve for silica gel has broad peak in the range of pore size 30–50 nm (Fig. 11.4b, curve 1). Samples with incorporated mesoporous silicas are characterized by increase in specific surface area from 115 to 377 m^2/g (Table 11.3). Pore size distribution curves exhibit peaks corresponding to pores of 3 nm size (Fig. 11.4b). Absence of any peaks in the diffractogram of the initial silica gel confirms its amorphous nature (Fig. 11.4c, curve 1).

It is clear from X-ray diffraction patterns that introducing micellar solution causes appearance of reflection intensity in low-angle region (Fig. 11.4c, curves 2–7). Broad low-angle diffraction peak should be a result of formation of worm-like pore structure, and weak intensity of reflection can be explained by small quantity of incorporated silica.

Thus, template synthesis of mesoporous silicas with pore diameter of 2.5 nm was carried out inside of nanoreactors based on large pores of silica gel. Surface area of the initial silica gel was 115 m^2/g and after the introduction of micellar solution, the calcined samples had a surface area about 377 m^2/g (Table 11.3).

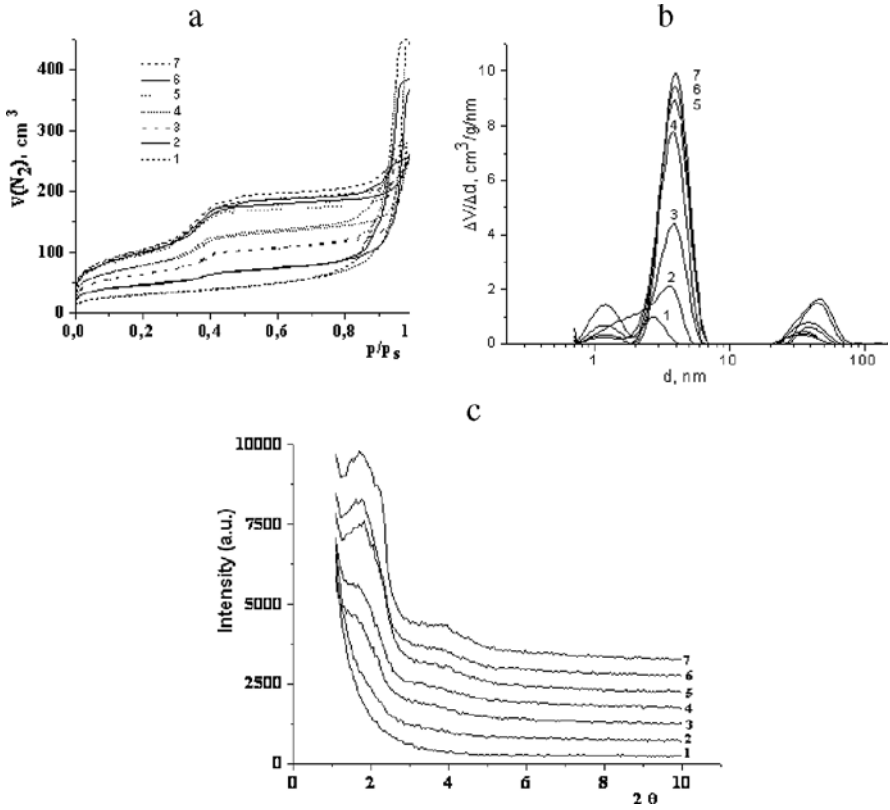

Fig. 11.4 Nitrogen adsorption–desorption isotherms (**a**), differential curves of dependence of pore size on pore volume (**b**), and diffractograms (**c**) for silicas synthesized inside of large pores of silica gel: the initial silica gel (*1*) and silica gels after the first (*2*), second (*3*), third (*4*), fourth (*5*), fifth (*6*), sixth (*7*) introducing of MCM-41

Table 11.3 Structural-adsorption characteristics of silicas synthesized inside of large pores of silica gel: initial silica gel (sample 1) and silica gels after the first (sample 2), second (sample 3), third (sample 4), fourth (sample 5), fifth (sample 6), sixth (sample 7) introducing of MCM-41 (DFT method)

	Structural-adsorption characteristics						
Sample	S_{meso} (m^2/g)	S_{macro} (m^2/g)	S_{micro} (m^2/g)	S_{total} (m^2/g)	V_{meso} (cm^3/g)	V_{macro} (cm^3/g)	V_{micro} (cm^3/g)
1	66	14	23	103	0.46	0.23	0.007
2	105	9	32	146	0.43	0.15	0.012
3	156	3	46	205	0.36	0.05	0.015
7	248	1.5	12	262	0.37	0.03	0.004
5	292	0.8	0.7	293	0.39	0.03	0
6	295	0.7	0.3	296	0.38	0.02	0
7	313	1	0.3	314	0.39	0.03	0

11.3 Synthesis of Gold and Silver Nanoparticles in Surface Layer of Silica Matrices

Nanoparticles attract considerable attention since they display unique electrical, optical, mechanical, and magnetic properties which are distinct from their bulk counterparts [17]. The most notable optical feature of metal nanoparticles is the surface plasmon resonance which arises from the collective oscillation of conducting electrons on the surface of the metal. The characteristic surface plasmon resonance of silver and gold nanoparticles has been used prominently in diverse areas of biological and biomedical science, such as in molecular labeling [18], SERS [19], and nonlinear optics, for the fabrication of biosensors, labeling of cells and biomolecules, therapies against cancer, and also for the fast detection of DNA macromolecules [20] and antibodies due to the change of the plasmon resonance.

For the preparation of mesoporous silica with grafted silicon hydride groups (≡SiH), we applied surface modification with triethoxysilane in the presence of acetic acid [21]. Then the modified silica was impregnated with chloroauric acid or silver nitrate solutions at room temperature and dried for 24 h in an oven at 150°C.

The presence of silicon hydride groups grafted to the silica surface was confirmed by FTIR spectral data (NEXUS FT-IR). The metal nanoparticles were characterized using X-ray powder diffraction (DRON-4-07, CuKα-radiation) and identified by TEM (JEM 100CXII) and UV–visible spectra recorded with a Carl Zeiss Jena spectrophotometer. Particle size distribution was estimated by photon correlation spectroscopy method using laser correlation spectrometer PCS 100 (Malvern Instrument Limited, UK) equipped with multi-computing correlator type 7032 CE.

The metal nanoclusters were immobilized due to a reduction of the metal complexes immediately in a place of the reducer attachment (surface ≡SiH groups). The reduction process is caused by the properties of the ≡SiH groups, accompanied by their hydrolysis and formation of highly dispersed metal nanoparticles.

Ordered mesoporous silica MCM-41 with silicon hydride groups in the grafted modified layer was used for synthesis of noble metal nanoparticles. In the IR spectrum of the silica (Fig. 11.5, curve 1), a sharp band is observed in the region

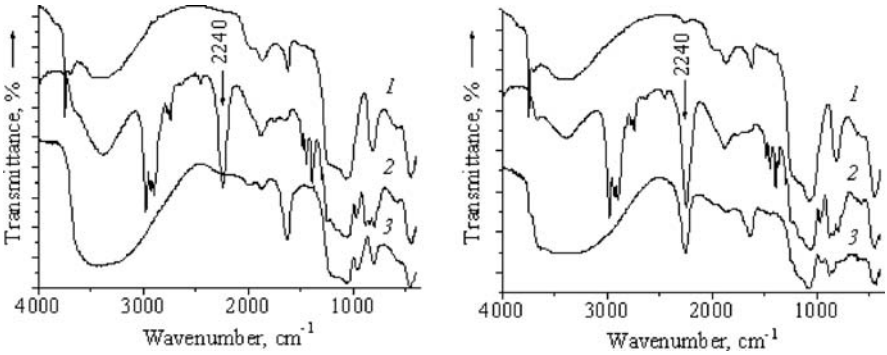

Fig. 11.5 FTIR spectra: *1* initial MCM-41 silica, *2* MCM-41 with grafted ≡SiH groups, *3* MCM-41 with reduced nanoparticles of silver (*left*) and gold (*right*)

of O–H vibration at 3750 cm^{-1} of isolated OH groups of the silica surface. In the spectrum of the silicon hydride-containing silicas (Fig. 11.5, curve 2), this band is absent and a broad band is seen at 2240 cm^{-1} providing evidence for the fact that attachment of the ≡SiH groups occurred. Also intensive narrow absorption bands at 1390 and 2976 cm^{-1} relating to deformation vibrations of the C–H bonds in CH_2 groups are observed.

Decrease of intensity of the absorption band at 2240 cm^{-1} of the ≡SiH groups and appearance of an absorption band of silanol groups at 3750 cm^{-1} as a result of reduction forming noble nanoparticles in surface layer of silica are observed.

It is possible to regulate the size of the metal particles by varying the concentration of the metal salt used for the reduction. A blue shift of the surface plasmon band (Fig. 11.6) is observed as a result of gradual decrease of the concentration of $AgNO_3$ from 11.25 to 1.25 mmol/l; the corresponding size of the nanoparticles decreases from 20 to 15 nm (Fig. 11.6b).

Silver nanoparticles of smaller sizes can be synthesized by reducing the time of interaction between the modified mesoporous silica and the $AgNO_3$ solution. Formation of the nanoparticles of larger sizes is accompanied by appearance of a long-wave wing in the spectrum and a small blue shift of the surface plasmon band in the region of 370–400 nm (Fig. 11.7a).

In accordance with XRD data, formation of silver nanoparticles in the range from 7 to 17 nm is observed (Fig. 11.7b).

TEM data (Fig. 11.8) of the prepared samples confirm formation of gold nanoparticles with average diameter of 20–30 nm and silver nanoparticles with diameter of 7–20 nm.

By varying the initial concentration of $HAuCl_4$, we were able to control the size of reduced metal nanoparticles formed on the surface of modified silicas which resulted in changes in the color of samples clearly seen visually. Indeed, a gradual decrease in the concentration of the initial solution of $HAuCl_4$ from 11.25 to 1.25 mmol/l was accompanied by a decrease in the size of gold nanoparticles from 30 to 20 nm (LCS – laser correlation spectroscopy data) (Fig. 11.9b). As the

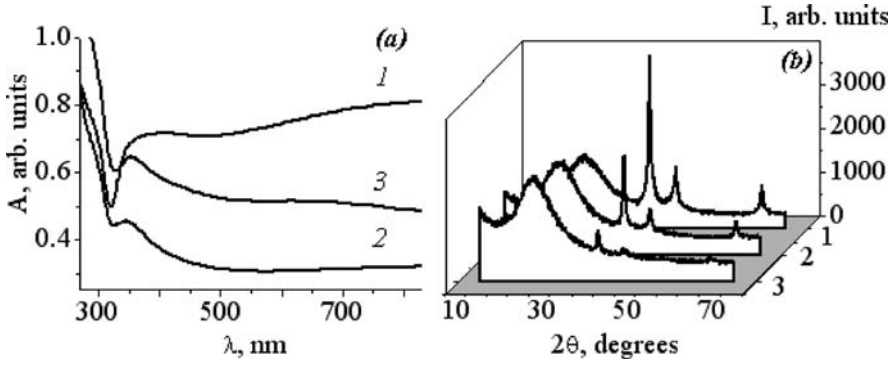

Fig. 11.6 (**a**) UV–visible spectra of colloid silver obtained after dissolution of the silica matrices modified with triethoxysilane after interaction for 24 h with $AgNO_3$ solutions with concentrations 11.25 mmol/l (*1*), 3.75 mmol/l (*2*), 1.25 mmol/l (*3*); (**b**) XRD measurements of the silver-containing silicas before dissolution

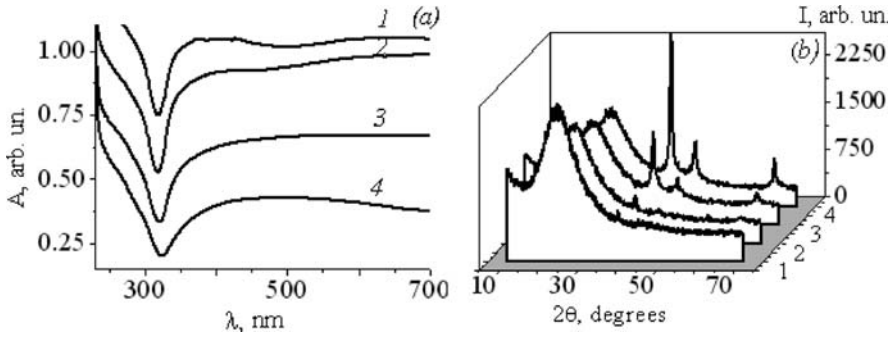

Fig. 11.7 (**a**) UV–visible spectra of colloid silver obtained after dissolution of silica matrices modified with triethoxysilane after their interaction with $AgNO_3$ solution (11.25 mmol/l) for 0.5, 1.5, 5.0, and 24.0 h (*1–4*, respectively); (**b**) XRD spectra of the silver-containing silicas before dissolution

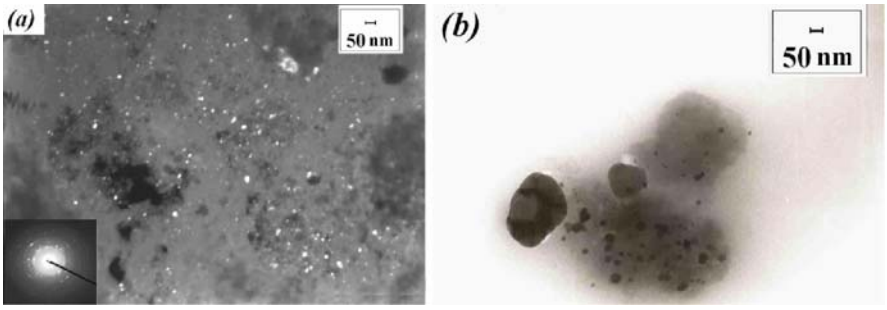

Fig. 11.8 TEM images of synthesized gold- (**a**) and silver-containing silicas (**b**)

concentration of the initial solution of $HAuCl_4$ lowers, matrix color changes from dark brick-red to dull brick-red which is likely caused by formation of smaller gold particles.

Decrease in the contact time between modified silica and $HAuCl_4$ caused formation of smaller gold nanoparticles, and the color of the gold-containing silica changed from brick-red to pink. This was accompanied by a bathochromic shift of the surface plasmon absorption peak and the long-wave spectrum wing lowered (Fig. 11.10a). At shorter reduction times, the size of gold nanoparticles decreased from 37 to 25 nm.

In the high-angle region at 2θ=30–90°, typical peaks of face-centered cubic structure of metallic silver were observed, which belong to (111), (200), and (220) diffractions. The crystallite sizes of nanoparticles were determined by the Scherrer equation [22].

The gold-containing silicas with 2 wt% gold concentration exhibited high catalytic activity in the oxidation of hydrogen with molecular oxygen [23].

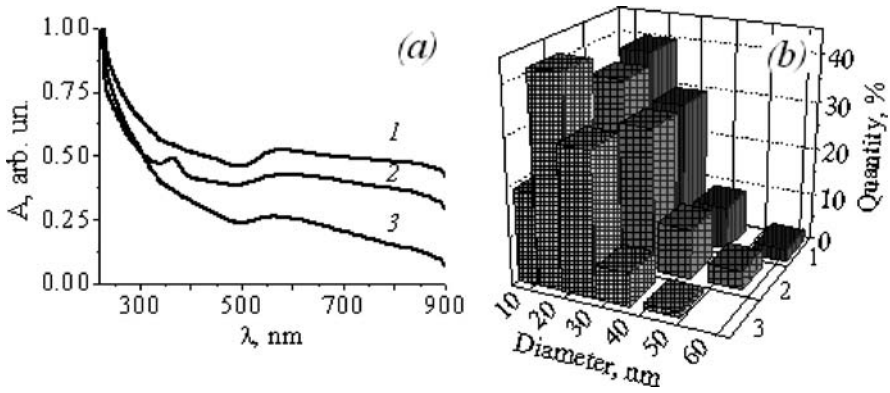

Fig. 11.9 (**a**) UV–visible spectra of colloid silver obtained after dissolution of the silica matrices modified with triethoxysilane after interaction for 24 h with $HAuCl_4$ solutions with concentrations of 11.25, 3.75, and 1.25 mmol/l (*1–3*, respectively); (**b**) size distribution of gold nanoparticles (LCS)

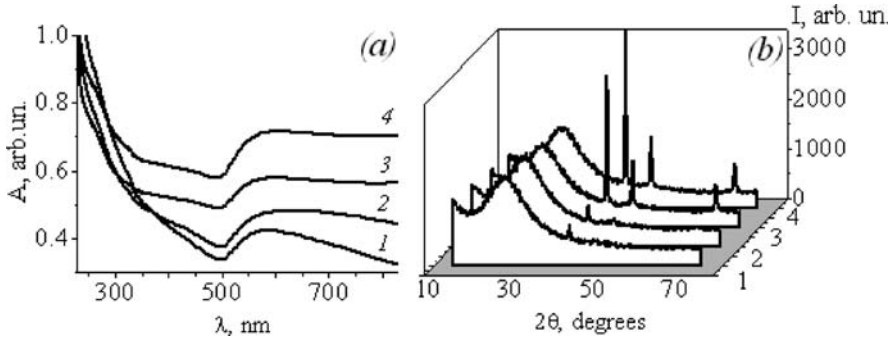

Fig. 11.10 (**a**) UV–visible spectra of colloid silver obtained after dissolution of silica matrices modified with triethoxysilane after their interaction with $HAuCl_4$ solution (11.25 mmol/l) for 0.5, 1.5, 5.0, and 24.0 h (*1–4*, respectively); (**b**) XRD spectra of the silver-containing silicas before dissolution

11.4 Conclusions

Structure-directing role of polyionene of the 1,4-MePh type in template synthesis of mesoporous silicas was investigated. Silicas with extremely high specific surface area and bimodal pore distribution were synthesized with the use of polyionene as structure-directing agent. Possibility of carrying out template synthesis of mesoporous silicas with pore diameter of 2.5 nm inside of nanoreactors based on large pores of silica gel was demonstrated. An approach of grafting of silicon hydride groups on silica surface with following application of modified silica in synthesis of gold and silver nanoparticles was elaborated. It is possible to regulate the sizes

of the metal particles by varying the concentration of the metal salt taken for the reduction and the time of reduction.

References

1. Ciesla U, Schuth F (1999) Ordered mesoporous materials. Microporous Mesoporous Mater 27:131–149
2. Corma A (1997) From microporous to mesoporous molecular sieve materials and their use in catalysis. Chem Rev 97:2373–2419
3. Grun M, Unger KK, Matsumoto A, Tsutsumi K (1999) Novel pathways for the preparation of mesoporous MCM-41 materials: control of porosity and morphology. Microporous Mesoporous Mater 27:207–216
4. Zhu W, Han Y, An L (2005) Silver nanoparticles synthesized from mesoporous Ag/SBA-15 composites. Microporous Mesoporous Mater 80:221–226
5. Katok KV, Tertykh VA, Brichka SYa, Prikhod'ko GP (2006) Catalytic synthesis of carbon nanotubes over ordered mesoporous matrices. J Therm Anal Calorim 86:109–114
6. Muller R (1950) Uber Silicone (I). Zur angewadten Chemie der Silicone (Synthese). Chemische Technik 2:7–13
7. Wagner GH, Pines AN (1952) Silicon oxyhydride. Ind Eng Chem 44:321–326
8. Budkevich GB, Slinyakova IB, Neimark IE (1966) Reductive properties of xerogel of hydridepolysiloxane. Kolloid Zh 28:21–25
9. Adeogun MJ, Hay JN (2001) Structure control in sol–gel silica synthesis using ionene polymers. 2. Evidence from spectroscopic analysis. J Sol–Gel Sci Technol 20: 119–128
10. Adeogun MJ, Fairclough JPA., Hay JN, Ryan AJ (1998) Structure control in sol–gel silica synthesis using ionene polymers – evidence from X-ray scattering. J Sol–Gel Sci Technol 13:27–30
11. Berezovska IS, Yanishpolskii VV, Tertykh VA, Lobunets TF, Ragulya AV (2006) Template synthesis of porous silica adsorbents with spherical morphology of particles. Ads Sci Technol 24:403–410
12. Berezovskaya IS, Yanishpolskii VV, Tertykh VA (2008) Morphology control of mesoporous silica and their template synthesis in silica gel. Russ J Phys Chem 82:1442–1446
13. Tatsumi T, Koyano K, Tanaka Y, Nakata S (1999) Mechanical stability of mesoporous materials MCM-48 and MCM-41. J Porous Mater 6:13–17
14. Williford RE, Li XS, Addeman RS, Fryxell GE, BAskaren S, Birnbaun JC, Coyle C, Zemanian TS, Wang G, Courtney AR (2005) Mechanical stability of templated mesoporous silica films. J Microporous Mesoporous Mater 85:260–266
15. Wang X, Li W, Zhu G, Qiu S, Zhao D, Zhong B (2004) Effects of ammonia/silica molar ratio on the synthesis and structure of bimodal mesopore silica xerogel. Microporous Mesoporous Mater 71:87–97
16. Gun'ko VM, Turov VV, Turov AV, Zarko VI, Gerda VI, Yanishpolskii VV, Berezovska IS, Tertykh VA (2007) Behavior of pure water and water mixture with benzene or chloroform adsorbed onto ordered mesoporous silicas. Cent Eur J Chem 5:420–454
17. Tertykh VA (2004) Functionalization of silica surfaces. In: Schwarz JA., Contesku C, Putyera K (eds) Dekker Encyclopedia of Nanoscience and Nanotechnology, Marcel Dekker, New York
18. Cai H, Wang Y, He P, Fang Y (2002) Electrochemical detection of DNA hybridization based on silver-enhanced gold nanoparticle label. Anal Chim Acta 469:165–172
19. Gong JL, Jiang JH, Liang Y, Shen GL, Yu RQ (2006) Synthesis and characterization of surface-enhanced Raman scattering tags with Ag/SiO_2 core–shell nanostructures using reverse micelle technology. J Colloid Interface Sci 298:752–756
20. Cao YC, Jin R, Thaxton CS, Mirkin CA (2005) A two-color-change, nanoparticle-based method for DNA detection. Talanta 67:449–455

21. Tertykh VA, Katok KV, Yanishpolskii VV (2008) Reduction nanoparticles of gold in surface layer of modified silica. Russ J Phys Chem 82:1438–1441
22. Genie A (1961) Radiographic Imaging of Crystals, State publisher of physico-mathematical literature, Moscow (in Russian)
23. Katok KV, Tertykh VA, Yanishpolskii VV (2008) Synthesis and application of metal-containing silicas. In: Vaseashta A, Mihailescu IN (eds) NATO Science for Peace and Security Series – B: Physics and Biophysics "Functionalized Nanoscale Materials, Devices, and Systems", Springer, Heidelberg

Chapter 12
Synthesis and Properties of Magnetosensitive Nanocomposites Based on Iron Oxide Deposited on Fumed Silica

V.M. Bogatyrov, M.V. Borysenko, I.V. Dubrovin, M.V. Abramov, M.V. Galaburda, and P.P. Gorbyk

Abstract A synthesis technique of magnetosensitive nanocomposites was proposed on the basis of nanocrystalline magnetite (Fe_3O_4) or maghemite (γ-Fe_2O_3) and highly disperse silica. Thermogravimetry, differential thermal analysis, XRD, and a vibrating magnetometer were used to characterize prepared nanocomposites. It was found that nanosilica prevents growth of Fe_3O_4 nanocrystallites stabilized at average sizes of 5–8 nm.

12.1 Introduction

Medical applications of magnetic nanoparticles cause a number of requirements of these materials dependent on the types of their use, e.g., as new contrasting agents in magnetic-resonance diagnostics, preparations for magnetic hyperthermy of cancerous diseases, and magnetic carriers for drug delivery to bad organs in vivo [1–3]. Special attention was given to the morphology of magnetic particles and their hydrophobic–hydrophilic properties. The creation of highly disperse magnetosensitive materials mainly deals with development of synthesis methods of the magnetic forms of such iron oxides as magnetite (Fe_3O_4) and maghemite (γ-Fe_2O_3). Magnetite as ferromagnet or uncompensated antiferromagnet is an inverted spinel $[Fe^{3+}]_A[Fe^{2+}Fe^{3+}]_BO_4$. The coercive force ($H_c$) and the remanence of disperse magnetite depend strongly on the particle sizes. Maximum H_c value of 375–440 Oe [4] is characteristic for particles being in single-domain state which exists in a narrow range of particle sizes from 30 to 50 nm [5]. The H_c value sharply drops to zero with decreasing particle size (because of enhanced effects of thermal fluctuations), and the system transforms to superparamagnetic state. For monodisperse particles of magnetite at the size of approximately 12 nm, the anhysteretic

M.V. Borysenko (✉)
O.O. Chuiko Institute of Surface Chemistry of the National Academy of Sciences of Ukraine, General Naumov St. 17, Kyiv 03164, Ukraine
e-mail: borysenko@naverex.kiev.ua

A.P. Shpak, P.P. Gorbyk (eds.), *Nanomaterials and Supramolecular Structures*,
DOI 10.1007/978-90-481-2309-4_12,

curve shape is characteristic for magnetization reversal curves recorded at room temperature [6]. On heating in air, maghemite irreversibly transforms into antiferromagnet state (α-Fe_2O_3) characterized by weak spontaneous magnetization. Curie temperature of α-Fe_2O_3 and γ-Fe_2O_3 is equal to 677°C [7], and on heating in non-oxygenous atmosphere, γ-Fe_2O_3 reversibly crosses the Curie point. The coercive force of γ-Fe_2O_3 reaches the limiting value of 340 Oe at the crystallite sizes of 40 nm [4].

Many methods have been developed to synthesize fine powders of iron oxides, e.g., sol–gel, co-precipitation, impregnation, hydrolysis, flame and laser pyrolysis, electrochemical and hydrothermal synthesis. The use of porous matrices, which can affect the particle size distribution and the physical properties of grafted nanoparticles, is of importance to the synthesis. Among similar systems silica/iron oxide is the most widely investigated one [8–13]. The nanocomposite systems with iron oxide deposited on the silica matrices were investigated by many researchers [1, 8–15]. However, the data on the role of the silica matrices on the formation of magnetic iron oxide deposits are contradictory, and the factors influencing the particle sizes of iron oxide require additional investigations for better control of the important characteristics of nanocomposites.

12.2 Experimental

Fumed silica "Biosil" (Pilot plant of the Institute of Surface Chemistry, Kalush, Ukraine; specific surface area S_{BET} =340 m^2/g) was used as the initial material. Iron acetyl acetonate ($Fe(acac)_3$), iron sulfate ($FeSO_4 \cdot 7H_2O$), iron trichloride ($FeCl_3$), isopropyl alcohol, and 25% aqueous solution of ammonia – all reactants and solvents – were of grade "chemically pure". Commercial iron oxides α-Fe_2O_3 and Fe_3O_4 (Nanostructured & Amorphous Materials Inc., USA, 98% purity) were used as samples for comparative investigations.

Magnetite and maghemite were synthesized in the presence of fumed silica at the final weight ratio of components SiO_2:Fe_3O_4 or Fe_2O_3 = 1:1. Magnetite was synthesized using a chemical condensation method [16, 17]

$$Fe^{2+} + 2Fe^{3+} + 8NH_4OH \rightarrow Fe_3O_4 + 4H_2O + 8{NH_4}^+,$$

based on fast precipitation of salts of divalent and trivalent iron by concentrated aqueous solution of ammonia. The solutions of Fe(II) sulfate, Fe(III) chloride, and ammonia were added to the aqueous suspension of silica on intensive stirring at room temperature. Sediment with magnetite/silica was separated and washed with distilled water five times using centrifugation, and the completing washing was carried out using acetone. Then samples were dried at 40°C for 10 h. During the synthesis, the order of mixing of components can affect the characteristics of the products; therefore, it was varied. In the first case the mixture of iron salts was added to the suspension of silica and then ammonia was

Table 12.1 Characteristic of Fe_xO_y/SiO_2 samples and fine powders of magnetite and hematite

Sample		S_{BET}	Crystallite size (nm) before and after calcination	
Label	Composition	m^2/g	40°C	1000°C (α-Fe_2O_3)
MT1	SiO_2/Fe_3O_4	248	5.3	44
MT2	SiO_2/Fe_3O_4	228	5.5	73
MT3	SiO_2/Fe_3O_4	297	7.7	62
MHT	SiO_2/γ-Fe_2O_3	203	30	154
MT	Fe_3O_4	92	11	212
α-Fe_2O_3	α-Fe_2O_3	17	178	–
Fe_3O_4	Fe_3O_4	34	56	–

added (this sample was labeled as MT1). In the second case the sequence was different: (Fe^{2+}+2Fe^{3+}) + NH_4OH + SiO_2 (sample MT2). The third sample corresponds to (Fe^{2+}+2Fe^{3+}) + (SiO_2 + NH_4OH) (sample MT3). A control sample of magnetite (labeled as MT) was synthesized without silica. The characteristics of samples of SiO_2/Fe_xO_y nanocomposites and fine powders of magnetite and hematite are shown in Table 12.1.

A silica/maghemite nanocomposite was also prepared. Isopropyl alcohol was added to a mixture of fumed silica and iron acetyl acetonate; then it was homogenized to uniform consistency. The dispersion was dried at 40°C, then the dry residue was heated in a muffler with gradually increasing temperature to 400°C.

A thermogravimetric (TG) study with differential thermal analysis (DTA) was carried out using a Derivatograph Q-1500 D (MOM, Hungary) at sample weight of 210–260 mg at a heating rate of 10 K/min.

To study the structure and phase composition of Fe_xO_y/SiO_2 samples, X-ray diffraction (XRD) patterns were recorded using a DRON-3M (Burevestnik, St. Petersburg) with Cu K_α radiation and a Ni filter. The average size (d) of Fe_xO_y crystallites was estimated according to the Scherrer equation [18].

The integral magnetic characteristics (magnetization curve and hysteresis loops) were measured using a vibrating magnetometer [19]. The dry demagnetized powders were used for the measurements. Frequency and amplitude of vibrations were controlled by an oscillator and a low-frequency amplifier. The measurements were carried out at 260 Hz and room temperature.

12.3 Results and Discussion

Iron oxide nanoparticles being in free state tend to be aggregated but their deposition onto a surface of carriers such as aggregates of primary particles of fumed silica can increase their stability, as well as the stability of whole nanocomposites. Iron oxide nanoparticles grafted onto the silica surface or incorporated in voids between silica nanoparticles undergo certain steric hindrances to be aggregated

themselves. However, they remain accessible for reagents (e.g., to be increased in size on subsequent reaction cycles) or adsorbates (on the practical use of these composites). Additionally, iron oxide deposits can not only preserve their fundamental physicochemical characteristics but also acquire new properties.

The specific surface area (S_{BET}) of synthesized control sample of magnetite is equal to 92 m^2/g. If the silica matrix did not affect the magnetite morphology then the S_{BET} values of Fe_3O_4/SiO_2 nanocomposite should be equal to 216 m^2/g (since $S_{BET} = 340$ m^2/g for silica) at equal weight ratio of components. However, the S_{BET} values of MT1–MT3 samples are greater (228–297 m^2/g) than that value. This result can be caused by smaller sizes of iron oxide particles in composites than that in the control sample synthesized without silica.

For samples MT1–MT3, the temperature dependences of TG, DTG, and DTA curves are close; therefore, these curves are shown only for MT2 (Fig. 12.1a). A major fraction of molecularly adsorbed water desorbs at $T < 120°$ and the maximal desorption rate (DTG) is observed at 100°C. Dissociatively adsorbed water (hydroxyls) desorbs associatively over a broad temperature range (200–900°C) but without DTG extrema characteristic for intact water. For the control magnetite (MT without silica), the shape of the TG and DTG curves (Fig. 12.1b) differs from those for MT2 (Fig. 12.1a). There are three maximal values of the weight loss rate for MT at 100, 170, and 250°C. The first one is linked to desorption of intact water. Subsequent two extrema at 170 and 250°C can be attributed to associatively desorbed water. The difference in the latter for MT2 and MT samples can be caused by the differences in the morphology of samples, sizes (Table 12.1), and structure of iron oxide particles, as well as by the effects of the amorphous silica matrix. An exothermic peak is observed on the DTA curve of MT at 460–620°C and $T_{max} = 550$°C. A similar exothermic effect but of smaller intensity is characteristic for MT2. This exothermic peak is located close to the Curie point of Fe_3O_4 (584°C) and it can be caused by the disordering of domain structures of iron oxide and the irreversible loss of its magnetic properties. The displacement of the peak

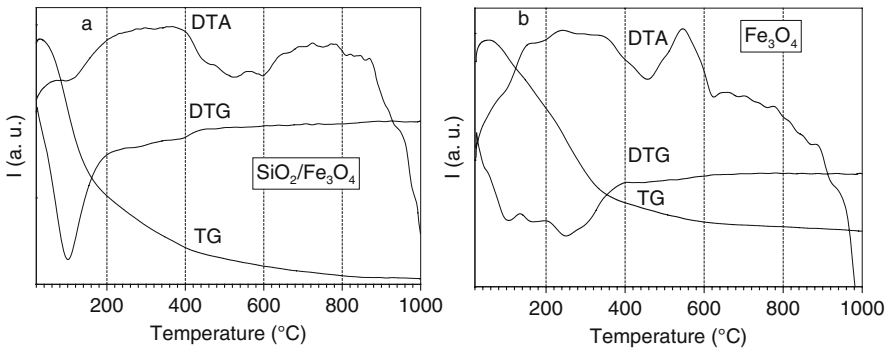

Fig. 12.1 TG, differential (DTG), and DTA curves of (**a**) MT2 and (**b**) synthesized control sample with magnetite

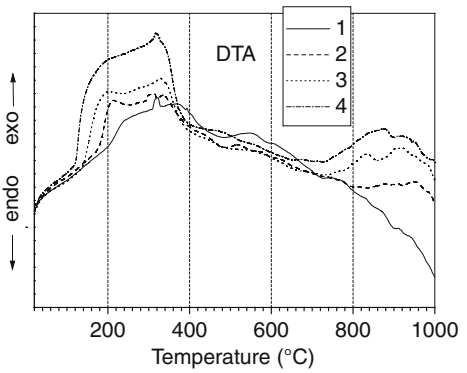

Fig. 12.2 DTA curves for $Fe(acac)_3/SiO_2$ at different contents of iron: (*1*) 0.5, (*2*) 1.0, (*3*) 2.0, and (*4*) 4.0 wt%

toward higher temperatures for MT2 in comparison with MT indicates an increase in the thermal resistance of nanoparticles of magnetite deposited onto the silica matrix against the phase transformation. Similar inhibitory effects of silica matrices were observed for other grafted oxides, e.g., on transformation of anatase to rutile [20, 21].

Thermograms of fumed silica with adsorbed iron acetyl acetonate (Fig. 12.2) as a precursor of iron oxide (sample MHT) differ from that for MT2 and MT. The DTA curves demonstrate three stages of thermal transformations of $Fe(acac)_3$. The exothermic effect at 120–400°C is linked to oxidation of organic ligands of $Fe(acac)_3$ and its value is proportional to a quantity of adsorbed $Fe(acac)_3$ (and $Fe(acac)_2$ chemically bonded to the silica surface). The second stage can be attributed to the formation of γ-Fe_2O_3 at the silica surface after the oxidation of residual acetyl acetonate fragments. The third stage (700–1000°C) corresponds to the formation of α-Fe_2O_3. The transformation of maghemite to hematite in iron oxide/silica nanocomposites investigated in detail elsewhere [12–14] occurs over the mentioned temperature range.

The XRD patterns (Fig. 12.3) show that magnetite is observed in MT1–MT3 samples and it transforms into α-Fe_2O_3 after heating of composites at 1000°C in air. It is known that solvents, time of gelation, and other parameters of sol–gel synthesis of nanocomposites (at the same content of oxide components) can affect the formation of the products and their characteristics [22].

However, the differences in the preparation techniques of MT1–MT3 samples do not affect the formation of magnetite and its subsequent transformation on heating to 1000°C. The formation of nonmagnetic α-Fe_2O_3 on calcination of magnetite grafted on silica confirms the nature of the exothermic peak observed on the DTA curves over the 460–620°C range and linked to the irreversible structural transformations of iron oxide. Despite the fact that the formation of Fe_2O_3 from Fe_3O_4 (due to oxidation by oxygen from air) should be accompanied by an increase in the sample weight, the corresponding changes in the TG curve are not observed (Fig. 12.1). However, an insignificant decrease in the sample weight at these temperatures can present only total balance of changes in the weight of samples caused by associative desorption of water and oxygen attachment to iron atoms on the mentioned

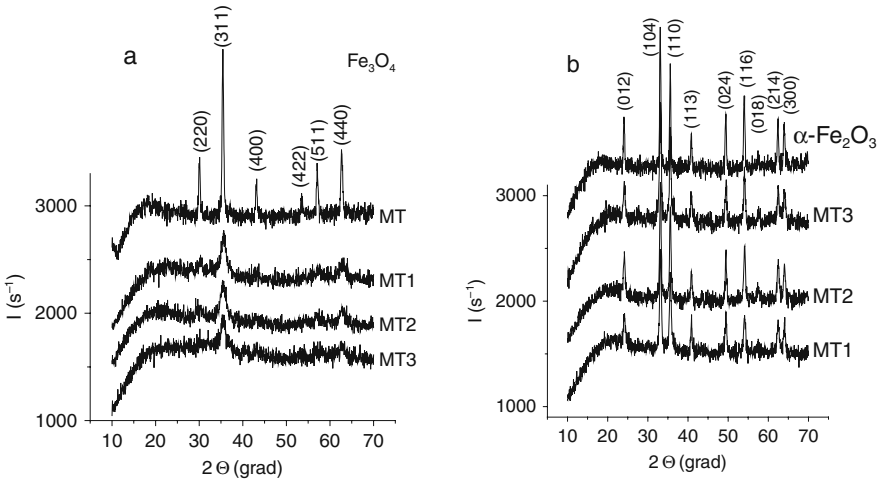

Fig. 12.3 XRD patterns of nanocomposites MT1–MT3 before (**a**) and (**b**) after calcination at 1000°C, and control sample of nanodimensional hematite

iron oxide transformation. Notice that Fe_2O_3/SiO_2 prepared from iron acetyl acetonate and heated at the last stage of the synthesis at 400°C in air represents mainly magnetic γ-Fe_2O_3 (Fig. 12.4).

The sizes of iron oxide crystallites calculated from the XRD data recorded before and after heating of samples at 1000°C (Table 12.1) are smaller for MT1–MT3 than that for MT by a factor of 1.4–2.1. These results are in agreement with changes in the specific surface area of these samples.

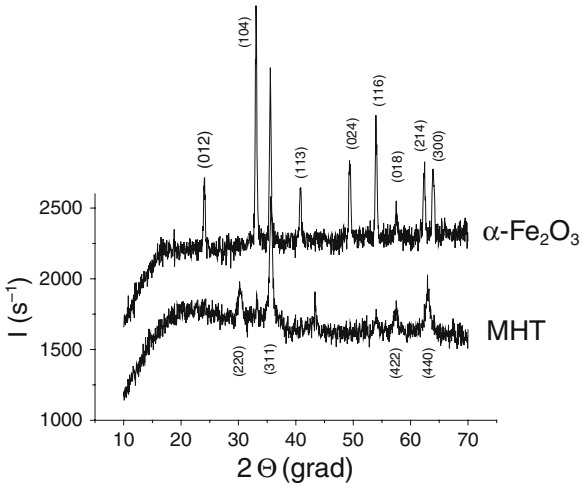

Fig. 12.4 XRD patterns of SiO_2/γ-Fe_2O_3 (MHT) and fine powder of α-Fe_2O_3

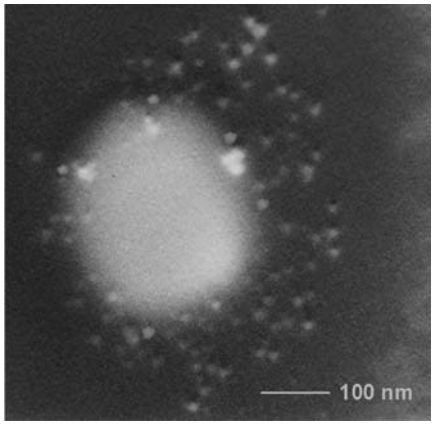

Fig. 12.5 SEM image of silica aggregate and nanoparticles of magnetite

The particle sizes and shapes of nanocomposite SiO_2/Fe_3O_4 were also studied using scanning electron microscopy (Fig. 12.5). It is known that primary particles of fumed silica A-300 of 5–15 nm in diameter form relatively stable aggregates of 100–1000 nm in size [23]. SEM image of SiO_2/Fe_3O_4 shows magnetite particles (average diameter 6–15 nm) against the background of silica aggregate of primary particles. Magnetite particles are randomly located around silica aggregate.

Relatively small sizes of magnetite particles formed at the surface of highly disperse silica can be determined by several factors. Silica nanoparticles which present in the dispersion in large quantity are characterized by a great number of surface sites (e.g., silanols) as centers of crystallization of magnetite nuclei that prevent aggregation of these nuclei. Additionally, highly developed silica surface can prevent the consolidation of primary nuclei of iron oxide because of reduction in their mobility and inhibit the oxidation of magnetite by atmospheric oxygen because of a significant adsorption potential of the silanol groups and the formation of magnetite particles in the interparticle voids in silica aggregates.

All Fe_3O_4/SiO_2 nanocomposites prepared here possess magnetic properties (Fig. 12.6). Commercial magnetite sample at the average size of crystallites of 56 nm (XRD) demonstrates coercive force $H_c \approx 100$ Oe, remanent magnetization $M_r \approx 3$, and saturation magnetization $M_s \approx 13$ a.u. A sample of synthesized magnetite (MT) is characterized by $H_c \approx 25$ Oe. This H_c value is lower than that for the commercial sample due to smaller sizes of particles of the synthesized magnetite.

It should be noted that samples MT1 and MT2 possess coercive force of 31 and 38 Oe, respectively, i.e., they are characterized by average sizes of magnetic particles compared with the average size of Fe_3O_4 particles synthesized without silica. The smallest particles of magnetite were, most probably, observed for sample MT3 since its H_c value was 22 Oe.

As was mentioned above, magnetite particles smaller than 12 nm in size are characterized by the anhysteretic curve shape of remagnetization at

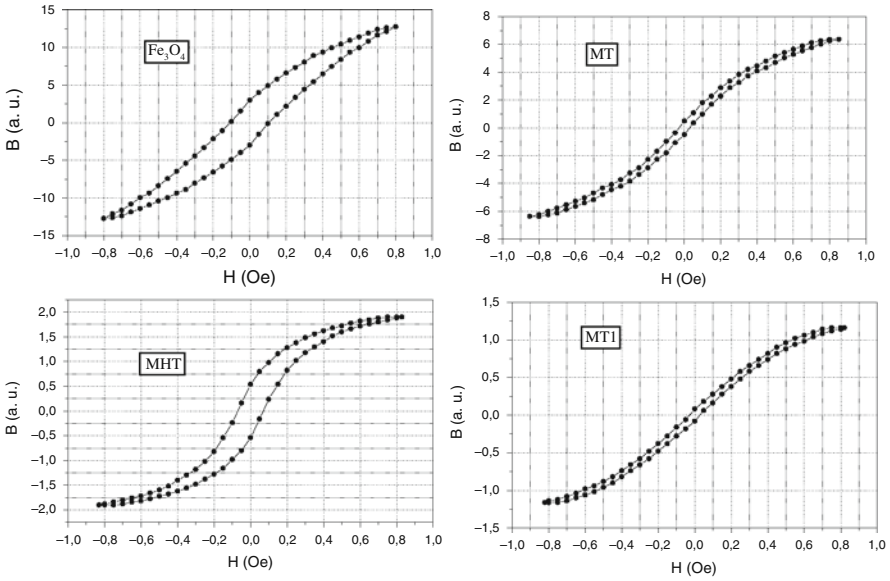

Fig. 12.6 Hysteresis loops for magnetic nanocomposites MT1, MHT, and individual Fe_3O_4

room temperature [6]. *Ex facte* the results obtained using the oscillator contradict the XRD data and changes in the S_{BET} values because the average size (estimated from the XRD data) of magnetite crystallites is smaller than 12 nm for MT and MT1–MT3 samples. However, synthesized particles are characterized by certain particle size distributions (Fig. 12.5); therefore, particles larger than 12 nm in size can be present in the systems. This fraction of larger particles is responsible for the appearance of the magnetic hysteresis. One can assume that MT3 (characterized by the smallest coercive force) has the most narrow particle size distribution among synthesized samples. The nanocomposite with a fraction of maghemite has the average size of magnetic particles of 30 nm and possesses coercive force of 70 Oe which is smaller than the limiting $H_c = 340$ Oe for γ-Fe_2O_3 at the average size of crystallites of 40 nm [4].

12.4 Conclusions

A synthesis procedure of magnetosensitive nanocomposites Fe_3O_4/SiO_2 was developed and tested using highly disperse silica as a matrix to create crystallization centers for the precipitation reaction of salts of iron(II) and iron(III) by ammonia solution. It was shown that the iron oxide nuclei formation at the silica surface allows the production of magnetic material at average sizes of crystallites of 5–8 nm and specific surface area larger by a factor of 2–3 than that of magnetite synthesized

using the Elmore method. The high sorption capacity of these materials and their significant magnetic characteristics suggest the possibility of their use as magneto-controlled preparations for decontamination of donor blood and other applications in medicine and industry.

It was shown that thermooxidation destruction of iron acetyl acetonate at the nanosilica matrix at 400°C is accompanied by the formation of $SiO_2/\gamma\text{-}Fe_2O_3$ nanocomposite possessing magnetic properties.

References

1. Gorbyk PP, Petranovskaya AL, Storozhuk LP et al (2006) Medico-biological nanocomposites based on magnetite: synthesis, modification, surface functionalization for application *in vitro*. Chem Phys Technol Surf 11–12:374–396
2. Duguet E, Vasseur S, Mornet S (2006) Magnetic nanoparticles and their applications in medicine. Nanomedicine 1:157–168
3. Mornet S, Vasseur S, Grasset F (2006) Magnetic nanoparticle design for medical applications. Prog Solid State Chem 34:237–247
4. Kotov EP, Rudenko MI (1990) Carriers for magnetic records. Radio i svyaz, Moscow
5. Kirschvink JL, Walker MM, Deibel C (2001) Magnetite-based magnetoreception. Curr Opin Neurobiol 11:462–467
6. Sun S, Zeng H, Robinson DB (2004) Monodispersed MFe_2O_4(M=Fe, Co, Mn) Nanoparticles. J Am Chem Soc 126:273–279
7. Vasilevsky YA (1989) Carriers for magnetic records. Iscusstvo, Moscow
8. Del Monte F, Morales MP, Levy D (1997) Formation of $\gamma\text{-}Fe_2O_3$ isolated nanoparticles in a silica matrix. Langmuir 13:3627–3624
9. Popovici M, Gich M, Savii C (2006) Ultra-light sol–gel derived magnetic nanostructured materials. Roman Rep Phys 58:369–378
10. Cannas C, Gatteschi D, Musinu A (1998) Structural and magnetic properties of Fe_2O_3 nanoparticles dispersed over a silica matrix. J Phys Chem B 102:7721–7726
11. Xu J, Thompson S, O'Keefe E (2004) Iron oxide-silica nanocomposites via sol–gel processing. J Mater Lett 58:1696–1700
12. Raileanu M, Crisan M, Petrache C (2005) Sol–gel Fe_xO_y nanocomposites. Roman J Phys 50:595–606
13. Cannas C, Concas G, Gatteschi D (2001) Superparamagnetic behaviour of $\gamma\text{-}Fe_2O_3$ nanoparticles dispersed in a silica matrix. Phys Chem Chem Phys 3:832–838
14. Battishaa IK, Afifya HH, Ibrahimb M (2006) Synthesis of Fe_2O_3 concentrations and sintering temperature on FTIR and magnetic susceptibility measured from 4 to 300 K of monolith silica gel prepared by sol–gel technique. J Magn Magn Mater 306:211–217
15. Bogatyrev VM, Gaeva MV, Chuiko AA (2006) IR spectral study of thermooxidation destruction of trimethylsilylated silica modified by acetylacetonate of Fe(III). Chem Phys Technol Surf 11–12:254–260
16. Sviridov VV (1987) Chemical precipitation of metals from aqueous solutions. Belarus, Minsk
17. Sviridov VV (1996) Inorganic synthesis. Belarus, Minsk
18. Oranska EI, Gornikov YI, Fesenko TV (1994) Automated method of determination of average sizes of crystallites of polycrystalline solids. Zavodsk Lab 60(1):28
19. Spak AP, Kunitsky YA, Zakharchenko MI, Voloschenko AS (2003) Magnetism of amorphous and nanocrystalline systems. Naukova Dumka, Kiev
20. Yang J, Ferreira JMF (1998) Inhibitory effect of the Al_2O_3–SiO_2 mixed additives on the anatase–rutile phase transformation. Mater Lett 36:320–324

21. Gun'ko VM, Zarko VI, Turov VV et al (1998) CVD-titania on fumed silica substrate. J Colloid Interface Sci 198:141–156
22. Cannas C, Concas G, Gatteschi D et al (2002) How to tailor maghemite particle size in γ-Fe_2O_3–SiO_2 nanocomposites. J Mater Chem 12:3141–3146
23. Gun'ko VM, Zarko VI, Leboda R et al (2001) Aqueous suspensions of fumed oxides: Particle size distribution and zeta potential. Adv Colloid Interface Sci 91:1–112

Chapter 13
Adsorption Modification of Nanosilica with Non-volatile Organic Compounds in Fluidized State

E.F. Voronin, L.V. Nosach, N.V. Guzenko, E.M. Pakhlov, and O.L. Gabchak

Abstract Adsorption modification of nanosilica allows effective regulation of its physicochemical, structural–mechanical, pharmacological, and biological properties thus broadening its field of application. Liquid-phase methods used for this purpose have several substantial drawbacks mainly of a technological and ecological character. Therefore a new effective and ecologically safe method was developed for adsorption modification of nanosilica with non-volatile organic compounds (bioactive compounds, polymers). The process is carried out in fluidized state in gaseous dispersion medium with the solvent atmosphere. The developed method allows one to achieve a defined degree of surface coverage and to conserve initial dispersity of silica required.

13.1 Introduction

Physicochemical properties of nanosilicas depend drastically on methods and conditions of their production [1–3]. Various methods of modification make it possible to confer new desired properties to nanosilicas. Nowadays silica modification is considered as a purposeful alternative to the properties by altering the surface topography, the morphology of particles, or the chemical nature of surface-active sites using various physicochemical processes.

Adsorption modification corresponds to silica surface coating with a layer of modificator strongly bound due to adsorption forces, mostly the hydrogen bonds. Substances of a relatively high molecular weight such as olygomers, polymers, and bioactive substances can be used as reagents for adsorption modification [4–6].

Methods of adsorption modification can be divided into liquid-phase and gas-phase ones depending on dispersion medium state [7]. Each of them has certain advantages and disadvantages.

E.F. Voronin (✉)
O.O. Chuiko Institute of Surface Chemistry of the National Academy of Sciences of Ukraine, General Naumov St. 17, Kyiv 03164, Ukraine
e-mail: e.voronin@rambler.ru

A.P. Shpak, P.P. Gorbyk (eds.), *Nanomaterials and Supramolecular Structures*,
DOI 10.1007/978-90-481-2309-4_13,

Liquid-phase method is universal and makes it possible to modify nanosilica with practically any compound. Nevertheless it has several substantial disadvantages mainly of a technological and ecological character, e.g., (i) the necessity of the use of solvents which are often toxic or ecologically dangerous, (ii) solvent removal that can be difficult due to filtration process, and (iii) utilization of spent solvents. Filtrate drying and then milling is a heat- and energy-intensive process taking additional expenses. Moreover, nanosilica can change some properties on liquid-phase modification and drying, for example, a strong increase in the bulk density, as well as irreversible loss of the dusty properties that can be undesirable [8].

Gas-phase modification devoid of a number of serious disadvantages is more appropriate, especially for high-disperse silica. This process can be carried out at underpressure (in vacuum), atmospheric or high (in autoclave) pressures. The main requirement to modificators limiting a wider usage of the gas-phase method is their volatility which is low or absent in the case of bioactive compounds and polymers.

Adsorption modification of dispersed solids has been successfully used to solve various scientific problems, such as production of adsorbents with different surface chemistry used in chromatography, industry (to increase compatibility of fillers to polymer systems, including lacquers and paints, and to increase stability of disperse systems), pharmacy, and cosmetology (to create new combined preparations, as well as diagnostic facilities for medical use) [5, 9].

It is worth noting that various properties of disperse systems depend in different ways on modification degree of silica with a monotonic character of this dependence in some cases and extremal in other ones. Therefore it is very important to have a possibility to achieve a given degree of surface coverage with controlled structure of the adsorption layer to synthesize modified silicas with a necessary set of the properties.

To modify nanosilica completely it is sufficient to drift on its surface a one-molecule-thick layer of a substance, i.e., unimolecular layer (monolayer). In general one can achieve unimolecular layer of non-volatile compounds on a surface of solids using (i) adsorption from solution, (ii) surface diffusion, and (iii) solvent evaporation from solution, containing non-volatile component (impregnation). By definition the first and the third methods of monolayer drifting are liquid-phase ones with all inherent drawbacks; in other words they are non-technological in the case of nanosilica modification.

Therefore the aim of the study consisted in development of a method of nanonosilica modification with non-volatile organic compounds in the absence of liquid dispersion medium.

13.2 Experimental

13.2.1 Modification of Nanosilica in Fluidized State in Controlled Atmosphere

Dust-like substance can be transferred into fluidized state in two ways: by blowing-over of pressurized gas or by mixing at high speed. In case of nanosilica the first

way is associated with significant problems, caused by carry-over of high-disperse fractions with airflow; therefore it has little promise for practical use.

Achievement of fluidized state by high-speed mixing of nanosilica in a reactor supplied with a mixer of regulated rotation frequency ranging from 0 to 3000 rpm appeared to be more effective. Such a reactor of intensive mixing (RIM) has an oil thermostat, allowing heating of samples up to 200°C, and an air or some other gas blowing-over system. This makes possible to carry out an adsorption modification of nanosilica with low volatile compounds in an atmosphere with controlled composition.

Representatives of different classes of organic compounds were used as modifiers, such as polymers – polyvinylpyrrolidone (PVP, $M \approx 12{,}000$), poly (ethyl-eneoxide) (PEO, $M \approx 40{,}000$), petrolatum ($M \approx 1000$);carboxylic acids –2-(4-isobutyl phenyl)propionic acid (ibuprofen); bis-quaternary ammonium compounds – 1,2-ethylene-bis-(*N*-dimethylcarbodecyloxymethyl)ammonium dihloride (ethonium),1,10-decamethylene-bis-[*N*-dimethyl(carbomethoxymethyl)ammonium] dichloride (decamethoxine); azoles – 1-(β-oxyethyl)-2-methyl-5-nitroimidazole (metronidazole),4-amino-*N*-(2-thiazolyl)benzenesulfonamide sodium salt (sulfathiazole sodium), *N*-(5-nitro-2-thiazolyl)acetamide (aminitrozole); polyphenoles– 4-(dimethylamino)-1, 4, 4a, 5, 5a, 6, 11, 12a-octahydro-3, 6, 10, 12, 12a-pentahydroxy-1,11-dioxo-naphthacene-2-carboxamide (tetracycline); sugars and polyols – glucose, mannitol, sorbitol, galactose, lactose, starch ($M \approx 200{,}000$), glycerin. All these compounds are widely used in medicine and pharmacy [10].

13.2.2 IR Spectroscopy Method

One of the most effective methods for investigation of physicochemical processes on silica surface is IR spectroscopy [11, 12]. The main sorption sites of nanosilica, free silanol groups, are located on the surface of primary particles statistically uniformly and appear in the IR spectra as a narrow intensive band at 3750 cm^{-1} [11–13]. Therefore a degree of their disturbance (Θ) caused by interaction with adsorbed molecules characterizes a degree of surface coverage. The Θ values for modified samples were calculated from a ratio of absorbances at 3750 cm^{-1} before and after adsorption (D_0 and D, respectively) by the formula $\Theta = 1 - D/D_0$, where $D = \lg I_o/I$; and I_o is the intensity of transmitted IR radiation ("baseline") and I is that of radiation at the maximum of the band at 3750 cm^{-1}.

The IR study was made using a ThermoNicolet FTIR spectrometer (Nicolet Instrument Corporation, USA). Silica samples studied were pressed using special press mold to tablets of 8×28 mm in size and 20 ± 0.5 mg in mass.

Parameter p which characterizes a part of polymer units in adsorption layer on silica surface directly interacting with active sites was calculated by the equation [14] $p = (\alpha_{OH} \cdot \Theta)/(A_{polymer}/M_{monomer})$, where α_{OH} is the concentration of free silanol groups, 0.6 mmol/g, Θ is a disturbance degree of silanol groups, $A_{polymer}$ is a value of polymer adsorption, mg/g, $M_{monomer}$ is the molar weight of a monomer unit of polymer macromolecule, mg.

For the aim of comparison, nanosilica was also modified using liquid-phase methods by adsorption under equilibrium conditions and by impregnation. For this purpose the sorbent was mixed with adsorbate solution, equilibrated, and then solvent with residual adsorbates was removed. The value of polymer adsorption on silica surface was calculated by the remainder of their concentrations before and after contact with the sorbent. The main difference for the impregnation method is that modification was carried out in non-equilibrium solution and only solvent is removed by evaporation.

13.3 Results and Discussion

13.3.1 Adsorption Modification of Nanosilica with Polyvinylpyrrolidone in Liquid Phase

PVP adsorption on nanosilica surface occurs with high speed and is characterized by complete polymer removal from solution at low temperatures [14]. Adsorption isotherm is well described by Langmuir equation and takes a linear form in *C*/*A*–*C* coordinates (Fig. 13.1a). Calculated value of maximum adsorption (A_{max}) amounts to 185 mg of PVP per gram of silica or 0.7–0.8 mg/m^2, which corresponds to the data given in the literature [5, 14, 15].

After the PVP adsorption on the silica surface from the aqueous solutions the IR spectra show lowering of band intensity at 3750 cm^{-1} symbate to polymer content and appearance of wide band of disturbed silanol groups with a maximum at about 3350 cm^{-1} (Fig. 13.1b). PVP interaction with high-disperse silica surface occurs due to formation of hydrogen bonds between oxygen of carbonyl groups and hydrogen of free silanol groups [14] (Fig. 13.2). Full disturbance of absorption band at 3750 cm^{-1} at 200 mg/g PVP content which is equal to monolayer capacity means

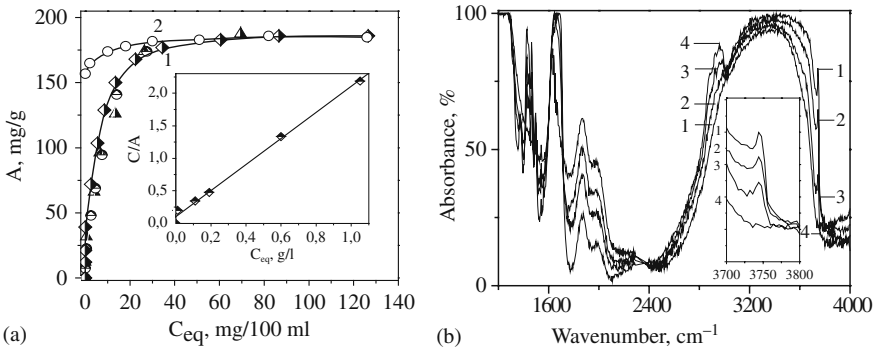

Fig. 13.1 (**a**) Isotherm of PVP adsorption from aqueous solution (*1* adsorption, *2* desorption); (**b**) IR spectra of initial nanosilica (*1*) and silica with adsorbed polyvinylpyrrolidone of 60 (*2*), 110 (*3*), and 200 mg/g (*4*)

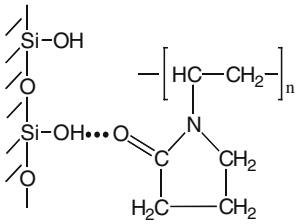

Fig. 13.2 Scheme of formation of hydrogen bonds between polyvinylpyrrolidone molecule and silanol group

that all surface of nanosilica is available to the interaction with adsorbate molecules, including large ones.

13.3.2 Modification in Fluidized State

Nanosilica (12.5 g) and the given polymer portion were consequently put into 0.5 dm^3 reactor of intensive mixing and then the mixer was turned on. The IR spectra show that in 1 h mixing under conditions of fluidization the homogeneous mixture obtained contains the components as different phases (Fig. 13.3a, curve 2). Then ethanol (5 g or 7.15 ml), which corresponds to 40 wt% of silica, was gradually brought in the reactor with a speed of 1–2 drops per second. Herein nanosilica conserves its friable state, which is the fact of principal importance. This phenomenon is caused by high oil absorption power of silica, in other words its ability to absorb fluids without loss in friability.

As early as after an hour the degree of disturbance of free silanol groups (Θ) came to ∼ 0.68, in 2 h 0.96, and then remained practically constant (0.98) (Fig. 13.3a, b).

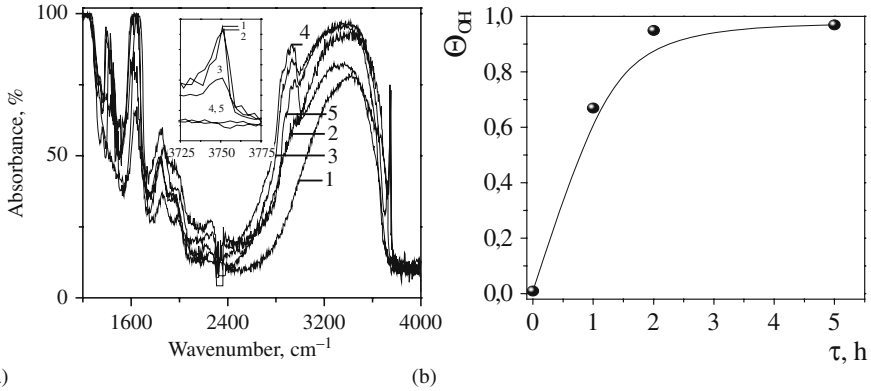

Fig. 13.3 (**a**) IR spectra of initial silica (*1*) and silica after mixing with PVP (175 mg/g) in RIM in air (*2*) and in air–ethanolic gaseous medium (40 wt% of silica) for 1 (*3*), 2 (*4*), and 5 h (*5*); (**b**) dependence of disturbance degree of free silanol groups with polyvinylpyrrolidone (175 mg/g) on time of modification in air–ethanol medium in RIM

A 1.5-fold increase (from 40 to 60%) of ethanol content in the reaction volume as well as prolongation of mixing time to 6 h made no effect on the final result. The mentioned conditions of modification in RIM are supposed to be close to optimum. It should be noted that the process is just as effective as that in case of air–aqueous and air–aqueous–ethanol gaseous medium.

The parameter p characterizing a part of monomer units forming bonds with silanol groups was calculated from the dependence of disturbance degree of free silanol groups on PVP content (Fig. 13.4). For PVP monolayer coverage obtained by adsorption under equilibrium and fluidization conditions, the parameter p was determined to be about 0.4 indicating that the polymer loops and tails contain 1–2 units only. This testifies that conformation of PVP monolayers is characterized by plane location of molecules in all mentioned cases and does not practically depend on interaction conditions.

From the analysis of the IR spectra and the dependences of the disturbance degree of free silanol groups and the parameter p on PVP content, the formation of a PVP adsorption layer on nanosilica surface in the reactor of intensive mixing can be schematically represented as in Fig. 13.5.

When the systems are mixed intensively in the reactor, a homogeneous mixture is formed, in which polymer particles contact directly with aggregates and other secondary structures of nanosilica. Due to the presence of a solvent in the atmosphere, PVP macromolecules swallow as a result of interaction with water or ethanol, its segments becoming mobile. The volume occupied by PVP molecules in dry state or solution is known to vary over one order of magnitude. Therefore a so-called swelling pressure similar to osmotic pressure arises when swallowing substance meets barriers. Swelling pressure can amount up to tens of millipascals.

Polymer molecules begin to spread onto silica surface due to increased mobility of segments. The driving force of surface diffusion of macromolecules is high

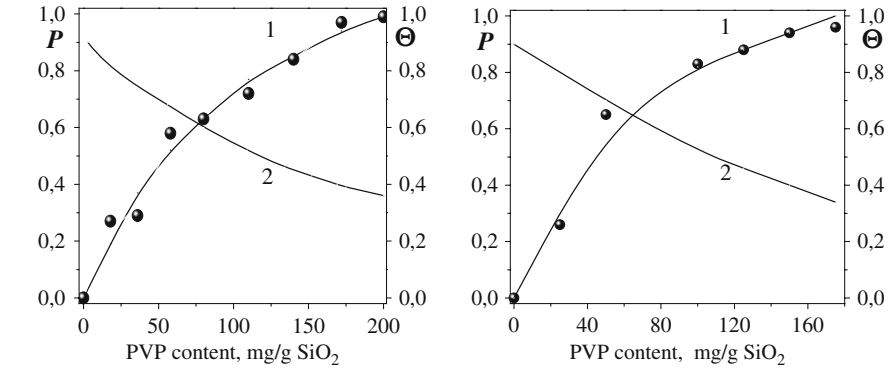

Fig. 13.4 Dependence of disturbance degree of free silanol groups (Θ) (*1*) and parameter p (*2*) on PVP content: (**a**) adsorption from equilibrium solution; (**b**) modification under conditions of fluidization

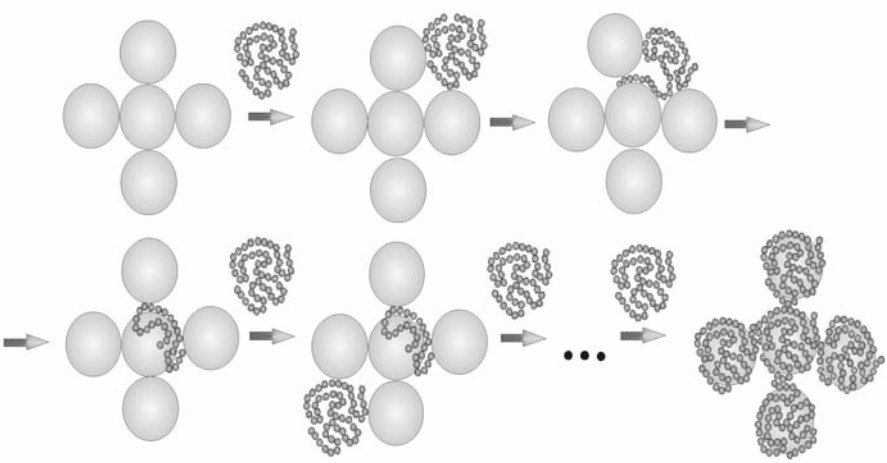

Fig. 13.5 Scheme of formation of PVP adsorption layer on nanosilica surface during modification under conditions of gaseous dispersion medium

energy of adsorbent–adsorbate interaction amounting to about 50 kJ/mol [14]. As far as interaction energy between silica particles does not exceed 20–25 kJ/mol (what one can find elsewhere [6]), PVP macromolecules can easily penetrate between them. This results in complete polymer coverage of nanosilica particles if necessary amount of modifier is available.

UV spectral study of iodine interaction with absorbed PVP showed plane location of the chains of polymer macromolecules on nanosilica surface [16].

13.3.3 Effectiveness Comparison for Methods of Nanosilica Modification

Similarly, the adsorption modification of nanosilica with another non-volatile organic compounds was carried out by adsorption, by impregnation, and in fluidized state. Since adsorption modification is the substitution of functional groups for other ones, the degree of silica surface coverage at equal modifier content can be assumed as criterion of effectiveness for modification methods when compared.

The literature data show that modification by adsorption is effective for polymers only. The degree of surface coverage in case of low molecular compounds adsorbed from solution amounts to one-third of monolayer at best (Table 13.1).

Table 13.2 shows data of maximum degree of silica surface coverage with studied compounds obtained using impregnation and fluidization.

It follows from the analysis of the tables that the method of silica modification under conditions of intensive mixing in gaseous dispersion medium is the most effective one. In this case total or almost total surface monolayer coverage was reached for all compounds studied.

Table 13.1 The maximum adsorption values (α_{max}) for compounds studied and the degree of silica surface coverage (θ)

Compound	Adsorption value, α_{max}		Coverage degree, $\theta = \alpha_{max}/0.6$	Reference
	mg/g	mmol/g		
PVP	195	–	1	[14]
POE	200	–	1	[17]
Ethonium	–	0.012[a]	0.02	[18]
		0.246[b]	0.41	
Decamethoxine	–	0.21	0.34	[19]
Tetracycline	–	0.017	0.03	[20]
Glucose	–	0	0	[21]
Sorbitol	–	0.0005	0.0008	[22]
Galactose	–	0	0	[21]

[a]Experimental value.
[b]Calculated value for monolayer capacity.

Table 13.2 Dependence of the degree of silica surface coverage (θ) on modification method

Compound	Modificator content		Degree of silica surface coverage (θ)	
	mg/g	mmol/g	Impregnation	RIM
PVP	200	–	1	1
POE	200	–	1	1
		–	–	0.58[a]
Vaseline oil	200	–	–	0.78[b]
		–	–	0.94[c]
Ibuprofen	–	0.60	1	–
Ethonium	–	0.30	1	1
Decamethoxine	–	0.17	1	–
	–	0.35	1	–
Tetracycline	–	0.60	0.80	– 0.71
		0.30	0.48	
Metronidazole	–	0.60	0.95	1
Sulfathiazole sodium	–	0.60	0.80	0.98
Aminitrozole	–	0.60	0.60	0.95
Glucose	–	0.60	0.58	0.90
Mannitol	–	0.60	0.29	0.90
Sorbitol	–	0.60	0.34	0.85
Galactose	–	0.60	0.37	0.90
Lactose	–	0.60	0.33	0.90
Starch	300	–	0.95	0.75
Glycerin	–	0.60	–	1[d]

[a]Mixing at 20° C.
[b]Mixing at 90° C.
[c]Mixing at 20° C in air–hexane atmosphere.
[d]Mixing at 90° C in air–ethanol atmosphere.

13.4 Conclusions

A new effective and ecologically safe method was developed for adsorption modification of nanosilica with non-volatile organic compounds (bioactive compounds, polymers) in fluidized state in conditions of gaseous dispersion medium in solvent atmosphere. The developed method allows one to achieve a defined degree of surface coverage and maintain practically full initial dispersity of silica.

References

1. Mironyuk I F, Voronin E F, Pakhlov E M et al (2000) Effect of manufacture conditions on hydrophilicity of high-disperse fumed silica. Ukr Chem J 66:81–83
2. Gun'ko V M, Mironyuk I F, Voronin E F et al (2001) Controlled effect on structure of high-disperse silicas. Phys Chem Solids 2:57–64
3. Sobolev V A, Khoma M I, Ogenko V M et al (1975) Study of the effect of vapour-phase conditions of high-disperse silica synthesis on its structural characteristics. Adsorption Adsorbents 3:79–83
4. Kiselev A V (1986) Intermolecular interactions in adsorption and chromatography. Visshaja shkola, Moscow
5. Iler R K (1978) The chemistry of silica: solubility, polymerization, colloid and surface properties and biochemistry of silica. Wiley-Interscience, New York
6. Legrand A P (ed) (1998) The surface properties of silicas. Wiley, New York
7. Lisichkin G V (2003) The chemistry of surface-drafted compounds. Physmathlit, Moscow
8. Chuiko A A (ed) (2001) The chemistry of silica surface. UkrINTEI, Kyiv
9. Chuiko A A (ed) (2003) The medical chemistry and clinical application of silica. Naukova dumka, Kiev
10. British Pharmacopoeia (2008) http://www.pharmacopoeia.co.uk/
11. Kiselev A V, Lygin V I (1972) Infrared spectra of surface compounds. Nauka, Moscow
12. Hair M L (1967) Infrared spectroscopy in surface chemistry. Marcel Dekker, New York
13. Zhdanov S P (1987) IR study of hydroxylated silica. Langmuir 3:960–967
14. Guzenko N V, Pakhlov E M, Lipkovskaya N A et al (2001) Sorption modification of fine silica with polyvinylpyrrolidone. Russ J Appl Chem 74:2017–2020
15. Parfit G D, Rochester C H (eds) (1983) Adsorption from solution at the solid/liquid interface. Academic Press, London
16. Guzenko N V, Voronina O E, Vlasova N N et al (2004) UV spectral study of iodine, polyvinylpyrrolidone and protein in solution and on silica surface. J Appl Spectrosc 71: 141–144
17. Nosach L V, Voronin E F (2006) Adsorption modification of high-disperse silica with non-volatile organic compounds under conditions of gaseous dispersion medium. Phys Chem Solids 3:540–543
18. Davidenko N K, Shevchenko N M, Bogomaz V I et al (1992) Ethonium adsorption on high-disperse silica surface. J Phys Chem 66:2778–2780
19. Goncharik V P, Kaspersky V O, Kozhara L I et al (2000) Decamethoxine adsorption on high-disperse silica. Pharm J 5:55–58
20. Slyshik N F, Nosach L V, Voronin E F (2004) Adsorption of tetracycline antibiotics on high-disperse silica surface. Chem Phys Technol Surf 10:170–174
21. Kulik T V, Palyanytsya B B, Galagan N P (2003) Molecular self-assembly in systems of nanosized particles and hydrocarbons. Nanosyst Nanomater Nanotechnol 2:681–690
22. Nastasienko N S, Mischanchuk B G, Galagan N P (2004) Mass-spectroscopic study of sorbitol and xylitol thermolysis. Chem Phys Technol Surf 10:198–201

Chapter 14
Synthesis of Functionalized Mesoporous Silicas, Structure of Their Surface Layer and Sorption Properties

Yuriy L. Zub

Abstract The routes of synthesis of polysiloxane xerogels functionalized by nitrogen-, oxygen-, phosphorus- and sulphur content ligand groups were investigated. Applying a number of physical methods (SEM, TEM, AFM, IR and Raman spectroscopy, ^{1}H, ^{13}C, ^{29}Si and ^{31}P CP/MAS NMR spectroscopy, EPR spectroscopy, ERS and thermal analysis) the structure of xerogels and their surface was established. The influence of some factors on the structural-adsorption characteristics of such xerogels and their sorption properties were analysed.

14.1 Introduction

Sol–gel method is most often applied for synthesis of polysiloxane mesoporous materials that contain complexing groups in their surface layer [1]. Use is usually made of its variant that is based on reaction of hydrolytic polycondensation of corresponding silicon derivatives (Eq. 14.1). Introduction of water and catalyst (e.g. H^+, OH^-, F^-) in the initial system leads to hydrolysis of alkoxysilanes with formation of silanol groups, ≡Si–OH. These groups interact with each other (or with alkoxysilyl groups, RO–Si≡) immediately, which leads to a creation of siloxane bonds (≡Si–O–Si≡), causing occurrence of oligomers. The results of further condensation of these oligomers are the occurrence of polymers of various structures. The growth of polymers results in occurrence of colloidal particles which consequently leads to occurrence of sol. The further integration of these particles and creation of aggregates causes transaction of sol into gel. The appropriate treatment of formed gel (its ageing, washing, drying, etc.) results in a polysiloxane xerogel with functional groups in its surface layer (FPX):

$$x\mathrm{Si}(\mathrm{OR})_4 + y(\mathrm{RO})_3\mathrm{SiR}' \xrightarrow[-\mathrm{ROH}]{+\mathrm{H_2O}\ (\mathrm{Solv}),\ \mathrm{catalyst}} \left(\mathrm{SiO}_{4/2}\right)_x \cdot \left(\mathrm{O}_{3/2}\mathrm{SiR}'\right)_y \qquad (14.1)$$

Y.L. Zub (✉)
O.O. Chuiko Institute of Surface Chemistry of the National Academy of Sciences of Ukraine, General Naumov St. 17, Kyiv 03164, Ukraine
e-mail: zub_yuriy@isc.gov.ua

A.P. Shpak, P.P. Gorbyk (eds.), *Nanomaterials and Supramolecular Structures*,
DOI 10.1007/978-90-481-2309-4_14,

Preparation of FPX is often effected using two-component systems (Eq. 14.1). This approach employs tetraalkoxysilane [usually tetraethoxysilane (TEOS), $Si(OC_2H_5)_4$] in the capacity of a structure-forming agent while the second component (trifunctional silane) is used to introduce a necessary ligand group R′. However, it is possible to use combinations of structure-forming agents and vary both composition and ratio of functionalizing agents. In this case the application of one-stage process allows to prepare polysiloxane adsorbents which would contain simultaneously several functional groups (R′) with different nature [2]. The possibility of making a wide choice of conditions that are acceptable for effecting the hydrolytic polycondensation reaction allows one to exert a rather strict control over properties of final products (FPX). The above-stated relates, in the first place, to parameters of their porous structure, nature and content of ligand groups. Taking into account an existence of huge number of alkoxysilane derivatives, it is possible to assert about the presence of significant prospect in search of new materials with unique properties including sorbents [3]. The cycle of Slinyakova team's papers, which were devoted to research of organosilicon adsorbents (xerogels) with alkyl and aryl radicals in their surface layer [4], was the base of this direction. In 1977 this team together with Voronkov's team also described a preparation of S-containing xerogel [5]. This short review was intended to consider the methods of synthesis and structure of xerogels containing complexing groups and the influence of some factors on the structural-adsorption characteristics of such materials and their sorption properties.

14.2 Synthesis of Functionalized Polysiloxane Xerogels

3-Aminopropyltriethoxysilane $(C_2H_5O)_3Si(CH_2)_2NH_2$ (APTES) was one of the first used for producing an amino-containing xerogel (TEOS was a structure-forming agent) [6]. Later it was shown that with decreasing TEOS/APTES ratio S_{sp} of samples decreases (at a ratio of 1:1 the xerogel becomes practically nonporous). As is known this characteristic has direct relation with functional groups' accessibility [7–9]. The influence of other conditions (nature of the nonaqueous solvent, gel ageing time, modes of washing, etc.) on structural-adsorption characteristics of the final products was also established. Some syntheses were carried out by the use of nonaqueous solvents. The procedure made it possible to prepare xerogels (in high alkaline medium) with reproducible main characteristics and a content of $[(SiO)_{2.6}(O_{3/2}Si(CH_2)_3NH_2)\cdot H_2O]$ [7–10]. Depending on the synthesis conditions the content of amine groups varied in the interval from 3.0 to 4.2 mmol/g. The obtained xerogels have high hydrolytic and thermal stability, for example, the decomposition of their surface layer begins beyond 275°C [10, 11].

The same approach involving application of ethanol, which often allowed to avoid appearance of two phases during formation of gels, was employed for producing xerogels with such functional groups as $\equiv Si(CH_2)_3NHCH_3$, $\equiv Si(CH_2)_3NH(CH_2)_2NH_2$, $\equiv Si(CH_2)_3NC_3H_5N$ (imidazolyl) and $[\equiv Si(CH_2)_3]_2NH$ [12–14]. In the last case the formation of so-called "arched structures"

$\equiv Si(CH_2)_3–NH–(CH_2)_3Si\equiv$ expected that obviously should have a high hydrolytic stability. The authors [12–14] also described a synthesis of porous xerogels with a bifunctional surface layer composed of $\equiv Si(CH_2)_3NH_2/CH_3$ (or C_6H_5).

Amino-containing xerogels were obtained by $(C_2H_5O)_3Si(CH_2)_2Si(OC_2H_5)_3$ (BTESE), $(C_2H_5O)_3Si(CH)_2Si(OC_2H_5)_3$ (BTEST) and $(C_2H_5O)_3SiC_6H_4Si(OC_2H_5)_3$ (BTESB) as structure-forming agents [15, 16]. It was shown that in order to avoid nonhomogeneous gelation it was necessary to use ethanol, to effect a preliminary hydrolysis of structure-forming agents (with F^- as a catalyst), and to enlarge the time for gel ageing (up to 14–30 days) with the purpose of increasing the polycondensation degree. The molar ratio "structure-forming agent/functionalizing agent" was equal to 4:1 or 2:1. The content of ligand groups in the xerogels prepared ranged from 1.0 to 2.6 mmol/g.

Voronkov and coworkers [5] described the synthesis of sulphur-containing sorbents using the hydrolytic polycondensation only of trifunctional silanes. One of the drawbacks of the offered approach is absence of any possibility for varying the contents of functional groups in the polymers. It should also be noted that the hydrolytic polycondensation of alkoxysilanes under such conditions gives precipitations but not gels. Hence, the set of factors that may be employed in the situation with such systems to exert an effect on properties of final products becomes substantially smaller in number. Therefore, the systems with two and three components were used for synthesis of xerogels with $\equiv Si(CH_2)_3NHC(S(O))NHR''$ functional groups ($R'' = –C_2H_5$, n-C_3H_7, $–C_6H_5$, etc.) (TEOS was a structure-forming agent; ethanol was a solvent; $F^-/Si \sim 1/100$) [17, 18]. Also the precursors forming arched structures are used [17, 19]. When the TEOS/trifunctional silane ratio is 2:1 the surface of formed xerogels possessed hydrophobic properties, and the xerogels did not have porosity, while at a ratio of 4:1 (or 8:1) they showed hydrophilic properties and porous structure [17, 18]. The xerogel surface acquired hydrophilic properties also in the case of introduction of additional amine groups [17]. The content of functional groups was 0.9–3.3 mmol/g. The obtained xerogels have high thermal stability, for example, the decomposition of xerogels with arched structure layer begins beyond 380–430°C [19].

Synthesis of xerogels with groups $\equiv Si(CH_2)_3SH$ is usually performed by applying such catalysts as $(n\text{-}Bu)_2Sn(CH_3COO)_2$ or HCl. However, the surface layer of such xerogels does not have high hydrolytic stability [20]. Besides that, the polymeric matrix composition includes tin [21]. Moreover, systems with 3-mercaptopropyltrimethoxysilane, $(CH_3O)_3Si(CH_2)_2SH$ (MPTMS), are noted to have often two phases, and the formed xerogel is practically nonporous [22]. These drawbacks could be avoided by using F^- as a catalyst [22]. The xerogel obtained at TEOS/MPTMS = 2:1 possessed an extended porous structure and the content of HS groups was equal to 4.5 mmol g^{-1}. The varying of alkoxysilanes ratio in the range of 5:1–1:1 allowed to obtain xerogels with thiol groups content from 1.9 to 5.3 mmol/g [23]. In the last case the sample consists of partly sticking together particles of spherical form (their size is 2.5–3.0 μm, Fig. 14.1a) that is not typical for xerogels of this class (Fig. 14.1b). The xerogels which contain 3-mercaptopropyl groups were synthesized with the use of BTESE and BTESB as

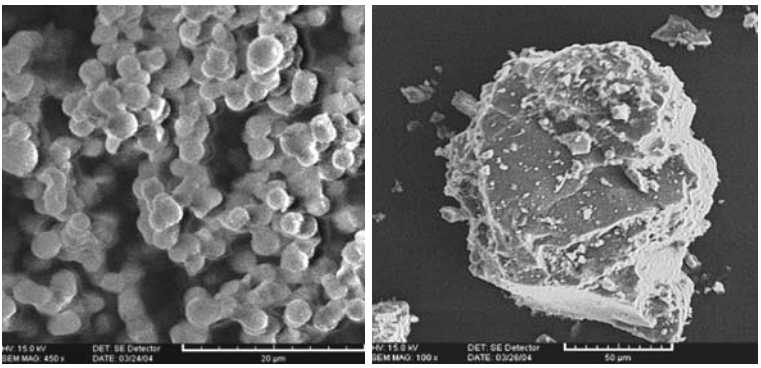

a b

Fig. 14.1 SEM micrographs of the xerogels with HS groups (TEOS/MPTMS = 1:1 (**a**) and 3:1 (**b**)) [23]

structure-forming agents [BTESE (or BTESB)/MPTMS = 2:1 or 4:1] [16, 24]. The content of functional groups was 1.0–2.7 mmol/g.

The authors [12, 22, 25] also described preparation of xerogels which contained a bifunctional surface layer of the SH/NH_2 type (the structure-forming agents were TEOS or bis(triethoxy)silanes). In the case of xerogels with $\equiv Si(CH_2)_3SH/\equiv SiCH_3$ (or $\equiv Si(CH_2)_2CH_3$) surface layer the variation of alkoxysilane ratio allowed to obtain xerogels with thiol groups content from 1.2 to 4.4 mmol/g [26, 27]. By means of AFM it is shown (Fig.14.2a) that these xerogels are composed of aggregated spherical particles with mean sizes of 35–45 nm. These results correlate with the data of SEM (Fig. 14.2b).

For the first time the xerogel with groups $\equiv Si(CH_2)_2COOH$ was synthesized in 1964 [28] by the acid hydrolysis of $(C_2H_5O)_3Si(CH_2)_3CN$ with following addition of TEOS. The obtained white product sorbed well the $NHEt_2$ and Py. Later using this approach the authors [29–31] described preparation of xerogels which contained

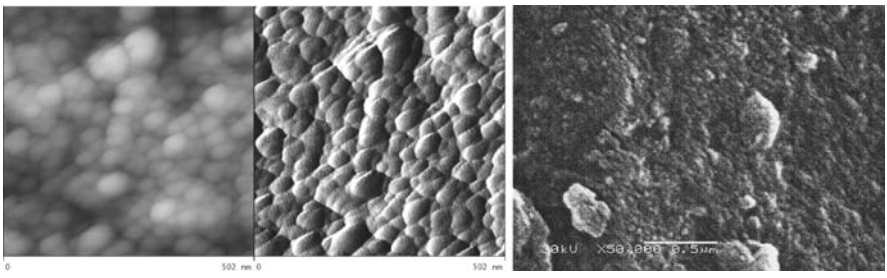

a b

Fig. 14.2 AFM (**a**) and SEM (**b**) images of HS-containing xerogels (TEOS/MPTMS/MTES = 2:0.5:0.5) [26]

groups $\equiv Si(CH_2)_2COOH$ and $\equiv Si(CH_2)_3COOH$. One of the salient features of the synthesized xerogels was that the content of carboxyl groups (according to the potentiometric titration data) was always lower than the content calculated from the element analysis data for carbon (1.8–3.7 mmol/g). By means of ^{13}C CP/MAS NMR spectroscopy it is shown that some part of these groups forms complex ethers.

The system with two components TEOS/$(C_2H_5O)_3Si(CH_2)_2P(O)(OC_2H_5)_2$ (DFTS) was used to obtain xerogels with P=O groups (the ratio of components was 2:1–10:1; ethanol was used as a solvent; $F^-/Si = 1/100$) [32]. The samples which were synthesized at the ratios of 6:1–10:1 had porosity. The content of functional groups in such xerogels was 1.2–1.4 mmol/g. The acidic treatment of nonporous xerogels leads to formation of porous samples with $\equiv Si(CH_2)_2P(O)(OH)_2$ functional group [33]. Its content was 2.6–3.5 mmol/g. Xerogels which contained amide derivatives of phosphonic and thiophosphonic acids, $\equiv Si(CH_2)_3NHP(O,S)(OC_2H_5)_2$, were obtained by application of two- and three-component systems (TEOS was a structure-forming agent) [34, 35]. 3-Mercaptopropyl and 3-aminopropyl groups were used in addition to P=O groups. The general content of functional groups reached 3.6 mmol/g.

Ethoxysilyl derivatives of α- and β-cyclodextrines (CD) were used for preparing xerogels with these macrocyclic molecules (the structure-forming agent was TEOS; DMF (or DMF/water) was used as solvent, $F^-/Si = 1/100$) [36]. It was also shown that the hydrolytic polycondensation of TEOS in the presence of 25,26,27,28-tetrahydroxycalix[4]arene can yield porous polysiloxane xerogels (S_{sp} = 381–643 m^2/g) with incorporated macrocyclic ligands [37]. It was elucidated that an increase in the concentration of macrocyclic ligands in the initial solution leads to an increase in the times of gel formation and aging. Probably, this did not allow one to prepare (under chosen conditions) samples with the macrocyclic ligand content higher than 1.0 mmol/g [38, 39].

14.3 Structure of Functionalized Polysiloxane Xerogels

14.3.1 Application of Vibration Spectroscopy

The vibrational spectroscopy, especially IR spectroscopy, is known to be a traditional technique used for FPX investigation. Its application makes it possible to ascertain that the obtained xerogels contain (a) siloxane bonds and introduced functional groups (and/or products of their transformation during the course of synthesis), (b) silanol groups (and/or alkoxysilane groups), (c) water and/or nonaqueous solvents used during synthesis, (d) systems of hydrogen bonds.

Thus, the most intensive adsorption band with a high-frequency shoulder is observed in the region 1000–1200 cm^{-1} of IR spectra of the xerogels with $\equiv Si(CH_2)_3SH/\equiv Si(CH_2)_3NH_2$ bifunctional surface layer [22] (Fig.14.3) consistent with the presence of a three-dimensional siloxane framework (≡Si–O–Si≡) [40]. In the IR spectrum of xerogel with thiol groups (Fig. 14.3, B) at 2565 cm^{-1} is legibly fixed the adsorption band which refers to ν(SH). The reduction of part of MPTMS

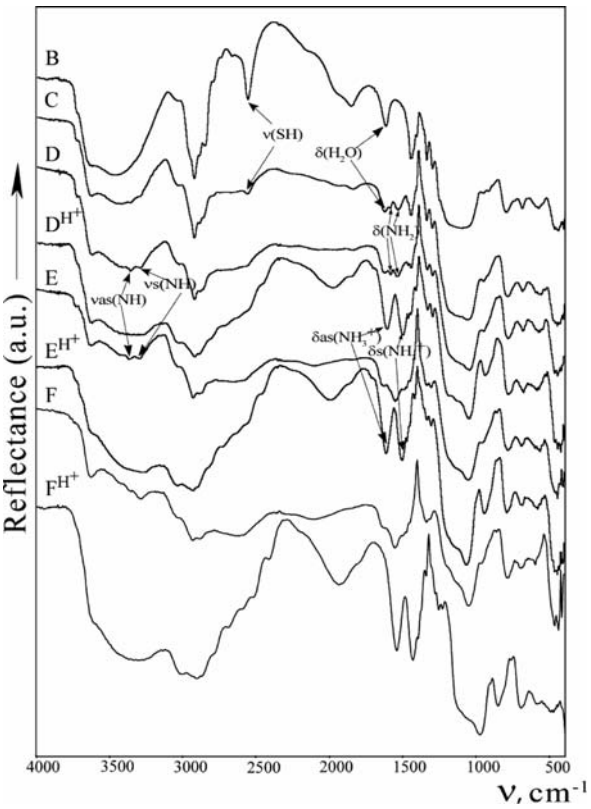

Fig. 14.3 IR reflection spectra of xerogels containing HS group (*B*); bifunctional surface layer with the ratio of $-SH/-NH_2 = 3.2$ (*C*), 1.1 (*D*) and 0.4 (*E*); amino group (*F*); the xerogels treated by 0.1 M HCl solution (D^{H+}, E^{H+} and F^{H+})

in a starting solution results in the decrease of its intensity and which becomes invisible in the IR spectra of xerogels D and E (Fig. 14.3). However, Raman spectra of these xerogels [11] have the line in 2570–2580 cm^{-1} region, assigned to ν(SH) [41], irrespective of a ratio in surface layer of thiol and amino groups. In the IR spectra of these samples there are two low intensive adsorption bands at ~3300 and ~3370 cm^{-1} which can be referred to as $\nu_{s,as}$(NH) of amino groups (Fig. 14.3). Besides in the IR spectra of samples C–F there are weak adsorption bands at 1585–1595 and 1540–1555 cm^{-1}. Occurrence of these bands is caused by deformation vibrations of amino group $\delta(NH_2)$. Such bands are absent in the IR spectrum of xerogel B containing only HS groups (Fig. 14.3). Since $-SH$ and $-NH_2$ groups exhibit different characteristics, it is not unreasonable to expect the protonation of amino groups even when thiol groups are present in a surface layer. In other words, the surface layer in such xerogels can possess a salt-like character of the type $[\equiv Si(CH_2)_3NH_3]^+[\equiv Si(CH_2)_3S]^-$. However, the line corresponding to ν(SH) in Raman spectrum is conserved even at dominating quantity of amino groups in the surface layer (sample E) [11]. Moreover, the adsorption bands which correspond to stretching vibrations of $\nu_{s,as}$(NH) and deformation vibrations $\delta(NH_2)$

of unprotonated amino groups are observed in the IR spectra of xerogels C and D (Fig. 14.3), where the quantity of thiol groups in the surface layers was in excess relative to that of the amino groups. If alkylammonium cations were formed in samples C–E, they would have exhibited several characteristic absorption bands in the 2500–2800 cm^{-1} region and a band of medium intensity at ca. 2000 cm^{-1} in their IR spectra [41]. However, such absorption bands are only observed in the IR spectra of samples D, E and F when the latter are treated with a 0.1 M HCl solution (Fig. 14.3), thereby providing additional evidence for protonation of the amino groups. Moreover, two intense absorption bands at ca. 1500 cm^{-1} and ca. 1610 cm^{-1}, referred to as $\delta_s(NH_3^+)$ and $\delta_{as}(NH_3^+)$, respectively, also appear in the IR spectra of such samples (Fig. 14.3). Similar absorption bands were observed in the IR spectra of the APTES/$Zr(HPO_4)_2$ intercalate which contains protonated hydrolysates and condensation of APTES [42]. Thus, the amino groups in the surface layer of the initial FPX are nonprotonated but are involved in the hydrogen bond formation [43, 44]. It should be noted that a weak absorption band at 1600 cm^{-1} assigned to a hydrogen bond between amino groups [41] appears in the IR spectrum of APTES itself [10]. In the IR spectra of xerogels C–F there is low intensive adsorption band in this region (see above) which often split into two components and shifted in low-frequency area at 7–70 cm^{-1} (Fig. 14.3). This fact may indicate the formation in xerogels of hydrogen bond of a different nature than in APTES. Similar observations have been made for bifunctional xerogels which were synthesized using BTESE as a structure-forming agent [25].

If in a surface layer of xerogels there appear functional groups that are more complex in their composition (for instance, $\equiv Si(CH_2)_2NHC(O,S)NHR''$ [17–19] or $\equiv Si(CH_2)_2P(O)(OC_2H_5)_2$) [32]), the IR spectra of the xerogels also become more complex. In the case of IR spectra of xerogels which contained $\equiv Si(CH_2)_2P(O)(OC_2H_5)_2$ groups, the most intense absorption band exhibits the second shoulder at ~1210 cm^{-1}corresponding to ν(P=O). This band is observed at 1241 cm^{-1} for individual DFTS. Hence, the shift of this band in a low-frequency region testifies to the presence of phosphoryl groups in the hydrogen bond formation [32]. The same situation is observed in the case of xerogels with such groups as $\equiv Si(CH_2)_2NHP(O)(OC_2H_5)_2$ [34, 35].

In the IR spectra for carboxyl-containing xerogels an intense band of absorption appears in the region 1720–1730 cm^{-1}. This is a typical feature of COOH groups which are connected with OH groups by hydrogen bonds [41, p. 139]. Moreover, another band appears at ~1645 cm^{-1}, which provides evidence to formation of some carboxyl groups of ester bonds [45].

14.3.2 Application of Solid-State NMR Spectroscopy

Solid-state NMR spectroscopy can furnish a valuable additional information about structure of xerogels and their surface layers. Here we considered solid-state NMR spectra of some xerogels which are typical for FPX.

Assignment of signals which are observed in ^{13}C CP/MAS NMR spectra of some xerogels with mono (−SH or $-NH_2$) and bifunctional (−SH/$-NH_2$) surface layer (Fig. 14.4) are presented in Table14.1. It is known that the resonance arising from the central propyl carbon atom of the $\equiv SiCH_2[\underline{C}H_2]CH_2NH_2$ group in the ^{13}C CP/MAS NMR spectrum is an indicator of the binding state of amino groups [46]. Thus, individual APTES molecules exhibit a resonance at ca. 28 ppm in the ^{13}C CP/MAS NMR spectrum while, after protonation of the grafted 3-aminopropyl groups to an SiO_2 surface, this resonance moves to the stronger field region (21–22 ppm) of the spectrum [46]. If it is assumed that the resonance in the ^{13}C CP/MAS NMR spectrum of sample D arises from the central carbon atom of the 3-aminopropyl fragment (Fig. 14.4 and Table 14.1), it is possible to conclude that protonation of the $-NH_2$ groups in the surface layer of this sample arises either from a proton of the thiol group or from a proton of the silanol group. However, this conclusion is not in agreement with that made on the basis of the IR and Raman spectroscopic data. Thus, if the 3-aminopropyl groups are not protonated in xerogel D, they may take part in the formation of hydrogen bonds. In this case, it is necessary to assume that

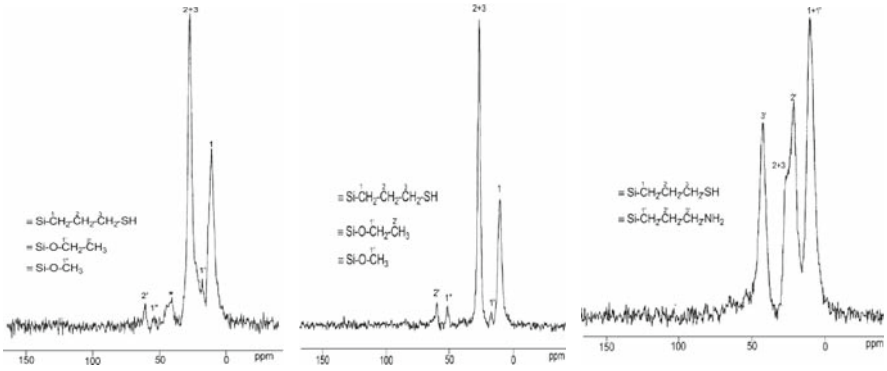

Fig. 14.4 ^{13}C CP/MAS NMR spectra of samples A (**a**), B (**b**) and D (**c**)

Table 14.1 Summary of ^{13}C CP/MAS NMR data for A, B, D and F xerogels

	Chemical shifts (ppm)			
Signals assignment	Sample A	Sample B	Sample D	Sample F
$\equiv Si\underline{C}H_2CH_2CH_2$(SH or NH_2)	10.9	10.8	10.0	10.4
$\equiv SiO\underline{C}H_2CH_3$	17.7	17.7	–	–
$\equiv SiCH_2\underline{C}H_2CH_2NH_2$	–	–	21.2	22.1;25.5 (sh)
$\equiv SiCH_2\underline{C}H_2\underline{C}H_2SH$	27.2	27.1	27.0	–
$\equiv SiCH_2CH_2\underline{C}H_2NH_2$	–	–	41.9	42.9
$\equiv SiO\underline{C}H_3$	~52	51.4	–	–
$\equiv SiOCH_2\underline{C}H_3$	60.4	59.7	–	–

the resonance from the central carbon atom of the propyl chain in the 20–23 ppm region of the ^{13}C CP/MAS NMR spectra can correspond either to the protonated amino group or to the formation of a hydrogen bond by this group. Analysis of the thermograms for sample D [47] indicated that it had a small water content (ca. H_2O on two functional groups). Making allowance for this fact, one may conclude that the 3-aminopropyl groups on the surface of sample D (and also on the surfaces of samples C and E) form hydrogen bonds with silanol groups. It is also probable that the water molecules associated with the surface layers of these xerogels form hydrogen bonds, for example, of the type $[\equiv Si(CH_2)_3H_2N\cdots H_2O\cdots HOSi\equiv]$. It is also possible to infer that the thiol groups exhibit partial "inertness" in comparison to amino groups, in accord with the Raman spectroscopic data. A similar assumption was made earlier [48] in considering the sorption of copper(II) ions by the same xerogels.

The hypothesis suggested above regarding surface layer structures in bifunctional xerogels agrees with the ^{13}C CP/MAS NMR [49] and ^{1}H MAS NMR spectral results for sample F [50]. Thus, the signal from the central carbon atom of the propyl chains for this sample also occurred in the same spectral range of 21–23 ppm (Table 14.1) as that existing in the ^{13}C CP/MAS NMR spectrum for the sample prior to treatment with HCl solution. After heating the initial xerogel in an oven, this signal moved to weaker fields in the ^{13}C CP/MAS NMR spectrum, i.e. to the region where the signal from the central carbon atom of APTES itself is located. In other words, the removal of water from the surface layers by heating results in the removal of a molecule of water forming a bridge between an amino group and a silanol group and to the formation of new hydrogen bonds, viz. a bond between individual amino groups, leading to re-organization of the surface layers in the xerogel. Hence, the state of the surface layers in such xerogels depends on the drying conditions employed for the samples.

On the basis of ^{1}H MAS NMR spectra analysis recorded for the initial xerogel F, its dried sample and a sample of the xerogel treated with an aqueous HCl solution it is possible to arrive at the following major conclusions [49, 50]: (a) the initial xerogel F contained a very small amount of ethanol (as shown by the area of the ^{1}H signals which were less than 0.1%) and residual ethoxysilyl groups (less than 1.5%); there was also some water in the sample; (b) during drying of this sample, all traces of ethanol and almost all the water were removed; the dried sample exhibited no signals which could be assigned to the presence of protonated amino groups (6.0–7.0 ppm); (c) upon treatment of the initial xerogel with 0.1 M HCl solution, the appearance of an intense signal at 6.2 ppm caused by formation of the alkylammonium cation $\equiv Si(CH_2)_3NH_3^+$ was observed (apparently overlapped by signals from the water protons); (d) finally, in summary, it may be noted that signals associated with the protons of silanol groups or amino groups were not observed in these spectra (the same was also reported earlier by some other authors [51] who undertook studies with similar systems).

The use of ^{31}P CP/MAS NMR spectroscopy allowed to reveal transformation of $\equiv Si(CH_2)_2P(O)(OC_2H_5)_2$ functional groups in the surface layer of xerogels after they were treated by boiling conc. HCl [33, 52]. Thus, ^{31}P CP/MAS NMR

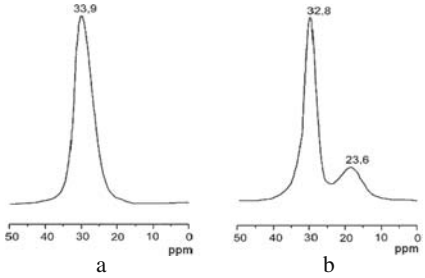

Fig. 14.5 ^{31}P CP/MAS NMR spectra of the xerogels containing $\equiv Si(CH_2)_2P(O)(OC_2H_5)_2$ groups: before (**a**) and after (**b**) the treatment of conc. HCl [33]

spectrum of the initial xerogel contains a single intense symmetric signal within the region from 20 to 35 ppm (Fig. 14.5a). The location of this signal is close to the one of phosphorus atom signal of the initial DFTS (32.9 ppm [53] or 34.5 ppm [54]). The appearance of an additional signal at 23–24 ppm in the ^{31}P CP/MAS NMR spectrum was observed after the treatment of the initial xerogel by conc. HCl and its drying in vacuum (Fig. 14.5b). The appearance of an additional signal in the ^{31}P CP/MAS NMR spectra of bifunctional xerogels most likely is due to formation of $\equiv Si(CH_2)_2P(O)(OH)–OSi\equiv$ bridges during the drying in vacuum at 120°C, by the part of P-containing groups.

The use of ^{13}C CP/MAS NMR spectroscopy allowed to reveal existence of ester groups $\equiv Si(CH_2)_2C(O)OC_2H_5$ in carboxyl-containing xerogels [45].

Solid-state NMR spectroscopy was found very useful for studying xerogels with complex functional groups, for instance, cyclodextrines [36]. Thus, in ^{13}C CP/MAS NMR spectrum of the xerogelwhich were functionalized by α-CD, ethoxysilyl groups are presented by distinct signals in contrast to IR spectroscopy data.

^{29}Si CP/MAS NMR spectra of functionalized polysiloxane xerogels contain, as a rule, two sets of resonance signals in the spectrum interval from –110 to −50 ppm relating to different structural units (Fig. 14.6a). In the first region there are three signals at about −110, −100 and −90 ppm that are related to $(\equiv SiO)_4\underline{Si}$ (Q^4),

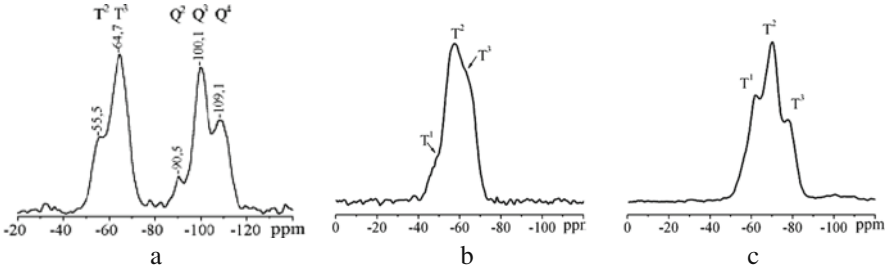

Fig. 14.6 ^{29}Si CP/MAS NMR spectra of HS-containing xerogel: **a** TEOS/MPTMS/MTES ratio was equal to 4:1:1 [27]; **b** BTESE/MPTMS=2:1, **c** BTESB/MPTMS=2:1 [16]

($\equiv$SiO)$_3$Si(OR) (Q^3) and ($\equiv$SiO)$_2$Si(OR)$_2$ (Q^2), respectively (R = H, Me or Et) [55]. The second region also contains one signal at −66 ppm with a shoulder at −57 ppm that are related to the structural units ($\equiv$SiO)$_3$SiCH$_3$/($\equiv$SiO)$_3$Si(CH$_2$)$_3$SH (T^3) and ($\equiv$SiO)$_2$(RO)SiCH$_3$/($\equiv$SiO)$_2$(RO)Si(CH$_2$)$_3$SH (T^2) in the case of xerogel with methyl and 3-mercaptopropyl groups (Fig. 14.6a) [27]. The absence of signals from structural units T^0, T^1 and Q^0, Q^1type in the considered spectra testifies about a high degree of course of hydrolytic polycondensation reaction.

Thus, irrespective of the functionality of a surface layer, nature of functional groups and structural-adsorption characteristics, the functionalized polysiloxane xerogels always contain silicon atoms of three types, with their environment consisting of only oxygen atoms. Besides, there are two more types of silicon atoms that are bonded (through alkyl chains) with ligand groups.

However, this picture changes in the case of xerogels obtained by the use of bis(triethoxy)silanes [16]. For the ^{29}Si CP/MAS NMR spectra of these systems there are no signals in the region of structural units Q^m. Therefore, their $\equiv$Si–C bonds are stabile. However, the group of intensive resonance signals in the range of (−48)–(−80) ppm indicates the existence of structure units of a T^n type (Fig.14.6b, c). In the case of xerogels with ethylene bridges these signals begin to overlap with each other especially in the case of amine functional groups. However, they can be identified distinctly in the spectra of xerogels with phenylene spacers (Fig.14.6b, c). The authors [16] made an attempt to estimate percentage of contribution of each structural unit T^n with a view to evaluate the degree of polycondensation of these xerogels. It was found that structure units of T^2 type are dominating in the framework of xerogels containing phenylene spacers, but structure units of T^1 and T^2 types are also present to a considerable degree for these samples. At the same time the framework of xerogels with ethylene spacers contains significantly lower amount of T^1-type structure units and contributions of T^2 and T^3 structure units are dominating. Therefore extent of polycondensation in case of xerogels with ethylene spacer is higher than that of xerogels with phenylene bridges – independently of a nature of functional group. This seems to be caused by a higher conformational mobility of ethylene spacers in comparison to phenylene bridges. Further, the analysis of these spectra allows one to infer that in the case of the samples with amine groups the contribution made by the structural units T^3 is higher in comparison to the samples with thiol groups. It is possible to assume that the phenomenon observed is a distinct manifestation of the difference in the nature of reaction media that are created during the course of the synthesis involving different functional groups [16].

Therefore, solid-state NMR spectroscopy application allows to make identification of the nature of functional groups in the surface layer of xerogels. It also reveals the transformation of these groups during the course of xerogel synthesis and allows to establish structural units' type, which form both xerogels and their surface layer. This spectroscopy application allows to fix the participation of functional groups in hydrogen bond formation and other interactions.

14.3.3 Application of Metal Microprobe Technique

The topography of FPX surface presents undoubtful interest. For its establishment the authors [48, 56–58] employed the metal microprobe technique: composition and structure of complexes coordination bundle, which forms during sorption of copper(II) ions by amine-containing xerogels from acetonitrile solutions, were identified by electron reflection spectroscopy (ERS) and EPR spectroscopy. It was found that irrespective of the degree of surface coverage by the metal on the surface there is the proceeded formation of complexes of one and the same composition $[CuO_2N_2]$ only. This means that at the equatorial plane of a coordination polyhedron of copper(II) there were two nitrogen atoms. A similar conclusion has also been made during the study of copper(II) complexes with amine groups on the surface of xerogels obtained by the use of bis(triethoxy)silanes [59]. It gave grounds to conclude about a specific and, probably, similar distribution of complexing groups in the surface layer of those materials. One cannot exclude that this is due to exist in their layer oligomers with the functional groups.

14.4 Adsorption Properties of Functionalized Polysiloxane Xerogels

14.4.1 Some Factors Contributing to Structural-Adsorption Characteristics

Early in [10] on the example of amine-containing xerogels, which were obtained using TEOS/APTES system, it was shown that (1) all of the obtained samples are classified as mesoporous adsorbents (for the majority of them their values of S_{sp} fall within the interval 90–315 m^2/g); (2) in all cases the introduction of a nonaqueous solvent results in a decrease of S_{sp} and V_s and an increase of d; (3) with decrease of TEOS/APTES ratio the porosity of samples decreases substantially; (4) a similar effect is exerted by relative increase of geometric sizes of the functional groups and a decrease in the amount of water taken for the hydrolysis; (5) drying of liogels at atmospheric pressure leads to large-pored sorbents; (6) washing of xerogels with water (before repeated vacuum drying) results in fine-pored adsorbents. As far as the xerogels with a bifunctional surface layer ($-NH_2/-CH_3$ or $-C_6H_5$) are concerned, it was found that the appearance of hydrophobic groups on the surface led to formation of globules of larger sizes and loosely packed structures [8, 11, 14]. These factors cause a substantial decrease in the specific surface area of xerogels.

These conclusions were confirmed and expanded in future by studying xerogels with functional groups of other nature. Thus, the increase of TEOS's loading in an initial solution caused the increase in S_{sp} of the xerogels which contained (thio)urea [17, 18], thiol [23], phosphoryl [32] and propionic acid [10, 45] groups. However, it should be mentioned that formation of porous structures was observed only for the systems with TEOS/trifunctional silane molar ratio which was higher than 1:1 in case of the HS groups [23], 2:1 in case of $-NHC(O,S)NHR''$ groups

[17–19] or 4:1 in case of the $-P(O)(OC_2H_5)_2$ groups [32]. Geometric sizes of the mentioned functional groups increases in the same sequence. An influence of the contained functional groups on structural-adsorption characteristics is clearly seen from samples of xerogels with calixarene or cyclodextrine groups [35–38]. It is interesting that the boiling-concentrated-HCl treatment of nonporous xerogels containing $\equiv Si(CH_2)_2P(O)(OC_2H_5)_2$ surface groups results in the hydrolysis of all ethoxygroups and the formation of porous xerogels with high values of a specific surface area (S_{sp} increases with the increasing TEOS/DFTS ratio) [33].

It was shown by the example of TEOS/(MPTMS + MTES) system that the change in molar ratio of trifunctional silanes in the initial solution from 2:1 to 1:2 leads to the formation of xerogels with the developed porous structure. Simultaneously, the tendency to the increase of other parameters, namely V_s and d, was observed [27]. A similar effect was also defined in the case of relative increase of TEOS's loading in an initial solution.

In the case of bridged polysilsesquioxane xerogels, which were functionalized by amine and thiol groups, their high values of S_{sp} attract attention, namely from 510 to 840 m^2/g for xerogels with ethylene bridges and from 650 to 970 m^2/g for xerogels with phenylene bridges [15, 16, 24, 60]. The type of isotherms of these xerogels depends, in the first place, on the nature of functional groups. In the case of amine groups the isotherms for xerogels with ethylene bridges are S-shaped and have a distinct hysteresis loop (in contrast to xerogels with phenylene bridges) while isotherms in the second case are more likely to be Langmuir isotherms. This difference is brought about by the nature of a medium that is created by these groups during the synthesis. It was shown [15, 16, 24, 60] that the parameters of the porous structure of such xerogels were substantially affected by the nature of a spacer, relative size of the functional group, ratio of reacting alkoxysilanes and gel ageing time. Finally it should be noted that these xerogels as a rule have narrow PSD curves.

Thus, taking into account the above-mentioned factors, it is possible to obtain FPX with controlled porosity, surface layer composition and loading of functional groups.

14.4.2 Adsorption Properties of FPX

Parish and coworkers [62] studyingin 1989 the adsorption of Ni(II), Co(II), Cu(II) and Zn(II) by amino-containing xerogels showed that an equilibrium in such systems is reached at least in 15 h. It is interesting that an increase of solution temperature (up to 50°C) causes significant decreases in the time of attainment of sorption equilibrium (up to 5 min) and at the same time increases the degree of gold extraction by xerogels whose surface layers contain thiourea and thiourea/amine groups [61]. However, even at optimal sorption conditions a part of xerogels' functional groups does not take part in complex formation [21, 62, 63, 64]. This is confirmed by HCl acid adsorption by amino-containing xerogels [65]. However, as was shown for the Cu(II) adsorption from acetonitrile solutions, almost all the amino groups are accessible for metal ions (adsorption time was 48 h) [56, 58].

It was shown that a separation of Ni(II) and Cu(II) is possible for xerogels with bifunctional surface layer (ethylenediamine and vinyl groups) [63]. In [61] attention has been given to sorption of microquantities of Au(III) from acidic solutions by xerogels whose surface layers contain thiourea and thiourea/amine groups. It has been found that the maximum degree of extraction of Au(III) is typical for the sorbent with a bifunctional surface layer. The same xerogel also has a high efficiency in sorbing mercury(II) from acidic solutions [47]. Hg(II) ions could be effectively extracted from their acidic solutions by xerogels with monofunctional surface layer containing thiol groups [66]. Good extraction of mentioned ions from their acidic solutions (pH $\sim$ 2) was achieved also for the xerogels that contain 3-mercaptopropyl and alkyl groups. The influence of surface layer's composition and pore structures' parameters of such xerogels on their complexing properties towards Hg(II) was studied in detail [66]. It was also found that xerogels which were functionalized by 3-mercaptopropyl groups have a high efficiency in sorbing Ag(I) ions [67, 68]. In [69] the sorption properties of silicas with mono- and bifunctional surface layers containing the complexing fragment $\equiv Si(CH_2)_3NHP(S)(OC_2H_5)_2$ were studied. It was found that xerogels can extract Hg(II) ions from acidified solutions (up to 450 mg/g).

Xerogels containing the phosphonic acid residues $\equiv Si(CH_2)_2P(O)(OH)_2$ sorbed uranyl and lanthanide ions from their nitrate solutions [69]. The resulting surface complexes contained two (for the UO_2^{2+} ion) or three inner-sphere ligand groups (for the Nd^{3+} and Dy^{3+} ions). Adsorptivity of such xerogels relative to *n*-hexane, triethylamine and acetonitrile was also investigated [70].

It was shown [37, 71] that xerogels with calixarene groups could adsorb Cs(I) ions from acidic aqueous solutions (1 M HNO_3). The adsorption equilibrium in the system is reached in less than 1 h. It was determined that the increase of functional groups contained leads to the increase of Cs(I) sorption degree. However, no more than 10–40% of functional groups takes part in Cs(I) extraction process [37].

14.5 Conclusion

Taking into account the presented results on sorption of metal ions as well as the results obtained by other authors [72, 73] especially by Voronkov's team [5, 74], it was possible to assert the significant perspectives of the usage of functionalized polysiloxane xerogels in sorptive technology and analytical chemistry.

Acknowledgements The author would like to acknowledge the partial financial support of NATO (Grant SfP–978006) and the Ministry of Education and Science of Ukraine for this work.

References

1. Zub YuL, Parish RV (1996) Functionalized polysiloxane sorbent: preparation, structure, properties and use. Stud Surf Sci Catal 99: 285–299
2. Melnyk IV, Dudarko OA, Stolyarchuk NV et al (2007) Polysiloxane xerogels with bifunctional surface layer. In: Shpak AP, Gorbyk PP (eds) Physico-chemistry of nanomaterials and supramolecular structures. Naukova Dumka, Kyiv

3. Zub YuL (2008) Design of functionalized polysiloxane adsorbents and their environmental applications. In: Innocenzi P, Zub YuL, Kessler VG (eds) Sol–gel methods for materials processing. Springer, Dordrecht
4. Slinyakova IB, Denisova TI (1988) Organo-silicon adsorbents: production, properties, and application (in Russ). Naukova Dumka, Kyiv
5. Voronkov MG, Vlasova NN, Pozhidaev YuN (2000) Organosilicon ion-exchange and complexing adsorbents. Appl Organometal Chem 14: 287–303
6. Chuiko AA, Pavlik GYe, Budkevich GB et al (1966) A method of preparation of silica gels containing aminoalkyl groups (in Russ). USSR Certificate of Authorship No 182719
7. Zub YuL, Gorochovatskaya MYa, Chuiko AA et al (1992) Polysiloxane matrices with functional groups as a basis of new sorbents. Ext Abstr Fourth Int Conf 'Fundamentals of Adsorption' (Kyoto, Japan) 461–463
8. Stechenko OV, Yurchenko GR, Matkovskii OK et al (2000) Adsorption properties of some polyaminosiloxanes. Sci Reports of Uzhgorod Univ (Ser 'Chemistry', in Ukrainian) 107–112
9. Matkovskii OK, Yurchenko GR, Stechenko OV et al (2000) Influence of solvent nature on structure-adsorption characteristics of poly(3-aminopropyl)siloxane. Sci Reports of Ternopil Univ (Ser 'Chemistry', in Ukrainian) 40–45
10. Zub YuL, Chuiko AA (2006) Salient features of synthesis and structure of surface of functionalized polysiloxane xerogels. In: Bergna HE, Roberts WO (eds) Colloidal silica: fundamentals and applications. CRC Press, Boca Raton
11. Zub YuL, Melnyk IV, Stolyarchuk NV et al (2006) Synthesis of functionalized polysiloxane xerogels, structure of their surface layer and sorption properties. Chem Phys Technol Surf (in Russ) 11–12: 165–203
12. Zub YuL, Drozd LS, Chuiko AA (1993) Factors influencing the porous structure of polyorganosiloxanes. Abstr IUPAC Symp 'Characterization of Porous Solids' (Marseille, France) 95
13. Stechenko OV, Zub YuL, Parish RV (1998) Polyaminosiloxane adsorbents: preparation and properties. Proc 3rd Int Symp 'Effects of Surf Heterogeneity in Adsorp and Catal on Solids' (Torun, Poland) 231–232
14. Zub YuL, Chuiko AA, Stechenko OV (2002) Synthesis, structure and structure-adsorption characteristics of some polyamonisiloxanes. Reports of NAS of Ukraine (in Russ) 150–155
15. Zub YuL, Chuiko AA, Stolyarchuk NV et al (2005) New amine-containing adsorbents on the basis of bridged polysilsesquioxanes. Reports of NAS of Ukraine (in Russ) 117–122
16. Dabrowski A, Barczak M, Stolyarchuk (Shvaykovska) NV et al (2005) Bridged polysilsesquioxane xerogels functionalizated by amine- and thiol-groups: synthesis, structure, adsorption properties. Adsorption 11: 501–517
17. Zub YuL, Melnyk IV, Chuiko AA et al (2002) Design of functionalized polysiloxanes: synthesis and investigation of sulfur-containing xerogels with mono- and bifunctional surface layer. Chem Phys Technol Surf 7: 35–45
18. Gona O, Melnyk IV, Zub YuL (2006) New mesoporous adsorption materials with $\equiv Si(CH_2)_3NHC(S)NHC_2H_5$ functional group in surface layer. Chem Phys Technol Surf (in Russ) 13: 87–98
19. Melnyk IV, Stolyarchuk NV, Zub YuL et al (2006) Polysiloxane xerogels containing arch-fixed urea groups. J Appl Chem (in Russ) 79: 992–997
20. Yang JJ, El-Nahhal IM, Maciel GE (1996) Synthesis and solid-state NMR structural characterization of some functionalized polysiloxanes. J Non-Cryst Solids 204: 105–117
21. Parish RV, Habibi D, Mohammadi V (1989) Insoluble ligands and their applications II. Polysiloxane-phosphine ligands, their complexes, and hydrogenation catalysts. J Organometal Chem 369: 17–28
22. Melnyk (Seredyuk) IV, Zub YuL, Chuiko AA et al (2002) Novel polyorganosiloxane xerogels with a bifunctional $\equiv Si(CH_2)_3SH/\equiv Si(CH_2)_3NH_2$ surface layer. Chem Phys Technol Surf 8: 125–133

23. Dobryanska HI, Melnyk IV, Zub YuL et al (2006) The influence of the $Si(OC_2H_5)_4$/$(CH_3O)_3Si(CH_2)_3SH$ ratio on the structure-adsorption characteristics of xerogels formed and accessibility of functional groups in their surface layers. J Phys Chem (in Russ) 80: 1071–1077
24. Zub YuL, Stolyarchuk NV, Melnyk IV et al (2005) New adsorbents based on bridged polysilsesquioxanes containing 3-mercaptopropyl functional groups. Mendeleev Commun 15: 168–170
25. Stolyarchuk NV, Melnyk IV, Zub YuL et al (2009) Bridge polysilsesquioxane xerogels with a bifunctional surface layer of the $\equiv Si(CH_2)_3NH_2/\equiv Si(CH_2)_3SH$ composition. Protect Metals Phys Chem Surf 45: 183–190
26. Dobryanskaya GI, Zub YuL, Barczak M et al (2006) Synthesis and structure-related adsorption characteristics of bifunctional polysiloxane xerogels with methyl and 3-mercaptopropyl groups. Colloid J (in Russ) 68: 548–557
27. Dobryanskaya GI, Melnyk IV, Zub YuL et al (2007) Porous xerogels with bifunctional surface layer of $\equiv Si(CH_2)_3SH/\equiv Si(CH_2)_2CH_3$ composition. J Phys Chem (in Russ) 81: 410–417
28. Chuiko AA, Pavlik GYe, Neimark IYe (1964) Method of preparation of organosilica gel. USSR Certificate of Authorship No 164680
29. Yashina NI, Zub YuL, Chuiko AA (1998) The synthesis of polyorganosiloxanes with the carboxyl groups on their surface. Abstr 3rd Polish-Ukrainian Symp 'Theor Experim Stud Interfacial Phenomena and Their Technol Application' (Lviv, Ukraine) 77
30. Prybora NA, Dzyubenko LS, Zub YuL et al (1999) Synthesis of the polysiloxane containing butyric acid residue on its surface layer. Collected Sci Papers of Nation Training Dragomanov Univ (Chem Sci, in Ukrainian) 41–47
31. Prybora NA, Zub YuL, Chuiko AA et al (2001) Synthesis and properties of some polycarboxylsiloxane sorbents. Abstr 2nd Int Conf on Silica Sci and Technol (Mulhouse, France) 171
32. Dudarko OA, Melnyk IV, Zub YuL et al (2005) Synthesis of polysiloxane xerogels using teraethoxysilane/(diethylphosphoneethyl)triethoxysilane system. Colloid J (in Russ) 67: 753–758
33. Dabrowski A, Barczak M, Dudarko OA et al (2007) Preparation and characterization of polysiloxane xerogels having covalently attached phosphonic groups. Polish J Chem 81: 475–483
34. Dudarko OA, Zub YuL, Semenii VYa et al (2007) The preparation of polysiloxane xerogels containing amide derivatives of phosphonic and thiophosphonic acids in the surface layer. Colloid J (in Russ) 69: 72–80
35. Dudarko OA, Zub YuL, Dabrowski A et al (2008) Polysiloxane xerogels with a bifunctional surface layer containing O/N, O/S, S/N and S/S donor centres. J. Appl Chem (in Russ) 81: 118–126
36. Kuchma OV, Zub YuL, Ryabov SV et al (2006) Hybrid organic–inorganic materials on a base of α- and β-cyclodextrins derivatives obtaining sol–gel method. Polym J (in Russ)28: 147–154
37. Kuchma OV, Zub YuL, Dabrowski A (2006) New sorption materials based on polysiloxane xerogels with incorporated calix[4]arene: synthesis and structure. Colloid J (in Russ) 68: 792–799
38. Kuchma OV, Zub YuL (2007) Hybrid polysiloxane matrixes with supramolecular surface layer: synthesis, structure, and properties. In: Shpak AP, Gorbyk PP (eds) Physico-chemistry of nanomaterials and supramolecular structures (in Russ). Naukova Dumka, Kyiv
39. Kuchma OV, Zub YuL (2006) Experimental approach to the synthesis of hybrid adsorbents on the basis of polysiloxane xerogels functionalized with calix[4]arenes and their derivatives. In: Loureiro JM, Kartel MT (eds) Combined and hybrid adsorbents: fundamental and applications. Springer, Dordrecht
40. Finn LP, Slinyakova IB (1975) Structure and thermodestruction of polyorganosiloxane xerogels using IR spectroscopy data. Colloid J (in Russ) 37: 723–729
41. Lin-Vien D, Colthup NB, Fateley WG et al (1991) The handbook of infrared and Raman characteristic frequencies of organic molecules. Academic Press, San Diego

42. Li L, Liu X, Ge Y et al (1991) Interaction and pillaring of zirconium bis(monohydrogenphosphate) with $NH_2(CH_2)_3Si(OC_2H_5)_3$. J Phys Chem 95: 5910–5914
43. Okabayashi H, Izawa K, Yamamoto T et al (2002) Surface structure of silica gel reacted with 3-mercaptopropyltriethoxysilane and 3-aminopropyltriethoxysilane: formation of the S-S bridge structure and its characterization by Raman scattering and diffuse reflectance Fourier transform spectroscopic studies. Colloid Polym Sci 280: 135–145
44. Shimizu I, Okabayashi H, Hattori N et al (1997) 13C- and 1H-NMR and FTIR spectroscopic evidence for aggregate formation of organosilanes in toluene. Colloid Polym Sci 275: 293–297
45. Dudarko OA, Zub YuL, Jaroniec M (2009) The sol–gel method for preparation of polysiloxane xerogels containing carboxylic functionality. Chem Phys Technol Surf 15 (in press)
46. Caravajal GS, Leyden DE, Qquinting GR et al (1988) Structural characterization of (3-aminopropyl) triethoxysilane-modified silicas by silicon-29 and carbon-13 nuclear magnetic resonance. Anal Chem 60: 1776–1786
47. Melnyk IV (2002) Synthesis and investigation of polyorganosiloxanes with bi- and trifunctional surface layer (Thesis for PhD Degree, in Ukrainian). ISC of NAS of Ukraine, Kyiv
48. Trofimchuk AK, Kuzovenko VA, Melnyk IV et al (2006) Comparison of complexing ability of bifunctional polysiloxane xerogels and chemical modified silica gels. J Appl Chem (in Russ) 79: 230–236
49. Zub YuL, Melnyk IV, White MG et al (2008) Structural features of surface layers of bifunctional polysiloxane xerogels containing 3-aminopropyl groups and 3-mercaptopropyl groups. Adsorp Sci Technol 26: 119–133
50. Stolyarchuk NV, Melnyk IV, Dobryanskaya GI et al (2007) A magic angle spinning NMR study of xerogels with functionalized by 3-mercaptopropyl groups. J Phys Chem (in Russ) 81: 1070–1075
51. Maciel GE (1998) NMR characterization of functionalized polysiloxanes. In: Ando I, Asakura T (eds) Solid state NMR of polymers. Elsevier, Amsterdam
52. Dudarko OA, Melnyk IV, Zub YuL (2006) Template synthesis of mesoporous silicas containing phosphonic acid derivatives in their surface layer. Inorg Mater (in Russ) 42: 413–420
53. Cardenas A, Hovnanian N, Smaihi M (1996). Sol–gel formation of heteropolysiloxanes from diethylphosphatoethyltriethoxysilane and tetraethoxysilane. J Appl Polym Sci 60: 2279–2288
54. Aliev A, Ou DL, Ormsby B et al (2000) Porous silica and polysilsesquioxane with covalently linked phosphonates and phosphonic acids. J Mater Chem 10: 2758–2764
55. Engelhardt G, Michel D (1987) High-resolution solid-state NMR of silicates and zeolites. Wiley, Chichester
56. Stechenko OV, Yakubovich TM, Teslenko VV et al (1997) Study of copper(II) absorption by some polyaminosiloxanes from the acetonitrile solutions. Chem Phys Technol Surf (in Ukrainian) 2: 62–67
57. Stechenko YeV, Yakubovich TN, Teslenko VV et al (1999) Copper(II) adsorption from acetonitrile solutions by nitrogencontaining polysiloxanes. Chem Phys Technol Surf (in Russ) 3: 46–50
58. Stechenko OV, Yakubovich TN, Teslenko VV et al (2003) Copper(II) ions adsorption from acetonitrile solutions by polyaminosiloxane xerogel with bifunctional surface layer. Ukr Chem J (in Russ) 69: 19–24
59. Stolyarchuk NV, Melnyk IV, Zub YuL et al (2006) Copper(II) adsorption from acetonitryl solutions by aminocontaining bridged polysilsesquioxane xerogels. Reports of Donestk Univ (in Ukrainian) A: 283–288
60. Shvaikovska NV, Melnyk IV, Yurchenko GR et al (2004) Synthesis and structure–adsorption characteristics of bridged polysilsesquioxanes with aminopropyl groups. Chem Phys Technol Surf (in Russ) 10: 80–84

61. Melnyk IV, Demchenko VYa, Zub YuL et al (2003) Sorption of aurum(III) using polysiloxane xerogels functionalized with thiourea groups. Chem Phys Technol Surf (in Ukrainian) 9: 31–36
62. Khatib IS, Parish RV (1989) Insoluble ligands and their application. I. A comparison of silica-immobilized ligands and functionalized polysiloxanes. J Organometal Chem 369: 9–16
63. El-Nahhal IM, Parish RV (1993) Insoluble ligands and their applications III. Polysiloxane diaminoethane derivatives. J Organometal Chem 452: 19–22
64. Ahmed I, Parish RV (1993) Insoluble ligands and their applications IV. Polysiloxane-bis(2-aminoethyl)amine ligands and some derivatives. J Organometal Chem 452: 23–28
65. El-Nahhal IM, Chehimi MM, Cordier C et al (2000) XPS, NMR and FTIR structural characterization of polysiloxane-immobilized amine ligand system. J Non-Cryst Solids 275: 142–146
66. Dobryanskaya GI, Goncharik VP, Kozhara LI et al (2009) Complex formation involving Hg^{2+} ions on the surface of the polysiloxane xerogels functionalized by 3-mercaptoprophl groups. Coord Chem (in Russ) 35: 264–271
67. Stolyarchuk NV, Melnyk IV, Zub YuL (2006) Ag(I) cations sorption by thiolcontaining bridged polysilsesquioxane xerogels. Proc X Int Conf 'Theoretical Problems of Surface Chemistry, Adsorption and Chromatography' (in Russ) 236–241
68. Melnyk IV, Zub YuL, Veron E et al (2008) Spray-dried mesoporous silica microspheres with adjustable textures and pore surface homogenously covered by accessible thiol functions. J Mater Chem 18: 1368–1382
69. Dudarko OA, Goncharyk VP, Semenii VYa et al (2008) Sorption of Hg^{2+}, Nd^{3+}, Dy^{3+}, and UO_2^{2+} ions at polysiloxane xerogels functionalized with phosphonic acid derivatives. Protect Metals 44: 207–212
70. Dudarko OA, Yurchenko GR, Matkovskii OK et al (2007) Adsorption properties of polysiloxane xerogels containing residues of phosphonic acid in their surface layer. Reports of Donestk Univ (in Ukrainian) A: 221–224
71. Ilchenko NN, Kuchma OV, Zub YuL et al (2007) Cesium cation complexation by 25, 27-dihydroxycalix[4]arene-crown-6: computational study. THEOCHEM 815: 83–86
72. Dai S (2001) Hierarchically imprinted sorbents. Chem Eur J 7: 763–768
73. Collinson MM (1998) Analytical applications of organically modified silicates. Mikrochim Acta 129: 149–165
74. Pozhidaev YuN (2004) Carbofunctional polyalkylsilsesquioxanes with ion-exchange and complexing properties (Thesis for DSc Degree, in Russ). IrIC, SB of RAN, Irkutsk

Chapter 15
Influence of Silica Surface Modification on Fiber Formation in Filled Polypropylene–Copolyamide Mixtures

M.V. Tsebrenko, A.A. Sapyanenko, L.S. Dzyubenko, P.P. Gorbyk, N.M. Rezanova, and I.A. Tsebrenko

Abstract Influence of unmodified and dimethylsilylated nanosilicas on rheological characteristics and structure formation on melt flow of polypropylene–copolyamide blends was studied using differential thermal analysis, viscometry, and optical microscopy with statistical treatment of the microstructure data. Nanosilica has an influence on the parameters of melting and crystallization of polymer blend extrudates. Modified nanosilica with grafted dimethylsilyl groups is a more effective additive on fiber formation than unmodified nanosilica because of a stronger affinity to polypropylene. Optimal compositions of the polymer blends and optimal extrusion conditions of production of filled polypropylene microfibers were determined. It was shown that addition of nanosilicas to the polypropylene–copolyamide blends is an effective method to control the formation of microfibers.

15.1 Introduction

Materials based on ultrathin synthetic fibers (microfibers) are widely used in industry for precise purification of gases and liquids, production of fabrics, synthetic leather, etc. Production technology of microfibers is based on a specific fiber formation upon processing of polymer mixture melts. Under rheological forces one (fiber forming) of the polymers forms numerous microfibers in the second polymer matrix which are strictly oriented in the extrusion direction. Microfibers are extracted from the composite extrudates by dissolution of the matrix polymer using an appropriate solvent [1]. Structure formation in polymer blend melts can be controlled using different additives such as plasticizers, surfactants, and compatibilizers [2–4]. One of the important methods to control the structure of polymers and their mixtures and alloys is the use of highly disperse solid additives [5, 6]. It is known that the polymer extrudate structure is determined by microrheological processes in

M.V. Tsebrenko (✉)
Kiev National University of Technologies and Design, 2 Nemirovich-Danchenko Street, Kiev 01011, Ukraine
e-mail: mfibers@i.com.ua

A.P. Shpak, P.P. Gorbyk (eds.), *Nanomaterials and Supramolecular Structures*,
DOI 10.1007/978-90-481-2309-4_15,

the processing stage, the capability of polymeric dispersion phase and dispersion medium to be crystallized, and crystallization conditions. To develop the production technology of microfibers containing nanosized additives by the use of polymer blend melts, it is necessary to know features of the effects of these nanoadditives on the rheological properties of the melts, the structure and the phase transition of the polymer composites. Therefore the aim of this work was to study the effects of surface modification of nanosilica used as an additive in the fiber formation in the polypropylene–copolyamide mixtures.

15.2 Materials and Methods

A polypropylene–copolyamide (PP/CPA) mixture was studied at the 30/70 w/w ratio. Used isotactic PP is characterized by melting temperature $T_m = 168°C$ and melt viscosity of 420 Pa s at shear stress $\tau = 5.69 \times 10^4$ Pa. Copolyamide was a co-polymer of ε-caprolactam and salt –[NH-$(CH_2)_5$-CO-NH-$(CH_2)_6$-NH-CO-$(CH_2)_4$-CO]$_n$– at 1:1 ratio at $T_m = 166°C$ and melt viscosity of 630 Pa s at $\tau = 5.69 \times 10^4$ Pa. The effects of unmodified and modified nanosilica additives on the rheological characteristics and structure formation of the PP/CPA blend melts were studied. Nanosilicas A-300 and A-200 (pilot plant of the O.O. Chuiko Institute of Surface Chemistry, Kalush Ukraine, specific surface area $S_{BET} = 300$ and 240 m^2/g, respectively) and modified nanosilica MA-200 (A-200 modified by dimethyldichlorosilane hydrolyzed, $S_{BET} = 242$ m^2/g) were used as solid additives in fiber-forming PP at concentration $C_a = 0.5$, 1, 3, and 5 wt% (in PP). Before the use, unmodified nanosilicas A-300 and A-200 were heated in a muffler at 400°C for 2 h, and modified silica MA-200 was dried in an oven at 150°C for 2 h. The polymer mixtures were prepared using a combined screw-disk extruder. The melt viscosity was determined using a capillary viscometer of constant pressure. The melt elasticity was evaluated using a swelling value (B) of the extrudate mixtures annealed at 170°C for 5 min. The effects of additives on the spinnability of the PP/CPA mixture melts were characterized by the maximum possible spinning jet value (Φ_{Max}) defined as the ratio of maximum velocity of the stream being winded onto the bobbin to velocity of melt outgoing from the die. The structure formation on flow of the mixture melts was studied using optical microscopy with the statistical analysis of structures in the residue (average diameter of long and short fibers, and sizes of particles and films) after the extraction of CPA from the extrudates.

To identify the functionalities at the nanosilica surface the FTIR spectra were recorded over the 1000–4000 cm^{-1} range using a ThermoNicolet Nexus FTIR spectrophotometer.

To study regularities in the phase transitions in the polymer blends, thermograms of melting and crystallization were recorded using a Q-1500D (Paulik, Paulik & Erdey, MOM, Budapest) apparatus with TG-DTA (thermogravimetry with differential thermal analysis), platinum crucibles for ground polymer samples (190 mg in weight) and Al_2O_3 powder as a standard. The thermograms of melting were

recorded at a heating rate $\beta = 5°C/min$ at $T = 20-200°C$ and then the crystallization curves of the melts were recorded on cooling at $\beta = 1.5°C/min$. Temperatures of the beginning of melting (T_1), melting (T_m), the beginning of crystallization (T_3), crystallization (T_{cr}), the end of melting (T_2), $\Delta T_m = T_2 - T_1$, and crystallization (T_4), $\Delta T_{cr} = T_3 - T_4$ were determined using the thermograms (relative mean errors $\pm 2°C$).

The enthalpy of melting (ΔH_m) was calculated using calibration of the peak area with respect to *n*-aminobenzoic acid characterized by $\Delta H_m = 152$ J/g. The crystallinity degree (α) was determined on the basis of the enthalpy of melting of entirely crystalline polymer ($\Delta H_{m,c}$):

$$\alpha = \frac{\Delta H_m}{\Delta H_{m,c}} 100(\%).$$

15.3 Results and Discussion

The FTIR spectrum of A-300 (Fig. 15.1a) shows intense absorption bands linked to the OH-stretching vibrations of free surface silanols at 3750 cm^{-1} and adsorbed water and disturbed silanols at 2500–3700 cm^{-1} [7].

Besides the mentioned bands the FTIR spectrum of modified silica MA-200 (Fig. 15.1b) includes the CH-stretching vibration bands at 2800–3000 cm^{-1} that testify the presence of grafted dimethylsilyl functionalities.

The rheological investigations of ternary blends PP/CPA/A-300 showed that the viscosity of the filled mixture melts changes weakly at great values of the shear stress (τ) (Fig. 15.2a). Apparently, at low τ values a role of the hydrogen bonds between the silanol groups of silica nanoparticles and electron-donor O- and N-containing groups of CPA and dispersion interactions at the phase boundary PP/CPA/A-300 affect the melt structurization. Therefore the viscosity

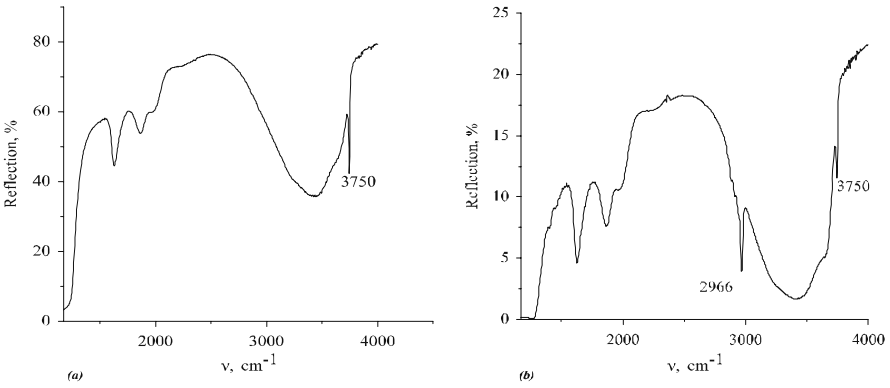

Fig. 15.1 FTIR spectra of (**a**) unmodified nanosilica A-300 and (**b**) modified nanosilica MA-200

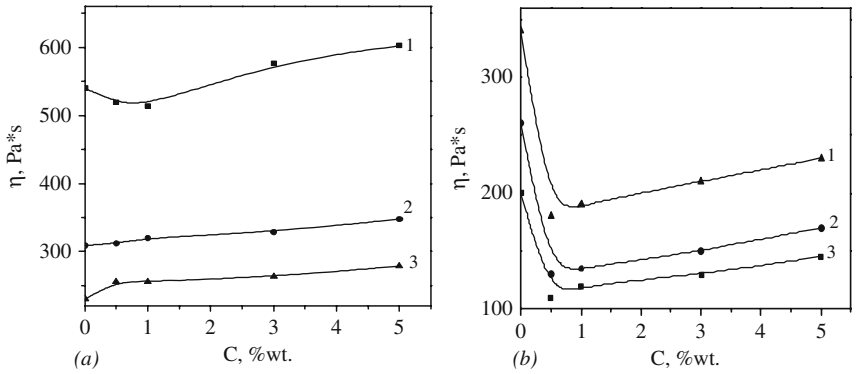

Fig. 15.2 Dependence of the melt viscosity on silica concentration for (**a**) PP/CPA/A-300 and (**b**) PP/CPA/MA-200 at τ of 1.62×10^4 Pa (curve *1*), 3.47×10^4 Pa (curve *2*), and 5.69×10^4 Pa (curve *3*)

of the mixture melts has a tendency to increase. On the processing of the mixture melts at $\tau \geq 5.69 \times 10^4$ Pa, an insignificant increase in the melt viscosity is observed.

The substitution of polar OH groups (A-200) for nonpolar dimethylsilyl groups at the silica surface (MA-200) enhances the affinity of nanosilica particles to PP macromolecules. This could lead to a more uniform nanoparticle distribution of silylated nanosilica in PP and, therefore, to improvement of the PP fiber formation in the CPA matrix. The character of the $\eta(C_a)$ dependence sharply changes for the PP/CPA/MA-200 mixture melts (Fig. 15.2) in comparison with PP/CPA/A-300, and the viscosity of PP/CPA/MA-200 decreases by a factor of 1.8–2 at $C_a = 0.5$ wt% (in PP). Subsequently the melt viscosity slightly increases with increasing content of MA-200 but it remains lower than that of unfilled PP/CPA blend, i.e., there is the thickening effect of the nanosilica additive. Thus, the obtained results allow us to conclude that the chemical nature of the silica additive surface noticeably influences the rheological properties of the PP/CPA mixture melts. Additionally, additive concentration affects such characteristics as swelling values of extrudates ($B(C_a)$) (Fig. 15.3) and maximum possible spinning jet value ($\Phi_{Max}(C_a)$) (Fig. 15.4). The $B(C_a)$ dependence for the ternary systems with unmodified and modified silicas has a maximum at $C_a = 1$ wt% (in PP) but for the mixtures with unmodified silica the B values are lower than that for the blends with modified silica at $C_a < 5$ wt% (in PP).

Previously [1] it was shown that the extrudate swelling value is an indirect characteristic of the fiber formation, since the greater the microfiber quantity and the thinner the fibers, the larger the swelling value. This is due to accumulation of high-elastic deformations at the fiber formation. Consequently, one can conclude that the MA-200 additive has certain advantages in comparison with unmodified nanosilica and its optimum content in the mixtures is close to 1 wt%. The improvement of the fiber formation with the presence of MA-200 is confirmed by results of the microscopic study (Table 15.1).

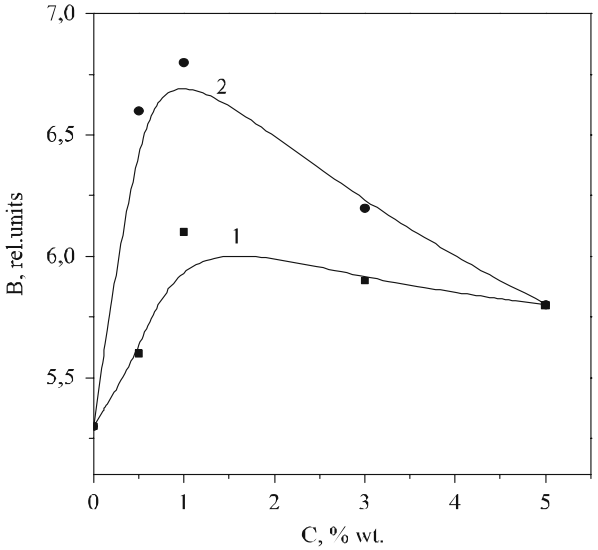

Fig. 15.3 Dependence of swelling value on content of silicas in blends PP/CPA/A−300 (*1*) and PP/CPA/MA−200 (*2*)

The Φ_{Max} value characterizes the capability of a melt for longitudinal deformation (i.e., spinnability). The $\Phi_{Max}(C_a)$ dependences for the mixtures with unmodified and modified silicas essentially differ (Fig. 15.4). The values of Φ_{Max} for streams with MA-200 are lower by two times in comparison with that for

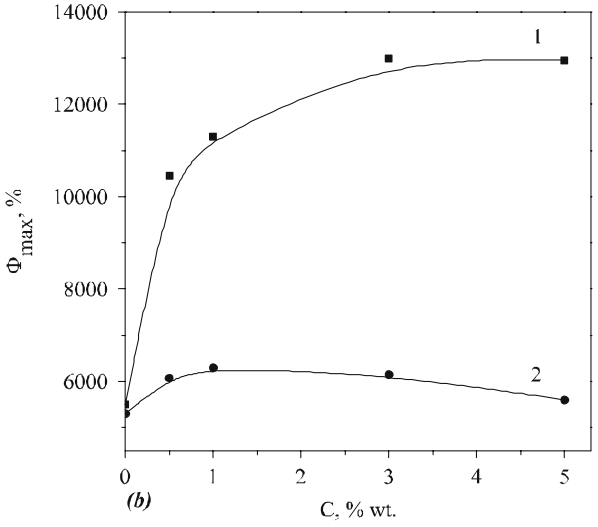

Fig. 15.4 Dependence of maximum possible of spinning draft value on silica content in blends: PP/CPA/A−300 (*1*) and PP/CPA/MA−200 (*2*)

Table 15.1 Microstructure characteristics of polypropylene–copolyamide (30/70 w/w) blends containing unmodified (A-200) or modified (MA-200) nanosilicas (1 wt% in PP)

Sample	*h*(mm)	Long fibers		Short fibers		Particles		Films	Fibrous cover
		d (μm)	*W* (%)	*d* (μm)	*W* (%)	*d* (μm)	*W* (%)	*W* (%)	*W* (%)
PP/CPA	4.8	4.0	57.6	3.2	2.8	4.1	0.1	30.0	19.5
PP/CPA/ A-200	4.8	3.6	60.8	3.2	7.2	4.7	2.8	21.4	7.6
PP/CPA/ MA-200	4.8	2.6	69.3	2.6	2.0	4.0	2.1	13.5	13.1
PP/CPA	6.0	3.9	69.4	3.1	14.0	4.05	0.7	15.9	–
PP/CPA/ A-200	6.0	2.6	74.1	2.3	2.9	3.1	0.8	14.5	7.7
PP/CPA/ MA-200	6.0	2.5	72.4	2.8	4.2	2.6	4.1	2.9	11.4
PP/CPA	9.0	The	films	are	structures		prevalent		
PP/CPA/ MA-200	9.0	1.5	80.0	2.1	5.0	2.1	1.0	6.0	8.0

h is the clearance size, *d* is the fiber diameter, *W* is the weight fraction of different PP structures, respectively.

streams containing silica A-300. This means that the streams containing A-300 are substantially strengthened in the longitudinal field stress due to strong interactions of surface silanols with electron-donor O- and N-containing functionalities of CPA. However, the durability of the stream containing MA-200 is lower because of weaker van der Waals forces between the methyl groups of modified silica and CPA macromolecules. Weakening of the stream (smaller Φ_{Max} values) of PP/CPA/MA-200 is also caused by its lower viscosity (Fig. 15.2).

Variation in the size of slit between mobile and stationary disks of an extruder is one of the methods to control the structurization of polymer mixture melts. On extrusion, tensile and shear stresses appear in the slit and their values increase with decreasing slit size. The smaller the slit size, the higher the dispersion degree, and achievement of a critical degree of the dispersion is more probable when the drops of the dispersed phase polymer become resistant to the tensile and shear stresses. Furthermore, as a result of heat generation in the disk zone the destructive processes can be enhanced. The mentioned phenomena are weakened with increasing slit size. The structure-formation data for the filled polymer mixtures (Table 15.1) reveal that the optimal slit size (*h*) from three tested ones is 9 mm. However, on the use of this slit size for the unfilled PP/CPA blend, the main structures in the extrudates correspond to film-like ones. As a result of thermodynamic incompatibility of PP and CPA, the interfacial layers between these polymers tend to be minimal because of weak interactions between the components. Therefore the stress appearing in the matrix on the polymer blend flow is non-passed entirely to drops of dispersed phase polymer and cannot deform them into streams. In this case for the fiber formation greater tensile and shear stresses are necessary that can be realized only at low slit sizes.

The effects of the chemical nature of the nanosilica surface and the slit size on the structure formation at the polymer mixture melt flow were evaluated on the basis of the quantitative data for the extrudate microstructures (Table 15.1). Obtained results testify that there are considerable effects of both unmodified and modified silica additives on the processes studied. The use of nanoadditives leads to an increase in weight fraction of long PP microfibers, a decrease in the mean diameter of PP microfibers and a quantity of films and particles, and appearing of external fine-fibrous cover (jacket) due to the migration processes. Comparison of the extrudate microstructure data for the systems containing A-200 and MA-200 confirms the advantages of the latter with respect to the efficiency of the fiber formation. Thus for the extrudates containing MA-200 and prepared at the slit size of 9 mm, the mean diameter of PP microfibers is minimal (1.5 μm) (Table 15.1). The improvement of the fiber formation for the blends containing MA-200 is explained by the affinity of silylated silica to PP due to high compatibility of their functionalities and much lower compatibility of polar CPA functionalities and nonpolar $=Si(CH_3)_2$ groups at the MA-200 particle surface. This effect is an indirect confirmation of the fact that a significant fraction of MA-200 particles is located at the interfacial layers and provides diminution of the interfacial tension. The interfacial tension (σ) was estimated from the kinetic data for fracture of a liquid cylinder in the matrix polymer using the Tomotika theory [8]. The σ value decreases from 2.4 mN/m for the PP/CPA (30/70 w/w) to 0.7 mH/m for the PP/CPA/MA-200 mixture at $C_a = 1$ wt%. This result reveals the surface activity of the additive (i.e., like to a surfactant) at the interfaces. From the obtained data, the optimal slit size is smaller for unfilled PP/CPA blend ($h = 4.8$ mm) than that for the filled blend ($h = 9$ mm), and the optimal content of nanoadditive is 0.5–1.0 wt% in PP.

It is known that the polymeric extrudate structure is determined not only by the microrheological processes at the processing stage but also by the capability of polymers of the dispersed phase and the dispersion medium to be crystallized and by conditions of their crystallization. Thermograms of melting and crystallization of extrudates of the binary and ternary mixtures of polymers are shown in Fig. 15.5. The melting peaks linked to melting of both polymers are weakly intensive since the extrudates were obtained on fast cooling in water and the crystallization under these conditions led to a low degree of crystallinity. It should be noted that there are additional low-temperature peaks of PP crystallization for both binary and ternary blends. This result is explained by disperse state of PP (microfibers of different diameters). Thinner PP streams are crystallized at lower temperatures than the streams of a greater diameter. The third low-temperature peak of PP crystallization (Fig. 15.5) can be linked to a PP fraction located at the interfaces and forming superthin fibrils at a fiber surface.

Analysis of the DTA data revealed that a certain narrowing of the melting temperature range (ΔT_m) for unfilled and filled PP/CPA mixtures in comparison with PP is due to an increase in temperature of the beginning of melting (Table 15.2). The reason for the latter is changes in the PP crystallization with the presence of a solid CPA fraction crystallized before PP on the preparation of these composites by the extrusion method. The ΔT_m range depends weakly on

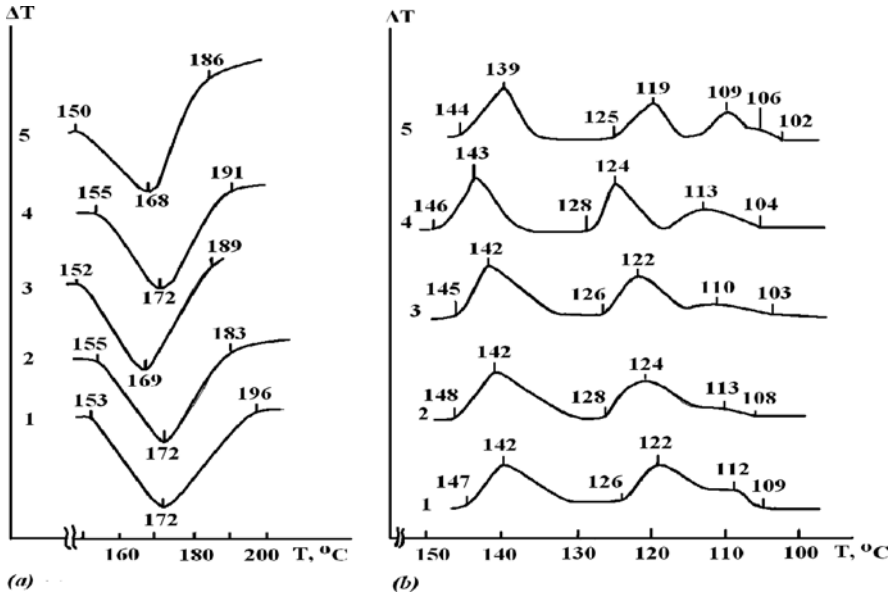

Fig. 15.5 Thermograms of (**a**) melting and (**b**) crystallization of PP/CPA (30/70 w/w) mixtures prepared at the slit size $h = 4.8$ (curves *1–3*), 6.0 (*4*), 9.0 mm (*5*) for PP/CPA (*1*), PP/CPA/A-200 (*2*), and PP/CPA/MA-200 (*3–5*) at $C_a = 1$ wt% in PP

the slit size, and the smallest ΔT_m values are for the compositions with MA-200 (Table 15.2).

An increase in the T_3 and T_4 values for the mixtures in comparison with individual PP observed on the thermograms of crystallization is regular since PP crystallizes at a surface of earlier crystallized CPA.

Addition of nanosilica changes the phase transitions in the PP/CPA mixtures, and on the addition of MA-200 an additional low-temperature peak of crystallization appears at 106°C that corresponds, apparently, to crystallization of PP in the interfacial layer. The temperature range of the PP crystallization in the ternary blends is expanded in comparison with the binary blend. This effect can be explained by finer dispersing of PP at the presence of nanosilica, i.e., the improvement in the PP fiber formation in the CPA matrix. The PP crystallinity degree in the binary mixture is lower than that for PP alone (Table 15.2) that is linked to disperse state of PP in the mixture. The fiber formation is low at $h = 9$ mm, PP is not in maximum disperse state, and the PP crystallinity degree (Table 15.2, α) increases to 60%. This value is much higher than that for PP alone and for PP/CPA mixture at $h = 4.8$ mm. These results can be explained by the fact that for the binary mixture obtained at $h = 9$ mm orientational crystallization is enhanced due to aggravation of fiber formation. On addition of nanosilica to the binary mixture the fiber formation is improved and a great portion of PP is located in the interfacial layers. These factors lead to a decrease in the PP crystallinity. On the other hand, nanoparticles can be crystallization centers causing an increase in the α value (Table 15.2). Additionally, the

Table 15.2 Characteristics of melting and crystallization processes in polypropylene–copolyamide (30/70 w/w) mixtures containing unmodified (A-200) or modified (MA-200) nanosilica (1 wt% in PP)

		Melting				Crystallization				
Sample	h (mm)	T_1(°C)	T_m(°C)	T_2(°C)	ΔT_m(°C)	T_3(°C)	T_{cr}(°C)	T_4(°C)	ΔT_{cr}(°C)	α(%)
PP	4.8	142	169	188	46	124	114	103	21	43.1
PP/CPA	4.8	153	172	196	43	126	122 112	109	17	38.0
PP/CPA	9.0	150	171	190	40	127	121 112	109	18	60.1
PP/CPA/A-200	4.8	155	169	189	44	128	124 113	108	20	56.7
PP/CPA/MA-200	4.8	152	172	189	37	126	122 110	103	23	40.1
PP/CPA	6.0	152	170	188	36	127	123 111	106	21	46.5
PP/CPA/A-200	6.0	153	170	190	37	126	121 110	106	20	44.2
PP/CPA/A-200	9.0	153	171	192	41	128	123 109	106	22	40.4
PP/CPA/MA-200	9.0	150	168	186	34	125	119 109 106	102	23	41.2

orientational processes on deformation of PP drops in the liquid streams play a certain role.

15.4 Conclusion

Modified nanosilica MA-200 with grafted dimethylsilyl groups more effectively influences on the fiber formation in the polypropylene–copolyamide mixture melts in comparison with unmodified nanosilica. The processing of the polypropylene/copolyamide/MA-200 mixture melts allows us to obtain polypropylene microfibers of 1.5 μm in diameter. The improvement of the fiber formation is explained by a better affinity of silylated silica to polypropylene than that of unmodified silica that is also confirmed by reduction of the interfacial tension. Substitution of surface silanols for dimethylsilyl groups affects on the microrheological processes that lead to changes in the macrorheological characteristics (viscosity, elasticity, capability for longitudinal deformation) of the polypropylene–copolyamide mixture melts. However, unmodified silica additives do not substantially change the melt viscosity of the blends. Addition of 0.5–1.0 wt% of silylated nanosilica to polypropylene diminishes the viscosity of the polypropylene–copolyamide mixture melts by a factor of 1.8–2.0 because of the improvement in the polypropylene fiber formation in the copolyamide matrix. In this case an additional low-temperature peak appears in the thermograms that corresponds to polypropylene crystallization in the interfacial layers. Thus the use of nanosilica additives with the different nature of surface functionalities is the effective method to control the fiber formation in the polypropylene–copolyamide mixture melts.

References

1. Tsebrenko MV (1991) Ultra-thin synthetic fibers. Khimiya, Moscow (in Russian).
2. Xu SA, Tjong SC (2000) Effect of compatibilizer content on the tensile properties and fracture toughness of high density polyethylene/polystyrene blends. J Polym 32: 208–214.
3. Rezanova VG, Tsebrenko MV (2008) Influence of binary additives of compatibilizers on the micro-and macrorheological properties of melts of polypropylene–copolyamide mixtures. J Phys Thermophys 81: 766–771.
4. Strobl GR (1996) The physics of polymers concepts for understanding their structures and behavior. Springer, Dordrecht.
5. Malysheva TL (2005) Wonders and technologies of the era of “clever” textile. Rev Market 471: 194–201 (in Russian).
6. Sreekala MS, Lehmann B, Freedrich R, Rony MZ (2006) Nanosilica reinforced polypropylene composites: microstructural analysis and crystallization behavior. Int J Polym Mater 55: 577–594.
7. Legrand LP (ed) (1998) The surface properties of silicas. John Wiley & Sons, New York.
8. Tomotika S (1935) On the stability of a cylindrical thread of a viscous liquid surrounded by another viscous fluid. Proc R Soc A 150: 322–337.

Chapter 16
Synthesis and Characterisation of Hollow Spherical Nano- and Microparticles with Silica and Magnetite

P.P. Gorbyk, I.V. Dubrovin, and Yu.A. Demchenko

Abstract The main principles and methods of synthesis of hollow structures with inorganic nanomaterials are described. Synthesis of hollow spherical silica particles was based on hydrolysis of $Si(CH_3)_2Cl_2$ and $SiCl_4$ in nonpolar solvents at a surface of aerosol drops. To synthesise hollow magnetite nano- and microparticles with magnetite, saturated solution of iron chlorides in acetone was used. Phase and element composition, morphology and structure of samples were studied using XRD, Auger electron spectroscopy, scanning electron and atom force microscopies.

16.1 Introduction

Hollow spherical particles with inorganic nanomaterials have prospective uses for industrial and biomedical purposes. Artificial porous or nonporous inorganic structures composed of hollow nanoparticles or microparticles can be used as hosts for encapsulated supramolecular compounds, therapeutic preparations based on polypeptides, antibodies, enzymes, nucleic acids, nanoparticles of different origin, magnetic fluids, chemical reactants, etc. Simultaneous destruction of a mixture of hollow particles containing different compounds can give intermediate or final products of certain technological processes [1, 2]. Application of hollow spherical particles possessing magnetic properties expands functional possibilities and area of practical utilisation of such materials. For instance, magnetically controlled movement of nanosized hollow particles used as highly efficient immunomagnetic sorbent and drug delivery system can be directed to tumour cells or injured organs and then particles can be magnetically fixed there.

Synthesis of hollow inorganic nanomaterials with the spherical geometry of particles and their characterisation were described in detail by many authors [3–11,

P.P. Gorbyk (✉)
O.O. Chuiko Institute of Surface Chemistry of the National Academy of Sciences of Ukraine, General Naumov St. 17, Kyiv 03164, Ukraine
e-mail: pgorbyk@mail.ru

A.P. Shpak, P.P. Gorbyk (eds.), *Nanomaterials and Supramolecular Structures*,
DOI 10.1007/978-90-481-2309-4_16,

13–25]. The formation of these ordered structures was controlled using special templates such as different organic compounds forming micelles and certain elements of dispersions or emulsion tending to reduce the surface area of the interfaces with hydrophilic and hydrophobic phases.

The aim of this work was to develop synthesis methodology of hollow spherical particles containing silica and magnetite at the interfaces of liquid aerosol drops with a certain vapour phase, to study regularities governing the formation of hollow particles, their phase and element compositions, morphology and structure depending on reaction and treatment conditions.

16.2 Synthesis Methodology of Hollow Spherical Nano- and Microparticles

The following points can be considered as a certain basis of worked-out synthesis methodology applied to preparation of hollow spherical particles:

- formation of hollow spherical particles can be carried out using chemical interactions of certain precursors at the interfaces of gas (vapour)–liquid phases which have a spherical shape, e.g. liquid aerosol drops in a certain gaseous phase;
- these chemical reactions should lead to the formation of poorly dissolved or insoluble compound or its precursor as the basis of formed stable walls of hollow particles.

For these purposes the use of chemical interactions at the fluid–gas (vapour) and liquid–liquid interfaces is the frequently applied technological method [1–3]. The formation of a separation layer due to sorption of inorganic compounds at a surface of spherical polymeric globules is used more rarely [4]. Preparation of porous and hollow ceramic particles can be based on sol–gel technology frequently used in combination with the emulsion method [5–11, 13]. During the synthesis particular attention should be focused on a choice of conditions appropriate to control changes in the form, size and some other characteristics of hollow particles prepared from different materials.

As a rule, removal of an organic template is carried out by thermal annealing of particles. However, re-crystallisation at high temperatures can lead to a decrease in the specific surface area of the materials, disappearance of narrow pores and changes in the functional properties [14].

The utilisation of volatile solvents can allow the synthesis without burn-out of organic components from the internal volume of spheres at high temperatures. This, in turn, makes it possible to preserve the native properties and characteristics of the synthesised materials.

The existing methodologies of hollow spherical particles formation do not allow implementation of constant control for regulating the shell thickness and porosity and are characterised by a low productivity. All these circumstances limit practical utilisation of these materials.

The synthesis of hollow spherical silica particles can be carried out using interaction of water vapour with aerosol drops containing the solution of dimethyldichlorosilane or silicon tetrachloride in a nonpolar organic solvent (heptane or carbon tetrachloride). These chlorides widely used in the industry are characterised by a low boiling temperature and can easily interact with water forming the Si−OH and Si−O−Si bonds and corresponding oligomers at the surface of aerosol drops. The intermediate products of the reaction transform at the surface of the drops into ultrafine silica particles which aggregate in the surface layer of drops to form a precursor of the walls of hollow particles.

For manufacturing of hollow spherical particles with magnetite, aerosol drops were prepared from a mixture of acetone solution of salts of di- and trivalent iron, and 25% aqueous solution of ammonia was used to form the vapour phase interacting with the drops. Magnetite was formed due to chemical reactions of the mentioned components in the surface layers of the aerosol drops transferred into the vapour phase of the ammonia solution. After removal of solvents, residual reactants and low molecular products, inorganic thin-walled spherical nano- or microparticles remained hollow.

16.3 Experimental

16.3.1 Installation for Synthesis

To synthesise hollow spherical particles of silica and magnetite, a specific installation (Fig. 16.1) was worked out.

The installation includes an ultrasonic disperser and two columns. The active component hydrolysis reaction proceeds in the first column. The reaction results in formation of precursors of the compounds to be synthesised on the surface of

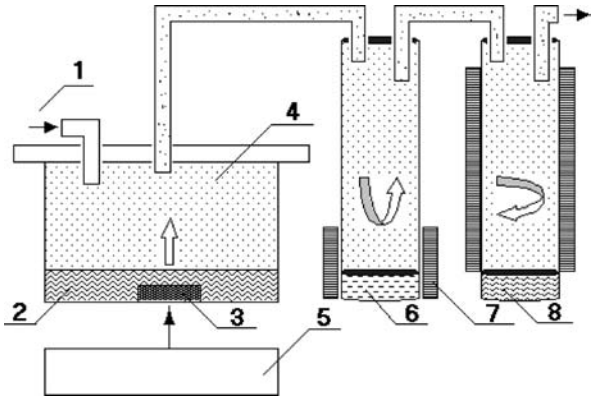

Fig. 16.1 Scheme of installation for synthesis of hollow oxide materials: (*1*) airflow; (*2*) mixture for dispersion; (*3*) ultrasonic emitter; (*4*) aerosol; (*5*) ultrasonic emitter; (*6*) water or ammonia solution; (*7*) heater; and (*8*) ethanol

aerosol drops. During the initial stage these precursors form walls of nanosized spheres. Formed particles are recovered, concentrated and dehydrated in the second column. Aerosol drop transport is carried out by dry airflow (1) at T= 293 K. The gas-carrier flow is controlled by rotameters. The stock solutions (2) are transformed into the aerosol state (4) using the ultrasonic disperser (3, 5) operated at 2.64 MHz. The aerosol liquid particle size is 0.1–5 μm. Partial pressure of water vapour (6) and temperature (293–313 K) in the reactor is controlled using heaters (7).

16.3.2 Synthesis Methodology

Such reactants as dimethyldichlorosilane and silicon tetrachloride rapidly react with water and form polydimethyl siloxane (PDMS) and silica by the reaction

$$n(CH_3)_2SiCl_2 + nH_2O \rightarrow (-(CH_3)_2Si-O-)_n \downarrow + 2n\text{HCl}, \tag{16.1}$$

$$SiCl_4 + 2H_2O \rightarrow SiO_2 \downarrow + 4\text{HCl}. \tag{16.2}$$

These compounds are quite appropriate because they are in the liquid state at 300 K and well dissolved in nonpolar (hydrophobic) solvents that allow the formation of aerosol at moderate pressure of saturate vapour. In our opinion, these circumstances can exclude the possibility of considerable supersaturation of the components in the vapour phase that could cause formation of silica nuclei out of the aerosol drop surface [1].

Any organic liquid chemically inert with respect to chlorosilanes (and the products of their hydrolysis) and immiscible with water can be used as a solvent for the active component to form the aerosol. Heptane or carbon tetrachloride was used as such a solvent. Concentration of silanes was changed in the 0–50 vol% range (at 5% step).

To synthesise hollow spherical magnetite nano- and microparticles, aerosol drops formed from the solution of the mixture of di- and trivalent (2:1) iron chlorides in acetone were transferred into the first column containing the vapour phase of 25% aqueous solution of ammonia at room temperature. Under these conditions the reactions resulting in the condensation of iron oxide in the surface layers of aerosol drops lead to the formation of magnetite:

$$2FeCl_3 + FeCl_2 + 4H_2O = Fe_3O_4 \downarrow + 8\text{HCl}. \tag{16.3}$$

The particles formed due to chemical reactions in the first column of the installation (Fig. 16.1) were transferred by the airflow to the second column with ethanol where they were collected. Then the synthesised product was separated from the residual solution by centrifuging and decantation after acetone washing to prevent (restrict) particle agglomeration. Residual water and solvents were eliminated by slow heating to 900 K at a heating rate of 0.003–0.01 K/s and at a low pressure of 1–10 Pa or in the oxygen flow over 620–920 K.

16.3.3 Characterisation Methods

The phase composition of the nanospherical materials prepared by evaporation of low-concentrated suspension of the particles on a polished surface of single-crystalline silicon was analysed using a DRON-3M (Burevestnik, St. Petersburg) diffractometer with Cu K_α ($\lambda = 0.15418$ nm) radiation and a Ni filter. Element composition of particles was studied using the Auger electron spectra recorded using a JAMP-10S (JEOL) spectrometer. The morphology of samples was studied using scanning electron microscopy (SEM) and atomic force microscopy (AFM). The specific surface area (S) of the synthesised materials was determined using adsorption of argon. The material density was determined using a pycnometer. The magnetic properties of spherical nano- and microparticles of magnetite were investigated using a magnetoelectric method (vibration frequency of a vibrator was 50 Hz).

16.4 Results and Discussion

Upon the synthesis of hollow spherical silica particles with silica in the first column (Fig. 16.1) the hydrolysis of one of the components in aerosol drops occurs in their surface layers. The radial gradient of concentration appearing with bonding of one of the components to the drop surface with subsequent growth of ultrafine particles with insoluble compound (e.g. silica) is the driving force of the formation of hollow spherical particles.

The water vapour excess at the boundary of the aerosol drops leads to the hydrolysis of total quantity of silane (dissolved in the hydrophobic solvent) located in restricted space of the surface layers and then its growth into the depth of the drops ceases. This is due to two circumstances: (i) the amounts of silane (dimethyldichlorosilane or silicon tetrachloride) did not exceed 40 wt%; therefore, the amount of the formed insoluble inorganic compound was sufficient only for building a relatively thin layer at the aerosol drop surface; and (ii) penetration of water into deeper layers of the drops of a hydrophobic solvent is restricted. Subsequent processes result in aggregation of the formed ultrafine particles into the surface oxide layers (i.e. walls of hollow particles) and their dehydration. Precipitation of aerosol particles occurs in the second column (Fig. 16.1). Primarily formed hollow spherical particles of silica gel filled with the liquid solvent (heptane, carbon tetrachloride) precipitate in ethanol (96%), and the processes of hydrolysis and coagulation are completed.

Figure 16.2 shows AFM image of nanosized PMDS particles deposited onto a flat single-crystalline silicon surface at the outlet from the first column and then dried at 300 K. It should be noted that these particles have an ellipsoidal shape because of significant elasticity of the particle walls formed at this synthesis stage and strained at the single-crystalline silicon surface. To prevent the strain of the hollow particles, their precipitation was carried out in anhydrous ethanol in the second column (Fig. 16.1). This preserves the spherical shape of the hollow particles. Additionally,

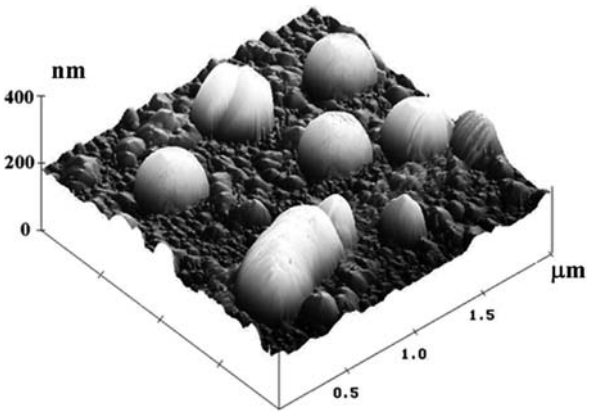

Fig. 16.2 AFM image of aerosol hollow silica particles

occurred partial dehydration of the particles leads to an increase in the mechanical strength of their walls.

The Auger electron spectra of hollow silica particles depict the presence of chlorine characterised by the weak intensity line due to residual chlorides of unknown compositions or adsorbed HCl. Complete removal of chlorine from silica particles occurs only upon annealing of the samples in the oxygen atmosphere at 623–773 K for 1 h. The XRD study of hollow spherical particles shows that silica is in the amorphous state.

According to SEM images, synthesised silica consists of hollow spherical particles (Fig. 16.3a) of 20–400 nm in diameter (*d*) and their wall thickness is equal to approximately *d*/10. Some spheres have partially destroyed walls revealing the

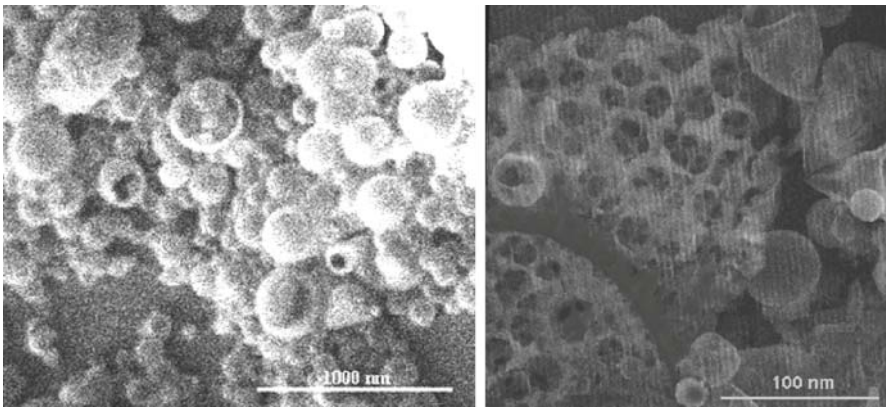

a b

Fig. 16.3 SEM images show (**a**) hollow spherical silica particles and (**b**) porous surface of hollow spherical particles of magnetite

empty internal space in particles. The specific surface area of the synthesised silica is about 40 m^2/g. According to the microscopic study, the volume of the internal voids in the hollow silica particles corresponds to 40–70% of their total volume and depends on the concentration of components upon synthesis. The bulk, true and apparent densities of this silica are equal to 0.27, 2.25 and 2.2 g/cm^3, respectively.

Separation of particles into fractions according to their sizes was carried out via sedimentation of the aerosol drops and the formed particles at the final stages of the synthesis. A study of the particle size distribution (PSD) of silica carried out using statistical treatment of electron-microscopic images showed that about 80% of the particles are 100 nm in diameter.

An increase in concentration of silane as an active component (C) in the dispersed mixture leads to an increase in the wall thickness of the hollow spherical particles and a decrease in the porosity of the walls. It should be noted that a considerable decrease in the fraction of correctly formed spheres was observed at $C \geq 40$ vol%. The maximum of the PSD curve shifted almost by 100 nm towards larger size with increasing velocity of the airflow from 5×10^{-5} to 5×10^{-4} m^3/s. These changes in the PSD can be caused by better transport of larger particles with increasing airflow velocity.

Intensive formation of agglomerates of the hollow silica particles occurs upon their storage in dispersion medium such as methyl isobutyl ketone or isopropyl alcohol. According to the electron-microscopic data, an isotropic type of agglomeration is inherent for the spherical silica particles.

The utilisation of the described methodology for synthesis of hollow spherical particles of magnetite yielded spheres of approximately 100 nm in diameter. Some large spheres had macropores in their walls through which smaller nanoparticles could penetrate into the internal volume and remain there due to strong intermolecular forces (mainly hydrogen bonding and dispersive interactions).

The thermogravimetric analysis of the materials shows that endothermic processes occur on heating due to removal of intact (< 400 K) and dissociatively adsorbed water (i.e. OH groups) and sublimation of NH_4Cl crystallites (610 K). The presence of NH_4Cl crystallites in magnetite particles is also confirmed by the XRD data. Annealing of spherical magnetite particles leads to formation of developed porous structure in the particle walls. Appearance of the pores (Fig. 16.3b) is due to removal of dendritic NH_4Cl crystallites formed on the synthesis of the material since sublimation of these crystallites begins at 610 K. The specific surface area of Fe_3O_4 samples was equal to approximately 80 m^2/g. This value is larger than the S value of the hollow silica particles because of the mentioned porosity of the walls of the magnetite particles.

The walls of the hollow spherical particles are formed on aggregation of primary ultrafine particles of magnetite. Subsequent partial re-crystallisation of Fe_3O_4 occurs on the formation of larger particles possessing more ordered crystalline structure. On low-temperature (323–393 K) treatment certain oxidation of the surface layer of magnetite occurs, and iron sesquioxide is formed. First of all this occurs

in amorphous surface layer that is confirmed by the Auger electron spectroscopy data. The study of the spectra in the low-energy range testifies to the presence of Fe_2O_3 at the particle surface. However, deeper layers in the walls of the hollow particles contain oxygen and iron at the stoichiometric ratio characteristic for magnetite.

The XRD analysis of magnetite samples heated at 10^{-1} Pa showed the presence of both amorphous and crystalline phases. The latter gives reflections at $2\theta = 30.1°$, 35.48° and 43.08° characteristic for magnetite. However, low intensity of these lines and the absence of other lines characteristic for the crystalline phases testify to the presence of a considerable quantity of amorphous iron oxide probably located in the surface layers of the particles. The lines characteristic for Fe_2O_3 (which can be formed on the synthesis of magnetite, its oxidation by atmospheric oxygen during washing, fractionation and drying) are absent; i.e. Fe_2O_3 is amorphous. This is in agreement with the Auger electron spectroscopy data revealing the presence of a thin surface layer of Fe_2O_3.

It is known [26, 27] that the dielectric–metal phase transition takes places for Fe_3O_4 at $T = 119-123$ K. At $T \approx 300$ K it is in the metallic state and has the electrical conductivity $\sigma = 10^3\ \Omega^{-1}\text{cm}^{-1}$. In the case of the spherical magnetite particles, the dc conductivity is low since $\sigma = 10^{-6}\ \Omega^{-1}\text{cm}^{-1}$. These results as well as the XRD and Auger electron spectroscopy data reveal that the synthesised material represents aggregates of Fe_3O_4 particles coated by a dielectric layer of Fe_2O_3 responsible for the low σ value.

Analysis of the magnetic characteristics of the synthesised magnetite spheres shows that the coercive force (H_c) has a value of 0.1 kOe. Therefore, one can assume that the prevailing quantity of Fe_3O_4 crystallites in hollow spherical particles corresponds to sizes smaller than 30 nm and these particles are in the superparamagnetic state [28, 29].

16.5 Conclusion

Physicochemical and technological conditions of the synthesis of hollow inorganic spherical nanomaterials based on silica and magnetite were determined. Hollow nanospheres of silica were synthesised using hydrolysis of dimethyldichlorosilane and silicon tetrachloride at a spherical surface of aerosol drops of organic hydrophobic solvents. About 80% of the hollow spherical particles are 100–300 nm in diameter. The hollow spheres of polycrystalline magnetite (from 40 nm to 10 μm in diameter) were synthesised using the reaction of di- and trivalent iron salts dissolved in acetone with the ammonia vapour at the spherical surface of aerosol drops. The wall thickness of the hollow particles was 10–20% of their outer diameter depending on the concentration of the active component (metal oxide precursor) dissolved in an organic solvent. The formation of pores in the walls of the hollow magnetite particles is due to the presence of dendritic NH_4Cl crystallites sublimating on heating of the material.

References

1. Gorbyk PP, Dubrovin IV, Spivak OA et al (2005) Synthesis of hollow nanospheres with silicon dioxide. Nanosyst Nanomater Nanotechnol 3:653–660.
2. Shen W, Zhu Y, Dong X et al (2005) A new strategy to synthesize TiO_2-hollow spheres using carbon spheres as template. Chem Lett 34:840–841.
3. Chen LY, Gu YL, Shi L et al (2004) A room-temperature approach to boron nitride hollow spheres. Solid State Commun 130:537–540.
4. Tan W, Wang K, He X et al (2004) Bionanotechnology based on silica nanoparticles. Med Res Rev 24:621–638.
5. Shu-Jiang D, Cheng-Liang Z, Mu Y et al (2006) Template synthesis of composite hollow spheres using sulfonated polystyrene hollow spheres. Polymer 47:8360–8366.
6. Shchukin DG, Ustinovich E, Sukhorukov GB et al (2005) Metallized polyelectrolyte microcapsules. Adv Mater 17:468–472.
7. Yong Z, Xintong Z, Jin Z et al (2008) Enhanced photocatalytic activity of hierarchically micro-/nano-porous TiO_2 films. Appl Catal B: Environ 83:24–29.
8. Radha G, Ashok K (2008) Bioactive materials for biomedical applications using sol–gel technology. Biomed Mater 3:034005 (15 pp).
9. Jiang P, Bertone JF, Colvin VL (2001) A lost-wax approach to monodisperse colloids and their crystals. Science 291:453–457.
10. Xinjian C, Min C, Limin W, Bo Y (2007) A novel and facile preparation method of hollow silica spheres containing small SiO_2 cores. J Polym Sci Part A Polym Chem 45: 3431–3439.
11. Dong C, Linlin L, Jianshu L et al (2007) Synthesis and self-assembly of monodisperse silver-nanocrystal-doped silica particles. J Colloid Interface Sci 308:351–355.
12. Jia H, Zhu G, Wang P (2003) Catalytic behaviors of enzymes attached to nanoparticles: the effect of particle mobility. Biotechnol Bioeng 84:406–414.
13. Strohm H, Löbmann P (2004) Assembly of hollow spheres by templated liquid phase deposition following the principles of biomineralisation. J Mater Chem 14:138–140.
14. Zhu Y-Z, Chen H-B, Wang Y-P et al (2006) Mesoscopic photonic crystals made of TiO_2 hollow spheres connected by cylindrical tubes. Chem Lett 35:756–757.
15. Aoi Y, Kambayashi H, Kamijo E, Deki Sh (2003) Synthesis of mesoscopic hollow spheres and inner surface functionalized hollow spheres of titanium dioxide by the liquid phase deposition method. J Mater Res 18:2832–2836.
16. Pei-Gen N, Bing-Ying C, Peng D, Dao-Zhong Z (2001) A novel titania membrane with uniform macropores. Chin Phys Lett 18:1610–1612.
17. Demchenko YuA, Gorbyk PP, Dubrovin IV, Filonenko MM (2008) Synthesis of hollow SiO_2 spheres. Proc. First International Scientific Conference "Nanostructural Materials – 2008" NANO-2008. April 22–25, 2008, Minsk, Belorussia Science, pp 660–661.
18. Shiho H, Kawahashi N (2000) Titanium compounds as coatings on polystyrene lattices and as hollow spheres. Colloid Polym Sci 278:270–274.
19. Wen P, Junwei Y, Guiling N, Yuan L, Jing W et al (2009) A novel synthesis of micrometer silica hollow sphere. Mater Res Bull 44:280–283.
20. Xinjun W, Fuquan W, Youjun G, Juan L, Kai J (2008) Synthesis of high-quality Ni2P hollow sphere via a template-free surfactant-assisted solvothermal route. J Cryst Growth 310: 2569–2574.
21. Ge C, Dingguo X, Zuoren N, Zhenyao W, Lei W, Lei Z, Jiujun Z (2007) Facile synthesis of Co− Pt hollow sphere electrocatalyst. Chem Mater 19:1840–1844.
22. Yun C, Zhen Q, Zhicheng Z (2007) Interface-initiated emulsion polymerization: synthesis of hollow sphere with a hole in the shell. Chem Lett 36:944–945.
23. Na L, Xing W, Hui C et al. (2007) Synthesis of a novel hollow sphere having rigid binaphthyl macrocycle as shell. Diffusion Defect Data Solid State Data Part B Solid State Phenom 121–123:219–222.

24. Yoshifumi A, Hisae K, Eiji K et al (2003) Synthesis of mesoscopic hollow spheres and inner surface functionalized hollow spheres of titanium dioxide by the liquid phase deposition method. J Mater Res 18:2832–2836.
25. Niu Z, Yang Z, Hu Z et al (2003) Polyaniline-silica composite conductive capsules and hollow spheres. Adv Funct Mater 13:949–954.
26. Phase DM, Tiwari Sh, Prakash R et al (2006) Raman study across Verwey transition of epitaxial Fe_3O_4 thin films on MgO (100) substrate grown by pulsed laser deposition. J Appl Phys 100:123703-123703-5.
27. Kirschvink JL, Jones DS, MacFadden BJ (eds) (1985) Magnetite biomineralization and magnetoreception in organisms. Plenum, New York.
28. Sun Sh, Zeng H, Robinson DB et al (2004) Monodispersed MFe_2O_4(M=Fe, Co, Mn) nanoparticles. J Am Chem Soc 126:273–279.
29. Gorbyk PP, Dubrovin IV, Filonenko MM (2007) Cryogenic synthesis of nanodimensional magnetite. Funct Mater 14:77–81.

Chapter 17
Synthesis of Silicon and Zinc Oxide Nanowhiskers and Studies of Their Properties

P.P. Gorbyk, I.V. Dubrovin, A.A. Dadykin, and Yu.A. Demchenko

Abstract The conditions and mechanisms for purposeful pattern formation on the surface of single-crystal silicon wafers by building up silicon or zinc oxide by the vapor–liquid–crystal (VLC) mechanism were studied. For the polished silicon surface we developed a procedure for preparation of areas with randomly distributed nanosized gold metal particles – whisker growth initiators. The arrays of randomly distributed silicon and zinc oxide whiskers were grown. The emission cells with a pointed surface pattern were fabricated. The morphology, structure, and field electron emission properties of the fabricated structures were studied.

17.1 Introduction

Development of new nanostructured materials for fabrication of highly efficient, economical, environment friendly, low-field cold electron emitters of large area is of interest for applied or pure scientific purposes [1]. The emitters of this kind may be used for production of flat displays, cathodoluminescent sources of light and other devices. Also they may be applied for brightening the liquid–crystal display images to ensure their intensity and contrast. Operating efficiency of the indicated devices depends substantially on the material's chemical composition and cathode's design features, in particular, on the surface pattern.

The required surface pattern may be prepared by ion or plasma treatment, thermal etching, vacuum deposition, selective chemical etching, or building-up of the specified surface structures [2]. For some time past, one of the intensively developing trends is concern for the growth of nanowhiskers, which are promising crystal nanomaterials with a unique set of properties [3, 4].

The indicated goals may be achieved with the use of highly attractive silicon and zinc oxide. These materials are widely used in phototechnique, optoelectronics, and

P.P. Gorbyk (✉)
O.O. Chuiko Institute of Surface Chemistry of the National Academy of Sciences of Ukraine, General Naumov St. 17, Kyiv 03164, Ukraine
e-mail: pgorbyk@mail.ru

A.P. Shpak, P.P. Gorbyk (eds.), *Nanomaterials and Supramolecular Structures*,
DOI 10.1007/978-90-481-2309-4_17,

semiconductor engineering [5–7]. However, until now the development of reproducible and relatively inexpensive processes for synthesis of silicon and zinc oxide nanowhiskers with a specified functionality remains very urgent.

In many respects a scope for practical use of whisker ensembles depends on perfection and reproducibility of growth technologies. Therefore the study of growth process for one-dimensional materials – nanowhiskers and nanowires – is one of priority trends in nanotechnology [8–10]. The unique properties of whiskers are due to a high ratio of their length and cross-dimensions. In our previous work we have established that the electron emission in the ZnO film structures with high ratio of geometrical measurements has occurred in fields that are about 2 orders lower than the theoretical values [11]. Therefore the synthesis of nanosized whiskers that are characterized by the maximum allowable values of this ratio will offer a possibility to fabricate patterns with the maximum performance. The growth mechanism of "vapor–liquid–crystal" type that was proposed by Wagner and Ellis [12] and generalized by Givargizov in the experiments on growing crystals on the silicon surface coated with a layer of activating gold [2] is generally accepted as a whisker formation mechanism.

The aim of this work is an analysis of conditions and mechanisms of changes in the silicon wafer surface patterns under chemical building-up of silicon and zinc oxide by the VLC mechanism, development of procedures for silicon and zinc oxide nanowhiskers, and analysis of their field emission properties versus their structure.

17.2 Experimental Procedures

Due to the complexity of fabrication of the identically oriented whisker systems in particular for flat-panel displays there is great interest in fabrication of regular structures consisting of elements with specified surface pattern by relatively simple methods (such as photolithography, thermal deposition with masks of various types). Also there is a certain interest in fabrication of cells with randomly distributed functional elements such as whiskers or tips. When the density of these elements is high it is more probable to achieve the optimal electrophysical parameters.

The regular areas coated with a gold film of about 5 nm in thickness (Fig.17.1) were produced on the (111) polished surface of silicon wafer by thermal deposition of gold through masks with regularly placed holes (about 100 μm) under a base pressure of about 10^{-5} Pa.

The wafer was heated in hydrogen atmosphere at a temperature of about 900°C. As a result the thin layer of liquid Au−Si alloy spontaneously coagulated to separated droplets of 10 nm−1 μm in size that were distributed with a surface density of about 10^7 cm^{-2}. This process was driven by diffusion and surface migration and resulted in a decrease in the cluster formation free energy.

The arrays of gold particles randomly distributed on the polished surface of Si wafers were also produced by sedimentation of gold colloid particles from carbon tetrachloride that well wets silicon surfaces. The colloid particles were synthesized

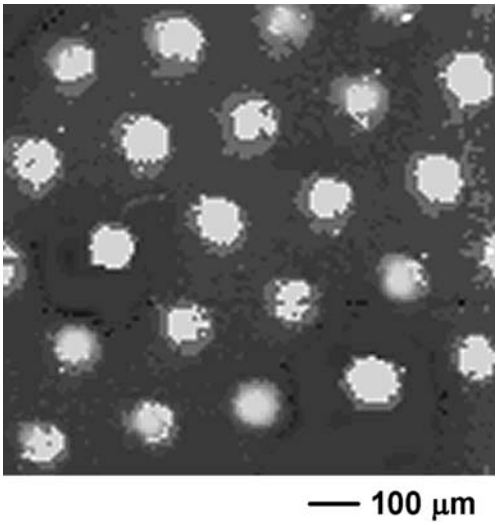

Fig. 17.1 SEM images of a gold film on the Si crystal surface

by reducing gold from strongly diluted solutions of chloroauric acid. Here colloidal solutions of different strong colors are produced. Upon addition of 0.0075% solution of $H[AuCl_4]$ to 0.005% solution of muriatic hydrazine the blue sol of gold was produced. When 0.005% solution of potassium carbonate was added to 0.0025% solution of $H[AuCl_4]$ and then tannin solution was poured by drops upon heating, the red sol was produced. According to AFM data the sol particles were 35–90 nm in size. The solutions' maximum optical absorption was shifted from 510 to 620 nm.

Synthesis of silicon and zinc oxide nanowhiskers was carried out in the process installation. Its block diagram is shown in Fig. 17.2. Silicon whiskers were

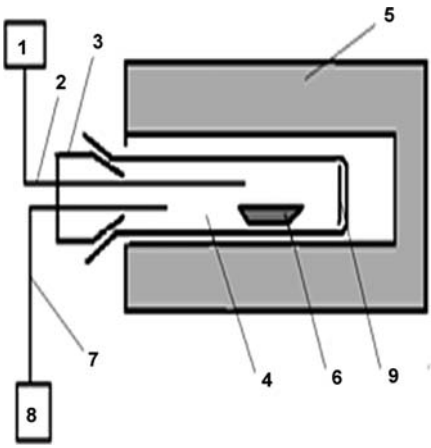

Fig. 17.2 Block diagram of the process installation for fabrication of silicon and zinc oxide nanowhiskers: *1* letting to gaseous components system, *2* gas nozzle, *3* joint, *4* alundum reactor, *5* electric oven, *6* ceramic boat, *7* gas withdrawal pipe, *8* water-lock, *9* substrate

grown on polished Si wafers coated with growth initiators (gold nanoparticles) at the temperature of about 900°C in the flow of $SiCl_4$, HCl, and hydrogen.

It should be noted that we also observed the growth of whiskers when the closed system with limited quantity of $SiCl_4$ had been used though the growth rate was lesser by an order of magnitude. In this case the gas phase must be replenished by silicon tetrachloride (and accordingly the solution-melt by silicon) due to interaction between the hydrochloric acid and nearby sections of the silicon substrate and formation of $SiCl_4$. In this case the formation of whiskers upon crystallization may be described by the following reactions:

$$12\,HCl + 3\,Si_{substrate} = 3\,SiCl_1 + 6\,H_2, \tag{17.1}$$

$$4\,AuCl_3 + 6\,H_2 = 4\,Au + 12\,HCl, \tag{17.2}$$

$$3\,SiCl_4 + 4\,Au = 3\,Si_{whisker} + 4\,AuCl_3. \tag{17.3}$$

The reaction equations (17.1–17.3) show that all components that participate in the transfer of silicon from the substrate to a whisker come back into the reaction zone.

Supersaturation of the produced solution-melt is removed by crystallization of the surplus silicon on the substrate surface. At that, the solution-melt acts as an off-beat whisker growth initiator and its zone ascends above the surface forming whiskers.

For growing zinc oxide whiskers (Fig. 17.2) the alundum reactor (4) was connected with a vacuum pump and a system for gases' purification and feeding. As a source material we used the pre-pressed tablets of zinc oxide. The tablets were laid into the alundum boat (6) and placed at the oven's central area. Before annealing the tablets of 5 mm in diameter and 1–5 mm in height were fabricated by cold pressing the zinc oxide powder of special purity grade. The synthesis was carried out in two stages. At the first stage the reactor was cleaned and growth initiators were prepared. The reactor was continuously pumped down to 10^{-1} Pa and linear heating was performed at the rate of 10 K/min up to 1623 K. Then the reactor was held for 5–10 min at 1632 K without a transporting agent (argon). At the second stage the controlled growth of whiskers was carried out. With the use of the purification and feed system argon was fed into the reactor at 1623 K. The rate of argon feed was 25 cm^3/s. ZnO was deposited on the polished (111) surface of silicon wafer in the areas where the Si−Au solution-melt was present.

17.3 Experimental Results and Discussion

The SEM studies of the silicon wafers' morphology show the presence of silicon whiskers with well-pronounced cuts (Fig. 17.3a) that indicate their crystalline structure. The surface density of whiskers is about 108 cm^{-2} and virtually is the same as the density of the Si−Au solution-melt particles on the silicon wafer surface. This

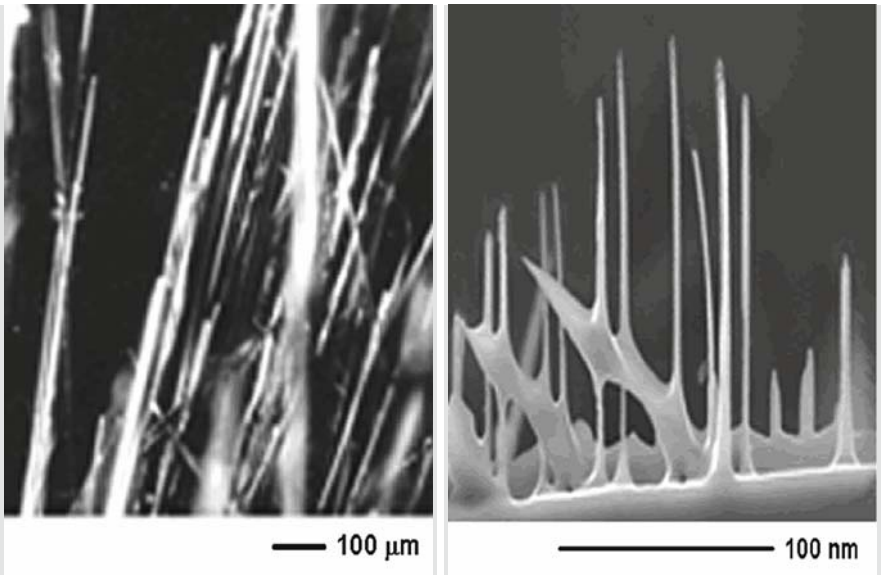

Fig. 17.3 SEM images of nanosized whiskers: **a** Si at angle of 900° with respect to a direction of growth; **b** ZnO

similarity is evidence of the fact that one gold particle is an initiator of a single whisker crystal. The whiskers have a certain distribution of sizes due to distribution of seed sizes.

The silicon nanotips were fabricated by etching the whiskers with the aqueous solution of a mixture of hydrofluoric and nitric acids. Under etching the whisker diameters decreased to less than 10 nm and the whisker upper parts with caps of eutectic alloy fell away. Also the technique of thermochemical sharpening was used [3]. At first, the specimen surface was oxidized by heating to a temperature of 900°C in the humid oxygen atmosphere. The tips had been covered with a layer of silicon dioxide which then was removed by hydrofluoric acid etching. For regular growth of whiskers the above-mentioned procedures ensure uniform field emission over the whole specimen surface that is very important for fabrication of cold electron sources.

The emission properties of the Si whisker array shown in Fig. 17.3a have been studied; Fig. 17.4a shows the current–voltage characteristic (VAC) for the field emission at 300 K from the whiskers with the caps of Si−Au solution-melt (curve 1) and after removal of the caps by etching in the mixture of nitric and hydrochloric acids (curve 2). After etching the structures we observed a substantial increase in the emission current and decrease in the operating voltages applied to the emission

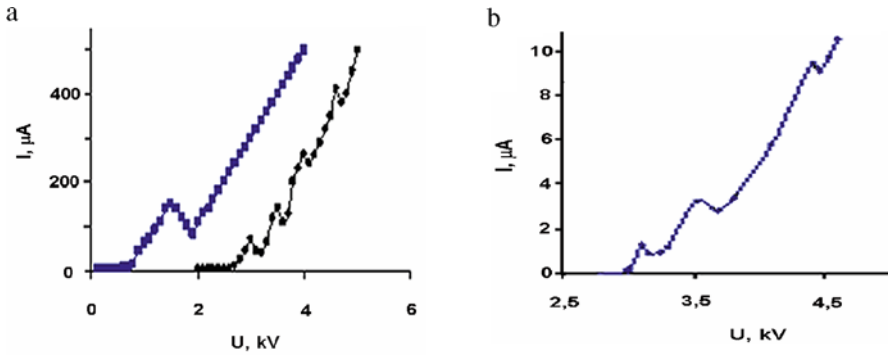

Fig. 17.4 Current–voltage characteristics for the field emission from the nanowhisker array: **a** from silicon (*1* with the caps of solution-melt; *2* after removal of the caps by etching); **b** from zinc oxide

cells. Such behavior may come from thinning of the nanowhiskers and decrease in the radius of curvature of the emitting surface that is due to dimensional effects. In our judgment the presence of resonance current peaks on the VAC curve is due to dimensional quantization of electron energy levels in the potential well [13] defined by the dimensions of the semiconductor whisker:

$$E_n = \frac{\pi^2 h^2}{2m^* \lambda^2} n^2, \tag{17.4}$$

where m^* is the effective electron mass, λ is the specimen size.

When the nanowhiskers are sufficiently thin there is only one quantizing level in the potential well and it is quite possible that this level results in only one current peak on the VAC curve. In the case of artificial atoms with size of less than 2 nm there are no energy quantizing levels in the potential well and the VAC curve becomes smooth and without any resonance peaks [14].

Indeed, upon further thinning of nanowhiskers the VAC curves without peaks have been obtained. It should be noted that the interest in the nanostructures of small sizes (<2 nm) is caused by a sharp increase in their light absorption coefficient due to quantum-dimensional effects. In the event of bulk specimens the transitions near band edges are indirect and light absorption (due to electron–phonon interaction) is rather small (about 1–10 cm^{-1}). In the case of quantum-dimensional objects forbidding on lateral transitions is removed [15] and the absorption coefficient increases sharply (about 10^5 cm^{-1}).

The presence of a number of peaks may be caused by the presence of whiskers of various diameters and heights. The main problem for the synthesis of such structures is fabrication of the arrays of whiskers that are uniform in size. This is particularly important for production of IR optoelectronic non-cooled transducers and flat cathodoluminescent displays.

The process of zinc oxide whiskers' growth consisted of three stages. At the first stage a layer of growth initiator (Au) was deposited on the prepared surface of Si (111) substrate. As stated above this layer was obtained by thermal deposition through the masks with regularly distributed holes and by sedimentation of colloidal particles. At the second stage the surface was heated to the temperature above the eutectic temperature for the binary system of substrate (Si) and growth initiator (Au). In that way an ensemble of liquid droplets of Si−Au solution-melt that were in the thermodynamic equilibrium with the substrate was formed on the surface. At the third stage the growth of zinc oxide whiskers took place at the fixed temperature.

The molecules of deposited material directly penetrate into a droplet from the vaporous medium. It should be noted that the ZnO vapor dissociates at the synthesis temperature (T=1623 K). Thus, the Zn^{+}, Zn^{2+}, and O^{2+} ions were detected in the mass spectra. Relative intensities of their peaks were in the ratio of 100:0.18:50.8 accordingly [16]. Besides, there was a diffusion flux of particles that penetrated into the droplet from the whisker's side surface. Penetration of molecules into the droplet had produced a state of supersaturation in the solution and crystallization of ZnO began at the liquid–crystal interface. The driving force of the growth process is a supersaturation of the gas phase. It is known [4] that the whisker growth rate depends on a diameter of catalyst droplet. The smallest droplets do not "rise" above a substrate at all. Furthermore, realization of the VLC mechanism requires the liquid layer's stability during growth. The indicated factors may critically restrict the number and sizes of generated whiskers. Therefore, for the synthesis of nanowhiskers with the specified parameters it is necessary to produce such droplets of the growth initiator that are similar in sizes. In our opinion the most promising method is a nanolithography by which the droplets of growth initiator of the same sizes may be deposited onto specified areas of various substrates.

The XRD analysis has shown the hexagonal wurtzite structure of the synthesized nanowhiskers with lattice constants of $a = 0.3240$ nm and $s = 0.5184$ nm that are in agreement with the data available in the literature (0.3249 nm and 0.5191 nm accordingly). The XRD data (Fig. 17.3b) show that the synthesized whiskers have a certain spread in sizes. The whisker sizes are strongly dependent on the synthesis duration and the gas flux rate.

The field emission properties were studied for the array of whiskers shown in Fig. 17.3b. The measurements were carried out in the standard diode cells with the anode coated with electron-excited phosphor for emission imaging. To reduce the local density of emission current and protect the screen against damages the cathode and anode were separated by a distance of about 300 μm. The field electron emission was registered with the local current density of about 10 A/cm^2 at the average electric fields of about 105 V/cm. The emission was stable even at the pressure of about 10^{-3} Pa.

Figure 17.4b shows a typical current–voltage characteristic (VAC) for the field emission from the zinc oxide nanowhiskers at 300°K. For quantum dots [17] the resonance current peaks were observed. Their occurrence was ascribed to quantization of electron energies in three-dimensional potential wells. In our case the

grown ZnO whiskers may be considered as quantum wires ($d/h \sim 1000$) with two-dimensional quantization and such an assumption is admissible for such dimensions and electron-effective masses in ZnO. We can estimate the dimensions of whiskers at which the quantum-dimensional effects will become apparent by equation (17.4). For zinc oxide the effective electron masses are in the range of 0.06–0.35 m^* depending on crystallographic directions. For separation of energy levels the whisker sizes shall be in the range 2–40 nm.

We intend to extend the study of the emission properties of synthesized nanowhiskers with allowance for zinc oxide piezoelectric properties. At that, the first-priority task will be fabrication of nanowhisker systems with a space uniformity and small spread in heights, which can be used for development of high-performance thermostable electron sources.

17.4 Conclusions

In summary, we developed the method for synthesis of silicon and zinc oxide nanowhiskers which allowed us to create the regular patterns with controlled densities of randomly distributed whiskers on the polished surfaces of single-crystal silicon. The silicon whiskers were grown on the polished silicon wafers coated with gold nanoparticles at the temperature of about 900°C in the flow of $SiCl_4$, HCl, and hydrogen. The ZnO whiskers were synthesized at the temperature of 1623 K in the flow of argon at the rate of 25 cm^3/s. The silicon nanotips of <10 nm in diameter were fabricated by etching the whiskers with aqueous solution of a mixture of hydrofluoric and nitric acids. The synthesized structures of silicon or zinc oxide nanowhiskers may be considered as quantum wires with the intrinsic low-field electron emission properties at room temperatures.

References

1. Dadykin AA, Naumovets AG, Kozyrev YuN et al (2005) Quantum Dots in High Electric Fields: Field and Photofield Emission from Ge Nanoclusters on Si(100), NATO Science Series II: Mathematics, Physics and Chemistry 190:353–367.
2. Givargizov EI (1975) Oriented growth of AIIIVV compound whiskers by the vapor–liquid–crystal mechanism. Kristallografiya 20:812–822.
3. Givargizov EI (1977) Vapor growth of whiskers and plate-type crystals. Science 304.
4. Givargizov EI, Chernov AA (1973) Whisker growth rate by the vapor–liquid–crystal mechanism and role of surface energy. Kristallografiya 18:147–153.
5. Gorbyk PP, Dadikin AA, Dubrovin IV et al (2006) Low-field electron emission from zinc oxide quantum-dimensional structures. Chem Phys Technol Surf 11,12:261–270.
6. Malvidskiy MG, Ufimcev VB (2000) Semiconductor materials at the modern stage of the development of solid-state electronics. Inorg Mater 36:360–368.
7. Atev BM, Kamilov IK, Mamedov VV (2002) Zinc oxide whiskers. Pis'ma Zh Tekh Fiz 23: 58–63.
8. Wang ZL (2004) Zinc oxide nanostructures: growth, properties and applications. J Phys Condens Matter 16:R829–R858.

9. Xu CX, Sun XW, Chen BJ et al (2005) Network array of zinc oxide whiskers. Nanotechnology 16:70–73.
10. Abduev AKh, Asvarov ASh, Akhmedov AK et al (2002) Vapor-phase synthesis of ZnO structures. Pis'ma Zh Tekh Fiz 28:59–63.
11. Dadykin AA, Gorbyk PP, Dubrovin IV et al (2002) Low–field electron emission and cathode luminescence of piezoelectric films of oxides and chalcogenides. Chemistry, Physics and Technology of Surfaces: Interdepartmental Collection of Scientific Papers/Chuiko Institute of Surface Chemistry, NAS of Ukraine, Publ. house "KM Academy" 7–8:163–176.
12. Wagner AG, Ellis WC (1964) Vapor–liquid–solid mechanism of single crystal growth. Appl Phys Lett 4:1053–1064.
13. Landau LD, Lifshits EM (1989) Quantum mechanics. Non-relativistic Theory, v. 3, p. 766, Nauka, Moscow.
14. Marcus RB, Rav TS, Gmtter T et al (1990) Formation of silicon tips with <1 nm radius. Appl Phys Lett 56:236–238.
15. Gorbyk PP, Dubrovin IV, Demchenko JuA et al (2007) Silicon whisker growth by the vapor–liquid–crystal method. Chemistry, Physics and Technology of Surfaces: Interdepartmental Collection of Scientific Papers/Chuiko Institute of Surface Chemistry, NAS of Ukraine, Naukova Dumka 13:294–300.
16. Zbejneva SG, Makarov AV (2002) Mass spectrometric analysis of vapors over crystalline zinc oxide. Vestn Mosk Univ Ser 2. Khim. 43:143.
17. Dadikin AA, Kozirev YuN, Naumovets AG (2002) Field electron emission from Ge–Si nanoclusters. Pis'ma Zh Eksp Teor Fiz 76:550–552.

Chapter 18
Sol–Gel Synthesis of Silica Glasses, Doped with Nanoparticles of Cerium Oxide

M.V. Borysenko, K.S. Kulyk, M.V. Ignatovych, E.N. Poddenezhny, A.A. Boiko, and A.O. Dobrodey

Abstract A method is suggested for creating nanoparticles CeO_2 incorporated into silica matrix using chemical modification of fumed silica surface with cerium acetylacetonate. A variant of the sol–gel method for synthesizing of silica glasses and optical composites containing nanoparticles of cerium oxide has been designed. Monolithic gels are produced on the basis of SiO_2/CeO_2, $Si(OC_2H_5)_4$, and gelation catalyst $(CH_2)_6N_4$. By the XRD, DTA, TG, photoluminescence, and measurements of specific surface area a research has been made into structural and physico-chemical properties of CeO_2/SiO_2 during the course of their thermal transformations up to formation of glasses.

18.1 Introduction

The modern technologies employed for production of various materials for optoelectronics and laser devices depend to a great extent on sol–gel processes. In particular, the well-known technology for production of silica sol–gel glass involves alkoxide processes with participation of ethers of silicic acid. It was shown that a substantial improvement of the quality of such materials and devices could be attained through filling of hydrolyzate with disperse silica [1, 2]. Under designed conditions the procedure for manufacture of a monolithic glass-like preform consists in several successive stages including preparation of a mixture of ingredients, hydrolysis and polycondensation of the mixture, gel formation, removal of the liquid to obtain xerogel, and sintering of the xerogel.

Variation of optical and luminescent properties of quartz silica materials can be effected by doping the glass produced with ions of transition and rare-earth metals [2, 3]. Doping additives are incorporated into xerogel using a liquid or

M.V. Borysenko (✉)
O.O. Chuiko Institute of Surface Chemistry of the National Academy of Sciences of Ukraine, General Naumov St. 17, Kyiv 03164, Ukraine
e-mail: borysenko@naverex.kiev.ua

A.P. Shpak, P.P. Gorbyk (eds.), *Nanomaterials and Supramolecular Structures*,
DOI 10.1007/978-90-481-2309-4_18,

gaseous medium. Unfortunately, various methods employed for impregnation of metal compounds with solutions or adsorption of reagent vapors are not free from some drawbacks related to an unhomogeneous distribution of a doping metal in the formed xerogel structure.

The main idea of the new method suggested by us for production of silica sol–gel glass [4, 5] consists in filling of hydrolyzate of tetraethoxysilane (TEOS) with a composite of the M_xO_y/SiO_2 type, with M_xO_y particles being nanoparticles of a doping metal oxide synthesized on the surface of highly disperse silica. Formation of nanodispersed composites of this type is based on the chemical modification of the fumed silica surface with compounds of metals.

Our preliminary studies were made using nanocomposite Cr_2O_3/SiO_2 obtained in a gas phase from vapor of chromium oxochloride CrO_2Cl_2 [5]. The chromium-containing silica was utilized to synthesize transparent glass that possessed a high homogeneity along the preform. The present chapter is concerned with the possibility of application of cerium-containing silica (CeO_2/SiO_2) as a filler and source of doping ions for optical sol-gel glasses.

18.2 Experimental

Nanocomposite CeO_2/SiO_2 was prepared using highly disperse fumed silica A-300 (Kalush Experimental Plant of the Institute of Surface Chemistry of the NAS of Ukraine) and acetylacetonate of cerium $[CH_3COCH{=}C(CH_3)O]_3Ce.H_2O$, $Ce(acac)_3$ (Aldrich). Modification of silica with cerium acetylacetonate was performed by a liquid-phase method (with carbon tetrachloride as a solvent).

Modification of silica was executed in double-throat glass reactor equipped with mechanical stirrer and refluxing tube. $Ce(acac)_3$ solution in CCl_4 was added to fumed silica (2 g previously calcinated at 500°C). Molar ratio $Ce(acac)_3/{\equiv}SiOH$ was 1:1 ($C_{SiOH} = 0.5$ mmol/g SiO_2). The reaction mixture was stirred in the reactor for 1 h at 76°C. In order to remove excess of modifier and reaction product acetylacetone (Hacac) sample was filtered and washed with two 25 ml portions of CCl_4. Then product was dried and calcinated for 1 h at 550°C. The content of grafted ceria was controlled using a set of subsequent processes of chemisorption of $Ce(acac)_3$ and its oxidation. The number of cycles was varied from 1 to 4 (SiCeM1−SiCeM4, Table 18.1).

The samples synthesized due to single-stage impregnation of SiO_2 by $Ce(acac)_3$ solution in CCl_4 were obtained for comparison. Impregnation of 0.2, 0.5, 1 mmol $Ce(acac)_3$ per gram of SiO_2 was performed (SiCeI0.2, SiCeI0.5, SiCeI1, Table 18.1). Temperature of SiO_2 advance pretreatment, drying and calcination conditions was identical with previous experiments. The CeO_2 content C_{CeO2} in CeO_2/SiO_2 samples was determined analyzing Ce^{3+} arsenazol complexes with a KFK-2MP spectrometer (LOMO, St. Petersburg) at 540 nm.

The procedure employed for synthesizing cerium-containing sol–gel glasses involved the following subsequent stages: hydrolysis of TEOS in a triple-component system $Si(OC_2H_5)_4$–H_2O–HCl of starting compounds with their molar ratio of

Table 18. 1 Characteristic of CeO_2/SiO_2 samples

Sample	C_{CeO2} (wt%)	S_{BET} (m^2/g)	D_{CeO2}(nm)				
			550°C	800°C	1000°C	1100°C	1200°C
SiCeM1	6.6	265	a	a	4	8	16
SiCeM2	12.3	230	3	3	5	9	19
SiCeM3	18.3	212	3	3	6	12	21
SiCeM4	23.3	189	3	3	6	14	25
SiCeI0.2	2.4	319	a	a	9	8	16
SiCeI0.5	6.9	264	a	11	5	9	17
SiCeI1.0	14.9	261	4	5	5	10	23

a amorphous.

1:16:0.01; addition of CeO_2/SiO_2; thorough dispersion in an ultrasonic bath; centrifugation for separation of coarse impurities and agglomerates; neutralization of the reaction mixture to pH = 5.5−6.5 using a solution of hexamethylenetetramine $(CH_3)_6N_4$; casting of the sol into plastic containers; gelation; drying of the gel; sintering in a muffle furnace; and holding at a temperature of 1140–1200°C for 1.5–2.0 h in air. A desired concentration of dopants was attained through introduction of an additional volume of pure silica.

Thermal destruction of the modified silica samples in air was studied using derivatograph Q-1500D (Hungary). The heating rate was 10°C per minute. The oxide structure formed during the thermooxidative destruction of grafted cerium acetylacetonate groups was investigated by X-ray powder diffractometry. The diffractograms presented in the figures below were registered on automatic diffractometer DRON-3M (Russia) (with copper anode-induced radiation and nickel filter). The spectra were recorded in the mode of reflected rays and the Bragg–Brentano geometry of focusing. The average size of the crystallites D_{CeO2} formed was determined according to the Scherrer equation. The specific surface area S_{BET} was measured by standard method using low-temperature adsorption of organ. Photoluminescence spectra were recorded with Perkin-Elmer LS50B luminescence spectrometer equipped with a pulsed zenon lamp. Optical absorption spectra were measured using a JASCO V-550 UV-Vis spectrometer. For spectral study, transparent colorless glasses of 5x10x2 mm dimensions in special sample holder were used. All spectra were taken at room temperature.

18.3 Results and Discussion

Interactions between metal acetylacetonates $M(acac)_x$ and silica surface can be accompanied by adsorption or chemisorption [6–9]. In the literature [6], there are reports about possibility of formation of adsorption complexes at the expense of bonds among hydrogen atoms of surface silanols and oxygen atoms of carbonyl groups or π-electrons of pseudoaromatic rings of acetylacetonate ligands.

Chemosorption of $M(acac)_x$ on the silica surface leads to the formation of SiO-M bonds can Hacac removal. Grafted groups $SiOM(acac)_{x-1(2)}$ were identified for $Cr(acac)_3$ [7], $Ni(acac)_2$ [8], $Ce(acac)_4$ [9] and $Zr(acac)_4$ [10]. During both chemisorption and physical adsorption, the IRS technique reveals a decrease in the intensity of the absorption band at 3748 cm^{-1} which is attributed to valence vibrations of bonds SiO–H. In $Zr(acac)_4$ instance this absorption band disappears completely [10].

The results of thermogravimetric and differential thermal analyses for precursor of SiCeM1 sample prepared by the liquid-phase modifications are presented in Fig. 18.1. The DTG curves make it possible to identify several stages of weight loss. At the first stage, removal of the water adsorbed on the surface (with $T_{max} = 100°C$) proceeds. The second stage observed in the interval of 210–300°C is the destruction of acetylacetonate ligands. The third stage of the destruction of intermediate carbonaceous structures proceeds in the temperature interval from 300 to 450°C. Such kind of sample behavior on heating is typical for all modificated and impregnated samples (see Table 18.1) without exception.

The X-ray powder diffractometry of the silica with cerium oxide structures was performed for the samples calcined at a temperature up to 1200°C. The peaks characteristic of the crystalline cerium oxide of the cubic structure (JCPDS # 75-76) are exhibited by the diffractograms for CeO_2/SiO_2 with ceria content of >6.6–6.9 wt%. With increasing content of cerium oxide up to 23.3 wt% the intensity of the peaks increases regularly. It is of interest to compare the curves recorded for the modified silica samples SiCeM1−4 after calcination at 550 and 1000°C (Fig. 18.2). The average size of crystallites of the cerium oxide phase CeO_2 is equal to 3–25 nm.

The newly synthesized nanocomposites for CeO_2/SiO_2 were used to produce samples of doped silica glass by the sol–gel method.

Sol obtained by TEOS hydrolysis in aqueous media without organic solvents was used for synthesis of glass-like materials. Formation of compositional sols

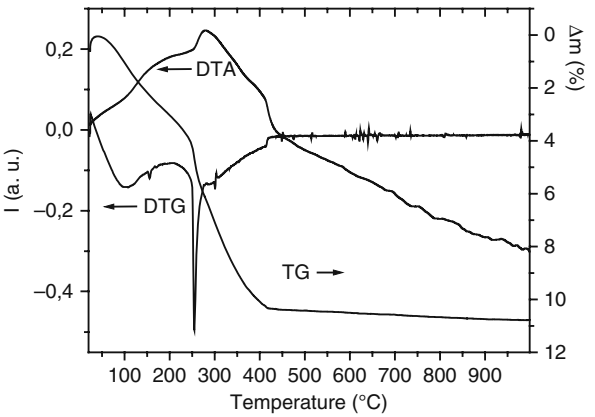

Fig. 18.1 TG, DTG, and DTA curves of silica with grafted cerium acetylacetonate groups (a precursor for SiCeM1 sample)

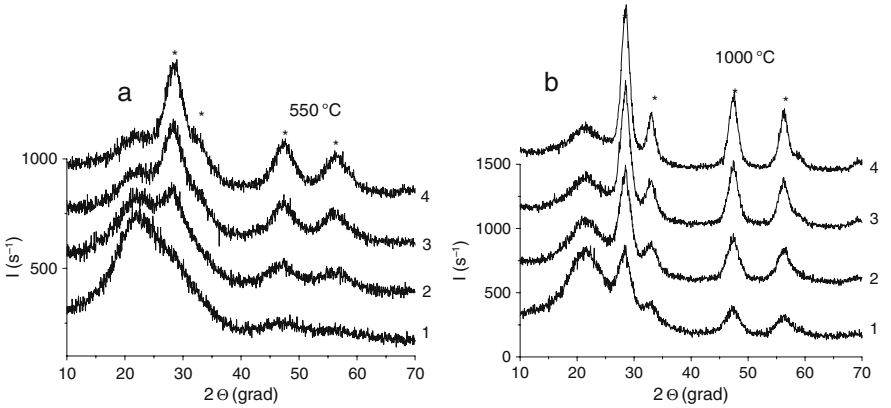

Fig. 18.2 XRD patterns of nanocomposites SiCeM1−4 after calcination at 550 (**a**) and 1000°C (**b**): (∗)lines due to CeO_2

was performed due to addition of fumed silica (A-300) to TEOS hydrolysates as fillers and SiO_2/CeO_2 as dopants. Silicas were previously dispergated by ultrasonic activation and additional mechanical stirring in aqueous media. In order to form homogenous colloidal systems compositional sols were exposed to ultrasonic activation with intensive mechanical stirring too. Centrifugal separation was used for the total exception of agglomerates of coalescent SiO_2 particles, grit and dust-like particles from compositional sols.

Then neutralization of compositional sols by solution of gelating agent $(CH_3)_6N_4$ to pH = 5.5–6.5 was performed. Neutralized sols were introduced to plastic vessels for gelation. Gel aging was performed in injection molds in syneresis liquid at room temperature. Then gels were exposed in distilled water bath for 24 h.

Formed gels were dried at 30–40°C in heat chamber in pasteboard boxes or directly in injection molds. Dried xerogels in various forms and sizes were initial intermediates for preparation of gel glasses and nanocomposites.

Thermal treatment of xerogels was performed in muffle furnace in air atmosphere using a set of subsequent processes: temperature rise to 120°C during 1 h, exposure to this condition for 2 h in order to remove free water; temperature rise to 250°C during 1 h, exposure to this condition for 2 h in order to remove adsorbed water; temperature rise to 600°C during 2 h, exposure to this condition for 2 h in order to burn out organic impurities; and temperature rise to 1150–1200°C, exposure to this condition for 1.5–2 h in order to obtain transparent monolithic nonporous glass.

Schematical model of nanocomposite formation on the basis of TEOS hydrolysis and ceria-modificated silica could be described in the following manner (Fig. 18.3). According to this model particles of modifier's phase during ultrasonic dispersion should remain associated with silica surface for the most part due to chemical bonding but transition of these particles into sol is also possible. Bonding with silica surface should prevent their free movement in porous liquid, "stamping" on the surface of volumetric samples during pore shrinking, and thermal condensation of

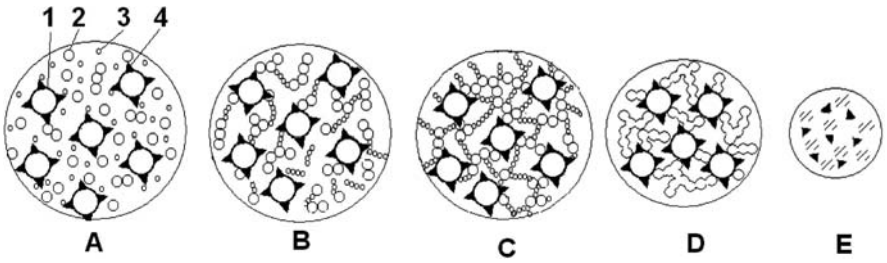

Fig. 18.3 Model of nanocomposite formation on the basis of TEOS hydrolysate and modificated silica. *A* compositional sol, *B* microgel phase, *C* wet gel phase, *D* dry gel phase, *E* glass composite phase. *1* fumed silica aggregates, *2* initial particles, *3* TEOS hydrolysate particles, *4* CeO_2 nanoparticles

xerogel; also this chemical bonding should inhibit aggregation and formation of crystalline phase islands; in consequence homogeneity of dopant distribution in sample bulk should rise. Thus, fumed silicas modificated by ceria nanoparticles could be used as dopants and fillers in the manufacturing of transparent sol–gel glasses and glass composites on the TEOS basis.

Thus, transparent, yellow-colored, luminescent in ultraviolet spectrum (max. 470 nm), nanocomposites were obtained due to ceria-modificated silica (Fig. 18.4).

Direct introduction of dopant in the form of modificated silica precludes operations of dosing addition of dopant salts or xerogel matrix impregnation, which present an advantage of developed method. For instance, traditional method of preparation of cerium-containing gel glasses due to introduction of solutions of cerium salts into colloidal system leads to formation of agglomerates of ceria particles distributed in silicate matrix and thermal treatment in air leads to formation of amorphous clusters with predominant content of optically inactive ions Ce^{4+} in the structure of composition Ce^{4+}/Ce^{3+}.

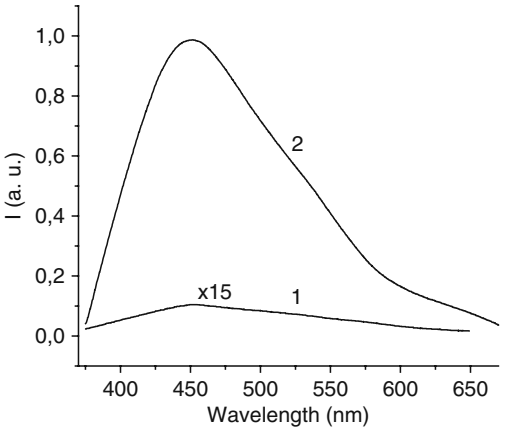

Fig. 18.4 Luminescence spectra of cerium-containing gel glasses, obtained due to introduction of cerium salt into liquid colloidal system (*1*) and due to addition of ceria nanoparticles modificated silica (*2*). $\lambda_{exc} = 340$ nm

18.4 Conclusions

Thus, if the fumed silica modified with such compounds as acetylacetonates of metals is subjected to heating in air at a temperature higher than that necessary for the complete removal of carbonaceous constituents, this thermal treatment is accompanied by formation of the metal oxides. The material synthesized by this method is nanocomposite M_xO_y/SiO_2 consisting of nanoparticles of fumed SiO_2 and the oxide M_xO_y formed in the course of this synthesis. The synthesis method exerts an effect on the phase state of the deposited metal oxide. By appropriate thermal treatment of the nanocomposite with an assigned metal content it is possible to vary the degree of crystallinity and size of crystallites of the oxide M_xO_y.

References

1. Toki M, Miyashita S, Takeuchi T (1988) A large-size silica glass produced by a new sol–gel process. J Non-Cryst Solids 100:479–483
2. Poddenezhny EN, Boiko AA (2002) Sol–gel synthesis of optical silica glasses. Sukhoi GGTU, Gomel
3. Schultz PC (1974) Optical absorption of the transition elements in vitreous silica. J Am Ceram Soc 57:309–313
4. Poddenezhny EN, Boiko AA, Alekseenko AA et al (2003) Sol–gel synthesis of doped vitreous materials with the use of modified aerosils. Glass Phys Chem 29:471–475
5. Borysenko MV, Bogatyrov VM, Poddenezhny EN et al (2004) Application of chromium-containing silica for synthesising functional glasslike materials by the sol–gel method. J Sol–Gel Sci Technol 32:327–331
6. White MG (1993) Uses of polynuclear metal complexes to develop designed dispersions of supported metal oxides. Catal Today 18:73–109
7. Borisenko NV, Sulim IYa, Borisenko LI (2008) Modification of highly dispersed silica with zirconium acetylacetonate. Theor Exp Chem 44:200–204

Chapter 19
Quantum Size Effects in Multilayer Si-Ge Epitaxial Heterostructures

Yu.N. Kozyrev, M.Yu. Rubezhanska, V.K. Sklyar, A.G. Naumovets, A.A. Dadykin, O.V. Vakulenko, S.V. Kondratenko, C. Teichert, and C. Hofer

Abstract A technology of epitaxial growth was developed making it possible to prepare monolayer and multilayer Ge nanocluster structures of different size and distribution density over silicon or oxidized silicon substrates. A stable field electron emission was obtained from Ge on Si quantum dot structures, showing current peaks in the current–voltage characteristics, which may be attributed to the resonant electron tunneling via the energy levels of the nanocluster potential well, manifesting in such a way the effects of energy quantization in the Ge quantum dots. Moreover, the field emission current showed a considerable photosensitivity in the wavelength range from 0.4 to 10 μm. Besides that, lateral photoconductivity spectra from the same structures revealed anomalous red shifts of the photocurrent excitation spectra to the boundary of about 0.3 eV, which shifted distinctly to lower energies as the number of Ge quantum dot layers increased. A pronounced correlation between these effects suggests a mechanism of the electron transport in Ge quantum dot structures involving the localized energy levels that appear near the band verges due to energy quantization effects.

19.1 Introduction

Ge−Si heterostructures with Ge quantum dots (QD) are widely investigated by both scientists and technologists all over the world because of the possibility of creation of objects that can manifest unique properties in view of the development of new Si-based nanoelectronic devices [1]. The promising properties of such systems can also essentially extend the abilities of infrared (IR) optoelectronic devices [2]. At the same time, creation of structures with inversion levels opens a prospect of elaboration of lasers operating in IR range. The presence and character of quantum size

Yu.N. Kozyrev (✉)
O.O. Chuiko Institute of Surface Chemistry of the National Academy of Sciences of Ukraine, General Naumov St. 17, Kyiv 03164, Ukraine
e-mail: kozyrev@iop.kiev.ua

A.P. Shpak, P.P. Gorbyk (eds.), *Nanomaterials and Supramolecular Structures*,
DOI 10.1007/978-90-481-2309-4_19,

effects occurring in such systems are defined first of all by morphological factors: the distribution density and regularity of Ge quantum dots, their size, and Ge mole fraction in them [3]. Investigations of low field emission [4, 5] and an anomalous shift of the lateral photo-EMF up to 1.5 eV attract a special interest [6]. If one clarifies the nature of these phenomena, the existing concepts of the character of energy-band structure changes and quantum effects in such structures would be possibly extended.

From this point of view, the formation process of Ge quantum dots, their distribution density over the surface, and size regularity are supposed to be very important aspects [3]. The essential difficulties that one encounters dealing with such quantum dot systems are connected with random distribution of self-assembled Ge nanoclusters over the substrate surface. This problem becomes even more essential, when one deals with epitaxial formation of multilayer Ge quantum dot heterostructures. To overcome this problem, a technology of epitaxial growth was developed making it possible to prepare monolayer and multilayer Ge nanocluster structures of different size and distribution density over silicon or oxidized silicon substrates with a predicted value of residual elastic strain in the nanoisland film. The latter defines the degree of wavefunction overlapping in the heterostructures of the second type, Ge quantum dots on Si in particular, in which the charge carriers are localized separately. Ge mole fraction in the quantum dots can vary from 40 to 90% during the epitaxial growth process.

Taking into account all these aspects, we present here our experimental results on lateral photoconductivity and photofield electron emission from multilayer Ge/Si heterostructures with Ge quantum dots. They seem to reveal quantum size effects which mirror the nature of electron transport in such structures. Thus one of the main purposes of the present work was to search for a correlation between the quantum regularities of the photofield electron emission and the lateral photoconductivity in multilayer Ge/Si heterostructures with Ge quantum dots.

19.2 Preparation of the Experimental Samples and Investigation Technique

The samples investigated were prepared using molecular-beam epitaxy (MBE) technique ("Katun'-B") that allowed forming multilayer Ge−Si(100) systems using the method of $Si_{(1-x)}Ge_{(x)}$ intermediate layers [3].

Nanocluster arrays with different number of Ge quantum dot layers (up to 10) of height $\sim$ 1.5–2.0 nm alternated by Si layers of thickness 2.0–2.5 nm were obtained in such a way at temperature $T_s = 500°C$. The growth process, in particular the stage of the 2D→3D transition, was controlled via reflection high-energy electron diffraction. Atomic force microscopy images of the last (surface) nanoisland layer of the investigated samples showed that the nanoclusters were shaped as tetrahedral pyramids with the base about 30 nm and height about 3 nm (Fig. 19.1). The

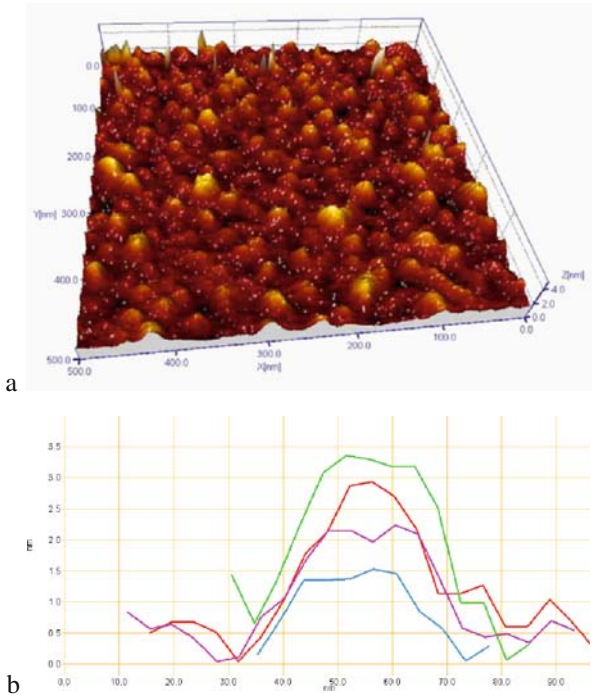

Fig. 19.1 AFM image of the surface of Ge/Si heterostructure with Ge quantum dots on Si(100) (**a**). Size distribution of the quantum dots in the investigated structure (**b**)

average nanoisland density was about 10_9 cm^{-2}. We suppose these Ge quantum dots to be vertically integrated, since we developed a technology of epitaxial growth allowing preparation of Ge quantum dot ensembles with a fixed elastic deformation in the nanoisland film. As we had shown earlier, the average elastic strain in the nanoisland film ε is proportional to the value $\sqrt{1/L}$, where L is the lateral size of a Ge quantum dot [3]. Using this estimate of the elastic strain in the nanoisland film, it was possible to prepare the ensembles of almost identical Ge nanoclusters in each layer.

The measurements of the field and photofield electron emission were carried out in two types of devices. On the one hand, we used flat diode cells, in which the distance between the electrodes was 50–300 μm, with a ZnS cathodoluminescent screen deposited onto a glass plate having a SnO_2 conducting layer. On the other hand, we tested Ge−Si emitters in diodes with a Mo anode shaped as a rod 1 mm in diameter (Fig. 19.2a).

In parallel with the photofield emission, we investigated lateral photoconductivity in the same monolayer and multilayer heterostructures with Ge quantum dots, according to the scheme given in Fig. 19.2b. To improve the sensitivity of the measurements, multipass waveguide geometry of photocurrent excitation was used.

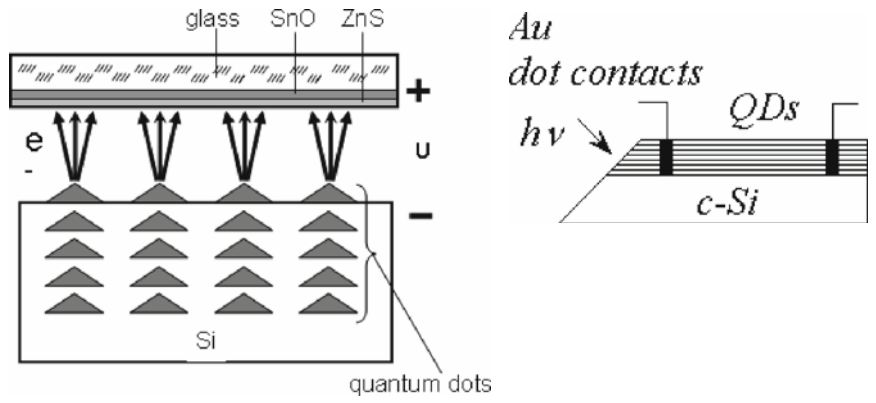

Fig. 19.2 Schemes of experimental device with light emitting diodes for investigation of field and photofield emission from Ge−Si nanocluster emitters (**a**) and lateral photoconductivity measurements (**b**)

19.3 Results and Discussion

A stable field electron emission was obtained from Ge quantum dot structures. The field emission from such systems was observed by several research teams, in particular by Tondare et al. [7–13]. The first works on this system recorded no peculiarities in the current–voltage curves of the field emission. However, a more careful study undertaken by us revealed reproducible peaks of current in the $I-V$ curves of the field emission from Ge nanocluster structures on Si(100). The number of peaks was found to depend on the cluster size (Fig. 19.3). These peaks are approximately equidistant when the $I-V$ curves are plotted in the semilogarithmic (Fowler–Nordheim) coordinates $\lg(I/V^2)$ versus reciprocal voltage $1/V$ (Fig. 19.4a). We suppose that the current peaks in the *I–V* curves may reflect the resonant tunneling of electrons via the energy levels existing in the nanocluster potential well.

Moreover, the field emission current showed a considerable photosensitivity in the wavelength range from 0.4 to 10 μm. It was found that with the photodiodes that were used, the field emission current increased for a multilayer Ge−Si nanocluster structure at room temperature by a factor of 5 to 3 under irradiation by light with wavelength of 2 and 10 μm, respectively (Fig. 19.4b).

We suppose that the current peak in the *I–V* curve of photofield emission (Fig. 19.3, curve 1) may also be connected with energy quantization, in particular the presence of discrete energy levels in the valence band of the quantum dots. In the absence of external electric field, Si/Ge heterojunction is referred to the second-type heterostructure, in which a potential well is formed for one type of carriers. Namely, the valence band of Ge nanoislands is a potential well for holes causing a localization of states. Possible energy-band diagrams for Si/SiGe heterojunction in the absence and presence of electric field are suggested in Fig. 19.5a

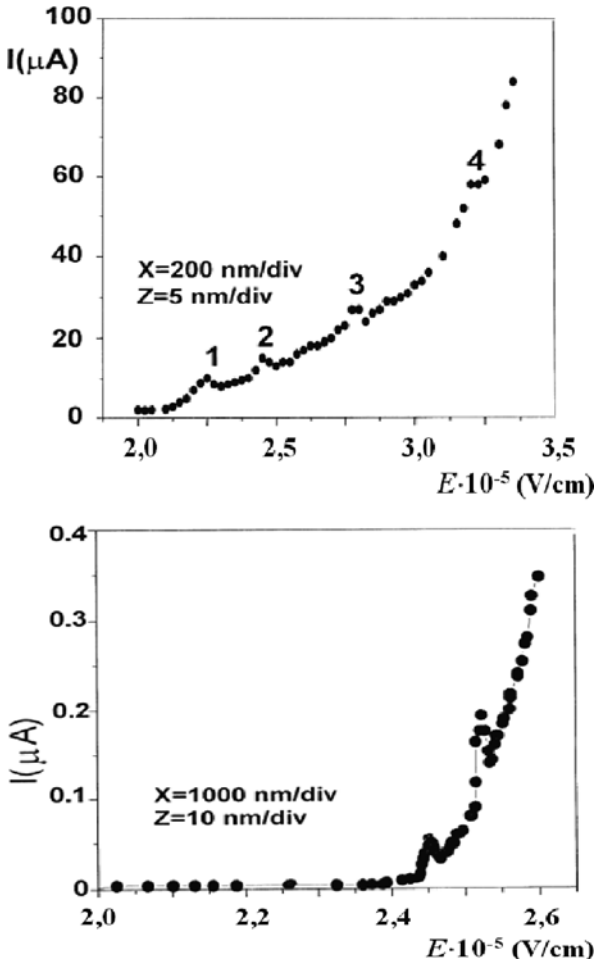

Fig. 19.3 Field emission current–voltage curves for Ge−Si nanostructures with Ge quantum dots with average lateral sizes about 100 nm (**a**) and 40 nm (**b**) measured at $T = 300$ K

and b, respectively. It should be stressed that the potential well near the surface is in any event highly asymmetric. Besides, the shape and transparence of the barrier Si/QD/vacuum depends drastically on the strength of applied electric field. That is why the considered Si/QD/vacuum "heterostructure" can neither be unambiguously classified as a first-type nor as a second-type heterojunction. We have thus to treat it as a special type of heterojunction whose properties depend upon the value of the applied electric field and require a separate approach.

In particular, the shape and width of the potential well for holes in the valence band of SiGe nanoislands changes essentially when the electric field is applied to the surface. As a consequence, the discrete energy values E_n change too.

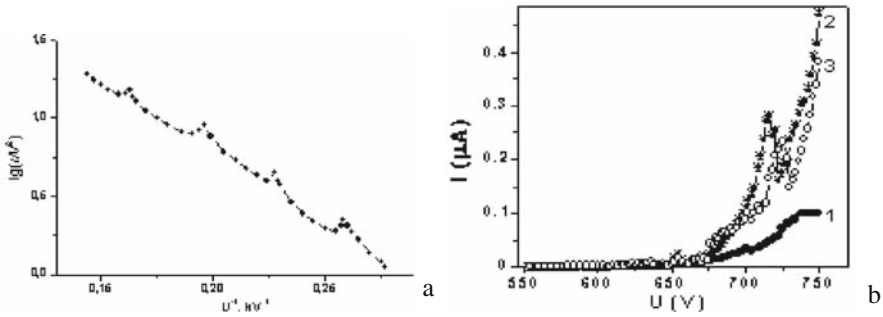

Fig. 19.4 Field emission current−voltage curve for Ge−Si nanostructure with Ge quantum dots plotted in the Fowler–Nordheim coordinates $\lg(I/V^2)$ versus $1/V$ (**a**). Effect of IR irradiation on field emission current–voltage characteristic for a multilayer Ge−Si nanocluster structure. (*1*) Dark current; (*2*) $\lambda \approx 2$ μm; (*3*) $\lambda \approx 10$ μm. $T = 300$ K (**b**)

At some value of the applied electric field, the energy position of a quantization level may coincide with the top of the Si valence band, so that resonance tunneling of electrons can become probable from this band into vacuum via the energy quantization level in the SiGe quantum dot (Fig. 19.5b). As the electric field is increased further, the potential well becomes shallower and resonance tunneling can proceed via the next energy level. The observation of a current peak for the structure with QDs about 2 nm high may indicate that at least one localized energy state exists in the valence band of SiGe nanoisland in the absence of electric field. Analyzing these effects, a question arises: where can these additional carriers originate that are responsible for such an essential current increase under irradiation. Let us consider this point applying the formula which was proposed by A. Modinos [14]

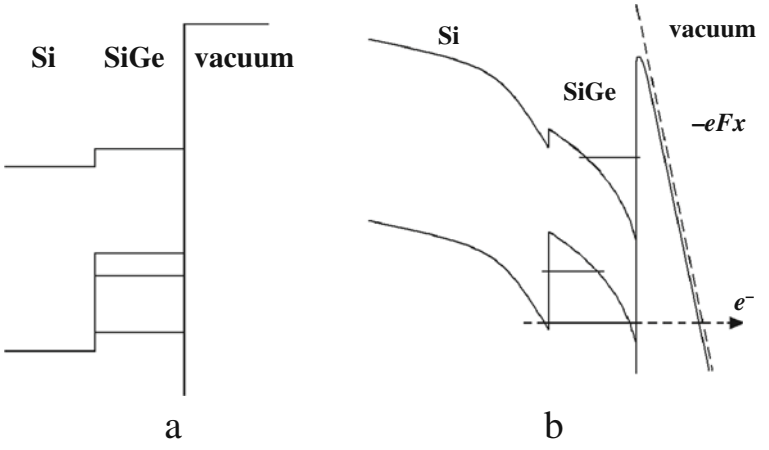

Fig. 19.5 An energy-band diagram of Si/SiGe heterojunction without (**a**) and in the presence of electric field F (**b**)

and represents the tunneling current density J for a certain energy E as

$$J(E) = S(E)T(E),$$

where $S(E)$ is the supply function depending on the density distribution of energy states in the subsurface region relevant to emission and $T(E)$ is a factor that describes the transparency of the surface potential barrier.

We suppose that the photoinduced field emission current can mainly be caused by electron excitation to additional energy levels in the quantum dots as well as to surface and subsurface states. These energy levels can be populated by interband and intraband optical transitions. Such transitions become possible, since the restriction imposed on optical transitions polarized in the plane of the emitter is lifted as a consequence of elastic deformation leading to a modification of the energy-band structure of the strained Ge/Si heterojunction. It should be noted that the elastic deformations not only induce the valley splitting and band offset lifting the restrictions imposed on optical transitions, but may also essentially influence the population of surface and subsurface states relevant to emission.

In parallel with the photofield emission, we investigated lateral photoconductivity in the same monolayer and multilayer heterostructures with Ge quantum dots. The investigated structures showed considerable photosensitivity for quanta energy in the range $0.48 \leq h\nu \leq 1.11$ eV that are smaller than the band-gap energies for silicon ($E_g = 1.1$ eV), germanium ($E_g = 0.67$ eV), and the strained solid solution $Si_{(1-x)}Ge_{(x)}$ [15]. In this solution, the valence band offset amounts to $\Delta E_{vb} \sim 0.54x \approx 0.16$ eV for $\varepsilon \approx 0.02$ at room temperature, where ε is the elastic strain (Fig. 19.6a). We suppose that the long-wave threshold of the lateral conductivity photosensitivity may also be attributed to formation of discrete energy levels at the band verges of the strained Ge/Si heterojunction, via which the electrons can participate in interband and intraband transitions. The photocurrent in the range

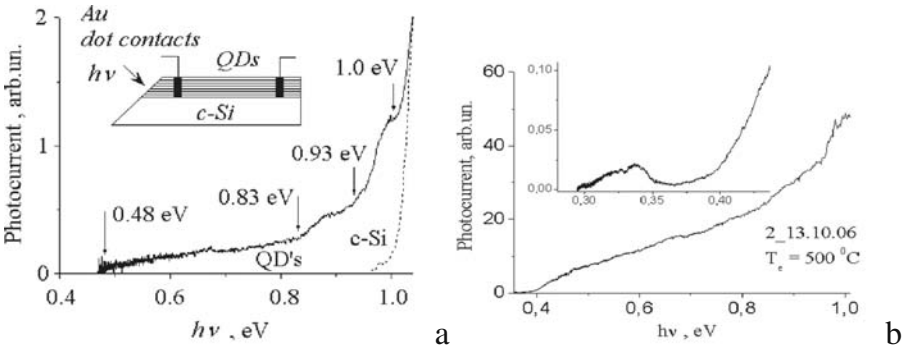

Fig. 19.6 Photoconductivity spectral dependence of Ge/Si heterostructure with eight layers of Ge quantum dots (*solid line*) and Si without the quantum dots (*dot line*) at 290 K (**a**). Photoconductivity spectral dependence of Ge/Si heterostructure with five layers of Ge quantum dots for lateral excitation (waveguide geometry) at $T = 77$ K (**b**)

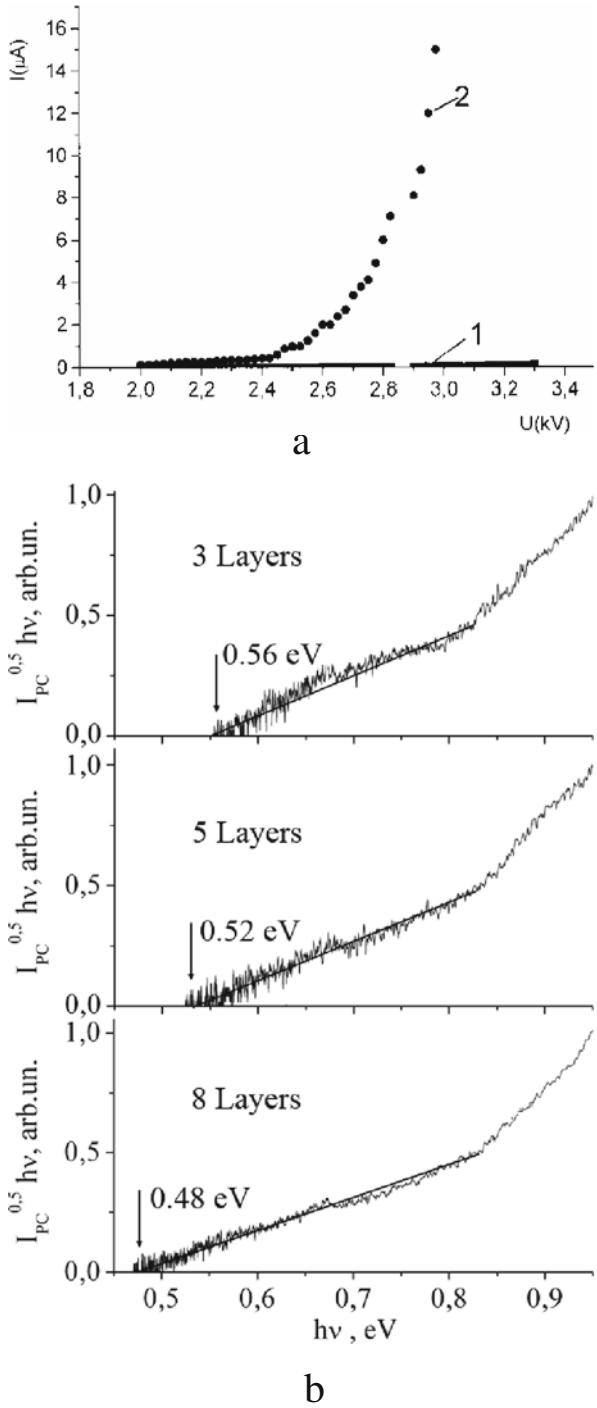

Fig. 19.7 (continued)

of 0.48–1.02 eV is possibly caused by generation of nonequilibrium carriers as a result of interband transitions in the Ge dots [16]. The photocurrent at 0.32–1.2 eV showing maxima at 0.32 and 0.34 eV observed at side excitation at 77 K may be produced by bound-to-continuum transitions of heavy holes of Ge nanoclusters from 2D delocalized states of the silicon wetting layer (Fig. 19.6b) [17].

To understand better the nature of the effects observed in photofield emission and lateral photosensitivity, we investigated the samples with different number of similar Ge quantum dot layers. These layers, which we supposed to be vertically integrated, contained Ge nanoclusters having an optimal height of about 2 nm.

We revealed that the field emission current from the multilayer Ge quantum dot structure increased several fold under irradiation by light with the wavelength of $\lambda \approx 0.7$ μm at $T = 77$ K (Fig. 19.7a). Then we investigated the lateral photoconductivity from similar multilayer Ge quantum dot heterostructures containing three, five, and eight layers of vertically integrated Ge quantum dots. We found that the red boundary of the lateral photoconductivity distinctly shifted to lower energies as the number of Ge quantum dot layers increased (Fig. 19.7b). At the same time, the photocurrent for the sample without Ge nanoclusters was observed only at $h\nu > 1.0$ eV. Thus, the two effects in Ge−Si quantum dot structures – the field emission and lateral conductivity – show a pronounced correlation: they both reveal a strong long-wave photosensitivity at an optimum size of the dots and are enhanced as the number of Ge quantum dot layers is increased. Hence, we can infer that the common features of these phenomena are connected with the energy quantization in the quantum dots. We suppose that the photoinduced field emission current can mainly be caused by electron excitation to additional energy levels in the quantum dots as well as to surface and subsurface states. These energy levels can be populated by interband and intraband optical transitions. Such transitions become possible, since the restriction imposed on optical transitions polarized in the plane of the emitter is lifted as a consequence of elastic deformation leading to a modification of the energy-band structure of the strained Ge/Si heterojunction. It should be noted that the elastic deformations not only induce valley splitting and band offset lifting the restrictions imposed on optical transitions, but may also essentially influence the population of surface and subsurface states relevant to emission.

19.4 Conclusions

Investigations of field and photofield emission and lateral photoconductivity in the structures of vertically integrated Ge quantum dots on Si(100) suggest a mechanism of electron transport in such structures involving the localized energy levels that appear near the band verges due to energy quantization effects.

Fig. 19.7 Effect of IR irradiation on field emission current–voltage characteristic for multilayer Ge−Si nanocluster structure. (*1*) Dark current; (*2*) $\lambda \approx 0.7$ μm. $T = 77$ K (**a**). Photoconductivity spectra of Ge/Si heterostructures with three, five, and eight layers of Ge quantum dots, correspondingly, given in coordinates $h\nu$ (**b**)

Elastic strains in the Ge/Si heterojunction determine the size characteristics of the grown Ge quantum dot structures. This opens a possibility to prepare more perfect Ge/Si heterostructures with optimum sizes of Ge quantum dots that may be used for elaboration of infrared devices and low-voltage electron emitters.

References

1. Gruetzmacher D (2003) Si/SiGe nanostructures: challenges and future perspectives. Physics, chemistry and application of nanostructures. World Scientific, Singapore: 3–10.
2. Masini G, Colace L, Assanto G (2003) Germanium-on-silicon infrared detectors. Encyclopedia of nanoscience and nanotechnology. American Scientific Publishers, Valencia, vol. X: 1–14.
3. Kozyrev YuN, Grechko LG, Lerman LB, Rubezhanska MYu, Chuyko AA (2005) Experimental investigation and simulation of size characteristics of Ge quantum dots on Si(100). Dopovidi NASU 10: 31–35.
4. Dadykin AA, Kozyrev YuN, Naumovets AG (2002) Field electron emission from Ge–Si nanostructures with quantum dots. JETP Lett 76: 472–474.
5. Dadykin AA, Kozyrev YuN, Naumovets AG, Rubezhanska MYu, Lytvyn PM, Litvin YuM (2003) Field and photo-field electron emission from self-assembled Ge–Si nanoclusters with quantum dots. Prog Surf Sci 74: 305–318.
6. Kondratenko SV, Vakulenko OV, Nikolenko AS, Golovinskiy SL, Kozyrev YuN, Rubezhanska MYu (2007) Lateral photoconductivity in Ge/Si heterostructures with Ge quantum dots. Semiconductors 41: 955–959.
7. Arthur JR (1965) Photosensitive field emission from p-type germanium. J Appl Phys 36: 3221–3227.
8. Fischer R, Neumann H (1966) Feld Emission aus Halbleitern. Fortschritte Phys 14: 603–692.
9. Borzyak PG, Jatsenko AF, Miroshnichenko LS (1966) Photo-field-emission from high-resistance silicon and germanium. Phys Stat Sol 14: 403–411.
10. Yatsenko AF (1970) On a model of photo-field-emission from p-type semiconductors. Phys Stat Sol (a) 1: 333–348.
11. Herman MH, Tsong TT (1979) Photon excited field emission from a semiconductor surface. Phys Lett 71A: 461–463.
12. Fursei GN (1996) Early field emission studies of semiconductors. Appl Surf Sci 94/95: 44–59.
13. Tondare VN, Birajdar BI, Pradeep N, Joag DS, Lobo A, Kulkami SK (2000) Self-assembled Ge nanostructures as field emitters. Appl Phys Lett 77: 2394–2396.
14. Modinos A. (1984) Field, thermionic, and secondary electron emission spectroscopy. Plenum Press, New York, Chapter 7.
15. Kondratenko SV, Vakulenko OV, Nikolenko AS, Kozyrev YuN, Rubezhanska MYu (2007) Photoconductivity spectra of Ge/Si heterostructures with Ge quantum dots. Nanotechnology 18: 185401–185406.
16. Peter Yu, Cardona M (2002) Fundamentals of semiconductors, physics and material properties. Springer, Heidelberg.
17. Kondratenko SV, Vakulenko OV, Nikolenko AS, Golovinskiy SL, Kozyrev YuN, Rubezhanska MYu (2007) Photocurrent spectroscopy of indirect transitions in Ge/Si multilayer quantum dots at room temperature. Surf Sci 601: L45–L49.

Part IV
Supramolecular Nanostructures on Surface of Silica

The surface of a solid state influences the processes of self-organization of molecules and nanoparticles greatly. Besides, the surface may itself represent a chemically active component which has a direct influence on forming of highly organized supramolecular nanostructures. Usage of solid-state matrixes with various structures, chemical nature of the surface, and given porosity provide control of self-organization processes of supramolecules and their groups.

Recent reports confirm that amorphous highly dispersive silica is characterized by nearly full physiological harmlessness and high adsorptive characteristics against proteins, toxins, and pathogenic microorganisms. Such complex of properties promises its usage for medical treatment of different diseases.

Purposive usage of supramolecular chemistry methodology, the effects of energetic and geometrical influence of highly dispersive silica surface, reactionary and adsorptive properties of its active centers allowed us to create new functional nanocomposites for medico-biological and technical applications.

Such materials preserve essential characteristics of highly dispersive silica, while substances immobilized on its surface may acquire new useful properties.

So, for instance, it was discovered that a nanocomposite containing immobilized bioactive substances on its surface exhibits synergetic properties, prolonged effect, higher bioaccessibility and bioactivity of the acting substances.

Specially constructed supramolecular structures on the silica surface may possess the functions of recognition and specific binding of molecules and microbiological objects according to the principle of complementarity: “key–lock,” “host–guest,” etc. They can be used as highly selective adsorbents.

The studies described in this part were directed to creation of new fundamental and application knowledge about regularities of synthetic processes and chemical modeling of organic, inorganic, and hybrid supramolecular systems at the surface of highly dispersed silica. Special attention was paid to determination of conditions for supramolecular structures’ formation, their targeted stabilization in adsorbed, chemisorbed, or encapsulated state, and usage of supramolecular templates for synthesis of new nanomaterials with designed molecular architecture. A strong emphasis was placed on understanding influence of highly dispersed silica in the synthetic process, evidences of structure of supramolecular complexes, creation of new prospective nanotechnologies and nanomaterials on this base, and determining the ways for their practical use.

Chapter 20
Designing of the Nanosized Centers for Adsorption of Mercury (II) on a Silica Surface

L.A. Belyakova, D.Yu. Lyashenko, and O.M. Shvets

Abstract The chemical design of nanosized centers for mercury (II)adsorption on a silica surface has been carried out. Chemically bonded molecules of β-cyclodextrin are the centers of adsorption. The kinetics of Hg (II) adsorption is analyzed within the framework of Lagergren model for processes of pseudo-first and pseudo-second orders. It was shown that the adsorption isotherm for β-cyclodextrin-containing silica is well described by Langmuir equation. The formation of inclusion complexes "β-cyclodextrin–nitrate-ion" with ratio 1:1 and supramolecules with composition $C_{42}H_{70}O_{34}\cdot 4Hg(NO_3)_2$ on a surface of β-cyclodextrin-containing silica has been proved using IR and ^1H NMR spectroscopy, spectrophotometry, elemental analysis, X-ray diffraction, and chemical analysis of surface compounds.

20.1 Introduction

It is known that functional organosilicas have high affinity to metal ions. They are used for express analysis of metal ions, separation of multicomponent ion mixtures, and synthesis of ion-exchange materials [1–7]. Silica is the most suitable support in the synthesis of functional materials due to reactivity of surface silanol groups, high chemical, thermal, radiation, antibacterial resistances, and no swelling [2, 3].

To solve complicated adsorption problems, for example, quantitative extraction and express analysis of toxic metal ions in water or dilute aqueous solutions, highly selective materials are necessary. One method for increase of functional silica selectivity can be immobilization of macro cyclic organic compounds as nanosized centers for adsorption of specified ions. Cyclodextrins are cyclic oligomers of α-D-glucose. They belong to the compounds which form stable inclusion complexes of the "host–guest" type due to steric correspondence of "guest" molecules

L.A. Belyakova (✉)
O.O. Chuiko Institute of Surface Chemistry of the National Academy of Sciences of Ukraine, General Naumov St. 17, Kyiv 03164, Ukraine
e-mail: isc412@ukr.net

A.P. Shpak, P.P. Gorbyk (eds.), *Nanomaterials and Supramolecular Structures*,
DOI 10.1007/978-90-481-2309-4_20,

and free space in molecules of cyclodextrins [8–10]. Cyclodextrins are widely used for enhancement of solubility and stability of medicines and bioactive compounds, chromatographic separation and purification of organic compounds of similar structure and composition [11], extraction of impurities of toxic substances [12]; creation of medicines with prolonged action; and decreasing toxicity of medicines [13, 14]. Cyclodextrins also are promising for creation of selective adsorbents and sensors [15–17].

At present, there has been pronounced tendency to obtain cyclodextrin-containing adsorbents by impregnation into organic polymer matrixes [18–21]. Immobilization of cyclodextrins on a surface of highly dispersed silicas has been studied not sufficiently [22–24]. We proposed reproducible methods of adsorptive and chemical immobilization of cyclodextrins on a surface of porous and nonporous silicas [25–28]. Sorption activity of cyclodextrin-containing silicas toward some metal ions was proved [27–29]. We suppose that the presence of inner hydrophobic cavity with strictly fixed size and hydrophilic lateral functional groups in the molecules of cyclodextrins must have an impact, in particular, on sorption peculiarities of these nanosized centers of adsorption and cyclodextrin-containing materials as a whole.

In the present work an influence of chemical immobilization of mono-tosyl-β-cyclodextrin on adsorption ability of highly dispersed silica to Hg (II) ions has been studied.

20.2 Results and Discussion

Chemical immobilization of mono-tosyl-β-cyclodextrin (Ts-β-*CD*) onto the silica surface has been realized in two stages. The first step is modification of hydroxylated silica surface with aminopropyl groups. The second step is chemical reaction between aminopropylsilica and mono-tosyl-β-cyclodextrin. The quantity of bonded β-cyclodextrin (β-*CD*) is 0.035 mmol g^{-1}. Chemically bonded β-cyclodextrin occupies ~50% of aminopropylsilica surface as the molecule area of β-*CD* equals 2.41 nm^2. The chemical immobilization of Ts-β-*CD* on the aminopropylsilica has been carried out on the lower rim of the torus, since tosyl group of Ts-β-*CD* is located in position 6 [27] (Fig. 20.1 and Sch. 20.1).

Effect of contact time of silica adsorbents I–III with aqueous solutions of 0.01 M mercury (II) nitrate on adsorption of Hg (II) ions was studied. Lagergren's kinetic models for processes of pseudo-first order and pseudo-second order were used for analysis of kinetic curves of Hg (II) adsorption onto adsorbents I–III (Table 20.1). The integral form of Lagergren kinetic model [30] for pseudo-first order processes can be expressed as

$$\ln\left(a_{\mathrm{eq}} - a_t\right) = \ln a_{\mathrm{eq}} - k_1 t, \tag{20.1}$$

where a_t and a_{eq} are the adsorption (mg g^{-1}) at time t (min) and at equilibrium state, respectively; k_1 is the rate constant of adsorption of pseudo-first order (min^{-1}).

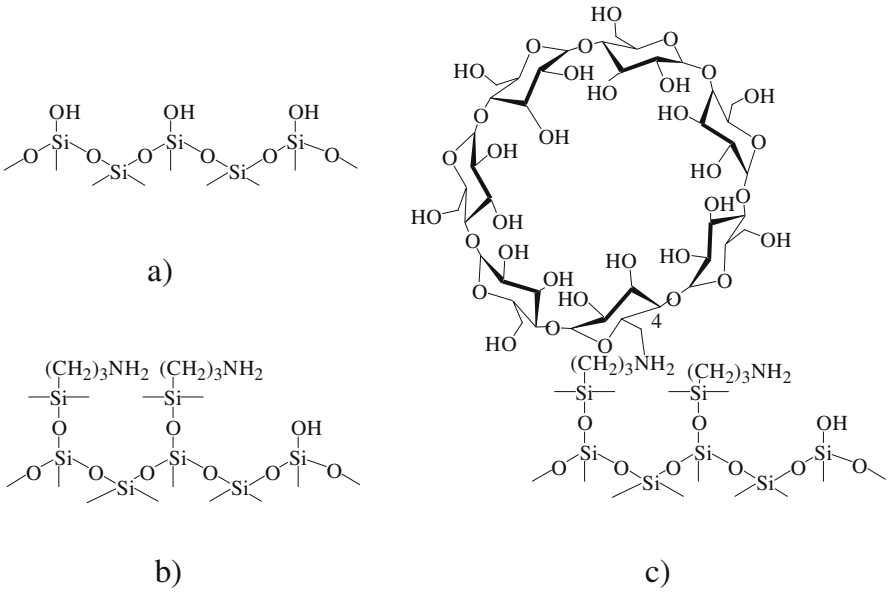

Sch. 20.1 Scheme of surface layer structure for adsorbents I (**a**), II (**b**), and III (**c**)

Table 20.1 Kinetic parameters of mercury (II) nitrate adsorption for processes of pseudo-first and pseudo-second order in Lagergren model

	Process of pseudo-first order		Process of pseudo-second order	
Adsorbent[a]	$k_1(\text{min}^{-1})$	R^2	$k_2(\text{g mg}^{-1}\ \text{min}^{-1})$	R^2
I	3.4 ± 0.2	0.98	0.29 ± 0.01	0.99
II	3.6 ± 0.2	0.98	0.18 ± 0.01	0.35
III	5.9 ± 0.3	0.92	0.055 ± 0.003	0.77

[a]Numbering of adsorbents corresponds to Scheme 20.1.

The equation for kinetic processes of pseudo-second order is given by

$$t/a_t = 1/\left(k_2 \cdot {a_{\text{eq}}}^2\right) + t/a_{\text{eq}}, \tag{20.2}$$

where k_2 is the rate constant of adsorption of pseudo-second order (g mg^{-1} min^{-1}).

The kinetic curves for adsorbents I–III are well fitted to linear form of the pseudo-first order process (Fig. 20.1). The rate constant of adsorption k_1 increases (Table 20.1) for kinetic processes of pseudo-first order in the sequence:

$$\text{I (starting silica)} < \text{II (aminopropylsilica)} < \text{III (β-cyclodextrin-containingsilica)}.$$

It proves that the rate of mercury (II) adsorption depends only on the type of functional groups onto silica surface.

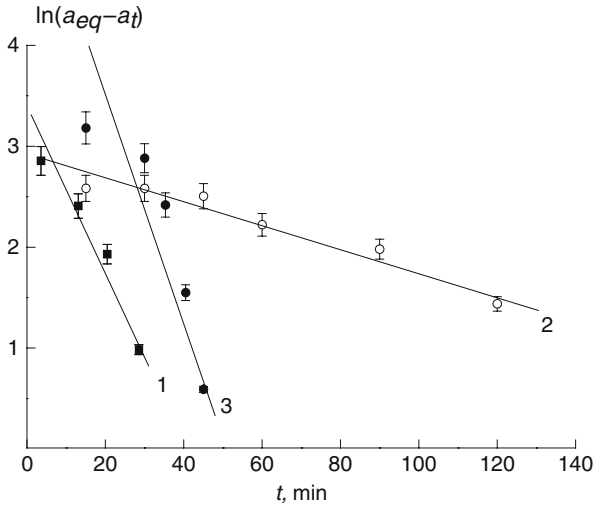

Fig. 20.1 Kinetic curves of mercury (II) adsorption (lines *1–3*) in Lagergren pseudo-first order equation for silicas I–III, respectively

The isotherms of mercury (II) adsorption from $Hg(NO_3)_2$ aqueous solutions with pH = 1–3 and concentrations 10^{-4}–10^{-3} M at 22°C are shown in Fig. 20.2. Predominant forms of mercury (II) in a weak acid range are Hg^{2+} and $Hg(OH)^{+}$ [29]. The uptake of mercury (II) for adsorbents I and II is negligible. For adsorbent III the isotherm of Hg (II) adsorption exhibits a sharp rise even at low equilibrium concentrations.

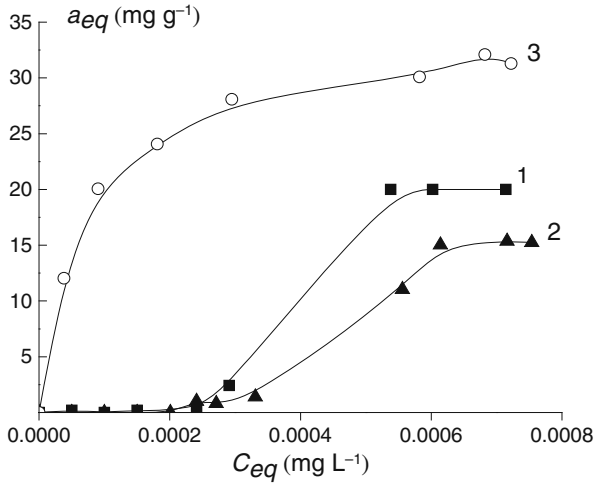

Fig. 20.2 Isotherms of mercury (II) adsorption (curves *1–3*) from mercury (II) nitrate aqueous solutions for adsorbents I–III, respectively

Weak acid silanol groups are present on a surface of adsorbent I ($pK_a = 6.90$, concentration of silanol groups is 0.40 mmol g^{-1}). Silanol groups are in the non-ionized state at pH < 2. At pH 3 the part of ionized silanol groups which participate in cation exchange is only 0.01%. As the adsorption of mercury (II) onto hydroxylated silica is insignificant at pH = 1–3, the centers of its adsorption are only ionized silanol groups. For adsorbent II two-thirds of silanols are replaced by aminopropyl groups ($[NH_2] = 0.28$ mmol g^{-1}) with the basicity constant $pK_b = 4.10$. However, most part of aminopropyl group in weak acid solutions is in protonated state and does not participate in complex formation with cation forms of mercury (II). Considerable enhancement of adsorption of mercury (II) ions by adsorbent III in comparison with adsorbents I and II is directly related to immobilization of mono-tosyl-β-cyclodextrin ($[\beta\text{-}CD] = 0.035$ mmol g^{-1}), as the total concentration of active centers of adsorbents I–III is constant, but only chemical composition of surface is varied. As Hg (II) uptake is four times higher than the quantity of immobilized β-*CD* it is possible to assume the formation of supramolecular structures on the surface of adsorbent III.

The results of adsorption measurements agree with the IR data. The IR spectrum of silica I after adsorption of mercury (II) is practically unchanged. For adsorbent II after contact with $Hg(NO_3)_2$ solution a little shift of the deformation vibrations bands in the N−H bonds for the primary aminopropyl groups (1570 and 1540 cm^{-1}) [31] in low-frequency area (1525 cm^{-1}) is observed as a result of interaction of uncharged amino groups with cations of mercury (II) [32]. In the IR spectrum of silica III after contact with mercury (II) nitrate solution the absorption bands of the valence vibrations of the O−H bonds for the secondary alcohol groups (3375, 3290 cm^{-1}) and the C−H bonds of β-cyclodextrin (2950, 2880 cm^{-1}) are shown less clearly. This confirms participation of chemically bonded β-cyclodextrin in the formation of surface supramolecular structures only for adsorbent III.

Figure 20.3 shows the isotherm of mercury (II) adsorption for adsorbent III in Freundlich and Langmuir equations. Freundlich model (Fig. 20.3a) for adsorption

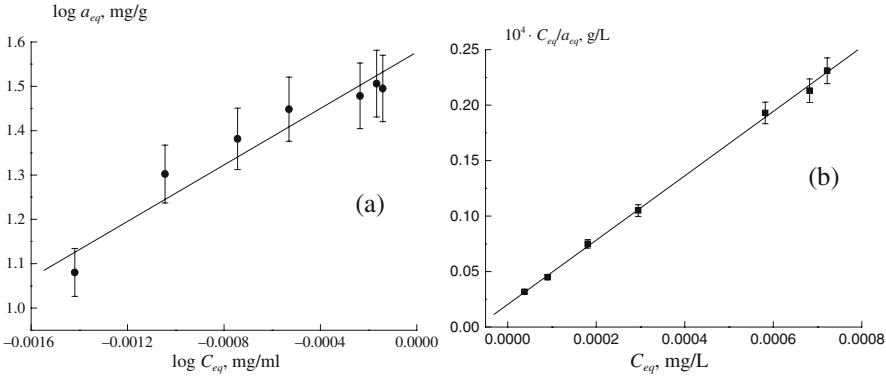

Fig. 20.3 Isotherm of mercury (II) adsorption in Freundlich (**a**) and Langmuir (**b**) equations for adsorbent III

Table 20.2 Parameters of mercury (II) adsorption at 22°C for β-cyclodextrin-containing silica III calculated by Freundlich and Langmuir equations

Freundlich equation			Langmuir equation			
R^2	n	K_F (mg g^{-1})	R^2	K_L(L mg^{-1})	a_m(mg g^{-1})	R_L
0.96	0.003	1.58 ± 0.08	0.999	14,400 ± 700	34 ± 2	0.65 ± 0.03

on heterogeneous surface is described by

$$\log a_{eq} = \log K_F + (1/n) \cdot \log C_{eq}, \tag{20.3}$$

where a_{eq} is the equilibrium adsorption (mg g^{-1}); K_F is Freundlich constant (adsorption capacity) (mg g^{-1}); $1/n$ is Freundlich constant characteristic of adsorption intensity; C_{eq} is the equilibrium concentration of adsorptive substance in a solution(mg L^{-1}).

Langmuir model (Fig. 20.3b) for monolayer adsorption on localized sites of energy uniform surface is described by

$$C_{eq/a_{eq}} = 1/(K_L \cdot a_m) + (1/a_m) \cdot C_{eq}, \tag{20.4}$$

where C_{eq} is the equilibrium concentration of adsorptive substance in a solution (mg L^{-1}); a_{eq} is the equilibrium adsorption (mg g^{-1}); K_L is Langmuir constant, which characterizes the energy of adsorption (L mg^{-1}); a_m is the adsorption capacity of monolayer (mg g^{-1}).

The parameters of adsorption are given in Table 20.2. The experimental data are well fitted to linear form of Freundlich and Langmuir equations (Fig.20.3). However, the correlation coefficient $R^2$is of higher value for Langmuir equation. The values of Langmuir equation (Table 20.3) were used for calculation of separation factor R_L [30]:

$$R_L = 1/\left(1 + K_L \cdot C^{\circ}\right), \tag{20.5}$$

where C° is the initial concentration of adsorbtive (mg L^{-1}).

Table 20.3 Chemical shifts in the ^{1}H NMR spectra for β-cyclodextrin and its inclusion complex with mercury (II) nitrate

Protons	Chemical shift δ (ppm) β-*CD*[a]	Chemical shift δ (ppm) β-*CD*	Chemical shift δ (ppm) "β-*CD*–$Hg(NO_3)_2$"	$\Delta\delta$ (ppm)
C(1)-H	4.820	4.821	4.819	−0.002
C(2)-H	3.290	3.200	3.270	0.070
C(3)-H	3.640	3.629	3.633	0.004
C(4)-H	3.340	3.317	3.318	0.001
C(5)-H	3.590	3.537	3.543	0.006
C(6)-H	3.640	3.629	3.633	0.004

[a]Literature data [38] .

The value $R_L = 0.65$ is evidence of high affinity of adsorbent III to Hg (II). Since the experimental adsorption isotherm is in a good agreement with equation of Langmuir adsorption isotherm these conclusions can be made: (1) the surface of chemically modified silica is sufficiently homogeneous; (2) the surface centers of adsorption do not interact with each other; (3) adsorption of Hg (II) is monolayer. These conclusions are not contradicted by our experimental result that the molecules of immobilized β-cyclodextrin are the unique centers of mercury (II) adsorption.

In the electronic spectrum of 0.001 M aqueous solution of mercury (II) nitrate symmetric absorption band with $\lambda_{max} = 302$ nm and $\varepsilon = 300$ L mol^{-1} cm^{-1} is registered. It corresponds to $n \rightarrow \pi^*$ transition of N=O chromophore in nitrate-ion [33]. The absorption band at 302 nm becomes asymmetric and its intensity sharply increases ($\varepsilon = 4600$ L mol^{-1} cm^{-1}) as a result of addition of given quantities of β-*CD* to an aqueous solution of $Hg(NO_3)_2$. β-Cyclodextrin does not have characteristic absorption bands in UV region of spectrum. The content of nitrate-ions in equilibrium solutions decreases. These facts together with the spectral changes of the absorption band of N=O chromophore are evidence of NO_3^- interaction with β-*CD*, namely, the anion penetration to inner cavity of β-cyclodextrin and the formation of inclusion complex "β-*CD*$-NO_3^-$." The composition of inclusion compound was determined by the method of equimolar series. Experimental points have linear correlation (Fig. 20.4) for complex "β-*CD*$-NO_3^-$" with ratio 1:1 in Benesi–Hildebrand equation [34]:

$$\left(C^\circ_{NO3^-} \cdot l\right)/D^\lambda = 1/\varepsilon^\lambda + 1/\left(K_s \cdot \varepsilon^\lambda \cdot C^\circ_{\beta\text{-}CD}\right), \tag{20.6}$$

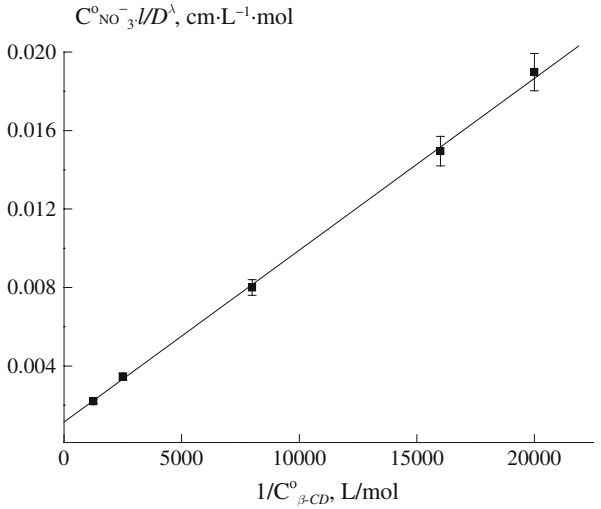

Fig. 20.4 Dependence of spectral characteristics of nitrate-ion on β-cyclodextrin amounts in water solutions in Benesi–Hildebrand equation

where C° is the initial concentration of the reagents (mol L^{-1}); D^{λ} is the optical density of equilibrium solutions (arbitrary units, a.u.); ε^{λ} is the molar extinction coefficient of the equilibrium solutions (L mol^{-1} cm^{-1}); K_s is the binding constant, or the constant of complex stability (L mol^{-1}); l is the thickness of the absorbing layer of analyzed solution (cm).

The value of the binding constant $K_s = 1290 \pm 60$ L mol^{-1} is evidence of the high strength of the "β-*CD*$-NO_3^-$" inclusion complex. Since the volume of inner cavity of β-*CD* molecule is *V* cavity β-*CD* = 0.262 nm^3, of its upper part is $V^1/_2$ cavity β-*CD* = 0.156 nm^3, the volume and diameter of hydrated nitrate-anion are $VNO_3^- = 0.153$ nm^3 and $dNO_3^- = 0.67$ nm [35], the penetration of the anion into the cavity of β-cyclodextrin is feasible through the wider edge. Location of NO_3^- is possible only in the upper part of β-*CD* torus. The reason for the high strength of the "β-*CD*$-NO_3^-$" inclusion complex is the equality of volumes of the upper part of β-*CD* inner cavity and hydrated anion.

Preparative quantity of product of interaction between β-cyclodextrin and mercury (II) nitrate as white needle-like crystals was obtained by precipitation at 5°C. The solution with pH = 1 contained equimolar quantities of β-cyclodextrin and mercury (II) nitrate. Hg^{2+} is the predominant form of mercury (II) at pH = 1. The presence of Hg^{2+} in the precipitated inclusion complex has been proved by chemical and elemental analysis, β-*CD*:$Hg(NO_3)_2$ = 1:4.

The study of the product by X-ray diffraction, IR and ^{1}H NMR spectroscopy confirms the formation of the "β-CD$-NO_3^-$" inclusion complex.

Three of the most intensive peaks with $2\theta = 12.57°$, 19.42°, 22.84° and $I = 7660$, 4140, 4570 a.u. are in the X-ray spectrum of crystalline β-cyclodextrin. Three main peaks of $Hg(NO_3)_2 \cdot H_2O$ attribute to $2\theta = 19.73$, 19.17, and 17.81. The X-ray spectrum of the product of β-cyclodextrin interaction with mercury (II) nitrate does not have peaks which belong to $Hg(NO_3)_2 \cdot H_2O$. The main peaks of β-cyclodextrin after interaction with mercury (II) nitrate are shifted ($2\theta = 12.42$, 19.57, 22.67), and their intensity essentially increases ($I = 14{,}030$, 10,740, 7400). Hence, the "β-cyclodextrin–mercury (II) nitrate" inclusion compound is formed.

β-Cyclodextrin consists of seven glucopyranose units which are connected by glycosidic α-(1→4)-bonds. The 7 primary (C-6) hydroxyl groups are located at the lower edge, and 14 secondary (C-2) and (C-3) alcohol groups are at the upper edge of β-*CD* molecule:

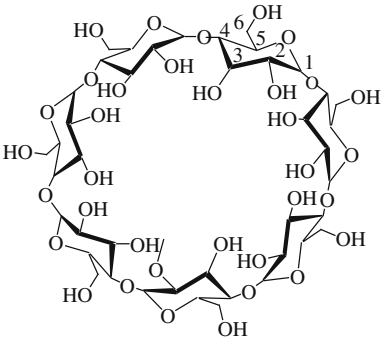

In the IR spectrum of β-cyclodextrin the wide intensive absorption band in the range of 3500−3000 cm^{-1} with maximum at 3380 cm^{-1} is observed. This band belongs to the valence vibrations of the O−H bonds in the secondary hydroxyl groups which are connected by the intramolecular hydrogen bonds [9]. The absorption band with maximum at 2930 cm^{-1} corresponds to the valence vibrations of the C−H bonds. In the range of 1400−1000 cm^{-1} the absorption bands of the valence vibrations of the C−O and C−C bonds and the deformation vibrations of the O−H bonds in alcoholic groups of β-*CD* are registered.

The IR spectrum of the "β-cyclodextrin–mercury (II) nitrate" inclusion complex has one absorption band with maximum at 3380 cm^{-1} which is ascribed to the valence vibrations of the hydrogen-bonded hydroxyl groups of β-*CD* [9]. The intensity of the absorption bands of the valence vibrations of the C−H, C−O, and C−C bonds decreases. Besides, the weak absorption band at 1385 cm^{-1} points to the presence of nitrate-anion [36] in the inclusion complex. Thus, it is possible to assume that nitrate-ion is placed in the inner cavity of the β-cyclodextrin molecule [37].

The shifts of all signals 1H of glucopyranose units are observed in the ^{1}H NMR spectrum of the "β-*CD*−$Hg(NO_3)_2$" inclusion complex in comparison with the spectrum of β-cyclodextrin. It points to interaction of β-cyclodextrin with mercury (II) nitrate (Table 20.3).

Slight variation of the chemical shift $\Delta\delta$ value is determined by the parameters of the studied system. It is known [39] that the values of chemical shifts for inclusion complexes increases with growing thermochemical radii of the anion-"guest" and with decreasing cavity size of cyclodextrins. For the system "β-cyclodextrin–nitrate-ion" slight changes of the chemical shifts of protons (Table 20.3) agree with the size of nitrate-ion (0.179 nm). The disappearance of the protons' resonance signals of the primary and the secondary hydroxyl groups of β-*CD* indicates that interior complex is formed [40]. The signals of the inner protons C(3)-, C(5)-, and C(6)-N of β-cyclodextrin are shifted into upfield region ($+\Delta\delta$) [39] after interaction with mercury (II) nitrate. It points to the penetration of the hydrated anion into the cavity of β-*CD*. The largest shift for C(5)-H allows us to conclude that the anion is kept near the vicinal C(5)-atom. For the protons of C(1)-, C(2)-, and C(4)-atoms of glucopyranose units which are located outside of the β-*CD*molecule torus, $\Delta\delta$ is usually smaller than that for C(3)-, C(5)-, and C(6)-H [39, 41]. In our case it was observed for C(1)- and C(4)-H signals. The downfield slight shift for C(1)-H indicates the absence of conformation changes in the β-*CD*molecule when nitrate-anion enters into the inner cavity of the β-*CD*. The large shift for C(2)-H is evidence of anion penetration into the cavity of β-*CD* through wider edge of the β-*CD* molecule, and it is kept near C(5)-H in the upper part of β-*CD*. These results agree with our conclusion about geometrical conformity of the hydrated nitrate-anion and upper part of the β-cyclodextrin cavity.

From obtained results conclusions about the mechanism of mercury (II) adsorption on the surface of β-cyclodextrin-containing silica are made. The quantity of adsorbed mercury (II) nitrate is four times more than the concentration of chemically bonded β-cyclodextrin. The inclusion compound of the "host–guest" type with ratio 1:1 between grafted molecules of β-cyclodextrin and nitrate-ions in a solution is formed on the surface of adsorbent III. Then NO_3^- ion incorporated into

the cavity of β-*CD* attracts Hg^2+, which, in turn, attaches yet another nitrate-anion. The linear molecule of mercury (II) nitrate spaced perpendicular to the plane of the macro cycle rim is formed. Three other molecules of mercury (II) nitrate are kept due to interaction with hydroxyl groups of wider edge of the β-*CD* molecule. Thus, the high affinity of β-cyclodextrin-containing silica to Hg^2+ is a result of the formation of neutral supramolecular structures (super molecules) with composition $C_{42}H_{70}O_{35}{\cdot}4Hg(NO_3)_2$ on the surface of β-cyclodextrin-containing silica:

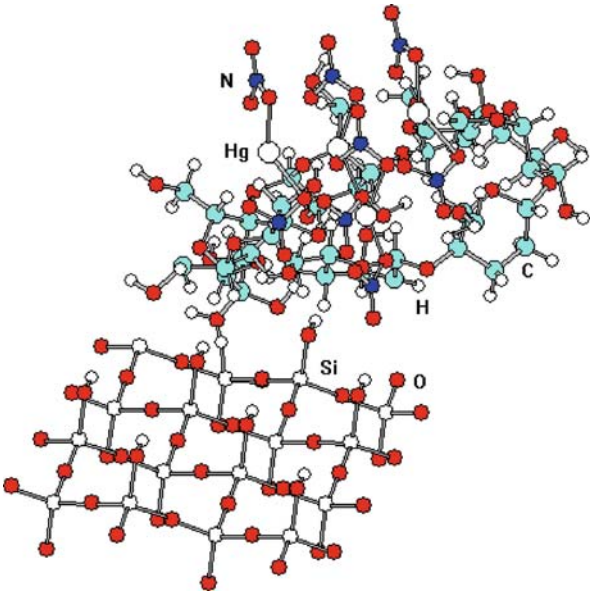

20.3 Conclusion

Chemical modification of the silica surface by β-cyclodextrin for increase of its affinity to mercury (II) was proposed. Substantial growth of mercury (II) ions uptake from dilute aqueous solutions by β-cyclodextrin-containing silica was shown. The value of the binding constant equals 14,400 ± 700 L mg^{-1}. The hydroxylated silica and aminopropylsilica do not adsorb mercury (II) under these conditions. Mechanism of β-cyclodextrin interaction with mercury (II) nitrate was established by IR spectroscopy, ^{1}H NMR spectroscopy, UV absorption, elemental analysis, X-ray diffraction, and chemical analysis of surface compounds. The formation of "β-cyclodextrin–nitrate-ion" inclusion complexes, with composition 1:1 and binding constant 1290 ± 60 M^{-1}, and super molecules with composition $S_{42}H_{70}O_{35}{\cdot}4Hg(NO_3)_2$ in a solution and on the surface of β-cyclodextrin-containing silica was proved.

Acknowledgments The work was done with financial support of the Complex Program of Fundamental Researches of the National Academy of Sciences of Ukraine "Nanostructure Systems, Nanomaterials, Nanotechnologies."

References

1. Iler RK (1979) The chemistry of silica: solubility, polymerization, colloid and surface properties and biochemistry of silica. Wiley-Interscience, New York
2. Tertykh VA, Belyakova LA (1991) Chemical reactions with participation of silica surface. Naukova Dumka, Kiev
3. Vansant EF, Van Der Voort P, Vrancken KC (1995) Characterization and chemical modification on the silica surface. Elsevier, Amsterdam
4. Dobrowski A, Tertykh VA (1996) Adsorption on new and modified inorganic sorbents. Elsevier, Amsterdam
5. Jal PK, Patel S, Mishra BK (2004) Chemical modification of silica surface by immobilization of functional groups for extractive concentration of metal ions. Talanta 62: 1005−1028
6. Dabrowski A, Hubicki Z, Podkościelny P, Robens E (2004) Selective removal of the heavy metal ions from waters and industrial waste waters by ion-exchange method. Chemosphere 56:91–106
7. Ariga K, Vinu A, Hill JP, Mori T (2007) Coordination chemistry and supramolecular chemistry in mesoporous nanospace. Coord Chem Rev 251:2562–2591
8. Lehn J-M (1995) Supramolecular chemistry: concepts and perspectives. VCH Verlagsgesellschaft, Weinheim
9. Szejtli J (1998) Introduction and general overview of cyclodextrin chemistry. Chem Rev 98:1743–1750
10. Hedges AR (1998) Industrial applications of cyclodextrins. Chem Rev 98:2035–2044
11. Khan AR, Forgo P, Stine KJ, D'Souza VT (1998) Methods for selective modification of cyclodextrins. Chem Rev 98:1977–1996
12. Shiraishi S, Komiyama M, Hiray H (1986) Immobilization of β-cyclodextrin on silica gel. Bull Chem Soc Jpn 59:507–510
13. Prousoontorn MH, Pantatan S (2007) Production of 2-*O*-α-glucopyranosyl L-ascorbic acid from ascorbic acid and β-cyclodextrin using immobilized cyclodextrin glycosyltransferase. J Incl Phenom Macrocycl Chem 57:39–46
14. Abe I, Fukuhara T, Kawasaki N, Hitomi M, Kera Y (2000) Characteristics of cyclodextrin adsorption onto activated carbons. J Colloid Interface Sci 229:615–619
15. Stancanelli R, Mazzaglia A, Tommasini S, Calabrò ML, Villari V, Guardo M, Ficarra P, Ficarra R (2007) The enhancement of isoflavones water solubility by complexation with modified cyclodextrins: a spectroscopic investigation with implications in the pharmaceutical analysis. J Pharm Biomed Anal 44:980–984
16. Panda SK, Schrader W, Andersson JT (2006) β-Cyclodextrin as a stationary phase for the group separation of polycyclic aromatic compounds in normal-phase liquid chromatography. J Chromatogr A 1122:88–96
17. Rozou S, Voulgari A, Antoniadou-Vyza E (2004) The effect of pH dependent molecular conformation and dimerization phenomena of piroxicam on the drug: cyclodextrin complex stoichiometry and its chromatographic behaviour. A new specific HPLC method for piroxicam:cyclodextrin formulations. J Pharm Sci 21:661–669
18. Seo T, Kajihara T, Iijima T (1987) Hydrolysis of phenyl esters in cyclodextrin-polymer systems. Makromol Chem 188:1295–1304
19. Martel B, Leckchiri Y, Pollet A, Morcellet M (1995) Cyclodextrin-poly(vinylamine) systems—I. Synthesis, characterization and conformational properties. Eur Polym J 31: 1083–1088

20. Ali MB, Kalfat R, Sfihi H, Ouada HB, Chovelon JM, Jafferezic-Renault N (1998) Cyclodextrin-polymethylhydrosiloxane gel as sensitive membrane for heavy ion sensors. Mater Sci Eng 6:53–58
21. Martel B, Morcellet M (1994) Sorption of aromatic compounds in water using polymer sorbents containing amino groups. J Appl Polym Sci 51:443–451
22. Akiyama T, Hishiya T, Asanuma H, Komiyama M (2001) Molecular imprinting of cyclodextrin on silica-gel support for the stationary phase of high-performance-liquid-chromatography. J Incl Phenom Macrocycl Chem 41:149–153
23. Raju GB, Holmgren A, Forsling W (1997) Adsorption of dextrin at mineral/water interface. J Colloid Interface Sci 193:215–222
24. Phan TNT, Bacquet M, Morcellet M (2002) The removal of organic pollutants from water using new silica-supported β-cyclodextrin derivatives. React Funct Polym 52:117–125
25. Belyakova LA, Varvarin AM, Khora OV, Oranskaya EI (2008) The interaction of β-cyclodextrin with benzoic acid. Russ J Phys Chem 79:228–232
26. Belyakova LA, Varvarin AM, Lyashenko DYu, Khora OV (2005) Designing adsorption centres for biological active molecules on a silica surface. Adsorpt Sci Technol 23:703–719
27. Belyakova LA, Kazdobin KA, Belyakov VN, Ryabov SV, Danil de Namor AF (2005) Synthesis and properties of supramolecular systems based on silica. J Colloid Interface Sci 283:488–494
28. Belyakov VN, Belyakova LA, Varvarin AM, Khora OV, Vasilyuk SL, Kazdobin KA, Maltseva TV, Kotvitskyy AG, Danil de Namor AF (2005) Supramolecular structures on silica surfaces and their adsorptive properties. J Colloid Interface Sci 285:18–26
29. Belyakova LA, Shvets OM, Danil de Namor AF (2008) Adsorption of mercury (II) onto silica surface modified β-cyclodextrin. Russ J Phys Chem 82:1357–1362
30. Gupta SS, Bhattacharyya KG (2006) Adsorption of Ni(II) on clays. J Colloid Interface Sci 295:21–32
31. Bellamy LJ (1968) Advances in infrared group frequencies. Methuen, London
32. Etienne M, Walcarius A (2003) Analytical investigation of the chemical reactivity and stability of aminopropyl-grafted silica in aqueous medium. Talanta 59:1173–1188
33. Rao CNR (1961) Ultra-violet and visible spectroscopy chemical applications. Butterworths, London
34. Wen X, Tan F, Jing Z, Liu Z (2004) Preparation and study of the 1:2 inclusion complex of carvedilol with β-cyclodextrin. J Pharm Biomed Anal 34:517–523
35. Chamberlain II RV, Slowinska K, Majda M, Buhlmann P, Aoki H, Umerawa YE (2000) Electrostatically-induced inclusion of anions in cyclodextrin monolayers on electrodes. Langmuir 16:1388–1396
36. West W (1956) Chemical applications of spectroscopy. Interscience Publishers, New York
37. Jambhekar S, Casella R, Maher T (2004) The physicochemical characteristics and bioavailability of indomethacin from β-cyclodextrin, hydroxyethyl-β-cyclodextrin, and hydroxypropyl-β-cyclodextrin complexes. Int J Pharm 270:49–166
38. Schneider HJ, Hacket F, Rudiger V, Ikeda H (1998) NMR studies of cyclodextrins and cyclodextrin complexes. Chem Rev 98:1755–1786
39. Matsui Y, Ono M, Tokunaga S (1997) NMR spectroscopy of cyclodextrin–inorganic anion systems. Bull Chem Soc Jpn 70:535–541
40. Borodkin GS, Borodkina IG, Uraev AI, Vasilchenko IS, Sadekov ID, Garnovskii AD (2004) Multinuclear spectroscopy NMR of ambidentat ligands. Russ Chem J 48:117–124
41. Chen M, Diao G, Zhang E (2006) Study of inclusion complex of β-cyclodextrin and nitrobenzene. Chemosphere 63:522–529

Chapter 21
Supramolecular Structures of Chitosan on the Surface of Fumed Silica

T.V. Kulyk, B.B. Palyanytsya, T.V. Borodavka, and M.V. Borysenko

Abstract The interaction of a chitosan biopolymer with the surface of fumed silica was investigated by temperature-programmed desorption mass spectrometry (TPDMS), thermogravimetry (TG), UV–visible spectroscopy (UV/vis), and Fourier transform infrared spectroscopy (FTIR). Mass spectra were used to estimate the number of chitosan segments non-connected and directly connected to the silica surface. The results indicate that as the amount of adsorbed chitosan increases the number of non-connected segments increases. A method was suggested for calculating the *p* parameter for chitosan adsorbed on silica directly from TPDMS data and without additional sample treatment. The experimental data indicate the formation of supramolecular iodine–chitosan surface complexes arranged in the form of two-layer cylindrically structured units.

21.1 Introduction

Research on adsorption of biopolymers on solid surfaces is important for advancing the knowledge on the fundamentals of macromolecules adsorption and for the development of applications in chemistry, biology, and medicine. On this venue, we are reporting some data related to the adsorption of chitosan (poly[(1-4)-2-amino-2-deoxy-D-glucose]) from water solutions onto the surface of fumed silica [1, 2].

Silica with varying chitosan surface content was obtained by equilibrium adsorption from water solutions of increasing concentration. Varying the degree of polysaccharide surface coverage allows modulating the final properties of the resulting composite and the properties of its single components. Chitosan is non-toxic and can be biodegraded to environmental and biota harmless low-molecular compounds [3]. It has a wide range of adsorption properties, can stimulate regeneration of

T.V. Kulyk (✉)
O.O. Chuiko Institute of Surface Chemistry of the National Academy of Sciences of Ukraine, General Naumov St. 17, Kyiv 03164, Ukraine
e-mail: tanyakulyk@gala.net

A.P. Shpak, P.P. Gorbyk (eds.), *Nanomaterials and Supramolecular Structures*,
DOI 10.1007/978-90-481-2309-4_21,

damaged tissues [4], and also has remarkable antibacterial, antiviral, antiradiation, and immuno-modulating properties [5–7]. This polymer is also used for drug delivery [8]. A vast number of studies are currently being carried out in order to obtain new chitosan-based materials for applications in biology and medicine [9–12].

As a rule, not all segments of an adsorbed polymer are in direct contact with the surface. The percentage of chain segments directly interacting with the surface, the so-called *p* parameter, becomes of practical importance to elucidate the structure of the adsorbed layer. The method for estimating the adsorbed polymer conformation from the knowledge of the *p* parameter is widely applied to describe polymer conformations on various solid surfaces [13]. Most often, the *p* parameter of polymers adsorbed on the surface of oxides is determined with the data from infrared spectroscopy, electronic paramagnetic resonance, and microcalorimetry [14].

In this work, we study the structure of the adsorption layer of chitosan on the surface of silica with the aid of thermogravimetry, Fourier transform infrared spectroscopy, UV–visible spectroscopy, and temperature-programmed desorption mass spectrometry. Particularly, the report describes the results of the estimation of the *p* parameter of silica-adsorbed chitosan from TPDMS data.

21.2 Experimental

21.2.1 Material

Samples of fumed silica (purity 99.87%, S_{BET}=270 m^2/g) were supplied by the Pilot Plant of the O.O. Chuiko Institute of Surface Chemistry, Kalush, Ukraine). Chitosan (low viscosity, obtained from crab shells) was supplied by Fluka (Switzerland). Silica-adsorbed chitosan (SiO_2/chitosan) samples were prepared by the equilibrium adsorption method. Chitosan contents varied from 5 to 60 mg/g of silica. After the adsorption step, the samples were dried at room temperature. Self-supported transparent pellets (20 mg) to be tested by FTIR were obtained by pressing the silica powder to 60 MPa. SiO_2/chitosan samples with no further treatment were analyzed by TPDMS (batches were 20.0 mg) and TG (batches were 240 and 170 mg of SiO_2 and SiO_2/chitosan, respectively). Silica–chitosan–iodine samples were prepared by the equilibrium adsorption method. An aqueous solution of KI−I_2 10 ml in volume was mixed with 0.1 g of SiO_2/chitosan (60 mg/g), and the mixture obtained was let standing for 2 h. The suspensions prepared were centrifuged and dried at room temperature.

21.2.2 Experimental Methods

Differential thermogravimetric analysis was performed in a MOM Q-1500 *derivatograph* and the 20–1000ºC temperature range was scanned. The heating rate was 0.167ºC/s.

FTIR spectra were recorded in the frequency range 4000−500 cm^{-1} using the Thermo Nicolet NEXUS FT-IR spectrophotometer. Samples were pressed into pellets without additional treatment.

UV–vis spectra were recorded in a Specord M-40 (Carl Zeiss Jena, Germany) spectrophotometer with an absorption mode for the solutions and a reflectance mode for the powders. The pH value was changed by addition of HCl or NaOH solution and controlled using a pH meter with a glass electrode.

TPDMS experiments were performed in an MKh-7304A monopole mass spectrometer (Electron, Sumy, Ukraine) with electron impact ionization, adapted for thermodesorption measurements. A typical test comprised placing a 20 mg sample on the bottom of a molybdenum–quartz ampoule, evacuating to $\sim 5 \times 10^{-5}$ Pa at ∼20°C and then heating at 0.15ºC/s from room temperature to ∼750°C. The volatile pyrolysis products passed through a high-vacuum valve (5.4 mm in diameter) into the ionization chamber of the mass spectrometer where they were ionized and fragmented by electron impact. After mass separation in the mass analyzer, the ion current due to desorption and thermolysis was amplified with a VEU-6 secondary-electron multiplier. The mass spectra were recorded and analyzed using a computer-based data acquisition and processing setup. The mass spectra were recorded within 1–210 amu. During each TPDMS experiment, ∼240 mass spectra were recorded. During a thermodesorption experiment, the sample was heated slowly while the rate of evacuation of the volatile pyrolysis products was high. Diffusion effects can thus be neglected and the intensity of the ion current can be considered proportional to the desorption rate. This made it possible to calculate the non-isothermal kinetic parameters such as the activation energy and the preexponential factor of desorption (thermal decomposition) and chemical reactions in the condensed phase and on the surface of the silica. Non-isothermal parameters and the p parameter were calculated using a computer program only for well-resolved peaks for which form and position on the temperature scale were reproduced in several experiments.

21.3 Results and Discussion

Figure 21.1 shows the FTIR spectra of silica samples with different amounts of adsorbed chitosan. Chitosan containing samples had increased absorption bands at 1524 cm^{-1} that are attributed to bending vibrations of N−H bonds in the protonated amino group. Other chitosan characteristic absorption bands were overlapped with absorption bands due to the silica and adsorbed water. It is known [14] that IR spectroscopy allows to determine the involvement of silica surface silanol groups in the interaction with modifier molecules. In this case no correlation was found between the absorption intensity of the 3750 cm^{-1} band due to stretching vibrations of the O−H bonds of isolated silanol groups and the amount of chitosan adsorbed on the silica surface.

Thermal analysis (Fig. 21.2) shows that chitosan-modified silica has an additional stage of weight loss corresponding to polymer destruction. According to the

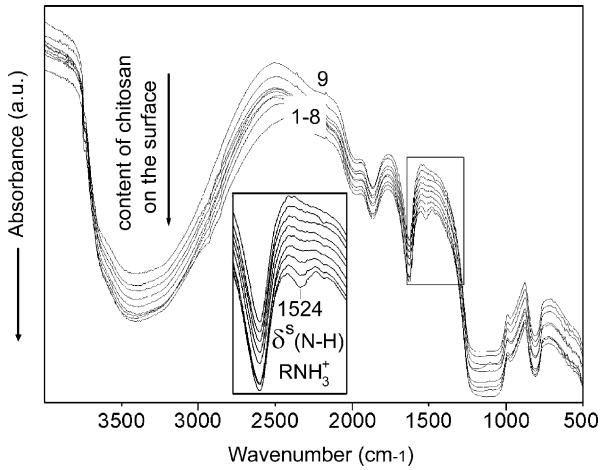

Fig. 21.1 FTIR spectra of samples. (*1*)–(*8*) Chitosan containing silica samples with 5, 10, 15, 20, 25, 35, 50, and 60 mg of chitosan per gram of silica, respectively. (*9*) The initial silica sample

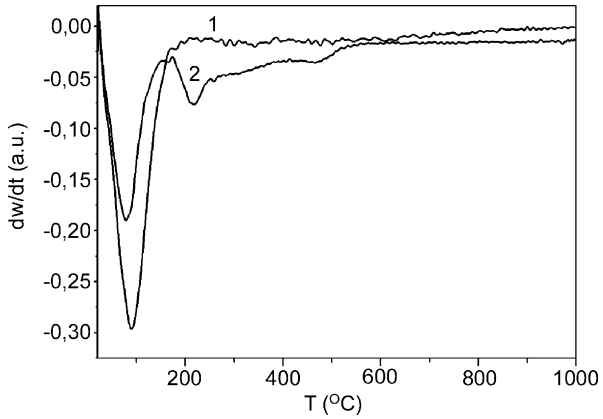

Fig. 21.2 DTG results. (*1*) The initial silica sample. (*2*) Silica modified by chitosan (60 mg/g)

differential curves, most of the chitosan adsorbed on the surface of silica decomposes at 70–500ºC. This is the close temperature range for in vacuo decomposition in the MS experiment.

Earlier TPDMS reports [15] have shown that most chitosan polymeric chains decompose without pyranose ring disruption. They seem to undergo 1,4-β-glycosidic bond cleavage, intramolecular β-elimination of two water molecules, and release of molecular unsaturated amino sugar (AS), the latter with molecular weight of 125 amu (see Scheme 21.1 and Fig. 21.3). Within the 220–400ºC range, mass spectra are observed with the molecular ion at *m*/*z* 125 and their regrouping ions

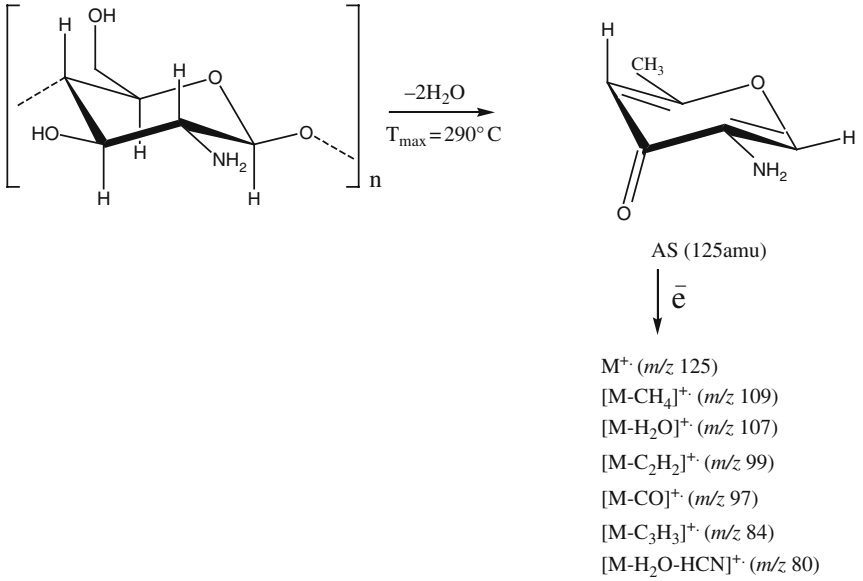

Scheme 21.1

formed in the ion source under the influence of electrons. The curve of thermal desorption corresponding to the ion with *m*/*z* 125 has one peak at $T_{max} = 290$ºC (Fig. 21.3).

The low-temperature stage of AS formation was found to appear during the pyrolysis of adsorbed chitosan (Fig. 21.4). The kinetic parameters of the first-order reaction of unsaturated AS (*m*/*z* 125) formation during pyrolysis of chitosan on the silica surface were calculated. At the low-temperature stage, the activation energy and the preexponential factor are $E^{\neq} = 54$ kJ/mol and $k_0 = 1.19 \times 10^4$ s^{-1}, respectively. The kinetic constant is significantly lower than that of the condensed state

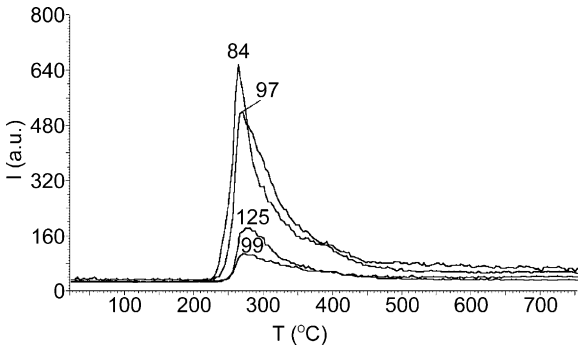

Fig. 21.3 Thermal decomposition of chitosan. TPD traces of the unsaturated amino sugar molecular ion (*m*/*z* 125) and their regrouping ions at *m*/*z* 99, 97, 84

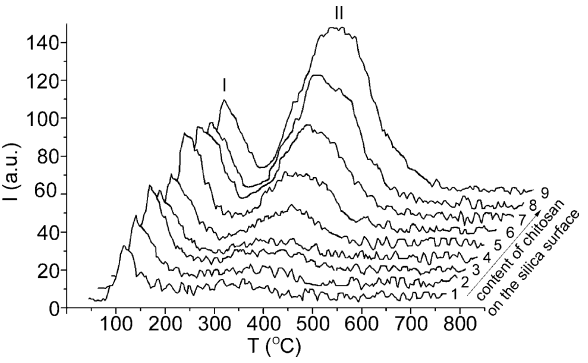

Fig. 21.4 Thermal decomposition of chitosan. TPD traces of the regrouping ion at *m/z* 107. (*1*)–(*9*) Chitosan-modified silica samples with 5, 10, 15, 20, 25, 35, 40, 50, and 60 mg of chitosan per gram of silica, respectively

($E^{\neq}$=124 kJ/mol, k_0 =2.43×10^9 s^{-1}). This effect is likely due to the formation of a $-NH_3^+\cdots{}^-OSi\equiv$ adsorption complex on the silica surface. Complexation results in the stabilization of a highly ordered transition state thus providing for a low activation energy for the elimination of two water molecules from the pyranose ring that results in the formation of AS. It is known that reactions in highly ordered transition states are characterized by negative values of d$S^{\neq}$ [16] as seen in this case. The preexponential factor and the activation energy are also likely reduced by the effects of surface heterogeneity and compensation.

Segment types of adsorbed polymers are usually referred to as trains, loops, or tails. Trains are segments directly interacting with the surface. Loops are areas of polymeric chains with two ends attached to the trains. Tails are so-called "lost ends" of an adsorbed chain. The *p* parameter is a ratio of the number of all train segments (A_{tr}) to the sum of all segments (A_{total}), i.e., $p=A_{tr}/A_{total}$.

Obviously, the two pyrolysis stages of the silica-adsorbed chitosan are caused by two types of chitosan: those directly bound to the surface (trains) corresponding to the formation of the $-NH_3^+\cdots{}^-OSi\equiv$ adsorption complex and those non-silica-bonded (loops and tails).

To study the adsorbed chitosan structure as a function of the degree of coverage of the silica surface, a series of samples were analyzed by both TPDMS and FTIR. The chitosan amount on the surface of these samples corresponded to the adsorption equilibrium value. Samples with higher concentration of chitosan had the stage II thermodesorption peaks of a higher intensity than the stage ones (Fig. 21.4). The integrated intensity of the stage II bands is proportional to the number of chitosan loops and tails while the integrated intensity of the stage I bands is proportional to the number of polymer segments directly bound to the surface. Therefore these values allow for the calculation of the *p* parameter.

The thermodesorption curves for the ion at *m/z*107 were mathematically processed for a series of samples with different chitosan content. The integrated intensity of the I and II peak types were thus obtained with R^2=0.91−0.98 (see Figs. 21.4 and 21.5). The ion at *m/z* 107 was particularly chosen because it is the most intense of the chitosan mass spectra. The *p* parameter was calculated from the integrated intensities (*int*) of the I and II peak types: $p=int^{I}/(int^{I}+int^{II})$.

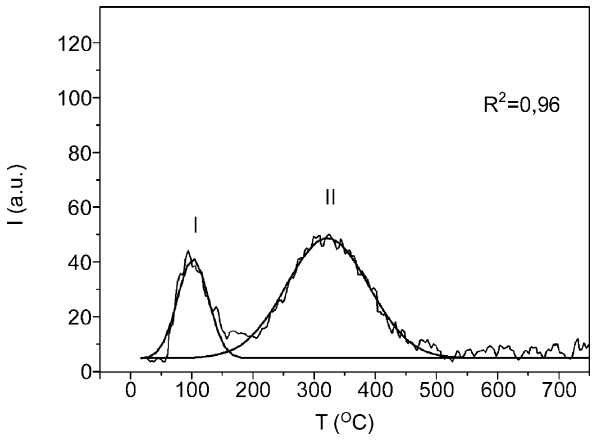

Fig. 21.5 Mathematical deconvolution of the TPD trace of the ion at *m*/*z* 107

A correlation between the amount of the adsorbed polymer and the *p* parameter was obtained (see Fig. 21.6). The higher is the polymer content, the lower is the *p* parameter. At the same time, the amount of polymer segments directly bound to the surface was reduced at growing values of the *p* parameter, i.e., the number of polymer-free segments grows at higher surface coverage densities. For a value of chitosan concentration of $\sim$ 60 mg/g corresponding to the saturation value of the adsorption isotherm, only 10% of pyranose rings appear to be bound. This means that at saturation, 90% of pyranose rings are in the form of loops and tails.

The above discussion sheds some light on the formation of chitosan–iodine supramolecular complexes when chitosan is adsorbed on the silica surface. It is known [17] that in certain conditions chitosan can form supramolecular complexes with iodine that have characteristic absorption band at λ_{max}=500 nm in the UV–vis spectra. Combined physical and chemical research methods have been previously used [17] to elucidate the structure of these complexes. Chitosan–iodine supramolecular complexes have been shown to consist of two-layer cylindrical

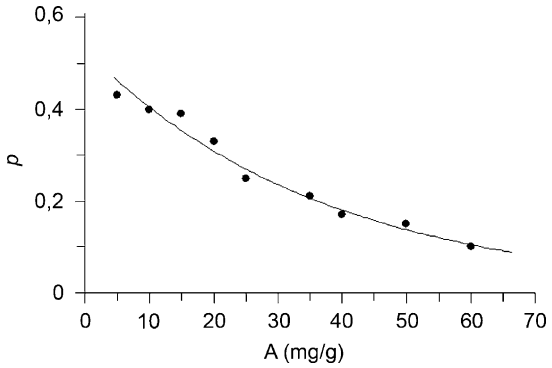

Fig. 21.6 *p* parameter as a function of the amount of chitosan on silica

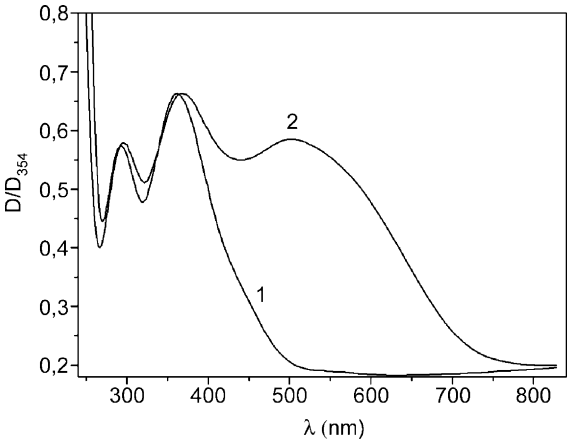

Fig. 21.7 Diffuse reflectance UV–vis spectra of iodine-treated samples. (*1*) Chitosan-free silica (0.1 mmol I_2/g). (2) Chitosan-modified silica (0.9 mmol I_2/g, 60 mg chitosan/g)

structures of inner polyiodide (I_3^-) chains surrounded by an assembly of crystalline-like extended chitosan chains involving intermolecular hydrogen bonds network.

Silica–chitosan sorbent samples become purple when in contact with KJ_3 solutions. Diffusive reflectance UV–vis spectra of silica–chitosan–iodine samples have an absorption band with a maximum at λ=500 nm (see Fig. 21.7). This is a sign of the formation of a chitosan–iodine supramolecular complex on the silica surface. The obtained samples are also easily decolorized by heating above 40°C, an expected result from the lability of these complexes [17].

A lack of absorption bands at λ=500 nm in the UV–vis spectra of the acid solutions (pH 2, Fig. 21.8a) and their presence in the spectra of the alkaline solutions (pH 8.3, Fig. 21.8b) show that at low pH values no chitosan–iodine supramolecular complexes can be formed. However, the complexes were found to be formed on silica–chitosan sorbent surfaces (Fig. 21.7) upon chitosan adsorption at low pH. Thus the ordered supramolecular structures of chitosan on silica can even

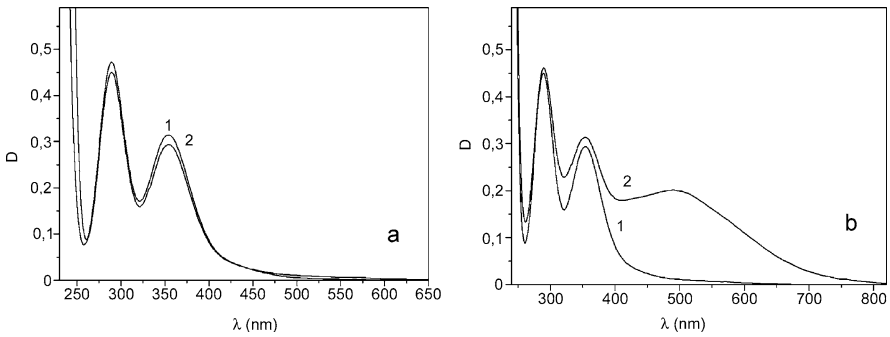

Fig. 21.8 UV–vis spectra of acidified (**a**, pH 2) and alkalized (**b**, pH 8.3) liquid samples. (*1*) Chitosan-free iodine solution (0.75 mmol I_2/l). (*2*) Chitosan–iodine solution (0.75 mmol I_2/l, 1 g chitosan/l)

be formed under acid conditions. Iodine adsorption can be used for testing if the chitosan polymeric chains form ordered or disordered patterns. In solution, the ordered structures are formed only in alkaline media while silica-induced orderly rearrangements can occur even at low pH. A possible explanation is that chitosan polymeric chains bonded with the silica surface are stable conformers, i.e., during adsorption from solution chitosan polymeric chains are formed on the silica surface as extended cylindrical structures. This explains the low value of the *p* parameter obtained. The existence of such conformers on the surface of the silica–chitosan sorbent promotes the formation of surface chitosan–iodine supramolecular complexes.

21.4 Conclusions

A method was suggested for calculating the *p* parameter for chitosan adsorbed on silica directly from TPDMS data and without additional sample treatment. A correlation between the *p* parameter and the amount of adsorbed chitosan was obtained.

The absorption band at λ=500 nm in the UV–vis spectra of silica–chitosan–iodine samples points out the formation of supramolecular chitosan–iodine surface complexes arranged in the form of two-layer cylindrically structured units. They would consist of inner polyiodide (I_3^-) chains surrounded by crystalline-like extended chitosan chains involving intermolecular hydrogen bond network.

TPDMS data presented in terms of the *p* parameter value and UV–vis spectra of silica–chitosan–iodine samples are the evidences of the structure-forming role of silica nanoparticles during chitosan adsorption and the existence of ordered chitosan structures on the silica surface.

References

1. Kulyk TV, Palyanytsya BB, Borodavka TV et al (2007) Physiko-chimiya nanomaterialov and supramolecularnykh struktur. Naukova Dumka, Kiev 1:229–242
2. Borodavka TV, Kulyk TV, Palyanytsya BB et al (2008) Pharm. Jurn. 3:94–98
3. Ravi Kumar MNV (2000) A review of chitin and chitosan applications. React Funct Polym 46(1):1–27
4. Sathirakul K, How NC, Stevens WF et al (1996) Application of chitin and chitosan bandages for wound healing. Adv Chitin Sci 1:490–492
5. Roberts GAF (1992) Chitin Chemistry. MacMillan Press, London
6. Shepherd R, Reader S, Falshaw A (1997) Chitosan functional properties. Glycoconj J 14(4):535–542
7. Chirkov SN (2004) The antiviral activity of chitosan (review). Appl Biochem Microbiol 38(1):1–8
8. Felt O, Buri P, Gurny R (1998) Chitosan: a unique polysaccharide for drug delivery. Drug Dev Ind Pharm 24:979–993
9. Anthonsen T (1990) Chitin and Chitosan: Sources, Chemistry, Biochemistry, Physical Properties and Application. Elsevier, London

10. Darder M, Collila M, Ruiz-Hutzky E (2005) Chitosan-clay nanocomposites: application as electrochemical sensors. Appl Clay Sci 28:199–208
11. Rashidova S, Shakarova D, Ruzimuradov O et al (2004) Bionanocompositional chitosan-silica sorbent for liquid chromatography. J Chromatogr 800(1–2):49–53
12. Ayers MJ and Hunt AJ (2001) Synthesis and properties of chitosan–silica hybrid aerogels. J Non-Cryst Solids 285(1–3):123–127
13. Fleer GJ, Cohen Stuart MA, Scheutjens JMHM, Cosgrove T, Vincent B (1993) Polymers at Interfaces. Chapman Hall, London
14. Lipatov YS, Sergeeva LM (1972) Adsorption of Polymers. Naukova dumka, Kiev
15. Kulyk TV, Palyanytsya BB, Borodavka TV et al (2006) Mass Spectrom 3:175–180
16. Moelwyn-Hughes EA (1971) The Chemical Statics and Kinetics of Solutions. Academic Press, London
17. Yajima H, Morita M, Hashimoto M et al (2001) Complex formation of chitosan with iodine and its structure and spectroscopic properties – molecular assembly and thermal hysteresis behavior. Int J Thermophys 22(4):1265–1283

Chapter 22
Supramolecular Complex Antioxidant Consisting of Vitamins C, E and Hydrophilic–Hydrophobic Silica Nanoparticles

I.V. Laguta, P.O. Kuzema, O.N. Stavinskaya, and O.A. Kazakova

Abstract Samples with varied amount of surface trimethylsilyl groups were obtained via gas-phase chemical modification of silica nanoparticles. The biocompatibility tests conducted in erythrocyte suspension have shown that hydrophobization of silica decreases its damaging effect to the cells. Being wettable in aqueous media, partially silylated silicas have higher affinity to hydrophobic bioactive molecules in comparison with the initial silica. Novel antioxidant consisting of vitamins C and E and silica with 40% of surface trimethylsilyl groups was formulated. It was found that supramolecular complexes are formed on the silica surface due to the affinity of water- and fat-soluble antioxidants to hydrophilic silanol and hydrophobic trimethylsilyl groups, respectively. Test reactions (total phenolic index determination, DPPH test) and in vitro studies (spectral analysis of erythrocyte suspensions undergoing UV irradiation) revealed the correlation between antioxidant activity of the complex antioxidant and the vitamins' content. The antioxidant remained active during long-term storage under standard conditions.

22.1 Introduction

Highly disperse silica is widely used in medicine as enterosorbent, drug carrier, filler for pills, toothpastes, and dental products [1]. Adsorption properties and workability of silica are defined by the presence of a large amount of hydroxyl groups on its surface. These groups specify the significant sorptivity of the particles with respect to water, proteins, microorganisms, bioactive compounds, and drugs whose molecules contain polar groups [1, 2]. However, hydroxylated silica is characterized by low adsorption activity with respect to non-polar molecules, and being introduced in an

I.V. Laguta (✉)
O.O. Chuiko Institute of Surface Chemistry of the National Academy of Sciences of Ukraine, General Naumov St. 17, Kyiv 03164, Ukraine
e-mail: laguta@i.com.ua

A.P. Shpak, P.P. Gorbyk (eds.), *Nanomaterials and Supramolecular Structures*,
DOI 10.1007/978-90-481-2309-4_22,

organism it can demonstrate the biological activity [3–5]. The adsorbents with partially hydrophobized surface are believed to be promising derivatives of hydrophilic silica with potential application in medicine. Partial substitution of silanol groups with methyl ones could diminish the damaging effect of silica upon a cell [3, 4] while keeping the necessary wettability of the particles with water as well as widen the variety of adsorbates owing to the appearance of new adsorption centers at the surface. Hydrophilic–hydrophobic silicas are of particular interest in relation to the idea of coadsorption of water- and fat-soluble bioactive compounds, e.g., vitamins C and E. Vitamins C (ascorbic acid) and E (α-tocopherol) are antioxidants and synergists [6]. One might expect that due to the presence of hydrophilic and hydrophobic groups on the silica surface the adsorbents would retain both water- (vitamin C) and fat-soluble (vitamin E) compounds, and the consecutive or simultaneous antioxidants' desorption would occur while nanocomposites are in contact with different media.

The goal of this work was to compare the properties of initial and modified silica adsorbents containing surface hydroxyl and trimethylsilyl groups, to formulate and study a complex antioxidant comprising vitamins C and E supramolecularly dispersed on the surface of silica nanoparticles. Adsorbents containing both vitamins on the surface might be of interest with regard to the possibility of their application, for instance in cosmetology, gerontology, dermatology, and as bioactive additives.

22.2 Experimental

Fumed silica A-300 (Pilot plant at the Institute of Surface Chemistry, Kalush, Ukraine; specific surface area $S_{BET} \approx 200$ m^2/g) was used as the initial adsorbent. Ascorbic acid (vitamin C, Merck) and all-rac-α-tocopheryl acetate (vitamin E acetate, Merck) were used as adsorbates. Folin-Ciocalteu's phenol reagent (Merck) was used to measure the total phenolic index. 2,2-Diphenyl-1-picrylhydrazyl (DPPH, Sigma) was used to measure the antioxidant activity.

Silica samples with different degrees of surface silylation were obtained using gas-phase chemical modification of highly disperse silica (A-300) surface by trimethylchlorosilane [7, 8]. Degree of substitution of the silanol groups by trimethylsilyl (TMS) groups was regulated by varying the amount of the modifying agent and monitored by IR spectroscopy. The extent of modification by $-Si(CH_3)_3$ groups is given by the TMS loading $\theta = 0.10$–0.70. Kinetics of the samples' wetting with water was investigated by capillary absorption [9]; the specific surface area was measured by the method of thermal desorption of nitrogen. Biocompatibility of the initial and modified silica was in vitro examined in erythrocyte suspension by using hemolysis test [10].

Antioxidant-containing composites were obtained via adsorption of the vitamins C and E from concentrated ethanol solutions at 20 °C for 1 h; after centrifugation, the sediment was dried under vacuum for several hours. Content of both vitamins in the obtained composite was about 50 μmol/g. Desorption of the vitamins into

distilled water, ethanol, and vaseline oil was studied at the adsorbent/solution ratio of 1 g/300 ml.

Antioxidant activity of the composites was characterized by using Folin-Ciocalteu method and DPPH assay [11, 12]. To measure total phenolic index, 9 ml of distilled water, 4 ml sodium carbonate solution, 1 ml of Folin-Ciocalteu's phenol reagent, and 5 ml of distilled water were subsequently added to 1 ml of nanocomposite suspensions or to the reference vitamins solutions. Obtained suspensions and solutions were then stored for 30 min, optical density D_{750} of supernatant was measured at $\lambda = 750$ nm, and the total phenolic index was calculated as $D_{750} \cdot 4$. To test antiradical activity, 0.15 mM solution of DPPH in 70% ethanol was added to the composite suspensions or to the vitamins solutions with the fixed composite/vitamins content; then the mixture was stirred for 30 min and the deposit was separated by centrifugation. Concentration of the DPPH radicals in the reaction mixture and in control solution was calculated from the optical density of supernatant/solution at $\lambda = 517$ nm.

Erythrocytes suspension in citrate buffer with red corpuscles content of about 10^4 per ml was used for in vitro investigation of antioxidant activity of the composites. Modified silica with adsorbed vitamins C and E and original antioxidants were added to the erythrocytes as a suspension and a solution in glycerin, respectively. The final mixtures contained 10% of glycerin and 0.1% of silica; concentration of both antioxidants in the suspensions was about 2 μmol/l. The mixtures were irradiated with UV light of mercury quartz lamp for different periods of time, with the aqueous filter being used to avoid overheat of the suspensions. To control the state of erythrocytes, the UV−Vis spectra of the suspensions were recorded periodically. According to the preliminary results, position of spectral bands has not been affected by the addition of silica or glycerin to the suspensions.

The IR and UV spectra were recorded using Specord M-80 (IR) and "Lambda" "PerkinElmer" UV/VIS spectrophotometers.

Structural and electronic characteristics of model clusters of silica (up to 36 tetrahedra), their complexes with vitamins, and free energies of adsorption (ΔG_{ads}) have been calculated using the solvation model SM5.42 with the 6-31G(d) basis set or the semiempirical method PM3 (GAMESOL program package, Version 3.1) [13]. Model silica clusters contained 40% of trimethylsilyl groups and 60% of silanol groups.

22.3 Results and Discussion

22.3.1 Physicochemical Properties and Biocompatibility of Partially Hydrophobized Silica

Table 22.1 contains some physicochemical data for initial silica A-300 and modified adsorbents TMS-0.10 to TMS-0.70 with different amounts of grafted trimethylsilyl groups.

Table 22.1 Degree of substitution of silanol groups with trimethylsilyl ones (θ), specific surface area (S_{sp}), rate constant of wetting with water (k_w), and maximum volume of absorbed liquid (V_{max}) per 50 mg for the initial and modified silicas

Sample	θ (%)	S_{sp} (m^2/g)	$k_w \times 10^3$ (1/s)	V_{max} (ml)
A-300	0	200	11.4	0.62
TMS-0.10	10	191	10.2	0.55
TMS-0.40	40	175	8.4	0.47
TMS-0.55	55	171	3.5	0.35
TMS-0.60	60	169	0	–
TMS-0.70	70	165	0	–

As one can see, specific surface area of the silica slightly decreases with an increase of the degree of modification. The samples with θ up to 40% are relatively well wetted with water. The samples with θ of 60% and higher are hydrophobic and unsuitable for use in aqueous media [8, 9].

Figure 22.1 gives the results of biocompatibility study of the initial and modified silica particles using hemolysis test.

The degree of erythrocytes hemolysis in the presence of modified silica is about three times less than in the case of the initial adsorbent, i.e., modified silica causes less damaging effect upon the cells. The conclusion drawn is in agreement with the results of studies of interaction between the silica particles and blood corpuscles by means of optical microscopy and EPR spectroscopy [14]. It is also supported by data of previous studies [3–5, 15]. According to the latter, highly disperse silica while in contact with cell acts as bioactive material [3–5, 15]. It may be related to, for instance, interaction of the particles with cell membrane as a result of hydrogen bond formation between silanol groups of the silica surface and biomolecules

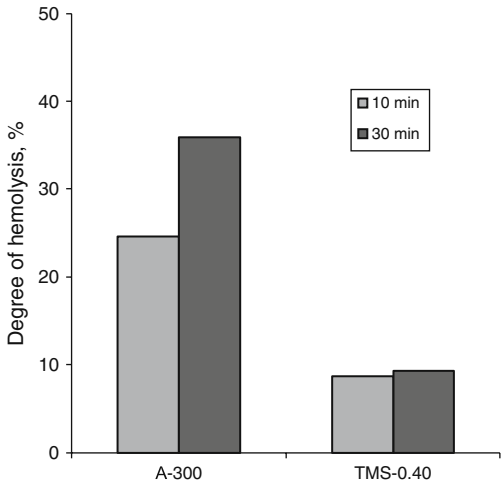

Fig. 22.1 The degree of erythrocytes hemolysis in the presence of initial and modified silicas

[5, 15]; correspondingly, decrease in the amount of silanol groups on the adsorbent surface should diminish the silica damaging action upon the cell [3, 5]. Thus, the data obtained indicate that partial substitution (up to 40%) of surface hydroxyls with trimethylsilyl groups does not lead to substantial decrease in specific surface area and wettability of silica particles, with biocompatibility of the adsorbent being improved considerably.

22.3.2 Hydrophilic–Hydrophobic Silica-Based Nanocomposites Containing Ascorbic Acid and α-Tocopherol

We have shown [16] that presence of trimethylsilyl groups on the surface of silica nanoparticles results in the increase of the adsorbent affinity to α-tocopherol molecules (Table 22.2) probably due to additional interaction between the vitamin molecules and hydrophobic surface sites.

Also, the data obtained previously [16, 17] show the appreciable retardation of oxidation of the dissolved ascorbic acid in the presence of the initial and modified silicas; improved stability of ascorbic acid in the suspensions appears to be caused by the peculiarities of the vitamin–silica interaction [17]. The ability of modified silicas to adsorb and stabilize ascorbic acid and their enhanced affinity to α-tocopherol molecules specify the possibility of formulation of complex antioxidant containing both vitamins. Such samples were obtained on the basis of TMS-0.4 adsorbent via its impregnation with ethanol solution containing mixture of ascorbic acid and α-tocopherol and subsequent vacuum drying.

Using quantum chemical calculation of the model systems in ethanol solution it was shown that vitamins C and E are adsorbed, respectively, on hydrophilic and hydrophobic fragments of modified silica surface (Fig. 22.2). It was found that the adsorption of vitamin E was thermodynamically unfavorable ($\Delta G_{ads} > 0$) on the surface of initial silica while in the case of modified silica ΔG_{ads} is equal to −29 kJ/mol. Interaction of vitamin C molecule with the silica particle occurs via hydrogen binding of OH groups of the adsorbate with silanol groups of silica surface; this leads to decrease in proton-donor ability of vitamin C and its stabilization [17]. Coadsorption of vitamins C and E on the surface of modified silica leads to a

Table 22.2 Physicochemical parameters of α-tocopherol adsorption from ethanol solutions on the initial and modified silicas

Adsorbent	A_∞ (μmol/g)	K (l/mol)	R
A-300	13 ± 3	290 ± 44	0.87
TMS-0.10	15 ± 2	393 ± 31	0.95
TMS-0.40	17 ± 4	660 ± 190	0.89
TMS-0.70	9 ± 1	904 ± 200	0.97

A_∞ limiting adsorption; Kadsorption equilibrium constant; R correlation coefficient for the linearized form of Langmuir isotherm.

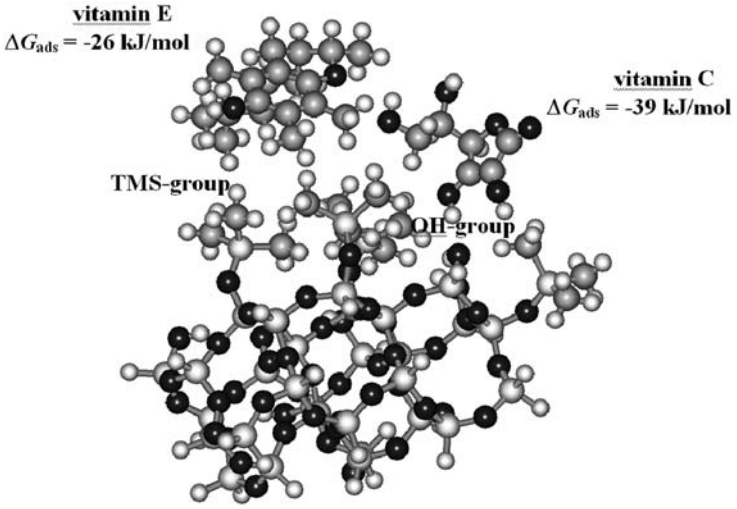

Fig. 22.2 Vitamins C and E molecules on the surface of modified silica particle modeled by a cluster with TMS and silanol groups (SM5.42/PM3)

small decrease in ΔG_{ads} (-39 kJ/mol instead of -31 kJ/mol) for ascorbic acid and small increase in ΔG_{ads} (-26 kJ/mol instead of -29 kJ/mol) for α-tocopherol. Thus, coadsorption of these antioxidants should not change the structure of adsorption complexes since they are adsorbed on different surface sites.

The additional concentration of active substance on the adsorbent surface probably occurs at solvent removal during the process of vacuum drying. According to IR spectroscopy data ~10% of the total amount of surface OH groups (0.02 mmol/g) is involved in interaction with ascorbic acid. At this stage, the surface contains about 0.05 mmol/g of ascorbic acid. From comparison of these values one may conclude that self-association of ascorbic acid molecules with participation of surface silanols has occurred, i.e., ascorbic acid is adsorbed in the form of clusters on the specific sites of silica surface. The same situation is assumed to take place in the case of vitamin E.

This conclusion about the adsorption of water- and fat-soluble vitamins on different sites of modified silica surface is not in contradiction with the results of mass spectrometric study of the dried nanocomposite. No essential influence of one vitamin on the kinetics of formation of the main volatile thermolysis products of the other vitamin was observed. This could be an evidence that the interaction between these antioxidants coimmobilized on the surface of the trimethylsilylated silica does not take place [18].

Thus, the presence of hydrophilic and hydrophobic groups on the silica surface makes it possible to adsorb and stabilize both water- and fat-soluble compounds, with the active substances of different nature being situated on different sites of the silica surface. In its turn, this arrangement of the vitamins should prevent their interaction between each other and improve their stability during storage.

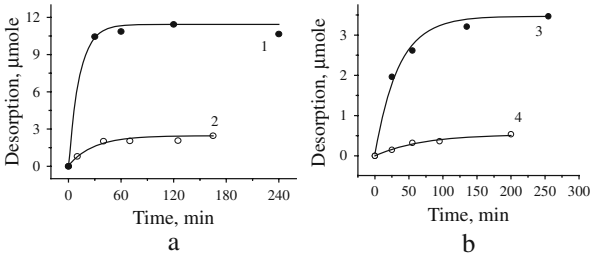

Fig. 22.3 Desorption of ascorbic acid (**a**) and α-tocopherol (**b**) from the surface of modified silica (TMS-0.40) into *1* water; *2*, *4* ethanol; *3* vaseline oil

22.3.3 Antioxidant Properties of the Nanocomposites

Antioxidant-containing silica may be used in more complex compositions and formulations, for instance in pills, creams, and ointments which should release the active compound into hydrophilic or lipophilic medium during application.

Figure 22.3 illustrates the data on the desorption of antioxidants from the nanocomposite into water, ethanol, and vaseline oil. Fast desorption of ascorbic acid into water as well as α-tocopherol into vaseline oil is observed; desorption of both antioxidants into ethanol is much slower. As expected, there was no desorption of ascorbic acid into oil as well as α-tocopherol into water. After keeping the silica with adsorbed vitamin C or E in oil or water, respectively, for 1–2 days the solvent was changed to water or ethanol and the desorption of vitamins was observed.

Being desorbed from the silica surface, antioxidants retain their reducing properties, which is confirmed by the data on antioxidant activity of the appropriate suspensions. The results of the study on antioxidant activity of the composites and control solutions of vitamins in test reactions with Folin-Ciocalteu's reagent and stable radical 2,2-diphenyl-1-picrylhydrazyl (DPPH) are given in Table 22.3.

Table 22.3 Total phenolic index and antioxidant activity in a reaction with DPPH for the nanocomposites and solutions of vitamins

Sample	Type/amount of AO in a probe (μmol)	Storage time	Total phenolic index	Quantity of DPPH radicals inactivated (%)
Vitamin C, solution	vitamin C/∼ 0.5	Fresh	1.0	95
Vitamin C, solution	vitamin C/∼ 0.5	30 min	0.3	–
Vitamin C on TMS-0.40	vitamin C/∼ 0.5	6 months	1.0	96
Vitamin E, solution	vitamin E/∼ 0.5	Fresh	–	25
Vitamin E on TMS-0.40	vitamin E/∼ 0.5	6 months	–	13
Vitamins C and E on TMS-0.40	vitamins C and E/∼ 0.25 and 0.25	6 months	0.5	59

AO antioxidant.

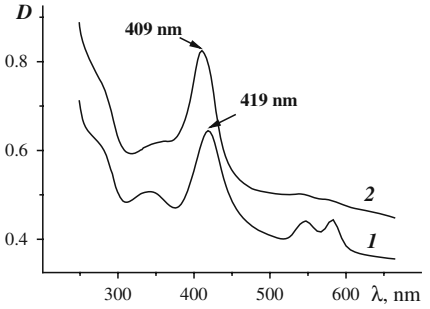

Fig. 22.4 UV–Vis spectra of the antioxidants-free erythrocytes suspensions before (*1*) and after (*2*) UV irradiation. Duration of irradiation is 25 min

It can be noticed that at equal content of the vitamins in a probe, the antioxidant properties of the composites and fresh solutions are identical. Long-term storage of dried composite (for 6 months) does not lead to the loss of its antioxidant activity whereas, for instance, ascorbic acid in a solution rapidly loses its reducing ability.

To test the antioxidant properties of the composites in vitro we used erythrocytes suspension undergoing UV irradiation. It is known [19] that UV irradiation of erythrocytes may result in the damage of the cell membranes with hemoglobin release, as well as in oxidation of oxyhemoglobin to methemoglobin. According to [20], the oxidation of the heme iron to trivalent state may be mediated, for instance, by peroxide species, which, in turn, may be formed in the system as a result of irradiation [21–24].

Figure 22.4, curves 1 and 2, gives the UV–Vis spectra of the antioxidants-free erythrocytes suspensions before and after irradiation.

As can be seen from the figure, the spectrum of the initial erythrocytes suspension is composed of the bands at 576, 540, 415–430 (the Soret band), 345, and 288 nm, which are characteristic of oxygenated hemoglobin [19, 23]. Irradiation of the suspension with UV light causes shift of the most intensive maximum into the region of the shorter wavelengths, the decrease in the intensity of the bands at $\lambda = 345$, 540, 576 nm, and the increase in the absorption at 360–370 and 500 nm. According to [19, 23], the bands at 500, 407, and 360–370 nm are characteristic of methemoglobin; thus, the changes in the spectra reveal transformation of oxyhemoglobin to methemoglobin. Position of the most intensive maximum in the spectra appears to depend on the percentages of oxyhemoglobin ($\lambda_{max} \sim 420$ nm [19]) and methemoglobin ($\lambda_{max} \sim 407$ nm [19]); then we used the value of the shift of the band to characterize qualitatively the extent of the oxyhemoglobin oxidation.

Figure 22.5 gives the data on UV-induced shift of the Soret band maximum for the erythrocytes suspension with and without vitamins versus time of UV irradiation. As one can see from the figure, upon irradiation of the antioxidant-free erythrocytes suspension the fast shift of the maximum from 419 to 409 nm is observed (Figs. 22.4, 22.5). Addition of vitamins solution to the suspension leads to inhibition of the hemoglobin oxidation during the first few minutes of irradiation,

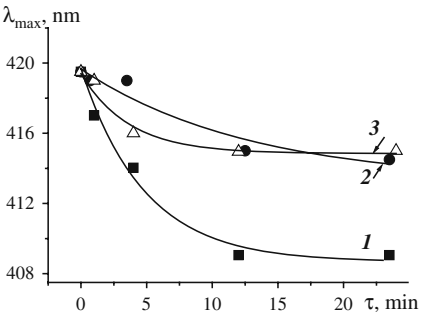

Fig. 22.5 Shift of the maximum of the Soret band versus time of UV irradiation: *1* antioxidants-free suspension, *2* erythrocytes – vitamins suspension, *3* erythrocytes – composite suspension

then the maximum of the band starts to shift into the region of shorter wavelengths (Fig. 22.5, curve 2). Presence of the composites with adsorbed vitamins also has protective effect against hemoglobin oxidation (Fig. 22.5, curve 3). Thus, vitamins C and E retard the oxidation of hemoglobin under UV irradiation, with the effect being practically the same for the antioxidants, both in solution and in the composite.

22.4 Conclusions

1. Substitution of up to 40% of surface silanols with trimethylsilyl groups does not lead to a substantial decrease in specific surface area and wettability of silica particles in aqueous solutions; however, it improves considerably their biocompatibility.
2. Presence of hydrophilic and hydrophobic groups on the silica surface allows implementing of coadsorption and stabilization of water- and fat-soluble compounds in a composite. In this case, active substances of different nature are situated on different sites of silica. This situation should prevent their interaction and improve the long-term stability during storage.
3. Adsorption of the antioxidants on the surface of silica nanoparticles allows introducing fat-soluble vitamin into hydrophilic medium as well as water-soluble one – into lipophilic medium. Antioxidant properties of vitamins in a composite remain intact: antioxidant activity of the composites containing vitamins C and E in the reactions with stable and short-lived radicals is the same as the activity of the equivalent amount of original vitamins.

Acknowledgments The work is performed within the framework of integrated program of fundamental research of Ukrainian National Academy of Sciences "Nanostructured systems, nanomaterials, nanotechnology". O.A.K. is grateful to Prof. V.M. Gun'ko for the use of the GAMESOL (Version 3.1) program package.

References

1. Chuiko A (ed) (2003) Medical chemistry and the clinical application of silicon dioxide. Naukova Dumka, Kiev.
2. Chuiko A, Gorlov Yu (1992) Surface chemistry of silica: surface structure, active sites, sorption mechanisms. Naukova Dumka, Kiev.
3. Lysenko L, Tchueshov V, Lavrushyna T (1977) Comparative toxicity of modified silica samples. Pharmaciya 26:56–58.
4. Fubini B, Wallace W (2000) Modulation of silica pathogenicity by surface processes. In: Papirer E (ed) Adsorption on silica surface. Marcel Dekker, New York.
5. Castranova V, Vallyathan V (2000) Silicosis and coal workers pneumoconiosis. Environ Health Perspect 108:675–684.
6. Carlotti M, Gallarate M, Gasco M et al (1997) Synergistic action of vitamin C and amino acids on vitamin E in inhibition of the lipoperoxidation of linoleic acid in disperse systems. Int J Pharm 155:251–261.
7. Kuzema P (2004) Properties of chemically modified highly disperse silicas with hydrophilic–hydrophobic surface. PhD Thesis, Kiev.
8. Pakhovchyshyn S, Matkovskiy K, Yurchenko G et al (2001) Hydrophilic–hydrophobic properties of methylsilicas. Dop Acad Nauk Ukrain 9:144–146.
9. Kuzema P, Laguta I (2004) Structural–mechanical properties of hydrophilic–hydrophobic silicas in water and decane. In: Proceedings of XI International Conference “Technologies of XXI Century”. Alushta, Ukraine.
10. Gatskiy O, Geraschenko I, Lutsyuk M (2004) *In vitro* study on hemolytic properties of highly disperse silica and its modified forms. Visn Morfol 10:257–260.
11. Alonso A, Domianguez C, Guillean D et al (2002) Determination of antioxidant power of red and white wines by a new electrochemical method and its correlation with polyphenolic content. J Agric Food Chem 50:3112–3115.
12. Yang J, Lee S, Han Ya et al (2003) Efficient transdermal penetration and improved stability of L-ascorbic acid encapsulated in an inorganic nanocapsule. Bull Korean Chem Soc 24: 499–503.
13. Xidos J, Li J, Zhu T et al (2002) GAMESOL–version 3.1. University of Minnesota, Minneapolis, based on the General Atomic and Molecular Electronic Structure System (GAMESS) as described in Schmidt M, Baldridge K, Boatz J et al (1993) J Comp Chem 14:1347–1363.
14. Stavinskaya O, Laguta I, Kuzema P et al (2006) Hydrophilic–hydrophobic silicas as potential adsorbents for medical application. Dop Acad Nauk Ukrain 4:152–157.
15. Gritsenko I, Osaulenko V, Roytman E (2004) Microscopic investigation of sorbent “Silics” action on erythrocytes of human blood. Klin Eksp Patol 3:526–528.
16. Kuzema P, Stavinskaya O, Kazakova O et al (2006) Hydrophobized silica nanocomposites with immobilized antioxidants (vitamins C and E). In: Blitz J, Gun’ko V (eds) Surface chemistry in biomedical and environmental science. NATO Science Series II: Mathematics, Physics and Chemistry.
17. Stavinskaya O, Kuzema P, Laguta I et al (2007) Interaction of ascorbic acid with hydrophilic–hydrophobic silicas. Ann U Mariae Curie-Sklodowska 62:124–135.
18. Laguta I, Stavinskaya O, Kuzema P et al (2007) Silica nanocomposites with immobilized antioxidants (vitamins C and E): synthesis and properties. In: Shpak A, Gorbyk P (eds) Physicochemistry of nanomaterials and supramolecular structures. Naukova Dumka, Kiev.
19. Timofeev K, Ryl’kov V, Shurygin A et al (1980) Spectral study of photochemical reactions in blood. Dokl Akad Nauk SSSR 255:751–755.
20. White A, Handler P, Smith E, Hill R, Lehman I (1978) Principles of biochemistry. McGraw-Hill, Inc., New York.

21. Vladimirov Y (1996) Free radical mechanism of action of UV and laser radiation on human blood tissues. In: Proceeding of the NATO ARW on free radicals in biology and environment. Bardolino, Italy.
22. Herrling T, Fuchs J, Rehberg J et al (2003) UV-induced free radicals in the skin detected by ESR spectroscopy and imaging using nitroxides. Free Radic Biol Med 35:59–67.
23. Puchala M, Szweda-Lewandowska Z, Leyko W (1979) γ-Irradiation of aqueous solutions of human hemoglobin in atmospheres of air and argon. Radiat Res 78:379–389.
24. Jurkovic P, Sentjurc M, Gasperlin M et al (2003) Skin protection against ultraviolet induced free radicals with ascorbyl palmitate in microemulsions. Eur J Pharm Biopharm 56:59–66.

Chapter 23
Physico-chemical Properties of Supramolecular Complexes of Natural Flavonoids with Biomacromolecules

V.M. Barvinchenko, N.O. Lipkovska, T.V. Fedyanina, and V.K. Pogorelyi

Abstract Polyvinylpyrrolidone (a water-soluble biopolymer) and human serum albumin (a globular protein) form supramolecular complexes with natural flavonoids quercetin and rutin in aqueous medium. The interaction with these biomacromolecules (BMM) causes the alteration of flavonoid spectral, protolytic, and other properties; in particular, it essentially increases their solubility. Absorption and solubility measurements revealed the supramolecular compounds of 1:1 stoichiometry for all systems studied. First it was demonstrated experimentally that the interaction with BMM promotes the tautomeric transformation in quercetin molecule. The mechanism of tautomerization via flavonoid molecular structure was discussed. Adsorption of BMM and their supramolecular compounds with flavonoids onto nanosilica was studied as a function of pH, and the properties of the biomacromolecules, flavonoids, and silica surface. It was found that BMM either complexed with quercetin (rutin) or preliminary immobilized on nanosilica increases the flavonoid adsorption.

23.1 Introduction

Flavonoids are bioactive polyphenolic compounds that occur ubiquitously in plants [1]. Recent interest in flavonoids stems mainly from their high therapeutic activity, acute-high potency, and low systemic toxicity. The most common flavonoids present in nature, quercetin (3,5,7,3',4'-pentahydroxyflavone, Qt) and rutin (5,7,3',4'-tetrahydroxyflavone-3-rutinoside, Rt), have potent antioxidant and metal ion chelating capacity, possess various biological and biochemical effects including anti-inflammatory, antisclerotic, antineoplastic, spasmolytic, diuretic, and cardio-protective activities [1–5].

N.O. Lipkovska (✉)
O.O. Chuiko Institute of Surface Chemistry of the National Academy of Sciences of Ukraine, General Naumov St. 17, Kyiv 03164, Ukraine
e-mail: lipkovska@ukr.net

A.P. Shpak, P.P. Gorbyk (eds.), *Nanomaterials and Supramolecular Structures*,
DOI 10.1007/978-90-481-2309-4_23,

However, the low solubility of the flavonoids and especially their aglycones in aqueous media and body fluids often presents a problem for medical applications of these substances. As the solubility is known to be one of the main biopharmaceutical drug properties [6], the development of water-soluble flavonoid composition is of great importance. Water-soluble natural and synthetic polymers [7], surfactants [8], cyclodextrines [9, 10], and other compounds are used in pharmacy and medicine as solubilizers. Earlier we have found [11] that β-cyclodextrin formed inclusion complex with Qt that resulted in considerable increase of quercetin solubility and bathochromic shift of its absorption spectra. In this work flavonoid interaction with polymer polyvinylpyrrolidone (PVP), known to be an effective and innocuous solubilizer [12], is investigated.

In body, bioavailability and bioactivity of flavonoids, their distribution, and their transformation in different tissues depend on the interaction with another biomacromolecule – proteins. It has been demonstrated that a plasma protein, human serum albumin (HSA), is a primary carrier of flavonoids in blood [13, 14]. Recently, a high affinity for quercetin toward HSA complexation was reported [14–20]. Therefore, the interaction of flavonoids with HSA is of major biological importance.

Nowadays, fumed nanosilica has become an important component of complex remedies as efferent therapy medicinal preparation, excipient, viscosity and dispersion stabilizer [21]. Recently, the authors conducted physico-chemical and medico-biological studies aimed to develop new complex medicinal preparations including herbal components and fumed nanosilica [22, 23]. Preliminary clinical trials showed the higher anti-inflammatory and immune-modulative activity of such combined pharmaceutical compositions [22].

Thus, the investigation of interactions in ternary system, flavonoid (Qt, Rt)–biomacromolecule (PVP, HSA)–fumed nanosilica, presented in this chapter is of fundamental and practical importance.

23.2 Experimental

23.2.1 Materials

Fumed nanosilica (Kalush OEZ, specific surface area S=300 m^2 g^{-1}), quercetin, rutin (Sichuan Xieli Pharmaceutical Co. Ltd., Korea), HSA (molecular weight 67,000, Biofarma, Ukraine), PVP (molecular weight 8000, BASF, Germany), and NaCl (Merck) were used. Stock quercetin and rutin solutions (2×10^{-4} M) were prepared by dissolving their weighted amounts in 40% ethanol solution. HSA and PVP solutions (1.5%) were obtained by dissolving their weighted amounts in distilled water. The solution pH in the range of 2–8 was adjusted using 0.05 M universal buffer solutions. In all experiments ethanol concentration was 4%, ionic strength μ=0.2 (NaCl).

The concentrations of free and bound Fl and BMM were determined by their molar absorption coefficients ϵ which were found earlier for the corresponding model solutions and pH values.

23.2.2 Phase Solubility Studies

Excess amounts of quercetin or rutin were put into 10 ml tubes containing aqueous solutions of increasing concentrations of BMM $(0–5)\times10^{-4}$ M and then shaken at 20°C. At the equilibrium after 72 h, all probes were centrifuged (3000 rpm, 5 min); an aliquot from each vial was put into a flask, then adequately diluted, and analyzed spectrophotometrically as described above.

23.2.3 Adsorption Studies

Fl and BMM sorption was studied using the batch technique. For this purpose 0.1 g of a sorbent was added to 5.0 ml of 6.72×10^{-5} M BMM and/or 2×10 M Fl aqueous solutions at appropriate pH and was shaken thoroughly at 298 K until the equilibrium was reached (120 min). The modified sorbent obtained was centrifuged (8000 rpm, 15 min), and Fl and BMM residual concentration in the solution after sorption ([C]) was controlled by spectrophotometry.

23.2.4 Apparatus

Absorption spectra of reagent solutions were registered with a UV/Vis spectrophotometer Specord M-40 (Carl Zeiss Jena, Germany). EV-74 potentiometer with a glass electrode was used for pH measurements.

23.3 Results and Discussion

23.3.1 UV–Visible Spectrophotometry

First, quercetin and rutin absorbance in aqueous ethanolic solutions both with and without the addition of BMM was investigated. It was reported [15, 16] that as a result of specific binding of quercetin to HSA, its absorption spectrum exhibits a red shift. The same was observedfor rutin. It was found that at pH 3–8 BMM addition causes the alteration and bathochromic shift of Fl electron spectra (Fig. 23.1a, b).

To testify quercetin and rutin interaction with BMM their dissociation constants without (pK^a_{Fl}) and with the addition of BMM ($pK^a_{Fl\text{-}BMM}$) were determined using UV–vis spectroscopic method according to [24]. The decrease of p*K*a values of quercetin and rutin in Fl:PVP and Fl:HSA compounds (see Table 23.1) in comparison with individual quercetin (pK^a_{Qt}=7.12) and rutin (pK^a_{Rt}=7.73) shows that complexation with BMM results in the alteration of Fl acid–base properties, namely in their acidity increase.

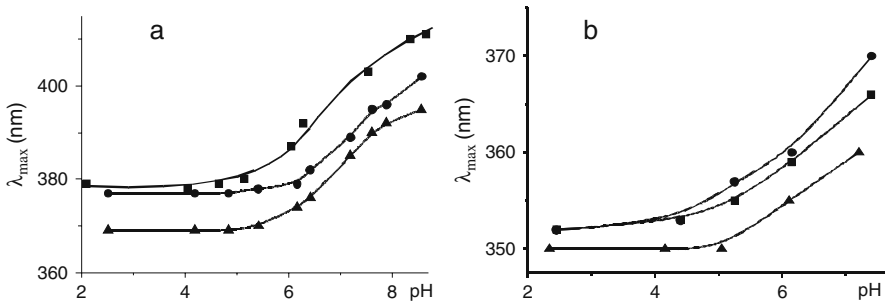

Fig. 23.1 The effect of solution pH on the wavelengths of absorption maximum for quercetin (**a**) and rutine (**b**) solutions without BMM (*triangle*) and with PVP (*circle*) and HSA (*square*) addition ($C_{Qt,\,Rt}$= 2.0×10^{-5} M, C_{BMM} =6.7×10^{-5} M)

Table 23.1 Alteration of flavonoid acid–base properties in the presence of BMM in aqueous solutions

Flavonoid	pK^a_{Fl}	$pK^a_{Fl:HSA}$	$pK^a_{Fl:PVP}$
Quercetin	7.12±0.04	6.89±0.02	7.00±0.01
Rutin	7.73±0.04	7.54±0.03	7.63±0.02

23.3.2 Phase Solubility Studies

The influence of increasing amounts of PVP and HSA on the flavonoid dissolution was studied (Fig. 23.2). For all the flavonoid/biomacromolecule systems type-AL diagrams were obtained, meaning that the solubility of the flavonoids is apparently increased in the presence of PVP or HSA, as a result of their complexation:

$$Fl + nBMM \leftrightarrow Fl \cdot BMM_n. \tag{23.1}$$

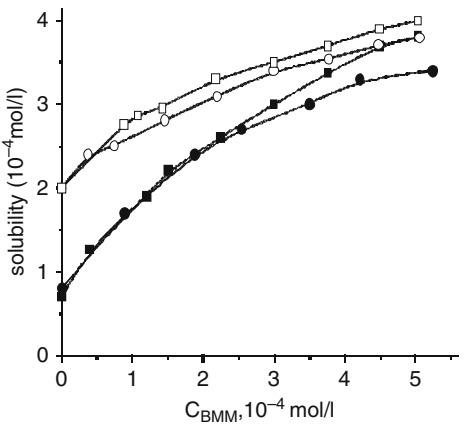

Fig. 23.2 Solubility of quercetin (*filled signs*) and rutine (*empty signs*) as a function of PVP (*circle*) and HSA (*square*) concentrations at 20°C

The stoichiometry and association constants K_A of the Fl·BMM compounds

$$K_A = [Fl \cdot BMM_n] / [Fl]^n [BMM] \quad (23.2)$$

were derived from the changes in the solubility of the substrates in the presence of increasing amounts of BMM.

Equilibrium concentration of $[Fl \cdot BMM_n]$ complex was found according to

$$[Fl \cdot BPM] = C_{Fl} - [Fl], \quad (23.3)$$

where C_{Fl} was the total flavonoid concentration after dissolving in the BMM solution, [Fl] the flavonoid equilibrium concentration in aqueous solution without BPM. The equilibrium concentration of [BMM] was assumed to be C_{BPM}.

The *n*-value was determined graphically as a tangent of line inclination in logarithmic coordinates: $-\lg[Fl \cdot BMM_n] - \lg[BMM]$. The graphs obtained (Fig. 23.3) were linear (R=0.998) and $tg\alpha \sim 1$ indicated the formation of complexes with component ratio Fl:BMM=1:1. This is in agreement with the data reported for Rt−HSA [25], Qt−HSA [15,16], and triphenylmethane dye−PVP (molecular weight <30,000) [26] molecular complexes. The association constants of Fl·BMM compounds were calculated according to Eq. (23.2) and presented in Table 23.2.

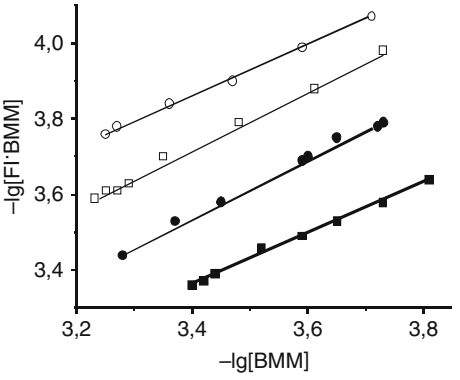

Fig. 23.3 The plot of $-\lg[Fl \cdot BMM]^{\sim}$ vs. lg[BMM] for PVP (*circle*) and HSA (*square*) flavonoid compounds

Table 23.2 Alteration of spectral and acid–base flavonoid properties on complexing with BMM and association constants of Fl·BMM complexes

BMM	Flavonoid	$\Delta\lambda_{max}$ (nm)	ΔpK_a	K_A ($10^4 M^{-1}$)
PVP	Qt	5	0.12	0.78
	Rt	4	0.10	0.083
HSA	Qt	17	0.23	11.0
	Rt	10	0.19	0.28

The variety of Qt–HSA constants reported in literature (26.7 [14], 19 [17], 5 [18], 91 [19], 52.6 [20], 1.4 [16], 1.46 [15]) is explained probably by different experimental conditions and procedures used for calculations. Hence the comparison of Fl·BMM complex stability is reliable if the association constants are obtained by the same procedure. Thus, for quercetin and rutin complexes with another albumin, BSA, the values of K_A were 10.3×10^4 M^{-1} and $0.86\times10^4 M^{-1}$, respectively [27], and their proportion is in agreement with our data for HSA. Comparison of Fl constants, $\Delta\lambda_{max}$ and ΔpKa values (Table 23.2), testifies that biomacromolecules form less stable complexes with Rt than with its aglycon Qt.

23.3.3 Time-Dependent Absorbance Studies

Time-dependent changes in the absorption spectra of Qt·BMM solutions were observed. To study kinetics of the complexation we examined changes in the absorption spectra of the reagents (Qt:BMM =1:3) in buffered solution at pH 7.4. It was shown that just after reagent mixing Qt·PVP(1) complex with λ_{max1}=335 nm and λ_{max2}=385 nm (Fig. 23.4a, solid curve) was formed. With time the band intensities

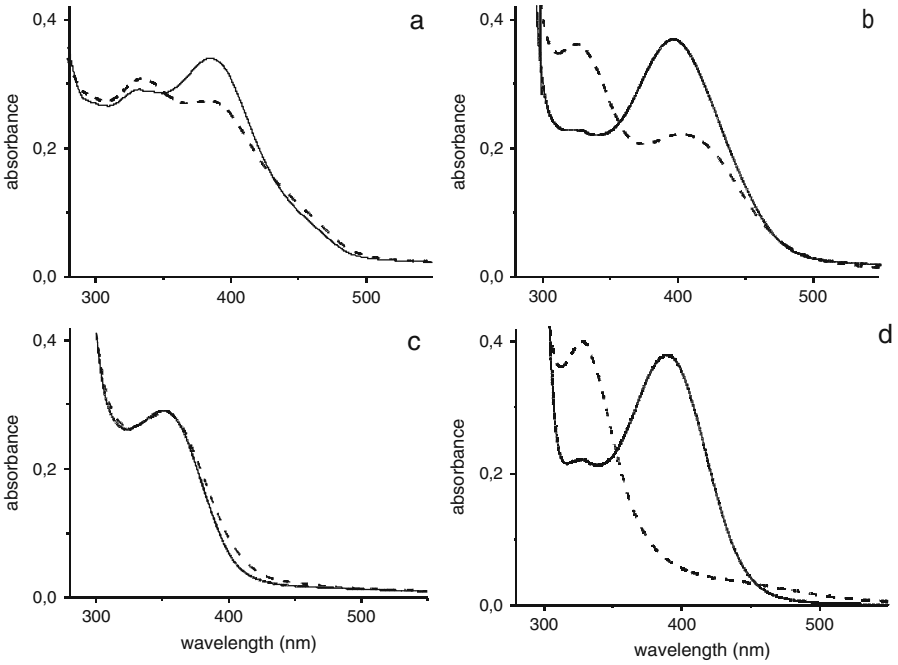

Fig. 23.4 Time-dependent spectra of quercetin (**a**, **b**, **d**) and rutin (**c**) solutions in the presence of PVP (**a**), HSA (**b**, **c**) and tryptophan (**d**) at Fl:BMM=1:3 and pH 7.4 after 10 min (Fl·BMM(I) *solid line*) and 21 h (Fl·BMM(II) *broken line*)

were redistributed apparently as a result of the transformation of Qt·PVP(I) complex into Qt·PVP(II) (Fig. 23.4a, broken curve). Spectral changes were more evident for Qt·HSA(I)→Qt·HSA(II) system (Fig. 23.4b) where considerable decrease of the absorption band intensity at λ_{max2}=399 nm took place together with the growth of the band at λ_{max1}=327 nm. Oxidation of Qt is hardly responsible for the changes observed as it occurs in more basic solutions or in the presence of oxidants (e.g., periodate) and the absorption spectra of quinone formed shows an absorption maximum at lower wavenumber: λ_{max1}=293 nm [27]. The observed spectral changes may probably indicate the transformation of Qt·BMM(1) complex into the more stable Qt·BMM(2) as a result of quercetin molecule tautomerization:

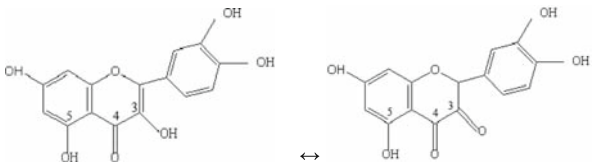

enolic form **ketonic form**

The observed hypsochromic shift of the peak of quercetin absorption spectrum from λ_{max2} to λ_{max1} under the influence of BMM may be caused by the alteration of π-conjugated bond system between γ-pyrone and phenol groups [28], similar to keto–enol tautomerism. Taking into account the chemical structure of the quercetin molecule the authors of [29] suppose more than 10 conformations of Qt. Quantum-chemical research of quercetin molecule by means of semi-empirical methods PM3 using the solvation model SM5.42 [30], MNDO/H (modified neglect of diatomic overlap) [31], or AM1 (Austin Model 1) [28, 29] demonstrated that the most probable tautomeric mechanism is the rotation of C_3-OH group followed by intramolecular proton migration along π-bonds and gradual dimensional restructure. This process is promoted by the breaking of intramolecular hydrogen bonds between C_5-OH, $C_4=O$, and C_3-OH fragments, which may occur at chemical interactions via these functional groups particularly at Fl binding to biomacromolecules.

To verify the suggested tautomeric transition of Qt molecule in the presence of BMM we carried out similar investigations with rutin which in fact is quercetin whose labile proton of C_3-OH group is replaced by rutinosa that would prevent such keto–enol tautomerism. No changes in rutin spectra were found in the presence of BMM in time (72 h) (Fig. 23.4c). This proves that keto–enol tautomerism does not occur in the absence of C_3-OH group labile proton and, therefore, may confirm our assumptions.

According to [1, 3, 4] the conformational variability was found to be one of the main structural factors of quercetin biological activity that enables Qt molecule to get "working" conformation at specific intermolecular interactions to form supramolecular complexes. The induction of quercetin keto-form influenced by BPM complexing is one of such examples.

In spite of multiplicity of donor–acceptor reaction centers in the molecules of the biopolymers studied they form 1:1 supramolecular complexes with flavonoids and some other polyphenols [14, 15, 25, 26]. It could be assumed that quercetin and rutin interact mainly with the end $RCOO^-$ or RNH^{3+} groups of albumin, as flavonoid bonding with polypeptide fragments along the chain is limited by steric factors preventing Fl molecule to penetrate inside the helix. Moreover, donor–acceptor centers of BMM are occupied with intramolecular hydrogen bonds.

However, the chemistry of bioregulatory processes [32] proves that cyclic and heterocyclic chemical compounds with asymmetrically located polar and hydrophobic groups, including flavonoids, are identified by special albumin receptors located apparently at the most flexible sections of polypeptide chain near open sides of each of three protein domains. The study of Qt−HSA complex structure using fluorescent technique [27] has shown that inside the Qt·HSA complex the energy transfer from tryptophan residue (Tr214) of protein in excited state to flavonoid chromophore takes place. Only Tr214 in the said protein is a part of IIA domain able to bond various ligands including warfarin [33] (of coumarin class that is structurally related to flavonoids) in its hydrophobic cavity. X-ray analysis data obtained from Qt−HSA complexing research also verified that ligands interact with Tr214 group located in IIA domain [27, 32].

We have investigated spectral characteristics of quercetin solutions with and without tryptophan in time. It was found that time-dependent changes in the absorption spectrum of Qt·Tr solution (Fig. 23.4d) are similar to those of Qt·HSA. This fact is an indirect evidence of quercetin localization namely in the hydrophobic cavity of A domain. Similar experimental results obtained for PVP suggest the similar mechanism of supramolecular complex formation in the case of this biopolymer which in dilute aqueous solutions has the random coil shape [34] in which hydrophobic cavities may exist.

As follows from the data in Table 23.2, quercetin forms more stable Qt−BMM complexes compared to those of rutin. According to [25] the presence of the sugar moiety in rutin may reduce affinity of this ligand to HSA in two ways: (i) The size of rutin approximately doubles that of quercetin. Moreover, rutin contains two more cyclic fragments that are less flexible to undertake conformational changes to accommodate within the protein or PVP binding sites. (ii) The sugar moiety of rutin bears additionally several polar hydroxyl groups that may perturb the relatively hydrophobic environment of the binding site.

23.3.4 Adsorption Studies

To ascertain the effect of flavonoid–BMM complexation on the adsorbability of individual reagents, adsorption of Fl, BMM, and Fl−BMM(1) on silica surface was studied according to the schemes:

Scheme 1

$$\mathrm{BPM} + \mathrm{Fl} \leftrightarrow (\mathrm{Fl}\cdot\mathrm{BPM})$$

$$\mathrm{SiO_2} + (\mathrm{Fl}\cdot\mathrm{BPM}) \leftrightarrow (\mathrm{SiO_2}-\mathrm{Fl}\cdot\mathrm{BPM})$$

Scheme 2

$$SiO_2 + BPM \leftrightarrow (SiO_2 - BPM)$$

$$(SiO_2 - BPM) + Fl \leftrightarrow (SiO_2 - Fl \cdot BPM)$$

According to Scheme 1, a supramolecular Fl·BMM complex is formed in solution and then absorbed on SiO_2 surface. On the contrary, accordingto Scheme 2, BMM is initially adsorbed on silica surface, and such modified sorbent is used for flavonoid adsorption.

Studies of Fl adsorption as a function of pH (Fig. 23.5) have shown that Qt adsorption was maximum (8 μmol/g) in the pH region of its molecular form domination (Fig. 23.5a, b). Contrarily, the adsorption of Rt (Fig. 23.5c, d) as well as of PVP is practically pH-independent. As a result of complexing with PVP flavonoids adsorbed more effectively and their pH-dependence curves were similar to those of respective Fl. Another type of pH-dependent adsorption curves were observed for Fl−HSA systems. Such bell-shaped adsorption curves (Fig. 23.5a, c, empty dots) with a peak at the pH range of protein isoelectric point (for HSA pH_{IP} = 4.9 [21])] are known to be typical for proteins and indicate that hydrogen bonds and electrostatic forces are responsible for BMM adsorption onto silica surface. Flavonoid complexation with HSA results in the essential increases of Fl adsorption. Corresponding pH-dependent adsorption curves are also bell-shaped (Fig. 23.5a, c, squares, triangles) and their peak positions are similar to those of HSA.

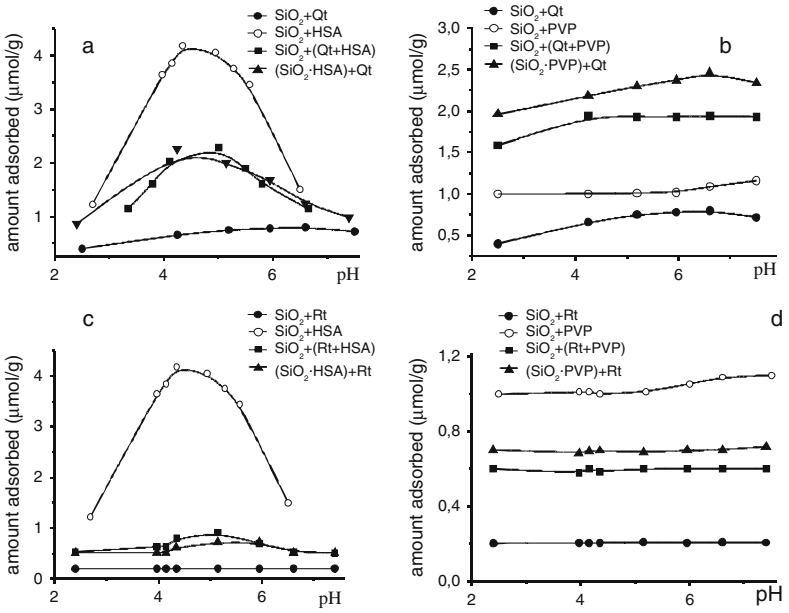

Fig. 23.5 The effect of pH on adsorption of flavonoids, biomacromolecules, and their complexes onto silica surface

As seen from Fig. 23.5 the adsorption of Qt with and without the BMM is 2–4 times higher than that of Rt. This indicates that the presence of a sugar moiety in Rt molecule markedly weakens both the rutin–BMM complexation and adsorption interaction with a sorbent.

So we have revealed considerable impact of adsorbate chemical nature on the adsorption of bioactive flavonoids of medicinal plants onto a surface of nanodispersed silica particles.

23.4 Conclusions

It was found that biomacromolecules (polyvinylpyrrolidone and human serum albumin) interact with natural flavonoids (quercetin and rutin) in aqueous solutions to form supramolecular complexes. Such complexing causes the alteration of flavonoid solubility, their spectral, adsorptive, and acid–base properties. Phase solubility studies pointed out the formation of 1:1 stoichiometric complexes between flavonoids and biomacromolecules.

It was pioneered to find that complexing with BMM causes the tautomerization of quercetin molecule. The regularities of adsorption interaction of medicinal plant bioactive flavonoids with nanodisperse silica particles depending on biomacromolecule, adsorbate, and solution nature were established. The results of flavonoid phase solubility studies and Fl−BMM interactions in aqueous solutions are important to comprehend the mechanism of flavonoid bioavailability increase in the presence of PVP as well as primary pharmaceutical reactions in the case of HSA.

Acknowledgements This research was supported by STCU (Grant 3832)

References

1. Harborne JB, Williams CA (2000) Advances in flavonoid research since 1992. Phytochemistry 55:481–504
2. Havsteen BH (2002) The biochemistry and medical significance of the flavonoids. Pharm Ther 96:67–202
3. Cook NC, Samman S (1996) Flavonoids – chemistry, metabolism, cardioprotective effects, and dietary sources. J Nutr Biochem 7:66–76
4. Yang CS, Landau JM, Huang MT, Newmark HL (2001) The effects of plant flavonoids on mammalian cells: implications for inflammation, heart disease, and cancer. Annu Rev Nutr 21:381–406
5. Rice-Evans C, Packer L (1998) Flavonoids in health and disease. Marcel Dekker, New York
6. Georgievsky VP, Konev FA (eds) (1996) The technology and standardization of medicines. RIREG, Kharkov (in Russian)
7. Florence AT, Attwood D (2006) Physicochemical principles of pharmacy, 4th edn. Pharmaceutical Press, London
8. Rangel-Yagui CO, Pessoa-Jr A, Tavares LC (2005) Micellar solubilization of drugs. J Pharm Pharm Sci 8:147–163
9. Tommasini S, Raneri D, Ficarra R et al (2004) Improvement in solubility and dissolution rate of flavonoids by complexation with β-cyclodextrin. J Pharm Biomed Anal 35:379–387
10. Uekama K, Hirajama F, Irie T (1998) Cyclodextrin drug carrier systems. Chem Rev 98: 2045–2076

11. Lipkovska NO, Barvinchenko VM, Pogorelyi VK (2000) The effect of β-cyclodextrin on quercetin properties in aqueous solutions. Pharm J 6:66–69 (in Russian).
12. Lauro MR, Torre ML, Maggi L et al (2002) Fast- and slow-release tablets for oral administration of flavonoids: Rutin and quercetin. Drug Dev Ind Pharm 28:371–379
13. Dangles O, Dufour C, Manach C et al (2001) Binding of flavonoids to plasma proteins. Methods Enzymol 335:319–333
14. Boulton DW, Walle UK, T Walle (1998) Extensive binding of the bioflavonoid quercetin to human plasma proteins. J Pharm Pharmacol 50:243–249
15. Zsila F, Bikadi Z, Simonyi M (2003) Probing the binding of the flavonoid, quercetin to human serum albumin by circular dichroism, electronic absorption spectroscopy and molecular modelling methods. Biochem Pharmacol 65:447–456
16. Kanakis CD, Tarantilis PA, Polissiou MG et al (2006) Antioxidant flavonoids bind human serum albumin. J Mol Struct 798:69–74
17. Sengupta B, Sengupta PK (2002) The interaction of quercetin with human serum albumin: a fluorescence spectroscopic study. Biochem Biophys Res Commun 299:400–403
18. Dufour C, Dangles O (2005) Flavonoid-serum albumin complexation: determination of binding constants and binding sites by fluorescence spectroscopy. Biochim Biophys Acta 1721:164–173
19. Bi S, Ding L, Tian Y et al (2004) Investigation of the interaction between flavonoids and human serum albumin. J Mol Struct 703:37–45
20. Rawel HM, Meidtner K, Kroll J (2005) Binding of selected phenolic compounds to proteins. J Agric Food Chem 53:4228–4235
21. Chuyko AA (ed) (1996) Medical chemistry and clinical application of silica dioxide. Naukova Dumka, Kyiv (in Russian)
22. Pogorelyi VK, Barvinchenko VN, Lipkovska NA, Turov VV, Chuiko AA (2001) Adsorption of bioactive molecules of medicinal plants. Chem Phys Technol Surf 4/6:301–309 (in Russian)
23. Chuiko OO, Barvinchenko VM, Pogorelyi VK (2002) The method of making of solid drug form with regulable active substance release – No 2001128631, Ukrainian patent 50289 A, MKB7 A61K9/22, Pend. 14.12.2001; Publ. 15.10.2002. Bull. No 10 (in Ukrainian)
24. Bernshtein IYa, Kaminsky JuL (1986) Spectrophotometrical analysis in organic chemistry. Chemistry, Leningrad (in Russian)
25. Pastukhov AV, Levchenko LA, Sadkov AP (2007) Spectroscopic study on binding of rutin to human serum albumin. J Mol Struct 842:60–66
26. Chmilenko FA, Kharun MV, Chmilenko TS et al (2001) Triphenylmethane dye of sulfophthalein series adducts with polyvinylpyrrolidone and their use in chemical analysis. J Anal Chim 56:483–486 (in Russian)
27. Dangles O, Dufour C, Bret S (1999) Flavonol-serum albumin complexation. Two-electron oxidation of flavonols and their complexes with serum albumin. J Chem Soc Perkin Trans 2:737–744
28. Gricenko OM, Degtyarev LS, Piliptchik LB (1999) Physical-chemical properties and electron structure of quercetin. Pharm J 2:34–37 (in Russian)
29. Gricenko OM, Piliptchik LB, Bogdan TV, Maksjutina NP (2003) Keto–enol tautomeria of quercetin molecule: quantum chemical. Pharm J 1:62–65 (in Russian).
30. Kazakova OA, Gun'ko VM, Lipkovska NA, Voronin EF, Pogorelyi VK (2002) Interaction of quercetin with fumed silica in aqueous suspensions. Colloid J 64:412–418
31. Potiagailo AL, Piliptchik LB, Govorun DM (2001) Cooperative intramolecular H-bonds in quercetine: MNDO/H quantum chemical investigation. Biopolym Cell 17:256–258 (in Ukrainian)
32. Kuchar VP, Luyk AI (eds) (1991) Chemistry of bioregulatory process. Naukova Dumka, Kyiv (in Russian)
33. Kragh-Hansen U, Brennan O, Galliano M, Sugita O (1990) Binding of warfarin, salicylate, and diazepam to genetic variants of human serum albumin with known mutations. Mol Pharmacol 37:238–242
34. Brandrup J (ed) (1999) Polymer hand-book, 4th edn. Wiley, New York

Chapter 24
Supramolecular Complexes Formed in Systems Bile Salt–Bilirubin–Silica

N.N. Vlasova, O.V. Severinovskaya, and L.P. Golovkova

Abstract The formation of supramolecular complexes between bilirubin and primary micelles of bile salts has been studied. The association constants of bile salts and binding of bilirubin with these associates have been determined. The adsorption of bilirubin and bile salts from individual and mixed aqueous solutions onto hydrophobic silica surfaces has been investigated. The interaction of bilirubin with primary bile salt micelles and the strong retention in mixed micelles, which are supramolecular complexes, result in the adsorption of bilirubin in free state only.

24.1 Introduction

Supramolecular chemistry is the interdisciplinary branch of science including chemical, physical and biological aspects of consideration of more-complex-than-molecules chemical systems connected in a single whole by means of intermolecular (noncovalent) interactions. The supramolecular chemistry covers and allows, considering from uniform positions, all kinds of molecular associates, from the least (dimer) up to the largest (the organized phases). It is necessary to emphasize once again that objects of supramolecular chemistry necessarily contain the parts (subsystems) not connected covalently.

The supramolecular structures formed as a result of interaction of bile salts with a bile pigment bilirubin and their adsorption on a surface of fumed hydrophobic (AMS) and partially hydrophobized silica (TMS) have been studied.

Bile acids are a group of acidic compounds, which are present in biological fluids in their ionized form [1]. They are produced from cholesterol in liver. One of the major functions of bile acids in an organism is solubilization and transport of fairly soluble substances in biological environments, such as cholesterol, lipids, fat acids and bilirubin. Specific properties of bile acids are determined by their structure. As

N.N. Vlasova (✉)
O.O. Chuiko Institute of Surface Chemistry of the National Academy of Sciences of Ukraine, General Naumov St. 17, Kyiv 03164, Ukraine
e-mail: vlabars@i.com.ua; vlasova@uni-mainz.de

A.P. Shpak, P.P. Gorbyk (eds.), *Nanomaterials and Supramolecular Structures*,
DOI 10.1007/978-90-481-2309-4_24,

products of cholesterol metabolism they consist of a steroid skeleton, containing 1, 2 or 3 hydroxyl groups, that differentiate the single compounds by number, position and orientation; they also bear short chain terminating with a carboxyl group. This carboxyl group can be free (unconjugated bile acid) or conjugated with glycine or taurine.

Ionized forms of bile acids are bile salts; they behave in aqueous solutions as association colloids. They are atypical surface-active agents: in this class of compounds the molecular polarity originated from dissimilarity between the two faces of the steroid rings. The face containing the hydroxyl groups is defined as α-face, while the other side formed by the hydrocarbon skeleton is the β-face.

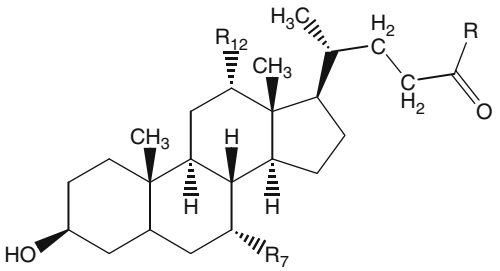

Bile acids

The aggregation occurs via a "back-to-back" contact between β-faces of two monomers to minimize the contact with water of these hydrophobic surfaces (primary micelles). Aggregation starts above a so-called critical micelle concentration (CMC). The CMC values are affected by the number, position and orientation of hydroxyls. The aggregation number is generally low and micelles can increase their size and number as the bile salt concentration increases; as a consequence, the aggregation is not really co-operative and critical. At a first approximation the following pattern of aggregation can be considered: at concentrations below CMC bile salts exist predominantly as monomers. Above this concentration value, formation of small aggregates starts: dimers – for trihydroxycholanic acid and trimers – for dihydrocholanic acids. At concentration of about 10–50 mmol/l large aggregates are formed, and these big species contain dimers or trimers as structural units.

Due to their special structure, bile salt micelles are able to solubilize many compounds forming inclusion complexes with them. One of these substances is bilirubin; its solubilization and transport is of great importance for organisms.

Bilirubin, the yellow-orange pigment associated with jaundice, is the catabolic product of haeme degradation in liver [2]. In normal individuals, bilirubin is first converted to more soluble mono- and diester derivatives prior to excretion in the biliary tract. However, the free dicarboxylic acid, commonly referred to as unconjugated bilirubin, is often involved in pathological conditions associated with this substance. Bilirubin is usually found as one of the component of gallstones.

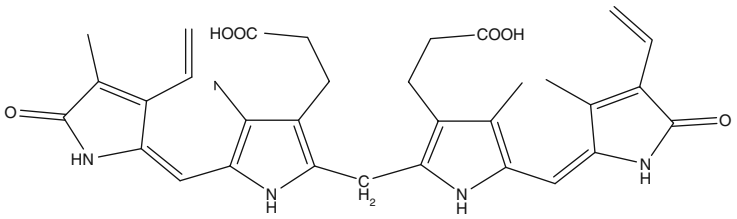

Bilirubin

Bilirubin is a nearly symmetrical tetrapyrrole, consisting of two rigid, planar dipyrrole units (dipyrrinones), joined by a methylene bridge. The structure thus resembles a two-bladed propeller, in which the blades could theoretically be joined at different angles and each blade could rotate about its bond to the methylene bridge. In the preferred "ridge-tile" conformation, the two dipyrrinones are syn-periplanar, as in a partially opened book, and the angle between the two planes is about 95°. This minimum energy conformation is further stabilized by two trios of internal hydrogen bonds formed between the carboxymethyl side chain of each dipyrrinone and the −CO−NH− and −NH− groups of the other dipyrrinone. This rigid structure, with its internal hydrogen bonds, was first demonstrated in the crystalline state [3], but it is also the preferred conformation in solution bilirubin in water and alcohols [4–6].

The aqueous solubility of bilirubin is practically negligible due to the propensity of the molecules to form intramolecularly hydrogen-bonded conformers. All hydrophilic regions of bilirubin molecule are involved in this hydrogen bonding with the result that polar groups are enclosed in a hydrophobic shell. In bile, bilirubin is solubilized by interaction with various amphiphilic lipid species, primarily the bile salts.

The excretion of bilirubin, particularly of its excess, from an organism is the important problem during treatment of gallstone disease and jaundices of different aetiologies. It has been shown that treatment of liver diseases is substantially facilitated by application of fumed silica as enterosorbent [7]. It may be explained by high adsorptive capacity of fumed silica with respect to many biologically active compounds including bilirubin.

Recently the adsorption of bile acids [8] and bilirubin [9] on the fumed silica surface from individual and mixed solutions [10, 11] has been studied, but the adsorption values were not very high at physiological pH. It is possible to explain this by mutual repulsion between negatively charged particles in solution and ionized surface silanol groups. Such supramolecular systems which are mixed micelles of bile salt with bilirubin possess strong hydrophobic properties. Therefore we have assumed that their adsorption on the surface of hydrophobic silicas may be higher than that on hydrophilic silica, and therapeutic action of hydrophobic silica sorbents may be strengthened.

The aim of this work was to study bilirubin adsorption onto hydrophobic silica surfaces from solutions containing bile salts.

24.2 Results and Discussion

The interaction of bilirubin (B) and some bile salts (BS) has been spectrophotometrically studied as comparison of absorption band of bilirubin in phosphate buffer (pH 7.4) and in bile salt solutions. Taurocholic, glycocholic, cholic (containing three hydroxy groups), deoxycholic and chenodeoxycholic (two hydroxy groups) acids were used in this investigation. They differ in some physicochemical properties which are presented in Table 24.1.

The interaction of bilirubin with bile salts in solution was studied using a specially prepared series of solutions with constant concentration of bilirubin (10 mkmol/l) and varied concentrations of bile salts (from 1 to 20 mmol/l) at pH 7.4 (phosphate buffer) and 37 °C. This temperature was chosen to avoid possible gel formation at higher bile salt concentrations and to approach physiological conditions. In buffer bilirubin solution the slightly asymmetric band has maximum at 438 nm.

As shown in Figs. 24.1 and 24.2 in the presence of bile salt the position of bilirubin absorption band changes: at concentrations of bile salts below CMC it shifts to shorter wavelength (about 420 nm); when bile salt concentrations increase (up to 20 mmol/l) this band shifts to longer wavelength (460–480 nm). The intensity of

Table 24.1 Chemical and physical properties of some bile acids [12]

Bile acid	R	R_7	R_{12}	Log $P_{O/W}$	CMC (mmol/l)
Cholic (C)	OH	OH	OH	2.02	11
Taurocholic (TC)	$NHCH_2CH_2SO_3H$	OH	OH	1.63	6
Glycocholic (GC)	$NHCH_2COOH$	OH	OH	1.65	10
Deoxycholic (DC)	OH	H	OH	3.50	3
Chenodeoxycholic (CDC)	OH	OH	H	3.28	4

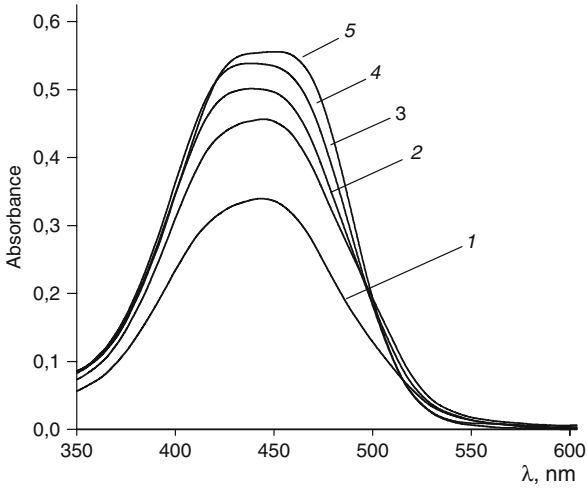

Fig. 24.1 Absorption spectra of individual bilirubin (*1*) and mixed bilirubin–DC solutions: bilirubin – 10 mkmol/l; DC concentrations of 4 (*2*), 6 (*3*), 8 (*4*) and 14 (*5*) mmol/l; and pathlength 1 cm

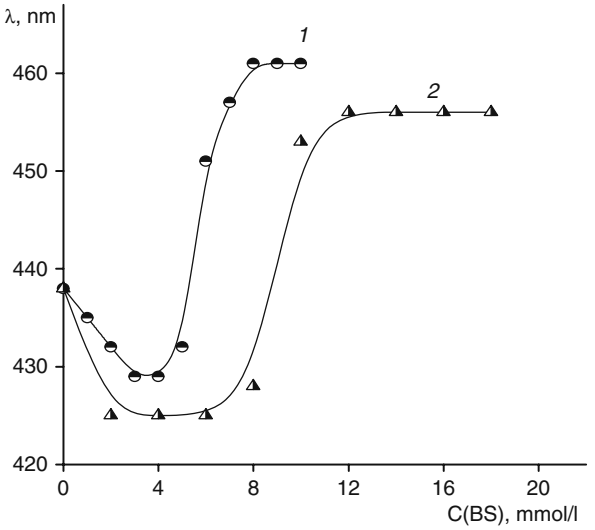

Fig. 24.2 The position of absorption band of bilirubin in mixed solutions with deoxycholate (*1*) and taurocholate (*2*) as a function of bile salt concentration

this absorption band strongly increases, and absorption band at shorter wavelength practically disappears.

According to [13] such behaviour of bilirubin absorption band could be explained as different types of interaction between bilirubin and bile salt which are dependent on bile salt concentration. Monomeric bile salts appear to interact with bilirubin hydrophilically. Hence hypsochromic shift of bilirubin absorption band is observed in comparison with its position in individual buffer solution. But dimers or trimers of bile salts form with bilirubin stronger complexes by hydrophobic interaction that is the reason for bathochromic shift of bilirubin absorption band. This assumption is proved by the positions of inflection points on the curves presented in Fig. 24.2, which approximately correspond to CMC of studied bile salts: 3–4 mmol/l for DC and 6–8 mmol/l for TC.

There are a number of data on interaction between bilirubin and different bile salts in literature [13–19], but all these studies have qualitative character. For quantitative description of interaction between bilirubin and bile salts we should consider the composition of bile salt solution in dependence on their concentrations. The composition and range of existence of aggregates formed by bile salts under investigation in aqueous solution were studied [20–22]. It was shown that the composition of aggregates is dependent on ionic strength, pH and concentration. We used the data which correspond to our experimental conditions and calculated association constants of bile salts assuming that TC, GC and C form only dimers, and DC and CDC form trimers:

$$n\mathrm{BS} \leftrightarrow (\mathrm{BS})_n,$$
$$K_{\mathrm{ass}} = \left[(\mathrm{BS})_n\right] / [\mathrm{BS}]^n .$$

Table 24.2 Association constants of bile salt and binding constants of bilirubin with bile salts

Bile salt (aggr. number)	Log K_{ass}	Log K_B
Taurocholic (n=2)	2.68	3.16
Glycocholic (n=2)	2.44	2.68
Cholic (n=2)	2.70	2.56
Deoxycholic (n=3)	6.25	3.50
Chenodeoxycholic (n=3)	6.00	3.40

The calculated constants are presented in Table 24.2. Primarily we ensured that aggregates with higher aggregation number than 2 and 3 are practically absent at the concentrations of bile salt up to 20 mmol/l.

Assuming that the intensity of long wavelength bands of bilirubin in presence of bile salts is determined by the formation of bilirubin complex with dimers or trimers of BS we analyzed the absorption data using the following equations:

$$\begin{aligned} D^{\lambda} &= \varepsilon_{B}^{\lambda}[B] + \varepsilon_{B-(BS)n}^{\lambda}[B-(BS)_n], \\ C_{BS} &= [BS] + n\left[(BS)_n\right] + n\left[B-(BS)_n\right], \\ C_B &= [B] + [B-(BS)_n], \end{aligned}$$

where [B], [BS], $[(BS)_n]$ and $[B-(BS)_n]$ are equilibrium concentrations of bilirubin, monomer and aggregates of bile salts and their complex with bilirubin, respectively. Molar extinction coefficients (at wavelength λ) of bilirubin, ε_B^{λ}, and its complex with bile salt, $\varepsilon_{B-(BS)n}^{\lambda}$, were determined for the individual solution of bilirubin and from the plot of optical density versus bile salt concentrations in mixed solutions. All these data allowed us to calculate the binding constants (Table 24.2) of bilirubin to small aggregates of bile salts:

$$\begin{aligned} B + (BS)_n &\leftrightarrow B-(BS)_n, \\ K_B &= \left[B-(BS)_n\right] / \left[(BS)_n\right][B]. \end{aligned}$$

The order of binding constants of B with BS aggregates is as follows: DC > CDC > TC > GC > C. This order does not coincide with the row of hydrophobicity of BS which is shown in Table 24.1 as partition coefficients (log $P_{O/W}$). It means that not only hydrophobic interactions of appropriate parts of bilirubin and bile salt molecules are involved but also hydrophilic interactions make some contribution to this complex formation [2]. The nonpolar parts of each dipyrrinone of B could interact by hydrophobic stacking interactions with the hydrophobic β-face of the bile salts. The polar side chains of B and BS could interact hydrophilically. In this case taurocholate likely has more possibilities to form additional bonds with bilirubin.

Using the binding constants of bilirubin with BS we calculated concentrations of free and bound bilirubin in bile salt solution with GRFIT program package [23]. These results are shown in Fig. 24.3. It is seen that at BS concentrations above their CMC values, virtually all bilirubin is complexed with BS aggregates.

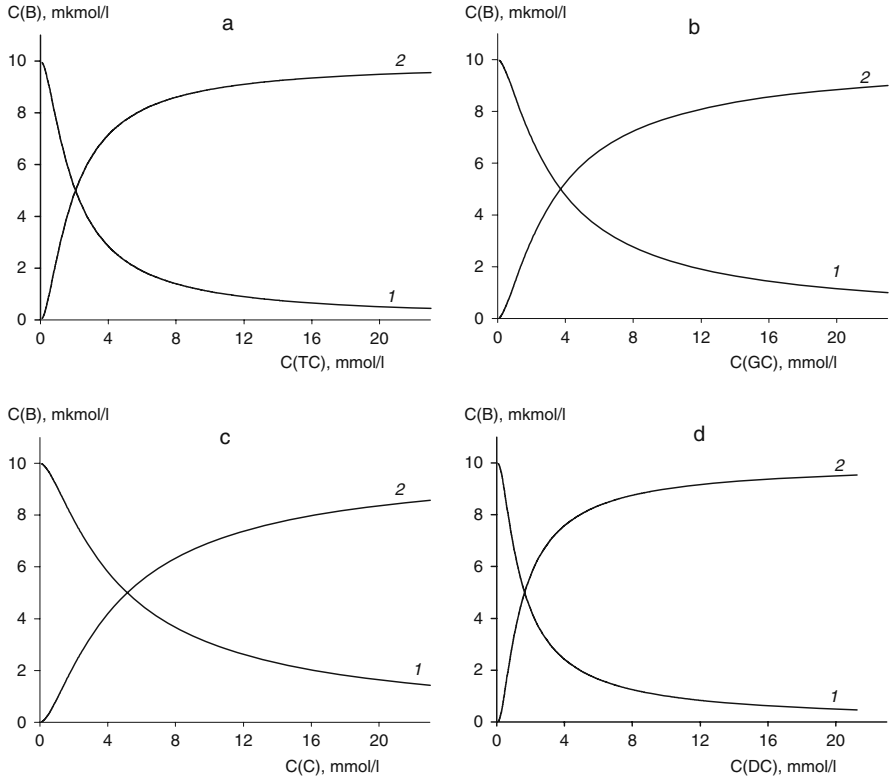

Fig. 24.3 Concentrations of free bilirubin (*1*) and its complexes with bile salt aggregates (*2*): taurocholate (**a**), glycocholate (**b**), cholate (**c**) and deoxycholate (**d**)

At the next stage of the work, we investigated the adsorption of bilirubin and bile salts from their mixed aqueous solutions on the surface of two hydrophobic silica sorbents: commercial hydrophobic silica AMS and partially modified by trimethylsilyl groups (appr. 50%) fumed silica, TMS. Both sorbents have specific surface area of about 300 m^2/g.

Primarily, the adsorption of bile salts from individual solutions was studied as a function of their initial concentrations. Isotherms of bile pigment adsorption from individual solutions are difficult to measure because of its low solubility even at pH 7.4 of a phosphate buffer. The data on bilirubin adsorption as dependent on initial concentrations of bile salts are presented in Fig. 24.4, from which it is seen that, as the concentration of the bile salts increases, the concentration of adsorbed bilirubin on the surface of both sorbents decreases. The shape of bilirubin adsorption curves resembles the curves of the variations in the concentration of free bilirubin in bile salts containing solutions. The character of changes in bilirubin adsorption with bile salts is sorbed on the surface of both sorbents.

This assumption is indirectly supported by the fact that bile salt adsorption from mixed solutions remains virtually unchanged in comparison with adsorption from

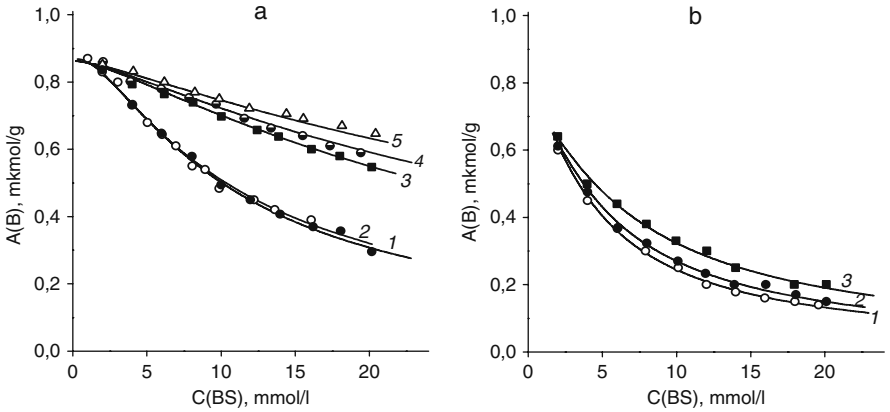

Fig. 24.4 Adsorption of bilirubin on the surface of AMS (**a**) and TMS (**b**) as a function of bile salts concentrations: deoxycholate (*1*), chenodeoxycholate (*2*), taurocholate (*3*), glycocholate (*4*) and cholate (*5*). The *symbols* and *lines* refer to experimental data and calculated adsorption curves, respectively

individual solutions. The data on bile salt adsorptions from solutions containing bilirubin are shown in Fig. 24.5.

Nonelectrostatic surface complexation model [24] and GRFIT program were used for quantitative estimation of the interaction of bilirubin and bile salts with the surface of silica sorbents. This model, which does not take into account the influence of surface charge on the equilibrium constants, was chosen because the structure of electrical double layer is unknown for the hydrophobic sorbents. Moreover all

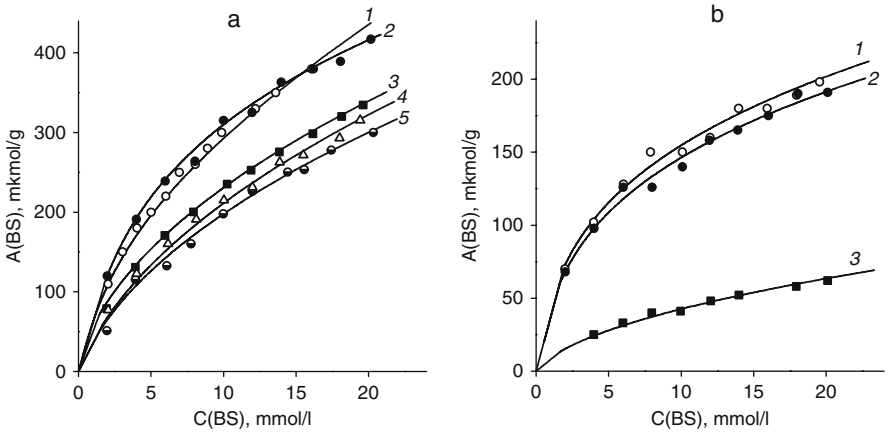

Fig. 24.5 Isotherms of bile salt adsorption from mixed bilirubin solutions on the surface of AMS (**a**) and TMS (**b**): deoxycholate (*1*), chenodeoxycholate (*2*), taurocholate (*3*), glycocholate (*4*) and cholate (*5*). The *symbols* and *lines* refer to experimental data and calculated adsorption curves, respectively. (Experimental data of adsorption from individual solutions are not shown)

Table 24.3 Equilibrium complexation constants (log *K*) of bile salts and bilirubin on the surface of hydrophobic silica sorbents

Adsorbate	AMS	TMS
Taurocholate	0.84	0.20
Glycocholate	0.88	–
Cholate	0.80	–
Deoxycholate	1.40	1.20
Chenodeoxycholate	1.34	1.10
Bilirubin	1.80	1.50

experiments were fulfilled at constant pH value. We assumed that in this case the contribution of electrostatic term to the surface complexation constants would be a permanent value. Therefore, we modelled the binding bilirubin and bile salts with the sorbent surface as an interaction in solution.

We assumed that adsorption is determined by the formation of bilirubin and bile salt complexes on the surface:

$$\equiv \mathrm{S} + \mathrm{B} \leftrightarrow \equiv \mathrm{S} - \mathrm{B},$$
$$\equiv \mathrm{S} + \mathrm{BS} \leftrightarrow \equiv \mathrm{S} - \mathrm{BS},$$

where ≡S refers to surface.

The GRFIT program enables us to select the equilibrium constants of a reaction to achieve the best correspondence between experimental and calculated adsorption curves. Equilibrium constants of the reaction corresponding to bile salts and bilirubin adsorption from individual and mixed solutions are listed in Table 24.3. These constants obtained from the interaction of bilirubin and BS with the surface reflect the observed regularities: the higher the hydrophobicity of sorbents (AMS is more hydrophobic than TMS) the greater the corresponding constants either of bilirubin or bile salts; the higher the hydrophobicity of bile salts the higher their affinity to sorbents.

Bilirubin is adsorbed only in the free state; bilirubin complexes with aggregates of bile salts are adsorbed on neither of the sorbents.

A lower affinity of bilirubin–bile salt complexes to the surface compared to bilirubin may be explained by the decrease in their nonpolar part and increase in the polar part, which is oriented towards water and negatively charged owing to dissociation of carboxyl groups of bile salt and bilirubin.

24.3 Conclusion

The interaction of bilirubin with small aggregates of bile salts (dimers or trimers) forming supramolecular complexes, and its strong retention in them, leads bilirubin to be adsorbed only in free state. Thus, we may assume that the application of silicas as enterosorbents must not disturb the vitally important processes involving bile salts and bilirubin and will result only in the adsorption of excess bilirubin which exhibits toxic action.

References

1. Carey MC (1985) Physical-chemical properties of bile acids and their salts. In: Danielson H, Sjövall J (eds) Sterols and bile acids, Elsevier, Amsterdam
2. Ostrow JD, Mukerjee P, Tiribelli C (1994) Structure and binding of unconjugated bilirubin. J Lipid Res 35:1715–1730
3. Bonnett R, Davies JE, Hursthouse MB et al (1978) The structure of bilirubin. Proc R Soc Lond B 202:249–268
4. Yang B, Morris MD, Xie M et al (1991) Resonance Raman spectroscopy of bilirubins. Biochemistry 30:688–694
5. Boiadjiev SE, Person RV, Puzicha G et al (1992) Absolute configuration of bilirubin conformational enantiomers. J Am Chem Soc 114:10123–10133
6. Pu YM, Lightner DA (1991) On the conformation of bilirubin dianion. Tetrahedron 47: 6163–6170
7. Shtat'ko EI, Moroz LV, Andreichin VA (2003) Complex therapy of infectious diseases. In: Chuiko AA (ed) Medical chemistry and clinical application of silicon dioxide, Naukova Dumka, Kiev
8. Vlasova NN, Belyakova LA, Golovkova LP et al (2003) Adsorption of bile acids on the highly dispersed silica surface. Russ J Phys Chem 77:902–905
9. Vlasova NN, Golovkova LP, Severinovskaya OV (2005) Adsorption of bilirubin from aqueous solutions on the surface of finely dispersed silica. Russ J Phys Chem 79:1312–1315
10. Vlasova NN, Golovkova LP, Severinovskaya OV (2006) Interaction between bilirubin and sodium deoxycholate and their adsorption from mixed solutions on the surface of silica sorbents. Colloid J 68:686–690
11. Vlasova NN, Golovkova LP, Severinovskaya OV (2007) Intermolecular interactions in system bilirubin–bile salt–silica. Russ J Phys Chem 81:1136–1139
12. Fini A, Feroci G, Roda A (2002) Acidity in bile acid systems. Polyhedron 21:1421–1427
13. Carey M, Koretsky A (1979) Self-association bilirubin IX-α in aqueous solution at pH 10 and physical-chemical interactions with bile salt monomers and micelles. Biochem J 179:675–689
14. Perrin JH, Wilsey M (1971) Induced optical activity of bilirubin in presence of sodium deoxycholate. J Chem Soc Chem Commun 14:769–770
15. Xu S, Hu J, Wang K (1986) Spectroscopic investigation of interaction of bilirubin with sodium taurochlate. J Mol Sci 4:675–689
16. Puranam KL, Balaram P (1987) Solubilization of bilirubin by cholate micelles. Proc Indian Acad Sci (Chem Sci) 98:453–468
17. Rege RV, Webster CC, Ostrow JD (1988) Interactions of unconjugated bilirubin with bile salts. J Lipid Res 29:1289–1296
18. Kurtin WE, Reck D, Lafontaine J et al (1993) Absorption and emission spectral studies of bilirubin complexes with sodium taurocholate in aqueous buffer at pH 8.0. J Chem Soc Perkin Trans II 2392–2397
19. Kurtin WE, Heo R, Breimer DJ et al (1998) Effects of pH on the adsorption, emission and light scattering spectroscopy of bilirubin and xantobilirubic acid in sodium taurocholate solution. J Chem Soc Perkin Trans II 1677–1682
20. Bottari E, Festa MR (1996) On the composition of sodium taurodeoxycholate micellar solutions. Langmuir 12:1180–1187
21. Bottari E, Festa MR, Franko M (1999) Structure and composition of taurocholate micellar aggregates. Analyst 15:2996–2998
22. Bottari E, Festa MR, Franko M (2002) Composition of sodium glycocholate micellar solutions. Langmuir 18:2337–2342
23. Ludwig C (1992) GRFIT, a program for solving speciation problems, evaluation of equilibrium constants, concentrations, and other physical parameters. Internal report, University of Berne
24. Davis JA, Kent DB (1990) Surface complexation modelling in aqueous geochemistry. Rev Miner 23:177–260

Chapter 25
Supramolecular Structures with Blood Plasma Proteins, Sugars and Nanosilica

V.V. Turov, V.M. Gun'ko, N.P. Galagan, A.A. Rugal, V.M. Barvinchenko, and P.P. Gorbyk

Abstract Supramolecular structures with blood plasma proteins (albumin, immunoglobulin and fibrinogen (HPF)), protein/water/silica and protein/water/silica/sugar (glucose, fructose and saccharose) were studied by NMR, adsorption, IR and UV spectroscopy methods. Hydration parameters, amounts of weakly and strongly bound waters and interfacial energy (γ_S) were determined over a wide range of component concentrations. The $\gamma_S(C_{protein},C_{silica})$ graphs were used to estimate the energy of protein–protein, protein–surface and particle–particle interactions. It was shown that interfacial energy of self-association (γ^{as}) of protein molecules depends on a type of proteins. A large fraction of water bound to proteins can be displaced by sugars, and the effect of disaccharide (saccharose) was greater than that of monosugars. Changes in the structural parameters of cavities in HPF molecules and complexes with HPF/silica nanoparticles filled by bound water were analysed using NMR-cryoporometry showing that interaction of proteins with silica leads to a significant decrease in the amounts of water bound to both protein and silica surfaces. Bionanocomposites with BSA/nanosilica/sugar can be used to influence states of living cells and tissues after cryopreservation or other treatments. It was shown that interaction of proteins with silica leads to strong decrease in the volume of all types of internal cavities filled by water.

25.1 Introduction

Detailed investigations of molecular interactions with the participation of proteins are stimulated by several problems whose solution is based on methods of control of interactions at protein–solid interfaces and on development of new biocompatible materials used in transplantation of organs and creation of artificial tissues [1, 2], cryopreservation of cells and tissues [3, 4], adsorbents for medical purposes [5], separation and purification of biomaterials [6, 7], etc. In this work we will analyse

V.V. Turov (✉)
O.O. Chuiko Institute of Surface Chemistry of the National Academy of Sciences of Ukraine, General Naumov St. 17, Kyiv 03164, Ukraine
e-mail: v_turov@ukr.net

A.P. Shpak, P.P. Gorbyk (eds.), *Nanomaterials and Supramolecular Structures*,
DOI 10.1007/978-90-481-2309-4_25,

the behaviour of a variety of colloidal and biocolloidal systems studied by ^{1}H NMR spectroscopy with layer-by-layer freezing-out of bulk and interfacial liquid phases. This method could be used to study supramolecular structures, hydrate shells of biomacromolecules and their changes occurring on interactions with low-molecular compounds or nanomaterials [8–10].

Diluted aqueous solutions of proteins obey the DLVO theory assuming that interactions between the protein molecules occur due to van der Waals and electrostatic forces [11]. Electrostatic repulsive forces are caused by charging of proteins as polyelectrolytes in the aqueous medium far from their point of zero charge (PZC). Dissociation of acidic groups in side functionalities of proteins or protonation of basic sites occurs depending on pH value that results in their negative or positive charges. Electrostatic components of surface forces at a flat surface covered by a protein layer were intensively studied [12, 13]. It was shown that at relatively large distances from the surface the experimental values of surface forces practically coincide with that calculated using the DLVO theory; however, in certain cases a large discrepancy between them was found [13–15]. The use of low-temperature NMR spectroscopy to determine the characteristics of water interactions with proteins and other biopolymers is effective due to the dependence of the mobility of the molecules and the freezing point depression of confined water on energy of these interactions. The mobility of molecules is directly linked to such spectral characteristic as relaxation time of nuclear spins [16]. The NMR experiments showed that the relaxation in a disturbed spin system can occur non-isotropically. A relaxation rate in the *XY* plane can be higher than that along the *Z* axis. Therefore times of longitudinal and transverse relaxations ($T1$ and $T2$, respectively) can be independently examined. The relaxation occurs because of energy exchange between disturbed and surrounding nuclei or paramagnetic particles, and the stronger is the interaction, the more rapidly is the equilibrium state achieved. The energy exchange most effectively occurs with magnetic dipoles participating in the molecular motions at a frequency coinciding with the resonance frequency of the disturbed nucleus. The molecular motions at the resonance frequency cause the relaxation processes both along the *Z* axis and in the *XY* plane. The difference in the $T1$ and $T2$ values is also due to an additional channel of energy dissipation for the transverse relaxation at very low frequencies. Therefore, temperature changes in the longitudinal and transverse relaxations differ. The $T1(1/T)$ dependence can correspond to a curve with a minimum which answers the equality of a frequency of the molecular motions and the resonance frequency, while a minimum of $T2(1/T)$ should be at lower temperatures [16, 17]. Investigations showed that the $T2$ values over entire temperature range were considerably lower than $T1$, and the minimum on the $T1(1/T)$ dependence was washed out; therefore, it is difficult to determine the characteristic parameters of the relaxation. A sufficiently accurate model could be developed assuming that there is correlation time distribution function characterising all types of bound water in the system. Another factor which should also be taken into account on the NMR measurements of heterogeneous systems is proton exchange at the interfaces. The mentioned features complicate interpretation of the NMR spectroscopy results. This was a reason to search for new approaches to

study the characteristics of confined water by the NMR spectroscopy, and layer-by-layer freezing-out of bulk and bound phases is one of such techniques. On freezing-out of bulk water at $T < 273$ K the ^{1}H NMR spectra include a signal of unfrozen water with decreased intensity with lowering temperature. This signal could be attributed to bound water characterised by certain freezing point depression due to the confining effects in pores of solid adsorbents or cavities (compartments) in biomacromolecules. Comparing the signal intensities of water before and after freezing-out, the amount of bound water as a function of temperature can be determined. However, the accuracy of these measurements depends on the presence of dissolved compounds and ions, the effects of supercooling of water on freezing and some other factors.

25.2 Materials and Methods

The ^{1}H NMR spectra were recorded using Bruker WP-100 SY (Germany) or Varian 400 Mercury spectrometers of high resolution using the 90° probe pulses with a duration of 4 or 2 μs, respectively. The temperature was controlled using a Bruker VT-1000 device with relative mean errors of ±1 K. Changes in concentration of unfrozen water were determined with the accuracy better than ±10%. To prevent supercooling of the studied systems, the measurements of the amounts (C_{uw}) of strongly (SBW) and weakly (WBW) bound unfrozen waters were carried out on heating of samples preliminarily cooled to 210 K and equilibrated for 5–7 min for each temperature. The ^{1}H NMR spectra recorded here at $T < 273$ K include the signals only of nonfreezable mobile water molecules. The signals of water molecules from ice, as well as protons from macromolecules and oxide materials, do not contribute to the ^{1}H NMR spectra because of features of the measurement technique and the short duration ($\sim 10^{-6}$ s) of transverse relaxation of protons in immobile structures which is shorter by several orders than that of mobile water. The characteristics of bound water were computed as described previously [9, 18, 19].

The bonding of low molecular organics to proteins was investigated for human (HSA) or bovine (BSA) serum albumins–water–sugar (glucose, fructose or saccharose) systems and on addition of nanosilica. BSA and HSA (Biopharma, Kiev, Ukraine), fructose, glucose and saccharose (Merck, Germany) were used as received. The solutions of the proteins and sugars were prepared using 0.9 wt% NaCl solution in distilled water.

Immunoglobulin (Ig) solutions were prepared by dilution of 10% Ig solution (Biopharma, Kiev, Ukraine, 97% purity with 92% of monomers and dimers, 3% of fragments and 5% of oligomers) by water or buffer solutions. Concentration of Ig was determined spectrophotometrically at $\lambda = 278$ and 550 nm using the Biuret method [20]. The pH values of the solutions were measured using an EV-74 pH meter with a glass electrode. The pH value was adjusted using the buffer solutions, HCl or KOH. Adsorption of proteins on nanosilica was determined spectrophotometrically. Desorption of proteins was measured for samples incubated at

room temperature for 1.5 h and centrifuged at 8000 rpm for 15 min, and protein concentration was determined in the supernatant liquid.

Highly disperse silicas (HDS, nanosilica or fumed silica) A-175 and A-300 (pilot plant of the Institute of Surface Chemistry, Kalush, Ukraine, specific surface area $S_{BET} = 186$ and 320 m^2/g, respectively) were heated at 700 K for several hours before use to remove adsorbed organics and residual HCl.

Human plasma fibrinogen (HPF) was obtained from plasma of donor blood on fractional salting out with sodium sulphate. Initial HPF concentration (C_{HPF}) was 2.6 wt% in an aqueous solution at 0.15 mol NaCl. HPF was frozen and stored at 245 K. Before studies frozen HPF was thawed in a water bath at 308–310 K for 15–20 min and maintained at room temperature for 10 min. To obtain the HPF solutions of given concentrations (0.6, 1.25 and 2.5 wt% at pH 5–8) a phosphate buffer solution (PBS) was used for dilution of the initial solution directly before experiments. Adsorption of HPF on nanosilica A-300 was studied at 293±1 K using 0.2 g of the dry powder and 40 ml of the HPF solutions at different concentrations. The HPF adsorption was studied at pH 7.4 because the pH value of blood is 7.35–7.45. Concentration of HPF before and after absorption was spectrophotometrically controlled using a Specord M-40 (Carl Zeiss, Germany) UV/vis spectrophotometer at $\lambda = 280$ nm. To reach the adsorption equilibrium, the samples were incubated for 1.5 h and then centrifuged at 8000 rpm for 15 min.

25.3 Interaction of Plasma Proteins with Water, Sugars and Nanosilica

Serum albumins (HSA, BSA) having native globular structure include a significant quantity of bound water affecting their characteristics. Albumins fulfil a transport function in the organisms; therefore they have labile and pH-dependent structures [21], and organic compounds present in a solution and competing with water molecules for albumin adsorption sites can influence the protein characteristics. The difference in the properties of albumins in unloaded and loaded states is used by the receptor system for utilisation of transported compounds.

Figure 25.1 shows the ^{1}H NMR spectra of unfrozen water bound to BSA and HSA in frozen solution at $T < 273$ K. At a high resolution (400 MHz, Fig. 25.1a) the spectra represent a broad asymmetrical signal whose width increases with lowering temperature because of a decrease in the mobility of water molecules [22]. The chemical shift of the proton resonance (δ_H) of this water is 4–5 ppm; i.e. it is strongly associated [9]. At low temperatures the asymmetry decreases, and the signal shifts towards the weak magnetic fields. This can be interpreted as the bonding of the water molecules to most polar sites of BSA [9]. A more complex signal is observed for the HSA solution with the presence of sugar (lower resolution at 100 MHz, Fig. 25.1b) as its components differ by ∼1 ppm. These features of the ^{1}H NMR spectra of unfrozen water bound to protein/sugar reveal the existence of

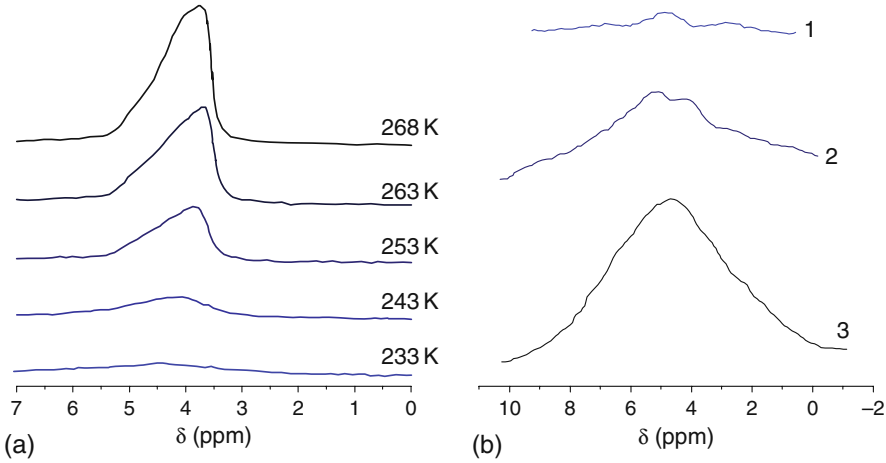

Fig. 25.1 ^{1}H NMR spectra of unfrozen water: (**a**) BSA/water at $C_{BSA} = 2$ wt% recorded at different temperatures and (**b**) HSA/saccharose/water at $C_{HSA} = 1$ wt% and saccharose concentration $C_{Sc} = 0$ (*1*), 0.1 (*2*) and 1 wt% (*3*) recorded at 250 K

several forms of water characterised by fast or slow (in NMR timescale) molecular exchange. The structural differentiation of water bound by proteins can occur due to its interactions with hydrophobic and hydrophilic protein functionalities [23, 24]. The water characteristics depend on the average number of the hydrogen bonds per molecule (n_H) [9, 24]. A decrease in the n_H value is accompanied by the displacement of the ^{1}H NMR signal towards the strong magnetic fields. Consequently, the signals at smaller δ_H values correspond to more strongly clustered (or more weakly associated) water characterised by a smaller number of the hydrogen bonds per molecule.

There is a regularity of the albumin/sugar/water system corresponding to a sugar concentration range giving a decrease in unfrozen water content. This is clearly observed for the HSA solution with saccharose (Fig. 25.1b) since addition of 1 wt% of saccharose leads to a decrease in the signal intensity of unfrozen water (at 250 K) more than five times. The obtained results testify about effective interaction of sugar with the protein molecules; i.e. the saccharose molecules can displace the major portion of water bound to protein [25].

Addition of very small quantities of sugars leads to a decrease in the amounts of unfrozen water. For fructose (Fig. 25.2a) this effect is in a narrow concentration range. For glucose (Fig. 25.2b) a considerable decrease in the C_{uw} value is observed only at $C_{Gl} < 0.38$ wt% and T near 273 K, and a section of an increase in C_{uw} versus C_{Gl} is over a wide range of concentrations and temperatures. The greatest changes in the amounts of unfrozen water are observed for the saccharose solution (Fig. 25.2c), and diminution in C_{uw} is greater at lower temperatures. At 250 K

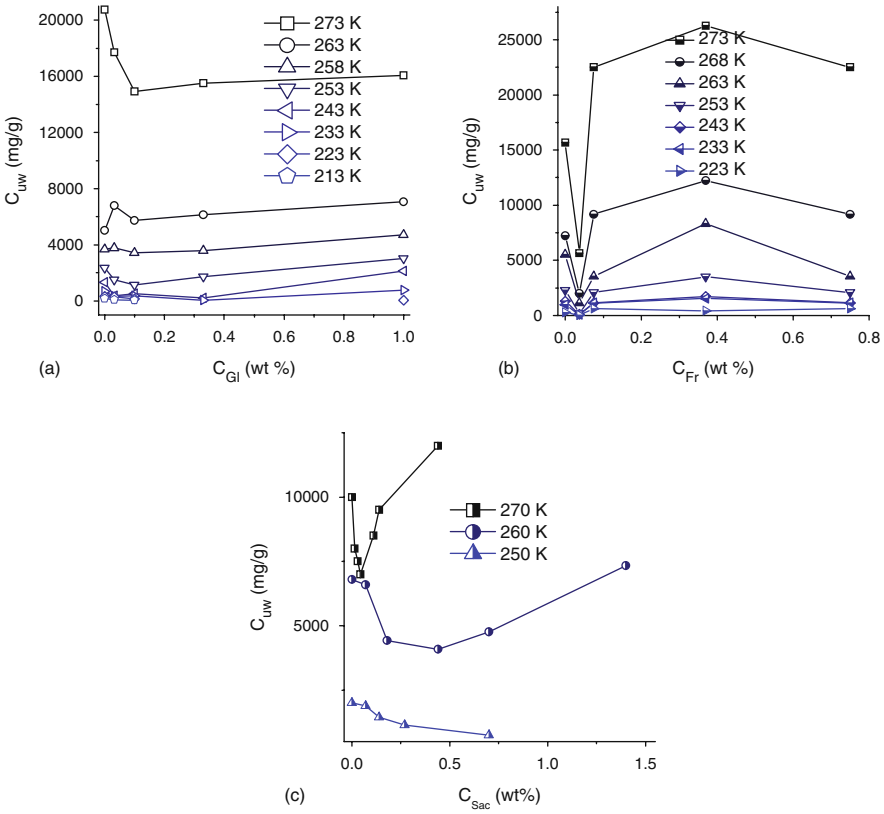

Fig. 25.2 Dependence of C_{uw} on concentration of sugars in aqueous solutions at different temperatures: (**a**) fructose, (**b**) glucose and (**c**) saccharose

the signal of unfrozen water is not observed with increasing saccharose concentration $C_{Sac} > 1$ wt%. Thus, the aqueous solutions of glucose, fructose and saccharose are characterised by different C_{uw} dependences on temperature and sugar content. Therefore, one can assume that the effects of these sugars on the aqueous solutions of proteins could be strongly different.

The interfacial energy γ_S diminishes with increasing concentration of BSA in the aqueous solution (Fig. 25.3a). Notice that similar dependences were observed for other heterogeneous systems [9, 24]. Protein molecules are strongly hydrated; therefore, to provide tight contacts between them (on self-association), a certain quantity of bound water should be removed from intermolecular gaps to the bulk that results in a decrease in the integral γ_S value. Thus, the amounts of bound water decrease as well as the γ_S value with increasing protein content in the solution. The difference in the γ_S values determines the energy of self-association of the protein molecules. Extrapolating $\gamma_S(C_{BSA})$ dependence to the zero concentration gives the interfacial energy of non-associated BSA molecules at $\gamma_S \approx 450$ J/g. The mentioned effects can change on addition of sugars to the aqueous solutions of proteins.

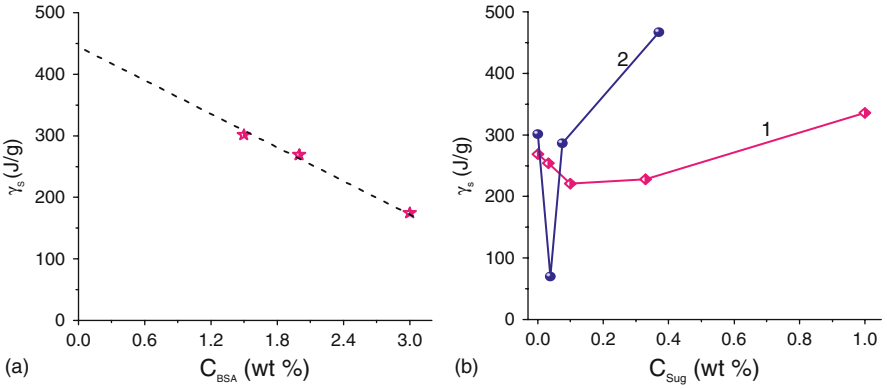

Fig. 25.3 Dependence of interfacial free energy on concentrations of (**a**) BSA in the aqueous solution and (**b**) glucose at $C_{BSA} = 2$ wt% (curve *1*) or fructose at $C_{BSA} = 1.5$ wt% (*2*) in the ternary systems BSA/monosugar/water

The $\gamma_S(C_{Sug})$ dependences (Fig. 25.3b) have the shapes similar to the $C_{uw}(C_{Gl(Fr)})$ graphs (Fig. 25.2). Simple estimations show that in the 2 wt% BSA solution 8.8×10^5 H_2O are present per protein molecule and $\sim 10^4$ H_2O from them are bound to macromolecules. Each sugar molecule can reduce a quantity of bound water by $\sim 10^3$ H_2O or even more since significant changes in the γ_S value are observed at $C_{Sug} < 0.1$ wt% (Fig. 25.3b). It is not possible to explain the substantial dehydration of BSA by only replacement of bound water by sugar molecules. Therefore, one can assume that on the bonding of sugars to the protein molecules, certain changes occur in the conformation of macromolecules that result in strong diminution of the quantity of bound water. The effect of the significant dehydration of protein molecules in the presence of sugars (maximal at low temperatures) can be one of the factors responsible for the cryoprotective properties of saccharides. Relatively small molecules of sugars (Fig. 25.4) can penetrate through cell membranes, cause certain dehydration of intracellular structures and reduce the

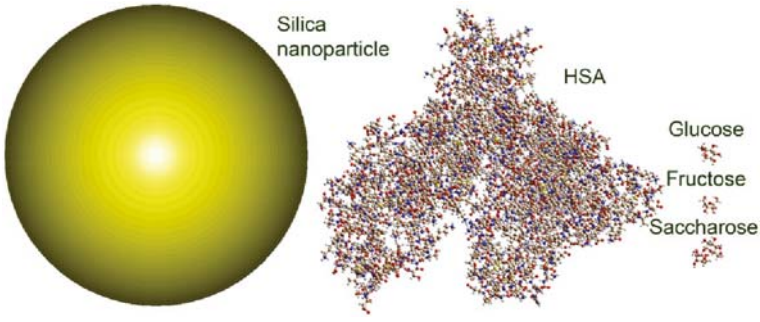

Fig. 25.4 Silica A-300 nanoparticle (8.5 nm) and HSA (8 × 9.2 nm) and sugar molecules

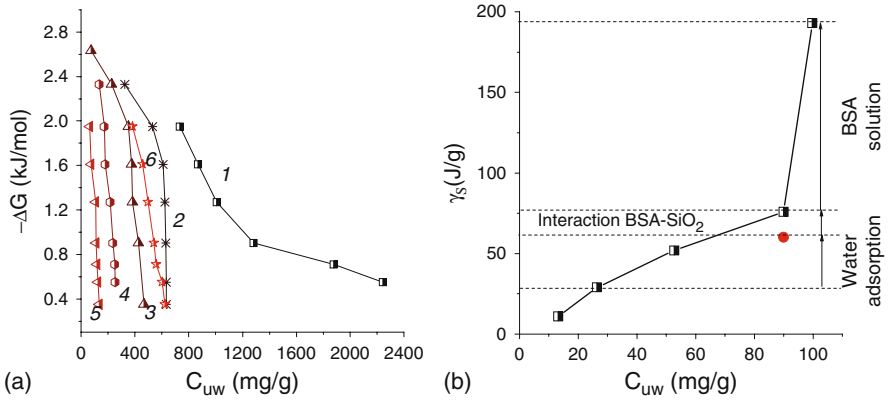

Fig. 25.5 Relationships between changes in the Gibbs free energy and the amounts of unfrozen water for (**a**) BSA differently hydrated at $C_{H2O} = 95.8$ (curve *1*), 90 (*2*), 52.8 (*3*), 26.4 (*4*) and 13.2 wt% (*5*) for protein alone and on addition of 1 wt% of silica A-175 at $C_{H2O} = 89$ wt% (*6*) and (**b**) interfacial energy as a function of C_{uw}

formation of intracellular ice crystallites. Additionally, sugars do not have a negative influence on living cells because they can be easily utilised in the cellular metabolism processes.

The relationships between the amounts of unfrozen water and its energetic characteristics for the solutions with BSA alone (Fig. 25.5a, curves 1–5) and on addition of nanosilica (curve 6) suggest that practically entire amounts of unfrozen water correspond to SBW. A section corresponding to WBW is observed only for the 0.25% BSA solution (Table 25.1).

The γ_S values for the hydrated powder and aqueous solution of BSA are characterised by almost linear increase with increasing C_{uw} value (Fig. 25.5b) dependent on protein hydration (total content of water C_{H2O}) (Fig. 25.2). For wet BSA powders, the maximum changes in the γ_S value caused by the water bonding are equal

Table 25.1 Characteristics of bound water in hydrated BSA

No	C_{BSA} (wt%)	γ_S (J/g)	C^s_{uw} (mg/g)	C^w_{uw} (mg/g)	$-\Delta G_s$ (kJ/mol)	$-\Delta G_w$ (kJ/mol)
1	0.25	193	1500	1700	3.4	1.6
2	10	76	620	–	2.8	–
3	47.2	52	528	–	2.8	–
4	73.6	29	264	–	2.8	–
5	86.8	11	132	–	3.0	–
6	10 (+1 wt% A-175)	65	700	–	2.8	–

Note. Types of water: strongly (C^s_{uw}, SBW frozen at T < 250 K and $\Delta G_s < -0.5$ kJ/mol) and weakly (C^w_{uw}, WBW frozen at $T > 250$ K and $\Delta G_w > -0.5$ kJ/mol) bound waters.

to 70 J/g (Fig. 25.5b). Addition of 1 wt% of nanosilica to the 10 wt% BSA solution leads to changes in the γ_S value decreased by 11 J/g. This value characterises the interaction of silica nanoparticles with BSA causing the displacement of interfacial water bound to both macromolecules and nanoparticles. Notice that silica (A-300) nanoparticles and albumin molecules (BSA and HSA molecules have close sizes) have close sizes (Fig. 25.4) and the A_m value (~500 mg/g [24]) corresponds to the protein monolayer adsorption at protein:silica ≈ 1:1, since their densities twice differ. Therefore on the adsorption of albumins, macromolecules and silica nanoparticles form hybrid aggregates characterised by certain changes in the protein conformation affecting the adsorption of sugars.

An important task in immunology is the development of new methods of immune activation using artificial antigens or vaccines, control of concentration and activity of antigens (antibodies such as immunoglobulin, Ig) [26]. Ig like other proteins can irreversibly adsorb on silica [27]. The characteristics of Ig were described in detail elsewhere [26, 28]. The Ig molecules (~160 kDa, length ~23 nm and average diameter ~5 nm) have a complex shape with two larger and two smaller polypeptide chains bonding by disulphide bridges. Ig adsorption (A) versus pH has a bell-shaped form at a maximum close to the PZC (or isoelectric point, IEP) of Ig at pH 6.6 (Fig. 25.6a). A similar A(pH) shape is typical for proteins as ionogenic macromolecules [24, 27, 29] because an area occupied by a molecule is minimal at the PZC when it has the most compact shape and the repulsive electrostatic interactions between adsorbed macromolecules are minimal. The appearance of negative charges on the molecules at $pH > pH_{PZC}$ leads to a decrease in the adsorption (in comparison with the adsorption at $pH < pH_{PZC}$) as a result of the electrostatic repulsion between them and negatively charged silica surface. At $pH < pH_{PZC}$ adsorption decrease is lesser because the electrostatic repulsion remains only between macromolecules but not between the molecules and silica having $pH_{PZC} \approx 3.5$ and low negative surface charge density at $pH_{PZC} < pH < 7$ [24].

The Ig adsorption isotherms (Fig. 25.6b) have the Langmuir shape and the corresponding monolayer adsorption capacity is $A_m = 105$ and 120 mg/g at pH 2.2 and 6.4, respectively. These A_m values correspond to a minimal thickness of the Ig adsorption layer due to its planar adsorption. Notice that for globular albumins $A_m = 300$–600 mg/g [24]. For proteins the adsorption and desorption isotherms do not coincide because of difficulties of macromolecule desorption requiring simultaneous breakage of all intermolecular bonds between macromolecules and a solid surface. Therefore, if desorption and adsorption ($A \leq A_m$) of Ig occurs at the same pH then the adsorption is practically irreversible. Desorption of Ig increases with increasing amount of adsorbed Ig but the quantity of desorbed protein is small (Fig. 25.6c) even at significant changes in pH.

The dependence of interfacial energy as a function of concentrations of Ig and silica (Fig. 25.7) includes three specific sectors. At $C_{SiO_2} = 0$, $\gamma_S(C_{Ig})$ represents the modulus of the total changes in the Gibbs free energy of bound water changing due to self-association of macromolecules. At $C_{Ig} = 0$ the $\gamma_S(C_{SiO_2})$ dependence describes the corresponding changes caused by interparticle interactions. If concentrations of both Ig and silica are not zero then the $\gamma_S(C_{Ig}, C_{SiO_2})$ dependence

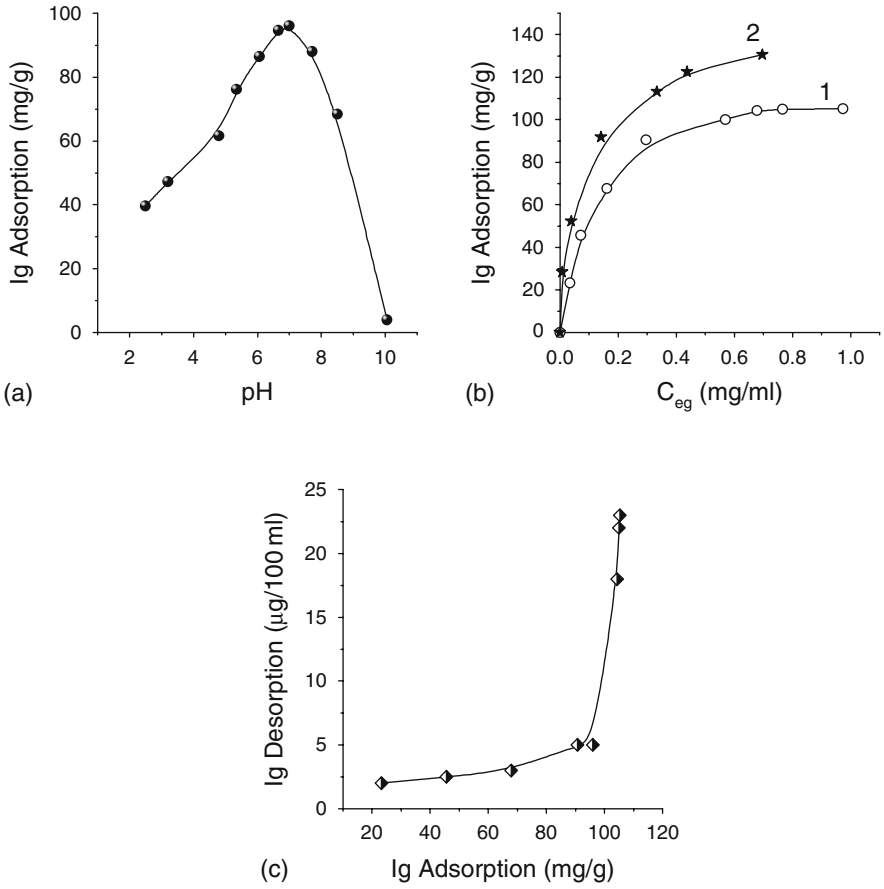

Fig. 25.6 Adsorption of Ig on silica A-300 as a function of (**a**) pH ($C_{Ig} = 0.075$ wt%), (**b**) C_{Ig} (pH 2.2 (*1*) and 6.4 (*2*)) and (**c**) desorption of Ig as a function of adsorbed amounts

is determined by both adsorption and coagulation processes. Taking into account the Langmuir shape of the Ig adsorption at $A < A_m$, one can assume that strong coagulation of macromolecules interacting with different silica particles does not occur at used concentrations. The Ig molecules are surrounded by a thick layer of bound water (Table 25.2) whose thickness increases in dilute solutions with decreasing concentration of proteins because in the dilute buffered solutions the probability of formation of protein oligomers is low and undistorted hydrate shells of macromolecules have a large thickness.

Maximum diluted Ig solutions (Table 25.2) are characterised by minimal Gibbs free energy of bound water (the γ_S value is maximal ~400 J/g and $C_{uw} \approx 10$ g/g at $C_{Ig} \to 0$) (Fig. 25.7). A small change in the interfacial energy at $C_{Ig} = 3-10$ wt% can be explained by increased interaction between macromolecules leading to a

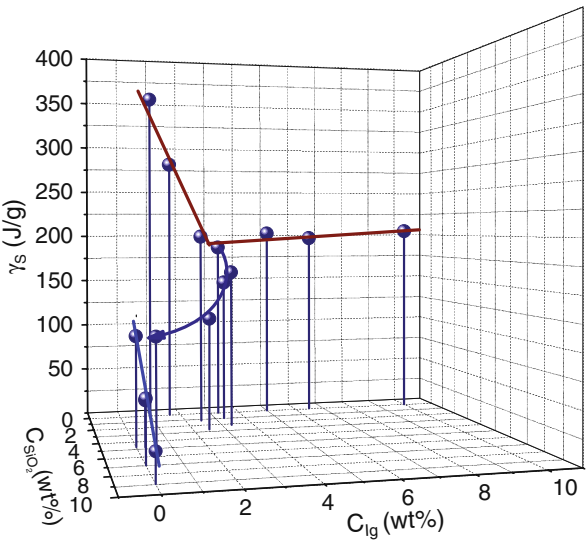

Fig. 25.7 Interfacial energy as a function of concentrations of Ig and silica A-300

Table 25.2 Characteristics of water bound in hydrated Ig and suspensions of A-300 and Ig/A-300

C_{Ig}/C_{SiO_2} (wt%)	C_{solid}· (wt%)	γ_S (J/g)	C^s_{uw} (g/g)	C^w_{uw} (g/g)	$-\Delta G_s$ (kJ/mol)	$-\Delta G_w$ (kJ/mol)
1/0	1	352	2.1	9.9	3	0.7
1.65/0	1.65	280	2.1	7.9	2.5	0.5
3.3/0	3.3	187	1.7	3.8	2.4	0.7
5/0	5	203	2.0	5.0	2.5	0.7
6.5/0	6.5	197	2.2	4.8	2.7	0.5
10/0	10	205	1.7	5.3	2.9	0.5
0/4.7	4.7	106	0.7	2.5	2.4	1
0/7	7	59	0.6	1.6	2.6	0.5
0/9	9	27	0.25	1.0	2.2	0.6
2.2/3.3	5.7	162	1.8	6.2	3	0.5
1/3.3	4.3	149	1.1	6.9	3	0.5
2.7/2.5	5.2	115	0.8	5.2	4	0.4
1.2/2.5	4.7	200	0.8	6.2	4.8	0.3
4.9/0.25	5.05	45	0.5	2.5	3	0.25
5.3/0.5	5.8	107	0.75	4.25	2.2	0.3

decrease in the amounts of bound water per macromolecule. Interactions between macromolecules and silica nanoparticles are much stronger than between macromolecules; therefore, silica added to the Ig solution leads to diminution of the amounts of water bound by protein. The reduction of the γ_S value for the system Ig/A-300/water is maximal at small C_{Ig} values because relative adsorption is

maximal at minimal C_{Ig} values (e.g. with increasing $C_{Ig,eq}$ from 0.1 to 1.0 mg/ml the adsorption increases only twice (Fig. 25.6b)). At $C_{Ig} > C_{SiO_2}$ changes in the γ_S values are relatively small due to weak interaction of Ig monolayer coated silica nanoparticles with dissolved protein molecules. This is confirmed by the rheometry results showing an extremal dependence of the viscosity of the protein (polymer)–nanosilica suspensions on concentration of proteins (polymers) [24].

For treatment of certain diseases (e.g. wound and purulent infections of internal cavities), preparations based on nanosilica are successfully used [5]. In some of these cases silica nanoparticles can contact blood. Blood as a multicomponent heterogeneous system contains many types of cells and macromolecules, and the aqueous solution of low molecular organic and inorganic compounds plays a role of the dispersion medium. Therefore investigations of hydrate shells of blood components, intermolecular interactions between them alone and on contact with solid nanoparticles are of importance for deeper understanding of the mechanisms of actions of medicinal nanocomposites.

Fibrinogen is one of the main plasma proteins participating in blood clotting [30, 31]. Its concentration in blood is 0.22–0.44 wt%. Native HPF molecules (340 kDa, 46 × 6.5 nm) are strongly hydrated, and bound water can play an important role in HPF interaction with other components of blood or solid nanoparticles. HPF molecule is composed of two identical molecular halves consisting of three non-identical Aα-, Bβ- and γ-chain subunits (compared in size with primary silica nanoparticles) held together by multiple disulphide bonds; or according to another model, a HPF molecule includes one central nodule (E domain) and two identical outer nodules (D domains) linked by two coiled-coil regions. HPF molecules have "loose ends" which are extremely mobile that can be functionally important, and they can play a specific role on the adsorption of HPF especially onto non-planar surfaces as of nanosilica. AFM investigations of adsorption of HPF on a silica surface showed that it is predominantly adsorbed through D and E domains [32].

The adsorption isotherm of HPF at pH 7.4 and $C_{eq} < 0.3$ mg/ml (Fig. 25.8a) has the Langmuir isotherm shape and $A_m = 156$ mg/g for planar-adsorbed long molecules at $C_{eq} \approx 0.25$ mg/ml, since for vertically adsorbed molecules $A_m \approx 500$ mg/g at $C_{eq} \approx 0.5$ mg/ml (Fig. 25.8a). A maximum of A(pH) is at pH 5.5–6.0 (Fig. 25.8b) close to the PZC of HPF. The adsorption decreases with increasing pH like other plasma proteins [24, 33]. Desorption of HPF is low [34] as for Ig shown above that suggests irreversible planar adsorption of HPF. The right term of the Langmuir equation was used as the kernel of integral adsorption equation [24, 34] to calculate the distribution function of Gibbs free energy of adsorption $f(\Delta G)$ (Fig. 25.8c). The position of the $f(\Delta G)$ maximum at $-\Delta G \approx 2.2$ kJ/mol corresponds to the slow rise of the adsorption isotherm and is in agreement with the ΔG_s values calculated from the ^{1}H NMR data for SBW (Table 25.3). These not-large values $-\Delta G < 5$ kJ/mol (Fig. 25.8c) are due to a considerable diminution of the solvation energy of HPF on adsorption to the silica surface.

The maximum concentration of water bound by HPF (or A-300 alone) and maximal γ_S values are observed in more diluted solutions (Table 25.3 and Fig. 25.9) like

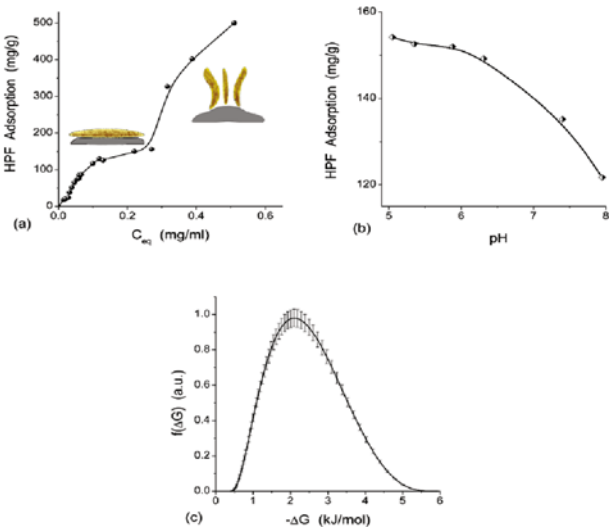

Fig. 25.8 HPF adsorption as a function of (**a**) equilibrium C_{HPF} (PBS, pH 7.4); (**b**) pH (C_{HPF} = 0.0795 wt%); and (**c**) distribution of Gibbs free energy of HPF adsorption at $A < 160$ mg/g

Table 25.3 Characteristics of weakly (WBW) and strongly (SBW) bound waters in solution of 0.15 M NaCl, HPF in PBS, suspensions of A-300 and HPF/A-300

Sample	C_{HPF} (wt%)	C_{SiO_2} (wt%)	C^s_{uw} (g/g)	C^w_{uw} (g/g)	$-\Delta G_s$ (kJ/mol)	S_{mes} (m^2/g)	S_{mac} (m^2/g)	V_{mes} (cm^3/g)	V_{mac} (cm^3/g)
NaCl			0.5	1.25	2.2	315	24	1.15	0.59
A-300[a]		4.7	0.7	2.5	2.4	115	64	1.20	2.00
A-300[b]		7.0	0.6	1.6	2.6	160	26	1.54	0.66
A-300[b]		9.0	0.25	1.0	2.2	169	2	1.19	0.06
HPF[c]	1.25		6.0	8.0	2.2	819	506	2.22	11.78
HPF[c]	2.5		1.25	6.75	3.0	545	185	3.02	4.96
HPF/ A-300[c]	0.6	2.5	0.35	3.65	2.6	71	145	0.16	3.84
HPF/ A-300[c]	2.5	1.7	1.25	1.75	3.0	323	43	2.31	0.69
HPF/ A-300[c]	2.5	3.5	0.6	3.1	3.0	57	137	0.21	3.49
HPF/ A-300[c]	2.5	5.2	0.4	0.4	4.5	112	6	0.70	0.10

[a]Aqueous suspension without addition of NaCl.
[b]0.15 mol NaCl.
[c]PBS.

Ig and BSA. For instance, at $C_{HPF} = 1.25$ wt%, HPF hydration corresponds to C_{uw} = 14 g of bound water per gram of protein, but $C_{uw} = 8$ g/g at $C_{HPF} = 2.5$ wt%; i.e. twice larger C_{HPF} value gives twice smaller C_{uw} value. A similar effect was

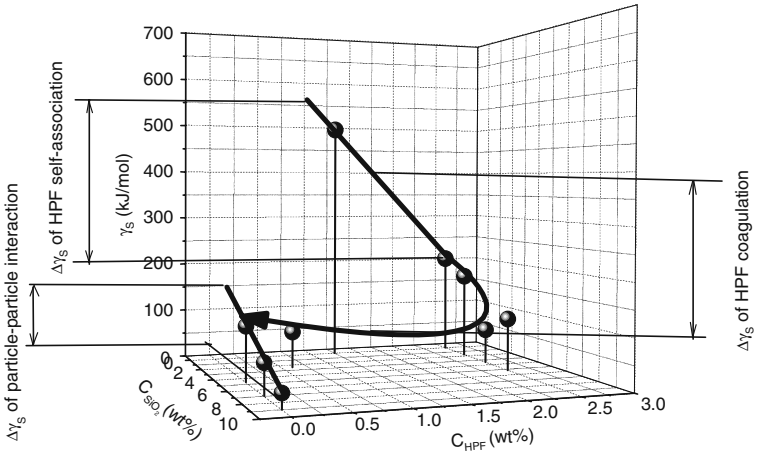

Fig. 25.9 Interfacial energy γ_S as a function of concentrations of HPF and silica

explained above for BSA and Ig as enhanced protein–protein interaction leading to the displacement of a fraction of bound water to the bulk. For HPF/A-300/water, a sharp decrease in the interfacial energy (in comparison with HPF alone) is characteristic similar to other proteins. In the HPF/A-300/water systems a decrease in concentrations of both SBW and WBW is observed (Table 25.3), and interpretation of this effect is the same as for Ig discussed above.

The surface forces (adhesive forces) at the interfaces of HPF/water can be estimated if the specific surface area of protein molecules is known. From the shape of HPF molecules [32] assuming a simplified geometry for them (two spheroids of 6.5 nm in diameter, a spheroid of 5 nm in diameter, cylindrical section of 1.5 nm in diameter and 29.5 nm in length) it is possible to calculate the surface of a molecule equal to 360 nm^2. This gives the specific surface area of protein $S = 750$ m^2/g (close to $S_{mes} + S_{mac}$ for the 2.5 wt% HPF solution, Table 25.3). ΔG as differential Gibbs free energy is numerically equal to differential energy of adhesion:

$$\Delta G = -W_a. \tag{25.1}$$

The interfacial energy γ_S is equal to the total energy of adhesion, and the adhesive forces can be estimated as [35]

$$F = \Delta G/x, \tag{25.2}$$

where x is the thickness of a bound water layer (estimated from the geometry of HPF molecule and the C_{uw} value). The range of adhesive forces increases up to 3 nm with decreasing concentration of HPF (Fig. 25.10) that is caused by a decrease in polymer–polymer interactions in the more diluted solution.

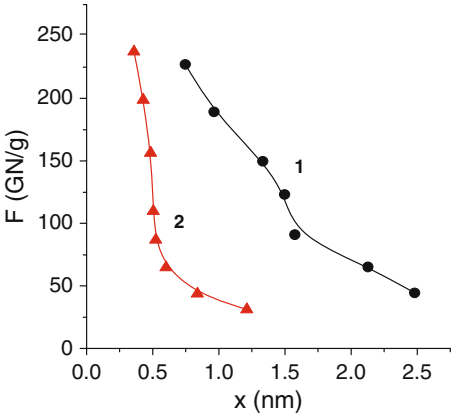

Fig. 25.10 Radial dependence of adhesive forces in the aqueous solution of HPF at $C_{HPF} = 1.25$ (curve *1*) and 2.5 wt% (*2*)

Water or other liquids can be frozen in narrower pores at lower temperatures as described by the Gibbs–Thomson relation for the freezing point depression

$$\Delta T_m = T_m(R) - T_{m,\infty} = \frac{2\sigma_{sl} T_{m,\infty}}{\Delta H_f \rho R} = -\frac{k}{R}, \tag{25.3}$$

where $T_m(R)$ is the melting temperature of a frozen liquid in pores of radius R, T_m the bulk melting temperature, ρ the density of the solid, σ_{sl} the energy of solid–liquid interaction, ΔH_f the bulk enthalpy of fusion and k a constant. This equation (or related integral equation) was used to calculate the size distribution functions of pores $f(R)$ (cavities, voids) filled by unfrozen water in frozen aqueous solutions of macromolecules, suspensions of nanosilica, etc. [9, 24, 36]. For the HPF solutions, these distributions are broad (Fig. 25.11b) as well as for the nanosilica suspension (Fig. 25.11a). For the HPF/A-300/water, a considerable rearrangement of hybrid aggregates occurs with increasing component concentration that reflects in $f(R)$ changes (Fig. 25.11c). These results reveal a significant decrease in the cavity volume filled by unfrozen water due to displacement of significant amounts of this water to the bulk because of strong macromolecular–particle interactions in hybrid aggregates becoming more compacted with increasing HPF and silica content.

HPF fulfils an important role in blood clotting. On contact with air HPF reacts with thrombin detaching a HPF fragment transforming it to active fibrin-monomer (Fm). Fibrin can easily polymerise to form supramolecular fibrin-polymer (Fb).

Transformation of HPF into fibrin-polymer through the stage of fibrin-monomer is accompanied by a significant change in the characteristics of bound water (Fig. 25.12), and a decrease in both SBW and WBW is observed. These changes reflect in the γ_S dependence on composition of the system since it decreases from 600 J/g for non-associated HPF molecules and 160 J/g for Fm to 10–20 J/g for Fb.

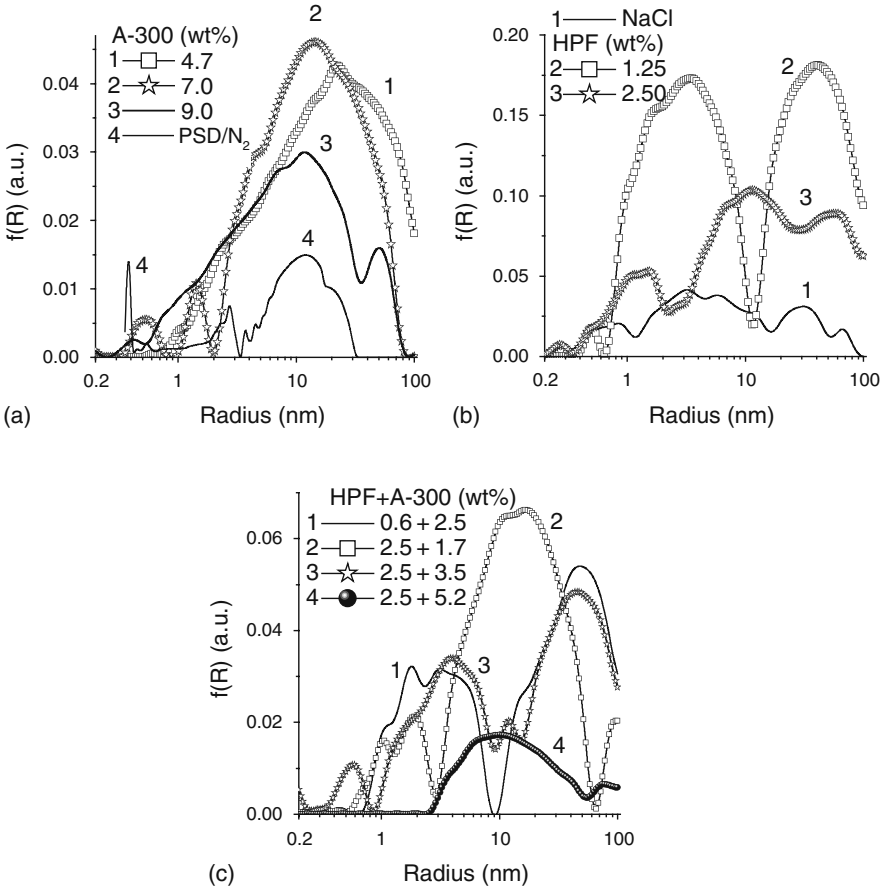

Fig. 25.11 The size distributions of voids (pores, PSD) filled by unfrozen water for (**a**) aqueous suspension of A-300 and PSD calculated from nitrogen adsorption (model of voids between spherical particles); (**b**) 0.15 mol NaCl or HPF solution at 1.25 and 2.5 wt%; and (**c**) HPF/A-300 at different concentrations of components

Notice that the changes in the γ_S value on self-association of Fb is much smaller ($\gamma_S{}^{as} \approx 50$ J/g) than that for HPF ($\gamma_S{}^{as} \approx 400$ J/g).

Thus, the significant changes in the interfacial energy on the transformation HPF $\rightarrow$ Fm $\rightarrow$ Fb reveal strong intermolecular interactions between Fb on clotting accompanied by removal of the major fraction of bound water to the bulk volume.

25.4 Biocomposites with Nanosilica, BSA and Sugars

The supramolecular systems with nanosilica, proteins and monosugars or disaccharides can possess a high bioactivity and be used in bionanocomposites perspective for biotechnology and medicine [33, 37, 38]. It was shown that composites on the

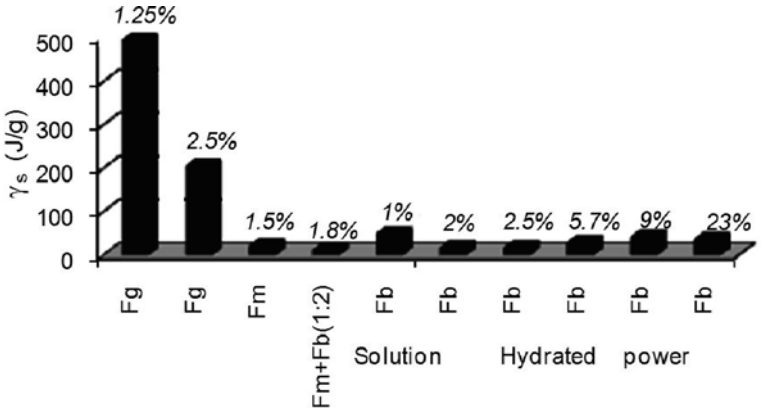

Fig. 25.12 Interfacial energy as a function of composition of the HPF/Fm/Fb system on transformation of fibrinogen into fibrin-monomer (Fm) and then fibrin-polymer (Fb)

basis of nanosilica [33], BSA, polyol (sorbitol, xylitol) or monosaccharides (fructose, glucose) in wide range of concentrations [39, 40] can stimulate activity [41] and prolong lifetime of cells after their cryopreservation.

The motion characteristics of bovine reproductive cells (BRCs) – rotation frequency, forward motion velocity and corresponding kinetic energy, E – were determined using laser Doppler spectroscopy [42]. These characteristics (Fig. 25.13) are linked to the capability of BRCs for their typical functioning.

The ratio $E/E_0 > 1$ (E_0 is for BRCs at 8×10^8 cells/ml in the 2.9 wt% TSC buffer solution) answers the stimulating effects of nanocomposite on BRCs, and $E/E_0 < 1$ corresponds to the suppressing effects. The activity was determined for ten concentrations of BRCs in the 2×10^{-6}–0.6 wt% range. Obtained results (Fig. 25.13) show that all studied composites (at certain concentrations) possess stimulating influence on BRCs.

The dependences of E/E_0 on lg C have a complex shape that indicates the multifactor nature of the effects of bionanocomposites on the BRC

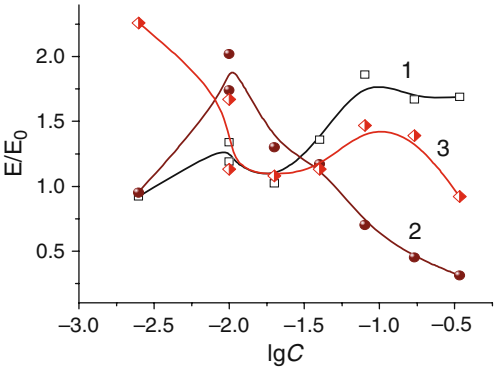

Fig. 25.13 Dependence of relative kinetic energy of BRCs after cryopreservation on concentration of nanocomposite in lactose/glycerol/vitelline medium: A-300/saccharose (curve *1*, $C_{Sac} = 0.8$ mg/g), A-300/BSA (*2*, $C_{BSA} = 570$ mg/g) and A-300/BSA/saccharose (*3*, $C_{BSA} = 515$ mg/g, $C_{Sac} = 1.06$ mg/g)

characteristics. Probably, the sign of the effects depends not only on concentration of solid nanoparticles (and their aggregation with BSA/sugars) but also on the BRC/bionanocomposite interfaces state determined by concentration and type of compounds adsorbed and desorbed there as well as by their conformation, rearrangement of supramolecular structures and desorption capability of sugars from BSA-coated nanoparticles on interaction with BRCs.

The experiments showed that bionanocomposites based on nanosilica, BSA and saccharose (at composite concentration of 0.0025 wt%) have the greatest positive effects on the BRCs. In the presence of the bionanocomposite, the BRC lifetime is longer by 2.5 h than that of the controls.

Since molecules of mono- and disaccharides poorly adsorb on the nanosilica surface one can assume that they adsorb to BSA molecules immobilised on silica. As was shown above, sugars can displace large amounts of water bound to albumins due to effective protein–sugar interactions. Especially great effects were observed on the use of saccharose. One can assume that sugars bound in protein–silica nanocomposites and desorbed on interaction with cells are responsible for significant changes in the stimulating effects on the BRCs.

Immobilisation of BSA on silica leads to an increase in the adsorption of saccharose by approximately 20% (Fig. 25.14). This difference is lower than could be expected from the data discussed above. However, it should be noted that conformational changes in adsorbed protein molecules are more difficult than in dissolved macromolecules alone. Additionally, BSA/nanosilica can form compacted hybrid aggregates with reduced accessible surface area of both protein molecules and silica surface for sugar molecules [24]. These effects can be responsible for the not-high increase in the adsorption of saccharose on BSA/silica in comparison with silica alone.

Two maxima on the $E/E_0(\lg C)$ graph (Fig. 25.13) are observed at concentrations of the solid phase of $\sim 10^{-2}$ and $\sim 10^{-1}$ wt%. Consequently, the BRC activation can occur at different concentrations of different nanocomposites that can correspond

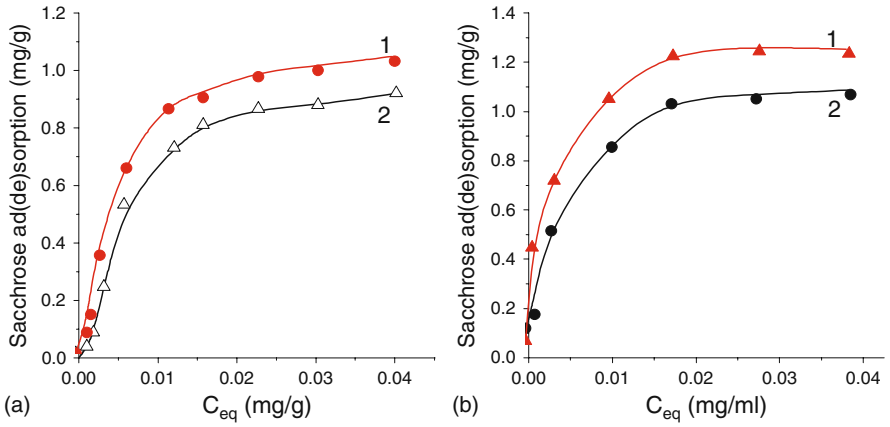

Fig. 25.14 Adsorption (*1*) and desorption (*2*) isotherms of saccharose on surface of (**a**) nanosilica and (**b**) BSA/nanosilica at $C_{BSA} = 515$ mg/g

to different mechanisms of the activation of the BRCs by desorbed sugars, BSA immobilised and dissolved and unmodified and modified silica nanoparticles, as well as by the adsorption of the products of the cell metabolism, etc.

Tendency to a decrease in the motion activity of the BRCs with increasing concentration of the dispersion phase can be caused by an increase in the viscosity of the dispersion medium and by undesirable interactions of integral proteins with silica aggregates resulting in agglutination of the cells [24, 33, 43]. Nanocomposites based on nanosilica, serum albumin and sugars demonstrated the stimulating influence on the vital activity of some other cells, e.g. red blood cells (RBCs) [44].

The effects of nanocomposites were studied at their concentration of 10^{-4}–1 wt% (aqueous suspensions of nanosilicas/BSA/sugar in 3.8 wt% trisodium citrate) and $C_{RBC} = 6 \times 10^7$ cell/ml. It was found that the shape of RBCs changes on interaction with unmodified and modified silicas from discocytes → echinocytes → spherocytes → deformed RBCs → shadow corpuscles depending on silica concentration [44]. The interaction of RBCs with bionanocomposites (in contact with nanosilica alone [44]) does not give shadow corpuscles (Fig. 25.15). The transformation of discocytes to echinocytes begins from distortion to a convexo-convex contour of normal RBCs. Rough spicules appear first on the edge of the disk and then on the whole RBC surface. The echinocyte spicules gradually become

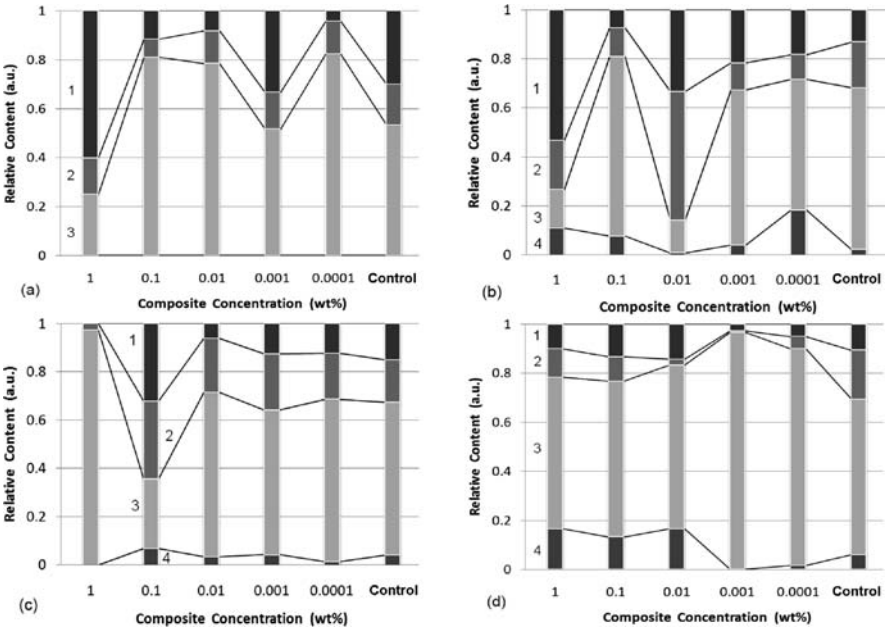

Fig. 25.15 Histograms of the RBC shape distributions: discocytes (*1*), echinocytes (*2*), spherocytes (*3*) and deformed RBCs (*4*) on addition of A-300/BSA (585 mg/g) with (**a**) fructose (2 mg/g), (**b**) glucose (2.25 mg/g) or (**c**) saccharose (1.25 mg/g) and (**d**) A-300/saccharose (0.8 mg/g) at total concentration of composites between 0.0001 and 1 wt% (control is for RBCs at 6×10^7 cells/ml in the 3.8 wt% TSC buffer solution)

thinner and more uniformly distributed on a cellular surface. Then cells become a spherical shape. On the final transformation, cells lose a part of the spicules and the transformation into the spherocyte shape becomes irreversible. A strong distortion of the membrane (e.g. on interaction with silica nanoparticles alone) leads to loss of its flexibility and resiliency. RBCs swell and increase in size in comparison with the spherocyte that leads to membrane break. Eliminated haemoglobin can be detected. However, the perforated cellular membrane remains as unique whole and forms the so-called shadow corpuscle. Notice that haemolytic activity of 1 wt% suspension of nanosilica A-300 corresponds to 100% in 20 min since only the shadow corpuscles are observed [44]. In the presence of fructose and glucose in nanocomposites, an increase in the concentration of discocytes is observed in comparison with the control (Fig. 25.15). However, interaction of RBCs with A-300/BSA/saccharose (Fig. 25.15c) or A-300/saccharose (Fig. 25.15d) leads to more negative effects since the number of normal discocytes decreases but the number of spherocytes increases. Consequently, composites with nanosilica–protein–monosugar can better stabilise the cell membrane or retard their destruction at the threshold concentrations of solid phase in comparison with nanosilica–protein–saccharose. Probably, the differences in the influence of di- and monosugars (as components of nanocomposites) on RBC depend on their chemical structure, interaction with BSA, changes in the free energy of solvation on adsorption/desorption and bonding to RBCs, as well as on their complement-fixing ability with respect to terminal carbohydrates of oligosaccharide functionalities of the receptor molecules of the supracellular matrix of RBCs. For instance, the free energy of solvation is $\Delta G_{\mathrm{sol}} = -541$ (glucose), -352 (fructose) and -344 (saccharose) J/g (calculated using IEFPCM/B3LYP/6-31G(d,p)//HF/6-31G(d,p) method). Consequently, the adsorption of saccharose on silica, albumin or albumin/silica from the aqueous solution could be better and the effects on bound water should be stronger than that for monosugars.

25.5 Conclusion

The low-temperature ^{1}H NMR spectroscopy used to determine the interfacial energy of biomacromolecules and related bionanocomposites has some advantages in comparison with other methods measuring similar characteristics. In contrast to calorimetric method determining the adhesion energy it does not require long time to reach equilibrium and it is more sensitive at low concentrations of solid phase. Additionally, it allows the determination of the radial dependences of adhesive forces in aqueous media, size distributions of cavities (pores, voids) filled by unfrozen bound water in any materials and the thickness of bound water layers up to 10 nm or larger that is impossible by using other methods. The concentration dependences of interfacial energy can be used to determine the energy of intermolecular interaction of protein molecules (energy of self-association) and the energy of swelling or destroying of protein gels, gel-like structures formed in the suspensions of nanoparticles or supramolecular systems. For aqueous solutions of biopolymers,

solid nanoparticles and low molecular organics (sugars), the dependence of interfacial energy on concentrations of dispersion components is quite informative since it is possible to trace the processes of adsorption, gel formation, coagulation, etc. The obtained results for supramolecular structures with nanosilica, proteins and mono- and disugars allow us to explain certain features of the influence of the bionanocomposites on living cells, in particular the effects of saccharose on the activity of BRCs and transformations of RBCs from normal discocytes to echinocytes, spherocytes to shadow corpuscles on interaction with bionanocomposites.

Acknowledgement This research was supported by Science & Technology Center in Ukraine (project No 3832) and National Academy of Sciences of Ukraine (Complex Program of Fundamental Investigations "Nanostructural Systems, Nanomaterials, and Nanotechnology").

References

1. Silver F, Doillon C (1989) Biocompatibility interaction of biological and implantable materials, Vol 1. VCH Publishers, New York, pp 1–24.
2. Lord GF, Williams FD (eds) (1986) Techniques of biocompatibility testing. CRC Press, Boca Raton.
3. Thomas ChC (ed) (1968) Cryosurgery. Wiley, New York.
4. Tsutsaeva AA (ed) (1983) Cryopreservation of cell suspensions. Naukova Dumka, Kiev.
5. Chuiko AA (ed) (1993) Silicas in medicine and biology. ISC, Kiev-Stavropol.
6. Porath J, Hansen P (1991) Cascade-mode multiaffinity chromatography fractionation of human serum proteins. J Chromatogr 550: 751–754.
7. Suen S, Elzel MR (1992) A mathematical analysis of affinity membrane bioseparations. Chem Eng Sci 47: 1355–1364.
8. Kabuta N, Kai E, Eguchi Y (1996) Preparation and protein adsorption properties of porous chitosan membranes modified with acetylsalycilic acid and tannic acid. Membrane 21: 386–393.
9. Gun'ko VM, Turov VV, Bogatyrev VM et al (2005) Unusual properties of water at hydrophilic/hydrophobic interfaces. Adv Colloid Interface Sci 118: 125–172.
10. Turov VV, Barvinchenko VN (1997) Structurally ordered surface layers of water at the SiO_2/ice interface and influence of adsorbed molecules of protein hydrolysate on them. Colloids Surf B 8: 125–132.
11. Verwey EJW, Owerbeek JThG (1948) Theory of the stability of liophobic colloids. Elsevier, New York.
12. Hato M, Murata M, Yoshida T (1996) Surface forces between protein adsorbed mica surfaces. Colloids Surf A 109: 345–361.
13. Derjaguin BV, Churaev NV, Muller VM (1987) Surface forces. Consultants Bureau, New York.
14. Molina-Bolivar JA, Galisteo-Gonzalez F, Hidalgo-Alvarez R (1999) The role played by hydration forces in the stability of protein-coated particles: non-classical DLVO behaviour. Colloids Surf B 14: 3–17.
15. Israelachvili H, Wennerstrom H (1996) Role of hydration and water structure in biological and colloidal interactions. Nature 379: 219–225.
16. Farrar T, Bekker E (1973) Pulse and Fourier NMR spectroscopy. Mir, Moscow.
17. Franks F (ed) (1985) Water and aqueous solutions at temperatures below 0 ^{o}C. Naukova Dumka, Kiev.

18. Turov VV, Volokhonsky IA, Pokrasen NM (1992) Unfrozen water in xerogels of polymethylsiloxane and influence of adsorbed serum albumin. Ukr Khim Zh 58: 640–644.
19. Leboda R, Turov VV, Charmas B et al (2000) Surface properties of mesoporous carbon-silica gel adsorbents. J Colloid Interface Sci 223: 112–125.
20. Krause J-P, Schwenke KD (2001) Behaviour of a protein isolate from rapeseed *(Brassica rapu*s) and its main protein components – globulin and albumin – at air-solution and solid interfaces, and in emulsions. Colloids Surf B 21: 29–36.
21. Chager SI (1975) Transport function of serum albumin. Academy of Sciences of SRR, Bucharest.
22. Mank VV, Lebovka NI (1988) Nuclear magnetic resonance spectroscopy in heterogeneous systems. Naukova Dumka, Kiev.
23. Shrade P, Klein H, Egry I et al (2001) Hydrophobic volume effects in albumin solutions. J Colloid Interface Sci 234: 445–447.
24. Gun'ko VM, Turov VV, Gorbyk PP (in press) Water at interfaces. Naukova Dumka, Kiev.
25. Turov VV, Bakay EA, Kornilov MY et al (1990) Study of interaction of sucrose with molecules of serum albumin by NMR spectroscopy method of frozen aqueous solutions. Biofizika 35: 824–829.
26. Freemel X, Brock Y (1986) Immunology fundamentals. Mir, Moscow.
27. Larsericsdotter H, Oscarsson S, Buijs J (2001) Thermodynamic analysis of proteins adsorbed on silica particles: electrostatic effects. J Colloid Interface Sci 237: 98–103.
28. Lehninger AL, Nelson DL, Cox MM (2004) Principles of biochemistry. Worth, New York.
29. Urano H, Fukuzaki S (2002) Kinetic study of desorption of two species of bovine serum albumin from alumina during alkali elution process. J Colloid Interface Sci 252: 284–289.
30. Varetska TV, Tsinkalovska SM, Demchenko OP (1972) Physicochemical properties of tryptic fragment of fibrinogen – inhibitor of fibrin polymerization. Ukr Biokhim Zh 44: 418–422.
31. Landau MA (1985) Molecular nature of certain physiological processes. Nauka, Moscow.
32. Hemmerlè J, Altmann SM, Maaloum M et al (1997) Direct observation of the anchoring process during the adsorption of fibrinogen on a solid surface by force-spectroscopy mode atomic force microscopy. Proc Natl Acad Sci USA Biophys 96: 6705–6710.
33. Chuiko AA (ed) (2003) Medical chemistry and clinical application of silicon dioxide. Nukova Dumka, Kiev.
34. Rugal AA, Gun'ko VM, Barvinchenko VN et al (2007) Interaction of fibrinogen with nanosilica. Cent Eur J Chem 5: 32–54.
35. Turov VV, Leboda R (1999) Application of ^{1}H NMR spectroscopy method for determination of characteristics of thin layers of water adsorbed on the surface of dispersed and porous adsorbents. Adv Colloid Interface Sci 79: 173–211.
36. Gun'ko VM, Turov VV, Leboda R et al (2007) Adsorption, NMR and thermally stimulated depolarization current methods for comparative analysis of heterogeneous solid and soft materials. Langmuir 23: 3184–3192.
37. Devis BG, Robinson MA (2002) Drug delivery systems based on sugar – macromolecule conjugates. Curr Opin Drug Discov Dev 5: 279–288.
38. Arce E, Nieto PM, Diaz V et al (2003) Glycodenolritic structures based on Boltorn hyperbranched polymers and their interactions with Zens culinaris Zectin. Bioconjug Chem 14: 817–823.
39. Galagan NP, Nastasienko NS, Gritsenko IV et al (2004) Investigations of nanocomposites based on highly disperse silica modified by polyols and bovine serum albumin. Nanosyst Nanomater Nanotechnol (RVV IMF, Kiev) 2: 597–608.
40. Galagan NP, Patey LM, Nastasienko NS et al (2006) Nanocomposites based on highly disperse silica and biomolecules and their thermal transformations. Nanosyst Nanomater Nanotechnol (RVV IMF, Kiev) 4: 599–612.
41. Stasy M, Barker S (1965) Carbohydrates of living tissues. Mir, Moscow.

42. Vlasenko VV, Galagan NP, Kulik TV, Pokrovskiy VO (2003) Studies on adsorption of carbohydrates on ultrafine silica surface by means of mass-spectrometry and laser Doppler spectrometry. VII Polish-Ukrainian of interfacial phenomena and their technological applications, September 15–18, Lublin, Poland, pp 312–314.
43. Gun'ko VM, Klyueva AV, Levchuk YuN, Leboda R (2003) Photon correlation spectroscopy investigations of proteins. Adv Colloid Interface Sci 105: 201–328.
44. Gun'ko VM, Galagan NP, Grytsenko IV et al (2007) Interaction of unmodified and partially silylated nanosilica with red blood cells. Cent Europ J Chem 5: 951–969

Part V
Nanotubes and Carbon Nanostructured Materials

This part is devoted to studies of new types of functional materials made on the base of silica and carbon nanotubes, diamond-like carbon films, highly dispersed graphites and diamonds, and porous diamond compacts.

Nanotubes are one of the most prospective nanomaterials for various applications due to possession of unique electrical, mechanical, thermophysical, adsorptive properties, etc., which depend on their chemical composition and structural features. Special attention in literature is paid to obtaining filled nanotubes, in particular, filled by metals. Studies of physical properties of such systems have a fundamental scientific importance. So, conductivity of electroconductive materials of few nanometers in diameter becomes close to unidimensional, thus providing a possibility for arising quantum effects, specific magnetic and emitting properties. Therefore development of design and assembly methods for nanotubes containing metal in their inner cavity is of great importance for improvement of existing and introduction of new scientific approaches for creation of the elemental base, nano- and molecular electronic devices and equipment.

The use of carbon nanotubes for the modification of polymeric matrixes not only provides increased electric, structural–mechanical, and thermophysical characteristics, but also improves their biocompatibility. Thus, such composites are prospective ones for producing chemical-resistant medical implants with improved strength and weight properties.

Composite materials based on polymers and various forms of graphite, modified by oxide clusters, are used for creation of gas-sensor elements. Their adsorption–desorption rate, selectivity to influence of various molecules, threshold of percolation, and the value of electric resistance can be controlled in a certain range via changing the type of polymer, graphite, and modifier and chemical composition of a composite. Gas-sensor elements are characterized by operation at room temperature, stability of characteristics, acceptable time of adsorption response, and a possibility of multiple use.

The features of diamond-like carbon films, highly dispersed diamonds, and porous diamond compacts were analyzed and compared with properties of certain nitride, carbide, oxide, graphite-like, and some metallic structures from the viewpoint of their usage as technical and biocompatible materials and coatings.

Combining experimental methods of scientific investigations allows high reliability forecasting of strength, tribology, adsorption characteristics, and corrosion resistance of materials upon their contact with biological environment.

Chapter 26
Design and Assembly of High-Aspect-Ratio Silica-Encapsulated Nanostructures for Nanoelectronics Applications

N.I. Kovtyukhova

Abstract This chapter summarizes our progress in design and assembly of new metal nanowire-based insulated interconnects and coaxially gated in-wire thin film transistors with the electrical characteristics closely approaching those of established large-scale planar thin film devices. Our approach relies on combining templated synthesis of nanostructures with wet successive adsorption techniques and electroplating. The strong advantages of this approach are (i) a possibility to easily incorporate various electronic materials into a single nanostructure, (ii) control of the device geometric parameters with sub-nanometer precision, and (iii) using low-energy-cost and environmentally friendly synthetic methods.

26.1 Introduction

A dramatic increase in research activity on nanoscale high-aspect-ratio inorganic structures has been motivated by their unique electronic, optical, catalytic, and mechanical properties determined by their shape, size, and, in many cases, single-crystal morphology. Among those, nanowires and nanotubes have received major attention as potential components of electronic circuits [1–5], photovoltaic cells [6–8], chemical and biological sensors [9, 10], battery anodes [11] and, very recently, nanomotors [12–14] and nanolocomotives [15, 16].

The chemical assembly of nanowires is now considered a potentially viable alternative to the conventional lithographic fabrication of nanoscale circuits, which is increasingly approaching physical and economic limits [1, 17, 18]. As high-aspect-ratio structures, nanowires and nanotubes appear to be ideal building blocks in chemically assembled electronic and optoelectronic nanotechnology. Their

N.I. Kovtyukhova (✉)
Department of Chemistry, The Pennsylvania State University, University Park, PA 16802, USA;
O.O. Chuiko Institute of Surface Chemistry of the National Academy of Sciences of Ukraine, General Naumov St. 17, Kyiv 03164, Ukraine,
e-mail: nina@chem.psu.edu

A.P. Shpak, P.P. Gorbyk (eds.), *Nanomaterials and Supramolecular Structures*,
DOI 10.1007/978-90-481-2309-4_26,

nanometer-size diameters and micron-size length allow for the fabrication of compact arrays of well-aligned parallel devices. Deposition of such an array on a lithographically pre-patterned substrate can be used to prepare planar ultradense electronic circuits composed of individually addressable device elements [19, 20]. Impressively, $\sim 10^{11}$ cross-point junctions can be fabricated on an area of 1 cm^2 [20]. Chemically grown arrays of vertically aligned parallel wires and tubes have been explored as 3D electron-harvesting and transport structures in solar cells [8], field emission displays [21], and multiple sensor arrays [9].

While most of this research has involved semiconductor nanowires and single-walled carbon nanotubes (SWNTs), functionalized metal nanowires have also been actively studied for this application [5, 20, 22–26]. Metal nanowires provide reliable control over physical dimensions, surface chemistry, and transport properties and can be easily prepared [27] and functionalized by low-temperature techniques [5, 22–26].

Our approach to electronically functional metal nanowires relies upon wet chemical assembly of established ultrathin film devices [6, 28] and their shaping into nanowire-based structures. This can be achieved by performing chemical and electrochemical synthesis inside the cylindrical pores of a template membrane. By exploiting surface chemistry of the metal wire and pore walls, the electroactive films can be deposited between two metal wire segments and/or around the wire body. The precise control over the film thickness is realized using successive adsorption techniques, such as layer-by-layer [23] or surface sol–gel deposition (SSG) [24, 25, 29, 30].

An important advantage of this strategy is a possibility to easily combine components with different electronic and chemical properties (such as metals, semiconductors, polymers, short SWNTs, and insulating oxides) in a single-wire structure. Multicomponent "all-in-wire" diodes [23, 26], transistors [25], photodetectors [31], and sensors [32] can be prepared in this way.

Additionally, the approach described here fulfills the requirements of future electronic applications particularly well because it (i) provides technologically simple preparation of a large number ($\sim 10^9$ per membrane) of relatively uniform nanowire devices with precise control over their geometric parameters and (ii) uses low-energy-cost and environmental friendly "green" synthetic methods.

Highly conductive metals offer some special advantages, particularly as low-resistance interconnects in high-speed circuits. A further reduction in RC (resistance–capacitance) and LC (inductance−capacitance) time constants for nanoscale circuits can be expected if low dielectric constant (low-*k*) materials can be introduced as insulating spacers between metallic nanowires [33]. For example, copper/low-*k* interconnect is currently a growing choice for high-performance chips [34]. Silicon dioxide is the relatively low-*k* dielectric material that is most widely used in CMOS integrated-circuit technology. Incorporation of SiO_2 into metal wire-based device structures requires new techniques for making ultrathin silica nanotubes of high quality with the thickness control at the sub-nanometer level.

This chapter summarizes our progress in design and assembly of ultrathin silica nanotubes, SiO_2-insulated metal nanowire interconnects, and coaxially gated in-wire thin film transistors with the electrical characteristics closely approaching

those of established large-scale planar thin film devices. We combine templated SSG synthesis of silica nanotubes on the pore walls of anodic aluminum oxide (AAO) membranes with electroplating of metal or composite metal–semiconductor−metal wire inside the tubes.

26.2 Template-Assisted Surface Sol–Gel Synthesis of SiO_2 Nanotubes

Replication of cylindrical pores of AAO membranes using deposition techniques, either vapor or liquid phase, developed for planar thin films has now widely been used to prepare oxide nanotubes of different compositions (see for recent review [8]). Conventional sol–gel methods, which involve immersing an AAO membrane in a precursor sol followed by gelation inside the pores, allow to adjust internal nanotube diameter by varying concentration and viscosity of the initial sol as well as the immersion times [35, 36]. However, by the beginning of this research, precise control over tube thickness and morphology, especially when the tube is only a few nanometers thick, has not been demonstrated yet.

More reliable control over the quality of planar thin films has been realized in layer-by-layer deposition methods, in which (i) preformed colloidal particles [37, 38] or (ii) molecular precursors [29, 30, 39] are successively adsorbed as a layer at a time onto the growing surface. Recently we demonstrated applicability of the first layer-by-layer technique to membrane substrates by preparing uniform and smooth free-standing semiconductor/polymer nanotubes and coated metal wires [23].

The second, SSG method, involves repeats of two-step deposition cycles, in which the adsorption of a molecular precursor and the hydrolysis (in the case of oxide film growth) steps are separated by a post-adsorption wash. The washing step desorbs weakly bound molecules that form additional layers [29]. Ideally, the SSG technique can limit each adsorption cycle to a single monolayer; however in practice, thicker layers have been found for planar oxide SSG films [29, 30]. Nevertheless, SSG allows very fine control over film thickness because a nanometer- or sub-nanometer-thick layer is grown in each two-step adsorption–hydrolysis cycle.

Here we describe growth of silica nanotubes on the pore walls of AAO membranes using the SSG technique. To understand the dynamics of tube growth, the process has been monitored by TEM and SiO_2 mass uptake measurements. The synthetic protocol is depicted schematically in Fig. 26.1, route 1 (for details see [24]). In the first step, $SiCl_4$ molecules are adsorbed on the hydrated surface of the alumina membrane. Subsequent washing with CCl_4 removes the unbound adsorbate molecules from the pores. In the second step, the adsorbed $SiCl_4$ is hydrolyzed to give SiO_2. Free-standing nanotubes were obtained by etching the alumina membranes in 50% H_2SO_4. Energy-dispersive X-ray (EDX) analysis of the product showed Si and O, with no detectable (< 0.5%) Cl or Al. Hence the conversion of $SiCl_4$ to silica is complete, and no aluminosilicate phase is present. This allows us to describe the chemical composition of the oxide as $(SiO_2)_x(SiOH)_y$.

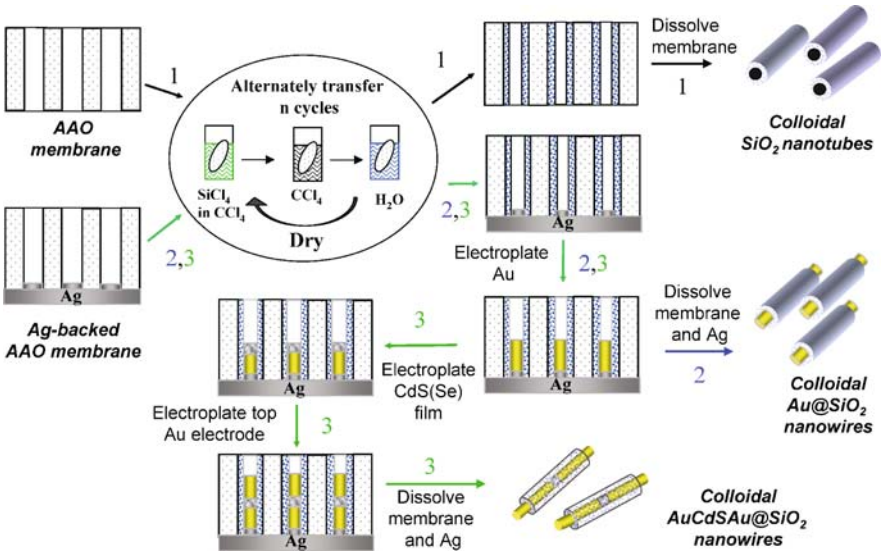

Fig. 26.1 Scheme of the template SSG synthesis of (*1*) SiO_2 nanotubes, (*2*) SiO_2-tube-encapsulated Au nanowires, and (*3*) coaxially gated in-wire thin film transistors. Commercial (Whatman Anodisc 25) and home-made AAO membranes can be used. Currently, AAO membranes with pore size in the range of 15–350 nm are available; however, scaling down to 15–50 nm pores will require longer SSG steps

TEM images (Fig. 26.2a, b) show robust SiO_2 nanotubes with smooth and uniform walls. Their shape clearly replicates the pore structure of AAO, including branches. Tubes 20–30 μm long can be found in optical micrographs (not shown) implying the growth of continuous tubules along the pore length. Figure 26.2a illustrates the remarkably high flexibility of these long silica nanotubes. A 100 nm diameter tube grown in five deposition cycles does not break even when bent at right angles. The external diameter of the tubes is determined by the pore diameter, and their internal diameter is adjustable by varying the number of deposition cycles and/or the concentration of $SiCl_4$. Nanotubes with external diameters ranging from 40 to 300 nm, and with wall thicknesses from 2 to 30 nm, were prepared.

The dependence of the nanotube wall thickness (which was estimated from TEM images of metal-filled nanotubes (Fig. 26.2c, d)) on the number of the deposition cycles is shown in Fig. 26.3a, trace 1. The graph is not linear: the amount of SiO_2 deposited per cycle increases gradually as the tubes are grown. For example, under the conditions shown in Fig. 26.3a, trace 1, the thickness change per cycle increases from 8.7 Å in the 4th–10th cycles to 15.3 Å in the 10th–20th cycles. Both values exceed the film thickness increase (~3 Å) expected if only one Si−O−H monolayer is added per cycle. The shape of this film thickness graph closely resembles that of the mass uptake of SiO_2 (Fig. 26.3a, trace 2). This correlation allows one to follow the process of nanotube growth by simply weighing the dry membrane after each SSG cycle.

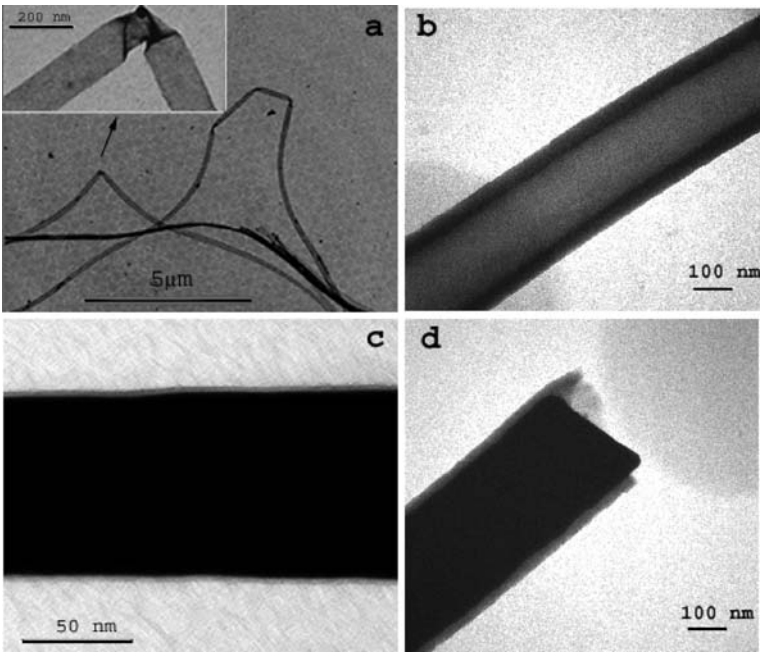

Fig. 26.2 TEM images of (**a, b**) SiO_2 nanotubes and (**c, d**) Au wires grown inside the SiO_2 nanotubes. (**a, c**) Five deposition cycles in 90 ± 20 nm diameter pores; (**b, d**) 20 deposition cycles in 280 ± 20 nm diameter pores. Reprinted with permission from [24]. Copyright 2003 Wiley-VCH Verlag GmbH & Co

The film growth at different $SiCl_4$ concentrations is shown in Fig. 26.3b. At any $SiCl_4$ concentration, a steep rise is observed in the first deposition cycle. After this, the film growth slows down significantly but the amount of SiO_2 deposited per cycle gradually increases. Ferguson and coworkers [38] attributed upward curvature in layer-by-layer growth of clay films to island nucleation and growth; however, this model is not consistent with the smooth morphology of SSG silica films seen in the TEM images.

Another possibility is that the upward curvature arises from occlusion of water in the growing film. Water is always present as a surface layer on hydrophilic surfaces under ambient conditions. The extent to which this surface-bound water will result in multilayer deposition depends on the amount of water present, the extent to which H_2O and CCl_4 molecules compete for interaction with $SiCl_4$, and the permeability of the deposited $[SiOCl_x(OH)_y]_n$ film to water, $SiCl_4$, and CCl_4. The coexistence of these three factors may cause the complex character of graphs shown in Fig. 26.3b, c. The fact that multiple layers of SiO_2 are grown in each cycle indicates that at high concentration, a multilayer of $SiCl_4$ molecules is present in the adsorption layer. In the subsequent washing step with CCl_4, all unreacted (unbound) $SiCl_4$ is removed. The following SSG step (immersion in water) completes hydrolysis of any remaining Si−Cl bonds and restores the water surface layer.

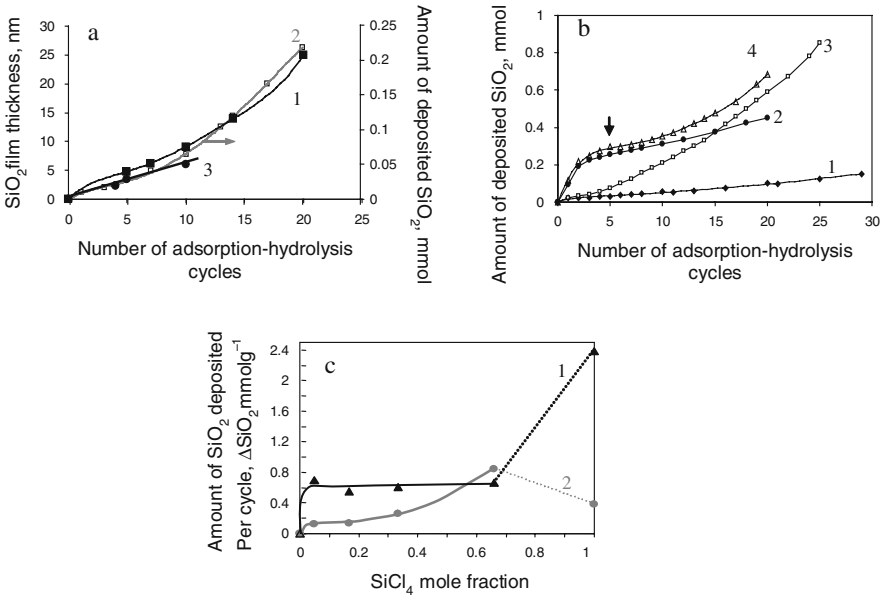

Fig. 26.3 **(a)** Plots of SiO_2 wall thickness (*1*, *3*) and amount of SiO_2deposited (*2*) from a 67 mol% solution of $SiCl_4$ versus the number of deposition cycles: pore diameter (*1*, *2*) 280 ± 20 nm and (*3*) 90 ± 20 nm. **(b)** Amount of SiO_2 deposited versus the number of deposition cycles for different concentrations of $SiCl_4$ in CCl_4: (*1*) 5 mol%; (*2*) 100 mol%; (*3*) 67 mol%; (*4*) 100% $SiCl_4$ was used in the first 5 cycles and 67% $SiCl_4$ was used in the next 15 cycles; *arrow* shows the point where the concentration was changed. Pore diameter 280 ± 20 nm. **(c)** Amount of SiO_2 deposited per cycle on (*1*) alumina and (*2*) silica-covered membrane surface versus $SiCl_4$ mole fraction. Pore diameter 280 ± 20 nm, bare membrane weight $0.033 \pm 2\%$, g. Reprinted with permission from [24]. Copyright 2003 Wiley-VCH Verlag GmbH & Co

We suggest that the amount of SiO_2 deposited in each SSG cycle is mainly determined by the amount of $SiCl_4$ adsorbed in the first step rather than by the hydrolysis step. In this case, a plot of SiO_2 amount deposited per cycle (ΔSiO_2) versus $SiCl_4$ mole fraction can be considered as a qualitative analogue of a $SiCl_4$ adsorption isotherm. Figure 26.3c, traces 1 and 2 shows two such plots taken (1) for the first deposition cycle and (2) as an average for the range of 5th−10th cycles, in which SiO_2 deposition is linear for all concentrations. The first isotherm (Fig. 26.3c, trace 1) characterizes $SiCl_4$ adsorption on the alumina surface while the second one (Fig. 26.3c, trace 2) is related to silica surface adsorption since, according to the TEM data, the pore walls are completely covered with SSG film after five cycles. The low concentration region of both plots is concave to the concentration axis, which is characteristic of strong interaction between surface and adsorbate [40], and is consistent with the chemical reaction of $SiCl_4$ with H_2O-covered alumina and silica surfaces. It is evident from the low concentration region of the plots that the $SiCl_4$ interaction with the alumina/H_2O surface is stronger.

Further flow of the adsorption isotherms for alumina and silica surfaces is different. On the silica/H_2O surface, the amount of SiO_2 deposited, as expected, increases gradually with the $SiCl_4$ mole fraction. However, on the alumina surface, the plot has a long plateau parallel to the concentration axis. We suggest that in the $SiCl_4$ mole fraction range of 0.05−0.67, fast formation of the $[SiOCl_x(OH)_y]_n$ layer at the alumina/H_2O//($SiCl_4 + CCl_4$) interface occurs, and this layer is dense enough to block further penetration of $SiCl_4$ through the film. An increase in adsorption on the alumina surface is observed when the $SiCl_4$ mole fraction equals 1. Apparently, in the absence of CCl_4 the hydrolysis reaction can continue until all water in the surface layer is consumed and replaced by the $[SiOCl_x(OH)_y]_n$ layer. Hence the amount of water available for hydrolysis of $SiCl_4$ determines its adsorption value. The fact that film growth is faster on the alumina pore walls (Fig. 26.3c, trace 1) than it is on several layers of the SSG film (Fig. 26.3c, trace 2) is consistent with the idea that the more polar alumina surface retains more water. Interestingly, in the plot of film grown on the silica/H_2O surface, a higher adsorption value is found at the $SiCl_4$ mole fraction of 0.67 than at that of 1 (Fig. 26.3c, trace 2).

Heat-treatment (100 °C, 3–13 h) of SiO_2-containing membranes dried at ambient temperature in Ar results in a weight loss of ∼ 4%, which can be ascribed to the removal of unbound water from the SiO_2 film. This indicates that the SiO_2 film is relatively porous, and pore fraction is estimated at ∼0.09 taking SiO_2 density at 2.17 g cm^{-3} [41]. This porosity is associated with relatively large pores and does not include micropores (if any) with radii approaching the thickness of an adsorbed water layer, because water in those pores can only be removed at higher temperatures. The porous structure of the SiO_2 film is consistent with the idea of occluded water assisting in multilayer film growth and is likely to be responsible for the gradual increase in the amount of SiO_2 deposited per cycle (Fig. 26.3a, b) rather than narrowing the pores during the SSG procedure. The tube growth inside the 90 nm wide pores is not found to be faster than that inside the 280 nm wide pores (Fig. 26.3a, traces 1, 3).

The same percent weight loss is observed for initial $SiCl_4$ concentrations of 5, 16, 33, and 100 mol%, while for 67 mol% $SiCl_4$ solution, the weight loss is 5.6% after 10th and 10% after 20th deposition cycle. Accordingly, estimated porosity is 0.126 for the SiO_2 film deposited in 10 cycles and it increases to 0.225 during the next 10 cycles. The porosity of the SiO_2 film measured under different growth conditions is consistent with the data shown in Fig. 26.3. In a 100% $SiCl_4$ solution the layer growth is actually slower than it is at 67 mol% $SiCl_4$ (Fig. 26.3b, traces 2, 3). The 100 mol% solution gives lower film porosity (0.09 after 5 deposition cycles), but upward curvature in film growth is found (Fig. 26.3b, trace 4) if the concentration is lowered to 67 mol%, which provides higher porosity (0.144 after 15 cycles). These facts suggest that, at relatively low CCl_4 concentration, thicker and poorer ordered $[SiOCl_x(OH)_y]_n$ layers, which may occlude both H_2O and CCl_4 molecules, are formed at the adsorption step of SSG cycles. Thus by an appropriate selection of synthesis conditions, one can control not only the thickness of nanotube walls, but also their porosity.

26.3 SiO_2-Insulated Metal Interconnects

While still in the membrane, the SiO_2-coated pores can be electrochemically filled with metal followed by membrane etching to give free-standing insulated wires (Fig. 26.1, route 2; for details on synthesis and electrical measurements see [24]).

Typical TEM images (Fig. 26.2c, d) show the gold wires inside uniformly thick and smooth silica tubes. The tube walls remain defect-free and no metal penetration of the walls is seen. The top ends of the wires are typically flat or convex, unlike nanowires grown in unmodified alumina membranes, which have cup-shaped ends. This cup-like shape has been explained as a consequence of the high surface tension of the alumina pore walls [23b]. The interaction of gold with the less polar silica pores is apparently weaker. The coulombic efficiency for plating Au and Ni wires is about 1.2 times higher (judging from wire lengths) in silica-modified pores than it is in unmodified anodic alumina.

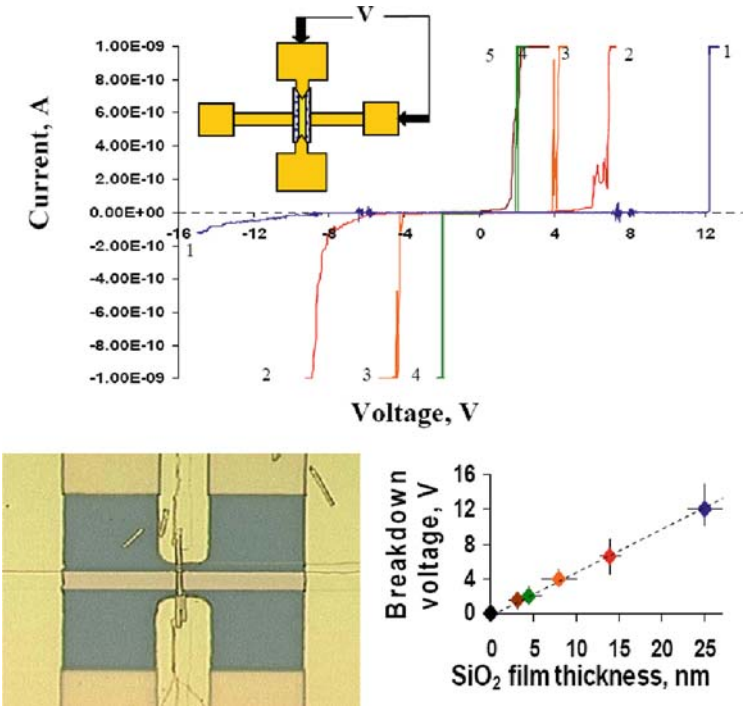

Fig. 26.4 *Top*: *I*–*V* characteristics of SiO_2-coated gold nanowires with different thickness of SiO_2 (nm): (*1*) 25, (*2*) 14, (*3*) 8, (*4*) 4.5, (*5*) 3.5. A scheme of a test structure for measuring the electrical properties is shown in the *inset*. *Bottom*: Optical micrograph of a test structure for measuring the electrical properties of SiO_2-coated gold nanowires (*left*). A plot of the breakdown voltage versus thickness (*right*). Reprinted with permission from [24]. Copyright 2003 Wiley-VCH Verlag GmbH & Co

When the silica-coated nanowires are released from the membrane, both ends are open, because the tube-shells break near the ends of the metal wire (Fig. 26.2d). This allows one to make electrical contact by evaporating metal onto the wire ends.

The $I-V$ characteristics of SSG SiO_2 films of different thicknesses (measured in Au@SiO_2/Au configuration) are shown in Fig. 26.4 (top). The curves show typical insulating behavior with breakdown voltages that increase linearly with film thickness (Fig. 26.4, bottom). The hard breakdown field is estimated at 4.8 MV cm^{-1}, which is only slightly less than the breakdown fields (10–15 MV cm^{-1}) of the SiO_2 dielectric used in CMOS integrated-circuit technology.

Because the SiO_2 tubes are porous, their dielectric constant is expected to be lower than that of dense silica ($\varepsilon = 3.8$ [10]). Porous silica is a promising dielectric material for nanoelectronics applications because of its relatively low dielectric constant [42]. Theoretical calculations predict a dielectric constant of 1.8–2.8 for a volume pore fraction of 0.4 and an almost linear decrease in ε with increasing porosity. In our experiments, it was difficult to measure the dielectric constant of the SiO_2 films precisely because of the uncertainty in the contact area in the Au@SiO_2/Au configuration. Nevertheless it is interesting to note that the synthesis offers some control over porosity, and that this will probably be reflected in the dielectric constant of the films.

26.4 Coaxially Gated In-Wire Thin Film Transistors

On the way toward realization of nano- and molecular-scale electronics, the development of strategies for promoting single devices to the level of integrated circuits is the key issue [17, 43–46]. In particular, for the realization of transistor circuits, each component transistor is required to give sufficient signal amplification and to be controlled by its own gate contact [17, 44–46]. Departing from this point, several approaches have been proposed to assembling logic circuits and nonvolatile memory from carbon nanotube [44] and semiconductor nanowire [45–47] building blocks. In the latter case, field-effect transistors (FETs) have been fabricated from cross-point nanowire junctions [45] or core-multishell nanowire structures [46], and the crossing nanowire or metal contact evaporated on the outer shell, respectively, have been used as the local gate contacts. The important advantage of the multishell-nanowire-based FETs lies in fact that they are by definition coaxially gated transistors, and in this implement a strategy of "wrap-around gate" projected for advancing conventional silicon transistors [1, 48, 49].

This chapter demonstrates the applicability of a "wrap-around gate" approach to nanoscale thin film transistors (TFTs). We describe the synthesis and characterization of coaxially gated in-wire TFTs. These devices consist of a cadmium chalcogenide thin film sandwiched between metal wire segments within a SiO_2 tube. The synthesis involves the above-described SSG deposition of SiO_2 tubes on the pore walls of an AAO membrane [24] and electroplating the composite nanowires within the tubes [31]. This approach is technologically simple and scalable with precise control over the diameter, segment lengths, and dielectric thickness. Two other

important advantages of the coaxially gated in-wire TFT structure are full encapsulation of the semiconductor segment, which prevents its oxidation, and possibility to use metal gate electrodes, which are compatible with a variety of gate dielectrics [1].

In-wire TFTs were prepared as shown in Fig. 26.1, route 3. First, the Ag-backed AAO membrane is subjected to deposition of SiO_2 nanotubes on the pore walls by repeating $SiCl_4$ adsorption–hydrolysis cycles [24]. The membrane is then used as the cathode in an electrochemical cell to electroplate 3–5 μm long Au segments inside the SiO_2 tubes. Semiconductor thin film segments are grown on the tip of the Au wire using electrochemically induced CdS film growth [50, 51] or cyclic voltametric CdSe deposition [31]. Top Au segments 3–5 μm long are electroplated onto the cadmium chalcogenide films. Finally, the Au/CdS(Se)/Au@$(SiO_2)_n$ (where n is the number of SSG cycles used for SiO_2–tube growth) nanowires are released by dissolving the Ag backing and AAO membrane. Metal/CdS/metal nanowires with different semiconductor segment lengths are prepared using 1 h and 15 min deposition times. In the latter case Ag clusters were chemically deposited prior to electrodeposition of the top metal segment in order to ensure good electrical contact. These devices are referred to as Au/CdS/Au@$(SiO_2)_{10}$ and Au/CdS/AgAu@$(SiO_2)_{14}$, respectively.

An optical micrograph and TEM images of the in-wire TFT structures are shown in Fig. 26.5a−c. The Au/CdS/Au junctions are clearly seen, and their thickness

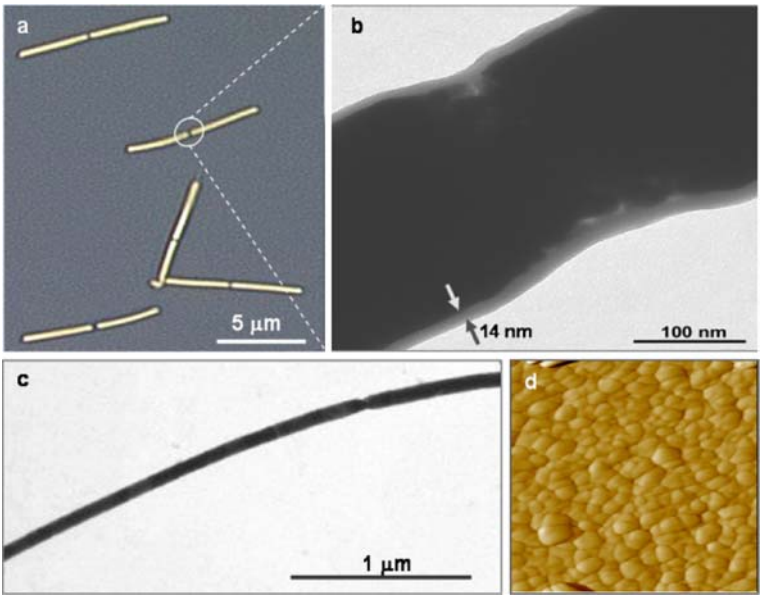

Fig. 26.5 Optical micrograph **(a)** and TEM images **(b, c)** of Au/CdS/Au@$(SiO_2)_{10}$ nanowires prepared in AAO membranes with pore size 280±20 nm (**a**, **b**) and 70±10 nm (**c**). (**d**) Tapping mode AFM image (585 × 585 nm, Z range 30.0°) of CdS film prepared on an Au-coated glass substrate using electrochemically induced deposition technique. Reprinted with permission from [25]. Copyright 2004 the American Chemical Society

can be roughly estimated at 100–200 nm for the wires prepared by using 1 h CdS deposition.

For the 15 min CdS deposition, TEM images show an approximate CdS film thickness at 30–50 nm. An AFM image of a 31 nm thick CdS film prepared the same way on a planar Au substrate shows densely packed 20–50 nm grains. An XRD pattern of the planar CdS film (not shown) shows one CdS-related peak at $2\Theta = 26.65^{o}$ ($d = 3.34$Å), the position of which corresponds to the (111) reflection of the cubic zinc blend structure ($d = 3.36$ Å) or the (002) reflection of the hexagonal wurzite structure ($d = 3.36$Å). However, the absence of other strong peaks from (100) and (101) planes of the hexagonal phase indicates that CdS crystallizes mainly in the cubic phase, in contrast to the hexagonal phase formed on ITO and SnO_2 substrates [50]. The average crystal size estimated from the X-ray line widths is 39.6 nm, which is consistent with the AFM data.

The thickness of the SiO_2 tubes that encapsulate the nanowires is uniform along the wire length and ranges from 12 to 14 nm for 10 SSG cycles (Fig. 26.5b) and from 16 to 18 nm for 14 SSG cycles. The flexibility of these shells allows them to precisely follow the shape of Au/CdS/Au junctions (Fig. 26.5b) thus enabling good adhesion of the gate dielectric to the semiconductor film.

The nanowires were aligned as shown in Fig. 26.6a for electrical measurements. $I_{DS}-V_{DS}$ characteristics of Au/CdS/Au@$(SiO_2)_{10}$ and Au/CdS/AgAu@$(SiO_2)_{14}$ devices are shown in Fig. 26.6b, c. At zero gate bias ($V_{GS} = 0$), turn-on potentials are -0.6 and -0.2 V, respectively, which is in reasonable agreement with the differences between the electron affinity of CdS ($\sim$4.5 eV) and the Au ($\sim$5.2 eV) and Ag ($\sim$4.7 eV) work functions, respectively. The Au/CdS/AgAu@$(SiO_2)_{14}$ devices show a zero gate bias DS resistivity 55 times lower than Au/CdS/Au@$(SiO_2)_{10}$, which may be attributed to better CdS/Ag electrical contact due to the formation of Ag$-$S bonds, and possibly to fewer grain boundaries in the thinner CdS film. However, the metal/semiconductor contacts of the in-wire TFTs are still much more resistive than those of planar TFTs [52, 53]. This implies a stronger effect of the contact resistance on the nanowire device properties. Therefore, all characteristics described below result from a field effect on both the CdS channel and Au(Ag)/CdS contacts.

The $I_{DS}-V_{DS}$ characteristics of both devices clearly show a field effect, which is more pronounced at negative drain voltage (Fig. 26.6b, c). At $V_{DS} = -2$ V, the Au/CdS/Au@$(SiO_2)_{10}$ devices have an ON/OFF current ratio of 10^3, a threshold voltage of 2.4 V, and a sub-threshold slope of 2.2 V per decade (Fig. 26.6d, gr. 1, 3). The Au/CdS/AgAu@$(SiO_2)_{14}$ devices show similar parameters at $V_{DS} = -0.2$ V and a gate sweep from 0 to 10 V. While the in-wire TFTs can operate at relatively low drain voltages, the above parameters are superior to those found with planar CdS [52] and nanocrystal-derived CdSe [53a]. TFTs in the gate voltage range from ± 9 to10V. The lower V_T and a threefold decrease in the sub-threshold slope (S) relative to planar nanocrystal-derived CdSe TFTs (S 7$-$10 V per decade [53a]) may result from the thinner dielectric layer and coaxial gating. A similar tendency was predicted for planar double-gated versus conventional FETs [48].

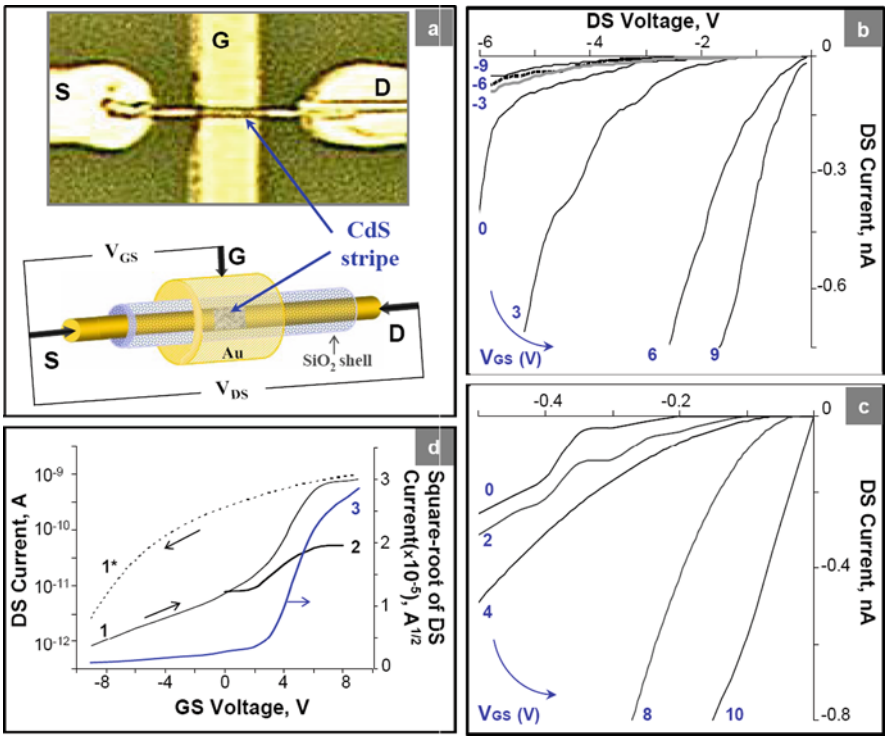

Fig. 26.6 **(a)** An optical micrograph and schematic presentation of the test structure and Au/CdS/Au@$(SiO_2)_{10}$ nanowire aligned for measuring the electrical properties. Letters *S*, *D*, and *G* indicate source, drain, and gate electrodes, respectively; (**b, c**) $I_{DS}-V_{DS}$ characteristics of in-wire TFTs for different values of gate voltage (V_{GS}): (**b**) Au/CdS/Au@$(SiO_2)_{10}$//Au (CdS deposition for 1 h); (**c**) Au/CdS/AgAu@$(SiO_2)_{14}$//Au (CdS deposition for 15 min). Gate leakage currents were in the range of 10^{-14}–10^{-12} A.; (**d**) $I_{DS}-V_{GS}$ characteristics of in-wire TFTs: Log I_{DS} (*1*, *1**) and $\sqrt{I_{DS}}$ (*3*) for Au/CdS/Au@$(SiO_2)_{10}$//Au at $V_{DS} = -2$ V for a gate sweep from −9 to 9 V (*1*) and vice versa (*1**); (*2*) Log I_{DS} for Au/CdSe/Au@$(SiO_2)_{14}$//Au at $V_{DS} = 5$ V for a gate sweep from 0 to 8 V. All measurements were performed in air at ambient temperature with a HP 4156B Precision Semiconductor Parameter Analyzer. Compliance current was set up at 1 nA. The TFTs were prepared using commercial AAO membranes with pore size 280 ± 20 nm. Reprinted with permission from [25]. Copyright 2004 the American Chemical Society

On the other hand, the channel mobility of the in-wire TFTs is approximately $5 \pm 2 \times 10^{-5}$ $cm^2\,V^{-1}s^{-1}$. This is 4–6 orders of magnitude lower than that found for TFTs with several micron long channels of planar nanocrystal-derived and vapor-deposited CdSe and CdS [13, 14]. To a certain extent, this decrease may be caused by the significant reduction of the channel length in the in-wire TFTs. The field-dependent mobility decrease is a predicted consequence of FET channel scaling [48, 54]. However, high Schottky contact resistance is most likely responsible for the low apparent mobility values. We believe that much higher mobility values can be achieved by further improving the metal/semiconductor interfaces and grain

structure of the semiconductor segment, as well as by using metal contacts with lower work function. Au/CdSe/Au@$(SiO_2)_{14}$ TFTs show poorer performance with an ON/OFF current ratio about 10 (Fig. 26.6d, gr. 2). This is consistent with observation by other groups [53] that planar CdSe TFTs fabricated without annealing exhibit very weak, if any, field effect.

Log $(I_{DS})-V_{GS}$ graphs with a gate sweep from -9 to 9 V and vice versa (Fig. 26.3d, gr. 1, 1*) show CCW hysteresis contrary to the CW one observed with planar CdSe TFTs [53]. The origin of the hysteresis is not currently understood but may be tentatively ascribed to trap states at the semiconductor/SiO_2 interface [53]. However, the chemical nature of the traps in our wet-assembled in-wire devices may differ from that in the thermally evaporated or annealed planar TFTs. Also a field effect on the Au/CdS contact properties may cause the CCW hysteresis. Oxidation of the planar TFTs [53a] is a less likely source of trap states in this case because the in-wire TFTs are encapsulated by SiO_2.

26.5 Conclusions

The surface sol–gel method is a simple way to prepare robust and flexible silica nanotubes. The thickness and porosity of the tubes can be precisely controlled by varying the composition of the precursor solution and the number of adsorption–hydrolysis cycles. The thickness of the SiO_2 layer deposited in each cycle, which always exceeds that of a monomolecular layer, can be explained assuming occlusion of water present as a surface layer. Free-standing SiO_2nanotubes with 2–30 nm walls, which are smooth and uniform along their length, were grown and characterized.

The SSG thin film deposition technique is well developed for other classes of materials, including metal oxides, chalcogenides, and phosphates. When performed in porous templates, as we have demonstrated here for SiO_2, the SSG method should offer a route to concentric multicomponent structures with well-controlled layer thickness and, presumably, tunable electrical and optical properties. The good control in film thickness that is obtained by SSG suggests that it should also be possible to precisely adjust the internal diameter of the AAO pores, and hence the diameter of nanowire replicas.

Electroplating metals inside the silica-coated pores of an AAO membrane is an easy route to nanoscale insulated metal interconnects of high quality. The hard breakdown field obtained for insulating SiO_2-nanotube coating on gold nanowires is only slightly lower than that of SiO_2 dielectric used in CMOS integrated circuits, and this is a surprising result given the fact that a wet chemical deposition method was used.

Coaxially gated in-wire thin film transistors can be made by using a combination of the templated SSG technique and electrochemical deposition of composite nanowires. The CdS-based TFTs can operate at drain voltages lower than 1 V and show better ON/OFF current ratio, threshold voltage, and sub-threshold slope than chemically similar planar TFTs. While the devices described here were not

optimized for performance, one might expect significant improvements by using strategies that have been developed or predicted for conventional FETs and TFTs [48, 52, 54]. The control of dimensions afforded by the template synthesis should make it possible to reduce the gate dielectric thickness, channel length, and diameter of the semiconductor body (see, e.g., Fig. 26.5c). The latter would extend the gate effect across the body region [48] and might also result in the formation of single-crystal semiconductor segments [51]. The SSG technique can be easily extended to other metal oxides that will allow substitution of higher *k* dielectrics, such as zirconium, titanium, and tantalum oxides for SiO_2 [29]. Finally, thermal annealing of the semiconductor segment prior to top electrode deposition is expected to improve the performance of the CdSe-based devices.

Acknowledgments I am grateful to Tom Mallouk for his deep interest and support of this work. I thank T.N. Jackson, T.S. Mayer, B. Kelley, and C.S. Kuo, who contributed to the work described in this chapter. This work was supported by the DARPA/ONR Moletronics program and by National Science Foundation grant CHE-0095394.

References

1. Vogel, E.: Technology and Metrology of New Electronic Materials and Devices. Nat. Nanotechnol. **2**, 25 (2007).
2. Chau, R., Doyle, B., Datta, S., Kavalieros, J., Zhang, K.: Integrated Nanoelectronics for the Future. Nat. Mater. **6**, 810–812 (2007).
3. Law, M., Goldberger, J., Yang, P. D.: Semiconductor Nanowires and Nanotubes. Annu. Rev. Mater. Res. **34**, 83–122 (2004).
4. (a) Dresselhaus, M. S., Dresselhaus, G., Jorio, A.: Unusual Properties and Structure of Carbon Nanotubes. Annu. Rev. Mater. Res. **34,** 247–278 (2004); (b) Chen, J., Klinke, C., Afzali, A., Avouris, P.: Self-Aligned Carbon Nanotube Transistors with Charge Transfer Doping. Appl. Phys. Lett. **86,** 123108 (2005).
5. Kovtyukhova, N. I., Mallouk, T. E.: Nanowires as Building Blocks for Self-Assembling Logic and Memory Circuits. Chem. Eur. J. **8**, 4355–4363 (2002).
6. Huynh, W., Dittmer, J., Alivisatos, A. P.: Hybrid Nanorod-Polymer Solar Cells. Science **295**, 2425 (2002).
7. Tian, B., Zheng, X., Kempa, T. J., Fang, Y., Yu, N., Yu, G., Huang, J., Lieber, C. M.: Coaxial Silicon Nanowires as Solar Cells and Nanoelectronic Power Sources. Nature **449**, 885–889 (2007).
8. Bae, C., Yoo, H., Kim, S., Lee, K., Kim, J., Sung, M. M., Shin, H.: Template-Directed Synthesis of Oxide Nanotubes: Fabrication, Characterization and Applications. Chem. Mater. **20**, 756–767 (2008).
9. Katz, E., Willner, I.: Biomolecule-Functionalized Carbon Nanotubes: Applications in Nanobioelectronics. Chem. Phys. Chem. **5**, 1084 (2004).
10. Heath, J. R.: Label-Free Nanowire and Nanotube Biomolecular Sensors for In Vitro Diagnostics of Cancer and Other Diseases. In: Mirkin, C., Niemeyer, C. M. (eds.) Nanobiotechnology II: Concepts, Applications, and Perspectives, Wiley, New York (2007).
11. Chan, C. K., Peng, H., Liu, G., McIlwrath, K., Zhang, X. F., Huggins, R. A., Cui, Y.: High-Performance Lithium Battery Anodes Using Silicon Nanowires. Nat. Nanotechnol. **3**, 31–35 (2008).
12. Paxton, W. F., Kistler, K. C., Olmeda, C. C., Sen, A., St. Angelo, S. K., Cao, Y., Mallouk, T., Lammert, P. E., Crespi, V. H.: Catalytic Nanomotors: Autonomous Movement of Striped Nanorods. J. Am. Chem. Soc. **126**, 13424 (2004)

13. (a) Fournier-Bidoz, S., Arsenault, A. C., Manners, I., Ozin, G. A.: Synthetic Self-Propelled Nanorotors. Chem. Commun. 441 (2005); (b) Ozin, G. A., Manners, I., Fournier-Bidoz, S., Arsenault, A.: Dream Nanomachines. Adv. Mater. **17**, 3011 (2005).
14. Kovtyukhova, N.: Toward Understanding of the Propulsion Mechanism of Rod-Shaped Nanoparticles That Catalyze Gas-Generating Reactions. J. Phys. Chem. C **112**, 6049 (2008).
15. Burghard, M.: A Freight Train of Nanotubes for Cargo Transport on the Nanoscale. Angew. Chem. Int. Ed. **47**, 8565–8566 (2008).
16. Sundararajan, S., Lammert, P. E., Zudans, A. W., Crespi, V. H., Sen, A.: Catalytic Motors for Transport of Colloidal Cargo. Nano Lett. **8**, 1271 (2008).
17. Tseng, G., Ellenbogen, J.: Toward Nanocomputers. Science **294,** 1293 (2001).
18. Goldstein, S. C., Budiu, M.: In: Proc. 28th Annu. Int. Symp. Computer Architecture 2001, Göteborg, Sweden, p. 178, ACM Press, New York (2001).
19. Sheriff, B. A., Wang, D., Heath, J. R., Kurtin, J. N.: Complementary Symmetry Nanowire Logic Circuits: Experimental Demonstrations and *In Silico* Optimizations. ACS Nano **2**, 1789–1798 (2008).
20. Green, J. E., Choi, J. W., Boukai, A., Bunimovich, Y., Johnston-Halperin, E., DeIonno, E., Luo, Y., Sheriff, B. A., Xu, K., Shin, Y. S., Heatrh J. R.: A 160-Kilobit Molecular Electronic Memory Patterned at 10(11) Bits Per Square Centimetre. Nature **445**, 414–417 (2007).
21. Meyyappan, M. (ed.): Carbon Nanotubes: Science and Applications, CRS Press, Boca Raton (2005).
22. (a) Martin, B. R., Dermody, D. J., Reiss, B. D., Fang, M., Lyon, L. A., Natan, M. J., Mallouk, T. E.: Orthogonal Self-Assembly on Colloidal Gold-Platinum Nanorods. Adv. Mater. **11**, 1021 (1999); (b) Mbindyo, J. K. N., Reiss, B. D., Martin, B. R., Keating, C. D., Natan, M. J., Mallouk, T. E.: DNA-Directed Assembly of Gold Nanowires on Complementary Surfaces. Adv. Mater. **13**, 249 (2001); (c) Reiss, B. D., Mbindyo, J. N. K., Martin, B. R., Nicewarner, S. R., Mallouk, T. E., Natan, M. J., Keating, C. D.: DNA-Directed Assembly of Anisotropic Nanoparticles on Lithographically Defined Surfaces and in Solution. Mater. Res. Soc. Symp. Proc. **635**, C6.2.1 (2001).
23. (a) Kovtyukhova, N. I., Mallouk, T. E.: Nanowire p-n Heterojunction Diodes Made by Templated Assembly of Multilayer Carbon-Nanotube/Polymer/Semiconductor-Particle Shells Around Metal Nanowires. Adv. Mater. **17,** 187–192 (2005); (b) Kovtyukhova, N. I., Martin, B. R., Mbindyo, J. K. N., Smith, P. A., Razavi, B., Mayer, T. S., Mallouk, T. E.: Layer by Layer Assembly of Rectifying Junctions in and on Metal Nanowires. J. Phys. Chem. B **105**, 8762–8769 (2001); (c) Kovtyukhova, N. I., Martin, B. R., Mbindyo, J. K. N., Mallouk, T. E., Cabassi, M., Mayer, T. S.: Layer by Layer Self-Assembly Strategy for Template Synthesis of Nanoscale Devices. Mater. Sci. Eng. C **19**, 255 (2002).
24. Kovtyukhova, N. I., Mallouk, T. E., Mayer, T. S.: Templated Surface Sol-Gel Synthesis of SiO_2 Nanotubes and SiO_2-Insulated Metal Nanowires. Adv. Mater. **15,** 780 (2003).
25. Kovtyukhova, N. I., Kelley, B. K., Mallouk, T. E.: Coaxially Gated In-Wire Thin Film Transistors. J. Am. Chem. Soc. **126**, 12738 (2004).
26. Park, S., Chung, S. W., Mirkin, C: Hybrid Organic–Inorganic, Rod-Shaped Nanoresistors and Diodes. J. Am. Chem. Soc. **126**, 11772–11773 (2004).
27. (a) Al-Mawlawi, D., Liu, C. Z., Moskovits, M.: Nanowires Formed in Anodic Oxide Nanotemplates. J. Mater. Res. **9**, 1014 (1994); (b) Nishizava, M., Menon, V. P., Martin, C. R.: Metal Nanotubule Membranes with Electrochemically Switchable Ion-Transport Selectivity. Science **268**, 700 (1995).
28. (a) Colvin, V., Schlamp, M., Alivisatos, A. P.: Light-Emitting Diodes Made from Cadmium Selenide Nanocrystals and a Semiconducting Polymer. Nature **370**, 354 (1994); (b) Cassagneau, T., Mallouk, T. E., Fendler, J. H.: Layer-by-Layer Assembly of Thin-Film Zener Diodes from Conducting Polymers and CdSe Nanoparticles. J. Am. Chem. Soc. **120**, 7848 (1998); (c) Gao, M., Richter, B., Kirstein, S., Mohwald, H.: Electroluminescence Studies on Self-Assembled Films of PPV and CdSe Nanoparticles. J. Phys. Chem. **102**, 4096 (1998); (d) Kaschak, D., Lean, J., Waraksa, C., Saupe, G., Usami, H., Mallouk, T.:

Photoinduced Energy and Electron Transfer Reactions in Lamellar Polyanion/Polycation Thin Films: Toward an Inorganic "Leaf". J. Am. Chem. Soc. **121,** 3435 (1999); (e) Feldheim, D., Grabar, K., Natan, M., Mallouk, T.: Electron Transfer in Self-Assembled Inorganic Polyelectrolyte/Metal Nanoparticle Heterostructures. J. Am. Chem. Soc. **118**, 7640 (1996).
29. (a) Ichinose, I., Senzu, H., Kunitake, T.: A Surface Sol-Gel Process of TiO_2 and Other Metal Oxide Films with Molecular Precision. Chem. Mater. **9**, 1296 (1997); (b) Fang, M., Kim, C. H., Martin, B. R., Mallouk, T. E.: Surface Sol–Gel Synthesis of Ultrathin Titanium and Tantalum Oxide Films. J. Nanoparticle Res. **1**, 43–49 (1999).
30. Kovtyukhova, N. I., Buzaneva, E. V., Waraksa, C. C., Martin, B., Mallouk, T. E.: Surface Sol-Gel Synthesis of Ultrathin Semiconductor Films. Chem. Mater. **12,** 383 (2000).
31. Pena, D., Mbindyo, J., Carado, A., Mallouk, T., Keating, C., Razavi, B., Mayer, T.: Template Growth of Photoconductive Metal-CdSe-Metal Nanowires. J. Phys. Chem. B **106**, 7458 (2002).
32. Cao, Y., Kovalev, A. E., Kim, J., Mayer, T. S., Mallouk, T. E.: Electrical Transport and Chemical Sensing Properties of Individual Conducting Polymer Nanowires. Nano Lett., **8**, 4653–4658 (2008).
33. Nalwa, H. S. (ed.): Handbook of Low and High Dielectric Constant Materials and Their Applications V1, Academic Press, New York (1999).
34. Riley, G.: The race to replace copper. In: Advanced Packaging, E-Newsletter, 20 February (2008). http://newsletters.pennnet.com/advancedpackaging/15734672.html.
35. (a) Mitchell, D. T., Lee, S. B., Trofin, L., Li, N., Nevanen, T. K., Soderlund, H., Martin, C. R.: Smart Nanotubes for Bioseparations and Biocatalysis. J. Am. Chem. Soc. **124**, 11864 (2002); (b) Lakshmi, B. B., Dorhout, P. K., Martin, C. R.: Sol-Gel Template Synthesis of Semiconductor Nanostructures. Chem. Mater. **9**, 857 (1997); (c) Lakshmi, B. B., Patrissi, C. J., Martin, C. R.: Sol-Gel Template Synthesis of Semiconductor Oxide Micro- and Nanostructures. Chem. Mater. **9**, 2544 (1997).
36. Zhang, M., Bando, Y., Wada, K.: Silicon Dioxide Nanotubes Prepared by Anodic Alumina as Templates. J. Mater. Res. **15**, 387 (2000).
37. (a) Iler, R. K.: Multilayers of Colloidal Particles. J. Colloid Interface Sci. **21**, 569 (1966); (b) Colvin, V. L., Golstein, A. N., Alivisatos, A. P.: Semiconductor Nanocrystals Covalently Bound to Metal Surfaces with Self-Assembled Monolayers. J. Am. Chem. Soc. **114**, 5221 (1992); (c) Fendler, J.: Self-Assembled Nanostructured Materials. Chem. Mater. **8**, 1616 (1996); (d) Mallouk, T. E., Kim, H.-N., Ollivier, P. J., Keller, S. W.: Ultrathin Films Based on Layered Materials. In: Alberti, G., Bein, T. (eds.) Comprehensive Supramolecular Chemistry V7, p. 189, Elsevier Science, Oxford (1996).
38. Kleinfeld, E. R., Ferguson, G. S.: Healing of Defects in the Stepwise Formation of Polymer/Silicate Multilayer Films. Chem. Mater. **8,** 1575 (1996).
39. Nicolau, Y. F., Menard, J. C.: Solution Growth of Zinc Sulfide, Cadmium Sulfide and Zinc Cadmium Sulfide Thin Films by the Successive Ionic-Layer Adsorption and Reaction Process; Growth Mechanism. J. Crystal Growth **92**, 128 (1988).
40. Parfitt, G. D., Rochester C. H. (eds.): Adsorption from Solution at the Solid/Liquid Interface, Academic Press, London (1983).
41. Weas, R. C. (ed.): Handbook of Chemistry and Physics, 68th Ed., CRS Press, Boca Raton (1987–1988).
42. Jin, C., Luttmer, J. D, Smith, D. M., Ramos, T. A.: Nanoporous Silica as an Ultralow-*k* Dielectrics. MRS Bull. **22**, 10, 39 (1997).
43. Zhong, Z., Wang, D., Cui, Y., Bockrath, M. W., Lieber, C. M.: Nanowire Crossbar Arrays as Address Decoders for Integrated Nanosystems. Science **302**, 1377 (2003).
44. Bachtold, A., Hadley, P., Nakanishi, T., Dekker, C.: Logic Circuits with Carbon Nanotube Transistors. Science **294**, 1317 (2001).
45. Huang, Y., Duan, X., Cui, Y., Lauhon, L., Kim, K., Lieber, C. M.: Logic Gates and Computation from Assembled Nanowire Building Blocks. Science **294**, 1313 (2001).
46. Lauhon, L., Gudiksen, M., Wang, D., Lieber, C. M.: Epitaxial Core-Shell and Core-Multishell Nanowire Heterostructures. Nature **420**, 57 (2002).

47. Duan, H., Huang, Y., Lieber, C. M.: Nonvolatile Memory and Programmable Logic from Molecule-Gated Nanowires. Nano Lett. **2**, 487 (2002).
48. Solomon, P. M.: Device Innovation and Material Challenges at the Limits of CMOS Technology. Annu. Rev. Mater. Sci. **30**, 681 (2000).
49. Leobandung, E., Gu, J., Guo, L., Chou, S.: Wire-Channel and Wrap-Around-Gate Metal–Oxide–Semiconductor Field-Effect Transistors with a Significant Reduction of Short Channel Effects. J. Vac. Sci. Technol. B **15**, 2791 (1997).
50. Yamaguchi, K., Yoshida, T., Sugiura, T., Minoura, H.: A Novel Approach for CdS Thin-Film Deposition: Electrochemically Induced Atom-by-Atom Growth of CdS Thin Films from Acidic Chemical Bath. J. Phys. Chem. B **102**, 9677 (1998).
51. Xu, D., Xu, Y., Chen, D., Guo, G., Gui, L., Tang, Y.: Preparation of CdS Single-Crystal Nanowires by Electrochemically Induced Deposition. Adv. Mater. **12**, 520 (2000).
52. Weimer, P. K.: The TFT – A New Thin-Film Transistor. Proc. IRE 1462 (1962).
53. (a) Ridley, B., Nivi, B., Jacobson, J.: All-Inorganic Field Effect Transistors Fabricated by Printing. Science **286**, 746 (1999); (b) Reita, C.: Theory for field-effect mobility enhancement in multilayer structure thin-film transistors. Inf. Display **2**, 10 (1993).
54. (a) Sze, S. M.: Physics of Semiconductor Devices, Wiley, New York (1981); (b) Ando, T., Fowler, A., Stern, F.: Electronic Properties of Two-Dimensional Systems. Rev. Mod. Phys. **54**, 437 (1982).

Chapter 27
Physicochemical Properties and Biocompatibility of Polymer/Carbon Nanotubes Composites

Yu.I. Sementsov, G. P. Prikhod'ko, A.V. Melezhik, T.A. Aleksyeyeva, and M.T. Kartel

Abstract Due to the unique structure and combination of extremely high durability, electrical and calorific conductivities, carbon nanotubes (CNTs) are prospective fillers for polymer materials. The reinforcement of polymer by developed set-like form of CNT provides an increase in mechanical, electrical, and thermophysical properties, chemical stability, and biocompatibility of nanocomposites. The manufacture of CNT and polymers (polypropylene, Teflon-4, and elastomers on the base of butadiene–nitrile and fluorinated rubbers) filled with nanotubes and nanofibers of various contents is described. The CNT and the nanocomposites are characterized in detail by structural and physicochemical methods. It is shown that not only bulk characteristics but also surface properties of filled polymers are changed and this explains better the biocompatibility of nanocomposites, which is observed in in vivo experiments.

27.1 Introduction

Development of medicine, especially for rehabilitation, is connected with searching for new materials to produce and substitute an organism's parts damaged due to illness. Presently there are vast possibilities to create artificial prosthetic appliances of practically any organ.

So the problem is to develop (to create) new materials which would have biomechanical characteristics similar to natural ones. Due to the unique structure and combination of high durability, electro- and thermoconductivity, carbon nanotubes are prospective fillings for creation of new composite materials [1]. In this work, structural features, physical and mechanical characteristics were studied of nanocomposites on the base of polytetrafluoroethylene (PTFE), isotactic polypropylene (PP), butadiene–nitrile, and fluorinated rubbers with CNT as filler. Also some biocompatibility properties were studied in experiments in vivo.

M.T. Kartel (✉)
O.O. Chuiko Institute of Surface Chemistry of the National Academy of Sciences of Ukraine, General Naumov St. 17, Kyiv 03164, Ukraine
e-mail: nikar@kartel.kiev.ua

A.P. Shpak, P.P. Gorbyk (eds.), *Nanomaterials and Supramolecular Structures*,
DOI 10.1007/978-90-481-2309-4_27,

27.2 Experimental

The method of obtaining multiwalled CNTs and their characterization are described in [2]. Typical TEM images of CNT are presented in Fig. 27.1. The average diameter of CNT was 10–20 nm, specific surface area determined by argon desorption was 200–400 m^2/g, and bulk density was within 20–40 g/dm^3. Ash residue of unpurified MWNT was 6–20% mass, while in purified ones it was less than 1% mass. According to X-ray analysis, the MWNT d_{002} parameter of graphite-like crystal lattice is within 0.3431–0.3451 nm. The small size of coherent-scattering region and strain lead to significant enlargement of the parameter as compared with that of graphite. It should be noted that TEM images, X-ray diffraction, Raman spectroscopy data, and temperature of the start of intensive oxidation in air (580–610°C) do not show the presence of noticeable amount of amorphous carbon.

According to XPS data, the content of oxygen in initial MWNT and oxidized ones (electrochemically or thermally in air) is 0.6, 1.1, 2.3 at.%, respectively. This is considerably lower than that for carbon fibers [3].

The concentration of oxygen-containing centers determined from 1s C electron bands is presented in Table 27.1 [4, 5].

Four types of nanocomposites based on polymeric matrices – polytetrafluoroethylene (PTFE), polypropylene (PP), and two types of rubbers – were studied.

The composites based on PTFE were obtained by methods of mixing PTFE powder (F4-PN20) with MWNT in the presence of liquids and following coagulation of PTFE aqueous dispersion with MWNT. The dried powdered mixtures were molded by hot-pressing.

The samples of composites with different MWNT contents (5, 10, 15, and 20%) were tested for uniaxial compression by using 2167-P50 recording device with automatic record of deformation diagrams. Thus conventional yield strength at compression ($\sigma_{0,2}$) and compression elasticity modulus (E_c) were determined. The surface of initial PTFE and PTFE–15% MWNT nanocomposite was studied using a NanoScope IIIa atomic-force microscope (Veeco corp). The data obtained were processed with the help of GWIDDION software. Samples' surfaces were also studied by AFM tip loaded with antibodies, immunoglobulin type G (IgG) obtained from the animal blood serum.

Nanocomposites on the base of polypropylene (PP) 21060 with content of MWNT within 0.05–5.0% mass were obtained by stirring a mixture of molten PP and nanotubes in an extruder at 50 rpm. Primary samples were got as granules and processed further by hot-pressing.

The samples of rubber filled with MWNT were obtained by rolling the raw rubber mass with MWNT powder. Two rubbers prepared were used:

(a) MBS 7V-14 oil- and petroleum-resistant systems based on butadiene–nitrile rubber SKN-18;
(b) IRP-1225 acid-resistant system based on fluorine-containing rubber SKF-32.

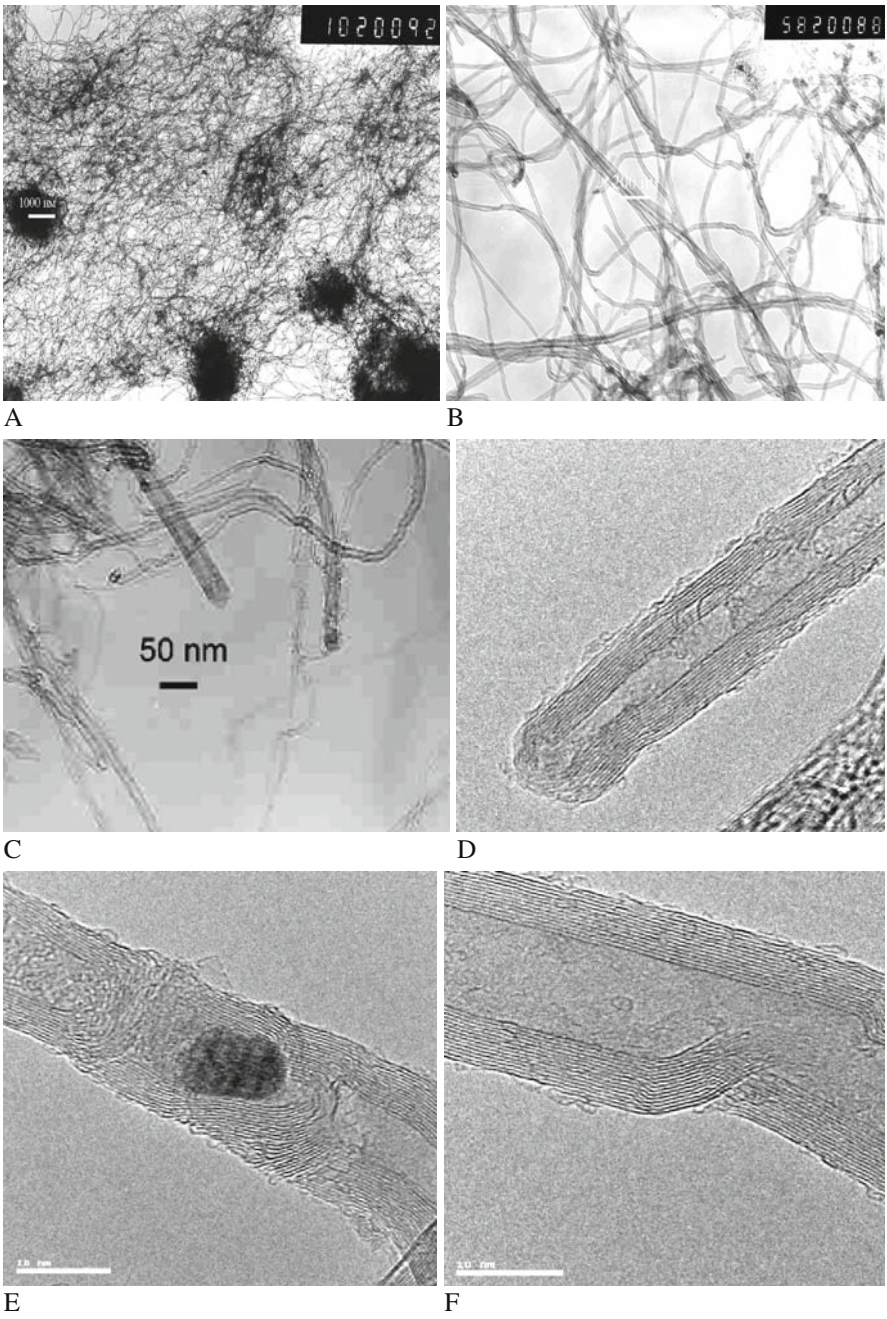

Fig. 27.1 TEM images of multiwalled CNT

Table 27. 1 Relative concentrations of oxygen-containing centers on MWNT and their classification by energy of 1s O electrons

	Relative concentration (%)			
MWNT samples	E_b = 286.1–286.3 eV Phenol, alcohol (C−OH)	E_b = 287.3–287.6 eV Carbonyl, quinone (C=O)	E_b = 288.4–288.9 eV Carboxyl, ether (C−OOH)	E_b = 290.4–290.8 eV Carbonate and/or absorbed CO, CO_2
Initial	49.1	17.2	17.2	16.5
Anode oxidation	53.8	19.8	13.6	12.8
Heat treatment	51.1	23.4	15.3	10.2

Nanocomposites of PP−MWNT with MWNT content of 0.05, 1.0, 3.0, and 5.0% mass, PTFE−MWNT with MWNT content of 15% mass, and initial polymer matrices were chosen for experiments in vivo.

27.2.1 Nanocomposite Physical and Mechanical Parameters

27.2.1.1 PTFE−MWNT

Rather large heterogeneity of MWNT distribution in the PTFE matrix is observed (Fig. 27.2a, b). Nanotubes form conglomerates that poorly interact with polymer matrix.

The influence of MWNT on properties of newly elaborated nanocomposites was determined by changes in the means of yield stress and modulus of elasticity and compared with the influence of other fillers, such as exfoliated graphite (EG) and superfine crystalline graphite.

As seen from the Table 27.2, strength characteristics of nanocomposite PTFE−MWNT are higher. Moreover, samples that were obtained by coagulation of aqueous PTFE dispersion with MWNT (the stable MWNT suspension was obtained by cavitation method) show the highest parameters.

Activation of MWNT with anode oxidation resulted in increasing conventional yield strength of nanocomposites (1500 mesh, flake size near 17 μm) and carbon soot (Table 27.2).

27.2.1.2 Polypropylene–MWNT

In the case of polypropylene, the strongest influence of MWNT on the structure of polymer matrix was observed. Structural characteristics and crystallization behavior of nanocomposites with different concentrations of CNT were studied by DTA-DTG and X-ray diffraction methods. The results are presented in Table 27.3.

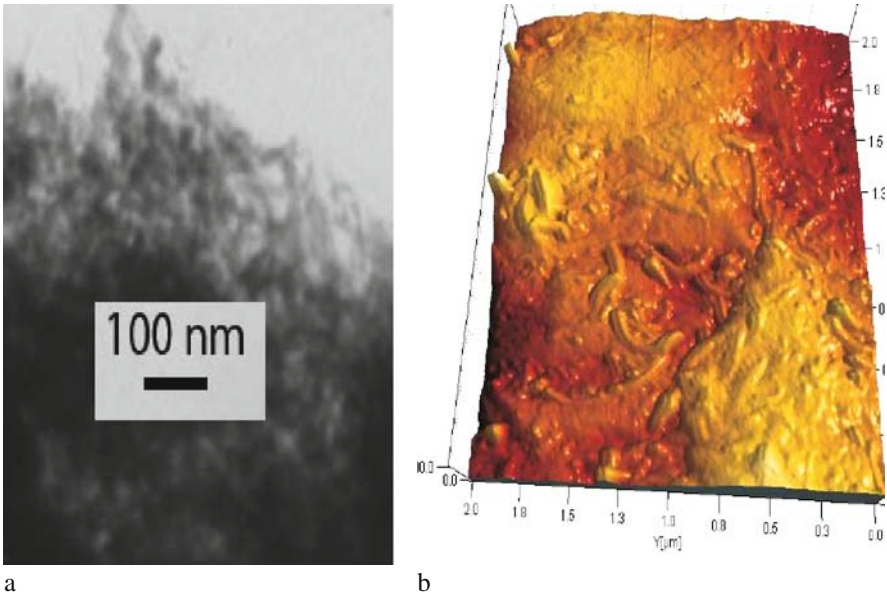

a b

Fig. 27.2 Images of nanocomposite PTFE−15% MWNT: **a** TEM of nanocomposite slice, **b** AFM image of nanocomposite surface

Table 27.2 Mechanical characteristics of PTFE and PTFE composites

Material/method	$\sigma_{0.2}$ (MPa)	E_C (MPa)
Composite/mixing powders of PTFE (F4-PN20) and MWNT	13–18	700–1500
Composite/coagulation PTFE aqueous dispersion with MWNT	16–24	800–1300
Industrial composite material F4K20	10.6	570
Composite material F4KVP−H2O	11.5	685
F4-PN20+exfoliated graphite foil/powder mixing	15.4	–
F4-PN20+graphite/powder mixing	9.8	320
F4-PN20+exfoliated graphite/powder mixing	11.8	863
F4-PN20+initial WNT, ρ=2.09 g/cm^3/powder mixing	9	616
F4-PN20+anode-oxidized MWNT, ρ=2.0 g/cm^3/powder mixing	13.4	940
F4-PN20+anode-oxidized and heat-treated MWNT, ρ=1.84 g/cm^3/powder mixing	16	560

According to the data presented, the characteristics of the melting temperature were slightly sensitive to the presence of filler and its concentration. At the same time, the beginning of crystallization temperature and other temperature characteristics were significantly influenced by CNT and changed in non-monotone mode with increasing CNT concentration in the polymer matrix. Thus, the lowest temperature

Table 27.3 Temperature characteristics of melting and crystallization processes and the level of crystallinity according to the X-ray and DTA data for the system PP−MWNT with different concentrations of filler

No	Content of MWNT (% mass)	Melting				Crystallization				Level of crystallinity (%)
		T_{start} (°C)	T_{max} (°C)	T_{end} (°C)	ΔT (°C)	T_{start} (°C)	T_{max} (°C)	T_{end} (°C)	ΔT (°C)	
1	PP	143	170	190	27	126	116	106	10	71.0
2	PP+0.05%	143	171	192	28	128	122	107	6	–
3	PP+0.1%	142	171	189	29	130	122	110	8	61.0
4	PP+0.5%	140	172	190	32	130	120	112	8	63.6
5	PP+1.0%	145	170	190	25	134	126	116	8	63.9
6	PP+3.0%	144	170	192	26	137	128	116	9	64.6
7	PP+5.0%	147	172	188	25	138	131	117	7	68.2

for melting to begin in the system PP−CNT was observed at 0.05% mass CNT. This concentration meets the maximum temperature process range, which decreases both at increasing and decreasing CNT concentration. For the crystallization process, there is monotonous, but non-linear temperature dependence of characteristic with increasing concentration of CNT in the studied range.

The data obtained agree well with the results [6] for the system PP+0.8% single-walled carbon nanotubes (SWNT) when compared with PP+1.0% MWNT: The crystallization temperature of PP+SWNT is higher as compared with pure PP, but the temperature interval (ΔT) for both melting and crystallization for nanocomposites is lower than that for initial PP. This indicates the similar influence of single- and multiwalled CNT on parameters of nanocomposites. In Fig. 27.3 XRD patterns of PP−MWNT nanocomposite samples with different concentrations of MWNT (0.5, 1.0, 3.0, and 5.0%) are presented. As follows from Fig. 27.3, there are no noticeable reflexes corresponding to a graphite-like structure.

The general view of XRD patterns agrees with DTA data on melting temperatures [6]. We can conclude that nanocomposites as well as initial PP have typical α-crystals habit; β-crystals are completely absent. Decomposition of XRD spectra into components corresponding to crystalline and amorphous phases shows the non-monotone changes of topological well-organized phase concentration with increase of nanotube content (Table 27.2, Figs. 27.3 and 27.4). This correlates with the change of melting process temperature.

If for initial PP degree of crystallinity is 71%, in case of nanocomposite containing 0.1% mass MWNT, the crystallinity falls to 61%. Further increasing of MWNT concentration up to 3.0% results in growth of crystallinity degree with satiation at 64.6%. At 5 mass% MWNT, content mean average degree of crystallinity reaches 68.2% (Fig. 27.4).

These facts can be explained, presumably, as follows. Insertion of MWNT into the polymeric matrix forms additional centers of crystallization, i.e., increases their number compared with that for initial (pure) PP.

Commonly, during polymer crystallization, irregular areas, the so-called “tails,” appear on the borders of crystalline clusters. So it means that increasing number of crystallization centers results in formation of greater number of crystalline clusters of less size and greater amount of “tails” with irregular molecular structure. Optical microscopy study [6] shows that in pure PP spherulites have larger size compared to nanocomposite PP−SWNT. These structural features are confirmed by dependence of half-width of XRD peaks in the system PP−MWNT on MWNT concentration (Fig. 27.4).

Moreover, recently it was shown by electron−positron annihilation method (EPA) [7] that in spectra of annihilation radiation angular correlation the additional narrow gauss component was observed for the system PP−CNT with CNT concentration up to 3 mass%. This indicates positrons’ capture and annihilation from positronium state in nanopores. In the interval studied, nanopore radii diminished from 0.45 to 0.35 nm with increasing CNT concentration, and at 5% content of CNT nanopores were not revealed by EPA method.

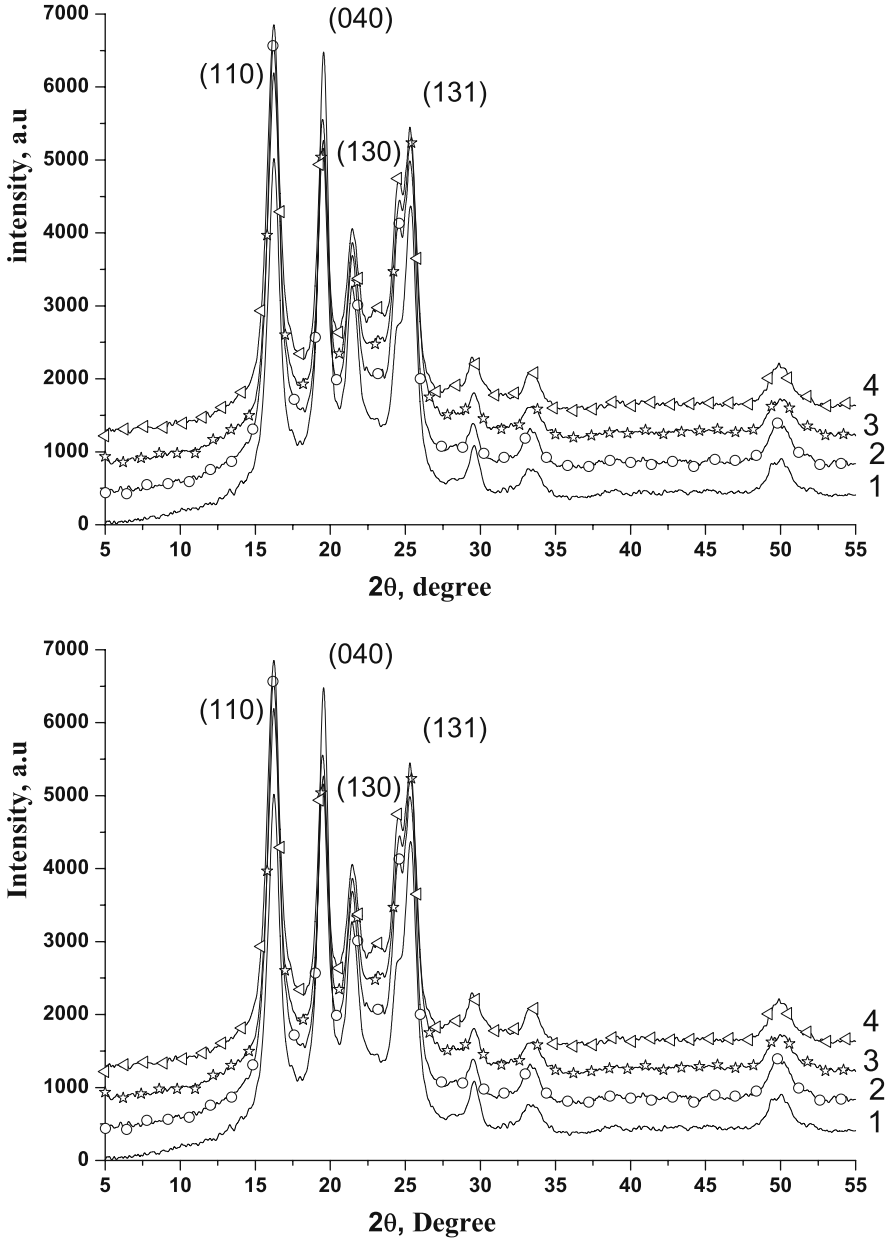

Fig. 27.3 XRD patterns of polypropylene−MWNT films with different concentrations of MWNT: *1* 0.5, *2* 1.0, *3* 3.0, *4* 5.0% mass. XRD of initial PP is inserted (λ_{Co}=0.179 nm)

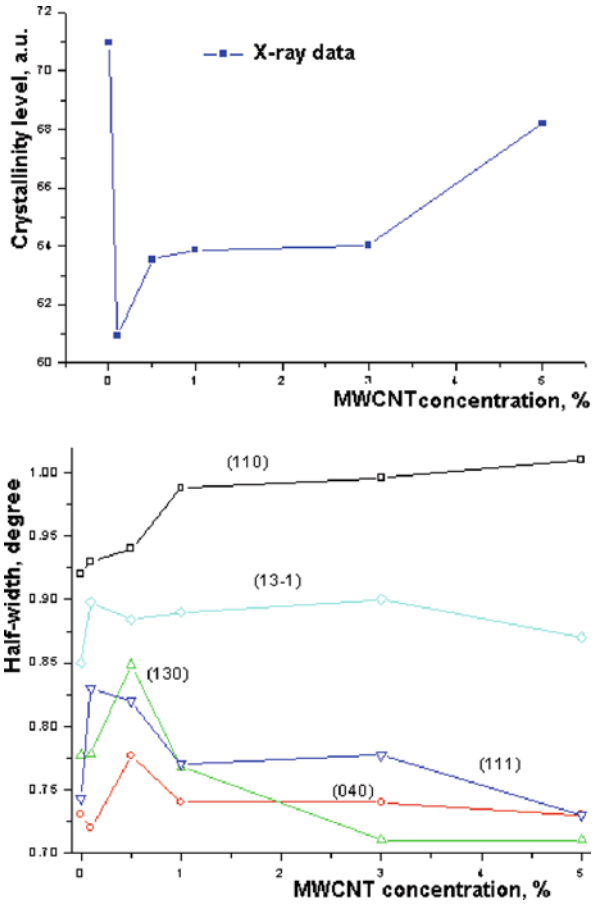

Fig. 27.4 Dependence of crystallinity level and half-width of diffraction peaks of PP−MWNT nanocomposite on MWNT concentration

Thus, the EPA study of PP−CNT system shows the presence of nanopores (of sizes mentioned above) just in area of low crystallinity. These facts, obviously, confirm the proposed explanation of dependence of PP−CNT system crystallinity on CNT concentration. Changes of CNT concentration in nanocomposites lead to changes in position, intensity peak values, half-width of diffraction reflexes which indicate the variation of grate's parameters, texture, size of coherent dispersion blocks, and microstress.

It follows from the data presented that carbon nanotubes influence the polymer supramolecular structure, particularly, its crystal orientation. On the other hand, alignment of nanotubes occurs in polymer matrix [8, 9].

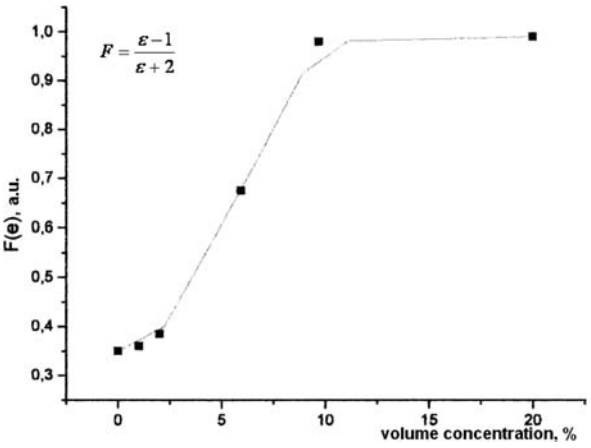

Fig. 27.5 Dependence of Clausius–Masotti function on CNT concentration in the system PP−CNT

Taking into account the non-monotonous change of structural parameters, it was interesting to find a percolation threshold for the PP−CNT system. Percolation threshold was determined by measuring the dielectric permeability (ε). A dependence of Clausius–Masotti function (F) on CNT concentration is shown in Fig. 27.5. Percolation threshold calculated from dielectric permeability dependence is observed within 2.5–5.0 mass% CNT volume concentration that approximately corresponds to 1.25–2.5 mass%. One can note that structural features determined by X-ray and DTA data were observed in the range below percolation transition, where CNT continuous cluster was not yet formed.

The temperature dependences of linear expansion coefficient for initial PP and PP+5% MWNT are presented in Fig. 27.6. One can conclude that after formation of MWNT continuous cluster, the temperature coefficient of expansion becomes negative, which is usually observed for graphite-like grates at rather low temperature.

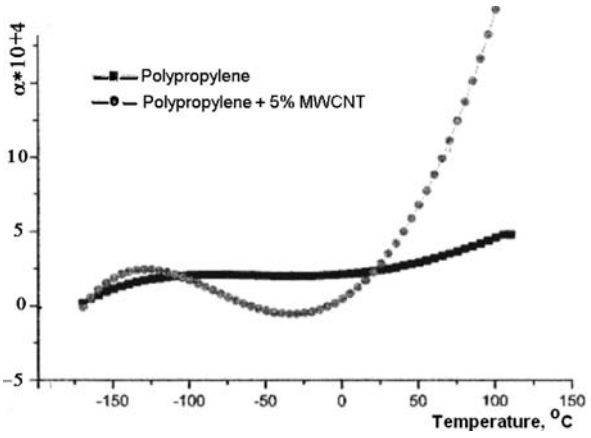

Fig. 27.6 Temperature dependence of linear expansion coefficient for PP and PP+5% CNT

27.2.1.3 Rubber−MWNT

In order to obtain nanocomposites based on the MBS 7V-14 rubber formulation containing carbon black, the latter was partially or completely replaced for CNT. The IRP-1225 rubber formulation was modified by incorporation of CNT at low concentration into the standard system.

Two series of samples of filled rubber MBS 7V-14 were tested for physical and mechanical parameters according to the standard GOST 270. The parameters measured at normal conditions (NC) and after aging for 24 h at 100°C are presented in Table 27.4, where

ε (%): ultimate tension strain;
F (kg/cm^2): ultimate tension stress limit;
Q (%): remaining deformation at strain;
A (cm): hardness by Shore.

The data for two series of samples show that incorporation of CNT influences all parameters of the nanocomposites studied: it reduces failure strain and increases durability strain and hardness. It should be noted that dependences of these parameters on CNT concentration are not linear, and it is possible to find the optimum value of CNT concentration for the industrial application.

In [10] similar CNT-containing system based on butadiene–styrene rubber with sulfur cure was studied. It was shown that introduction of 0.66 mass% MWNT followed by vulcanization at 150°C resulted in increasing elasticity modulus and tensile strength without deterioration of stretching strain. The authors explained such a result by high CNT distribution homogeneity and good interfacial adhesion between oxidized CNT and matrix.

In Table 27.5 the results of abradability tests are shown of samples based on MBS 7V-14 formulation with carbon black replaced for CNT, according to the standard GOST 426.

Table 27.4 Physical and mechanical characteristics of the elastomer MBS 7V-14 filled with CNT, according to standard GOST 270

	CNT content (% mass)		ε (%)		F (kg/cm^2)		Q (%)		Shore hardness	
Sample	In carbon component	In the sample	NC	Ageing	NC	Ageing	NC	Ageing	NC	Ageing
C[a]	0	0	234	210	107	121	0	0	70	75
01	12.5	5.1	176	146	131	141	0	0	79	83
02	25.0	10.2	158	134	151	157	4	0	81	86
03	37.5	15.2	156	134	166	175	8	0	82	88
04	50.0	20.3	126	113	173	184	7	0	85	90
05	12.5	5.1	148	150	138	159	2	0	80	84
06	25.0	10.2	130	118	175	189	2	0	83	90
07	37.5	15.2	104	83	198	187	4	0	86	91
08	50.0	20.3	84	92	222	234	4	0	89	91

Table 27.5 Dependence of MBS 7V-14 based rubber abradability on carbon filler (CNT) concentration

CNT concentration (% mass)		C[a]	0.68	1.35	2.01	2.66	3.31	6.41	9.32	12.05	14.62
Abradability	cm^3/kWh	244	137	117	81	87	116	145	217	260	251
	m^3/kJ	68	38	33	23	24	32	41	61	73	70

[a]Rubber of standard composition.

The data obtained show that incorporation of MWNT leads to reduction of abradability in CNT concentration from 0 to ~2.5%. Further increasing of CNT concentration leads to increasing abradability. The minimal value of abradability (three times lower than for initial matrix) is observed at CNT concentration of 2.0–2.5% mass. Obviously, increasing abradability at high CNT concentration is caused by development of sample porosity.

27.2.2 Chemical Resistance of Rubber

Changes of nanocomposites' samples weight after interaction with different media according to standard GOST 9.030 at different conditions are represented in Table 27.6:

Oil AMG-10, temperature 70°C, duration 24 h;
Petrol-benzyl (p-b) 75:25 mass parts, normal condition, duration 24 h;
Oil SZR-3, temperature 100°C, duration 24 h.

Dependence of nanocomposites' parameters on CNT concentration after interaction with different media was not monotonous. The optimal CNT concentration corresponding to maximum chemical resistance of these materials is within 6–12 mass%.

The system IRP-1225 based on fluorinated rubber SKF-32 of standard composition is known as acid-resistant rubber for special applications. Chemical resistance

Table 27.6 Changes of nanocomposites' sample weight after interaction with different media according to standard GOST 9.030

CNT content (wt%)	Sample's code	Δm (%) AMG-10	Δm (%) p-b	ΔV (%) SZR	Sample's code	Δm (%) AMG-10	Δm (%) p-b	ΔV (%) SZR
0	C	−0.6	20.5	23.4	C	−0.6	20.5	23.4
5.1	01	−0.48	19.4	19.3	05	−0.16	17.9	21.4
10.2	02	−0.14	17.2	20.7	06	−0.27	18.5	20.4
15.2	03	0.31	20.2	22.8	07	0.37	18.9	21.1
20.3	04	0.19	19.1	20.2	08	0.74	19.9	22.6

Table 27.7 Weight changes of composites IRP-1225-CNT after exposure to sulfuric acid

Sample	CNT content (% mass)	Initial density (g/cm^3)	Weight changes (%)
C	Initial IRP-1225	1.98±0.02	0.23±0.04
1	0.29	2.03±0.03	0.38±0.01
2	0.6	2.02±0.04	0.47±0.02
3	0.89	1.99±0.03	0.62±0.08
4	1.5	2.0±0.02	0.68±0.01

of IRP-1225 filled with CNT in different concentrations was studied for weight changes of samples after interaction with 94% sulfuric acid at different temperatures. In Table 27.7 the results are represented of tests after exposing the rubber composites to 94% sulfuric acid during 2 h at 85°C and then 60 h at room temperature.

First, we can note that incorporation of CNT in amount of up to 1.5% does not change the density of samples in limits of measuring error (Table 27.7). So it could not lead to appearance of porosity in the samples.

Dependence of increase of sample weight on CNT concentration for different times of exposure to 94% sulfuric acid at room temperature is presented in Fig. 27.7. As can be seen, maximum relative increase of weight is observed at minimum CNT concentration. In other words, incorporation of 0.3% CNT results in maximum

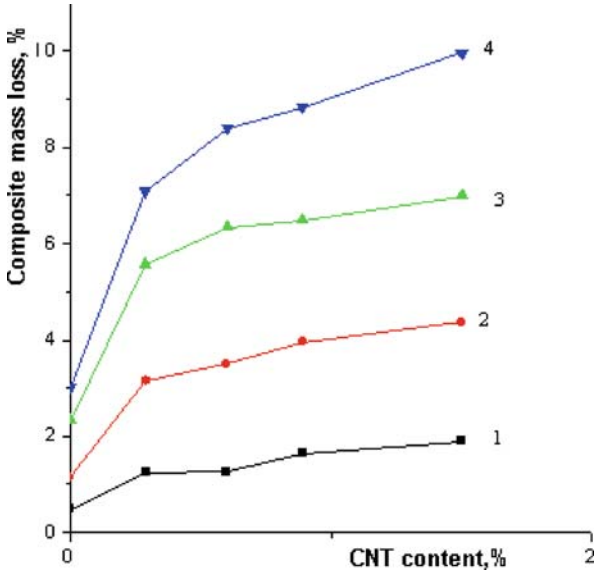

Fig. 27.7 Dependence of relative increase of system IRP-1225-CNT weight on CNT concentration for different times of exposure to 94% sulfuric acid (h): *1* 65, *2* 113, *3* 329, *4* 425

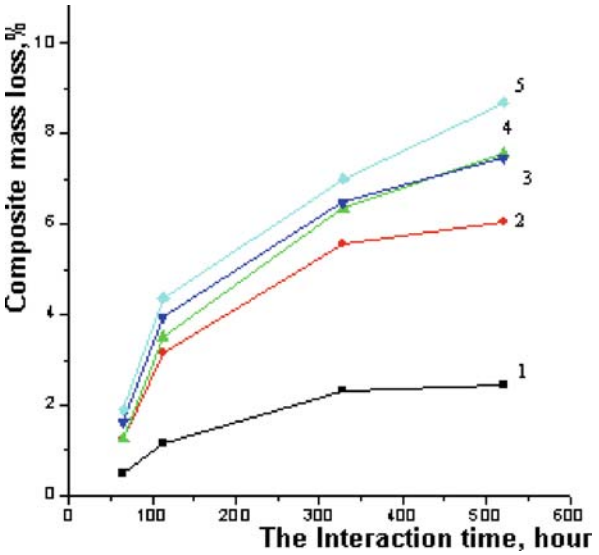

Fig. 27.8 Dependence of relative increase of system IRP-1225-CNT weight on time exposure with 94% sulfuric acid for different CNT concentration: *1* initial, *2* 0.29% mass, *3* 0.6% mass, *4* 0.89% mass, *5* 1.5% mass

relative increase of weight. Further increase of CNT concentration in the range up to 1.5% gives lesser relative increase of mass.

In Fig. 27.8 dependence is shown of increase of weight for the samples IRP-1225-CNT with different CNT concentrations on the time of exposure at room temperature. No saturation was observed for weight changes of the samples with CNT even after exposure over 500 h, in contrast to initial IRP-1225 rubber. However, the total change of weight for samples of nanocomposites after all exposure times was relatively small and did not exceed 10%.

Obviously, this industrial rubber composition is optimized so that during the structure formation all bonds are saturated. At first approximation, this is a thermodynamically stable system. The mode of CNT interaction with different matrices can be various and can influence their parameters.

The carbon black (soot) is a component of initial MBS 7V-14 composition and is used as reinforcing filler. It is known that reinforcement effect of soot or other active fillers arises due to the formation of "net" penetrating the rubber matrix in all directions because of the joining of active particles. In other words, the rubber matrix and filler form two interpenetrative continuous clusters. Oxygen-containing functional groups present at the soot surface (–OH, –OOH, >C=O, and so on) provide chemical coupling with sulfur and rubber during vulcanization. The number of unsaturated bonds in rubber decreases during formation of chemical bonds between soot and rubber. It is conventional that only bonds which are at distance no more than 0.3 nm from soot's particles surface can participate in the formation of net (average diameter of soot particles is near 3 nm). Approximately 1.5% of total amount of

unsaturated rubber's bonds is located at such distances. As a result of the interaction, the rubber molecules become less mobile.

It is clear that CNT is a more effective filler, first of all due to form factor. For CNT the ratio of maximum size (length) to minimum size (diameter) is 100–1000. The specific surface area of CNT usually is ≥ 200 m^2/g. For comparison, specific surface area of carbon black usually is ≤ 100 m^2/g. For instance, surface area of the soot P-803 (PM-15, a component of MBS 7V-14) is ~ 15 m^2/g. Surface concentration of oxygen-containing centers for CNT and carbon black (soot) also is different: for CNT $\sim$ 1 at.%, for carbon KAU $\sim$10 at.% [11].

So partial replacement of carbon black in the MBS 7V-14 system for a more effective filler − CNT strongly influences the physical and chemical parameters. First of all, mechanical characteristics are changed. Increase of CNT concentration resulted in monotonous increase of breaking strength (Table 27.4) and decrease of failure strain. More complex behavior of this system was observed on heating. CNT concentration of 10–15 mass% provided minimal changes in breaking strength at "aging" process. At the same CNT concentration minimal changes were observed in system parameters (weight, volume) after interaction with different media (Table 27.6). Dependence of abradability on CNT concentration shows an extremum at 2 mass% of CNT (Table 27.5).

Influence of CNT on the MBS 7V-14 system parameters, which obviously is caused by interaction of CNT with rubber and vulcanizer (sulfur), can be divided into two types. In the first one we see an extremum in dependence of parameters on CNT concentration at 10–15 mass% CNT as a result of competition of two or several processes. This is observed for chemical and thermal stability at partial replacement of soot for CNT. The second type exhibits a monotonous change of parameters with increasing CNT concentration in the studied range (breaking strength and failure strain at partial replacement of soot for CNT).

In the IRP-1225 system, where, as a first approximation, all bonds can be considered to be saturated, incorporated CNTs do not affect the good-tempered matrix. In this case the effect of increasing chemical stability was not observed. It should be noted than for the initial matrix a saturation was observed in tests with sulfuric acid (Fig. 27.8). On the contrary, for nanocomposites, containing different concentrations of CNT, no saturation on the weight–time plots was observed. This can be a result of weak interaction of CNT with this matrix.

However, mechanical testing of initial system and nanocomposites containing 1.5 mass% CNT before and after interaction with sulfuric acid gave unpredictable results (Fig. 27.9). CNT incorporation into IRP-1225 matrix smoothly decrease the loop's width in loading–deformation co-ordinates (Fig. 27.9a, b). Such behavior of parameters means the change in mode of deformation of the system. The system elasticity increases due to incorporation of the high elasticity modulus component such as CNT. The decrease of loop's area means that the energy losses are reduced. The energy loss coefficient can be determined as

$$k = (S_1 - S_2)\,/S_1,$$

where S_1 and S_2 are areas under loading and unloading curves, respectively.

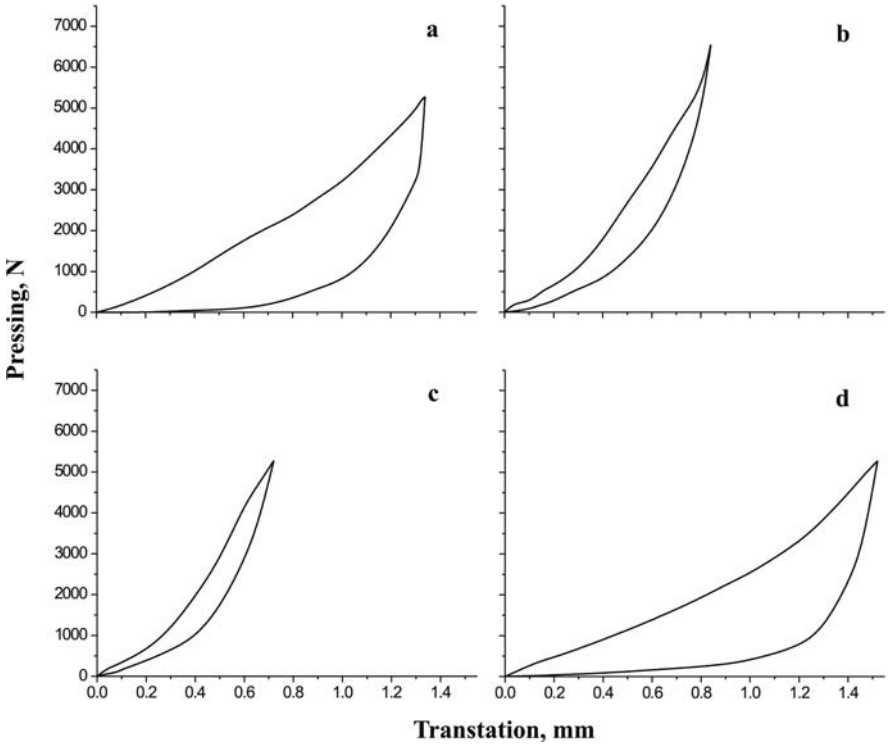

Fig. 27.9 Compression diagram of samples IRP-1225 (**a**, **b**) and IRP-1225-1.5% CNT (**c**, **d**) in co-ordinates "loading–deformation" before testing (**a**, **c**) and after exposure to 94% sulfuric acid for 600 h at room temperature (**b**, **d**). Energy loss coefficient: **a** $k = 0.70$, **b** $k = 0.36$, **c** $k = 0.33$, **d** $k = 0.74$

So CNT incorporation into IRP-1225 matrix leads to decreasing of the energy loss coefficient k from 0.70 to 0.36.

Heat treatment and interaction with active chemical compounds that effected on vulcanizates commonly lead to their gradual degradation. This should result in change of mechanical parameters, for instance, in decrease of matrices elasticity and increase in resiliency and hardness. The loop of deformation becomes narrower; coefficient of energy losses also reduces. For the system studied the coefficient k decreases from 0.70 to 0.33 (Fig. 27.9a, c). However, the system filled with CNT exhibits reverse behavior. After interaction with sulfuric acid the system becomes "softer" (Fig. 27.9b, d). The deformation loop becomes broader, and coefficient k increases from 0.36 to 0.74. This indicates increasing of energy losses due to the system structure rebuilding which is not connected with plastic deformation, because the loading curve is very smooth and gets to origin of co-ordinates.

Thus, the data obtained demonstrate that incorporation of CNT into butadiene–nitrile rubber SKN-18 and fluorinated rubber SKF-32 matrices dramatically changes the complex of physical, chemical, and mechanical properties. This was observed in

systems where carbon component was used as active reinforcing filler (MBS 7V-14), as well as in systems where filler of other nature was used (IRP-1225).

27.2.3 Nanocomposites Biocompatibility

The concept "biocompatibility" has no certain determination for all types of implantation of foreign material. It was suggested in [12, 13] to determine the compatibility of artificial materials with living body by the thickness of fibrous-connective capsule (pocket) that formed around foreign body. Thus, the rejection reaction can be determined by

Measurement of the thickness of fibrous-connective capsule (pocket) formed around implant 4 weeks after installation;

Determination of biochemical parameters of recipients' blood plasma before and at the end-point of the study; at that, not the absolute values of parameters but rather their rate before and after implantation should be taken into account.

27.2.3.1 Histological Study of Surrounding Tissue

The suggested method of evaluation of implants' biocompatibility is reasonable for in vivo experiments. In the case of correlation between histological data, biochemical parameters, and physical data this method could be the effective instrument for lifetime diagnosis of implants' biocompatibility with recipient's body.

Evaluation of initial polymer matrices biocompatibility in comparison with nanocomposites with different CNT concentration: Testing of materials was carried out by implantation of the preformed samples into the muscle "pockets" on the back of experimental animals. In order to decrease the number of animals in study and to receive the unbiased results by comparison of the body reaction to different material types the samples were implanted on one animal in different parts of the back. For example, the preformed initial PTFE and PTFE+MWNT were implanted on one animal.

The study was carried out with eight rabbits, breed "Grey Giant," male, weight 2.5–3.0 kg. Samples of materials were implanted into the muscle pockets 0.8 × 0.8 cm which were formed by incision of all skin layers on the back. The two types of samples implanted per animal were (a) initial PTFE and (b) PTFE filled with 15% mass MWNT. In the case of PP−MWNT the samples with different contents of MWNT (0.05, 0.1, 3, and 5% mass) were implanted along both sides of spinal (vertebral) column. Four weeks after operation, the samples with surrounding tissue were excised for further histological study and for investigation of the samples' surface. The level of experimental animal body reaction was determined by measuring the thickness of fibrous-connective capsule which formed around the sample. As we compared samples that were implanted on one animal there was no reason to conduct biochemical study.

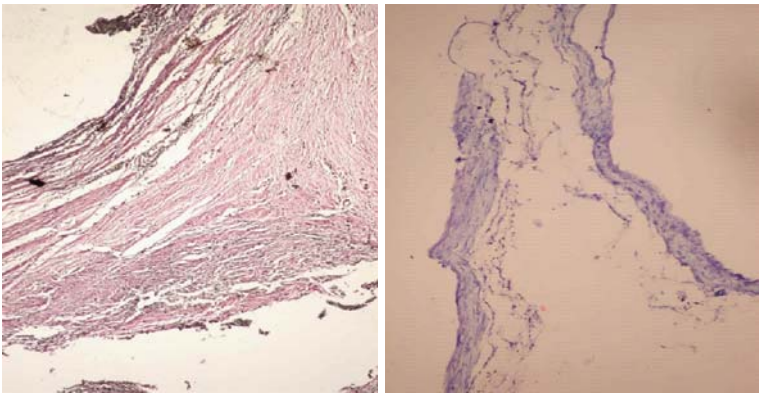

PTFE PTFE+MWNT

Fig. 27.10 Thickness of fibrous-connective tissue around PTFE and PTFE+15% mass MWNT

According to the histological data the insertion of 15 mass% MWNT into PTFE matrix essentially influences the fibrous-connective formation around the sample.

Histological slides (Fig. 27.10) have shown that the capsule thickness around initial PTFE was appreciably larger.

Morphometry data are presented in Figs. 27.11 and 27.12, which demonstrate the influence of MWNT on biocompatibility of the PTFE+MWNT and PP−MWNT nanocomposites.

On the basis of histological study of PP−MWNT implantation we can conclude that nanocomposite biocompatibility is connected with the presence of MWNT in initial matrix. Introduction of even 1 mass% MWNT into PP resulted in lower thickness of fibrous-connected capsule. Further morphometric data analysis shows that biocompatibility is a non-linear function of MWNT concentration in polymer matrix. It has the same mode as the crystallinity level for the nanocomposites.

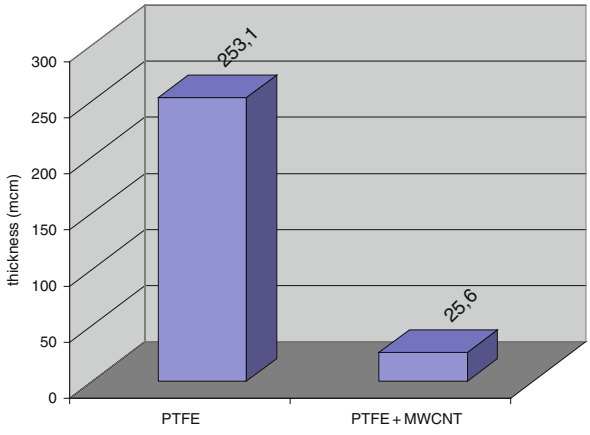

Fig. 27.11 Thickness of fibrous-connective tissue around PTFE+MWNT composite samples

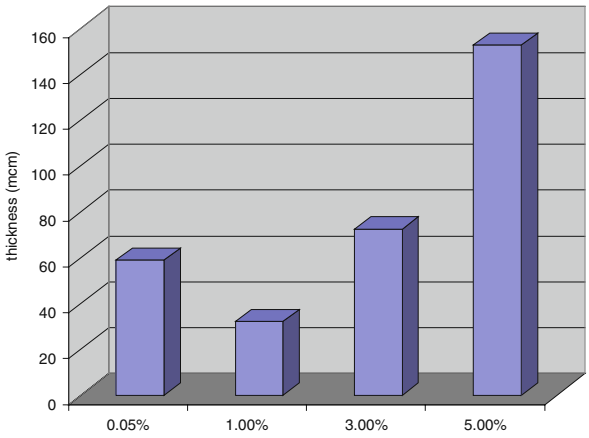

Fig. 27.12 Thickness of fibrous-connective tissue around PP+MWNT composite samples

27.2.3.2 Experiment on Knee-Joint's Replacement

Tree rabbits, breed "Grey Giant," male, weight 2.5 kg, were operated for knee-joint segment excision under total anesthesia with "ketanol" (2 ml/kg) and replacement for artificial prosthesis made of PTFE and PTFE+MWNT (on the right and left legs, respectively). Joints were fixed by equal methods. Fourteen days after operation, all animals at the site of PTFE prosthesis had strong edema, inflammation, and limitation of extremity mobility. In the case of nanocomposite prosthesis the joint's mobility was satisfactory, and practically edema or inflammation was not observed. The X-ray study on the 28th day after operation confirmed these results: pure PTFE induced edema and inflammation of surrounding tissue that lead to knee-joint immobilization in comparison with PTFE+MWNT ones that did not cause tissue reaction – the joints were mobile according to surgical operation.

27.2.4 AFM Samples' Study

It is known that implants' surface is of critical significance for realizing the living body's rejection reaction. In particular, the surface triggers the mechanism of foreign body recognition by immunoglobulin type G adhesion [13]. So it is useful to find a correlation between the results of histological studies and AFM data by measuring the interaction forces between samples' surface and AFM tip modified with immunoglobulin G of certain animal.

The scheme of measuring is represented in Fig. 27.13. The force curves (dependence of interaction force on tip-surface distance) were registered at room temperature. The speed of scanning was equal to 0.3 Hz (0.45 μm/s). In all studies standard silicon nitride AFM tip was used (DNP-20, Veeco corp.) with nominal cantilever flexibility of 0.06 N/m.

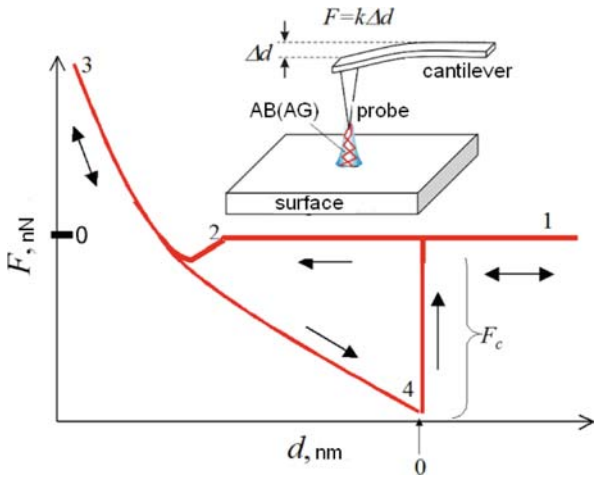

Fig. 27.13 Scheme of pull-off forces evaluation F_c by ACS method. Bioadhesion force (retention) was determined by evaluation of tip cantilever compliance Δd as $F=k\Delta d$, where k is cantilever elastic constant

Experimental animals' blood was collected twice during the study: just before manipulation and at the end-point.

Immunoglobulin G was obtained from blood serum by sedimentation with ammonium sulfate by routine method. The residue obtained was dissolved in 0.9% sodium chloride and purified from sulfate by dialysis. Purified immunoglobulin G was deposited on AFM tip from solution. The measurements were carried out in contact mode. Results are given in Table 27.8.

The force of interaction of modified AFM tip with initial matrix surface was higher than with nanocomposite. It means that the initial PTFE matrix is recognized

Table 27.8 Data of surfaces testing with AFM tip modified by IgG

	Air		Water	
Sample	Jump to	Pull off	Jump to	Pull off
	"Clear" Si3N4 tip/force interaction (nN)			
PTFE	0.79±0.26	10.64±0.33	0.28±0.06	3.72±0.22
PTFE−MWNT	0.13±0.01	8.32±0.38	0.08±0.01	0.92±0.06
PTFE initial	0.22±0.02	10.32±0.28	Is not detected	2.43±0.07
	Si3N4 +IgG tip/force interaction (nN)			
PTFE	2.37±0.22	26.28±0.28	Is not detected	1.82±0.06
PTFE−MWNT	1.29±0.03	9.63±0.21	Is not detected	0.48±0.06
PTFE initial	3.86±0.11	23.83±0.70	Is not detected	4.72±0.15
PTFE−MWNT initial	1.93±0.14	13.10±0.22	Is not detected	Is not detected

by living organism as foreign material which triggers bodies' protective reaction. The interaction of PTFE−MWNT system and modified AFM tip is lower and it means that body's protective reaction would be lower. The data obtained agree with histological results which unambiguously show that PTFE−MWNT composites cause the least fibrous-connective capsule formation around them. In other words, presence of MWNT in matrix improves biocompatibility.

27.3 Conclusions

Carbon nanotubes (CNT) are prospective fillers for polymer materials due to their unique structure and outstanding combination of strength, electrical and thermal properties of CNT.

Reinforcement of polymers including elastomers with infinite CNT net results in change of both three-dimensional material parameters and surface properties. In the systems polytetrafluoroethylene−MWNT, polypropylene−MWNT, and rubber elastomers−MWNT, increase of mechanical parameters was observed such as yield strength, elasticity modulus, breaking strength, wearing resistance, as well as chemical stability and electrical conductivity. Filling of polymers with CNT changes their surface properties and improves biocompatibility. This was demonstrated by experiments in vivo with polytetrafluoroethylene−MWNT and polypropylene−MWNT systems. Filling of polymers with CNT leads to decreasing of interaction forces between AFM tip modified with antibody and nanocomposite surface. This effect can be used as a method for measuring artificial implants' biocompatibility.

At low MWNT concentration (below percolation threshold) the structure peculiarities were observed due to the presence of disordered phase. This phase probably appears around nanopores, and its existence correlates with other characteristics of the system.

Polymer−CNT composites are prospective materials for manufacturing endoprosthesis for medicine.

References

1. Lacerda L, Bianco A, Prato M, Kostarelos K (2006) Carbon nanotubes as nanomedicines: from toxicology to pharmacology. Adv Drug Del Rev 58:1460–1470
2. Sementsov YuI, Melezhek OV, Prikhod'ko GP et al (2007) Synthesis, structure, physicochemical properties of nanocarbon materials. In: Shpak AP, Gorbyk PP (eds) Physical chemistry on nanomaterials and supramolecular structures, vol. 2. Naukova dumka, Kyiv
3. Yue ZR, Jiang W, Wang L et al (1999) Surface characterization of electrochemically oxidized carbon fibers. Carbon 37:1785–1796
4. Boehm HP (2002) Surface oxides on carbon and their analysis: a critical assessment. Carbon 40:145–149
5. Boehm HP (1994) Some aspects of the surface chemistry of carbon blacks and other carbons. Carbon 32:759–769

6. Bhattacharyya AR, Sreekumar TV, Liu T et al (2003) Crystallization and orientation studies in polypropylene single wall carbon nanotube composite. Polymer 44:2373–2377
7. Nischenko MM, Tsapko EA, Prikhod'ko GP, Sementsov YuI (2007) Positron spectroscopy of polypropylene composites with carbon nanotubes. In: Schur DV, Zaginaichenko SYu, Veziroglu TN, Skorokhod VV (eds) Hydrogen materials science and chemistry of carbon nanomaterials. AHEU, Kiev
8. Latypov ZZ, Pozdnyakov OF (2006) Investigation of conditions of synthesis of polymer films containing ordered structures of carbon nanotubes and higher fullerenes. Tech Phys Lett (Russia) 32:28–33
9. Barber AH, Zhao Q, Wagner HD, Baillic CA (2004) Characterization of E–glass–polypropylene interfaces using carbon nanotubes as strain sensors. Comp Sci Technol 64:1915–1919
10. Zhou X-W, Zhu Y-F, Liang Li (2007) Preparation and properties of powder styrenebutadiene rubber composites filled with carbon black and carbon nanotubes. Mater Res Bull 42:456–464
11. Sementsov YuI, Senkevitch AI, Prikhod'ko GP et al (2007) Exfoliated graphite. Structural performance and surface condition. Chem Ind Ukraine 2:19–24
12. Tirrell M, Kokkoli E, Biesalski M (2002) The role of surface science in bioengineered materials. Surf Sci 500:61–83
13. Castner DG, Ratner BD (2002) Biomedical surface science: foundations to frontiers. Surf Sci 500:28–60

Chapter 28
Gas-Sensing Composite Materials Based on Graphite and Polymers

L.S. Semko, Ya.I. Kruchek, and P.P. Gorbyk

Abstract A series of composite materials (CMs) based on polymers (polyethylene, polytetrafluorethylene, polyvinylchloride) and non-modified thermally expanded graphite (EG) and SiO_2-modified EG have been prepared. Graphite contents in the CM vary from 0 to 100 wt% and modifier contents from 0 to 50%. The structural, electrical, and gas-sensing properties of CM have been studied. An influence of polymer nature, EG modifications by SiO_2 on percolation processes, percolation threshold values (Θ_C), and resistivity of obtained systems have been investigated. An influence of gaseous species (acetone, toluene, ethanol, ammonium, diethyl ester, propane, ozone) on the electric resistance of such CM has been analyzed. It is shown that by varying the type of polymer, the composition of the composites, and modification of the EG surface by SiO_2, studying the effect of these on the shape of adsorption curves, velocity of adsorption–desorption process, selectivity of the CM to an influence of various substances, and other properties is possible. Uses of obtained materials as sensitive elements of sensors for determination of some gaseous compounds have been proposed.

28.1 Introduction

Creation of new prospective materials sensitive to the influence of gaseous compounds and efficient sensors is needed for control of hazardous gases at factories, enterprises, and homes. At present, semiconductive metal oxides (tin, zinc, zirconium, titanium), mixed oxides, alloyed oxides, electroconductive polymers (polyaniline, polypyrroles, phthalocyanines), and metal- and polymer-based composites are used for development of sensors [1–6]. Certain materials for sensitive elements (SEs) comprise carbon components (soot, fullerenes, graphites, nanotubes) [1, 2, 7–10]. Semiconductive sensors are the most widespread.

P.P. Gorbyk (✉)
O.O. Chuiko Institute of Surface Chemistry of the National Academy of Sciences of Ukraine, General Naumov St. 17, Kyiv 03164, Ukraine
e-mail: gorbyk_petro@isc.gov.ua

A.P. Shpak, P.P. Gorbyk (eds.), *Nanomaterials and Supramolecular Structures*,
DOI 10.1007/978-90-481-2309-4_28,

However, in most cases, a number of metrological parameters of the sensitive elements of the existing sensors do not fit the contemporary requirements (instability of electrical parameters, high work temperature, low repetition factor, irreversibility of adsorption–desorption processes) [4]. Therefore, we had an important task to create gas sensor systems operating at ambient conditions with fast and reversible adsorption–desorption of gaseous compounds, high repetition factor, and sensitivity to certain gaseous compounds.

It is rational to use the concept developed by the authors for creation of contemporary prospective gas sensor systems [11]. The concept is based on a cluster approach, use of the phenomena of percolation toward formation of polymer composite systems (PCS), principles of similarity and self-similarity of the clusters, and ideas about PCS fractal structures formation [12]. The concept provides a relation between composite material (CM) parameters at a certain filler content and PCS macrostructural characteristics. Nevertheless, the developed concept requires further development accounting for processes of gas molecules adsorption on the surface of sensor CM.

CMs based on polymers, various graphite forms, and additives (e.g., silica) are the prospective materials for SE of sensors operating at ambient conditions [10–15]. We demonstrated in those works that CMs based on polymers and thermally expanded graphite (TEG) operate at the ambient conditions providing stable parameters and reversible adsorption–desorption processes. However, a number of issues related to the relationship between composition, structure, electrophysical properties, and gas sensor properties are not clear enough. Regularities of influence of polymer nature, additives, and graphite modifications on CM gas sensor parameters are not determined. Moreover, there are no approaches at present as to how the CM selectivity toward adsorption and desorption of gaseous compounds can be tuned and how to change these processes.

The aim of this work comprises determination of regularities of composition and structure influence on electrical and gas sensor properties of CM for the systems polymer–TEG and polymer–TEG–SiO_2.

28.2 Experimental Part

28.2.1 Preparation of CM

The following materials were used as a main electroconductive component for preparation of CM sensitive toward influence of gaseous compounds:

- TEG of the type GAKV-2 (loose density 8 kg/m^3, average particle size 0.475 mm, specific surface area 30 m^2/g)
- TEG modified with silica (average particle size 0.32 mm, specific surface area 25 m^2/g, average SiO_2 particle size 0.2 μm).

TEG surface modification with silica was carried out using tetraethoxysilane (TEOS) as a modifying agent (precursor). The procedures for the modification are described in [10]. The SiO_2 content in TEG was varied from 1 to 50%.

Electron microscopy studies of the modified TEG showed that its surface is coated with clusters of ultradisperse SiO_2 particles.

Polytetrafluoroethylene (PTFE), polyethylene (PE), and polyvinylchloride (PVC) were used as binding components for creating gas sensor materials.

Preparation of the CM on the basis of PE and TEG, PTFE and graphites, PVC and TEG is described in [10, 13, 14], respectively. Graphite content was varied from 0 to 100 wt% (0 to 1 volume part (Θ)). The thickness of the CM samples was 0.5 + 0.03 mm.

28.2.2 Methods of Analysis

We used optical and electron microscopies at magnifications 10–200 and 500–10,000 times, respectively, for evaluation of the CM structure. Electron microscopy studies were carried out with a scanning electron microscope JEOS JSM-35 (Japan). The samples were fixed on a holder with silver paste. Additional electroconductive coating was not applied.

Fourier transform infra-red (FTIR) spectroscopy was applied for identification of SiO_2 on the surface of modified TEG. The spectra were recorded with an FTIR spectrometer NEXUS Thermo Nicolet (USA) in the region 600–4000 cm^{-1}. The powders of TEG and SiO_2-modified TEG were placed between NaCl plates and fixed in a holder.

The specific volume electric resistance (ρ_{CM}, Ω·m) of the electroconductive CM ($\rho_{CM} < 10^6$ Ω·m) was determined by the standard four-probe potentiometric method at permanent current according to GOST 6433.14-71. The contact electrodes were fabricated in the form of hold-down screws. The chosen current strength passing through a sample (0.01–15 mA) excluded heating of the sample. The ρ_{CM} value was measured along the longitudinal axis of a sample (perpendicular to the compressing axis). The ρ_{CM} value of high-resistance CM samples with low TEG content was measured with a teraohmmeter E6-13A.

From analysis of various types of sensor equipment [1–10], we concluded that the most suitable method of registration of the impact of gaseous compounds is measuring material electroconductivity. This method is simple enough and does not require sophisticated equipment. Sensitivity of CM toward vapors of gaseous compounds was determined using specially developed models. A similar design of sensors was described in [10, 13–15]. A gas-sensitive material was placed between electrodes, fixed, and introduced into a chamber (gas-controlled volume) for identification of a certain gaseous compound. The following characteristics were chosen as informative parameters: R_0 initial electric resistance; R_X electric resistance at a certain moment of time; ΔR_X change in electric resistance ($R_X - R_0$); R_{max} electric resistance corresponding to the maximal adsorption of a gaseous compound; $\Delta R_X/R_0$ the relative change in electric resistance; t impact time of a gaseous compound. The R_0 parameter was measured and compensated prior to introduction of gaseous compounds to the chamber. Then vapors of gaseous compounds were directed to the chamber, and the function of electric conductivity change (ΔR_X) on impact time of

a gaseous compound (t) was recorded. After the adsorption maximum was achieved, the chamber was vented with air in order to remove the compounds' vapors, and the desorption process was monitored (decrease $\Delta R_X = f(t)$). Samples of CM with varied content of graphite were used for the determination of the impact of various compounds (toluene, acetone, ethanol, ozone, propane, diethyl ether, and ammonia) on the SE of the sensor. A series of adsorption response curves ($\Delta R_X = f(t)$) was obtained as a result.

28.3 Results and Discussion

28.3.1 Structure and Electrophysical Properties of CM

We studied the electrophysical properties of CM in the systems PE−TEG, polypropylene (PP)−TEG, and polyamide (PA)−TEG [10, 12, 13]. Processes of cluster formation in the polymer–electroconductive component system can be modified via changing graphite type, chemical nature of the polymer, manufacturing technology, composition, etc. It was found that the polymer−TEG system can have one or two thresholds of percolation depending on cluster structure and preparation conditions [12, 13]. Figure 28.1 shows a typical character of the function $\rho_{CM}(\Theta)$ for the systems PE−TEG with two percolation thresholds (curve 1) and PVC−TEG with one percolation threshold (curve 2). Figure 28.1 shows that there are two sudden changes in the concentration function curve $I_{KM}(\Theta)$ for the PE−TEG system which correspond to the first (Θ_C =0.075 of TEG volume part) and the second ($\Theta_C' = 0.41$ of TEG volume fraction) percolation thresholds. The function $\rho_{KM}(\Theta)$ for the PVC−TEG system has only one sudden change at the concentration $\Theta = \Theta_C = 0.04$ of TEG volume part which is typical for systems with one percolation threshold.

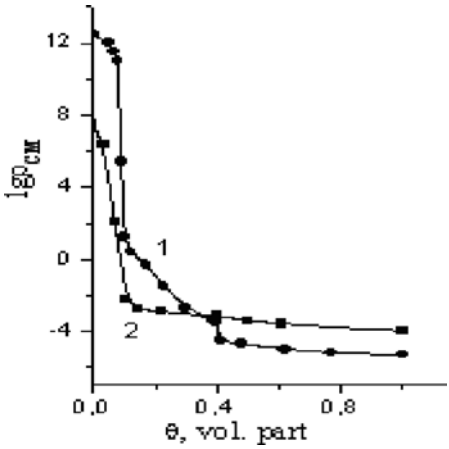

Fig. 28.1 Function of specific volume electric resistance logarithm (lg ρ_{CM}) on TEG content (Θ, volume part) for the longitudinal axis of CM samples of the systems PE−TEG (*1*) and PVC−TEG (*2*)

For both systems being discussed, formation of an uninterrupted infinite cluster (UIC) of TEG at $\Theta \geq \Theta_C$ causes an abrupt decrease of ρ_{CM} values by several orders. This phenomenon is similar to a second-order phase transition by its operation effect; however, no phase changes occur in TEG, only its uninterrupted structure is formed. Our previous studies [10, 11] showed that the polymer UIC in the PE−TEG system with two percolation thresholds does not disappear in the region $\Theta_C < \Theta < \Theta_C$' but co-exists with TEG UIC; the UIC of the polymer disappears upon a condition that $\Theta \geq \Theta_C$' [10]. Only TEG UIC (similar to a matrix) and isolated polymer clusters (inclusions) exist in the region $\Theta_C' < \Theta < 1$.

The CM structure of both systems PE−TEG and PVC−TEG upon the TEG content $0 < \Theta < \Theta_C$ is a matrix of polymer clusters with TEG inclusions (Fig. 28.2a). However, at $\Theta \geq = \Theta_C$, formation of UIC from TEG for a system with one percolation threshold (on the contrary, to a system with two percolation thresholds) is accompanied by disappearance of UIC of PVC, and only TEG UIC and isolated polymer clusters exist upon the TEG content $\Theta_C < \Theta < 1$ (Fig. 28.2b).

Study of the CM microstructure in the PTFE−TEG system showed that cluster formation in this system occurs in accordance with the same principle as in the PVC−TEG system, while the percolation threshold is equal to $\Theta_C = 0.02$ of the TEG volume part [13].

From comparison of percolation thresholds in the PTFE–graphite system, it was found for a number of graphites that the percolation threshold values decrease in the following order: GAK-2 > GSM-1 > C-0 > TEG. This fact can be explained by peculiarities of TEG particles and their surface structure. The TEG particles are destroyed and shortened, and their shape is changed upon CM fabrication. Nevertheless, the fracture places of the TEG particle, quinone and hydroquinone groups, on its surface form active centres which promote active TEG structure formation in a polymer binding component, formation of long electroconductive fragments. The factors named above determine low values of percolation thresholds and high CM electroconductivity upon use of TEG with respect to other carbon fillers (not expanded graphite, soot, carbon fiber) [13, 16].

Analysis of voltage–current characteristics and functions of electric resistance (R) on voltage (U) and temperature (T) revealed the following regularities. Linearity

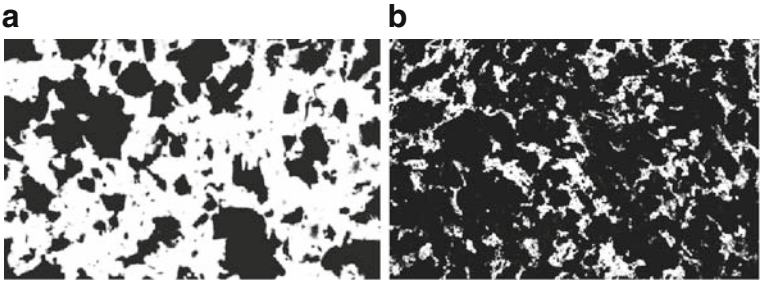

Fig. 28.2 Optical microphotographs of thin films of the CM samples on the PVC basis containing the 0.015 (**a**) and 0.106 (**b**) TEG volume fraction

of the function $R(U)$ and a negative temperature coefficient of resistance (TCR) are observed in the TEG concentration region $\Theta \gg \Theta_C$ similar to pure TEG. This fact testifies for current streaming through direct contacts between TEG particles. A non-linear function $R(U)$ and a positive TCR are representative for both systems being studied in the region of small TEG content near the percolation threshold ($\Theta \geq \Theta_C$) which may indicate possible streaming of electric charge through both the direct contacts between TEG particles and the gaps between them. We reported more detailed analysis of similar phenomena in polymer−TEG system earlier in [10, 15, 17].

We found from comparison of polymer nature influence on percolation thresholds that the Θ_C values in the polymer−TEG systems decrease toward PE > PVC > PTFE from 0.07 to 0.02 volume part.

We addressed a question, how do SiO_2 contents on the TEG surface influence the percolation processes in the PVC−TEG−SiO_2 system. It was found that this system has the percolation threshold in the region of values $\Theta \sim 0.07$ volume part.

The results obtained from optical and electron microscopy studies of CM thin films showed that the macrostructure of PVC- and modified TEG-based CM in the region of the TEG contents $0 < \Theta < \Theta_C$ (the CM sample is not conductive) consists of a UIC of PVC (matrix) phase and isolated inclusions of the modified TEG. Upon the TEG contents of $\Theta_C < \Theta < 1$ (the concentration region in which the CM is electroconductive), the CM sample consists of a UIC of the TEG particles on which modifier clusters are located and polymer (PVC) inclusions in the TEG matrix. It should be noted that increase in modifier contents on the TEG surface from 0 to 50% leads to increase of specific volume electric resistance in the PVC−modified TEG system.

28.3.2 Sensor Properties of CM

Sensor properties of CM depend to a high extent on cluster macrostructure of the components of the PCS being reviewed. The typical shapes of the curves corresponding to adsorption of a gaseous compound (rise of the R_X values) are presented in Fig. 28.3a, while Fig. 28.3b shows descending curves corresponding to desorption from the CM surface (at the temperature 22±1°C and air humidity 65±5%). The curve shape reflects whether adsorption occurs only on the CM surface (a typical Langmuir curve) or capillary condensation takes place (concave curvature).

The following regularities were found from analysis of the sensor properties of the polymer−TEG systems upon varying TEG contents. The CM structure exhibits sensitivity toward impact of gaseous compounds only in certain TEG concentration intervals: for the systems PE−TEG at $\Theta_C<\Theta<\Theta_C$' (0.1–0.4 volume part), for systems PVC–TEG and PTFE–TEG in the region $\Theta_C<\Theta\ll1$ (0.07–0.2 volume part). The highest CM sensitivity is exhibited near the percolation threshold ($\Theta_C<\Theta\ll1$).

Thus the system of the PE-based CM with varying TEG contents shows that the highest rate of electric conductivity increase is observed for the sample containing

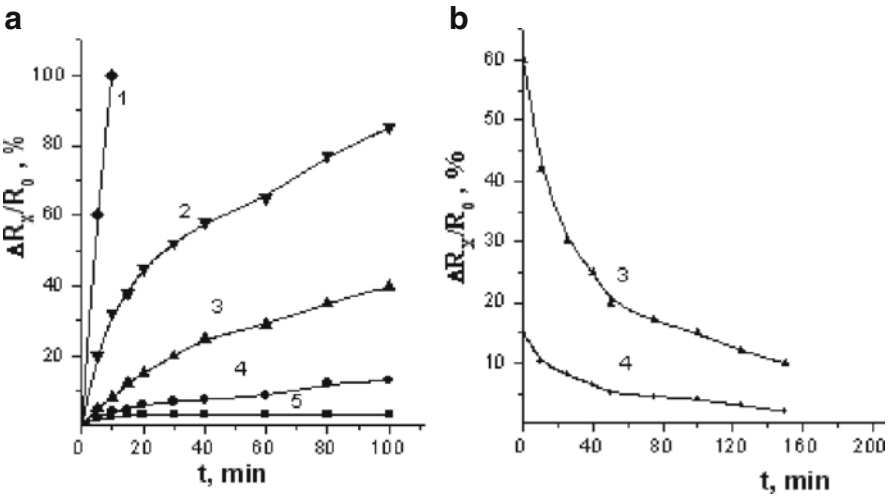

Fig. 28.3 Functions of relative electric resistance ($\Delta R_X/R_0$) on time of toluene saturated vapors' impact for the CM on the basis of PE and TEG upon adsorption (**a**) and desorption (**b**). TEG contents in the CM (Θ, the volume part): *1* 0.10; *2* 0.15; *3*0.20; *4* 0.25; *5* 0.40

0.10 volume part of TEG. The SE of the sensor responds practically immediately to toluene vapors; its adsorption occurs with high enough rate while the equilibrium adsorption value at saturation $\Delta R_{max}/R_0$ is equal to 276%. Increase in the TEG contents to 0.41 volume part leads to decrease of the ΔR_X and$\Delta R_X/R_0$ growth rates and a drop of the $\Delta R_{max}/R_0$ values. Analysis of the $\Delta R_X/R_0 = f(\Theta)$ function for CM based on PVC and TEG and PTFE–TEG also testifies for a similar trend of $\Delta R_{max}/R_0$ decrease upon increase of $\Theta > \Theta_C$.

We analyzed the functions $\Delta R_X/R_0 = f(t)$ (Figs. 28.3, 28.4, and 28.5) in order to evaluate selectivity of the obtained CM toward adsorption of various compounds. The figures show that the CM possesses individual selectivity toward various compounds. Each curve of a function of electric resistance on time ($\Delta R_X = f(t)$ or $\Delta R_X/R_0 = f(t)$) corresponding to processes of adsorption–desorption of gaseous compounds is specific for a certain compound only and different from curves for other compounds in the following parameters: time required for adsorption response (t_0), electric resistance growth rate, times of achievement of an equilibrium value of $R_X = R_{max}$ (saturation), R_{max} (the value which is equivalent to adsorption at saturation), time of desorption.

We found that the sensitive element made on the basis of PE and TEG is more sensitive toward toluene vapors than to other compounds (Fig. 28.4a). The values $\Delta R_X/R_0$ decrease in the following order for the solvent vapors at their equal impact time: toluene → petroleum → acetone → xylene → ethanol → ammonia → hydrogen chloride.

In a difference from solvents which have a positive ΔR_X value, hydrogen chloride gives decreasing resistance for CM based on PE and TEG. Behind this a

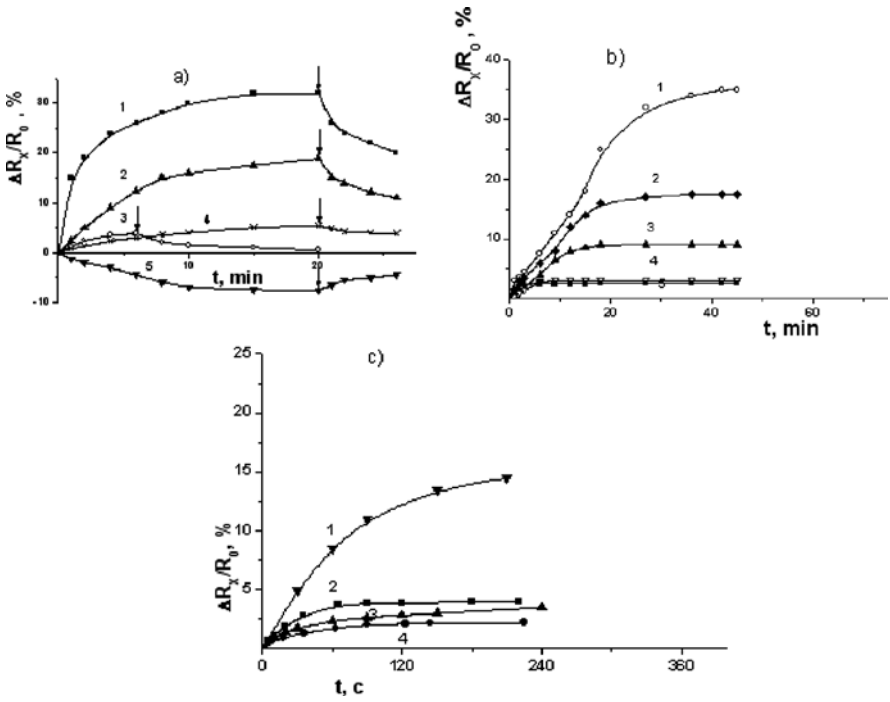

Fig. 28.4 Function of relative electric resistance ($\Delta R_X/R_0$) on time of impact of saturated vapors of gaseous compounds for CM on the basis of PE and TEG (**a**), PVC and TEG (**b**), PTFE and TEG (**c**). Contents of TEG in the CM $\Theta = 0.16$ (**a**), $\Theta = 0.07$ (**b**), $\Theta = 0.1$ (**c**). Gaseous compounds: for (**a**) *1* toluene; *2* petroleum; *3* acetone; *4* xylene; *5* hydrogen chloride; for (**b**) *1* acetone; *2* ammonia; *3* petroleum; *4* ethanol; *5* toluene. ↓ indicates the beginning of desorption, for (**c**) *1* ammonia; *2* acetone; *3* toluene; *4* ethanol

low desorption velocity of hydrogen chloride from the surface of the material is observed.

In a difference from the above system a CM based on PVC and TEG is more sensitive toward acetone. For this CM we observe a decreasing of $\Delta R_X/R_0$ value in such order (for different compounds): acetone → ammonia → ethanol → petroleum → toluene.

We found that the CM based on PTFE and TEG is more sensitive toward ammonia than to other compounds. At equal time of vapors' impact (e.g., 2 min), the values $\Delta R_X/R_0$ decrease in the following order for compounds: ammonia → acetone → toluene → ethanol. For the CM on the basis of PTFE and 10% TEG, the values $\Delta R_{max}/R_0$ comprise 14% upon ammonia impact; the adsorption and desorption times upon achievement of $\Delta R_{max}/R_0$ are equal to 200 and 300 s, respectively. The characteristics for toluene vapors decrease to 3.5%, 120 s, and 80 s, respectively.

Figures 28.3 and 28.4 demonstrate that the sensor properties of the CM substantially depend on the macrostructure of the CM component clusters, polymer chemical nature, and type of gaseous compound.

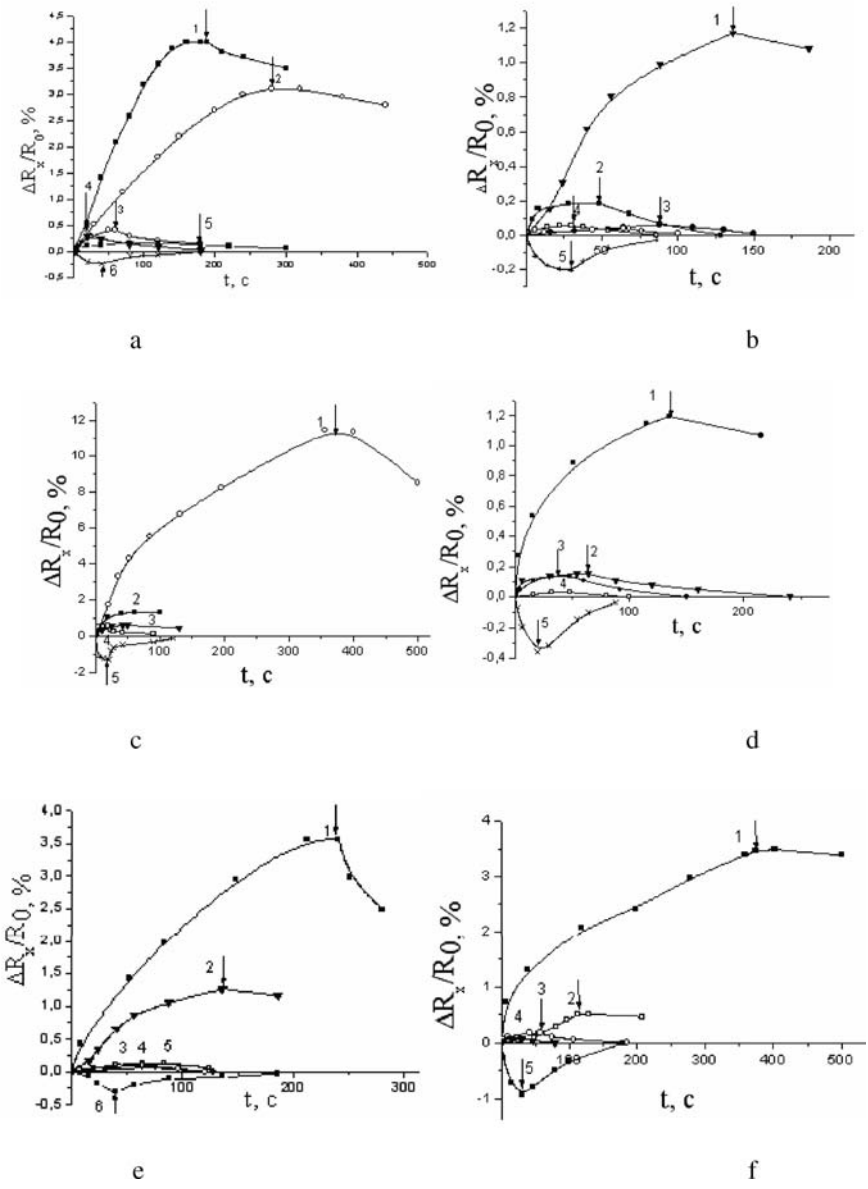

Fig. 28.5 Function of relative electric resistance ($\Delta R_X/R_0$) on impact time of saturated vapors of various gaseous compounds for the CM on the basis of PVC and TEG, unmodified (**a**) and modified with SiO_2 (**b**–**e**). Contents of TEG (%): **a** 10 ($\Theta = 0.07$ volume part), **b**, **c** 15 ($\Theta = 0.1$ volume part), **d**–**f** 20 ($\Theta = 0.15$ volume part). SiO_2 contents of the TEG surface (%): **b**, **d** 10; **c**, **e** 20; **f** 50. Gaseous compounds: acetone *1* (**a**, **d**–**f**), *2* (**c**); toluene *2* (**a**, **f**), *3* (**b**, **d**, **e**), *1* (**c**); diethyl ether *1* (**b**), *2* (**d**, **e**), *3* (**c**), *4* (**a**, **f**); ethanol *3* (**a**), *4* (**b**); ammonia *5* (**a**, **e**); propane *4* (**c**–**e**), *3* (**f**); ozone *6* (**a**, **e**), *5* (**b**–**d**, **f**)

We addressed also the question, how modification of TEG, type of the modifying agent (SiO_2), and its contents influence the selectivity of CM samples toward impact of gaseous compounds (acetone, toluene, ethanol, ammonia, diethyl ether, propane, ozone), processes of adsorption–desorption of these compounds, shape of adsorption response curves, etc.

We found from analysis of Fig. 28.5 that modifying TEG surface with SiO_2 leads to a change of the adsorption response curve shape. Comparison of influence of various gaseous compounds on SE based on PVC and unmodified TEG (Fig 28.5a) showed a trend in selectivity of the CM that the value $\Delta R_X/R_0$ decreases in the following order for a number of solvent vapors: acetone → toluene → ethanol → ozone → diethyl ether → ammonia.

The value $\Delta R_X/R_0$ for ozone has the negative sign for all samples. Change in selective ability of CM toward influence of gaseous compounds occurs and the adsorption–desorption rates increase upon introduction of TEG modified with silica into the CM. The composite material containing 15% TEG modified with 10% SiO_2 (Fig. 28.5b) is the most sensitive toward diethyl ether and does not respond to ammonia and propane, while $\Delta R_X/R_0$ for this CM decreases for the order of vapors: diethyl ether → acetone → ozone → toluene → ethanol. The value $\Delta R_{max}/R_0$ upon impact of diethyl ether and the time required for achievement of $\Delta R_{max}/R_0$ are equal to 1.2% and 140 s, respectively. The following trend is observed in decrease of selective ability of CM upon increase of SiO_2 content on the TEG surface to 20% (Fig. 28.5c): toluene → acetone → diethyl ether → propane. Decrease of adsorption–desorption rates and increase of sensitivity toward influence of gaseous compounds are observed at TEG content 20% in CM and increase of SiO_2 concentration on the TEG surface from 10 to 50% (Fig. 28.5d−f). For the sample containing TEG modified with 10% SiO_2, decrease of the $\Delta R_X/R_0$ values is observed in the order: acetone → diethyl ether → ozone → toluene → propane. Increase of sensitivity by three times toward the compounds listed above is observed upon increase of SiO_2 content on TEG surface to 20 and 50%, while the selectivity does not significantly change.

Thus the data analysis testifies that even a minor change in CM composition leads to a change in CM selectivity toward various compounds, the trend of changes in selectivity, adsorption–desorption rate, the maximal ΔR_{max} values, time of adsorption and desorption, and other sensor characteristics. The time (t_1) required for achievement of ΔR_{max} upon adsorption of gaseous compounds for the CM being studied lies within 20–120 s and the time of desorption within 40–600 s and depends on the CM composition at a notable degree.

Multiple tests of CM at ambient temperature showed good reproducibility of the adsorption response curves upon cycling of adsorption–desorption of vapors of gaseous compounds. This testifies for equilibrium of adsorption–desorption of gaseous compounds on the CM surface at ambient temperature. Such equilibrium is related to physical adsorption of these compounds on the surface. We assume that the gaseous compounds interact with all components of CM (TEG particles, SiO_2, polymer molecules) because shapes of adsorption response curves, the values

$\Delta R_{max}/R_0$, and other sensor characteristics change upon change of the TEG content in the CM.

It should be noted that fractal structures of the CM components and their dimensionality are of a substantial importance upon forming CM gas sensor properties. It was shown earlier [10, 14, 15] that the skeleton of a UIC near the percolation threshold ($\Theta \geq \Theta_C$) in the CM based on PVC and TEG contains bulbs linked by thin bridges with maximal resistance. The thickness of the bridges can be regulated via addition of other components to a CM (in particular, SiO_2 and TiO_2). Electric resistance of a conductive sample of a CM in the region of TEG contents of $\Theta_C \leq \Theta < 1$ can be presented as

$$R_{CM} = R_1 + R_2 + R_3, \tag{28.1}$$

where R_1 is the total electric resistance of TEG particles, R_2 is the resistance derived from direct contacts of the TEG particles, and R_3 is the resistance arising from electric current in the gap between the particles.

In accord with our experimental data, electric resistance of the CM sample is $R_{CM} \sim R_1$ in the region of TEG concentrations $\Theta \gg \Theta$. In this case, sensitivity of CM to influence of gaseous compounds is determined mostly by their interaction with parts of TEG located on the CM surface. The authors of [18] report that electric conductivity in TEG is performed by electrons and holes. Therefore, adsorptive interaction causes change in the number of charge carriers on the surface of TEG and their mobilities due to withdrawal of electrons from the surface or change in electrons and holes concentration ratio. Consequently, concentration of charge carriers in TEG volume changes which leads to a change of electric resistance of a CM sample. It is necessary to note that CM samples have low specific resistance ($\rho_{CM} = 10^{-3}-10^{-5}$ Ω·m) at high TEG contents, while the change in resistance resulting from interaction of gaseous compounds with TEG is small. Therefore, sensitivity of CM in the TEG concentration region $\Theta \gg \Theta_C$ upon interaction with gaseous compounds is low. It was found for polymer−TEG systems that the values $R_{CM} \gg R_1$ in the range of concentrations $\Theta_C \leq \Theta \ll 1$ (near the percolation threshold upon approaching it from the right), therefore $R_{CM} \approx R_2 + R_3$. The value of contact resistance R_2 and size of the gap between TEG particles may vary upon influence of gaseous compounds. The contact resistance and the gap between fractal structures of TEG may change most significantly near the percolation threshold Θ_C upon formation of UIC from TEG which expands throughout the whole sample of CM. This fact explains a substantial increase in rate of electric conductivity growth near the percolation threshold ($\Theta \geq \Theta_C$) of CM samples upon influence of gaseous compounds.

It is necessary to note that the selective ability of CM toward influence of gaseous compounds depends to a high extent on affinity of these compounds to the polymer, the electroconductive component, and the modifying additive [10, 15, 17]. It is known [10] that toluene and acetone have high affinity to PE and PVC, respectively. However, these polymers are stable against treatment with aqueous solutions

of ammonia and ethanol. Since polymers and additives (SiO_2) are insulators, adsorptive interaction with polymer clusters located on CM surface cannot change electric conductivity of a sample directly. However, one can assume that adsorption of gaseous compounds on polymer surface leads to some extending of the polymer surface layer and, consequently, to a change of linear sizes of other constituents and the whole sample. Thus, papers [19, 20] report that linear size of samples can vary as a result of adsorption of gaseous compounds on surfaces of porous bodies. Usually, adsorption of gaseous compounds induces extension of a sample; however, contraction is also possible (e.g., upon adsorption of ammonia on glass). In the case of extension of a sample upon adsorption of gaseous compounds on CM surface, the gap between fractal structures increases and the area of the contact spot between particles of TEG decreases. These processes are accompanied by increase of resistances R_1 and R_2 and the value of R_{CM}. In the case of contraction of the gap between the fractal structures and decrease of contact resistance and the R_{CM} value upon adsorption, the response of a sensor material becomes negative ($\Delta R_X/R_0 < 0$). Thus the overall response of a sensor depends on the influence of gaseous compounds on all levels of CM structure.

It should be noted that most of the developed gas sensor materials work at ambient conditions (temperature 10–30°C) and have the initial response period less than 1 s, small time of adsorption–desorption, complete reversibility of adsorption–desorption processes, stability of performance parameters, and selectivity toward certain gaseous compounds.

The obtained materials on the basis of TEG and polymers can be used as sensor materials. The CM containing 84–87% PE and 13–16% TEG is recommended for determination of toluene and petroleum; the CM on the basis of PVC and 10% TEG, PVC and 15% TEG modified with 20% SiO_2, PVC and 15% TEG modified with 10% SiO_2 are recommended for detecting acetone, ozone, and diethyl ether, respectively.

28.4 Conclusions

A number of CMs based on polymers (PE, PTFE, PVC) and unmodified TEG and TEG modified with SiO_2 possessing a broad range of electrophysical (ρ_{CM} varies from 10^{16} to 10^{-6} Ω·m) and sensor characteristics were studied.

Regularities of influence of composition, polymer nature, SiO_2 contents on percolation processes, percolation thresholds in the systems polymer–graphite and structure, electrophysical, and sensor properties of the obtained CM were found. We showed that the PTFE−TEG system has the lowest value of percolation threshold ($\Theta_C = 0.02$ of the TEG volume part) from comparison of percolation thresholds in systems containing PE, PVC, PTFE as polymers.

We demonstrated that every obtained CM has an individual response of adsorption–desorption processes (“sensor portrait”) and exhibits selective sensitivity toward influence of certain gaseous compounds (toluene, acetone, ethanol,

diethyl ether, ammonia, propane, ozone). The materials exhibit different times required for achievement of ΔR_{max}, desorption times, ΔR_{max} and $\Delta R_{max}/R_0$ values, adsorption and desorption rates. We showed that the highest sensitivity of CM toward influence of gaseous compounds is observed near the percolation threshold ($\Theta_C<\Theta\ll1$). Regulating sensor characteristics and selectivity of CM toward various gaseous compounds is possible via tuning chemical nature of polymer, contents of TEG and the SiO_2 additive. Most of the obtained materials possess response time less than 1 s; time of adsorption–desorption of gaseous compounds lies within the range 20–200 s; the processes of adsorption–desorption are completely reversible upon multiple use at ambient temperatures; the performance parameters are stable.

References

1. Miasnikov IA, Sukharev VYa, Kuprianov LYu, Zav'yalov SA (1991) Semiconducting sensors in physico-chemical studies. Nauka, Moscow (in Russian)
2. Talanchuk PM, Shmatko BA, Zaika LS, Tsvetkova OE (1992) Semiconductive and solid electrolyte sensors. Tekhnika, Kiev (in Russian)
3. Manea F, Radovan C, Pop A, Corb I, Burtica G, Malchev P, Picken S, Schoonman J (2009) Carbon composite electrodes applied for electrochemical sensors. In: Baraton M-I (ed) Sensors for environment, health and security. Springer, Netherlands, pp 179–189
4. Galyamov BSh, Zav'yalov SA, Kupriyanov LYu (2000) Microstructure and gas-sensing properties of nano-inhomogeneous composite films. Zh. Fiz. Khim. 74:459–464
5. Yasumasa T, Masanobu A, Mutsuo S (2000) Multilayered gas sensor/No. 9/10/106. US patent 6263723, G 01 No. 27/00, G 01 No. 27/12. Filed 20.05.1998, Printed 14.04.2000
6. Semko LS, Shevlyakov YuA, Garashchenko II, Chuiko OO, Gorbyk PP, Kruchek YaI (2005) Gas sensing material and gas sensor No. 2003076763. Ukraine patent 72367, G 01 N 27/00, G 01 N 27/12. Filed 18.07.2003, Printed 15.02.2005, vol. 2
7. Rakov EdG (2006) Chemistry of carbon nanotubes. In: Gogotsi Y (ed) Nanomaterials. Hand Book. CRC Press, Boca Raton, pp 103–173 (in Russian)
8. Kupriyanov LYu (2004) Nanotechnology application for the creation a new type of high sensitive chemical sensors. Novosti Nauki 1:30–35 (in Russian)
9. Chen SG, Hu JW, Zhang MQ, Li MW, Rong MZ (2004) Gas sensitivity of carbon black/waterborne polyurethane composites. Carbon 42(3):645–651
10. Semko LS, Gorbyk PP, Kruchek YaI (2007) Gas sensing materials based on graphites, polymers, titanium oxide and silica. Physics and chemistry of nanomaterials and supramolecular structures. Naukova Dumka 2:159–191 (in Ukrainian)
11. Semko LS (1997) Advanced approaches to controlling the microstructure of polymer-matrix composites. Khim Prom-st Ukr 4:46–50
12. Semko LS, Dzubenko LS, Chernysh IG, Kocherov VL, Popov RE (1997) Badanie wlasciwosci kompozytow z polipropylenu i grafitu termorozszerzalnego. Polimery. Cz. II. Wplyw grafitu termorozszerzalnego na procesy topnienia polipropylenu w kompozytach 42(6):380–385
13. Kruchek YaI, Semko LS, Shevlyakov YuA, Garashchenko II (2004) Electrical and gas-sensing properties of polytetrafluoroethylene-graphite composites. Khim. Fiz Tekhnol Poverkhn 10:156–160
14. Semko LS, Kruchek YaI, Shevlyakov YuA (2005) Effect of silica on the electrical and gas-sensing properties of poly(vinyl chloride). Expanded graphite composites. Dokl Nats Akad Nauk Ukr 11:93–100
15. Semko LS, Kruchek YaI, Shevlyakov YuA, Gorbyk PP, Oranskaya EI (2007) Effect of TiO_2 nanoparticles on the resistivity and gas-sensing performance of poly(vinyl chloride)-expanded graphite composites. Inorg Mater 43(4):1–7

16. Chernysh IG, Karpov II, Prihodko GP, Shuy VM (1990) Physical-chemical properties of graphite and their compounds. Naukova Dumka (in Russian)
17. Semko LS, Kruchek YaI, Shevlyakov YuA, Dzyubenko LS, Gorbyk PP, Chuiko OO (2004) Correlation between structure, electrical and sensory properties of composite materials based on polyvinylchloride and expanded graphite. Phys Chem Solid State 6(4):685–691 (in Ukrainian)
18. Vovchenko LL, Semko LS, Chernysh IG, Matsui LYu (1993) Thermo-EMF of composite materials based on polyethylene and thermally expanded graphite. Neorg Mater 29(7):920–922 [Inorg Mater (Engl. Transl.) 29(7):804–806]
19. Little LH (1966) Infrared spectra of adsorbed species. Academic Publishers, New York
20. Gubin SP, Koksharov YuA, Khomutov GB, Yurkov GYu (2005) Magnetic nanoparticles: methods of preparation, structure, and properties. Adv Chem 74(4):539–574 (in Russian)

Chapter 29
Films and Disperse Materials Based on Diamond-Like and Related Structures

V. M. Gun'ko, S.V. Mikhalovsky, L.I. Mikhalovska, P. Tomlins, S. Field, D.G. Teer, S. FitzGerald, F. Fucassi, V. M. Bogatyrev, T. V. Semikina, S. P. Turanska, M.V. Borysenko, V. V. Turov, and P. P. Gorbyk

Abstract Structural, adsorption, mechanical and other properties of diamond-like carbon (DLC) films, ultradisperse diamonds and porous diamond compacts were studied in comparison with Ti, TiO_X, TiN_X, TiC, Zr, ZrO_X, ZrN_X, ZrC, SiO_2, graphite-like carbon film and graphitised carbon black. Control of the properties of DLC materials by doping or surface modification, high mechanical characteristics and tribological behaviour, chemical passivity, biocompatibility and nontoxicity allow the use of these materials in industry and medicine.

29.1 Introduction

Development of biomaterials attracts considerable attention [1]. The organism response on biomaterials depends on the structure of the material surface. Surface composition optimisation allows decreasing negative effects: undesirable chemical reactions, implant corrosion, surface wear and formation of wear particles, surface accumulation of bacteria, and strengthening of thrombogenesis [1, 2]. Biomaterials with optimal volume properties rarely have optimal surface properties; therefore surface modification of them to develop hard-, wear- and corrosion-resistant coatings with high biocompatibility is one of the main methods to improve the characteristics. Diamond-like carbon films (DLCFs) possessing unique physicochemical properties [3] are used to develop coatings with low friction coefficient, chemical inertness, high electrical resistance, appropriate hardness, etc. [4, 5]. Experiments in vitro and in vivo showed high biocompatibility of DLCF-coated CoCr and Ti [6], and composites with diamond-like carbon (DLC) and Ti, Si and Zr or even toxic Ag, Cu and V were developed [7, 8] that allow the creation of biomaterials with high biocompatibility for cardiovascular [9] and ureteral stents [10] and bone implants [11]. Sulzer CarboMedics and other companies reported the improvement in biocompatibility of

V.M. Gun'ko (✉)
O.O. Chuiko Institute of Surface Chemistry of the National Academy of Sciences of Ukraine, General Naumov St. 17, Kyiv 03164, Ukraine
e-mail: gun@voliacable.com

A.P. Shpak, P.P. Gorbyk (eds.), *Nanomaterials and Supramolecular Structures*,
DOI 10.1007/978-90-481-2309-4_29,

Si-doped DLCF and coatings with Si and pyrolytic carbon alloy. CaO-doped DLCF is characterised by decreased film hardness, wetting angle and sp^3/sp^2-C state ratio [8]. Adhesion of blood particles to the DLC surface is lower than to Ti [12, 13]. In the experiments in vitro [14, 15] DLCF is characterised by considerably smaller area covered by blood particles in comparison with Ti, TiN and TiC. A smaller adsorption of blood plasma proteins with a high albumin/fibrinogen (HSA/Fg) ratio on DLCF in comparison with Ti, TiN and TiC indicates the efficiency of DLCF in the prevention of thrombogenesis [16]. A higher ratio of HSA/Fg concentrations was observed for DLCF in comparison with silicone materials widely utilised in implants [4]. The activation of antigens of thrombocytes CD62p and CD63 on DLCF was analysed [17]. The experiments in vitro showed that DLCFs on cardiovascular stents with stainless steel 316L diminish activation of thrombocyte antigens that decrease the thrombogenesis. A decrease in elimination of metal ions from alloy 316L was observed for DLCF-coated stents. H-containing and H-free DLCFs are characterised by good biocompatibility and a lower number of adsorbed thrombocytes in comparison with pyrolytic carbon, Ti, 316L and other biomaterials [18, 19]. The wear of coating with polyethylene was reduced 10–600 times by the use of DLCF coating with a low roughness coefficient close to that in native knee joint [2]. Appropriate haematocompatibility of DLCF allows the production of commercial implants with DLCF coating, e.g. Cardio Carbon Company Ltd produces DLCF-covered Ti implants, and Sorin Biomedica manufactures cardiac valves and catheters covered by 0.5 μm Carbofilm.

Diamond materials such as powders, compacts and related composites can be prepared by sintering of ultradisperse diamond (UDD) powders produced at high pressure and temperature (HPHT) forming polycrystalline diamond compacts (PDCs) [20–25] (e.g. commercial Compax, Stratapax and Syndite). Nanoparticles in PDC have strains observed in some natural minerals [20]. One shortcoming of PDC is caused by the presence of a metallic phase generated on synthesis that diminishes the thermostability and influences other properties of the materials. However, composites including UDD phase-submerged in soft metal/graphite matrix are used because of wide regulation of abrasive wear and other parameters by changing the composition of the soft phase and the morphology of particles. Surface properties of PDC play an essential role in the use of these materials. Porous PDCs are chemically inert as porous graphitised carbon (PGC); however, their mechanical properties are much better [20–25]. Additionally, many surface properties of diamond materials differ significantly from that of PGC because of the difference in contributions of sp^3 and sp^2-C states. The aim of this work was to study the properties of DLCF, porous PDC and UDD as materials for technical and biomedical applications in comparison with other materials.

29.2 Materials and Methods

Materials. Medical grade 316L stainless steel (St) discs (Goodfellow, Huntingdon, UK, 10 and 15 mm in diameter) coated with Ti, TiO_x, TiC, TiN_x, Zr, ZrO_x, ZrC, isotropic DLCF and graphite-like (G) films were prepared by plasma vapour

deposition (PVD) using the unbalanced magnetron sputtering technique (Teer Coatings Ltd) [26–30]. The coating thickness was 1.5–4 μm: 2.3 μm (Ti), 2.7 μm (TiO_x), 3 μm (TiN_x), 1.5 μm (G and DLC) and 4 μm (Zr and ZrN_x). For quartz crystal microbalance (QCM) investigations, quartz crystal blanks (8.6 mm diameter, $f_0 = 10$ MHz, Spartan Europe, Portsmouth, UK) were furnished on both faces with a thin microcrystalline Au film (≈100 nm thickness, 5 mm diameter). Quartz crystals with the Au films or St discs or stents were covered by DLC, Ti- or Zr-containing films (Teer Coatings Ltd).

Commercial PDC (Institute of Superhard Materials, Kiev, 0.5–4 μm in size) was used in a comparative study with Carbopack X (Supelco), silica gel Davisil 643 (Aldrich) initial or modified by octadecyldimethylsilyl groups (loading 0.6 mmol/g) [28], and silica gel Si-60 (Merck) [29, 30]. Particle sizing of PDC was carried out using photon correlation spectroscopy with a Malvern MasterSizer giving the average particle size of 3.94 μm. The characteristics of UDD ("SINTA", Belarus) particles (4–6 nm in size) are similar to primary particles in PDC.

Nitrogen Adsorption. Nitrogen adsorption isotherms at 77.4 K were recorded using Micromeritics Gemini II and ASAP 2010 adsorption analysers. The specific surface area (S_{BET}) was calculated according to the standard BET method [31]. The pore volume (V_p) was estimated on nitrogen adsorption at relative pressure $p/p_0 \approx 0.98$. The pore size distributions (PSD) were calculated using a method described previously [32–34].

FTIR. The infrared spectra over the 4000–900 cm^{-1} range were recorded using a ThermoNicolet FTIR spectrometer in a diffusive reflectance mode.

XRD. X-ray diffraction (XRD) patterns were recorded over $2\theta = 10°-70°$ range using a DRON-3 M (Burevestnik, St. Petersburg) diffractometer with Cu K_α ($\lambda = 0.15418$ nm) radiation and a Ni filter. The average size of crystallites was estimated according to the Scherrer equation.

High-Performance Liquid Chromatography (HLPC). PDD was packed in a stainless steel chromatographic column 10 cm × 4.6 mm i.d. (Phenomenex, UK) from methanol slurry. The amount of diamond in the column was 1.65 g, packing pressure 3500 psi. Chromatographic studies were carried out using a Shimadzu HPLC system with UV detection at 254 nm with an injection volume of 20 μl, a flow rate of 1.0 ml/min and ambient column temperature. Experiments with PDD were done in comparison with commercial Hypersil® C18-silica 3μ column or Spherisorb® 5μ silica column (Waters) [25].

^1H NMR. The ^1H NMR spectra with layer-by-layer freezing-out of bulk and bound liquids were recorded using a Bruker WP-100 SY spectrometer of high resolution [35].

Scanning Electron Microscopy (SEM) and Energy Diffraction Analysis of X-rays (EDX). The morphology of metal-, ceramic- and carbon-coated discs were analysed by the SEM (model JSM-6310, Japan Electron Optics Ltd) method. The elemental composition of the coatings at different depths was analysed using EDX at the accelerating voltage of 5 and 10 keV and a Philips XL20 scanning electron microscope fitted with the EDX system.

Raman Spectroscopy. A LabRAM 300 microscope (Jobin Yvon, UK) with 300 mm focal length spectrometer (providing ∼ 1 cm^{-1}/pixel spectral dispersion),

532 nm (50 mW) and 633 nm (18 mW) laser excitation and −70°C TE air-cooled CCD detection was used to record the Raman spectra of the coatings. The used apparatus incorporates a true confocal Raman microscope.

Hydrophilicity/Hydrophobicity. Discs (10 × 0.25 mm) with studied coatings were washed in detergent (5% 7X-PF), rinsed in distilled water, followed by 2% acetic acid, distilled water and acetone and left to air-dry before dynamic contact angle (DCA) measurements using a CAHN Dynamic Contact Angle (DCA) Analyser.

Micro-roughness. A UBM laser profilometer, which tracks across a surface to be measured using a red laser beam, was applied to estimate surface micro-relief. The device uses a PZT transducer to maintain focus of the beam and thereby monitors changes in the height (≥ 0.1 μm) of the surface features.

Quartz Crystal Microbalance. The QCM sensors were mounted in PEEK^{TM} cartridges using a viscosity elastomer (RS, Corby, UK). The cartridges were in turn mounted within a peltier temperature-controlled block, held at 25±0.1°C. Human plasma fibrinogen (Fg, Chromogenic) and albumin (HSA, Sigma) were dissolved in phosphate-buffered sodium saline (PBS) and dialysed overnight to get rid of any other ions. The solutions were centrifuged at $1.3\times10^4\times$g and concentration was measured using an extinction coefficient ${E_{280\text{nm}}}^{1\%} = 16$ for Fg and E280nm1% = 6.7 for HSA. The final concentration of Fg was 2.5 mg/ml and HSA 20 mg/ml (because of their different amounts in blood). The QCM measurements were performed for individual Fg and HSA solutions and after injection of the second protein, HSA after Fg (first pair Fg–HSA) and Fg after HSA (second pair HSA–Fg). The QCM method is described in detail elsewhere [24, 26, 36].

Lowering of frequency of quartz crystal oscillations in liquid media is [24, 36]

$$\Delta f = -f_0^{1.5}\left(\frac{\eta_\text{l}\rho_\text{l}}{\pi\mu_\text{q}\rho_\text{q}}\right)^{0.5}, \tag{29.1}$$

where Δf is the measured frequency shift, f_0 is the resonant frequency of the unloaded quartz crystal, ρ_l and η_l are the density and the viscosity of a liquid, respectively, ρ_q and μ_q are the specific density and the shear modulus of quartz, respectively. On adsorption of mass m_a as a film from a liquid, the f value decreases:

$$\Delta f = -f_0^{1.5}\left(\frac{\eta_\text{l}\rho_\text{l}}{\pi\mu_\text{q}\rho_\text{q}}\right)^{0.5} - cm_\text{a}(1-x), \tag{29.2}$$

where c is a constant and x is the viscous correction factor dependent on mechanical properties of an adsorbed film and an aqueous solution. If this film (with the thickness h_f and the specific density ρ_f) is relatively rigid and the liquid is Newtonian, then the load from this layer and the liquid load are additive [24]:

$$\Delta f = -f_0^{1.5}\left(\frac{\eta_\text{l}\rho_\text{l}}{\pi\mu_\text{q}\rho_\text{q}}\right)^{0.5} - \frac{2f_0^2\rho_\text{f}h_\text{f}}{(\mu_\text{q}\rho_\text{q})^{0.5}}. \tag{29.3}$$

Table 29.1 Content (%) of elements in coatings according to the EDX data

Coating	Ti	O	C	N	Coating	Zr	O
Ti	99.7				Zr	99.8	
Ti	99.7				Zr	99.8	
Ti	99.7				Zr	99.8	
TiO_x	65	35			ZrO	70.6	29.4
TiO_x	65	35			ZrO	72.2	27.8
TiO_x	63.2	36.8			ZrO	72.8	27.2
TiC	76.1		23.9				
TiC	76.7		23.3				
TiC	75.8		24.2				
TiN_x	62.1			37.9			
TiN_x	61.4			38.4			
TiN_x	61.4			38.6			
DLC+G			99.9				

Note: St includes 63.5% Fe, 24.8% Cr and 7.1% Ni.

This equation was used for estimation of the h_f values for adsorbed proteins (Table 29.1). Time dependence of a $\Delta f(t)$ curve portion corresponding to a sharp decrease in frequency because of the protein loading to the sensor surface is [24]

$$\ln \frac{\Delta f}{A} = -kt, \tag{29.4}$$

where k is the adsorption rate constant, which decreases with time because of increasing coverage Θ depending on adsorption and unfolding of macromolecules. $\Theta = \Theta_a + \Theta_u$, where Θ_a and Θ_u are the surface fractions covered by intact and unfolding protein molecules. Equation (29.4) can be re-written as follows [24]:

$$\Delta f = A\left\{\exp\left[-\frac{\gamma(t-\alpha)^{\nu}}{1+\beta(t-\alpha)}\right]-1\right\}, \tag{29.5}$$

where α is a constant corresponding to the time between the protein injection to the liquid flow and the beginning of its adsorption on the sensor surface; β, γ and ν are the equation parameters; exp[] < 1; $\nu > 1$; and $A \approx -\Delta f_m$ is the maximal change. To describe the protein adsorption over a large time interval, changes in frequency can be given by

$$\Delta f = A\left\{(t-\alpha)^{\delta}\exp\left[-\gamma(t-\alpha)^{\nu}\right]-b(t-\alpha)+c(t-\alpha)^{\lambda}\right\}, \tag{29.6}$$

where A, b, c, α, δ, γ, λ and ν are the equation parameters. Equation (29.4) can be re-written with consideration for diminution of the adsorption rate $d\Gamma/dt$ with increasing surface coverage Θ in the form of integral equation

$$\Delta f_{exp}(t) = A\int_0^{k_{max}} \exp\left[k(t-\alpha)^{\nu}\right]\times\left[1-(t-\alpha)/\chi\right]\varphi(k)dk, \tag{29.7}$$

where ν and χ are the equation parameters and $\varphi(k)$ is the distribution function of the adsorption rate k.

29.3 Characteristics of Biomaterials

Results of EDX elemental analysis (Table 29.1) suggest that the composition of each coating was consistent with an expected composition with a low amount of impurities. The SEM images show surface features of initial St discs (Fig. 29.1) and after coating with metallic, ceramic and carbon films (Fig. 29.2). They confirm the integrity of the coatings, although some batches of coated discs have surface cracks. The TiO_x and ZrO_x surfaces look like microcrystalline ($\sim$ 0.1–1 μm) in contrast to other more homogeneous surfaces. However, the carbon surfaces showed various micro-roughnesses compared to relatively smooth metal coatings. The TiN_x coating is akin to ZrN_x and many of their properties such as the hardness and elastic recovery (Fig. 29.3) are very similar. These two coatings demonstrate the best hardness and elastic recovery properties. The lowest values of these parameters are observed for related metallic coatings with Zr and Ti. In total, the order for hardness is ZrN_x > TiN_x > ZrC > TiC > G > DLC > ZrO_x > TiO_x > Ti > Zr. For the elastic recovery the order differs: DLC > ZrN_x > G > TiN_x > ZrC > TiC > ZrO_x > TiO_x > Zr > Ti (Fig. 29.3).

The DCA analysis (Fig. 29.4) confirmed that TiO_x is the most hydrophilic surface. The Zr and Ti surfaces have a low DCA value because they are hydrophilic due to a thin surface oxide layer [37, 38] but for St this value is higher. Both carbon coatings and ZrC are the most hydrophobic; however, DCA < 80° because of the presence of polar surface functionalities.

The DLC and G-like carbon (GLC) coatings (Fig. 29.5) are characterised by broad Raman bands that reveal their amorphicity [20, 39]. Two D and G bands in the spectra of DLCF (Fig. 29.5a) correspond to diamond- and graphite-like structures, respectively. However, the G structures give certain contributions to the D band because the difference between these bands in this range is only 20 cm^{-1} [20, 39]. The G band corresponds to ordered graphite and amorphous structures

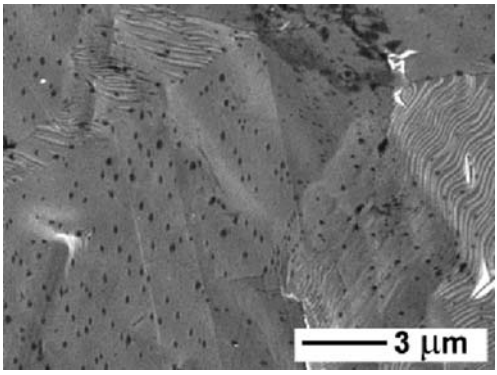

Fig. 29.1 SEM image of stainless steel surface

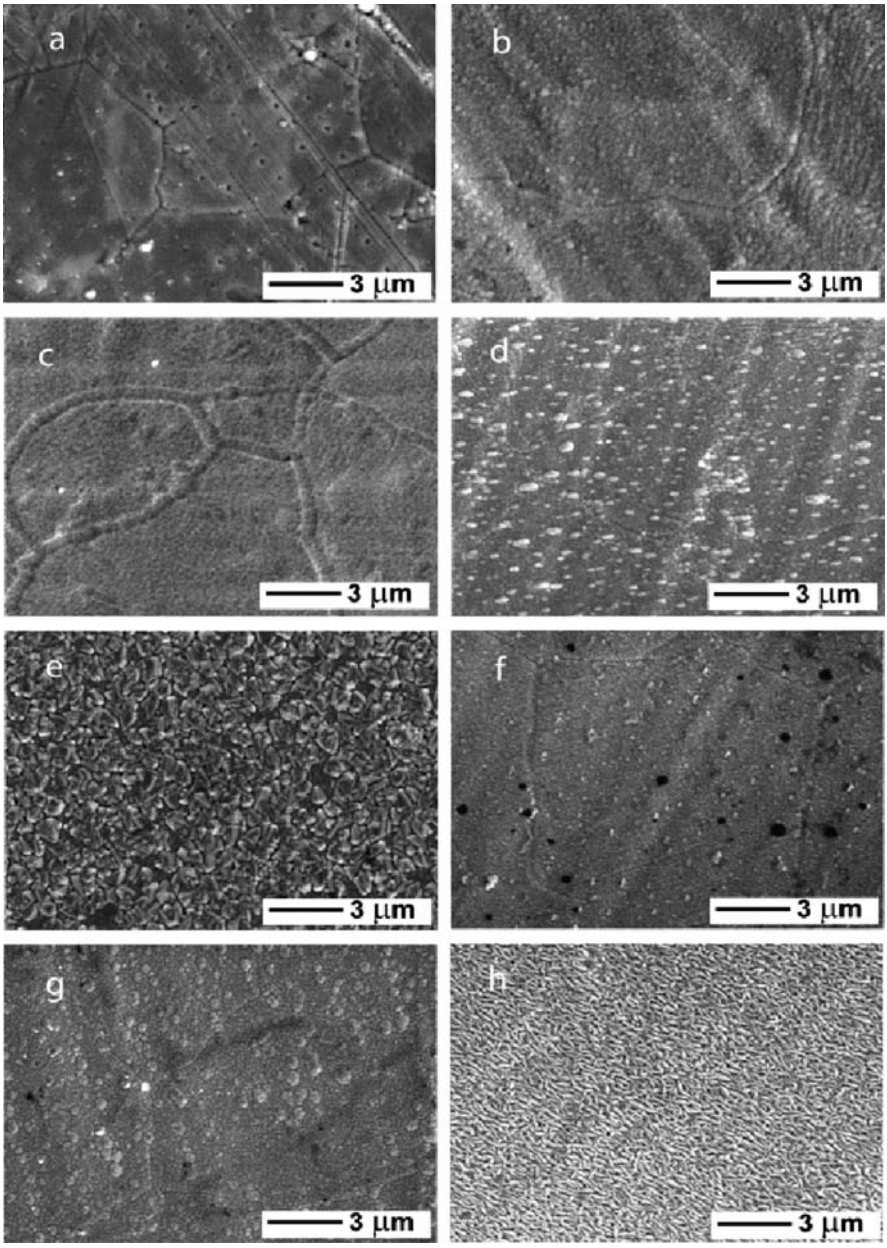

Fig. 29.2 SEM images of coatings: **a** DLC, **b** G, **c** Ti, **d** TiN_x, **e** TiO_x, **f** Zr, **g** ZrN_x and **h** ZrO_x

characterised by the difference of 80–90 cm^{-1} [20, 39]. Typically, three types of carbon structures are observed in the DLC and GLC films such as diamond (1328–1332 cm^{-1}), graphite (1347–1350 and 1573−1580 cm^{-1}) and amorphous carbon (1460–1500 cm^{-1}). The spectra of the GLCF (Fig. 29.5) are broader than that of

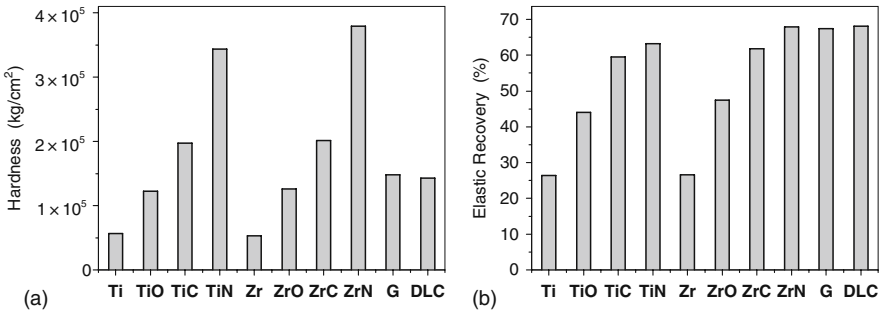

Fig. 29.3 Fisherscope microhardness tests of coatings: **a** ultra low load dynamic microhardness and **b** elastic behaviour

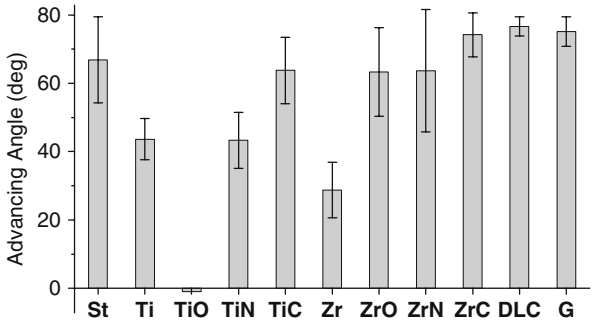

Fig. 29.4 DCA values for the tested coatings

the DLCF because of a larger structural disorder and a larger content of amorphous carbon. The similarity of the Raman spectra (Fig. 29.5) of different carbon coatings suggests the uniformity of these coatings as well as SEM images (Fig. 29.2).

The Raman spectra of St stents covered by DLC and GLC (Fig. 29.5) are typical for similar materials with a low concentration of non-carbon elements (e.g. N, O, H). A band at 1100 cm^{-1} and the difference in the sloping background for GLC and DLC coatings indicate increased hydrogen content.

According to the Raman spectra of TiO_x (Fig. 29.6), its surface is non-uniform (in agreement with SEM images (Fig. 29.2)); anatase and rutile bands are observed. Titania includes a major portion of anatase on the side B. The side A of the same disc consists of rutile, anatase and amorphous phase (with non-stoichiometric ratio Ti/O). Notice that the spectra recorded from different points ($\sim 1 \times 1$ μm) of TiO_x-covered St stent and disc are close. The largest nanoparticles include mainly rutile (Fig. 29.6b). In the case of TiO_x-covered stent, anatase gives the main contribution. ZrO_x coatings include monoclinic and tetragonal phases (Fig. 29.7), and the first one is the main contributor. The Raman spectra of ZrO_x coatings of discs and stents are close and are practically the same for different points of coatings.

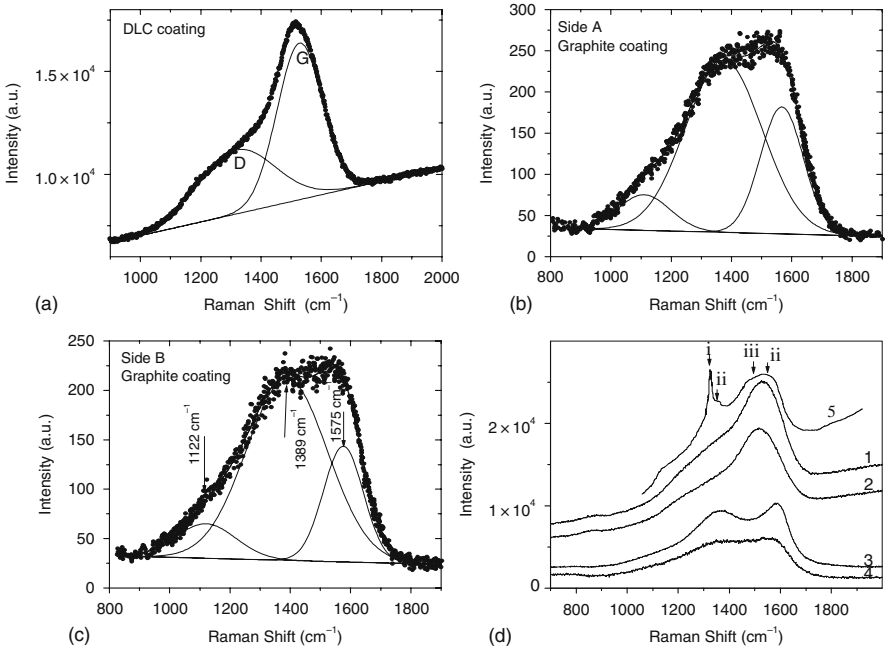

Fig. 29.5 Raman spectra of **a** DLC, **b** GLC, **c** commercial Carbofilm-coated stent and **d** DLC (curves *1* and *2*) and G (*3* and *4*) coatings at St stent for different points of the surface; (*5*) DLCF at St with the positions of (*i*) diamond, (*ii*) graphite and (*iii*) amorphous carbon bands

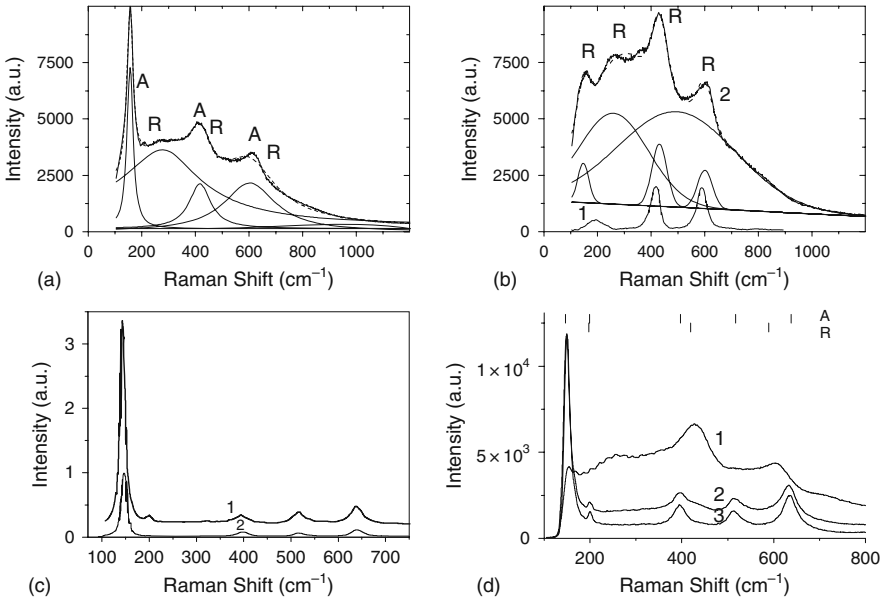

Fig. 29.6 Raman spectra of different points at sides (**a**, **b**, **d**(*1*)) A and (**c**, **d**(*2*)) B of stainless steel disc coated by TiO_x; individual (**b**(*1*)) rutile and (**c**(*2*)) anatase; and (**d**(*3*)) TiO_x-covered stainless steel stent; labels *A* and *R* correspond to anatase and rutile, respectively

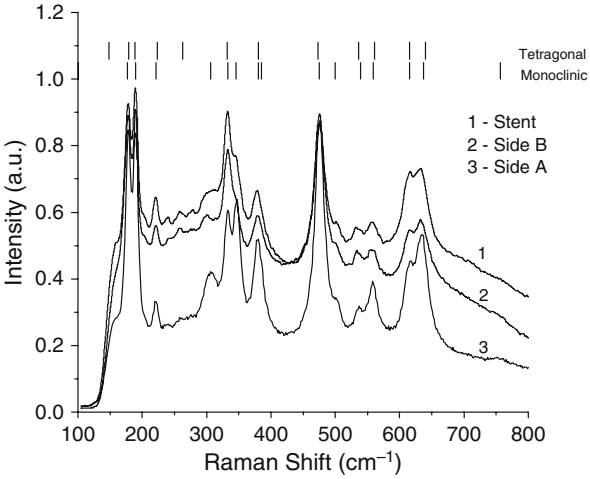

Fig. 29.7 Raman spectra of stainless steel (*1*) stent and (*2*, *3*) disc covered by zirconia film

These results reveal that ZrO_x coatings are uniform with respect to phase composition. The spectra character suggests that the coatings have a significant crystallinity with a low content of amorphous phase. This is in agreement with SEM image (Fig. 29.2) demonstrating uniform ZrO_x microcrystalline surface.

The kinetics of changes in the corrosion potential E_c (Fig. 29.8) reveals that Ti and Zr surfaces can be quickly passivated to reach the positive (passive) values in contrast to St and TiO_x surfaces. The smallest changes of the potential with time are observed for the DLC and G surfaces at $E_c > 100$ mV (DLC) and $E_c > 50$ mV (G). The TiN_x and ZrN_x coatings starting at different initial values of the corrosion potential (50 and −100 mV, respectively) reach approximately +100 mV in 16 h. These data suggest that the most corrosion-resistant coatings correspond to

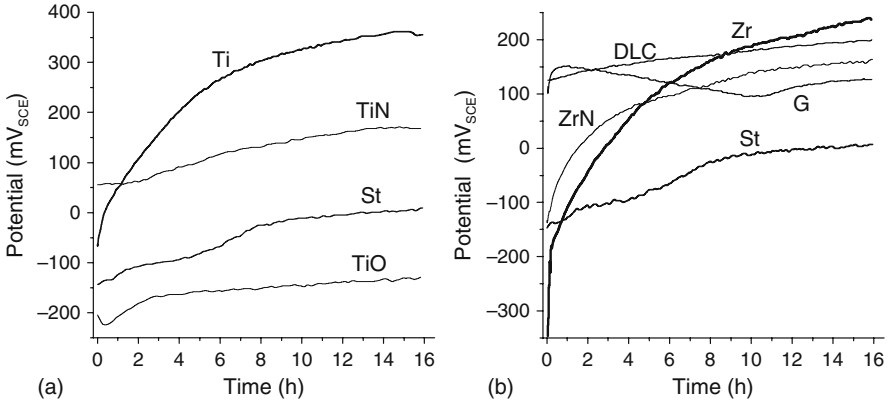

Fig. 29.8 Corrosion potential (reference SCE) as a function of time for different coatings

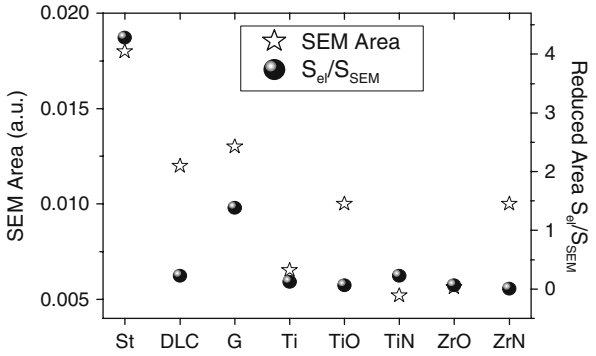

Fig. 29.9 Relative surface area according to the SEM data (S_{SEM}) and the ratio of relative electrochemically active surface area (S_{el}) to S_{SEM} for different coatings

DLC and G. Estimation of the ratio between the SEM area and the electrochemically active area gives values lower than 0.5 for the majority of the surfaces with the exception of St and G coatings (Fig. 29.9). From the data it follows that DLC, carbides and nitrides of zirconium and titanium are the most promising coatings of biomaterials in contrast to TiO_x and ZrO_x coatings.

Comparative study of biomaterials is continued on adsorption of HSA and Fg since their concurrent adsorption on biomaterials in blood determines the haematocompatibility. Despite a larger HSA concentration as $C_{HSA}/C_{Fg} = 8$ (corresponding to that in blood), the amount of adsorbed HSA ($\Gamma \sim -\Delta f(t)$) is always lower (on the same surfaces) than that of fibrinogen $\Gamma_{Fg}/\Gamma_{HSA} = 1.3$–$3.4$ (Fig. 29.10a). This ratio depends, however, on the type of the surface (Figs. 29.10 and 29.11).

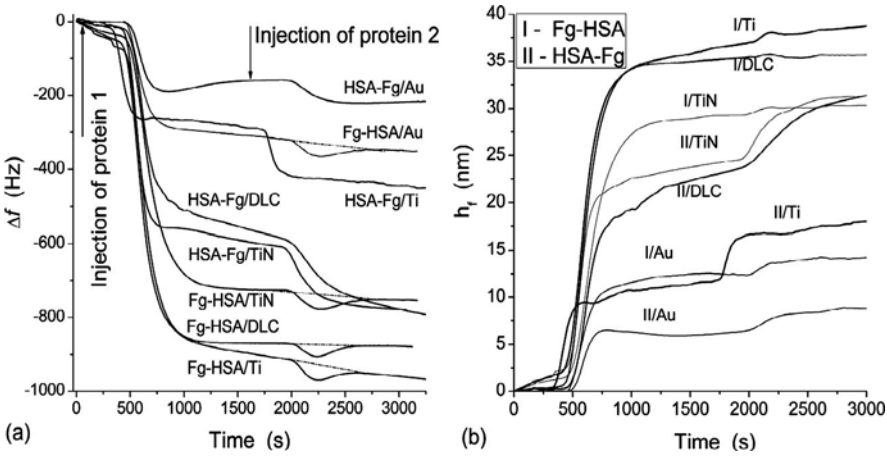

Fig. 29.10 **a** Frequency shift on adsorption of Fg–HSA or HSA–Fg on Au, DLC, Ti and TiN; **b** the layer thickness as a function of time of the adsorption of (*I*) fibrinogen then HSA and (*II*) HSA then fibrinogen on Au, DLC, Ti/TiO_x, TiN surfaces

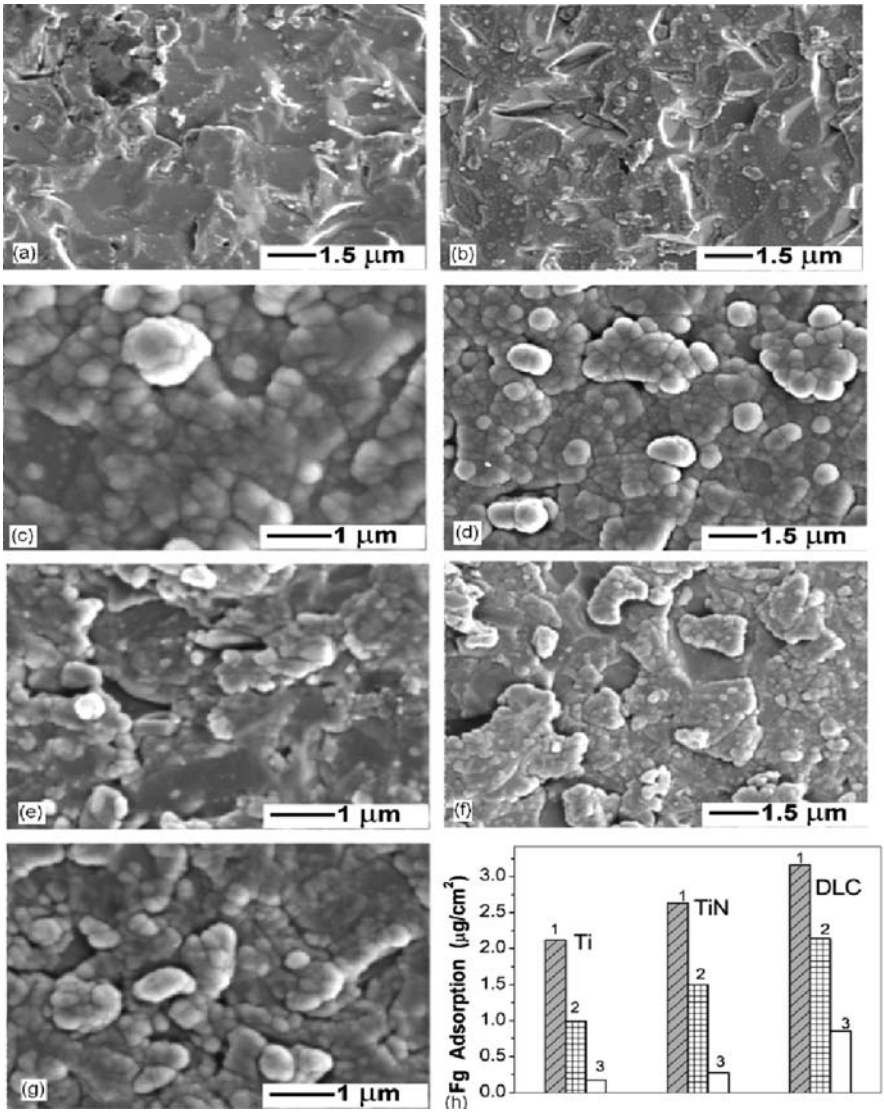

Fig. 29.11 SEM images (×20,000) of Au surface (**a**, **b**), DLC (**c**, **d**), Ti (**e**, **f**) and TiN_X (**g**) initial (**a**, **c**,**e**, **g**) and after adsorption of Fg and drying; (**h**) adsorption of Fg on Ti, TiN_X and DLC determined after fivefold washing off in PBS (*1*), 2% solution of sodium dodecyl sulfate (*2*) and 5% β-mercaptoethanol at 37°C (*3*)

A maximal difference in their adsorption is observed on Ti surface (covered by TiO_x), and a minimal one is on TiN_x. The ratio of the adsorption values is substantially smaller than that of the molecular weights $\Gamma_{Fg}/\Gamma_{HSA} < MW_{Fg}/MW_{HSA} \approx 5.1$. Consequently, relative packing density of adsorbed Fg molecules is lower than that

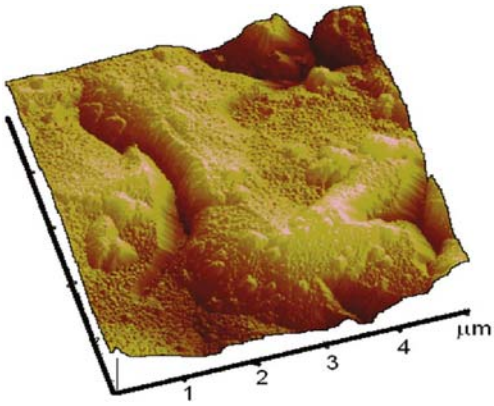

Fig. 29.12 AFM (Nanoscope IIIa, Digital Instruments) image ($5 \times 5 \times 0.5$ μm) microcrystalline Au film on quartz substrate

of HSA. Additionally, smaller molecules of HSA can penetrate in narrower shallow surface "pores" (Figs. 29.2, 29.11 and 29.12) in comparison with larger Fg. Since the ratios of adsorption Γ and molecular weights of proteins differ, one may assume that the structure of their adsorption layers (rather monolayer, Table 29.2, h) differs too. This difference depends on the surface type. The studied surfaces are non-smooth on the nano- and micro-scales (Figs. 29.11 and 29.12). The "hilly" topography of the surfaces remains after protein adsorption and drying because the adsorption protein layer is monolayer (Table 29.2, h) and its thickness is smaller than the roughness scale of the surfaces. For Fg adsorbed on all the studied surfaces $d_{\min} < h < d_{\max}$ where $d_{\min}$ and $d_{\max}$ are the minimal and maximal sizes of protein molecules. This relation is valid for HSA adsorbed on Au and Ti/TiO_x but in the case of DLC and TiN, $h > d_{\max}$ (Table 29.2). One may assume that the difference in the h values depends on the surface roughness (R_x) affecting the amounts of adsorbed proteins. The relative roughness (R_r) of DLC, Ti and TiN_x can be estimated with respect to

Table 29.2 Additional relative coverage Θ_2 of surfaces by Fg after pre-adsorption of HSA, advancing dynamic contact angle (θ) and micro-roughness criterion R_{mr}

Parameter	Au	DLC	Ti/TiO_x	TiN
Θ_2	0.30	0.29	0.22	0.29
θ (deg.)	47.9	76.7 ± 1.6	43.7 ± 3.0	27.1 ± 9
h_{Fg} (nm)	12.3	34.8	35.6	28.9
h_{HSA}(nm)	5.2	21.0	10.1	22.5
$h_{HSA–Fg}$ (nm)	8.9	31.0	17.8	30.9
$h_{Fg–HSA}$ (nm)	13.5	35.3	37.8	30.0
R_{mr}	1.00005	1.06	1.094	1.094

$\Theta_2 = (h_{HSA–Fg} - h_{HSA})/h_{Fg}$; for the Fg–HSA pair, the Θ_2 values cannot be calculated because of the absence of a clear effect of the HSA adsorption on the surfaces with pre-adsorbed Fg due to the entire relaxation; h_{Fg}, h_{HSA}, h_{Fg-HSA} and h_{HSA-Fg} are the thicknesses of the film formed on the QCM crystals calculated using Eq. (29.3); $\theta = -1 \pm 0$ for TiO_2.

the roughness of Au (R_{Au}) as $R_r = R_x/R_{Au} \sim h(X)/h(Au)$. This estimation gives R_r between 2.35 and 2.89 for individual Fg and between 1.94 and 4.33 for HSA. The difference in the R_x values estimated from the Fg and HSA adsorption can be explained by the smaller size of the HSA molecule. The h value for HSA adsorbed on the Au surface is relatively close to the smaller size (d_{min}) of the molecule. However, HSA can partially keep its globular structure in the adsorbed monolayer. Therefore, the effective h value of the HSA monolayer on ideally flat surface should be smaller than the molecular size.

Since $h > d_{min}$ one can assume that $R_{Au} > 1$. The ratio between larger and smaller sizes of the Fg molecule is significantly greater than that of HSA, since the albumin molecule has a compact globular form in contrast to the long Fg molecule. Consideration of the micro-roughness of the studied surfaces (Table 29.2, R_{mr}) and the adsorbed layer thickness h reveals the influence of the hydrophobic effect, which is maximal for DLC (Table 29.2, θ) and causes the maximal average h value for this material. Additionally, the average h value for TiN is greater than that for Ti; however, they are characterised by the same R_{mr} value. A minimal adsorption of individual proteins is observed for HSA on Au surface (HSA adsorption increases in the order Au < Ti < DLC < TiN_x), and a maximal one is for Fg adsorbed on Ti/TiO_x (Au < TiN_x < DLC < Ti) (Figs. 29.10 and 29.11). This result can be connected to the surface roughness, the molecular size of Fg and HSA and the chemical nature of the surfaces and protein molecules. Ti deposited on Au/quartz crystal is covered by a thin TiO_x layer with surface hydroxyls. At pH 7.2 the surface charge density on the titania surface is low, since its p*I* is close to 6. It is known that highly disperse titania can effectively adsorb proteins [40], and this result is in agreement with a marked adsorption of Fg on the microcrystalline Ti/TiO_x surface (Fig. 29.10). According to [41], proteins are not adsorbed on a hydrophilic surface but they are associated with it through an interfacial water layer. The Fg desorption from the sensor surfaces under the liquid flow is not observed (Fig. 29.10). Consequently, its binding to the surfaces is strong enough to consider this interaction as adsorption. The adsorption of HSA on Ti/TiO_x is significantly lower than that of Fg. This provides a faster loading of Fg on Ti/TiO_x non-densely covered by HSA (Fig. 29.10, $t < 1600$ s) in comparison with other surfaces.

The DLC surface is less polar than other materials (Table 29.2). Therefore electrostatic interaction with protein molecules is weaker (as DLC is less hydrophilic) and dispersive forces provide a greater contribution to the adsorption of proteins on DLC (as well as on TiN). The protein adsorption layer can be denser on more hydrophobic surfaces because the amounts of the remaining interfacial water are smaller than that on adsorption on hydrophilic surfaces [41]. The Fg adsorption on DLC and TiN_x is greater (Fig. 29.10) than that of HSA. Additionally, Fg adsorbs on these surfaces covered by pre-adsorbed HSA in a significant amount in contrast to HSA adsorbed after Fg. Fibrinogen molecules, which are larger and possess a greater affinity to the studied surfaces than HSA, can replace adsorbed HSA molecules according to the Vroman effect [41] observed for the HSA–Fg pair (Fig. 29.10 and Table 29.2). This effect corresponds to competitive adsorption of different proteins with replacement of a smaller protein, which is adsorbed faster, by

a larger one that is adsorbed slower. It is easily seen from comparison of the h values (Table 29.2), estimated relative roughness R_r and changes in $\Delta f(t)$ after injection of Fg as the second protein that the larger the roughness the greater the Vroman effect. This result may be explained by the non-uniformity of distribution of adsorbed HSA at "hilly" surfaces: peaks remain unoccupied and Fg molecules begin the adsorption from interaction with these peaks. Then Fg molecules can displace HSA molecules located in "valleys". However, this effect is absent for Fg–HSA. Notice that the rate of frequency diminution $d(\Delta f)/dt$ is greater on adsorption of Fg after HSA than that in the opposite order of the protein adsorption (Fig. 29.10). This effect is connected with changes in the second right term in Eqs. (29.2) and (29.3). It corresponds to adsorption weakly affected by changes in the characteristics of the liquids (η_l and ρ_l) since $C_{HSA} >> C_{Fg}$ (i.e. changes in the viscosity should give the opposite effect to the observed one). Efficiency of the replacement of HSA by Fg depends on the type of the surface (Table 29.2). For instance, the loading differs significantly on the Au and DLC surfaces. Notice that changes in $\Delta f(t)$ after the adsorption of the second protein are maximal for HSA–Fg/DLC and minimal for Fg–HSA adsorbed on the same surface. Changes in the h value (between 21 and 35 nm) are minimal for DLC among the studied systems (Table 29.2). In the case of Fg–HSA, changes in $\Delta f(t)$ because of the presence of HSA at the Au, Ti and TiN surfaces covered by Fg are close. Relative coverage of the surfaces with pre-adsorbed HSA by Fg (Θ_2 is calculated with respect to monolayer adsorption of individual Fg on the same surface) is maximal for Au or TiN and minimal for Ti/TiO_x (Table 29.2). This result may be of importance for estimation of the haemocompatibility of the TiO_x surfaces. Calculations of the adsorption rate using two methods with Eqs. (29.5), (29.6) and (29.7) give qualitatively closely related results. For instance, $k_{Fg}(t) > k_{HSA}(t)$ with time (Fig. 29.13); however, initially the opposite relationship is observed.

This effect corresponds to the displacement of a peak of the distribution function $\varphi(k)$ for HSA towards larger k values in comparison with that for Fg (Fig. 29.14).

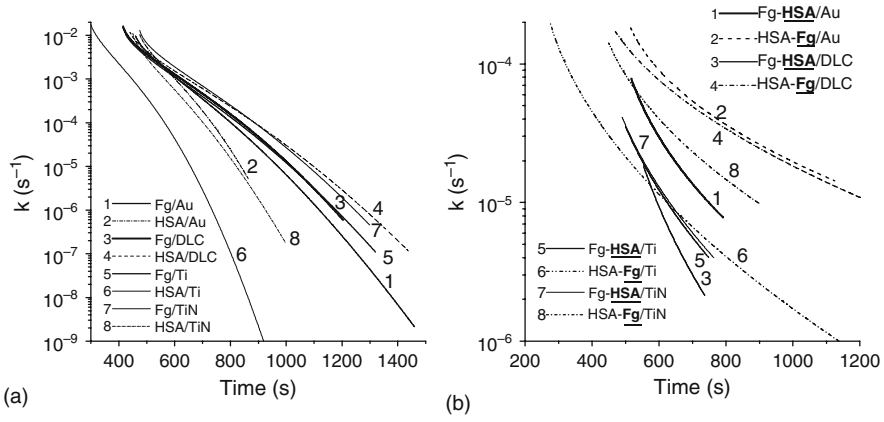

Fig. 29.13 Adsorption rate constants calculated using Eqs. (29.4), (29.5) and (29.6), **a** Fg (curves *1*, *3*, *5*, *7*), HSA (*2*, *4*, *6*, *8*) and **b** HSA after Fg (*1*, *3*, *5*, *7*) and Fg after HSA (*2*, *4*, *6*, *8*) (second shift Δf) on Au (*1*, *2*), DLC (*3*, *4*), Ti (*5*, *6*) and TiN_X (*7*, *8*)

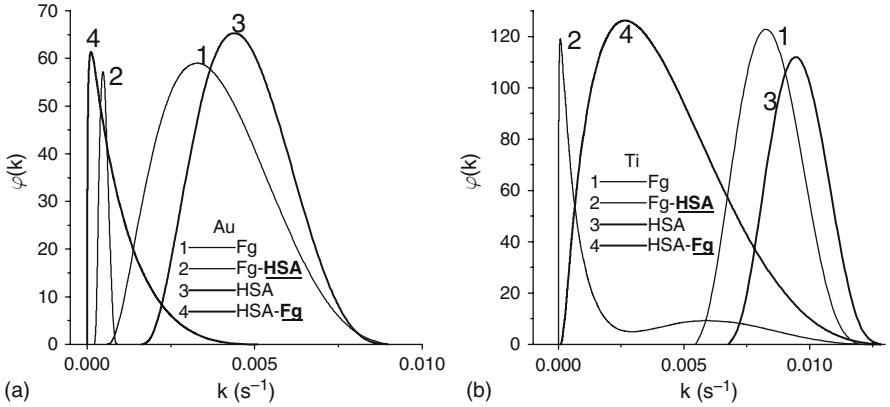

Fig. 29.14 Distribution functions of the adsorption rate constants $\varphi(k)$ of Fg (*1*), HSA after Fg (*2*), HSA (*3*) and Fg after HSA (*4*) on **a** Au and **b** Ti

At the same time for the second protein, $k_{\mathrm{Fg-HSA}} < k_{\mathrm{HSA-Fg}}$ (Fig. 29.13b) and the corresponding $\varphi(k)$ peak for Fg (as the second protein in the HSA–Fg pair) shifts towards greater k values in comparison with that for HSA (as the second protein in Fg–HSA). The $\varphi(k)$ peaks on the Fg and HSA adsorption on Ti/TiO_x shift towards larger k values (Fig. 29.14b) in comparison with those on their adsorption on the Au surfaces (Fig. 29.14a). This result is in agreement with the positions of the corresponding $k(t)$ curves (Fig. 29.13a). The Au surface covered by HSA looks more uniform (smaller its roughness) for adsorbed Fg since the $\varphi(k)$ peak is narrower than that for Ti/TiO_x (Fig. 29.14). A similar effect is also observed for Fg–HSA.

29.4 Highly Disperse and Porous Diamonds

Ultradisperse diamond (UDD) particles (4–6 nm in size estimated from XRD peak broadening) form PDC (~4 μm in size, Fig. 29.15). Primary UDD nanoparticles are sufficiently tightly packed in the compacts, since the pore volume (Table 29.3, V_{p}) is relatively small. Micropores (S_{mic}) mainly contribute to the specific surface area S_{BET} although their volume (V_{mic}) is less than that of mesopores (V_{mes}) but $S_{\mathrm{mes}} < S_{\mathrm{mic}}$. These structural features depend not only on the morphology of UDD particles forming the skeleton of PDC but also on the parameters of graphite and metal phases included in PDC as a result of the synthesis method.

A broad band at 3400 sm^{-1} is observed in the FTIR spectrum of UDD (Fig. 29.16a, curve 1) which corresponds to O−H stretching vibrations of surface OH groups (interacting with water) and adsorbed water. A band at 1640 sm^{-1} corresponds to deformation vibrations of OH groups [42, 43]. Absorption at 1510-1530 sm^{-1} can be assigned to vibrations of NO_2 groups formed on acidic clearing of UDD. A band at 1730 sm^{-1} relates to the C=O stretching vibrations. Bands in the 1070–1140 sm^{-1} range can be caused by admixed nitrogen centres of the type A

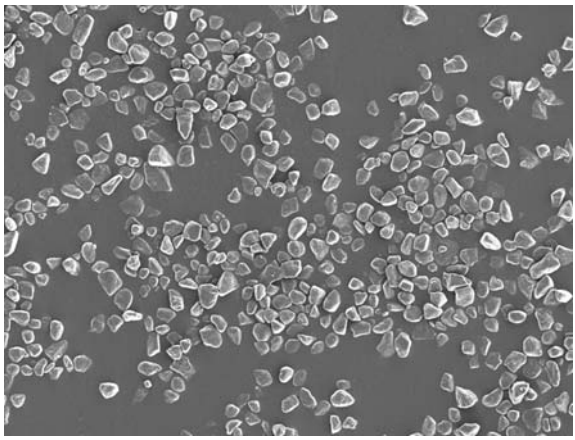

Fig. 29.15 SEM image of PDD compacts (×1000)

Table 29.3 Structural characteristics of PDC, graphitised carbon black Carbopack X, silica gels Si-60 and Davisil 643 unmodified and with ODS groups

Material	S_{BET} (m^2/g)	S_{mic} (m^2/g)	S_{mes} (m^2/g)	V_p (cm^3/g)	V_{mic} (cm^3/g)	V_{mes} (cm^3/g)	V_{mac} (cm^3/g)	Δw	D_{AJ}
PDC	216	124	91	0.18	0.03	0.15	0.01	−0.08[a]	2.637
Carbopack X	223	72	150	0.48	0.04	0.42	0.02	0.32[b]	2.286
Davisil 643	344	124	218	1.14	0.04	1.03	0.07	−0.09[c]	2.220
Davisil 643/ODS	192	7	185	0.65	0.0	0.65	0.0	0.42[c]	< 2
Si-60	369	0	369	0.74	0	0.73	0.01	0.05[c]	2.389

V_{mic}, V_{mes}, V_{mac}, S_{mic}, S_{mes} and S_{mac} are the pore volume and the specific surface area of micro-, meso- and macropores, respectively, calculated on integration of $f_V(R)$ and $f_S(R)$ at the radii (half-width) of pores $R = 0.2-1.0$ nm, 1−25 nm and 25−100 nm, respectively.
Models of pores: [a]voids between spherical particles + cylindrical and slit-shaped pores; [b]slit-shaped pores and [c]cylindrical pores.

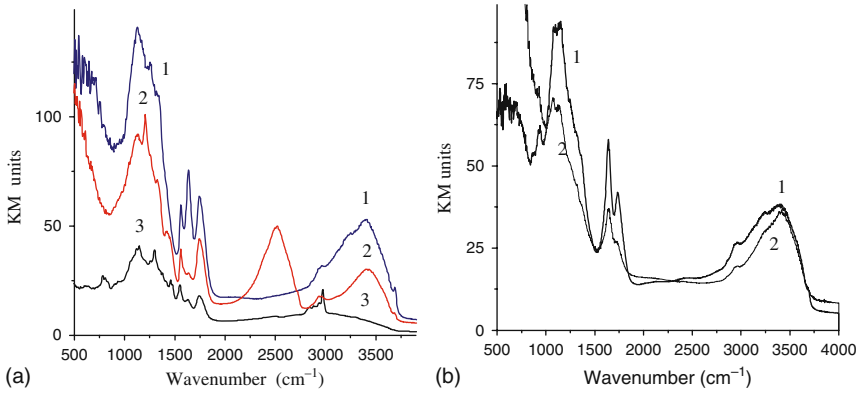

Fig. 29.16 FTIR spectra of **a** UDD initial (curve *1*), after H−D exchange (*2*) and with adsorbed diethylamine (*3*) and **b** PDC fractions with particles of 0.5–1.0 μm in size (curve *1*) and 2–4 μm (*2*)

(two N atoms in adjacent lattice points) [43]. A band at 2800–3000 sm^{-1} corresponds to the C−H stretching vibrations. The presence of O−H and C−H surface groups is confirmed by the FTIR spectra of UDD before and after the adsorption of D_2O (H−D exchange was carried out in saturated D_2O vapour at room temperature for 24 h) and diethylamine which leads to an essential decrease in the intensity of the bands related to O−H vibrations (Fig. 29.16a). Some properties of UDD were described previously [44, 45]. The chemical composition of the PDD compacts is relatively complex as it includes several elements (C, O, P, S, Cl, Pd, Na and Cu); however, the contribution of carbon is substantially prevalent (Fig. 29.17). The carbon phase in PDC consists of both the sp^3-C (diamond) and sp^2-C (graphite) structures. Surface functionalities with carbon and non-carbon atoms provide specific interaction (e.g. hydrogen bonding) of PDD microparticles with their surroundings. Surface groups of C−O−H and C−H (Fig. 29.16b) possessing hydrophilic and hydrophobic properties, respectively, can cause effective attachment of both polar and non-polar adsorbates.

The interfacial interactions depend also on the pore structure of PDC, since the adsorption potential in narrow pores is substantially higher than that of a flat surface of the same chemistry. To understand deeply the relationships of the "structure–properties" type we will compare structural and adsorptive characteristics of PDC with those of well-characterised materials such as (i) Carbopack X (since PDC includes graphite-like fragments); (ii) Hypersil and Davisil 643 with ODS functionalities (a role of C−H in adsorption phenomena); and (iii) unmodified silica gels Davisil 643 and Si-60 (a role of O−H groups in the interaction with polar compounds) [28]. The pore size distribution of PDC is broad and includes narrow pores at the pore half-width $x < 1$ nm, broader pores at $x > 1$–70 nm (Fig. 29.18). However, the main contribution to the specific surface area is linked with narrow pores at $x <$ 8 nm. Carbopack X having a similar S_{BET} value (Table 29.3) has a broader PSD.

The models of pores used give relatively small deviation (Table 29.3, Δw) in the pore shape from model one for PDC (mixture of three types of pores) and unmodified silica gels (cylindrical pores). However, in the case of modified silica gel Davisil 643/ODS [28] (model of cylindrical pores) and Carbopack X (model of

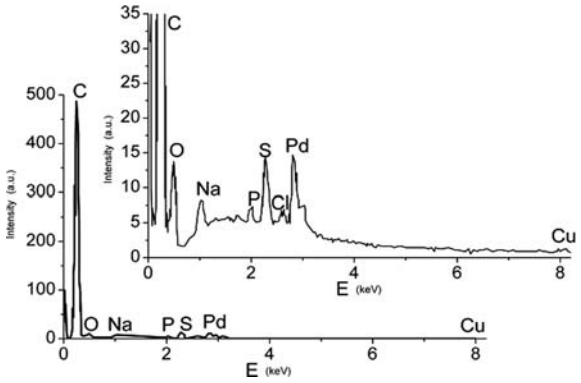

Fig. 29.17 EDX data for PDC

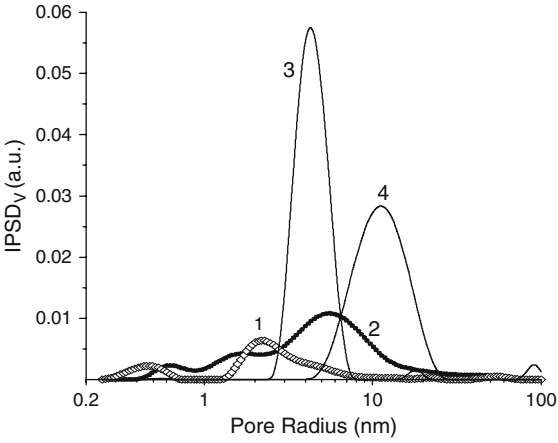

Fig. 29.18 Incremental PSD of PDC (*1*), Carbopack X (*2*), Si-60 (*3*) and Davisil 643/ODS (*4*)

slit-shaped pores), the Δw values show that errors are larger than 30%. This result can be explained by the deviation of the pore shape of broad pores of Carbopack X from the slit-like one (that is typical for non-microporous carbon adsorbents [24]) and the influence of the modification of the silica surface on the pore shape for Davisil 643/ODS. The pore wall surface of this silica with ODS functionalities has larger surface area than that for smooth cylinders. Notice that the fractal dimension D_{AJ} [26] for PDC is relatively high in comparison with that of other adsorbents because of a large contribution of narrow pores in the PSD. Additionally, estimation of the fractal dimension [26] of a surface with a very low adsorption potential A (Fig. 29.19, Davisil 643/ODS) can give an underestimated value (e.g. $D_{AJ} < 2$ for modified silica gel) in comparison with values estimated using other methods. Despite the mentioned structural features, Carbopack X possesses higher adsorption potential and higher energy of the nitrogen adsorption (Fig. 29.19) in comparison

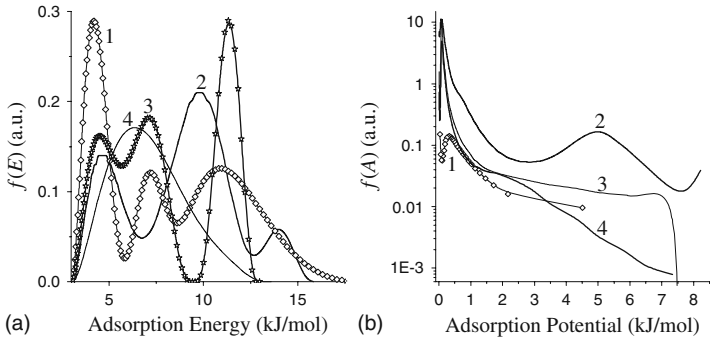

Fig. 29.19 Distribution functions of nitrogen adsorption energy (**a**) and adsorption potential (**b**) for PDD compacts (*1*), Carbopack X (*2*), Davisil 643 (*3*) and Davisil 643/ODS (*4*)

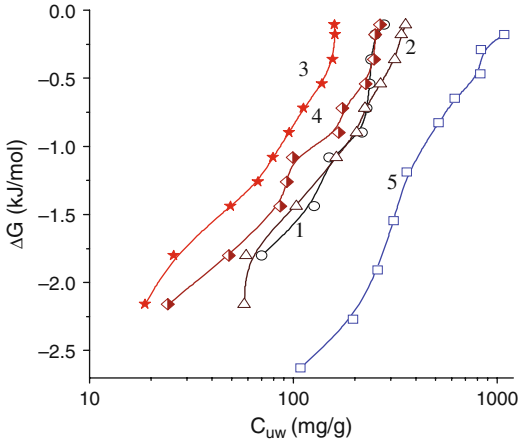

Fig. 29.20 Relationship between concentration of unfrozen water (C_{uw} in mg per gram of dry adsorbent) and changes in the Gibbs free energy of boundary water (ΔG) at different total contents of water: 0.268 (curve *1*), 1.222 (*2*), 3.347 (*3*), 4.882 (*4*) for PDC and 95.0 g/g for Si-60 (*5*)

with PDC because of stronger dispersion interactions of graphite sheets with non-polar molecules. All the $f(A)$ and $f(E)$ peaks of Carbopack X shift towards higher potential or energy values than those of the PDC. The $f(A)$ distribution function demonstrates lower adsorption potential at $A > 3$ kJ/mol corresponding to the nitrogen adsorption in narrow pores of PDC in comparison with both Carbopack X and unmodified silica gel. However, Davisil 643/ODS demonstrates significantly lower adsorption energy (Fig. 29.19b, curve 4 at $E > 10$ kJ/mol) than PDC (curve 1). Additionally, the latter provides higher $f(E)$ than that for unmodified silica gel (curve 3 at $E > 12$ kJ/mol) due to the effect of the sp^2-C fragments of PDC.

The difference in the shape of the high-energy $f(E)$ peak of PDC and Davisil 643 can be caused by a more ordered pore structure and pore walls of the silica gel. This also corresponds to the lower D_{AJ} value and narrow PSD of the silica gel. Therefore, one can assume that PDC will interact more weakly with non-polar compounds than the graphitised carbon Carbopack X or unmodified silica gel but more strongly than silica with non-polar surface functionalities (akin to Hypersil or Davisil 643/ODS). This aspect as well as interaction of the PDC with polar compounds can be investigated using the ^{1}H NMR method with layer-by-layer freezing-out of bulk water (Fig. 29.20) and the HPLC method applied to polar and non-polar analytes using various polar or non-polar eluents (Tables 29.4, 29.5 and 29.6). Comparison of changes in the Gibbs free energy of water disturbed by PDC and silica gel Si-60 surfaces (Fig. 29.20) reveals a weaker effect of the diamond compacts on the interfacial water in comparison with unmodified silica gel, despite narrower pore characteristic for PDC (Fig. 29.18). This effect is caused by a larger content of surface hydroxyls on the Si-60 surface than that on the PDC surface. These hydroxyls are the main effective adsorption sites for such polar adsorbates as water. The volume of unfrozen water in PDC (at $C_{H2O} = 122$ wt%) is twice larger than the V_p value because of the influence of the external surfaces of microparticles on a relatively thick layer of the interfacial water. In the case of unmodified silica gel Si-60 the amount of non-freezable water is also larger than the V_p value but this difference is smaller

Table 29.4 Influence of eluent polarity on retention time of toluene and phenol in HPLC columns with PDC and Hypersil®

	Retention time (min)			
Eluent water/methanol (%/%)	PDC Toluene	Phenol	Hypersil® Toluene	Phenol
100/0[a]	2.06	5.52	–	–
90/10	1.86	4.58	–	–
80/20	1.83	4.27	–	–
50/50	1.40	2.77	–	–
25/75	1.49	2.19	1.69	7.25
20/80	–	–	1.32	2.23
10/90	–	–	1.37	1.60
0/100	1.15	1.96	1.51	1.77

[a]0.05 ml of toluene was dissolved in 10 ml of a mixture of methanol and deionised water, then 10-fold dilution by water was carried out; phenol (20 mg) was dissolved in 10 ml of deionised water.

Table 29.5 Influence of polarity (dielectric constant) of analyte on retention time (min)

Analyte	ε	PDC[a]	Hypersil[b]
Benzene	2.28	1.99	5.54
Methyl benzoate	6.59	3.10	5.18
Aniline	6.89	3.27	2.95
Phenol	9.78	5.90	2.07

Eluent [a]100% deionised water and [b]water:methanol = 1:1.

Table 29.6 Parameters of separation of ortho- and para-isomers of xylol

	PDC		Spherisorb	
Parameter	Ortho	Para	Ortho	Para
Retention time t_r (min)	2.63	2.29	1.75	1.79
Resolution R_s	0.895	0.895	–	–

than that for PDC. A contribution to this effect is connected with an enlargement of pores on water freezing there because of a larger volume of ice (V_{ice}) than that of liquid water (V_{lw}). Sometimes this effect is greater than the ratio V_{ice}/V_{lw} for the same water weights [28, 34]. Nitrogen can adsorb on the external surface of the PDC compacts only weakly and it cannot entirely fill pores at $x > 50$ nm (but water can fill them more effectively) which gives a small contribution to the V_p value.

The HPLC results showing the effect of increasing solvent polarity on the retention time of toluene and phenol are given in Table 29.4. As a whole the retention time for the PDC columns increases for polar analytes and eluents (Tables 29.4, 29.5 and 29.6). The PDC column resolved better in highly polar eluents and the best eluent for PDC is pure water (Table 29.4). The free energy of solvation calculated using the IEFPCM/B3LYP/6-31G(d,p)//6-31G(d,p) method [28] for phenol

and toluene is −24 and −2 kJ/mol in water and −31 and −12 kJ/mol in methanol, respectively. These values and Tables 29.4, 29.5 and 29.6 reveal that an increase in the polarity of an analyte leads to an increase in the retention time for the PDC column sometimes in contrast to that for the Hypersil and Spherisorb columns. This difference in the effects of the polarity of the analytes and the eluents for the HPLC results with the PDC and other columns is linked to the nature of the surfaces of the materials used as a stationary phase. Comparison of the $f(E)$ distribution functions for Davisil 643/ODS and PDC (Fig. 29.19) shows that the hydrophobic coverage of the silica surface leads to disappearance of the high-energy peak. This fact corresponds to a decrease in the adsorption potential of Hypersil (with similar ODS groups) for both polar and non-polar analytes, which leads to a decrease in the retention time in comparison with that for the PDC column. However, the effect of the polarity of analytes with the PDC columns depends also on the polarity of eluents. Table 29.6 shows that the PDC column can separate the two positional isomers of xylene, whereas the Spherisorb® column produces worse result. These preliminary results suggest that porous diamond is an interesting material for HPLC separations and has a potential due to its combination of unconventional surface properties.

29.5 Conclusion

Comparative investigations of physicochemical properties of biomaterials such as DLC and GLC films, ZrN_x, TiN_x, ZrC, TiC, ZrO_x, TiO_x, metals (Ti, Zr, Au, stainless steel) on Au or steel substrates showed high strength and anticorrosive properties of the materials; and many of these properties are the best for DLC. ZrO_x coatings have a microcrystalline structure. TiO_x films are least uniform and include anatase, rutile, amorphous and non-stoichiometric phases.

The Vroman effect is observed for proteins HSA and Fg subsequently adsorbed on Au, Ti/TiO_x, DLC and TiN_x surfaces. On the adsorption of Fg followed by HSA this effect is absent because HSA is significantly smaller than Fg and its ability in replacing adsorbed Fg molecules is negligibly low. A minimal adsorption of individual proteins is observed for HSA on Au (Au < Ti < DLC < TiN) and a maximal one is for Fg on Ti/TiO_x (Au < TiN < DLC < Ti). The effective thickness of the adsorbed protein layers is larger than the minimal size of the protein molecules but smaller than the maximal one. Changes in this value can be explained by changes in the surface roughness and hydrophobicity.

PDCs are characterised by relatively low adsorption potential for non-polar (in comparison with activated carbons) and polar (in comparison with silica gel) compounds. However, PDC interacts with polar compounds more strongly than modified silica gels. Therefore PDC may be considered as a more biocompatible adsorbent than activated carbons and similar to materials with aliphatic surface functionalities. PDC can be a more effective adsorbent than silica covered by hydrophobic functionalities because of certain amount of hydroxyls present on the PDC surface.

References

1. Cui FZ, Li DJ (2000) A review of investigations on biocompatibility of diamond-like carbon and carbon nitride films. Surf Coat Technol 131:481–487.
2. Tiainen V-M (2001) Amorphous carbon as a bio-mechanical coating – mechanical properties and biological applications. Diamond Rel Mater 10:153–160.
3. Semikina TV (2006) Application of diamond-like films in electronics. Electron Commun 2:9–16.
4. Hauert R (2003) A review of modified DLC coatings for biological applications. Diamond Rel Mater 12:583–589.
5. Donnet Ch, Erdemir A (eds) (2007) Tribology of diamond-like carbon films: Fundamentals and applications. Springer, Dordrecht.
6. De Scheerder I, Szilard M, Yanming H et al (2000) Evaluation of the biocompatibility of two new diamond-like stent coatings (Dylyn) in a porcine coronary stent model. J Invasive Cardiol 12:389–394.
7. Dorner-Reisel A, Schürer C, Irmer G et al (2002) Diamond-like carbon coatings with Ca-O-incorporation for improved biological acceptance. Anal Bioanal Chem 374:753–755.
8. Schroeder A, Francz G, Bruinink A et al (2000) Bone marrow cell responses to titanium containing amorphous hydrogenated carbon films: a contribution to surface biocompatibility. Biomaterials 21:449–456.
9. Salahas A, Vrahatis A, Karabinos I et al (2007) Success, safety, and efficacy of implantation of diamond-like carbon-coated stents. Angiology 58:203–210.
10. Laube N, Kleinen L, Bradenahl J, Meissner A (2007) Diamond-like carbon coatings on ureteral stents – a new strategy for decreasing the formation of crystalline bacterial biofilms? J Urol 177:1923–1927.
11. Saldamli B, Thorwarth G, Jürgens P (2007) Morphology of osteoblasts grown on doped diamond-like carbon coatings – an electron microscopy study. Eur Cells Mater 13(3):39.
12. Tran HS, Puc MM, Hewitt CW et al (1999) Diamond-like carbon coating and plasma or glow discharge treatment of mechanical heart valves. J Invest Surg 12:133–140.
13. Krishnan LK, Varghese N, Muraleedharan CV et al (2002) Quantitation of platelet adhesion to Ti and DLC-coated Ti *in vitro* using ^{125}I-labeled platelets. Biomol Eng 19: 251–253.
14. Jones MI, McColl IR, Grant DM et al (2000) Protein adsorption and platelet attachment and activation, on TiN, TiC, and DLC coatings on titanium for cardiovascular applications. J Biomed Mater Res 52:413–421.
15. Jones MI, McColl IR, Grant DM et al (1999) Haemocompatibility of DLC and TiC–TiN interlayers on titanium. Diamond Rel Mater 8:457–462.
16. Gutensohn K, Beythien C, Bau J et al (2000) *In vitro* analyses of diamond-like carbon coated stents. Reduction of metal ion release, platelet activation, and thrombogenicity. Thrombosis Res 99:577–585.
17. Alanazi A, Nojiri C, Noguchi T et al (2000) Improved blood compatibility of DLC coated polymeric material. ASAIO J 46:440–443.
18. Yu LJ, Wang X, Wang XH (2000) Haemocompatibility of tetrahedral amorphous carbon films. Surf Coating Technol 128–129:484–488.
19. Yamazaki K, Litwak P, Tagusari O et al (1998) An implantable centrifugal blood pump with a recirculating purge system (cool-seal system). Artif Organs 22:466–474.
20. Lux B, Haubner R, Holzer H, De Vries RC (1997) Natural and synthetic polycrystalline diamond, with emphasis on ballas. 'Ballas' – radially grown, polycrystalline diamonds? Int J Refractory Metal Hard Mater 15:263–288.
21. Larson P, Axén N, Eksrtöm T et al (1999) Wear of a new type of diamond composite. Int J Refractory Metals Hard Mater 17:453–460.
22. Vlasov A, Ralchenko V, Gordeev S et al (2000) Thermal properties of diamond/carbon composites. Diamond Rel Mater 9:1104–1109.

23. Lee J, Novikov N (eds) (2005) Innovative superhard materials and sustainable coatings for advanced manufacturing. NATO science series II: mathematics, physics and chemistry, vol 200. Springer, Dordrecht.
24. Vadgama P (ed) (2005) Surfaces and interfaces for biomaterials. CRC Press and Woodhead Publishing Ltd, Cambridge.
25. Mikhalovsky SV, Patel BA, Rutt KJ et al (2005) Structural and adsorption characteristics of porous industrial diamond. In: Lee J, Novikov N (eds) Innovative superhard materials and sustainable coatings for advanced manufacturing. NATO science series II: mathematics, physics and chemistry, vol 200. Springer, Dordrecht, pp 169–182.
26. Mikhalovsky SV, Mikhalovska LI, James SL et al (2006) Characterization of hard and soft porous materials and tissue scaffolds. In: Loureiro JM, Kartel MT (eds) Combined and hybrid adsorbents, fundamentals and applications. NATO security through science series C: environmental security. Springer, Dordrecht, pp 309–320.
27. Mikhalovsky SV, Gun'ko VM, Turov VV et al (2005) Investigation of structural and adsorptive characteristics of various carbons. Adsorption 11:657–662.
28. Blitz JP, Gun'ko VM (eds) (2006) Surface chemistry in biomedical and environmental science. NATO science series II: mathematics, physics and chemistry, vol 228. Springer, Dordrecht.
29. Borysenko MV, Gun'ko VM, Dyachenko AG et al (2005) CVD-zirconia on fumed silica and silica gel. Appl Surf Sci 242:1–12.
30. Gun'ko VM, Turov VV, Skubiszewska-Ziba J et al (2004) Structural and adsorptive characteristics of pyrocabon/silica gel Si-60. Adsorption 10:5–18.
31. Gregg SJ, Sing KSW (1982) Adsorption, surface area and porosity, 2nd edn. Academic Press, London.
32. Gun'ko VM, Mikhalovsky SV (2004) Evaluation of slitlike porosity of carbon adsorbents. Carbon 42:843–849.
33. Gun'ko VM (2000) Consideration of the multicomponent nature of adsorbents during analysis of their structural and energy parameters. Theor Exp Chem 36:319–324.
34. Gun'ko VM, Turov VV, Leboda R (2002) Structure–adsorption characteristics of carbon-oxide materials. Theor Exp Chem 38:199–228.
35. Gun'ko VM, Turov VV, Bogatyrev VM et al (2005) Unusual properties of water at hydrophilic/hydrophobic interfaces. Adv Colloid Interface Sci 118:125–172.
36. Scheller FW, Schubert F, Fedrovitz J (eds) (1997) Frontiers in biosensorics. Birkhauser Verlag, Basel.
37. Fendler JH (ed) (1998) Nanoparticles and nanostructured films. Wiley-VCH, Weinheim.
38. Morrison SR (1977) The chemical physics of surfaces. Plenum Press, New York.
39. Buijnsters JG, Shankar P, Fleischer W et al (2002) CVD diamond deposition on steel using arc-plated chromium nitride interlayers. Diamond Rel Mater 11:536–544.
40. Gun'ko VM, Klyueva AV, Levchuk YN, Leboda R (2003) Photon correlation spectroscopy investigations of proteins. Adv Colloid Interface Sci 105:201–328.
41. Horbett TA, Brash JL (eds) (1995) Proteins at interfaces II: fundamentals and applications. ACS Symposium Series 602. American Chemical Society, Washington, DC.
42. Mironov E, Koretz A, Petrov E (2002) Detonation synthesis ultradipersed diamond structural properties investigation by infrared absorption. Diamond Rel Mater 11:872–876.
43. Dolmatov VY (2003) Ultradisperse diamonds of denotation synthesis. Preparation, properties, application. SPBSPU, St. Petersburg.
44. Gubarevich TM, Chernukho LE, Akhremkova GS, Lapina VA (2004) Properties of surface of modified nanodiamonds. Proceedings of III International Seminar "Nanostructural Materials – 2004: Belarus-Russia", Minsk, Belarus, 12–15 October 2004, pp 44–45.
45. Gubarevich TM (2004) Technical control of quality of ultradisperse diamonds. Proceedings of III International Seminar "Nanostructural Materials – 2004: Belarus-Russia", Minsk, Belarus, 12–15 October 2004, pp 50–51.

Index

A.P. Shpak, P.P. Gorbyk (eds.), *Nanomaterials and Supramolecular Structures*,
DOI 10.1007/978-90-481-2309-4_BM2, © Springer Science+Business Media B.V. 2009